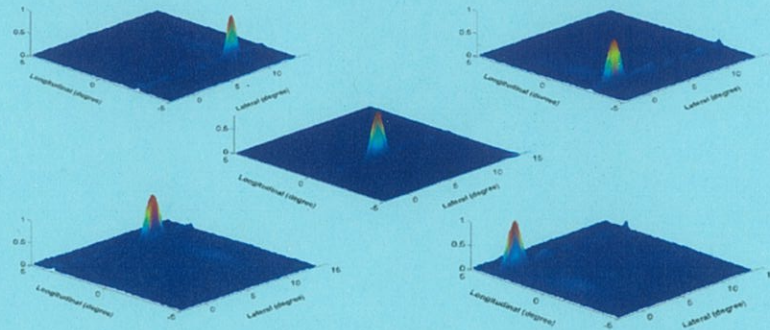
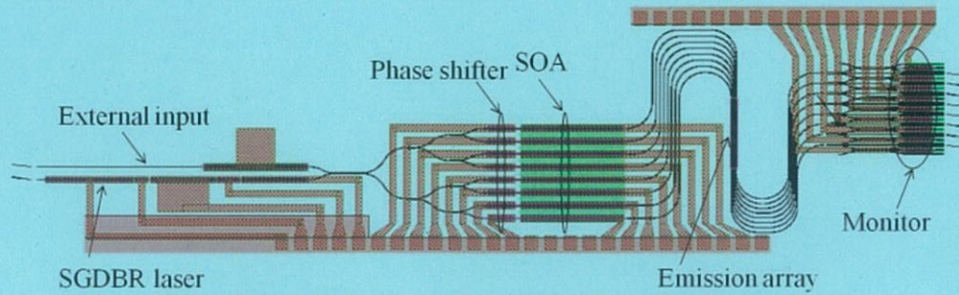


Research in Optoelectronics (A)



2012 Reprints of
Professor Larry A. Coldren
and Collaborators

ECE Technical Report 13-01
Department of Electrical & Computer Engineering
University of California, Santa Barbara

Introduction:

In 2012 some 36 papers were published in journals and conference proceedings that resulted within, and from collaborations with, Professor Coldren's research group. Copies are reprinted in this volume. The majority of these works also have originated from proposals generated within Coldren's group, but a few are due to efforts that originated elsewhere and were supported by Coldren and his group members. As in recent years, the work has a focus on III-V compound semiconductor materials as well as the design and creation of photonic devices using these materials—mostly diode lasers and photonic integrated circuits (PICs). The work spans efforts from basic materials and processing technology, through device physics, design and formation, to their characterization within systems environments.

The reprints have been grouped into three areas: **I. Photonic Integrated Circuits; II. Vertical-Cavity Surface-Emitting Lasers (VCSELs); and III. Materials and Device Technology.** Most of the work is in the first area, which has been further subdivided into *A. Tutorials, Reviews, and Books; B. Integrated Mode-Locked Lasers; C. Integrated Optical Phase-Locked Loops; and D. Coherent Beam Steering PICs.* Integrated coherent transmitters and receivers continues to be the leading theme. MOCVD growth remains a support effort for this work. Our MBE growth effort is key to the second major activity on VCSELs (II). In this section are six papers describing efforts on high-speed and polarization modulation of VCSELs using new and novel approaches. The third section on materials and device technology (III) summarize some MOCVD lateral overgrowth efforts with Prof. Bowers' as well as a new, simplified quantum-well intermixing approach. In nearly every project the work requires efforts in materials research, device physics, device design, process development, device fabrication, and device characterization. Most students are deeply involved in several, if not all, of these efforts, so our graduates tend to be known for their "bandwidth."

The work was performed with funding from several grants from industry and government, some gift funds from industry, and support from the Kavli Endowed Chair in Optoelectronics and Sensors. Several projects were funded by the MTO Office of DARPA, most notably under the CIPHER and SWEEPER projects. One was supported by the UC-Discovery program in collaboration with Rockwell-Collins, and industry support included work with Ziva, JDS-Uniphase, Telcordia, Corning, and Rockwell-Collins.

The first group of reprints (*IA.*) gives overviews of our work over the past couple of years. The first item gives the Table of Contents and Preface of the second edition of our textbook which now includes quite a bit of updated information as well as many worked examples to make the material more easy to comprehend. Nearly all of the papers are INVITED, either directly by the journal or as invited conference talks in major international venues. All papers also center about the photonic integration technology we have originated, which incorporates our widely-tunable Sampled-Grating Distributed-Bragg-Reflector (SGDBR) Laser. A new emphasis on single-chip integrated coherent transmitters and receivers, especially those incorporating our efforts on miniature optical phase-locked loops (OPLLs) are highlighted.

The second group of five papers (1B) reports work on single-chip mode-locked lasers (MLLs) for comb generation and other applications. One concept is to use OPLLs with rf off-set locking to tune an SGDBR from one line to the next of a frequency-stabilized MLL so that optical frequencies can be synthesized across the entire ~ 5 THz tuning range of the SGDBR. Figure 1 illustrates one of the MLLs studied together with its rf spectrum, which shows a mode spacing of about 18.2 GHz.

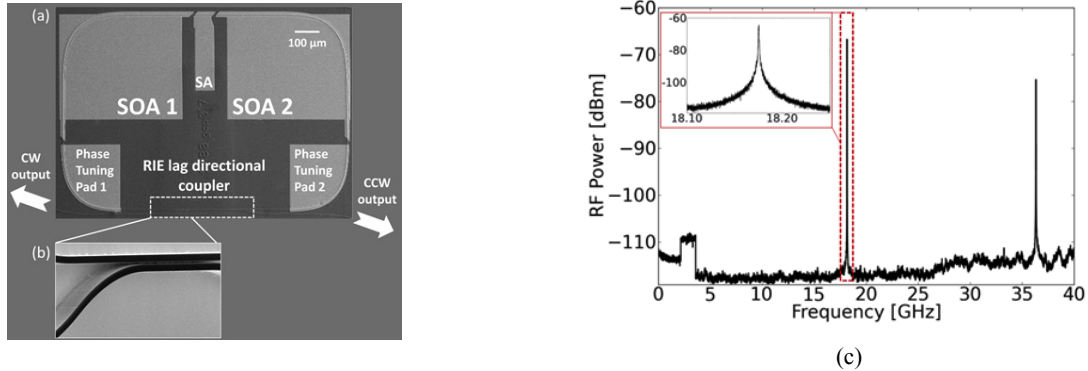


Fig. 1. (a) Scanning electron microscope (SEM) image of fabricated ring mode-locked laser with semiconductor optical amplifiers (SOAs), saturable absorber (SA), phase tuning pads, and directional coupler. (b) SEM side-view of two waveguides coming together to form the directional coupler. (c) Measured RF-spectrum $I_{SOA} = 210$ mA, $V_{SA} = -4.5$ V. Step discontinuity at 3 GHz is due to electronic amplifier. The locked mode comb had a 5.3 nm FWHM, and a 10dB width of about 10 nm or 1.25 THz.

The third group of papers (1C) includes seven papers that describe work on integrated OPLLs—a collaboration with Prof. Rodwell. As indicated by the schematic and photo in Figs 2 and 3, respectively, the OPLL consists of a photonic IC (PIC) and electronic IC (EIC) together with a discrete loop filter on a single ceramic carrier which measures about a square centimeter in size.

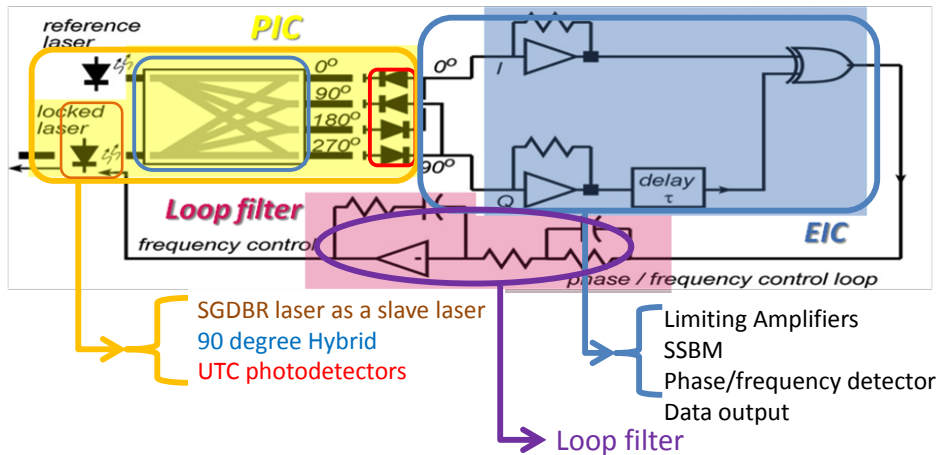


Fig. 2. Schematic of optical phase-locked loop, indicating various elements.

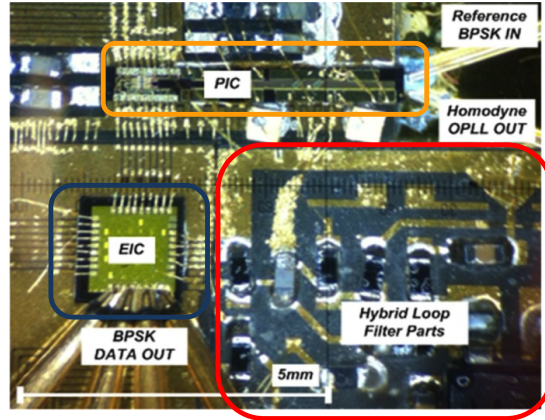


Fig. 3. Photo of OPLL on common carrier (rearranged from Fig. 2). Net loop delay = 120 ps: PIC—40 ps, EIC—50 ps, LF and lines—30 ps

Part (1D) in the PIC section gives papers describing a collaborative effort with Prof. Bowers' group and Rockwell-Collins on coherent 2-D beam sweeping. Figure 4 summarizes some results from the Coldren group.

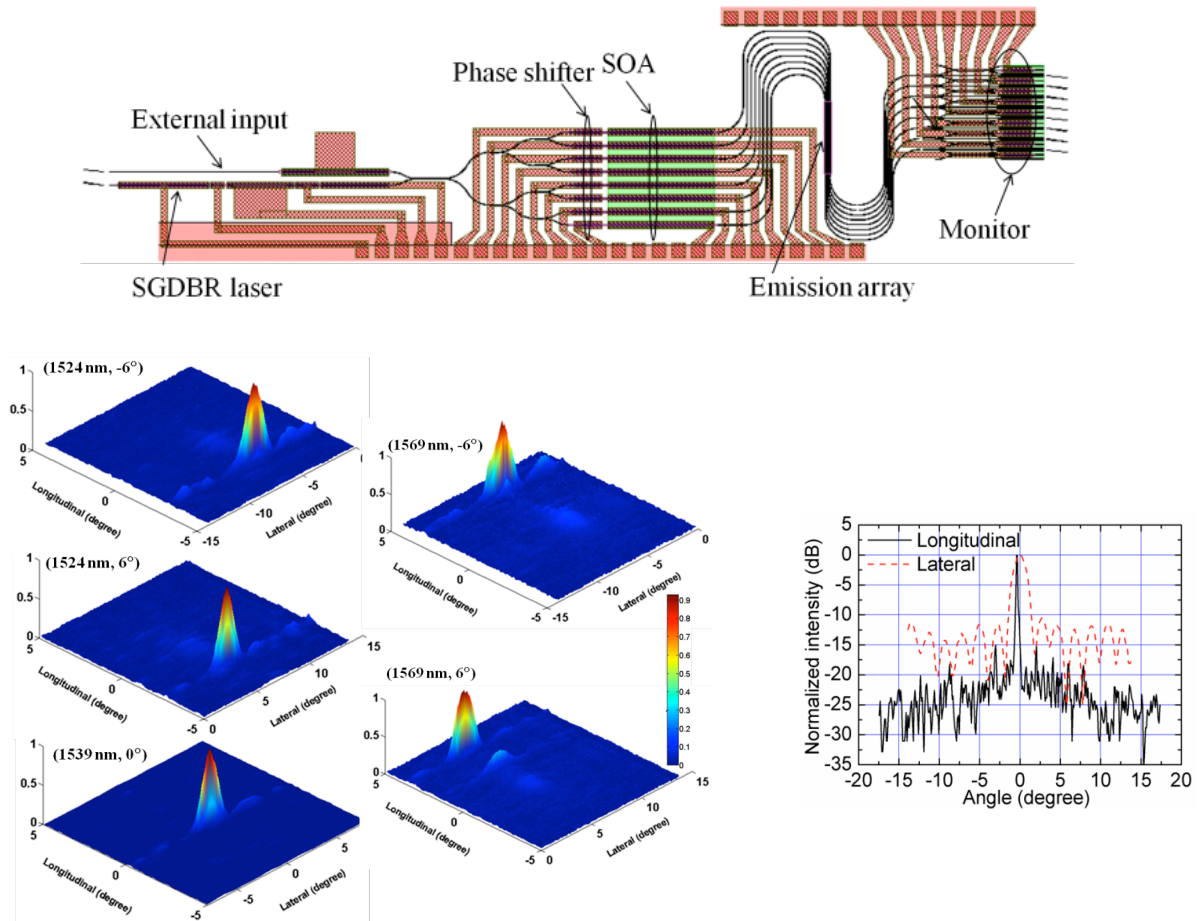


Fig. 4. (top) Mask-layout of 8-channel beam sweeper with integrated SGDBR tunable laser; (left) representative far-field images; (right) detailed beam shape in central location.

The second major element of work in Prof. Coldren's group is on high-speed and polarization modulated VCSELs, Section II. The high-speed work involves both investigating more highly strained materials reaching into the 1060 nm wavelength range on GaAs as well as novel three-terminal structures. In the past year these 3-terminal field-induced carrier-separation lasers (FICSLs) have been successfully fabricated and characterized as depicted in Fig. 5.

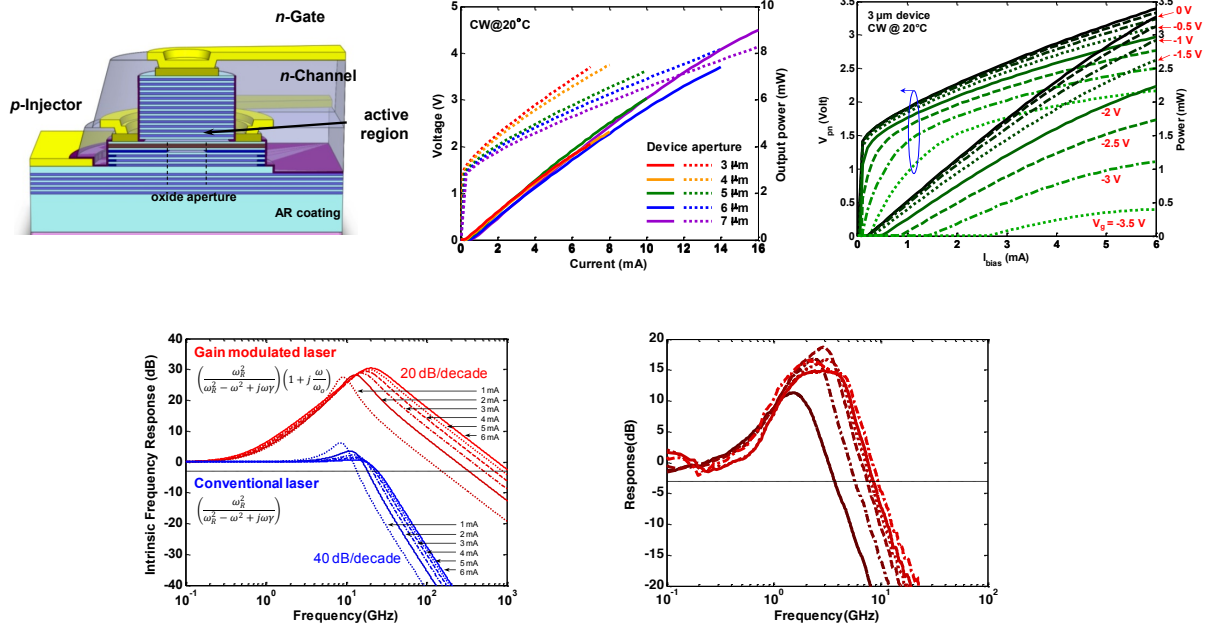
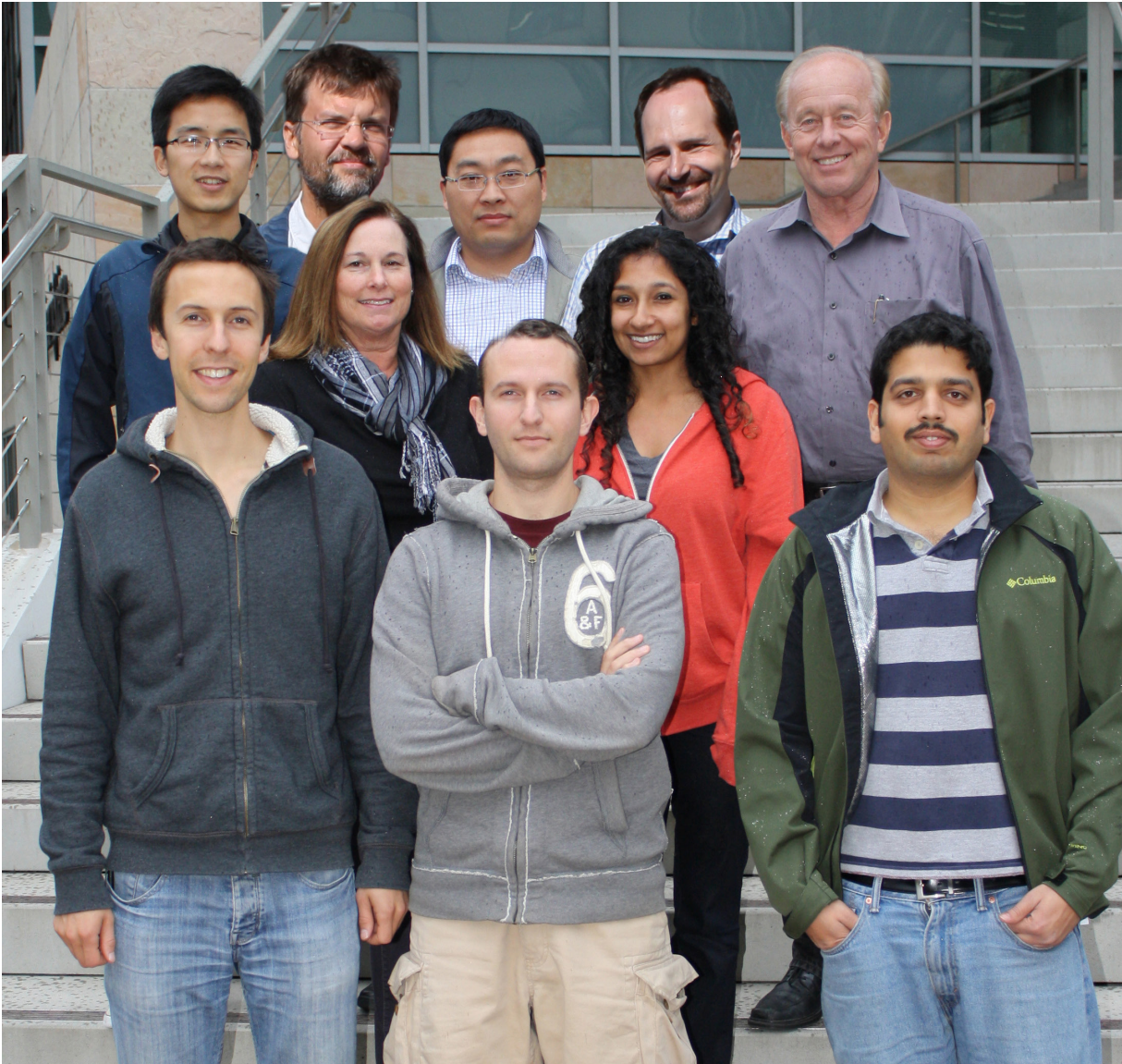


Fig. 5. (top) Schematic; DC PIV; and PIV vs gate bias for FICSL-VCSEL. (bottom) Theoretical and measured small-signal modulation for various dc biases.

Not shown are new results for fast polarization modulation of diode VCSELs, which are presented in the last two papers in this section. This breakthrough uses a switching of an rf-modulation frequency to stimulate the polarization switching. It has been shown that this is not a thermal effect, and the speed of switching is in the gigahertz range.

The first two publications in Section III, **Materials and Device Technology**, describe two different technological advances. The first, in collaboration with Prof. Bowers, describes work on MOCVD overgrowth of InP through dielectric masks, and the second demonstrates that viable active-passive PICs can be fabricated following all epitaxial growths (no regrowths) using impurity-free quantum-well intermixing (QWI). The third paper gives design details for injection-locked lasers.

Professor Coldren's Group



Back Row: Mingzhi Lu, Leif Johansson, Weihua Guo, Milan Mashanovitch, Professor Larry Coldren
Middle Row: Libby McCollum, Abi Sivananthan **Front Row: John Parker, Pietro Binetti, Ajit Barve**

Professor Coldren's Group

I. Researchers

A. Barve	Postdoctoral Scholar, UCSB
A. Bhardwaj	Visiting Scientist, UCSB, now at JDSU
P. Binetti	Postdoctoral Scholar, UCSB
W. Guo	Project Scientist, UCSB
L. Johansson	Associate Research Engineer, UCSB
M. Masanovic	Project Scientist, UCSB

II. Students

C. Althouse	Master's Program
R. Guzzon	Ph.D. Program, now at Aurrion
C. Lin	Ph.D. Program, now at JDSU
M. Lu	Ph.D. Program
E. Norberg	Ph.D. Program, now at Aurrion
J. Parker	Ph.D. Program
A. Sivananthan	Ph.D. Program
Y. Zheng	Ph.D. Program, now at Booz Allen Hamilton

III. Staff

D. Cohen	Principal Development Engineer, reports to Prof Nakamura
L. McCollum	Center Assistant, OTC

Collaborators

I. Faculty

J. Bowers	UCSB
S. DenBaars	UCSB
P. Petroff	UCSB
D. M. Gvozdic	University of Belgrade
D. Ritter	Technion Israel - ITT
M. Rodwell	UCSB
S. Stemmer	UCSB

II. Researchers

H. Ambrosius	Director of Clean Room, Optoelectronics Devices Group, Eindhoven University of Technology
E. Bloch	Research Scientist, Technion Israel University of Technology and UCSB (Rodwell)
S.W. Corzine	Design Engineer, Infinera
J. V. Crnjanski	Teaching and Research Assistant, University of Belgrade
J. Doylend	Postdoctoral Scholar, UCSB (Bowers)
Z. Griffith	RF Design Engineer, Teledyne Scientific & Imaging
M. Heck	Postdoctoral Scholar, UCSB (Bowers)
Y-Jr. Hung	Postdoctoral Scholar, National Tawiwian University of Science and Technology
A. Husain	CEO, ZIVA Corporation
S. Kraemer	Senior Development Engineer, Materials Dept., UCSB
M.M. Krstic	Teaching and Research Assistant, University of Belgrade
P. Mages	Project Scientist, UCSB (Bowers)
A. Mehta	Ziva Corporation
J. Peters	Senior Development Engineer, UCSB (Bowers)
B. Thibeault	Project Scientist, UCSB (Rodwell)

III. Collaborating Students

J. Bovington	UCSB, Bowers
M. Davenport	UCSB, Bowers
N. Julian	UCSB, Bowers
H. Park	UCSB, Rodwell
T. Reed	UCSB, Rodwell
C. Zhang	UCSB, Bowers
J. Zhang	UCSB, Materials

Table of Contents:

<u>I. Photonic Integrated Circuits</u>	Page
<i>IA. Tutorials, Reviews, and Books</i>	
L.A. Coldren , S.W. Corzine, and M. Mašanović, “ <i>Diode Lasers and Photonic Integrated Circuits</i> ,” Second Edition, John Wiley & Sons, Inc, New York, January 2012	1
R.S. Guzzon , E.J. Norberg, and L.A. Coldren, “Spurious-Free Dynamic Range in Photonic Integrated Circuit Filters with Semiconductor Optical Amplifiers,” <i>IEEE Journal of Quantum Electronics</i> , 48 , (2), pp.269-278, February 2012 INVITED PAPER	17
P.R.A. Binetti , M. Lu, E.J. Norberg, R.S. Guzzon, J.S. Parker, A. Sivananthan, A. Bhardwaj, L.A. Johansson, M.J. Rodwell, and L.A. Coldren, “Indium Phosphide Photonic Integrated Circuits for Coherent Optical Links,” <i>IEEE Journal of Quantum Electronics</i> , 48 , (2), pp. 279-291, February 2012 INVITED PAPER	27
L.A. Coldren , L.A. Johansson, M.J. Rodwell, M. Lu, A. Sivananthan, and J.S. Parker, “Photonic Integrated Circuits as Key Enablers for Coherent Sensor and Communications Systems,” <i>Proc. GOMAC 2012</i> , paper no. 2.4, Las Vegas, NV (March 19-22, 2012)	40
L.A. Coldren , L.A. Johansson, M. Lu, A. Sivananthan, and M.J. Rodwell, “Single-Chip Integrated Transmitters and Receivers,” <i>Proc. CLEO 2012</i> , paper no. CW1K.1, San Jose, CA (May 6-11, 2012) INVITED TUTORIAL	42
L.A. Coldren , L.A. Johansson, M. Lu, A. Sivananthan, and M.J. Rodwell, “Single-Chip Integrated Transmitters and Receivers,” <i>Proc. ECOC 2012</i> , paper no. Tu.1.G.1, Amsterdam, Netherlands (September 15-21, 2012) INVITED TUTORIAL	44
L.A. Coldren , “From Tunable Lasers to Photonic Integration,” <i>40th Anniversary of Dynamic Single-mode Semiconductor Lasers: From Invention Toward New Era</i> ,” paper no. C-2, Tokyo Institute of Technology, Tokyo (November 2012) INVITED TALK	79
L.A. Coldren , L.A. Johansson, M. Lu, A. Sivananthan, and M.J. Rodwell, “Single-Chip Integrated Transmitters and Receivers,” <i>Optics Express</i> , 20 , (26), pp. B377–B385 (December 10, 2012)	81
<i>IB. Integrated Mode-Locked Lasers</i>	
J.S. Parker , A. Bhardwaj, P.R.A Binetti, Yung-Jr. Hung, and L.A. Coldren, "Monolithically Integrated Gain-Flattened Ring Mode-Locked Laser for Comb-Line Generation," <i>Photonics Technology Letters, IEEE</i> , 24 , (2), pp.131-133, January 15, 2012	93
J.S. Parker , R.S. Guzzon, E.J. Norberg, A.Bhardwaj, P.R.A. Binetti, and L.A. Coldren, "Theory and Design of THz Intracavity Gain-Flattened Filters for Monolithically Integrated Mode-Locked Lasers," <i>IEEE Journal of Quantum Electronics</i> , 48 , (2), pp.114-122, February 2012	96
J.S. Parker , A. Sivananthan, M. Lu, L. Johansson, and L.A. Coldren, “Integrated Phase-locked Multi-THz Comb for Broadband Offset Locking,” <i>Proc. OFC/NFOEC 2012</i> , paper no. OM3E.5, Los Angeles, CA (March 4-8, 2012)	105

J.S. Parker, P.R.A. Binetti, Y-Jr Hung, and L.A. Coldren, "Frequency Tuning in Integrated InGaAsP/InP Ring-Mode-locked Lasers," *Journal of Lightwave Technology*, **30**, (9), pp. 1278-1283, May 2012 108

J.S. Parker, M. Lu, H. Park, E. Bloch, A. Sivananthan, Z. Griffith, L.A. Johansson, M.J. Rodwell, and L.A. Coldren, "Offset Locking of an SG-DBR to an InGaAsP/InP Mode-locked Laser," *Proc. IEEE Photonics Conference*, paper no. ThR3, Burlingame, CA (September 23-27, 2012) 114

IC. Integrated Optical Phase-Locked Loops

M. Lu, H. Park, E. Bloch, A. Sivananthan, A. Bhardwaj, L.A. Johansson, M.J. Rodwell, and L.A. Coldren, "Highly Integrated Optical Heterodyne Phase-locked Loop with Phase/frequency Detection," *Optics Express*, **20**, (9), pp. 9736-9741 (April 2012) 119

M.Lu, H. Park, E. Bloch, A. Sivananthan, Z. Griffith, A. Bhardwaj, L.A. Johansson, M.J. Rodwell, and L.A. Coldren, "A Highly Integrated Optical Phase-locked Loop with Single-sideband Frequency Sweeping," *Proc. CLEO 2012*, paper no. CW1K, San Jose, CA (May 6-11, 2012) 125

E. Bloch, H. Park, M Lu, T.Reed, Z. Griffith, L.A. Johansson, L.A. Coldren, D.Ritter, and M.J. Rodwell, "A 1–20 GHz InP HBT Phase-lock-loop IC for Optical Wavelength Synthesis," *Microwave Symposium Digest (MTT), 2012 IEEE MTT-S International*, paper no. WEPN-4, pp. 1-3, Montreal, Canada (June 17-22, 2012) 127

H. Park, M. Lu, E. Bloch, T. Reed, Z. Griffith, L.A. Johansson, L.A. Coldren, and M.J. Rodwell, "40Gbit/s Coherent Optical Receiver Using a Costas Loop," *Proc. ECOC 2012*, paper no. Th.3.A.2, Amsterdam, Netherlands (September 15-21, 2012) POST DEADLINE 130

M.Lu, H. Park, E. Bloch, A. Sivananthan, Z. Griffith, L.A. Johansson, M.J. Rodwell, and L.A. Coldren, "A Highly Integrated Optical Phase-locked Loop for Laser Wavelength Stabilization," *Proc. IEEE Photonics Conference*, paper no. ThR2, Burlingame, CA (September 23-27, 2012) 133

M.Lu, H. Park, E. Bloch, A. Sivananthan, J.S.Parker, Z. Griffith, L.A. Johansson, M.J. Rodwell, and L.A. Coldren, "A Photonic Integrated Circuit for a 40Gbaud/s Homodyne Receiver using an Optical Costas Loop," *Proc. IEEE Photonics Conference*, paper no. PD1.4, Burlingame, CA (September 23-27, 2012) POST DEADLINE 135

H. Park, M. Lu, E. Bloch, T. Reed, Z. Griffith, L.A. Johansson, L.A. Coldren, and M.J. Rodwell, "40Gbit/s Coherent Optical Receiver Using a Costas Loop," *Optics Express*, **20**, (26), pp. B197-B203 (December 10, 2012) 137

ID. Coherent Beam Steering PICs

J.K. Doyle, M.J.R. Heck, J.T. Bovington, J.D. Peters, L.A. Coldren, and J.E. Bowers, "Free-space Beam Steering in Two Dimensions Using a Silicon Optical Phased Array," *Proc. OFC/NFOEC 2012*, paper no. OM2J.1, Los Angeles, CA (March 4-8, 2012) 147

W.H. Guo, P.R.A. Binetti, C. Althouse, H.P.M.M. Ambrosius, L.A. Johansson, and L.A. Coldren, "Improved Performance of Optical Beam Steering through an InP Photonic Integrated Circuit," *Proc. CLEO 2012*, paper no. CW1K.2, San Jose, CA (May 6-11, 2012) 150

W.H. Guo , P.R.A. Binetti, C. Althouse, H.P.M.M. Ambrosius, L.A. Johansson, and L.A. Coldren, “InP Photonic Integrated Circuit with an AWG-like Design for Optical Beam Steering,” <i>Proc. IPRM 2012</i> , paper no. Tu-2D.4, Santa Barbara, CA (August 27 -30, 2012)	152
W.H. Guo , P.R.A. Binetti, C. Althouse, H.P.M.M. Ambrosius, L.A. Johansson, and L.A. Coldren, “Very fast ($>10^7$ degree/s) 2D Optical Beam Steering through an InP Photonic Integrated Circuit,” <i>Proc. IEEE Photonics Conference</i> , paper no. ThR1, Burlingame, CA (September 23-27, 2012)	156
W.H. Guo , P.R.A. Binetti, C. Althouse, H.P.M.M. Ambrosius, L. A. Johansson, and L. A. Coldren, “InP Photonic Integrated Circuit with On-chip Monitors for Optical Beam Steering,” <i>Proc. 23rd IEEE Semiconductor Laser Conference</i> , paper no. MA6, San Diego, CA (October 7-10, 2012)	158
J.K. Doylend , M.J.R. Heck, J.T. Bovington, J.D. Peters, M.L. Davenport, L.A. Coldren, and J.E. Bowers, “Hybrid III/V Silicon Photonic Source with Integrated 1D Free-Space Beam Steering,” <i>Optic Letters</i> , 37 , (20), pp. 4257-4259 (October 15, 2012)	160
W.H. Guo , P. R. A. Binetti, C. Althouse, H. P. M. M. Ambrosius, L. A. Johansson, and L. A. Coldren, “InP Photonic Integrated Circuit for 2D Optical Beam Steering,” <i>Proc. POEM 2012: International Photonics and Optoelectronics Meetings</i> , IF3B.2, Wuhan, China, (November 1-2, 2012)	163
INVITED TALK	

II. Vertical-Cavity Surface-Emitting Lasers (VCSELs)

A.V. Barve , Y. Zheng, L.A. Johansson, and L.A. Coldren, “Frequency Dependent Polarization Dynamics in Vertical Cavity Surface Emitting Lasers with Electrical Injection,” <i>Proc. IEEE Photonics Conference</i> , TuF3, Burlingame, CA, (September 23-27, 2012)	167
C.-H. Lin , B.J. Thibeault, Y. Zheng, J.S. Parker, M.J. Rodwell, and L.A.Coldren, “Ultra-compact Intra-cavity Contacts for Multi-terminal VCSEL Power Enhancement,” <i>Proc. IEEE Photonics Conference</i> , paper no. MN3, Burlingame, CA (September 23-27, 2012)	169
Y. Zheng , C.H. Lin, A V. Barve, L.A. Coldren, "P-Type D-Doping of Highly- Strained VCSELs for 25 Gbps Operation," <i>Proc. IEEE Photonics Conference</i> , paper no. MP3, Burlingame, CA (September 23-27, 2012)	171
C.-H. Lin , Y. Zheng, L. A. Johansson, M. J. Rodwell and L.A. Coldren, “Electro-thermal Single-mode Tuning in Field-Induced Charge-Separation Lasers,” <i>Proc. 23rd IEEE Semiconductor Laser Conference</i> , paper no. WB5, San Diego, CA (October 7-10, 2012)	173
A.V. Barve , Y.Zheng, L.A.Johansson, A. Mehta, A. Husain and L.A. Coldren, "Fast Polarization Modulation in Vertical Cavity Lasers with Electrical RF Injection," <i>Proc. 23rd IEEE Semiconductor Laser Conference</i> , paper no. PD1.4, San Diego, CA (October 7-10, 2012) POST DEADLINE	175
A.V. Barve , Y. Zheng, L.A. Johansson, A. Mehta, A. Husain, and L.A. Coldren, “Ultrafast Polarization Modulation in Vertical Cavity Surface Emitting Lasers with Frequency Dependent Current Injection,” <i>Applied Physics Letters</i> , 101 , (25), pp. 1-4, (November 2012)	177

III. Materials and Device Technology

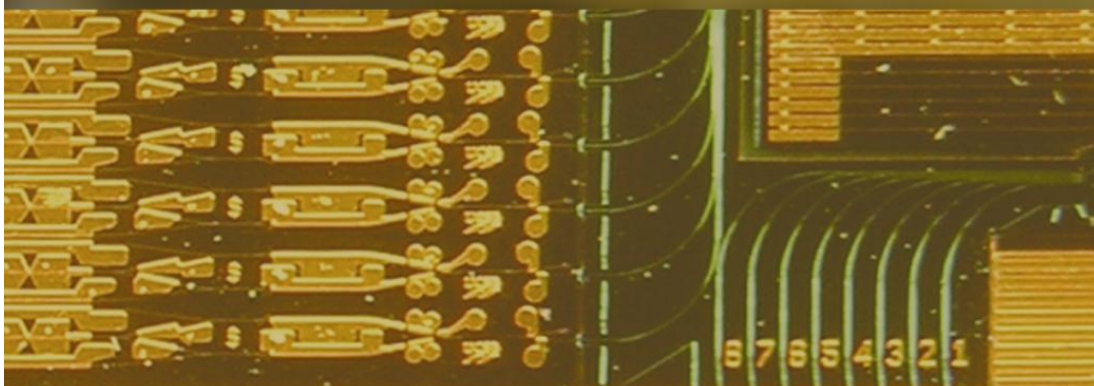
- N. Julian**, P. Mages, C. Zhang, J. Zhang, S. Kraemer, S. Stemmer, S. Denbaars, LA. Coldren, P. Petroff, and J. Bowers, "Coalescence of InP Expitaxial Lateral Overgrowth by MOVPE with V/III Ratio Variation," *Journal of Electronic Materials*, **41**, (5), pp. 845-852, May 2012 183
- J.S. Parker**, A. Sivananthan, E.J. Norberg, and L.A. Coldren, "Regrowth-free High-gain InGaAsP/InP Active-passive Platform via Ion Implantation," *Optics Express*, **20**, (18), pp. 19946-19955 (August 27, 2012) 191
- M.M. Krstic**, M.L. Masanovic, J.V. Crnjanski, LA. Johansson, LA. Coldren, and D.M. Gvozdic, "Detailed Stability Map and Bistability Investigation for Injection-locked Fabry-Perot Semiconductor Lasers," *Proc. 23rd IEEE Semiconductor Laser Conference*, paper no. TuP27, San Diego, CA (October 7-10, 2012) 201

I. Photonic Integrated Circuits

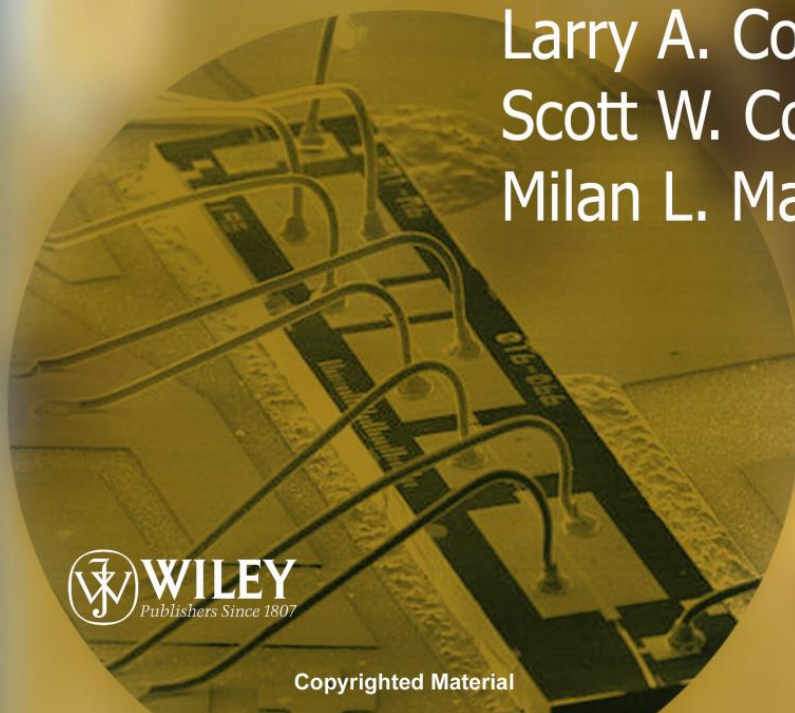
A. Tutorials, Reviews, and Books

SECOND EDITION

Diode Lasers and Photonic Integrated Circuits



Larry A. Coldren
Scott W. Corzine
Milan L. Mašanović



 **WILEY**
Publishers Since 1807

Copyrighted Material

Contents

Preface	xvii
Acknowledgments	xxi
List of Fundamental Constants	xxiii
1 Ingredients	1
1.1 Introduction	1
1.2 Energy Levels and Bands in Solids	5
1.3 Spontaneous and Stimulated Transitions: The Creation of Light	7
1.4 Transverse Confinement of Carriers and Photons in Diode Lasers: The Double Heterostructure	10
1.5 Semiconductor Materials for Diode Lasers	13
1.6 Epitaxial Growth Technology	20
1.7 Lateral Confinement of Current, Carriers, and Photons for Practical Lasers	24
1.8 Practical Laser Examples	31
References	39
Reading List	40
Problems	40
2 A Phenomenological Approach to Diode Lasers	45
2.1 Introduction	45
2.2 Carrier Generation and Recombination in Active Regions	46

2.3	Spontaneous Photon Generation and LEDs	49
2.4	Photon Generation and Loss in Laser Cavities	52
2.5	Threshold or Steady-State Gain in Lasers	55
2.6	Threshold Current and Power Out Versus Current	60
2.6.1	Basic P–I Characteristics	60
2.6.2	Gain Models and Their Use in Designing Lasers	64
2.7	Relaxation Resonance and Frequency Response	70
2.8	Characterizing Real Diode Lasers	74
2.8.1	Internal Parameters for In-Plane Lasers: $\langle\alpha_i\rangle$, η_i , and g versus J	75
2.8.2	Internal Parameters for VCSELs: η_i and g versus J , $\langle\alpha_i\rangle$, and α_m	78
2.8.3	Efficiency and Heat Flow	79
2.8.4	Temperature Dependence of Drive Current	80
2.8.5	Derivative Analysis	84
	References	86
	Reading List	87
	Problems	87
3	Mirrors and Resonators for Diode Lasers	91
3.1	Introduction	91
3.2	Scattering Theory	92
3.3	S and T Matrices for Some Common Elements	95
3.3.1	The Dielectric Interface	96
3.3.2	Transmission Line with No Discontinuities	98
3.3.3	Dielectric Segment and the Fabry–Perot Etalon	100
3.3.4	S-Parameter Computation Using Mason’s Rule	104
3.3.5	Fabry–Perot Laser	105
3.4	Three- and Four-Mirror Laser Cavities	107
3.4.1	Three-Mirror Lasers	107
3.4.2	Four-Mirror Lasers	111
3.5	Gratings	113
3.5.1	Introduction	113
3.5.2	Transmission Matrix Theory of Gratings	115
3.5.3	Effective Mirror Model for Gratings	121

3.6	Lasers Based on DBR Mirrors	123
3.6.1	Introduction	123
3.6.2	Threshold Gain and Power Out	124
3.6.3	Mode Selection in DBR-Based Lasers	127
3.6.4	VCSEL Design	128
3.6.5	In-Plane DBR Lasers and Tunability	135
3.6.6	Mode Suppression Ratio in DBR Laser	139
3.7	DFB Lasers	141
3.7.1	Introduction	141
3.7.2	Calculation of the Threshold Gains and Wavelengths	143
3.7.3	On Mode Suppression in DFB Lasers	149
	References	151
	Reading List	151
	Problems	151
4	Gain and Current Relations	157
4.1	Introduction	157
4.2	Radiative Transitions	158
4.2.1	Basic Definitions and Fundamental Relationships	158
4.2.2	Fundamental Description of the Radiative Transition Rate	162
4.2.3	Transition Matrix Element	165
4.2.4	Reduced Density of States	170
4.2.5	Correspondence with Einstein's Stimulated Rate Constant	174
4.3	Optical Gain	174
4.3.1	General Expression for Gain	174
4.3.2	Lineshape Broadening	181
4.3.3	General Features of the Gain Spectrum	185
4.3.4	Many-Body Effects	187
4.3.5	Polarization and Piezoelectricity	190
4.4	Spontaneous Emission	192
4.4.1	Single-Mode Spontaneous Emission Rate	192
4.4.2	Total Spontaneous Emission Rate	193
4.4.3	Spontaneous Emission Factor	198
4.4.4	Purcell Effect	198

4.5	Nonradiative Transitions	199
4.5.1	Defect and Impurity Recombination	199
4.5.2	Surface and Interface Recombination	202
4.5.3	Auger Recombination	211
4.6	Active Materials and Their Characteristics	218
4.6.1	Strained Materials and Doped Materials	218
4.6.2	Gain Spectra of Common Active Materials	220
4.6.3	Gain versus Carrier Density	223
4.6.4	Spontaneous Emission Spectra and Current versus Carrier Density	227
4.6.5	Gain versus Current Density	229
4.6.6	Experimental Gain Curves	233
4.6.7	Dependence on Well Width, Doping, and Temperature	234
	References	238
	Reading List	240
	Problems	240
5	Dynamic Effects	247
5.1	Introduction	247
5.2	Review of Chapter 2	248
5.2.1	The Rate Equations	249
5.2.2	Steady-State Solutions	250
	Case (i): Well Below Threshold	251
	Case (ii): Above Threshold	252
	Case (iii): Below and Above Threshold	253
5.2.3	Steady-State Multimode Solutions	255
5.3	Differential Analysis of the Rate Equations	257
5.3.1	Small-Signal Frequency Response	261
5.3.2	Small-Signal Transient Response	266
5.3.3	Small-Signal FM Response or Frequency Chirping	270
5.4	Large-Signal Analysis	276
5.4.1	Large-Signal Modulation: Numerical Analysis of the Multimode Rate Equations	277
5.4.2	Mode Locking	279
5.4.3	Turn-On Delay	283
5.4.4	Large-Signal Frequency Chirping	286

5.5	Relative Intensity Noise and Linewidth	288
5.5.1	General Definition of RIN and the Spectral Density Function	288
5.5.2	The Schawlow–Townes Linewidth	292
5.5.3	The Langevin Approach	294
5.5.4	Langevin Noise Spectral Densities and RIN	295
5.5.5	Frequency Noise	301
5.5.6	Linewidth	303
5.6	Carrier Transport Effects	308
5.7	Feedback Effects and Injection Locking	311
5.7.1	Optical Feedback Effects—Static Characteristics	311
5.7.2	Injection Locking—Static Characteristics	317
5.7.3	Injection and Feedback Dynamic Characteristics and Stability	320
5.7.4	Feedback Effects on Laser Linewidth	321
	References	328
	Reading List	329
	Problems	329
6	Perturbation, Coupled-Mode Theory, Modal Excitations, and Applications	335
6.1	Introduction	335
6.2	Guided-Mode Power and Effective Width	336
6.3	Perturbation Theory	339
6.4	Coupled-Mode Theory: Two-Mode Coupling	342
6.4.1	Contradirectional Coupling: Gratings	342
6.4.2	DFB Lasers	353
6.4.3	Codirectional Coupling: Directional Couplers	356
6.4.4	Codirectional Coupler Filters and Electro-optic Switches	370
6.5	Modal Excitation	376
6.6	Two Mode Interference and Multimode Interference	378
6.7	Star Couplers	381
6.8	Photonic Multiplexers, Demultiplexers and Routers	382
6.8.1	Arrayed Waveguide Grating De/Multiplexers and Routers	383

6.8.2	Echelle Grating based De/Multiplexers and Routers	389
6.9	Conclusions	390
	References	390
	Reading List	391
	Problems	391
7	Dielectric Waveguides	395
7.1	Introduction	395
7.2	Plane Waves Incident on a Planar Dielectric Boundary	396
7.3	Dielectric Waveguide Analysis Techniques	400
7.3.1	Standing Wave Technique	400
7.3.2	Transverse Resonance	403
7.3.3	WKB Method for Arbitrary Waveguide Profiles	410
7.3.4	2-D Effective Index Technique for Buried Rib Waveguides	418
7.3.5	Analysis of Curved Optical Waveguides using Conformal Mapping	421
7.3.6	Numerical Mode Solving Methods for Arbitrary Waveguide Profiles	424
7.4	Numerical Techniques for Analyzing PICs	427
7.4.1	Introduction	427
7.4.2	Implicit Finite-Difference Beam-Propagation Method	429
7.4.3	Calculation of Propagation Constants in a z -invariant Waveguide from a Beam Propagation Solution	432
7.4.4	Calculation of Eigenmode Profile from a Beam Propagation Solution	434
7.5	Goos–Hanchen Effect and Total Internal Reflection Components	434
7.5.1	Total Internal Reflection Mirrors	435
7.6	Losses in Dielectric Waveguides	437
7.6.1	Absorption Losses in Dielectric Waveguides	437
7.6.2	Scattering Losses in Dielectric Waveguides	438
7.6.3	Radiation Losses for Nominally Guided Modes	438
	References	445
	Reading List	446
	Problems	446

8 Photonic Integrated Circuits	451
8.1 Introduction	451
8.2 Tunable, Widely Tunable, and Externally Modulated Lasers	452
8.2.1 Two- and Three-Section In-plane DBR Lasers	452
8.2.2 Widely Tunable Diode Lasers	458
8.2.3 Other Extended Tuning Range Diode Laser Implementations	463
8.2.4 Externally Modulated Lasers	474
8.2.5 Semiconductor Optical Amplifiers	481
8.2.6 Transmitter Arrays	484
8.3 Advanced PICs	484
8.3.1 Waveguide Photodetectors	485
8.3.2 Transceivers/Wavelength Converters and Triplexers	488
8.4 PICs for Coherent Optical Communications	491
8.4.1 Coherent Optical Communications Primer	492
8.4.2 Coherent Detection	495
8.4.3 Coherent Receiver Implementations	495
8.4.4 Vector Transmitters	498
References	499
Reading List	503
Problems	503

APPENDICES

1 Review of Elementary Solid-State Physics	509
A1.1 A Quantum Mechanics Primer	509
A1.1.1 Introduction	509
A1.1.2 Potential Wells and Bound Electrons	511
A1.2 Elements of Solid-State Physics	516
A1.2.1 Electrons in Crystals and Energy Bands	516
A1.2.2 Effective Mass	520
A1.2.3 Density of States Using a Free-Electron (Effective Mass) Theory	522
References	527
Reading List	527

2	Relationships between Fermi Energy and Carrier Density and Leakage	529
A2.1	General Relationships	529
A2.2	Approximations for Bulk Materials	532
A2.3	Carrier Leakage Over Heterobarriers	537
A2.4	Internal Quantum Efficiency	542
	References	544
	Reading List	544
3	Introduction to Optical Waveguiding in Simple Double-Heterostructures	545
A3.1	Introduction	545
A3.2	Three-Layer Slab Dielectric Waveguide	546
	A3.2.1 Symmetric Slab Case	547
	A3.2.2 General Asymmetric Slab Case	548
	A3.2.3 Transverse Confinement Factor, Γ_x	550
A3.3	Effective Index Technique for Two-Dimensional Waveguides	551
A3.4	Far Fields	555
	References	557
	Reading List	557
4	Density of Optical Modes, Blackbody Radiation, and Spontaneous Emission Factor	559
A4.1	Optical Cavity Modes	559
A4.2	Blackbody Radiation	561
A4.3	Spontaneous Emission Factor, β_{sp}	562
	Reading List	563
5	Modal Gain, Modal Loss, and Confinement Factors	565
A5.1	Introduction	565
A5.2	Classical Definition of Modal Gain	566
A5.3	Modal Gain and Confinement Factors	568
A5.4	Internal Modal Loss	570

A5.5	More Exact Analysis of the Active/Passive Section Cavity	571
A5.5.1	Axial Confinement Factor	572
A5.5.2	Threshold Condition and Differential Efficiency	573
A5.6	Effects of Dispersion on Modal Gain	576
6	Einstein's Approach to Gain and Spontaneous Emission	579
A6.1	Introduction	579
A6.2	Einstein <i>A</i> and <i>B</i> Coefficients	582
A6.3	Thermal Equilibrium	584
A6.4	Calculation of Gain	585
A6.5	Calculation of Spontaneous Emission Rate	589
	Reading List	592
7	Periodic Structures and the Transmission Matrix	593
A7.1	Introduction	593
A7.2	Eigenvalues and Eigenvectors	593
A7.3	Application to Dielectric Stacks at the Bragg Condition	595
A7.4	Application to Dielectric Stacks Away from the Bragg Condition	597
A7.5	Correspondence with Approximate Techniques	600
A7.5.1	Fourier Limit	601
A7.5.2	Coupled-Mode Limit	602
A7.6	Generalized Reflectivity at the Bragg Condition	603
	Reading List	605
	Problems	605
8	Electronic States in Semiconductors	609
A8.1	Introduction	609
A8.2	General Description of Electronic States	609
A8.3	Bloch Functions and the Momentum Matrix Element	611
A8.4	Band Structure in Quantum Wells	615
A8.4.1	Conduction Band	615

A8.4.2	Valence Band	616
A8.4.3	Strained Quantum Wells	623
	References	627
	Reading List	628
9	Fermi's Golden Rule	629
A9.1	Introduction	629
A9.2	Semiclassical Derivation of the Transition Rate	630
A9.2.1	Case I: The Matrix Element-Density of Final States Product is a Constant	632
A9.2.2	Case II: The Matrix Element-Density of Final States Product is a Delta Function	635
A9.2.3	Case III: The Matrix Element-Density of Final States Product is a Lorentzian	636
	Reading List	637
	Problems	638
10	Transition Matrix Element	639
A10.1	General Derivation	639
A10.2	Polarization-Dependent Effects	641
A10.3	Inclusion of Envelope Functions in Quantum Wells	645
	Reading List	646
11	Strained Bandgaps	647
A11.1	General Definitions of Stress and Strain	647
A11.2	Relationship Between Strain and Bandgap	650
A11.3	Relationship Between Strain and Band Structure	655
	References	656
12	Threshold Energy for Auger Processes	657
A12.1	CCCH Process	657
A12.2	CHHS and CHHL Processes	659

13 Langevin Noise	661
A13.1 Properties of Langevin Noise Sources	661
A13.1.1 Correlation Functions and Spectral Densities	661
A13.1.2 Evaluation of Langevin Noise Correlation Strengths	664
A13.2 Specific Langevin Noise Correlations	665
A13.2.1 Photon Density and Carrier Density Langevin Noise Correlations	665
A13.2.2 Photon Density and Output Power Langevin Noise Correlations	666
A13.2.3 Photon Density and Phase Langevin Noise Correlations	667
A13.3 Evaluation of Noise Spectral Densities	669
A13.3.1 Photon Noise Spectral Density	669
A13.3.2 Output Power Noise Spectral Density	670
A13.3.3 Carrier Noise Spectral Density	671
References	672
Problems	672
14 Derivation Details for Perturbation Formulas	675
Reading List	676
15 Multimode Interference	677
A15.1 Multimode Interference-Based Couplers	677
A15.2 Guided-Mode Propagation Analysis	678
A15.2.1 General Interference	679
A15.2.2 Restricted Multimode Interference	681
A15.3 MMI Physical Properties	682
A15.3.1 Fabrication	682
A15.3.2 Imaging Quality	682
A15.3.3 Inherent Loss and Optical Bandwidth	682
A15.3.4 Polarization Dependence	683
A15.3.5 Reflection Properties	683
Reference	683

16 The Electro-Optic Effect	685
References	692
Reading List	692
17 Solution of Finite Difference Problems	693
A17.1 Matrix Formalism	693
A17.2 One-Dimensional Dielectric Slab Example	695
Reading List	696
Index	697

Preface

Diode lasers and related photonic integrated circuits have become even more commercially important since the first edition of this book was published, in 1995. They are used in a wide variety of applications ranging from the readout sources in DVD and Blu-ray disk players, laser printers, mice and pointers, to the complex multiwavelength transmitters and receivers in optical fiber communication systems that carry hundreds of gigabits per second of information. New applications, such as solid-state lighting sources, or sources for high-spectral-efficiency telecommunications networks continue to emerge as the devices become more varied, reliable, manufacturable, and inexpensive.

In this edition, the GaN-based materials, which have become important in the UV/blue/green wavelength regions as well as for solid-state lighting, are included with equal emphasis to the GaAs and InP-based materials, which provide emission from the red to about 1 micron in wavelength on GaAs and over the 1.3–1.6 micron wavelength range on InP. Thus, the range of applications that can be addressed with a mastery contents of this edition is very broad.

This book has been written to be a resource for professors, graduate students, industry researchers, and design engineers dealing with the subject of diode lasers and related photonic integrated circuits for a range of applications. The depth of coverage is relatively advanced, but the initial chapters provide a working knowledge of semiconductor lasers before delving into much of the advanced material. Appendices are used both to provide a review of background material as well as some of the details of the more advanced topics. Thus, by appropriate use of the appendices, the text can support teaching the material at different academic levels, but it remains self-contained.

Significant new material has been added, to both improve on the original text, and to address important technology developments over the last decade. One of the key novel features is the addition of many worked examples throughout all the chapters to better illustrate how to apply the theory that is being covered. New homework problems have also been added to supplement the previous ones, some

of which are less complex than the previous problems, because many found them too difficult for beginning students or casual reference readers.

New topics that are being covered in this second edition are more introductory material related to benefits, applications and basics of laser diodes and photonic ICs; additional methods for analytic calculation of S parameters based on Mason's rule; expanded treatment of DFB and VCSEL lasers; additional material on quantum dots, gain and other material parameters for both GaN, InP and GaAs based active regions and devices; treatment of the mode-locked lasers and injection locking; total internal reflection mirrors and beam splitters; a new appendix and section on multimode interference effects and devices; treatment of star couplers and photonic multiplexers, demultiplexers and routers, and their design; expanded treatment of losses in dielectric waveguides; treatment of light propagation in curved waveguides; significantly expanded treatment of tunable and widely tunable laser diodes; expanded treatment of externally modulated lasers, including Mach-Zehnder modulators and semiconductor optical amplifiers; additional material on waveguide photodiodes, optical transceivers and triplexers; and a full section on basics and PICs for coherent communications.

Also available online with the second edition will be a number of password-protected tools, such as BPM and S and T matrix computation code, DFB laser code, mode solving code, as well as color versions of all figures, all of which should be useful for instructors and students, as well as other readers.

The full text is intended for use at the graduate level, although a fairly comprehensive introductory course on diode lasers at an advanced undergraduate level could be based around the material in Chapters 1 through 3 together with Appendices 1 through 7.

It is assumed that the readers have been exposed to elementary quantum mechanics, solid-state physics, and electromagnetic theory at the undergraduate level. It is also recommended that they have had an introductory optoelectronics course. Appendices 1 and 3 review most of the necessary background in just about all of the required detail. Thus, it is possible to use the book with less prior educational background, provided these review appendices are covered with some care.

For use in a more advanced graduate class, it would not be necessary to cover the material in the first seven appendices. (Of course, it would still be there for reference, and the associated homework problems could still be assigned to ensure its understanding. Nevertheless, it is still recommended that Appendix 5, which covers the definitions of modal gain and loss, be reviewed because this is not well understood by the average worker in the field.) The coverage could then move efficiently through the first three chapters and into Chapters 4 and 5, which deal with the details of gain and laser dynamics in a first course. For more focus on the gain physics some of Appendices 8 through 12 could be included in the coverage. In any event, their inclusion provides for a very self-contained treatment of this important subject matter.

Chapters 6 and 7 deal more with the electromagnetic wave aspects of photonic ICs and diode lasers. This material is essential for understanding the more advanced PIC type of devices used in modern fiber-optic links and networks.

However, keeping this material to last allows the student to develop a fairly complete understanding of the operation of diode lasers without getting bogged down in the mathematical techniques necessary for the lateral waveguide analysis. Thus, a working understanding and appreciation of laser operation can be gained in only one course. Chapter 6 deals with perturbation, coupled-mode theory and modal excitation while Chapter 7 deals with dielectric waveguide analysis. Putting Chapter 6 first emphasizes the generality of this material. That is, one really does not need to know the details of the lateral mode profile to develop these powerful techniques. Using the coupled-mode results, gratings and DFB lasers are again investigated. Historically, these components were primarily analyzed with this theory. However, in this text grating-based DFB and DBR lasers are first analyzed in Chapter 3 using exact matrix multiplication techniques, from which approximate formulas identical to those derived with coupled mode theory result. The proliferation of computers and the advent of lasers using complex grating designs with many separate sections has led the authors to assert that the matrix multiplication technique should be the primary approach taught to students. The advent of the vertical-cavity laser also supports this approach. Nevertheless, it should be realized that coupled-mode theory is very important to reduce the description of the properties of complex waveguide geometries to simple analytic formulae, which are especially useful in design work. Chapter 7 also introduces some basic numerical techniques, which have become indispensable with the availability of powerful personal computers and efficient software for solving complex numerical algorithms. The finite-difference technique is introduced for optical waveguide analysis, while the beam-propagation method is discussed as a key tool for analyzing real PIC structures.

Chapter 8 pulls together most of the material in the first seven chapters by providing a comprehensive overview of the development of photonic integrated circuits, with a series of design examples of relatively complex photonic integrated circuits.

Unlike many books in this field, this book is written as an engineering text. The reader is first trained to be able to solve problems on real diode lasers, based on a phenomenological understanding, before going into the complex physical details such as the material gain process or mode-coupling in dielectric waveguides. This provides motivation for learning the underlying details as well as a toolbox of techniques to immediately apply each new advanced detail in solving real problems. Also, attention has been paid to accuracy and consistency. For example, a careful distinction between the internal quantum efficiency in LEDs and injection efficiency in lasers is made, and calculations of gain not only illustrate an analysis technique, but they actually agree with experimental data. Finally, by maintaining consistent notation throughout all of the chapters and appendices, a unique self-contained treatment of all of the included material emerges.

L. A. COLDREN
S. W. CORZINE
M. L. MAŠANOVIĆ

Spurious-Free Dynamic Range in Photonic Integrated Circuit Filters with Semiconductor Optical Amplifiers

Robert S. Guzzon, Erik J. Norberg, and Larry A. Coldren, *Fellow, IEEE*

(Invited Paper)

Abstract—Among other advantages, radio-frequency (RF) signal processing in the optical domain using photonic integrated circuits (PICs) offers unprecedented bandwidth and tunability. However, modern RF-photonic link applications demand PICs with high spurious-free dynamic range (SFDR). The SFDR of active PICs integrating semiconductor optical amplifiers (SOAs) is limited by amplified spontaneous emission noise and distortion caused by four-wave mixing. Here, we derive an analytical model for the SFDR of SOAs, and extend it to PICs with arbitrary transfer functions integrating many SOAs. The model is general and applicable to any photonic signal-processing circuit operating in the linear amplification regime below saturation. We show analytically the importance of SFDR-driven photonic design over noise-figure-driven design. Using this model, we explore the SFDR of coupled-ring bandpass filters integrated on a high saturation power integration platform and show SFDR as high as $117.0 \text{ dB} \cdot \text{Hz}^{2/3}$ for filters with bandwidths in the 1–2 GHz range. We show how the material parameters and PIC design determine the SFDR. Tradeoffs between SFDR and filter bandwidth, extinction, and stopband roll-off are investigated.

Index Terms—Integrated optoelectronics, microwave photonics, optical filters, photonic integrated circuits, semiconductor optical amplifiers.

I. INTRODUCTION

OPTICAL analog signal processing at telecom wavelengths for RF applications has attracted attention due to the advantages provided by RF photonic links. Radio over fiber (RoF) systems provide low-loss transmission, wide bandwidth, and immunity to electromagnetic interference (EMI) [1]. Within such systems, photonic filters can provide widely tunable and high quality factor (Q) filters with operating bandwidths not achievable in current RF electronic technology for new applications demanding center frequencies up to 100 GHz [2]. In addition, analog signal processing in the optical domain can potentially provide size, weight, and power (SWaP) dividends [3].

Manuscript received August 1, 2011; revised October 18, 2011; accepted October 22, 2011. Date of current version January 24, 2012. This work was supported in part by DARPA under Program PhASER. A portion of this work was completed in the UCSB nanofabrication facility, part of the National Science Foundation-National Nanotechnology Infrastructure Network.

The authors are with the Department of Electrical and Computer Engineering and Department of Materials, University of California Santa Barbara, Santa Barbara, CA 93106 USA (e-mail: guzzon@ece.ucsb.edu; norberg@ece.ucsb.edu; coldren@ece.ucsb.edu).

Color versions of one or more of the figures in this paper are available online at <http://ieeexplore.ieee.org>.

Digital Object Identifier 10.1109/JQE.2011.2174618

Microwave photonic filtering can be achieved in a variety of ways using bulk optics [4], and more recently, photonic integrated circuits (PICs) [5]–[10]. PICs can capitalize on SWaP and stability improvements over bulk optical solutions while providing a high level of programmability and tunability to the filtering application. However, RF link performance must not be compromised by the photonic subsystem. Traditionally, signal fidelity is quantitatively described by the system spurious-free dynamic range (SFDR). The theoretical and experimental SFDR limitations in RF photonic links involving passive PIC filters have been evaluated [2], [11]. In these systems, filters introduce optical loss, but do not add noise or signal distortion. Therefore, SFDR is limited by the modulation and detection nonlinearities; laser, shot, and receiver noise; and link gain.

Recently, we have described and evaluated active PIC filters in the InGaAsP/InP material system [9]. Fig. 1 displays a fabricated PIC filter and measured bandpass spectra. Integrated semiconductor optical amplifiers (SOAs) provide high tunability to active filters and compensate for passive waveguide loss within ring structures, allowing for the synthesis of near-ideal filter shapes incorporating high Q resonators. With intra-ring gain, filter design relies less on the exact specification of inter-ring coupling values, and becomes more flexible. Filter bandwidth can be set independently of pole magnitude, guaranteeing a flat-topped filter design regardless of bandwidth. In addition, filters can be designed with passband gain. Fabrication in the InGaAsP/InP material system is also advantageous for integration with other active photonic components such as transmitters and receivers. These benefits come at the expense of added amplified spontaneous emission (ASE) noise [12] and nonlinearities stemming from the four-wave mixing (FWM) phenomenon created by carrier population oscillations (CPO) [13].

A full theoretical SFDR treatment has been conducted for a single SOA operating in the nonlinear large-signal regime [14]. In this paper, we extend ASE and CPO theory to determine the PIC-limited SFDR of a coherent heterodyne RF photonic link. This general model describes any PIC integrating SOAs that operate below saturation. Here, we outline the model and apply it to PIC bandpass filters utilizing low-gain SOAs. When integrated on a high-saturation power integration platform [15], the model predicts SFDR as high as $117.0 \text{ dB} \cdot \text{Hz}^{2/3}$ for

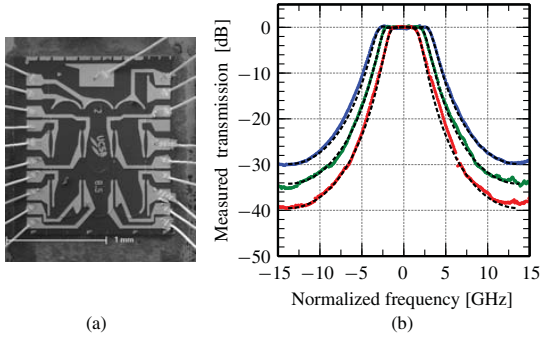


Fig. 1. (a) SEM picture of a fabricated and wire-bonded third-order coupled ring filter. (b) Third-order bandpass filters measured in the RF domain, normalized in frequency and amplitude for clarity. These filters were measured to have between 0.0 and 5.0 dB optical passband gain. The dotted lines are a theoretical fit. More details in [9].

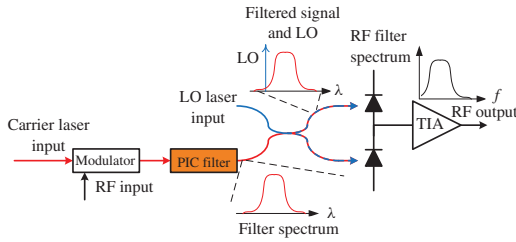


Fig. 2. RF photonic link including modulator, PIC filter, and balanced receiver. The optical signal is in red, RF electrical signals in black, and LO in blue.

a second-order coupled-ring bandpass filter with a 1.75 GHz bandwidth. Results show clear trade-offs between linearity and filter bandwidth, extinction, and roll-off, while shedding light on optimal filter design. The model also shows that noise figure alone may not provide the optimal design of an analog optical link, and that SFDR provides a more useful metric.

II. THEORETICAL BACKGROUND

Fig. 2 schematically represents a coherent heterodyne RF photonic link. In such a system, a strong local oscillator (LO) downconverts the PIC-filtered optical signal through a balanced detection receiver. The link could be over a long distance in fiber, or be contained on a single PIC depending on the application.

A. SFDR in Terms of Optical Powers

The SFDR of a system describes the range over which a signal remains above the noise level, while spurious distortion power remains below the noise level. In particular, the third-order intermodulation distortion (IMD) products between two input tones $2f_2 - f_1$ and $2f_1 - f_2$ are of prime interest because of their proximity to the signal band. The two-tone SFDR can be written as the ratio of the third-order electrical intercept power to the electrical noise power in the receiver [16]

$$SFDR = \left[\frac{P_{OIP3,elec}}{N} \right]^{\frac{2}{3}} = \left[\frac{\langle i_{OIP3}^2 \rangle}{\langle i_N^2 \rangle} \right]^{\frac{2}{3}} \quad (1)$$

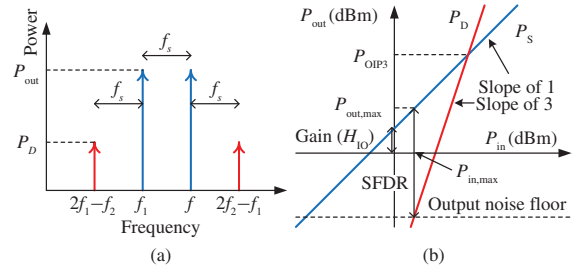


Fig. 3. Schematic representation of two-tone SFDR showing. (a) Relationship of the fundamental tones with separation frequency f_s to the IMD tones $2f_2 - f_1$ and $2f_1 - f_2$. (b) Signal (P_S) and IMD distortion power (P_D) as a function of input signal power. SFDR and the output intercept point are labeled on this dB-dB plot.

where $P_{OIP3,elec}$ is the output third-order intercept electrical power, N is the electrical noise power, $\langle i_{OIP3}^2 \rangle$ is the output third-order intercept mean-square current, and $\langle i_N^2 \rangle$ is the noise equivalent mean-square current. A schematic representation of the two-tone SFDR is presented in Fig. 3. Since the impedance seen by all currents in the receiver are equal, signal and noise quantities are written above in terms of mean-square currents, where the angle brackets denote averaging. In order to concentrate on the effect of the PIC on SFDR, we will assume an ideal transmitter and receiver where laser RIN and thermal noise do not dominate. In a real system, this may not be the case. In particular, the receiver noise may be appreciable. However, the aim of this paper is not to investigate the SFDR of a realistic link, but look at how a PIC with integrated SOAs impacts a link independently of other noise sources. In such a case, noise in a heterodyne RF photonic link with optical amplification is dominated by shot noise and LO-ASE beat noise. The mean squared shot noise current at the receiver where the LO power is much greater than the signal power is given by [17]

$$\langle i_{shot}^2 \rangle = 2qRP_{LO}\Delta f \quad (2)$$

where q is the electron charge, $R = q/\hbar\omega$ is the responsivity of an ideal detector, P_{LO} is the optical power of the LO, and Δf is the bandwidth of the receiver. Only the LO optical power appears in (2) because the LO power is assumed to be much larger than the signal and noise. The LO-ASE beat noise for single-sideband detection is given by [17]

$$\langle i_{LO-ASE}^2 \rangle = 2R^2P_{LO}S_{ASE}\Delta f \quad (3)$$

where S_{ASE} is the power spectral density of ASE in the mode. Single-sideband detection is assumed because the noise spectrum is filtered by the PIC such that only one sideband is dominant. This results in the pre-factor of 2 rather than 4 in Eq. (3). The mean-squared third-order intercept current is given by

$$\langle i_{OIP3}^2 \rangle = 2R^2P_{LO}P_{OIP3} \quad (4)$$

where P_{OIP3} is the power at the third-order optical output intercept point (OIP3). Thus, in an optical heterodyne system where the LO power is much greater than the signal power, the SFDR can be written in terms of optical powers. Substituting

(2), (3), and (4) into (1), the SFDR in terms of optical powers is

$$SFDR = \left[\frac{P_{OIP3}}{(S_{ASE} + \hbar\omega)\Delta f} \right]^{\frac{2}{3}} \quad (5)$$

SFDR can be written in terms of noise factor as

$$SFDR = \left[\frac{P_{OIP3}}{H_{IO}\hbar\omega F_n \Delta f} \right]^{\frac{2}{3}} \quad (6)$$

where H_{IO} is the power transfer function from input to output, and the noise factor is given by [17]

$$F_n = \frac{S_{ASE}}{H_{IO}\hbar\omega} + \frac{1}{H_{IO}}. \quad (7)$$

The first term represents LO-ASE beat noise, and the second term represents the shot noise contribution. SFDR is typically multiplied by $\Delta f^{2/3}$ and quoted on a receiver bandwidth independent dB scale as $\text{dB} \cdot \text{Hz}^{2/3}$.

SFDR is a range over which the signal power can swing without inducing distortion and without falling below the noise floor. For each SFDR, it is convenient to calculate the maximum optical input power or output power of the PIC needed to take advantage of the full dynamic range. These maximum optical powers can be deduced from Fig. 3(b) as:

$$P_{\text{out,max}} = \frac{P_{OIP3}}{\sqrt{SFDR}} \quad (8)$$

$$P_{\text{in,max}} = \frac{P_{OIP3}}{H_{IO}\sqrt{SFDR}}. \quad (9)$$

B. ASE Noise Generation in a Single SOA

To determine the ASE noise at the receiver, we first look at the noise generated by a single SOA. Starting with the spontaneous photon density rate equation for a traveling wave amplifier, writing it as a differential equation with respect to position in the SOA, and writing it in terms of power spectral density we have [12]

$$\frac{dS_{ASE}}{dz} = (\Gamma g - \alpha_i)S_{ASE} + \Gamma g n_{sp} \hbar\omega \quad (10)$$

where S_{ASE} is the ASE power spectral density in the mode, Γg is the modal gain, α_i is the modal loss, and n_{sp} is the population inversion factor. Solving the differential equation and integrating over the length of the SOA, L [12]

$$S_{ASE} = \frac{n_{sp}\hbar\omega}{\zeta}(G - 1) = N_{\text{mat}}(G - 1) \quad (11)$$

where G is the single-pass power gain given by $G = e^{(\Gamma g - \alpha_i)L}$, and $\zeta = (\Gamma g - \alpha_i)/\Gamma g$. For a particular material and waveguide design, and at a particular operation point (current density) and wavelength, n_{sp} , ζ , and $\hbar\omega$ are constant, and are therefore lumped into the material noise parameter N_{mat} . The total ASE power in the mode is simply $P_{ASE} = S_{ASE}\Delta f$ where Δf is the ASE bandwidth.

C. Intermodulation Distortion Generation in a Single SOA

The theory of FWM through CPO in SOAs has been studied extensively in the past [13]–[15], [18]–[22]. When certain assumptions are made, an analytical solution can be attained for the intermodulation distortion power generated by an SOA [13], [19]. First, a small-signal approach is taken, where the input tones are assumed to be much larger than the distortion products, and modulation of the carrier density is small compared to its average. Also, higher-order modulation of the carrier density by beating of input tones with distortion products can be ignored. Finally, the carrier density is assumed to be constant along the length of the SOA. These assumptions are valid for a system operating in the linear amplification regime, well below saturation. This is the regime in which we hope to operate. [13], [19] also make the additional assumption of high single-pass gain. The filters presented here often incorporate SOAs with very low single-pass gain, rendering this assumption invalid. Here, we present a new result that does not require high single-pass gain. Additionally, [13], [19] utilize the slowly-varying envelope approximation to simplify the second order differential wave equation to a first order differential equation. Here, we analytically solve the second order differential equation directly and derive an equation for the optical power generated in a third-order IMD tone by two equal input tones.

Starting with the carrier density rate equation

$$\frac{dN}{dt} = \frac{I_a}{qV} - \frac{N}{\tau} - \frac{g(N)}{\hbar\omega}|E|^2 \quad (12)$$

where N is the carrier density, I_a is the current into the active region, V is the active volume, τ is the carrier lifetime, $g(N)$ is the material gain, and E is the electric field in the active region, normalized by the factor $\sqrt{n\epsilon_0 c/2}$ such that $I = |E|^2$ is the optical intensity in the active region. Using the saturation intensity in the active region $I_S = \hbar\omega/a\tau$ and $g(N) = a(N - N_0)$ where a is the differential gain and N_0 is the transparency current density, the rate equation can be written in time-harmonic form as

$$j\omega N I_S \tau = \frac{I_a I_S \tau}{qV} - N I_S - (N - N_0)|E|^2. \quad (13)$$

The electric field for 2 input tones of equal amplitude is given by

$$E = E_0 + E_1 = E_e \left(e^{j\omega_0 t} + e^{j\omega_1 t} \right) \quad (14)$$

where $E_e = E_{in} e^{(\Gamma g - \alpha_i)z/2}$ is the electric field envelope along the SOA and E_{in} is the input electric field magnitude. The carrier density can be separated into an average value and a value modulated at the difference frequency between the input tones

$$N = \bar{N} + \Delta N \left(e^{j(\omega_1 - \omega_0)t} + e^{-j(\omega_1 - \omega_0)t} \right). \quad (15)$$

Substituting (14) and (15) into (13) and solving for \bar{N} and ΔN gives

$$\bar{N} = \frac{I_a I_S \tau / qV + 2N_0 E_e^2}{I_S + 2E_e^2} \quad (16)$$

$$\Delta N = \frac{-(\bar{N} - N_0)E_e^2}{(1 + j\omega_s \tau)I_S + 2E_e^2} \quad (17)$$

where $\omega_s = \omega_1 - \omega_0$ is the separation between the input tones. Now, using the wave equation, the distortion power generated and amplified in each IMD tone can be determined. Keeping only the field component at the IMD frequency, the wave equation for the IMD tone, E_D , in the propagation (z) direction can be written [18]

$$\frac{d^2 E_D}{dz^2} + \tilde{k}_D^2 E_D = \Gamma a(\alpha + j\zeta) \Delta N k_D E_e e^{jk_D z} \quad (18)$$

where α is the linewidth enhancement factor, $\tilde{k}_D = k_D - j(\Gamma g - \alpha_i)/2$ is the complex propagation constant for the distortion field, and k_D is the real part of the propagation constant. Now, substituting (16) into (17), the result into (18), using $g = a(N - N_0)$, and keeping only the dominant term in the denominator, the wave equation becomes

$$\frac{d^2 E_D}{dz^2} + \tilde{k}_D^2 E_D = \frac{-\Gamma g(\alpha + j\zeta) k_D E_e^3 e^{jk_D z}}{(1 + j\omega_s \tau) I_S}. \quad (19)$$

Solving (19) with the boundary conditions $E_D(0) = 0$ and $E'_D(0) = 0$, using $I = |E|^2$ and the optical power in the mode $P = IA_{\text{active}}/\Gamma$, and keeping only dominant terms, the total distortion power at the output of the SOA is

$$\begin{aligned} P_D(L) &= \frac{(1 + \alpha^2/\zeta^2) P_{in}^3}{4(1 + (\omega_s \tau)^2) P_S^2} G [G - 1]^2 \\ &= A_{\text{mat}} P_{in}^3 G [G - 1]^2 \end{aligned} \quad (20)$$

where P_{in} is the input power of each tone, P_S is the modal saturation power, and $G = e^{(\Gamma g - \alpha_i)L}$ is the single-pass power gain. For a particular material and waveguide design, and at a particular operating current density, α , ζ , P_S , and τ are constant, and are therefore lumped into the material parameter A_{mat} . According to Eq. (20), IMD power is inversely proportional to P_S^2 . It is therefore important for best SFDR performance to operate SOAs at their optimal current density where the peak gain and peak saturation power are obtained. Eq. (20) then relates the third-order IMD power generated in each SOA to the optical power at the input of the SOA and the total SOA gain. Contrary to [13] and [19], this result is valid for low single-pass gain where the assumption $G \gg 1$ is not valid. The presence of the $[G - 1]^2$ term in (20) and the $G - 1$ term in (11) indicates a low-gain operation regime where high SFDR can be obtained. Photonic microwave filters integrating SOAs in rings such as the ones presented in this paper operate within such a regime.

The IMD output intercept power is related to the distortion power by

$$P_{\text{OIP3}} = \left[\frac{(H_{\text{IO}} P_{in})^3}{P_D} \right]^{\frac{1}{2}} \quad (21)$$

where H_{IO} is the power transfer function from input to output, which is simply equal to G in the case of a single SOA. If we define a unit-less distortion

$$D = \frac{P_D}{A_{\text{mat}} P_{in}^3} = G [G - 1]^2. \quad (22)$$

P_{OIP3} can be written independently of P_{in}

$$P_{\text{OIP3}} = \left[\frac{H_{\text{IO}}^3}{D A_{\text{mat}}} \right]^{\frac{1}{2}}. \quad (23)$$

Eq. (11) and (23) relate the noise and OIP3 of an SOA to its material parameters N_{mat} and A_{mat} and its single-pass gain, G . In a more complex system involving multiple SOAs and multiple waveguide paths, S_{ASE} and D can be determined for each SOA, and the contribution summed at the receiver.

D. Noise and Distortion in a System with Multiple SOAs

In a PIC integrating multiple SOAs and waveguide paths like the ones schematically shown in Fig. 4(a) and (b), each SOA generates noise and distortion at the receiver depending on its total gain and location in the PIC. The single-pass SOA gain is determined by active material length. The location of an SOA in the PIC determines the wavelength-dependent transfer function from the input to the SOA, and the transfer function from the SOA to the output. The input-to-SOA transfer function determines P_{in} for that SOA, and the SOA-to-output transfer function determines the wavelength-dependent amplification or loss incurred by the IMD power and ASE power as they propagate to the receiver. From Eq. (11), the contribution to ASE noise at the receiver from the n^{th} SOA can be written

$$S_{\text{ASE},n}(\lambda) = N_{\text{mat}}(G_n - 1)H_{SO,n}(\lambda) \quad (24)$$

where $H_{SO,n}(\lambda)$ is the SOA-to-output power transfer function for the n^{th} SOA. Then, the total ASE power is incoherently summed at the receiver

$$S_{\text{ASE,total}}(\lambda) = \sum_{n=1}^N S_{\text{ASE},n}(\lambda). \quad (25)$$

Extending Eq. (22), the contribution to IMD at the receiver from the n^{th} SOA can be written

$$D_n(\lambda) = G_n [G_n - 1]^2 H_{IS,n}^3(\lambda) H_{SO,n}(\lambda) \quad (26)$$

where $H_{IS,n}(\lambda)$ is the input-to-SOA power transfer function for the n^{th} SOA. Since the distortion is created from a coherent signal, it is likewise coherent, and is created in-phase in each SOA. Therefore, the total IMD is coherently summed at the receiver

$$D_{\text{total}}(\lambda) = \left[\sum_{n=1}^N \sqrt{D_n(\lambda)} \right]^2. \quad (27)$$

The summation in (27) accounts for the in-phase coherent addition of the distortion created by each SOA. Eq. (27) is equivalent to simply adding the IMD electric fields from each SOA in-phase.

Once the ASE and IMD power contributions from each SOA are deduced at the output, the OIP3 power [Eq. (23)] and SFDR [Eq. (5)] are calculated as a function of wavelength. This ‘‘spot-SFDR’’ output reflects the noise and the distortion generated by two closely-spaced tones [$\omega_s \tau \ll 1$ in Eq. (20)] at each frequency. This is a different approach than the conventional method for reporting SFDR, which assumes constant distortion and noise across the receiver bandwidth. However, for wide bandwidth signals, the frequency dependence of distortion and noise should be considered [16]. The actual SFDR for a signal falling in the bandwidth of the filter depends on the signal bandwidth and placement in the filter passband,

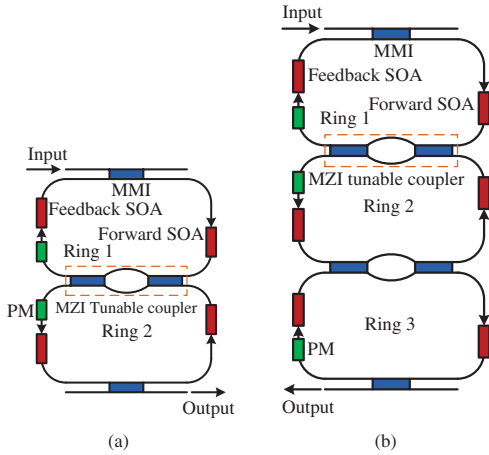


Fig. 4. Schematic representation of (a) second-order and (b) third-order coupled-ring filter. MMIs are in blue, SOAs in red, and phase modulators (PMs) in green.

and is a complex function of many-tone interactions [16]. However, the minimum and maximum spot-SFDR across the filter bandwidth provide an upper and lower bound for the third-order SFDR of an arbitrary signal.

E. Example: SOA on a Waveguide

The simple example of a single SOA on a waveguide demonstrates the importance of considering SFDR as a figure of merit in lightwave systems as opposed to relying solely on noise figure. We will consider two cases: 1) a lossy waveguide with an SOA at the beginning of the waveguide, and 2) a lossy waveguide with an SOA at the end of the waveguide. Using the equations in the preceding sections, it can be shown that the SFDR of case 2 is equal to

$$SFDR_2 = \left[\frac{n_{sp}/\zeta(G-1) + 1/H_{SO}}{n_{sp}/\zeta(G-1) + 1} \right]^{\frac{2}{3}} SFDR_1 \quad (28)$$

where H_{SO} is the SOA-to-output transfer function in case 1 and G is the SOA gain for both cases. $G > 1$, and for a lossy waveguide, $0 < H_{SO} < 1$, so the prefactor on the right hand side of Eq. (28) is always greater than 1. Therefore, the SFDR of case 2 is always greater than the SFDR of case 1, implying that for an arbitrary amount of lossy waveguide and an arbitrary amount of gain, it is always better to place the gain at the end of the waveguide. This is contrary to the typical noise-figure-based design rule, which is to place gain elements at the beginning of a string of lossy elements in order to minimize noise figure [17]. Eq. 28 is valid as long as the signal remains above the shot noise limit, which is the case for the PIC systems described in the next sections.

III. SIMULATION OF SFDR IN A PIC FILTER

A. Description of the PIC Filter

PICs incorporating SOAs can provide high-quality photonic signal processing for RF applications. As described above, noise and distortion generated in the SOAs negatively impact

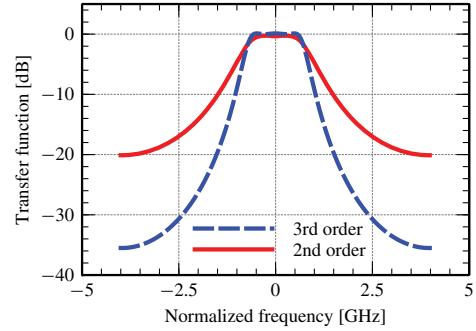


Fig. 5. Optical power transfer functions of second and third-order bandpass filters utilizing the same ring length and inter-ring coupling value. The filters are not normalized, but are shown at the passband gain which produces the optimal SFDR. Pole magnitudes were chosen to produce flat-topped bandpass filter responses [9].

signal fidelity. Using the results from Section II, we developed a simulation package that calculates the PIC-limited SFDR of an ideal RF-photonic link. The results are shown in Figs. 7–10. The simulation models an RF-photonic link utilizing coherent detection via optical heterodyne downconversion, and assumes an LO power much greater than the signal, allowing for a simple expression of SFDR in terms of optical powers [Eq. (5)]. Using the transfer functions of a PIC, the simulation package determines the PIC-limited SFDR of any design operating in the linear amplification regime. The SFDR in a real system may be lower due to laser RIN and receiver noise, and depends on the particular transmitter and receiver utilized, and on the optical LO power. Coupled-ring filters like the one described in [9] are adept at creating high-quality bandpass filters [23]. Here, we investigate the SFDR of such systems. [9] describes how the input-to-output transfer functions of coupled-ring PIC filters are calculated. Similarly, input-to-SOA and SOA-to-output transfer functions can be derived using Mason's Formula [24]. Fig. 4(a) and (b) schematically represent the second and third-order coupled ring filters investigated here. Fig. 5 shows their transfer functions.

From Eq. (11) and (20), it is clear that minimizing total SOA gain in a PIC filter while maintaining the desired functionality is crucial for obtaining high SFDR. Within rings, SOAs compensate for loss in order to obtain pole magnitudes sufficient for synthesis of flat-topped bandpass filters. Therefore, low waveguide propagation loss and coupler insertion loss directly translate to higher SFDR. In general, trade-offs exist between filter shape ideality and SFDR. High-quality flat-topped bandpass filters with high extinction and fast stop-band roll-off require high-order filters with high pole magnitudes [23]. Increasing the filter order (number of rings) increases waveguide propagation loss and in turn requires more gain. In addition, higher pole magnitudes require higher SOA gain. Increasing both filter order and pole magnitudes therefore decreases SFDR.

In order to reduce filter bandwidth, ring delay lengths must be increased and/or pole magnitudes must be increased. Adding waveguide length adds propagation loss. Therefore narrow bandwidth filters produce a lower SFDR per unit

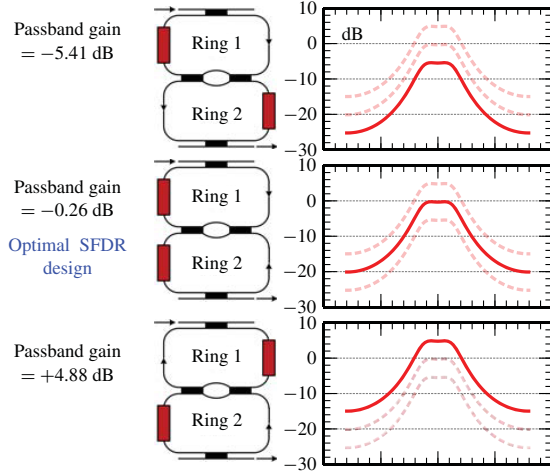


Fig. 6. Schematic representation of a second-order coupled ring bandpass filter with certain SOA configurations and the resulting transfer function. (a) Lowest passband gain configuration, with both SOAs in the feedback segments. (b) Optimal SFDR configuration with a passband gain near 0 dB. The ring 1 SOA is in the feedback segment and the ring 2 SOA is in the forward segment. (c) Highest passband gain configuration, with both SOAs in the forward waveguide segments.

TABLE I
SIMULATION PARAMETERS

Symbol	Parameter	Value
n_{sp}	Population inversion factor	1.3
N_{mat}	ASE material parameter [15]	1.78×10^{-9} J
A_{mat}	IMD material parameter [15]	127 W^{-2}
P_S	Saturation power [15]	19.1 dBm
n_g	Group index	3.78
λ	Center wavelength	$1.55 \mu\text{m}$
α_{ip}	Passive waveguide loss [15]	1.0 cm^{-1}
α_i	Active waveguide loss [15]	2.0 cm^{-1}
Γ_g	Modal gain [15]	19.7 cm^{-1}

of bandwidth than wide bandwidth filters. Filter geometry can also affect the filter SFDR. A coupled-ring system is investigated here, because such systems inherently require less SOA gain than cascaded-ring systems (systems where there is no feedback between rings). A fraction of the input power to each ring is discarded in a cascaded-ring system in the input coupler of each ring [9]. This excess loss decreases SFDR compared to coupled-ring systems.

B. Simulation Results and Discussion

Table I displays the simulation parameters used in the following results. All parameters are kept constant unless otherwise noted. The material constant A_{mat} is extracted from IMD measurements of a new high-dynamic range InGaAsP/InP integration platform [15]. This platform integrates deeply-etched waveguides and low-confinement-factor quantum-well (QW) SOAs to allow for high SFDR PICs with tight waveguide bends and low waveguide propagation loss. The filters in [9] are integrated on a similar platform. Using Γ_g and α_i from [15], we assumed $n_{sp} = 1.3$ [25] in order to find N_{mat} . As a check of the IMD theory, the linewidth enhancement factor

TABLE II
2nd-ORDER FILTER SIMULATION PARAMETERS

Symbol	Parameter	Value
p_{r1}, p_{r2}	Intrinsic pole magnitude 1, 3 [9]	0.58
C	Inter-ring power coupling	15%
	Filter 3 dB bandwidth	1.75 GHz
	Maximum extinction ratio	19.8 dB
	Maximum roll-off	11.7 dB/GHz
	MMI insertion loss	0.5 dB
	Ring length	1.0 cm
	Feedback to forward waveguide ratio	10.0

TABLE III
3rd-ORDER FILTER SIMULATION PARAMETERS

Symbol	Parameter	Value
p_{r1}, p_{r3}	Intrinsic pole magnitude 1, 3 [9]	0.61
p_{r2}	Intrinsic pole magnitude 2 [9]	0.85
C	Inter-ring power coupling	15%
	Filter 3 dB bandwidth	1.55 GHz
	Maximum extinction ratio	35.6 dB
	Maximum roll-off	27.7 dB/GHz
	MMI insertion loss	0.5 dB
	Ring length	1.0 cm
	Feedback to forward waveguide ratio	10.0

is determined from A_{mat} in (20) to be $\alpha = 1.37$. This is low for InGaAsP/InP-based QW devices, but is within an order of magnitude of the expected value [26], showing that the theory of IMD generation is reasonably accurate. With the A_{mat} parameter extracted from real measurements, we expect the results presented here to be realistic.

In the following sections we present simulation results for second and third-order coupled-ring bandpass filters. Each SFDR result is accompanied by other system parameters that result from the particular configuration of SOAs and waveguides used for that filter. For instance, in a coupled-ring system, each ring has a forward and feedback segment of waveguide. In order to create a certain filter shape, the pole magnitude of each ring is set by the amount of gain and loss in the ring [9]. However, the IMD, ASE, and passband gain characteristics of the filter are dependent on the distribution of waveguide length and SOA gain between the forward and feedback segments. The shape of the filter does not change as long as the total gain and loss in each ring remains the same. However, SFDR is dependent on the IMD, ASE, and total input-to-output transfer function (H_{IO}). An optimal SFDR can be found, or passband gain modified, by adjusting the distribution of waveguide and SOA between the forward and feedback segments of each ring. The “shape” of the filter is here defined as the dB transfer function. Fig. 6 shows several SOA configurations that result in the same second-order filter shape, but different levels of passband gain. As SOA distribution is varied from fully in the feedback segment to fully in the forward segment in either ring, the passband gain of the filter will increase. The filter shape will not change however, as long as the total SOA gain in the ring remains the same. The distribution of waveguide length between the forward and feedback segments also affects the passband gain. The feedback to forward ratio given in Tables II, III is defined as the ratio of the feedback waveguide length to the forward waveguide length. As this ratio is varied from small to large values, the passband gain of the filter will increase (without any change

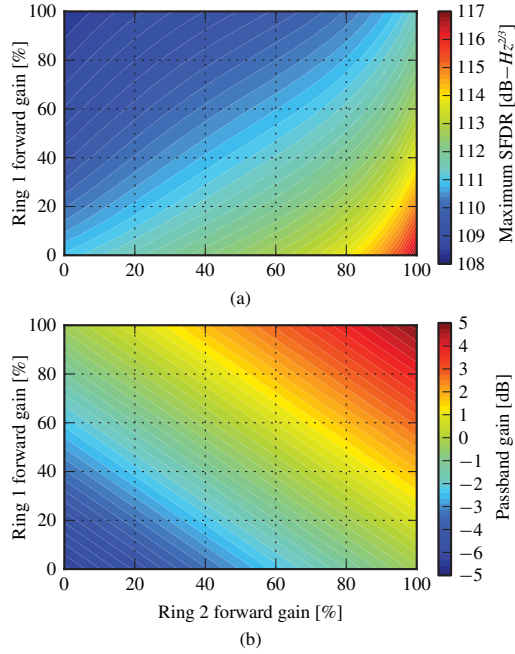


Fig. 7. (a) Peak SFDR and (b) peak passband gain across the 3 dB bandwidth of a second-order bandpass filter as a function of the distribution of SOA gain between the forward and feedback segments of rings 1 and 2. Total SOA gain per ring is held constant in order to produce the same filter shape for all points on the map. 100% forward gain means that all of the SOA is located in the forward segment, and none is located in the feedback segment. There is a clear optimal SFDR point when the ring 1 SOA is fully in the feedback segment and the ring 2 SOA is fully in forward segment. The passband gain can be swept from -5.4 dB to $+4.9$ dB by adjusting the SOA placement.

to the filter shape) as waveguide propagation loss is removed from the forward segment and added to the feedback segment.

1) *Second-Order Coupled-Ring Filter*: Fig. 4 shows a schematic representation of a second-order coupled ring bandpass filter and Fig. 5 displays the transfer function of a filter across one free spectral range (FSR) with specifications outlined in Table II. A more detailed signal flow diagram can be found in [9]. The filter has a bandwidth of 1.75 GHz, a maximum extinction ratio of 19.8 dB, and a maximum stopband roll-off slope of 11.7 dB/GHz. Like the design described in [9], Mach-Zehnder Interferometer (MZI) tunable couplers comprised of two multi-mode interference (MMI) couplers are modeled between the coupled rings. These allow for complete control of inter-ring coupling. The inter-ring coupling value sets the bandwidth of the filter [9]. Input and output couplers are single MMI couplers. Total ring length is 10 mm, which is split between the couplers and the forward and feedback waveguides of each ring, as given by the feedback to forward ratio in Table II.

With the parameters in Table II, and with all SOAs placed at the end of their respective waveguide segments, there are two remaining degrees of freedom: the distribution of gain between the forward and feedback waveguide segments in the two rings. Fig. 7(a) plots the maximum SFDR in the 3 dB bandwidth of the filter as a function of these two variables. There is a clear maximum when the ring 1 SOA is fully in

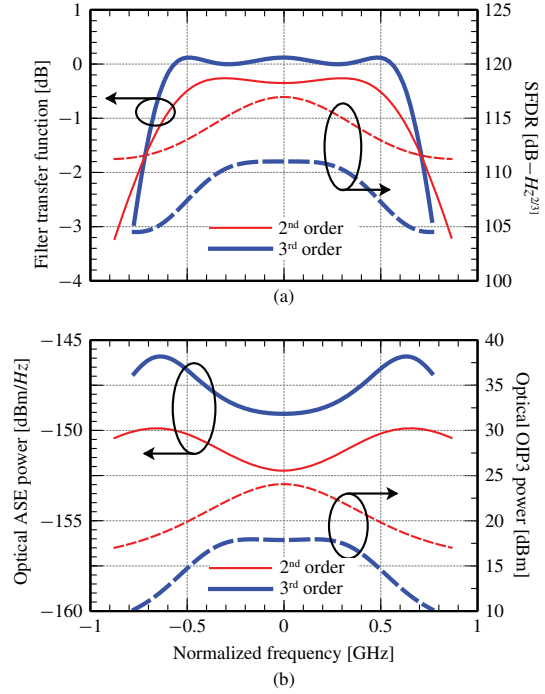


Fig. 8. (a) Second and third-order filter transfer functions and spot-SFDR over the 3 dB bandwidth of the filters. SFDR falls off away from the center of the filter. However, the third-order filter has a wider constant-SFDR plateau that extends for 0.66 GHz with less than 1 dB variation. (b) ASE power and OIP3 power over the 3 dB bandwidth of the second and third-order filters. There is a clear degradation of ASE noise and OIP3 power at the edges of the filter passband.

the feedback segment, and the ring 2 SOA is fully in the forward segment. Intuitively, this can be explained as follows. As seen in Section II-E, IMD is the dominant source of SFDR degradation for an SOA on a waveguide, and the highest SFDR is obtained by limiting the optical power in the SOA. In the example of Section II-E, this is accomplished by placing the SOA at the end of a lossy waveguide. In the second-order coupled ring filter, this is accomplished by placing the ring 1 SOA at the end of the feedback segment. In ring 2, there is no added benefit to placing the SOA in the feedback segment, since the SOA in ring 1 is already the IMD limiting factor. In this case, placing the ring 2 SOA in the feedback segment reduces IMD and ASE at the output, but at the expense of reduced passband gain. Since OIP3 power is proportional to $H_{IO}^{3/2}$ [Eq. (23)], and the ring 1 SOA is already the IMD limiting factor, the best SFDR is obtained when the ring 2 SOA is placed in the forward segment.

Fig. 7(b) plots the passband gain of the second-order filter as a function of forward/feedback gain distribution in the two rings. The maximum gain is obtained when the SOAs in both rings are fully in the forward segment, but any passband gain between -5.4 dB and $+4.9$ dB is attainable. The optimal SFDR of 117.0 dB \cdot Hz $^{2/3}$ is obtained for a passband gain of -0.26 dB. Fig. 6(b) shows this configuration, along with (a) the lowest passband gain configuration, and (c) the highest passband gain configuration. As mentioned in Section III-B,

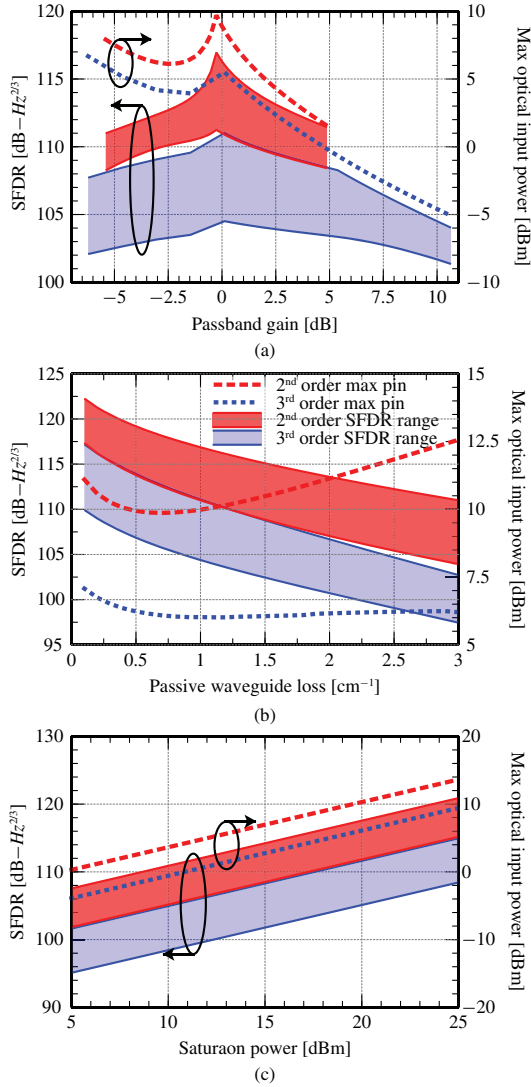


Fig. 9. SFDR range and maximum optical input power (9) seen over the 3 dB bandwidth of the second and third-order filters (a) as a function of passband gain, (b) as a function of passive waveguide loss, and (c) as a function of SOA saturation power. The passband gain is varied by adjusting the distribution of SOA gain in the forward and feedback segments of waveguide in each ring. Since there are multiple ways to achieve each passband gain level, the arrangement that generates the highest SFDR is plotted here. The methods for generating these curves are discussed in Sections III-B.1 and III-B.2. SFDR degrades for both types of filters with increased propagation loss, and increases for increased saturation power. The latter relationship is very simple, and is given by $\text{SFDR} \propto P_S^{2/3}$. Continued experimental increases in saturation power and decreases in passive waveguide loss bode well for photonic integrated filters. The integration platform in [15] (and used for all results in this paper) has $\alpha_{ip} = 1 \text{ cm}^{-1}$ and $P_S = 19.1 \text{ dBm}$.

the passband gain can also be adjusted by varying the feedback to forward waveguide length ratio.

Fig. 8 shows the transfer function, SFDR, OIP3 power, and ASE power as a function of frequency across the 3 dB bandwidth of the filter at the optimal SFDR point. ASE power and IMD power are higher at the edges of the filter (OIP3 power is lower), causing a degradation in the SFDR.

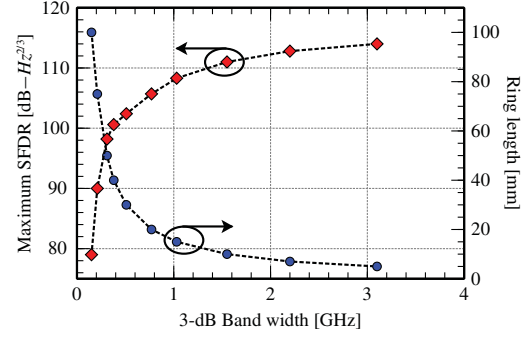


Fig. 10. Maximum SFDR in the 3 dB bandwidth of third-order filters as a function of the bandwidth. Also plotted are the ring lengths needed to reach such bandwidths. SFDR degrades quickly below 1 GHz due to the inverse relationship between ring length and bandwidth. Waveguide propagation loss increases with ring length, negatively impacting SFDR.

Fig. 9 show the effect of varying passband gain, passive waveguide loss, and SOA saturation power on SFDR for both second and third-order filters. The range of SFDR across the 3 dB bandwidth of the filter is plotted along with the optical input power needed to obtain the peak SFDR. In Fig. 9(a), passband gain is varied in such a way as to maximize the SFDR for each point. First, starting with both ring 1 and ring 2 SOA distributions fully in the feedback segment (the point of minimum passband gain), the ring 2 SOA distribution is varied smoothly from fully in the feedback segment to fully in the forward segment. This is the point of maximum SFDR. Then, the ring 1 SOA is varied smoothly from fully in the feedback segment to fully in the forward segment to complete the curve with both ring 1 and ring 2 SOAs fully in the forward segment (the point of maximum passband gain). In Fig. 9(b), (c) as expected, increased passive waveguide loss degrades SFDR, and higher saturation power improves SFDR. The integration platform demonstrated in [15] achieves improvements in both of these parameters over previous active integration platforms with deeply etched waveguides. The maximum input power is high at low loss values because very little gain is needed to compensate for waveguide loss, so very little distortion is generated. However, maximum input power begins to increase again above $\sim 1 \text{ cm}^{-1}$ because high propagation losses degrade signal power, and higher SOA gain pushes up the noise floor.

2) *Third-Order Coupled-Ring Filter*: A third-order coupled ring filter with same inter-ring coupling value and ring length as the second-order filter in Section III-B.1 can provide narrower bandwidth, higher extinction, and faster stopband roll-off at the expense of a higher pole magnitude in the center ring [9]. The higher pole magnitude and increased waveguide propagation loss associated with the extra ring result in a degradation in SFDR compared to the second-order filter. Fig. 4 is a schematic representation of a third-order coupled ring filter, and Fig. 5 displays the transfer function of a filter across one FSR with specifications outlined in Table III. Compared with the second-order filter, the extinction ratio is improved by 15.8 dB to 35.6 dB, and the maximum roll-off slope is improved by 16 dB/GHz

to 27.7 dB/GHz. The bandwidth of the third-order filter is 1.55 GHz.

Similarly to the second-order filter, there is an optimal design and passband gain which maximizes the SFDR. Like the second-order design, the SOA in ring 1 is located fully within the feedback segment. To complete the design, the ring 2 SOA is placed fully in the forward segment, and the ring 3 SOA is placed fully in the feedback segment. This provides a passband gain of 0.12 dB and a maximum SFDR of $111.0 \text{ dB} \cdot \text{Hz}^{2/3}$. As shown in Fig. 9(a), passband gain can be varied from -6.22 dB to 10.65 dB by adjusting the distribution of SOAs in the rings with a penalty in SFDR. The gain is varied in such a way as to maximize the SFDR for each point, and can be varied further by adjusting the feedback to forward waveguide length ratio. In order to produce Fig. 9(a), for the lowest passband gain, all SOAs were located fully in the feedback segment of their respective rings. Then, the ring 2 SOA is varied smoothly from fully in the feedback segment to fully in the forward segment. This is the arrangement that produces the optimum SFDR. In order to increase passband gain beyond this point, the ring 1 SOA is varied smoothly from fully in the feedback segment to fully in the forward segment. Once this point is reached, the ring 3 SOA distribution is varied in a similar fashion until all SOAs are located fully in the forward segments of their respective rings. This is the point of maximum passband gain.

Fig. 8 shows the transfer function, SFDR, OIP3 power, and ASE power as a function of frequency across the 3 dB bandwidth of the filter at the optimal SFDR point. Like the second-order filter, ASE power and IMD power are higher at the edges of the filter (OIP3 power is lower), causing a degradation in the SFDR. Fig. 9(b), (c) show the effect of variations in passive waveguide loss and SOA saturation power. As expected from substituting Eq. (20) into (21) and the result into (5), SFDR varies linearly with saturation power on a dB-dB scale with a slope of $2/3$ for both second and third-order filters.

Fig. 10 shows the variation of SFDR across filters of varying bandwidth. In order to reduce bandwidth, ring lengths are increased, increasing waveguide propagation loss. The resulting reduction in SFDR accelerates below 1 GHz because of the inverse relationship between ring length and bandwidth. Ever more ring length is required to reduce the bandwidth by an appreciable amount. At 0.15 GHz, 100 mm of waveguide is required per ring, degrading SFDR to $79.0 \text{ dB} \cdot \text{Hz}^{2/3}$. With current waveguide propagation loss and saturation power numbers, the active InGaAsP/InP material platform is useful for coupled-ring bandpass filters with bandwidths greater than 1 GHz.

IV. CONCLUSION

In this paper, we have derived an expression for the PIC-limited SFDR of an RF-photonics link incorporating integrated optical amplifiers in terms of optical powers. The model treats ASE noise, shot noise, and IMD rigorously for a system operating below saturation and in the linear small-signal regime. We have shown simulation results for two systems

in particular: second and third-order coupled-ring bandpass filters with 10 mm ring lengths and $\sim 1.75 \text{ GHz}$ bandwidths. However, the model presented in Section II-D is applicable to any active analog signal processing system operating in the linear regime. Our examples also utilize results from a new high saturation power integration platform [15]. The results depict trade-offs between filter quality and SFDR performance, with a peak SFDR of $117.0 \text{ dB} \cdot \text{Hz}^{2/3}$ for a second-order filter. A more reasonable third-order filter offering 35.6 dB of extinction results in a peak SFDR of $111.0 \text{ dB} \cdot \text{Hz}^{2/3}$. Recent results measuring the SFDR of RF-photonics links incorporating passive integrated filters are limited to the same range by modulator nonlinearities, link loss, and receiver noise. [2] measures a $105 \text{ dB} \cdot \text{Hz}^{2/3}$ SFDR for a link incorporating an all passive CMOS filter. In their experiment, an attenuator simulates the filter insertion loss in order to avoid excess chip fiber-coupling losses. The filter is assumed to have 6 dB passband insertion loss. [11] also measures a link by substituting an attenuator for a passive filter and reports a maximum SFDR of $108 \text{ dB} \cdot \text{Hz}^{2/3}$ for a link that includes the attenuator and does not use distortion compensation methods. Our results here show that the PIC-limited SFDR of a link incorporating active filters is comparable with that of current passive links. More investigation is required to determine to what extent the modulator nonlinearities, laser RIN noise, and receiver noise of a real link degrade the theoretical PIC-limited SFDR derived in this paper.

Active PIC filters have important advantages over passive filters, including operation without insertion loss or with passband gain, reducing demands on the optical transmitter and receiver. In addition, active filters can synthesize very high quality filter shapes like those in [9]. SOAs are designed to provide the optimal SFDR, but also add an extra element of tuning for “tweaking” filter shapes in-situ. In particular, as filters are tuned in frequency via current-injection phase modulators, loss is introduced via free-carrier absorption. SOA current can be modified in small amounts to retain an optimal shape over the frequency tuning range with negligible effect on SFDR. Continued improvements in passive waveguide loss and SOA saturation power can drive up SFDR such that RF-photonics links are limited by other mechanisms. Practical limits on saturation power in the integration platform discussed here are determined by the trade-off between gain and saturation power, by higher order modes in the transverse direction, and by two-photon absorption [15]. Improvements will need to be made, however, in order to push the SFDR of practical active photonic microwave filters into the $120 \text{ dB} \cdot \text{Hz}^{2/3}$ range required for military radar applications [27]. With the current state of the art in low propagation loss and high saturation power integration platforms, bandpass filters in the InGaAsP/InP material system are limited to bandwidths greater than 1 GHz. For narrower bandwidths, low-loss hybrid-integration platforms such as hybrid InP/Si could provide a solution [8]. For example, with all other parameters kept constant, a reduction in passive waveguide loss by a factor of 10 to 0.1 cm^{-1} would make possible a ten-fold increase in ring length. This would create 0.15 GHz filters with SFDR equal to the 1.55 GHz filters presented here (see Fig. 10).

The ability to implement other active components on-chip along side optical signal processing circuits continues to make the active InGaAsP/InP material system interesting for RF-photonics. Active material systems also provide design versatility that is not possible with passive filters. With a high saturation power material platform and optimal SFDR design, active photonic integrated circuits can provide high quality and high fidelity signal processing for RF-photonics systems.

REFERENCES

- [1] J. Yao, "Microwave photonics," *J. Lightw. Technol.*, vol. 27, no. 3, pp. 314–335, Feb. 2009.
- [2] K.-Y. Tu, M. S. Rasras, D. M. Gill, S. S. Patel, Y.-K. Chen, A. E. White, A. Pomerene, D. Carothers, J. Beattie, M. Beals, J. Michel, and L. C. Kimerling, "Silicon RF-photonics filter and down-converter," *J. Lightw. Technol.*, vol. 28, no. 20, pp. 3019–3028, Oct. 2010.
- [3] T. K. Woodward, T. C. Banwell, A. Agarwal, P. Toliver, and R. Menendez, "Signal processing in analog optical links," in *Proc. IEEE Conf. Avionics Fiber-Opt. Photon. Technol.*, San Antonio, TX, 2009, pp. 17–18.
- [4] J. Capmany, B. Ortega, and D. Pastor, "A tutorial on microwave photonic filters," *J. Lightw. Technol.*, vol. 24, no. 1, pp. 201–229, Jan. 2006.
- [5] M. S. Rasras, D. M. Gill, S. S. Patel, K.-Y. Tu, Y.-K. Chen, A. E. White, A. T. S. Pomerene, D. N. Carothers, M. J. Grove, D. K. Sparacino, J. Michel, M. A. Beals, and L. C. Kimerling, "Demonstration of a fourth-order pole-zero optical filter integrated using CMOS processes," *J. Lightw. Technol.*, vol. 25, no. 1, pp. 87–92, 2007.
- [6] N.-N. Feng, P. Dong, D. Feng, W. Qian, H. Liang, D. C. Lee, J. B. Luff, A. Agarwal, T. Banwell, R. Menendez, P. Toliver, T. K. Woodward, and M. Asghari, "Thermally-efficient reconfigurable narrowband RF-photonics filter," *Opt. Express*, vol. 18, no. 24, pp. 24648–24653, 2010.
- [7] P. Dong, N.-N. Feng, D. Feng, W. Qian, H. Liang, D. C. Lee, B. J. Luff, T. Banwell, A. Agarwal, P. Toliver, R. Menendez, T. K. Woodward, and M. Asghari, "GHz-bandwidth optical filters based on high-order silicon ring resonators," *Opt. Express*, vol. 18, no. 23, pp. 23784–23789, 2010.
- [8] H.-W. Chen, A. Fang, J. D. Peters, Z. Wang, J. Bovington, D. Liang, and J. Bowers, "Integrated microwave photonic filter on a hybrid silicon platform," *IEEE Trans. Microw. Theory Tech.*, vol. 58, no. 11, pp. 3213–3219, Nov. 2010.
- [9] R. S. Guzzon, E. J. Norberg, J. S. Parker, L. A. Johansson, and L. A. Coldren, "Integrated InP-InGaAsP tunable coupled ring optical bandpass filters with zero insertion loss," *Opt. Express*, vol. 19, no. 8, pp. 7816–7826, 2011.
- [10] E. J. Norberg, R. S. Guzzon, J. Parker, L. A. Johansson, and L. A. Coldren, "Programmable photonic microwave filters monolithically integrated in InP/InGaAsP," *J. Lightw. Technol.*, vol. 29, no. 11, pp. 1611–1619, Jun. 2011.
- [11] A. Agarwal, T. Banwell, and T. K. Woodward, "Optically filtered microwave photonic links for RF signal processing applications," *J. Lightw. Technol.*, vol. 29, no. 16, pp. 2394–2401, Aug. 2011.
- [12] T. Numai, *Laser Diodes and Their Applications to Communications and Information Processing*. New York: Wiley, 2010.
- [13] R. M. Jopson and T. E. Darcie, *Coherence, Amplification, and Quantum Effects in Semiconductor Lasers*, Y. Yamamoto, Ed. New York: Wiley, 1991.
- [14] P. Berger, J. Bourderionnet, M. Alouini, F. Bretenaker, and D. Dolfi, "Theoretical study of the spurious-free dynamic range of a tunable delay line based on slow light in SOA," *Opt. Express*, vol. 17, no. 22, pp. 20584–20597, 2009.
- [15] E. Norberg, R. S. Guzzon, J. S. Parker, S. DenBaars, and L. Coldren, "An InGaAsP/InP integration platform with low loss deeply etched waveguides and record SOA RF-linearity," in *Proc. Eur. Conf. Opt. Commun.*, Geneva, Switzerland, Sep. 2011, pp. 1–3.
- [16] J. Lerdworatawee and W. Namgoong, "Revisiting spurious-free dynamic range of communication receivers," *IEEE Trans. Circuits Syst I*, vol. 53, no. 4, pp. 937–943, Apr. 2006.
- [17] D. M. Baney, P. Gallion, and R. S. Tucker, "Theory and measurement techniques for the noise figure of optical amplifiers," *Opt. Fiber Technol.*, vol. 6, no. 2, pp. 122–154, 2000.
- [18] G. P. Agrawal, "Population pulsations and nondegenerate four-wave mixing in semiconductor lasers and amplifiers," *J. Opt. Soc. Amer. B*, vol. 5, no. 1, pp. 147–159, 1988.
- [19] T. E. Darcie and R. M. Jopson, "Nonlinear interactions in optical amplifiers for multifrequency lightwave systems," *Electron. Lett.*, vol. 24, no. 10, pp. 638–640, May 1988.
- [20] Y. C. Chung, J. M. Wiesenfeld, G. Raybon, U. Koren, and Y. Tu, "Intermodulation distortion in a multiple-quantum-well semiconductor optical amplifier," *Photon. Technol. Lett.*, vol. 3, no. 2, pp. 130–132, Feb. 1991.
- [21] M. J. Adams, D. A. O. Davies, M. C. Tatham, and M. A. Fisher, "Nonlinearities in semiconductor laser amplifiers," *Opt. Quantum Electron.*, vol. 27, no. 1, pp. 1–13, Jan. 1995.
- [22] T. Marozsak, E. Udvardy, and T. Bercei, "Transmission characteristics of all semiconductor fiber optic links carrying microwave channels," in *Proc. Eur. Microw. Conf.*, Oct. 2000, pp. 1–4.
- [23] C. K. Madsen and J. H. Zhao, *Optical Filter Design and Analysis: A Signal Processing Approach*. New York: Wiley, 1999.
- [24] P. Saeung and P. P. Yupapin, "Generalized analysis of multiple ring resonator filters: Modeling by using graphical approach," *Optik Int. J. Light Electron Opt.*, vol. 119, no. 10, pp. 465–472, Aug. 2008.
- [25] T. Saitoh and T. Mukai, *Coherence, Amplification, and Quantum Effects in Semiconductor Lasers*, Y. Yamamoto, Ed. New York: Wiley, 1991.
- [26] M. Osinski and J. Buus, "Linewidth broadening factor in semiconductor lasers—an overview," *IEEE J. Quantum Electron.*, vol. 23, no. 1, pp. 9–29, Jan. 1987.
- [27] J. Choe, "Defense RF systems: Future needs, requirements, and opportunities for photonics," in *Proc. IEEE Conf. Microw. Photon.*, 2005, pp. 307–310.

Robert S. Guzzon received the B.S. degree in electrical engineering and physics from Lehigh University, Bethlehem, PA, in 2007. He is currently pursuing the Ph.D. degree in electrical engineering with the University of California, Santa Barbara.

His current research interests include the design and fabrication of versatile photonic integrated microwave filter systems that achieve high spurious free dynamic range, large-scale photonic integration, and microwave photonic signal processing.

Erik J. Norberg received the B.S. and M.S. degrees in engineering nanoscience from Lund University, Lund, Sweden, in 2008. He is currently pursuing the Ph.D. degree in electrical engineering with the University of California, Santa Barbara.

He is currently working on the development of high dynamic range integrated optical filters for microwave signal processing. His current research interests include the design and metal organic chemical vapor deposition growth of large scale photonic integrated circuits on InP.

Larry A. Coldren (F'82) received the Ph.D. degree in electrical engineering from Stanford University, Stanford, CA, in 1972.

He is the Fred Kavli Professor of optoelectronics and sensors and the Acting Richard A. Auhll Dean of engineering with the University of California, Santa Barbara (UCSB). After 13 years in the research area with Bell Laboratories, Holmdel, NJ, he joined UCSB in 1984, where he is currently with the Department of Materials and the Department of Electrical and Computer Engineering. In 1990, he co-founded optical concepts, later acquired as Gore Photonics, to develop novel vertical-cavity surface-emitting laser (VCSEL) technology, and in 1998, he co-founded Agility Communications, Inc., Goleta, CA, later acquired by JDS Uniphase Corporation (JDSU), Milpitas, CA, to develop widely tunable integrated transmitters. At Bell Laboratories, he was initially on waveguided surface-acoustic-wave signal processing devices and coupled-resonator filters. He later developed tunable coupled-cavity lasers using novel reactive-ion etching technology that he created for the new InP-based materials. At UCSB, he continued work on multiple-section tunable lasers, in 1988, inventing the widely tunable multi-element mirror concept, which is currently used in some JDSU products. Near this same time period, he also made seminal contributions to efficient VCSEL designs that continue to be implemented in practical devices to present. More recently, his group has developed high-performance InP-based photonic integrated circuits as well as high-speed VCSELS, and they continue to advance the underlying materials growth and fabrication technologies. He has authored or co-authored over 1000 journals and conference papers, seven book chapters, and one textbook and has been issued 63 patents. He has presented dozens of invited and plenary talks at major conferences.

Prof. Coldren is a member of the National Academy of Engineering. He was a recipient of the John Tyndall and the Aron Kressel Awards in 2004 and 2009, respectively.

Indium Phosphide Photonic Integrated Circuits for Coherent Optical Links

Pietro R. A. Binetti, Mingzhi Lu, Erik J. Norberg, Robert S. Guzzon, John S. Parker, Abirami Sivananthan, Ashish Bhardwaj, Leif A. Johansson, *Member, IEEE*, Mark J. Rodwell, *Fellow, IEEE*, and Larry A. Coldren, *Fellow, IEEE*

(Invited Paper)

Abstract—We demonstrate photonic circuits monolithically integrated on an InP-based platform for use in coherent communication links. We describe a technology platform that allows for the integration of numerous circuit elements. We show examples of an integrated transmitter which offers an on-chip wavelength-division-multiplexing source with a flat gain profile across a 2 THz band and a new device design to provide a flattened gain over a 5 THz band. We show coherent receivers incorporating an integrated widely tunable local oscillator as well as an optical PLL. Finally, we demonstrate a tunable optical bandpass filter for use in analog coherent radio frequency links with a measured spurious-free dynamic range of 86.3 dB-Hz^{2/3} as well as an improved design to exceed 117 dB-Hz^{2/3}.

Index Terms—Coherent detection, microwave photonics, monolithic integrated circuits, optical filters, optical receivers, optical transmitters, photonic integrated circuits.

I. INTRODUCTION

TRADITIONALLY, sufficient performance has been provided by optical links using on-off keying (OOK) for modulating data and direct detection for receiving data. Examples include intensity modulation for digital or analog optical links and time-domain reflectivity for ranging or sensing applications such as pulsed light detection and ranging (LIDAR) or optical time domain reflectometry (OTDR) [1]. Phase encoded signals and the coherent receiver necessary to detect them, such as homodyne detection or heterodyne detection via a local oscillator (LO), are more technically difficult and have been used only where the significant performance or architectural advantages of such links are required. However,

Manuscript received August 5, 2011; revised November 3, 2011; accepted November 25, 2011. Date of current version January 24, 2012. This work was supported in part by the Defense Advanced Research Projects Agency Microsystems Technology Office, under Contract including Photonic Integration for Coherent Optics and Photonic Analog Signal Processing Engines with Reconfigurability. Device fabrication was done in the UCSB nanofabrication facility.

P. R. A. Binetti, M. Lu, E. J. Norberg, R. S. Guzzon, J. S. Parker, A. Sivananthan, L. A. Johansson, M. J. Rodwell, and L. A. Coldren, are with the Department of Electrical Engineering, University of California, Santa Barbara, CA 93106 USA (e-mail: pbinetti@ece.ucsb.edu; mlu@ece.ucsb.edu; norberg@ece.ucsb.edu; guzzon@ece.ucsb.edu; JParker@ece.ucsb.edu; asivananthan@umail.ucsb.edu; leif@ece.ucsb.edu; rodwell@ece.ucsb.edu; coldren@ece.ucsb.edu).

A. Bhardwaj was with the Department of Electrical Engineering, University of California, Santa Barbara, CA 93106 USA. He is now with JDS Uniphase Corporation, San Jose, CA 95134 USA (e-mail: Ashish.Bhardwaj@jdsu.com).

Color versions of one or more of the figures in this paper are available online at <http://ieeexplore.ieee.org>.

Digital Object Identifier 10.1109/JQE.2011.2178590

in the past decade, interest in coherent optical links has grown for both analog and digital communications because of their increasingly stringent performance requirements.

Today's data traffic in residential, business, and mobile digital communications is mainly driven by a combination of video, social networking and advanced collaboration applications, often referred to as "visual networking." This is illustrated in Figure 1, which shows the current and forecast trend of the Internet data traffic in Exabytes (1 Exabyte = 1E18 Bytes) for some of the most resource-hungry applications, video being the largest [2]. In order to meet the exponentially growing bandwidth demands of such applications, fiber-optic networks need to dramatically increase their capacity to offer a suitable communication infrastructure. This can be done by deploying more fiber channels in parallel, or in a more cost-effective and energy-efficient way, by increasing the spectral efficiency of the existing channels. Thus, enhanced spectral efficiency (SE) motivated the research and development of more complex modulation formats, such as phase-shift keying (PSK) modulation formats, at the expense of more complex hardware requirements, with respect to the simpler OOK technology [3], [4]. Higher spectral efficiency (SE) is available using quadrature phase-shift keying (QPSK)—double the SE, or polarization-multiplexed QPSK (PM-QPSK) modulation—quadruple the SE, as shown in [5]. A higher sensitivity and improved dispersion compensation is also possible when a coherent optical link is used to (de)modulate real and imaginary parts of the optical signal [3], [5]. Even higher spectral efficiency is possible by modulating both the amplitude and phase, quadrature-amplitude modulation (QAM), to more completely utilize the available complex vector-field space, given the signal-to-noise and dynamic range at the receiver, as exhaustively discussed and demonstrated in [5].

Analog optical communications benefit from coherent links as well. Optical phase modulation offers highly-linear optical modulators and very large optical modulation depth, allowing high-dynamic-range optical links to be demonstrated [6]. These benefits extend to sensing as well, where frequency modulated continuous-wave (FMCW) light ranging offers improved sensitivity and resolution compared to time-domain ranging techniques [7].

The larger hardware complexity and cost required for the implementation of a coherent optical link provides motivation for the research and the applications of photonic integrated

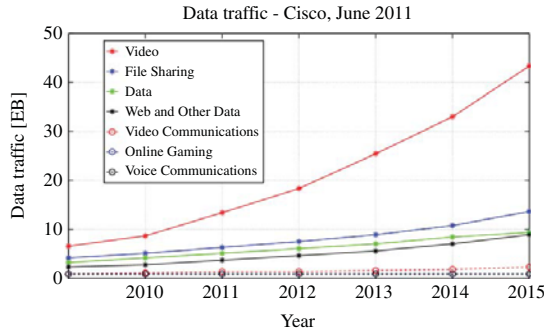


Fig. 1. Cisco "Visual Network Index": current view and forecast of the Internet data traffic (in Exabytes) for some of the most popular applications. Source publicly available at <http://www.cisco.com>.

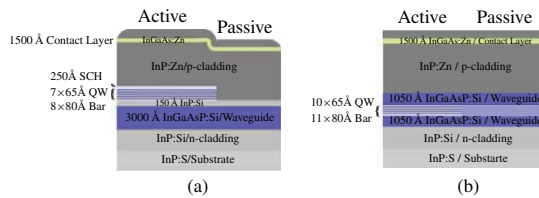


Fig. 2. (a) OQW and (b) CQW material platforms for high saturation power and high gain, respectively.

circuits (PICs) in this field. PICs offer a substantial cost reduction due to a greatly reduced system footprint, lower power consumption and packaging costs, and the possibility of performing many signal processing steps in the optical domain, thus avoiding the low-speed and power-hungry optical-to-electronic-to-optical (OEO) conversions [8], [9]. State-of-the-art PICs employing the above mentioned technologies for coherent-link applications have been recently reported in [6], [10], [13].

In this paper, we will overview recent advances in integrated photonic ICs for coherent communication and sensing applications within our research group at UCSB and present new results for each PIC. The development of PICs which take advantage of the compactness and phase stability of integrated optical waveguides to realize coherent building blocks for a wide range of applications will be included. In Section II, we describe the integration platform which we developed to monolithically integrate such building blocks. Afterwards, some examples will be given. First, efforts to create a digitally-controlled widely-tunable transmitter incorporating a widely-tunable laser together with an optical phase locked loop (OPLL) will be introduced. Details of this transmitter PIC layout and fabrication are given for the first time in this paper. Second, new results from compact optical comb generators to synthesize optical frequencies over a wide frequency range (5 THz) with a very high relative and absolute precision, will be given. These can be combined within the OPLL of the tunable transmitters to generate very wide bandwidth LIDAR waveforms [6]. Third, we will show how the small dimensions of a monolithic PIC can be taken advantage of to form a homodyne Costa's loop coherent receiver where the requirement for post-detection frequency and phase compensation

to decouple the LO phase is eliminated. New measurement results are presented in Section V. Then in our fourth and final example, reconfigurable microwave signal processing devices are reviewed using compact, integrated ring-resonator based optical filters for analog coherent optical link applications. The progress on such filter work carried out at UCSB is shown and improved design and technology developed to improve the dynamic range are presented for the first time in Section VI.

II. INTEGRATION PLATFORM

Before diving into the details of each PIC, it is worth describing the technology that allows the monolithic integration of all the core active and passive components of our PICs in a high-yield, low-cost, and efficient way. This also demonstrates the strength and flexibility of the library of PICs for use as transmitters, receivers, and signal processing circuits for coherent optical links that we present in this paper.

Light sources, waveguide elements, modulators, amplifiers, phase shifters, and photodetectors were monolithically integrated in the PICs reported in this paper on two material platforms used at UCSB: offset quantum-well (OQW) and centered quantum-well (CQW) platforms, shown schematically in Figure 2. In the OQW active-passive platform, the multiple quantum-well (MQW) active layer is grown on top of the waveguide layer, which is common to active and passive components. The MQW layer is removed from the areas where passive components are desired and a single blanket regrowth of the upper cladding is finally performed on the wafer. The CQW active-passive configuration is similarly fabricated with an unpatterned cladding regrowth, but in this case the common waveguide contains the MQW-active region, and the bandgap of the MQW region has been selectively increased by a patterned implant and multiple annealing steps to selectively intermix the quantum-well barriers and wells in regions that are to become passive, or perhaps modulator sections, if the shift is not as large [14]. The CQW platform provides the highest confinement factor and gain per length, but also the lowest saturation power. As the QWs are moved away from the waveguide layer for OQW designs, the gain is reduced, while the saturation power is increased. We will discuss this technique further in Section VI.B. By incorporating both OQWs and CQWs, PICs can use both high gain semiconductor optical amplifiers (SOAs) for lasers and high saturation/linear SOAs. The integration is simply done by adding a regrowth step where the OQWs are grown on top of the CQW base-structure, in the intermixed region. The blanket cladding regrowth is then done as usual. In the same way, uni-travelling carrier (UTC) detectors can be integrated on the CQW platform for applications requiring high-speed photodetection. We have previously demonstrated such integration for wavelength converter and routing applications [9], [15]. For a more detailed description of these platforms, we refer to [8] and references therein.

Regardless which active-passive variation on the integration platform is chosen, the processing steps necessary to complete the PIC fabrication after regrowth are the same. More specifically, deeply etched waveguides are defined with photoresist

on a Cr/SiO₂ bilayer hardmask. The Cr is etched using a low power Cl₂/O₂(23.3 / 6.8 sccm) inductively coupled plasma (ICP) reactive ion etch (RIE) with 50 W applied to the ICP coil and 15 W on the substrate bias at a chamber pressure of 10 mT. The SiO₂ is etched using an SF₆/Ar (50 / 10 sccm) ICP-RIE with 600 / 50 W (ICP coil / substrate bias) at a chamber pressure of 7.5 mT. The SiO₂ to Cr selectivity is >30:1, and the etch chemistry provides a highly vertical etch of the silicon dioxide. The resulting 600 nm SiO₂ mask acts as a hardmask to define the InGaAsP/InP deeply etched waveguides using a Cl₂/H₂/Ar (9/18/2 sccm) ICP-RIE with 850 / 125W (ICP coil / substrate bias) at a chamber pressure of 1.5 mT and substrate temperature of 200 °C [16]. Conventional III-V wet-etching techniques are used to integrate surface-ridge waveguides in the same chip when necessary, such as in large PICs that require both the small footprint offered by the deeply etched waveguides, and the reduced propagation losses and better heat dissipation of surface-ridge structures.

After removing the SiO₂ waveguide mask, blanket deposition of a 350 nm isolation layer of silicon nitride is performed. Vias are opened for top-side p-metal contacts. N-metal contacts are realized through backside deposition of Ti/Pt/Au onto the n-doped conducting InP substrate or top-side deposition on patterned vias when a semi-insulating (SI) substrate is needed (e.g. high-speed ICs).

Finally, a contact anneal at ~400 °C is performed in order to decrease the electrical resistance at the metal-semiconductor interface.

III. DIGITALLY-SYNTHESIZED TRANSMITTERS

The transition from analog to digital frequency synthesis mirror recent development in RF sources. Analog optical frequency synthesis uses a precisely tuned and controlled optical resonator to generate a target frequency. Digital optical frequency synthesis involves multiplication of fixed frequency reference oscillators to be able to precisely synthesize any optical frequency within a band of interest, such as the C-band. In this section we briefly introduce the scope of this work within the context of coherent links, and then we describe our approach for the realization of a digitally-synthesized transmitter IC using a low-linewidth laser and an RF reference.

Optical phase-locked loops are a key technology in the development of chip-scale generic integrated coherent transmitters that can be used for a variety of applications, such as terahertz frequency generation, coherent beam forming and high resolution frequency swept LIDAR sources [17], [18]. The resolution and range of frequency swept LIDAR systems are inversely proportional to the linearly chirped signal frequency bandwidth and laser linewidth, respectively. Sampled grating distributed Bragg reflector (SG-DBR) lasers, with their small footprint, 5 THz tuning range and high speed tuning, are ideal sources for μ m resolution LIDAR [19]. An OPLL, in conjunction with an RF signal synthesizer, can be used to precisely and linearly control the frequency of the SG-DBR. Since the loop bandwidth of the feedback loop must be larger than the sum of the LO and reference laser, semiconductor lasers, e.g. SG-DBRs, with their large linewidths, require

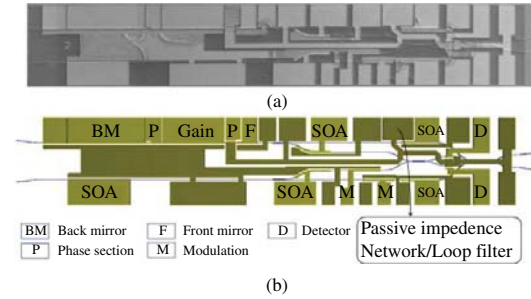


Fig. 3. (a) SEM image and (b) mask layout of design of an all-optical OPLL.

extremely short loop delays [6]. Monolithic integration along with custom built electronic circuits can enable an OPLL for heterodyne locking, realizing low linewidth, digitally synthesized THz dynamic range LIDAR sources.

We have designed and fabricated a PIC with SG-DBR lasers, SOAs, 2×2 multi-mode interference (MMI) couplers, modulators and balanced detectors integrated on one chip, as shown in Figure 3. The PIC can be used in two configurations; one is all optical and uses a passive feedback loop to offset lock at a fixed frequency and the other uses custom designed electronics to synthesize a wavelength sweep. In the all optical design, both the LO and reference laser signals are split in a 1×2 MMI. At the MMI output, the LO is modulated by an RF source, mixed with half the reference power in a 2×2 MMI and detected by balanced detectors. The signal from the balanced detectors goes directly to the phase section of the SG-DBR, with a passive impedance network providing loop stability. This allows us to create an extremely low loop delay PLL. From the second MMI port, the LO signal mixed with the reference signal for optical output of the heterodyne signal. The unmodulated LO signal, which will be used for LIDAR interrogation, can be coupled out from the back mirror of the SG-DBR.

These devices have been fabricated, however work toward a full LIDAR demonstration is still underway. In operation, to achieve a linear frequency sweep up to 5 THz, the SG-DBR LO can potentially be locked to a comb line from a wide bandwidth comb source, as shown in Figure 5. This is feasible as the linewidth of the comb source is comparable to the master SG-DBR used in the previous phase-locking experiment demonstrated in [6]. It is then possible to sweep the SG-DBR LO from one comb line to the next using a swept RF source applied to an electronic single sideband mixer in the feedback loop. Once it is within the loop bandwidth of the next comb line, the SG-DBR can then be locked to that line. Then, the RF sweep begins again, until the laser is swept over all the comb lines. The required bandwidth of the modulator and RF swept frequency source is only as large as the comb spacing.

These devices use the CQW platform described in Section II, and are processed on a SI InP:Fe substrate. Gratings were defined by electron-beam lithography before the p-cladding regrowth step. The integrated waveguides are both surface ridge (SR) for high power SG-DBRs and deep ridge (DR) for device compactness, incorporating a waveguide

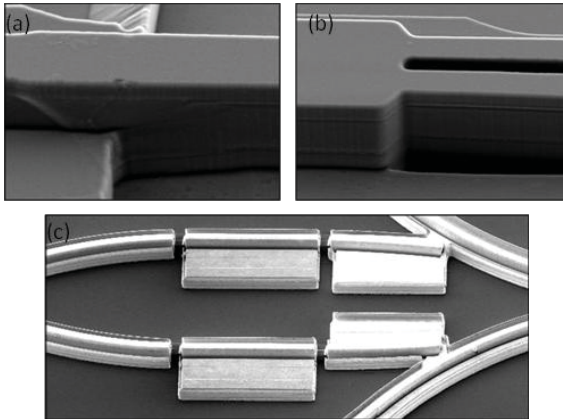


Fig. 4. SEM images of (a) surface ridge to deep ridge waveguide transition, (b) MMI lag etch at entrance of 2×2 MMI, and (c) Au He implant hardmask.

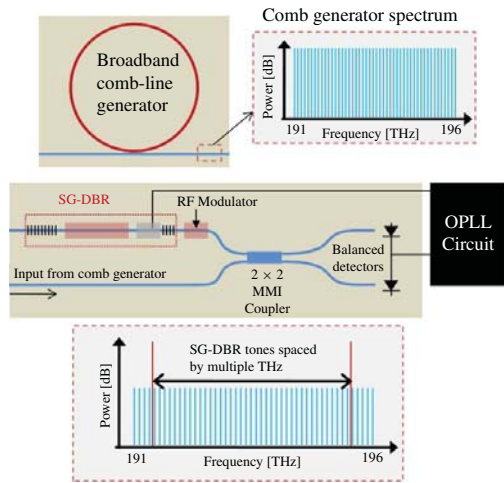


Fig. 5. LIDAR architecture showing comb generated from the ring mode-locked laser PIC at the top. In center, the SG-DBR laser is mixed with the comb generator signal in the 2-by-2 multimode interference coupler. The output from the optical mixing is measured on balanced detectors and the difference signal is fed back to the SG-DBR phase section, shifting the cavity frequency. This allows the OPLL circuit to track the incoming signal. RF modulation is added to the SG-DBR widely tunable laser for offset locking.

transition between them. Following regrowth, the ridge was defined using the bilayer Cr/SiO₂ mask described earlier and etched for 1 μm everywhere. Then the DR sections were protected by PR and the SR sections were wet-etched. The SR sections were protected using a low temperature SiO₂ deposition and liftoff, and the DR sections were dry-etched using the chamber conditions described in section II. The entrance waveguides to the 2×2 MMIs need an additional etch step due to the RIE lag effect in which the etch rate is decreased drastically when waveguides are less than 1 μm apart. A SiO₂ mask is used to protect the ridge everywhere but the MMI regions, to avoid etching through the n-contact layer, and another dry etch is performed. After this, a n-mesa is created by wet etching and stopping on the n-InGaAs contact

layer and n-metal is patterned via e-beam evaporation and liftoff. Next, a series of He implants, with the highest implant energy at 1675 keV, is used to create n-contact isolation between the balanced detectors. The hardmask process for the He implant consists of a two-stage angled Au deposition, with 2.5 μm of Au evaporated in each stage for a total of 5 μm in the planar regions, and is patterned via liftoff; this hardmask thickness is necessary to protect the waveguide from the high-energy implant [20]. The via openings for the n and p contacts are then formed as described in section II for a SI substrate. Several processing steps from the fabricated transmitter are shown in Figure 4.

IV. COMB GENERATION IN COHERENT LINKS

A. Broadband Phase-Locked Comb Applications

As discussed in the previous section, a broadband phase-locked frequency comb is very desirable for providing a reference grid for offset locking tunable lasers [6]. It can be also be used in a variety of other applications for coherent communication, such as a single cavity wavelength-division-multiplexing (WDM) source on the transmitter side [21], or multiple LOs on the receiver side. Enhanced performance could be expected from these latter examples if also combined with our recently demonstrated integrated optical phase-locked loops. For example, a coherent homodyne or heterodyne link using digital signal processing (DSP) would typically require each channel to have its own high-speed processing chip and a stable LO. The next generation of dense WDM grids spaced by 25 or 50 GHz with high spectral efficiency will contain 100 to 200 channels in the optical C-band. Thus as grid density increases, the required overhead to operate such a link with a DSP and an LO for each channel becomes quite costly, and the advantages realized from an integrated PIC with more functionality are apparent.

A 5 THz comb source with lines spaced by 25 GHz has the potential to replace 200 single frequency lasers with considerable savings in packaging and manufacture. Furthermore, with integrated OPLLs we can lock the frequency lines of the comb to the incoming signal avoiding the need for 200 DSP modules in a receiver array. If we use a phase-locked comb source on the transmitter side as well, only two OPLLs in the receiver are necessary to track the phase and frequency spacing. Phase locking combs to two frequency references for complete comb frequency stabilization has been studied extensively in fiber MLL based experiments [22]. As a result, by combining OPLLs and a compact broadband comb source we can reduce the overhead by as much as 200X. One potential drawback of the system, might be due to phase-noise, which can be significant at frequencies < 1 GHz from acoustic phonon modes in long fiber links [23]. The interaction of phonon modes with phase-noise in this coherent systems is subject to many factors, and deserves careful examination, however it is outside the scope of this article.

MLLs typically consist of a laser cavity with a saturable absorber (SA) element. For semiconductor MLLs, an SA is fabricated using a reverse biased P-i-N junction of bulk, QW, or quantum-dot (QD) material. The SA becomes transparent

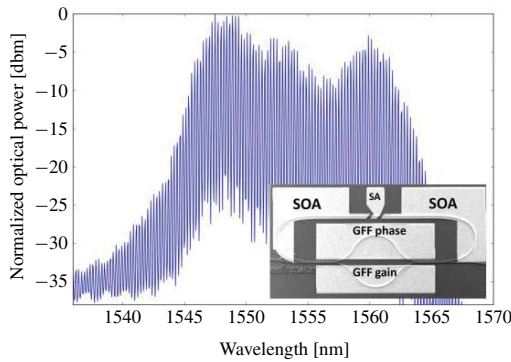


Fig. 6. Optical spectrum from gain flattened mode-locked laser. An SEM image of the GFF-MLL is shown in the inset. SOA: semiconductor optical amplifier. SA: saturable absorber. MZI: Mach-Zehnder interferometer.

above a certain power, as carrier accumulation prevents further absorption of photons, providing less loss to narrower pulses with a high peak power. This mechanism shifts the cavity's lowest-loss operating state from continuous-wave (common in single-mode lasers) to periodic pulse-trains. A quick application of the Fourier transform, reveals that such temporal pulse-trains are only possible with multiple phase-locking frequency tones. Thus, phase-locked comb generation is the expected output from MLLs [24].

When combined with SG-DBR widely tunable lasers, the comb generator can be used to precisely place two tones at up to multiple THz intervals enabling RF generation and LIDAR. As shown in Figure 5, by applying RF modulation to the SG-DBR output before mixing with the comb, the laser can be offset locked from the discrete comb lines. When two of these lasers are mixed together, a beat tone is formed and broadband digital frequency sweeping becomes possible by adjusting the offset locked frequency.

B. Gain Flattening for Comb Generation

In a semiconductor MLL, the span of the comb is determined by the cavity dispersion and the gain competition between its various lasing modes. While the semiconductor medium can generate gain that spans over 100 nm, the gain competition arising from the nonuniform material gain as a function of wavelength limits the bandwidth of the resulting frequency comb. We have overcome such limitations by introducing an intracavity filter with the inverse of the spectral shape of the material gain. Hence, the resulting net gain appears flattened, creating a more uniform spectral profile. This allows for wider comb generation as demonstrated with bench-top MLLs [25].

We have been pursuing some of the first work to incorporate a gain flattening filter (GFF) into integrated passively MLLs. With the intracavity filter enabled, the GFF-MLL shows significant improvement in pulse-width and comb span compared to similar rings without the filter [26], [27]. These GFF-MLLs produce the widest combs yet generated by integrated quantum-well based lasers with combs spanning more than 2 THz within their -10 dB bandwidth [28], as shown in

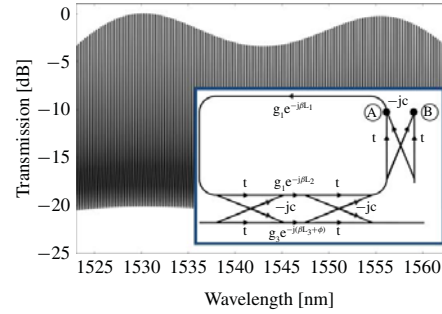


Fig. 7. Calculated output power response from a ring with a GFF. The inset shows the corresponding signal flow diagram where the power response taken from points A-to-B.

Figure 6; this is more than 70 phase-locked lasing lines from a device with a footprint of $0.6 \times 1.5 \text{ mm}^2$. This lasing span matches state-of-the art QD and quantum-dash MLLs [29]. These material platforms can provide an inherently flatter gain due to their nonuniform growth distribution, however reproducible QD gain spectra can be challenging as small growth changes can greatly alter the distribution of QDs. Moreover, such GFFs can be used to improve the gain flatness on any material platform, including: QDs, QWs, and bulk as future devices may require different semiconductor gain media.

The GFF-MLL is fabricated on the InGaAsP/InP offset quantum well (OQW) platform described in Section II. The active material is used to define SOAs and the SA, whereas the passive material is used to define the low-loss waveguides and current injection based phase shifters.

The fully fabricated GFF-MLL PIC has a round-trip cavity length of $2600 \mu\text{m}$, corresponding to lasing lines spaced by 29.7 GHz, as shown in Figure 6. For offset locking SG-DBR tunable lasers or for use in WDM communication, 10-100 GHz frequency spacing is desired for the cavity modes. This requires ring circumferences to be ~ 1 to 10 mm, making integrated cavities ideal for these applications. The $600 \mu\text{m}$ asymmetric MZI filter uses two 3 dB couplers with connecting arms that differ in length by $16 \mu\text{m}$ providing a free-spectral-range (FSR) of 40 nm. One of the arms of the MZI filter has an SOA that can be used to control the extinction ratio (ER) of the GFF, whereas the other arm has a phase shifter allowing adjustment of the filter center frequency. The optical power coupled into a lens fiber is -6 dBm. The measured -20 dB RF linewidth is < 500 KHz and FWHM pulse-width is 900 fs [30]. Such linewidth and pulse-width measurements are consistent with other QW based passively mode-locked lasers [31], indicating that the gain flattening does not degrade phase-locking and moreover that hybrid mode-locking the cavity can be used to greatly reduce the linewidth further [32].

Using scattering matrix theory, we predict that further improvements in the GFF to achieve a 5 THz span are possible. As discussed in [28] and shown in the inset of Figure 7, the optimal filter has three 78% bar couplers, two of which are used for the filter, while the third serves as the output for the desired flattened response. The simulated output comb has

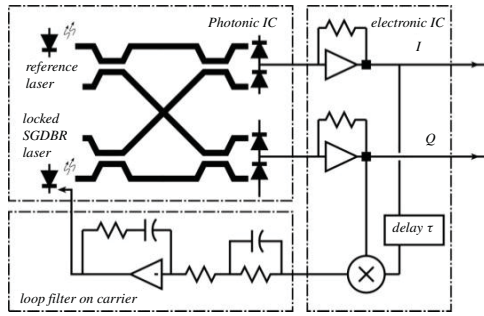


Fig. 8. Architecture of the coherent receiver showing three parts of this receiver: a photonic integrated circuit, an electrical integrated circuit, and a loop filter.

a 3.5 dB power variation over its 40 nm operating window (see Figure 7). Therefore, while 2 THz bandwidths have been demonstrated on-chip, GFF-MLLs have the potential for comb generation spanning 5 THz or more.

V. COHERENT RECEIVERS

As a part of optical coherent links, coherent optical receivers for digital communication applications have received a lot of interest recently. Compared to traditional direct detection receivers, coherent optical receivers have many advantages, such as higher detection sensitivity, greater tolerance to noise, compatibility with different modulation formats (such as multi-level phase shift keying or QAM), and their intrinsic ability to demultiplex wavelength-division multiplexed (WDM) channels without the use of optical filters [5], [33]–[36].

The most commonly used implementation of an optical coherent receiver is by using a free-running LO. Limited by laser linewidth and stability, high-speed digital signal processing is required to perform phase and frequency offset estimation and correction. However, the state-of-the-art high-speed digital signal processors that are used currently have high power consumption, limited speed and high cost.

One solution to this problem is to implement an optical phase-locked loop (OPLL) where an LO tracks the frequency and phase of the transmitter laser [6], [36], [37]. Although studies of optical phase-locked loops can be traced back almost fifty years, the OPLL has proven to be hard to implement. The main difficulty is that it requires a short loop delay and generally narrow linewidth lasers. For example, to achieve a 1 GHz loop bandwidth, the loop delay is normally required to be less than 100 ps. This is not feasible using fiber pigtailed components. However, by integrating all the photonic components monolithically, the footprint of the whole receiver becomes much smaller and therefore the loop delay can be significantly decreased.

To realize this phase-locked coherent receiver, we monolithically integrated a widely-tunable laser, a 90 degree hybrid and four high-speed photodetectors on an InGaAsP/InP-based photonic integrated chip. Besides the PIC, the receiver also includes an electrical integrated circuit (EIC) and a loop filter. The EIC is composed of two transimpedance amplifiers and an XOR gate. The loop filter is built on the carrier to provide

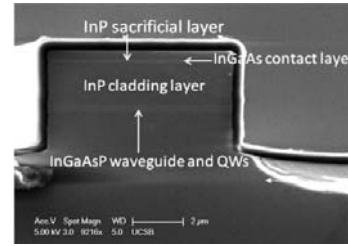


Fig. 9. Cross section of a waveguide.

more gain to the phase-locked loop and, more importantly, to introduce the correct filter function to keep the phase-locked loop stable. This architecture is shown in Figure 8. An integrated delay between I- and Q-data results in a DC component that is dependent on the frequency offset between input and LO laser, and provide frequency pull-in before the loop acquires phase-lock. Further, this architecture forms a Costa's loop, capable of coherent demodulation of BPSK modulated optical signals.

The PIC uses a widely-tunable SG-DBR laser [37] as the LO laser. Two variations of 90 degree hybrid designs are realized. One uses four MMI couplers, and the other uses a star coupler [38].

To monolithically integrate these optical components, we have used the InGaAsP/InP CQW platform presented in Section II, with an InP:S conducting substrate. The full epitaxial structure is shown in Figure 2, and Figure 9 is a SEM picture of a deeply etched waveguide cross section showing the epi layers. After quantum well intermixing, sampled gratings with a pitch size of 238 nm (shown in Figure 10(a)) are defined using electron beam lithography before the blanket regrowth of the p-cladding and InGaAs contact layer. For better laser performance and device compactness, we integrated both surface ridge waveguides and deeply etched waveguides on the same device with a low-loss waveguide transition between them, as previously described in Section III.

The $\text{Cl}_2/\text{H}_2/\text{Ar}$ based ICP-RIE dry etch resulted in very smooth ridge side walls and minimum undercut (Figure 10(b)) [16]. The surface ridge waveguide, the deeply etched waveguide, and the transition between them are shown in Figure 10(c).

Following the waveguide etching is the RF ground metal deposition and the bisbenzocyclobutene (BCB) definition steps. After that, the waveguide tops are opened for p-metal contacts followed by the opening of BCB vias for detectors and by our standard metal evaporation. In order to connect PIC and EIC by wire bonding, four 50-Ohm microstrip transmission lines are also fabricated on the PIC to bring all the signals from the photodetectors to the same side of the PIC. All the metal traces are 430 μm long and BCB is used as a dielectric layer. Figure 11(a) is the microscope picture of a PIC that is designed using MMI couplers as the 90 degree hybrid and Figure 11(b) shows the PIC that is designed using a star coupler.

The SG-DBR laser has been characterized. The output power is measured by an on-chip photodetector assuming unity

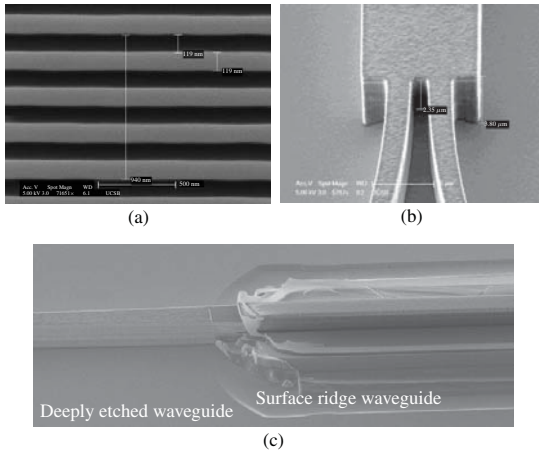


Fig. 10. SEM images of the fabricated PIC showing, (a) Gratings definition for SG-DBR lasers. (b) Vertical and smooth waveguide etch. (c) Waveguide transition from surface ridge to deeply etched waveguide. A linear tape is well designed to decrease the transition loss.

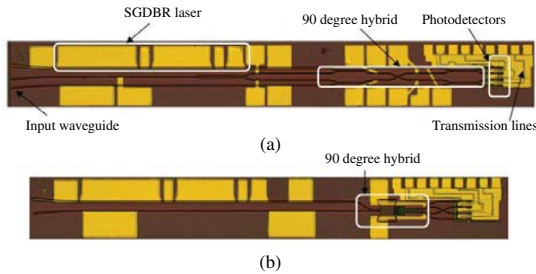


Fig. 11. Microscope images of the PIC showing. (a) PIC using MMI couplers as a 90 degree hybrid. (b) PIC using star coupler as a 90 degree hybrid.

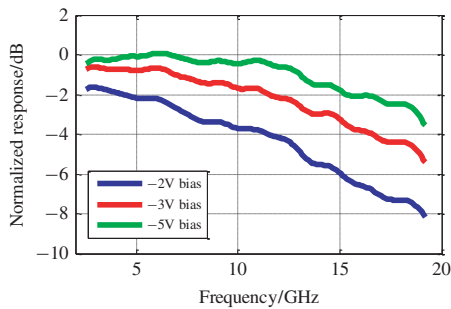


Fig. 12. Normalized frequency response of the photodetector with -2 V, -3 V, and -5 V DC bias.

quantum efficiency. The measured threshold current of the laser is around 40 mA and the maximum output optical power is 18 mW. A 40 nm tuning range has been achieved. The high-speed photodetector has also been tested. Figure 12 shows the relative frequency response of the detector with different DC biases. With a -5 V DC bias, an 18 GHz bandwidth can be achieved.

Back-to-back system characterization shows the functionality of the receiver without a phase-locked loop. The test

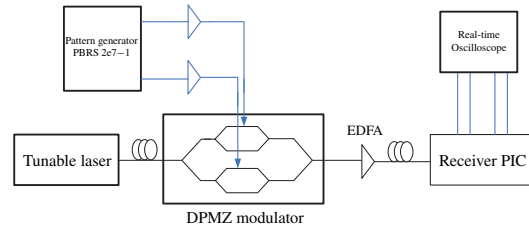


Fig. 13. Measurement setup for the coherent receiver.

setup is shown in Figure 13. Using the on-chip laser as an LO, the QPSK signal can be demodulated. The in-phase and quadrature data are detected on chip and sampled by a four-channel real-time oscilloscope. The sample rate is 40 GSa/s for each channel. While the measurements of the coherent receiver with an OPLL are currently being carried out, digital post-processing was performed offline on a computer for the first chip testing presented here in order to demonstrate the functionality of the coherent receiver PIC. The constellation diagram corresponding to a data rate of 10 Gb/s is shown in Figure 14.

VI. HIGH DYNAMIC RANGE PIC FILTERS FOR COHERENT ANALOG OPTICAL LINKS

A. Introduction and PIC Filter Results

As mentioned in Section I, the power of coherent photonic systems extends beyond the digital telecom applications. Analog RF-photonic links can provide low-loss, very high bandwidth microwave transmission systems that are immune to electromagnetic interference [39]. Within analog photonic links, RF signal processing can be conducted in the optical domain. The wide-bandwidth nature of photonic systems opens the door to signal processing over bandwidths not attainable in RF electronics. In particular, microwave filtering in the optical domain can relieve demands placed on analog-digital converters or digital circuits normally tasked with performing the filtering application [40].

Recently, much attention has been given to photonic microwave filter PICs because of their size, weight, power, and stability improvements over bulk optical systems [41]-[46]. The optical stability provided by an integrated device allows for coherent signal processing of the optical signal. In this way, PICs can fulfill signal processing requirements for coherent optical links. In addition, process compatibility with the other components described in this paper allows for the integration of signal-processing functions on coherent link transmitter and receiver PICs, improving link functionality while reducing the total demands placed on digital post processing or electronic RF analog signal processing.

Integration on a direct-bandgap semiconductor material system like InGaAsP/InP provides design and operational flexibility because of the integration of SOAs on-chip. SOAs make it easier to produce high-quality filter shapes without introducing excess loss into the system [45]. They also provide a level of tunability and programmability not available in passive systems. When integrated with fast current-injection phase

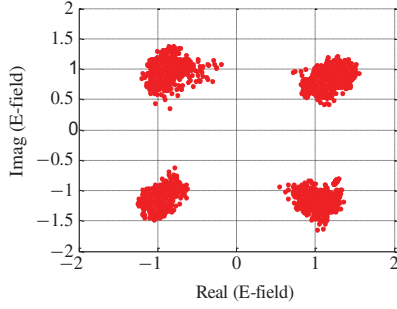


Fig. 14. Constellation diagram of the demodulated QPSK signal. The data rate is 10 Gb/s. Data are measured on a star-coupler-based device.

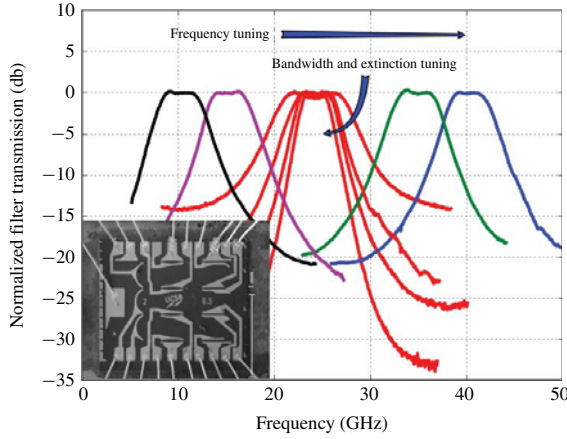


Fig. 15. Second-order coupled ring bandpass filters measured in the RF domain showing tunability in bandwidth and frequency. Filters are normalized to 0.0 dB passband gain for clarity, but have passband optical gain of 0–5 dB. The inset is an SEM image of a fabricated device. See [38] for more details on the device and measurement.

modulators, filters can be tuned in bandwidth and frequency in real-time. Recently, we fabricated and demonstrated cascaded [46] and coupled-ring [45] bandpass filters showing high levels of tunability and near-ideal filter shapes. Figure 15 shows the tuning capabilities of a 2nd order coupled-ring bandpass filter. Coupled-ring structures easily synthesize bandpass filters whose bandwidth is controlled by the inter-ring coupling value. Pole magnitudes are set by the intra-ring SOAs [45]. The InGaAsP/InP material platform is also advantageous for monolithic integration with other link components like transmitters and receivers, as discussed in Section II.

While highly-tunable and high-quality filters were demonstrated, it is important that RF link performance not be compromised by the photonic subsystem. Integrated SOAs produce amplified-spontaneous-emission (ASE) noise and distortion via four-wave mixing that negatively impact the system spurious-free dynamic range (SFDR). The SFDR of a fabricated second-order bandpass filter was measured to be 86.3 dB-Hz^{2/3}, indicating the need for a high-dynamic-range design [46]. Such a design is achieved through the use of a high-saturation-power and low-loss material platform, and a high-SFDR device layout, as we discuss in the following sections B and C.

B. High Dynamic Range SOAs

The noise and distortion that negatively impact the SFDR of an RF-photonic link incorporating a PIC filter originate in the integrated SOAs. ASE noise is generated in any SOA operating in the linear amplification regime, and in-band intermodulation distortion (IMD) is generated via carrier population oscillations that produce four-wave mixing [47]. The SFDR of a coherent link with an LO power much greater than all other optical powers can be written in terms of optical noise and third-order IMD output intercept point (OIP3) as [48],

$$SFDR = \left[\frac{P_{OIP3}}{S_{ASE} + \hbar\omega} \right]^{2/3}. \quad (1)$$

Where S_{ASE} is the power spectral density of ASE in the mode, and P_{OIP3} is the optical third-order IMD output intercept point. SFDR is given on a bandwidth-independent dB-Hz^{2/3} scale. Using the definitions for S_{ASE} and P_{OIP3} from [48], we derive an equation for the SFDR of a single SOA in a link as

$$SFDR = \left[\frac{P_S G}{M[n_{sp}(G-1)/\zeta + 1](G-1)} \right]^{2/3}. \quad (2)$$

Where P_S is the SOA saturation power, G is the single-pass power gain, n_{sp} is the population inversion factor, and $\zeta = (\Gamma g - \alpha_i)/\Gamma g$, where Γg is the modal gain, and α_i is the modal loss. For two closely spaced tones (the worst case), M is a material parameter given by

$$M = \frac{\hbar\omega}{2} \sqrt{1 + \alpha^2/\zeta^2}. \quad (3)$$

Where α is the linewidth enhancement factor and τ is the carrier lifetime. M is constant for a certain material platform and for constant bias current. The SFDR of a system of many SOAs is a complex function of SOA gain and placement in the PIC, but (1) and (2) show that the best performance for an SOA is obtained at high current density, when n_{sp} is small, ζ is close to 1, and saturation power is highest. Maximizing SFDR for a single SOA is equivalent to maximizing saturation power and minimizing total gain used. In a PIC, minimizing total gain used is equivalent to minimizing passive waveguide propagation loss and component insertion loss. If less loss is accrued, less gain is needed, and the structure achieves a higher SFDR. Thus, the key material attributes needed to achieve a high linearity integration platform are high P_S and low loss.

We have fulfilled both these requirements by slightly modifying the well-established OQW material platform, previously described in the Section II of this paper. P_S can be increased by lowering Γ without reducing the active region cross section. This is done by inserting an extra InP layer in between the waveguide and the active region, there through lowering Γ . The penalty of increasing P_S comes with trading off for lower modal gain, since Γ is decreased. The lower gain is not a problem for our filter designs, which rely on reducing the incorporated SOA gain (G) to maximize SFDR ((1) and (2)). More importantly, having the CT-layer in the passive sections exponentially reduces the propagation loss since the modal overlap with the p-cladding and thus the inter-valence band absorption is reduced [49]. Figure 16 schematically illustrates this integration platform, with the key CT-layer highlighted.

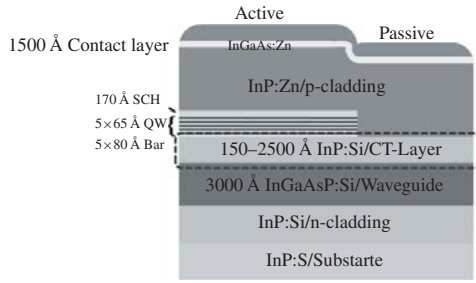


Fig. 16. Schematic illustration of the InGaAsP high dynamic range platform for active/passive device integration.

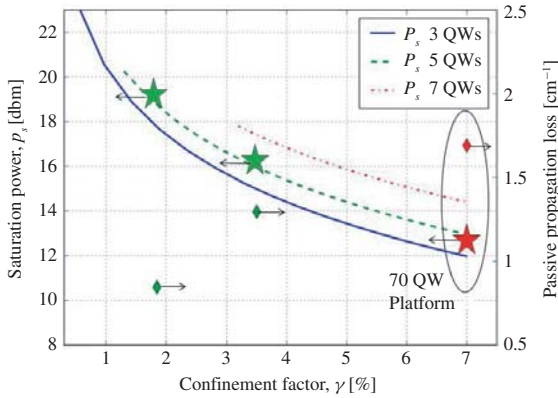


Fig. 17. Simulated P_s as a function of Γ , varying number of QWs and CT-layer thickness (lines). Superimposed with measured output saturation powers (stars), and averaged passive losses (diamonds) for corresponding CT-layer designs. For the passive loss measurement, the standard deviation is $<0.087 \text{ cm}^{-1}$ for all points. The standard OQW with 7QWs is highlighted for reference.

One boundary condition for the CT-layer technique is that the CT-layer cannot be made too thick, such that higher order transverse modes are guided. This effectively limits the number of wells that can be used for a given P_s , and is manifested by the broken lines in the simulation of P_s in Figure 17. The active/passive integration for this platform is analogous to the standard OQW platform, with a simple wet-etch step removing the quantum wells in passive sections, and a single blanket regrowth of the p-cladding. We have characterized this high linearity platform using a deeply etched waveguide design. The deep etching allows for maximum flexibility in device integration since the mode has large lateral confinement and the dry etch fabrication does not require a specific crystallographic direction. The filter PICs described previously use deeply etched waveguides.

Figure 17 shows the measured output saturation power and passive loss for a few different Γ designs. The measured results match theory very well; P_s increases and passive loss decreases with decreasing Γ (increasing CT-layer thickness). The loss with the lowest confinement OQW design is 0.34dB/mm, improved by factor over the standard OQW design. At the same time, P_s was improved by $>7\text{dB}$ to 19.1dBm, this is the highest reported P_s to our knowledge using $\leq 3\mu\text{m}$ wide waveguides. The gain for this design is

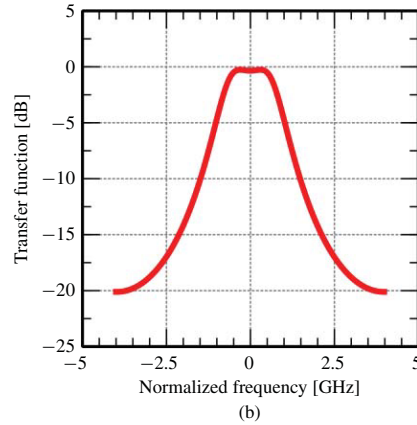
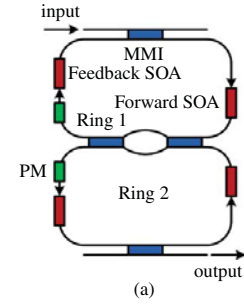


Fig. 18. (a) Schematic representation of a second-order coupled ring filter. MMIs are in blue, SOAs in red, and phase modulators (PM) in green. The inter-ring coupling value is controlled by the Mach-Zehnder interferometer (MZI) tunable coupler comprised of two MMIs and two waveguides of equal length. (b) Simulated transfer function of a second-order coupled ring bandpass filter with inter-ring coupling of 15%. This optimal-SFDR filter provides a passband gain of -0.26 dB .

measured to be 7.8 dB/mm, which is sufficient to balance the accrued loss in our PIC filters. The proven loss and saturation improvements for the OQW platform promise to facilitate high dynamic range PIC filters, which will be discussed in the next section.

As mentioned in the end of the Integration Platform section, it is fully possible to integrate high-gain CQW sections with these high-linearity SOA structures, simply by adding a second regrowth. This way an LO laser and balanced receiver could be integrated with the RF-filter application.

C. Next Generation High Dynamic Range Microwave PIC Filters

In [48], we develop a model to calculate the SFDR of an arbitrary PIC system with SOAs operating in the linear amplification regime. ASE and IMD are calculated for each SOA, and their contributions summed at the receiver depending on the frequency-dependent transfer function from the PIC input to the SOA, and from the SOA to the PIC output. This model creates a method for investigating the impacts of device design on SFDR.

In addition to the importance of integration on a high-saturation-power material platform proven in the last section, the layout of a signal-processing PIC is crucial for obtaining

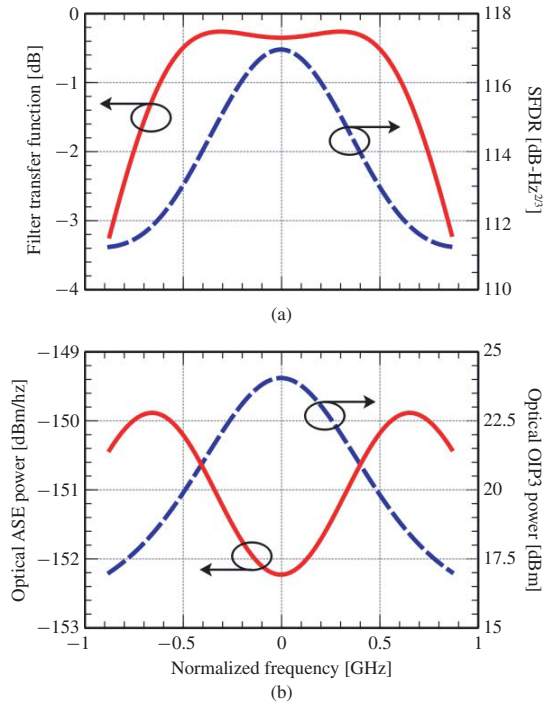


Fig. 19. (a) Simulated transfer function and SFDR over the 3 dB bandwidth of the SFDR-optimal second-order coupled ring bandpass filter. (b) Simulated ASE noise output and OIP3 power over the 3 dB bandwidth at the output of the same filter.

high SFDR. Here, we will use a second-order coupled ring bandpass filter as an example to demonstrate the design process.

The second-order coupled-ring filter shown in Figure 18(a) produces two transfer function poles, the magnitudes of which are set by the net ring gain and loss. The phases of the poles are set by the round-trip phase accumulation, and are tuned by the phase modulators. When the two ring resonances are located at the same frequency, the coupled nature of the transfer function causes the poles to split in frequency. The frequency separation is determined by the magnitude of the inter-ring coupling. As inter-ring coupling increases, the poles move away from each other and the filter bandwidth increases. By appropriately setting the pole magnitudes and inter-ring coupling value, a flat-topped bandpass filter can be synthesized. An example of this flat-topped filter is shown in Figure 18(b).

The pole magnitudes used to create the filter shape are dependent on the total gain and loss in the ring, but not on the location of that gain and loss. For example, SOA gain can be located either in the “feedback” or “forward” waveguide segments as shown in Figure 18(a). By adjusting the distribution of gain between these forward and feedback segments, the filter transfer function will move up and down on a dB scale, while the filter shape remains the same. In this way, the filter can be designed for a specific passband gain. As the SOA distributions are changed, the SFDR will also vary. It is also crucial for high SFDR to locate all SOAs at the end of their respective waveguide segments in order to

minimize signal power (and hence distortion generation) in the SOAs [48].

For this filter, the optimal SFDR is obtained when the ring 1 SOA is located in the feedback segment, and the ring 2 SOA is located in the forward segment. Figure 19 shows the transfer function, SFDR, ASE, and OIP3 power as a function of frequency over the 3 dB bandwidth for this arrangement. The model uses the measured results presented in Section VI-B to calculate the SFDR of a device fabricated on the high-saturation-power integration platform. An SFDR range of 111.2–117.0 dB-Hz^{2/3} is predicted over the 3dB filter bandwidth. ASE power and IMD are higher at the edges of the passband (OIP3 is lower) causing a degradation of SFDR in those areas. The SFDR of an arbitrary signal in the passband is a complex function of many-tone interactions, but the SFDR range reported here provides an upper and lower bound [48].

The PIC-limited SFDR calculated with this model is comparable to recent measurements of coherent RF-photonic links incorporating passive microwave photonic filters [50], [51]. Importantly, active PIC filters like the example in Figure 19 do not have insertion loss, which can relieve demands on the transmitter and receiver. With the possibility to monolithically integrate PIC filters with a transmitter or receiver, the active InGaAsP/InP material system is attractive for use in next-generation coherent RF-photonic links.

VII. CONCLUSION

We have demonstrated photonic circuits monolithically integrated on an InP-based platform for use in coherent communication links. We have shown examples of an integrated transmitter that uses an optical phase locked loop to both accurately set the wavelength as well as possibly narrow the linewidth. Compatible mode-locked ring lasers are illustrated as possible on-chip WDM sources, which have been demonstrated with a flat gain profile across a 2 THz band. New device designs promise to provide a flatted gain over a 5 THz band. We have shown coherent receivers incorporating an integrated widely tunable laser: open-loop measurements demonstrated a 10 Gb/s QPSK transmission. Paired with an OPLL, the coherent receiver has the potential to demonstrate phase-locked operation without DSP post-processing. This is a preferable solution especially for short-haul links where dispersion is less of an issue, since our OPLL offers an easier and more power-efficient integration. Finally a tunable, programmable optical bandpass filter for use in analog coherent RF links is demonstrated. With an established higher-saturation and lower-loss OQW design, improved filter designs can potentially exceed 117 dB-Hz^{2/3} SFDR.

ACKNOWLEDGMENT

The authors would like to thank the many former and present University of California, Santa Barbara, students and colleagues that have performed much of the work presented herein and especially the collaboration of J. E. Bowers on much of the research.

REFERENCES

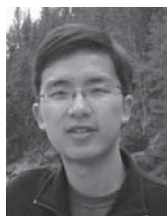
- [1] A. J. Rogers, "Polarization-optical time domain reflectometry: A technique for the measurement of field distributions," *Appl. Opt.*, vol. 20, no. 6, pp. 1060–1074, 1981.
- [2] Cisco Systems. (2011, Jun.). *Visual Networking Index*, San Jose, CA [Online]. Available: <http://www.cisco.com>
- [3] M. Nakazawa, K. Kikuchi, and T. Miyazaki, *High Spectral Density Optical Communication Technologies*, vol. 6. Berlin, Germany: Springer-Verlag, 2010, pp. 103–127.
- [4] P. Magill, "100 Gigabit Ethernet from a carrier's perspective," in *Proc. IEEE Lasers Electro-Opt. Soc. Ann. Meet.*, Lake Buena Vista, FL, Oct. 2007, pp. 21–25.
- [5] R.-J. Essiambre, G. Kramer, P. J. Winzer, G. J. Foschini, and B. Goebel, "Capacity limits of optical fiber networks," *J. Lightw. Technol.*, vol. 28, no. 4, pp. 662–701, Feb. 2010.
- [6] S. Ristic, A. Bhardwaj, M. J. Rodwell, L. A. Coldren, and L. A. Johansson, "An optical phase-locked loop photonic integrated circuit," *J. Lightw. Technol.*, vol. 28, no. 4, pp. 526–538, Feb. 2010.
- [7] K. Iiyama, W. Lu-Tang, and H. Ken-Ichi, "Linearizing optical frequency-sweep of a laser diode for FMCW reflectometry," *IEEE J. Lightw. Technol.*, vol. 14, no. 2, pp. 173–178, Feb. 1996.
- [8] L. A. Coldren, S. C. Nicholes, L. Johansson, S. Ristic, R. S. Guzzon, E. J. Norberg, and U. Krishnamachari, "High performance InP-based photonic ICs-A tutorial," *IEEE J. Lightw. Technol.*, vol. 29, no. 4, pp. 554–570, Feb. 2011.
- [9] S. C. Nicholes, M. L. Masanovic, B. Jevremovic, E. Lively, L. A. Coldren, and D. J. Blumenthal, "An 8×8 InP monolithic tunable optical router (MOTOR) packet forwarding chip," *IEEE J. Lightw. Technol.*, vol. 28, no. 4, pp. 641–650, Feb. 2010.
- [10] R. Nagarajan, J. Rahn, M. Kato, J. Pleumeekers, and D. Lambert, "10 channel, 45.6 Gb/s per channel, polarization multiplexed DQPSK, InP receiver photonic integrated circuit," *IEEE J. Lightw. Technol.*, vol. 29, no. 4, pp. 386–395, Feb. 2011.
- [11] P. Evans, M. Fisher, R. Malendevich, A. James, P. Studenkov, G. Goldfarb, T. Vallaitis, M. Kato, P. Samra, S. Corzine, E. Strzelecka, R. Salvatore, F. Sedgwick, M. Kuntz, V. Lal, D. Lambert, A. Dentai, D. Pavinski, B. Behnia, J. Bostak, V. Dominic, A. Nilsson, B. Taylor, J. Rahn, S. Sanders, H. Sun, K.-T. Wu, J. Pleumeekers, R. Muthiah, M. Missey, R. Schneider, J. Stewart, M. Reffle, T. Butrie, R. Nagarajan, C. Joyner, M. Ziari, F. Kish, and D. Welch, "Multi-channel coherent PM-QPSK InP transmitter photonic integrated circuit (PIC) operating at 112 Gb/s Per wavelength," in *Proc. Opt. Fiber Commun. Conf.*, Los Angeles, CA, Mar. 2011, pp. 1–3.
- [12] L. Johansson, U. Krishnamachari, A. Ramaswamy, J. Klamkin, S. Ristic, H.-F. Chou, L. A. Coldren, M. Rodwell, and J. E. Bowers, "Linear coherent optical receivers," in *Proc. Opt. Fiber Commun. Conf.*, San Diego, CA, Mar. 2010, pp. 1–3.
- [13] E. J. Norberg, R. S. Guzzon, J. S. Parker, L. A. Johansson, and L. A. Coldren, "Programmable photonic microwave filters monolithically integrated in InP-InGaAsP," *IEEE J. Lightw. Technol.*, vol. 29, no. 11, pp. 1611–1619, Jun. 2011.
- [14] E. J. Skogen, J. S. Barton, S. P. Denbaars, and L. A. Coldren, "A quantum-well-intermixing process for wavelength-agile photonic integrated circuits," *IEEE J. Sel. Topics Quantum Electron.*, vol. 8, no. 4, pp. 863–869, Jul.–Aug. 2002.
- [15] J. W. Raring, M. N. Sysak, A. T. Pedretti, M. Dummer, E. J. Skogen, J. S. Barton, S. P. Denbaars, and L. A. Coldren, "Advanced integration schemes for high-functionality/high-performance photonic integrated circuits," *Proc. SPIE*, vol. 6126, pp. 1–12, Jan. 2006.
- [16] J. S. Parker, E. J. Norberg, R. S. Guzzon, S. C. Nicholes, and L. A. Coldren, "High verticality InP/InGaAsP etching in Cl₂/H₂/Ar inductively coupled plasma for photonic integrated circuits," *J. Vac. Sci. Technol. B*, vol. 29, no. 1, pp. 011016-1–011020-5, 2011.
- [17] L. Ponnampalam, M. J. Fice, F. Pozzi, C. C. Renaud, D. C. Rogers, I. F. Lealman, D. G. Moodie, P. J. Cannard, C. Lynch, L. Johnston, M. J. Robertson, R. Cronin, L. Pavlovic, L. Naglic, M. Vidmar, and A. J. Seeds, "Monolithically integrated photonic heterodyne system," *J. Lightw. Technol.*, vol. 29, no. 15, pp. 2229–2234, Aug. 2011.
- [18] N. Satyan, A. Vasilyev, G. Rakuljic, V. Levya, and A. Yariv, "Precise control of broadband frequency chirps using optoelectronic feedback," *Opt. Exp.*, vol. 17, no. 18, pp. 15991–15999, 2009.
- [19] L. A. Coldren, "Monolithic tunable diode lasers," *IEEE J. Sel. Topics Quantum Electron.*, vol. 6, no. 6, pp. 988–999, Nov.–Dec. 2000.
- [20] J. Klamkin, J. M. Hutchinson, J. T. Getty, L. A. Johansson, E. J. Skogen, and L. A. Coldren, "High efficiency widely tunable SGDBR lasers for improved direct modulation performance," *IEEE J. Sel. Topics Quantum Electron.*, vol. 11, no. 5, pp. 931–938, Sep.–Oct. 2005.
- [21] Y. B. M'Sallem, Q. T. Le, L. Bramerie, Q. Nguyen, E. Borgne, P. Besnard, A. Shen, F. Lelarge, S. LaRochelle, L. A. Rusch, and J. Simon, "Quantum-dash mode-locked laser as a source for 56-Gb/s DQPSK modulation in WDM multicast applications," *IEEE Photon. Technol. Lett.*, vol. 23, no. 7, pp. 453–455, Apr. 2011.
- [22] B. R. Washburn, S. A. Diddams, N. R. Newbury, J. W. Nicholson, M. F. Yan, and C. G. Jrgensen, "Phase-locked, erbium-fiber-laser-based frequency comb in the near infrared," *Opt. Lett.*, vol. 29, no. 3, pp. 250–252, 2004.
- [23] K. Blotekjaer, "Thermal noise in optical fibers and its influence on long-distance coherent communication systems," *J. Lightw. Technol.*, vol. 10, no. 1, pp. 36–41, Jan. 1992.
- [24] P. J. Delfyett, S. Gee, M. T. Choi, H. Izadpanah, W. Lee, S. Ozharar, F. Quinlan, and T. Yilmaz, "Optical frequency combs from semiconductor lasers and applications in ultrawideband signal processing and communications," *J. Lightw. Technol.*, vol. 24, no. 7, pp. 2701–2719, Jul. 2006.
- [25] M. M. Mielke, G. A. Alphonse, and P. J. Delfyett, "Multiwavelength modelocked semiconductor lasers for photonic access network applications," *IEEE J. Sel. Areas Commun.*, vol. 25, no. 3, pp. 120–128, Apr. 2007.
- [26] J. S. Parker, A. Bhardwaj, P. R. A. Binetti, Y.-J. Hung, C. Lin, and L. A. Coldren, "Integrated 30 GHz passive ring mode-locked laser with gain flattening filter," in *Proc. IEEE Int. Semiconductor Laser Conf.*, Kyoto, Japan, Sep. 2010, pp. 1–2.
- [27] J. S. Parker, P. R. A. Binetti, A. Bhardwaj, R. S. Guzzon, E. J. Norberg, Y. Hung, and L. A. Coldren, "Comparison of comb-line generation from InGaAsP/InP integrated ring mode-locked lasers," in *Proc. Lasers Electro-Opt.*, Baltimore, MD, May 2011, pp. 1–2.
- [28] J. S. Parker, R. S. Guzzon, E. J. Norberg, A. Bhardwaj, P. R. A. Binetti, and L. A. Coldren, "Theory and design of intracavity gain-flattening filter for monolithically integrated mode-locked lasers," *IEEE J. Quantum Electron.*, vol. 48, no. 3, p. 1, Nov. 2011.
- [29] J. P. Tourrenc, A. Akrou, K. Merghem, A. Martinez, F. Lelarge, A. Shen, G. H. Duan, and A. Ramdane, "Experimental investigation of the timing jitter in self-pulsating quantum-dash lasers operating at 1.55 μm," *Opt. Exp.*, vol. 16, no. 22, pp. 17706–17713, 2008.
- [30] J. S. Parker, A. Bhardwaj, P. R. A. Binetti, and L. A. Coldren, "Monolithically integrated gain flattened mode-locked laser for comb-line generation," *IEEE Photon. Technol. Lett.*, 2011, to be published.
- [31] K. Merghem, A. Akrou, A. Martinez, G. Moreau, J.-P. Tourrenc, F. Lelarge, F. Van Dijk, G.-H. Duan, G. Aubin, and A. Ramdane, "Short pulse generation using a passively mode locked single InGaAsP/InP quantum well laser," *Opt. Exp.*, vol. 16, no. 14, pp. 10675–10683, 2008.
- [32] B. R. Koch, A. W. Fang, O. Cohen, and J. E. Bowers, "Mode-locked silicon evanescent lasers," *Opt. Exp.*, vol. 15, no. 18, pp. 11225–11233, 2007.
- [33] F. Derr, "Coherent optical QPSK intradyne system: Concept and digital receiver realization," *J. Lightw. Technol.*, vol. 10, no. 9, pp. 1290–1296, 1992.
- [34] R. Nagarajan, D. Lambert, M. Kato, V. Lal, G. Goldfarb, J. Rahn, M. Kuntz, J. Pleumeekers, A. Dentai, H.-S. Tsai, R. Malendevich, M. Missey, K.-T. Wu, H. Sun, J. McNicol, J. Tang, J. Zhang, T. Butrie, A. Nilsson, M. Reffle, F. Kish, and D. Welch, "10 channel, 100 Gbit/s per channel, dual polarization, coherent QPSK, monolithic InP receiver photonic integrated circuit," in *Proc. Opt. Fiber Commun. Conf.*, Los Angeles, CA, Mar. 2011, pp. 1–3.
- [35] A. Beling, N. Ebel, A. Matiss, G. Unterborsch, M. Nölle, J. K. Fischer, J. Hilt, L. Molle, C. Schubert, F. Verluise, and L. Fulop, "Fully-integrated polarization-diversity coherent receiver module for 100 G DP-QPSK," in *Proc. Opt. Fiber Commun. Conf.*, Los Angeles, CA, Mar. 2011, pp. 1–3.
- [36] M. J. Fice, A. Chiuchiarelli, E. Ciaramella, and A. J. Seeds, "Homodyne coherent optical receiver using an optical injection phase-lock loop," *IEEE J. Lightw. Technol.*, vol. 29, no. 8, pp. 1152–1164, Apr. 2011.
- [37] M. Lu, A. Bhardwaj, A. Sivananthan, L. A. Johansson, H. Park, E. Bloch, M. J. Rodwell, and L. A. Coldren, "Widely-tunable integrated coherent optical receiver using a phase-locked loop," in *Proc. IEEE Photon. Conf.*, Arlington, VA, Oct. 2011, no. ThL4.
- [38] C. R. Doerr, M. D. Gill, A. H. Gnauck, L. L. Buhl, P. J. Winzer, M. A. Cappuzzo, A. Wong-Foy, E. Y. Chen, and L. T. Gomez, "Monolithic demodulator for 40-Gb/s DQPSK using a star coupler," *IEEE J. Lightw. Technol.*, vol. 24, no. 1, pp. 171–174, Jan. 2006.
- [39] J. Yao, "Microwave photonics," *IEEE J. Lightw. Technol.*, vol. 27, no. 3, pp. 314–335, Feb. 2009.
- [40] J. Capmany, B. Ortega, and D. Pastor, "A tutorial on microwave photonic filters," *IEEE J. Lightw. Technol.*, vol. 24, no. 1, pp. 201–229, Jan. 2006.

- [41] M. S. Rasras, D. M. Gill, S. S. Patel, K.-Y. Tu, Y.-K. Chen, A. E. White, A. T. S. Pomerene, D. N. Carothers, M. J. Grove, D. K. Sparacin, J. Michel, M. A. Beals, and L. C. Kimerling, "Demonstration of a fourth-order pole-zero optical filter integrated using CMOS processes," *IEEE J. Lightw. Technol.*, vol. 25, no. 1, pp. 87–92, Jan. 2007.
- [42] N.-N. Feng, P. Dong, D. Feng, W. Qian, H. Liang, D. C. Lee, J. B. Luff, A. Agarwal, T. Banwell, R. Menendez, P. Toliver, T. K. Woodward, and M. Asghari, "Thermally-efficient reconfigurable narrowband RF-photonics filter," *Opt. Exp.*, vol. 18, no. 24, pp. 648–24 653, Nov. 2010.
- [43] P. Dong, N.-N. Feng, D. Feng, W. Qian, H. Liang, D. C. Lee, B. J. Luff, T. Banwell, A. Agarwal, P. Toliver, R. Menendez, T. K. Woodward, and M. Asghari, "Ghz-bandwidth optical filters based on high-order silicon ring resonators," *Opt. Exp.*, vol. 18, no. 23, pp. 23784–23789, Nov. 2010.
- [44] H.-W. Chen, A. Fang, J. D. Peters, Z. Wang, J. Bovington, D. Liang, and J. Bowers, "Integrated microwave photonic filter on a hybrid silicon platform," *IEEE Trans. Microw. Theory Tech.*, vol. 58, no. 11, pp. 3213–3219, Nov. 2010.
- [45] R. S. Guzzon, E. J. Norberg, J. S. Parker, L. A. Johansson, and L. A. Coldren, "Integrated InP-InGaAsP tunable coupled ring optical bandpass filters with zero insertion loss," *Opt. Exp.*, vol. 19, no. 8, pp. 7816–7826, 2011.
- [46] E. J. Norberg, R. S. Guzzon, J. Parker, L. A. Johansson, and L. A. Coldren, "Programmable photonic microwave filters monolithically integrated in InP/InGaAsP," *IEEE J. Lightw. Technol.*, vol. 29, no. 11, pp. 1611–1619, Jun. 2011.
- [47] G. P. Agrawal, "Population pulsations and nondegenerate four-wave mixing in semiconductor lasers and amplifiers," *J. Opt. Soc. Amer. B*, vol. 5, no. 1, pp. 147–159, Jan. 1988.
- [48] R. S. Guzzon, E. J. Norberg, and L. A. Coldren, "Spurious-free dynamic range in photonic integrated circuit filters with semiconductor optical amplifiers," *IEEE J. Quantum Electron.*, 2011, to be published.
- [49] E. J. Norberg, R. S. Guzzon, and L. A. Coldren, "An InGaAsP/InP integration platform with low loss deeply etched waveguides and record SOA RF-linearity," in *Proc. Eur. Conf. Opt. Commun.*, Geneva, Switzerland, 2011, pp. 1–3.
- [50] K.-Y. Tu, M. S. Rasras, D. M. Gill, S. S. Patel, Y.-K. Chen, A. E. White, A. Pomerene, D. Carothers, J. Beattie, M. Beals, J. Michel, and L. C. Kimerling, "Silicon RF-photonics filter and down-converter," *IEEE J. Lightw. Technol.*, vol. 28, no. 20, pp. 3019–3028, Oct. 2010.
- [51] A. Agarwal, T. Banwell, and T. Woodward, "Optically filtered microwave photonic links for RF signal processing applications," *IEEE J. Lightw. Technol.*, vol. 29, no. 16, pp. 2394–2401, Aug. 2011.



Pietro R. A. Binetti received the Ph.D. degree in electrical engineering from COBRA Research Institute, Eindhoven University of Technology, Eindhoven, The Netherlands, in 2009.

He is currently a Post-Doctoral Fellow with the University of California, Santa Barbara. His current research interests include design, fabrication, and characterization of photonic integrated circuits for analog and digital applications.



Mingzhi Lu received the B.S. degree in electrical engineering from Southeast University, Nanjing, China, in 2008. He is currently pursuing the Ph.D. degree in electrical engineering with the University of California, Santa Barbara.

His past research experience includes microwave and THz frequency selective surfaces and metamaterials. His current research interests include InGaAsP/InP based photonic integrated coherent receivers and optical phase-locked loops.



Erik J. Norberg received the B.S. and M.S. degrees in engineering nanoscience from Lund University, Lund, Sweden, in 2008. He is currently pursuing the Ph.D. degree in electrical engineering with the University of California, Santa Barbara.

He is currently working on the development of high dynamic range integrated optical filters for microwave signal processing. His current research interests include design and metal organic chemical vapor deposition growth of large scale photonic integrated circuits on InP.



Robert S. Guzzon received the B.S. degree in electrical engineering and physics from Lehigh University, Bethlehem, PA, in 2007. He is currently pursuing the Ph.D. degree in electrical engineering with the University of California, Santa Barbara.

His current work focuses on the design and fabrication of versatile photonic integrated microwave filter systems that achieve high spurious-free dynamic range. His current research interests include large-scale photonic integration, particularly applied to microwave photonic signal processing.



John S. Parker received the B.S. degree in engineering from Harvey Mudd College, Claremont, CA, in 2007, and the M.S. degree in electrical and computer engineering from the University of California, Santa Barbara, in 2009, where he is currently pursuing the Ph.D. degree.

His current research interests include radio frequency photonics, coherent communication, and compact components for dense photonic integrated circuits.



Abirami Sivanathan received the B.S. degree in engineering physics from the University of Illinois at Urbana-Champaign, Urbana, in 2007, and the M.S. degree in electrical and computer engineering from the University of California, Santa Barbara, in 2009. She is currently pursuing the Ph.D. degree in electrical engineering with the University of California.

Her current research interests include optical phase locked loops to achieve low linewidth semiconductor lasers and widely tunable photonic integrated transmitters on the InGaAsP/InP integration platform.



Ashish Bhargwaj received the B.Sc. (honors) and M.Sc. degrees in physics from the Indian Institute of Technology, Kharagpur, India, in 1994 and 1996, respectively, and the Ph.D. degree in applied physics from the California Institute of Technology, Pasadena, in 2001.

He was with Bell Laboratories, Lucent Technologies, Holmdel, NJ, from 2001 to 2007, as a Technical Staff Member, where he was engaged in research on fast wavelength switching in tunable lasers for applications in optical packet switching. He also

led research in the design, fabrication, and characterization of large-scale monolithically integrated InP-based photonic integrated circuits employing semiconductor optical amplifiers. From 2007 to 2011, he was with the Department of Electrical and Computer Engineering, University of California, Santa Barbara, where he led research in the design and fabrication of monolithically integrated optical phase locked loops as coherent receivers for high dynamic range radio frequency/photonic links. He is currently with JDS Uniphase Corporation, San Jose, CA.



Leif A. Johansson (M'04) received the Ph.D. degree in engineering from University College London, London, U.K., in 2002.

He is currently a Research Scientist with the University of California, Santa Barbara. His current research interests include design and characterization of integrated photonic devices for analog and digital applications and analog photonic systems and sub-systems.



Mark J. Rodwell (F'03) received the Ph.D. degree from Stanford University, Stanford, CA, 1988.

He received the IEEE Sarnoff Award in 2010 and the IEEE Microwave Prize in 1997. He received the Doluca Family Endowed Chair in Electrical and Computer Engineering, University of California, Santa Barbara (UCSB). He directs the UCSB node of the National Science Foundation Nanofabrication Infrastructure Network and the Semiconductor Research Corporation Nonclassical Complementary-Metal-Oxide Research Center.



Larry A. Coldren (S'67–M'72–SM'77–F'82) received the Ph.D. degree in electrical engineering from Stanford University, Stanford, CA, in 1972.

He is Fred Kavli Professor of optoelectronics and sensors with the University of California, Santa Barbara (UCSB). After 13 years in the research area at Bell Laboratories, Murray Hill, NJ, he joined UCSB in 1984, where he now holds appointments with the Department of Materials and the Department of Electrical and Computer Engineering. In 1990, he co-founded Optical Concepts, later acquired as Gore

Photonics, Newark, DE, to develop novel vertical-cavity surface-emitting laser (VCSEL) technology, and in 1998, he co-founded Agility Communications, later acquired by JDS Uniphase (JDSU) Corporation, Milpitas, CA, to develop widely-tunable integrated transmitters. At Bell Laboratories, he initially worked on waveguided surface-acoustic-wave signal processing devices and coupled-resonator filters. He later developed tunable coupled-cavity lasers using novel reactive-ion etching technology that he created for the new InP-based materials. At UCSB, he continued work on multiple-section tunable lasers in 1988, inventing the widely-tunable multi-element mirror concept, which is now used in some JDSU products. During this period, he also made seminal contributions to efficient designs that continue to be implemented in practical devices to this day. More recently, his group has developed high-performance InP-based photonic integrated circuits as well as high-speed VCSELs and they continue to advance the underlying materials growth and fabrication technologies. He has authored or co-authored more than 1000 journal and conference papers, seven book chapters, and one textbook and has been issued 64 patents.

Prof. Coldren is a fellow of the Optical Society of America and the Institution of Electrical Engineers, and a member of the National Academy of Engineering. He was a recipient of the 2004 John Tyndall and 2009 Aron Kressel Awards. He has presented dozens of invited and plenary talks at major conferences.

Photonic Integrated Circuits as Key Enablers for Coherent Sensor and Communication Systems

Larry A. Coldren, Leif Johansson, Mark J. Rodwell, Mingzhi Lu, Abirami Sivananthan, John S. Parker
 Electrical and Computer Engineering Department, University of California, Santa Barbara, CA 93106
 <coldren@ece.ucsb.edu>

Abstract— InP-based Photonic ICs (PICs), together with closely integrated Electronic ICs, have recently been shown to enable robust, compact coherent optical communication and sensor systems that have not been possible in the past. Experimental results will illustrate these functionalities.

I. INTRODUCTION

SOME years ago, coherent communication was intensively investigated as a means of increasing receiver sensitivity and repeater spacing in fiber telecommunication systems [1]. When wavelength division multiplexing (WDM) systems became more practical and inexpensive with the advent of the erbium-doped fiber amplifier (EDFA) these relatively costly and temperamental coherent communication approaches were put on the shelf for such fiber optic systems [2,3]. Nevertheless, they have continued to be explored in free-space communications as well as sensing applications where the cost and the difficulties are worth the benefits [4]. In recent years coherent techniques have also reemerged in the telecommunications sector, mainly driven by spectral efficiency, as we again are running out of fiber bandwidth, now driven totally by data, mostly from social networking, HD video, and other exponentially growing data demands on the network [5,6].

Recently, we have been exploring more integrated approaches, where only a single photonic integrated circuit (PIC) may contain all of the transmitter or receiver optics (except for coupling) and the feedback to lock the local oscillator or transmitter to some reference may be done with a single electronic IC, or perhaps with no electronic IC (EIC) at all [7-9]. These approaches have the potential to vastly simplify coherent transmitters and receivers and make them much more robust. Environmental controls are relaxed, locking and capture ranges increased, and overall stability is significantly improved in a much smaller, lighter, less costly, and lower power package.

Figure 1 describes a heterodyne experiment in which two SGDBR lasers are offset-locked together [7]. The circuit schematic shows that an integrated modulator is used to generate sidebands on the mixed signal, so that the OPLL can lock on one of these. In this case a 5GHz fundamental offset locking is illustrated. With deep phase modulation of the on-chip modulator it is possible to generate a number of sidebands and such modulators can be made with bandwidths up to ~100GHz, so it is anticipated that such offset locking might be

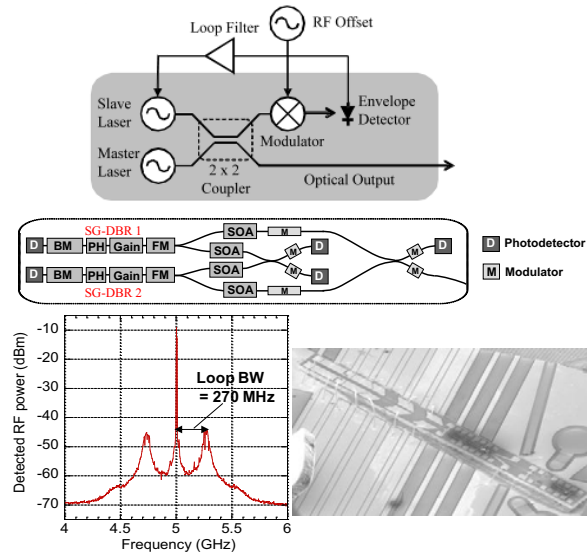


Fig. 1. Circuit schematic; PIC schematic; heterodyne result; and SEM of InP-based PIC

possible up to the THz range without having to generate rf higher than 100 GHz.

Fundamental offset locking as high as 20 GHz was demonstrated with the current set up. Although a balanced detector pair was available on the chip, the electronics used only had a single-input amplifier, so only a single detector was used, and this resulted in more AM and noise in the feedback loop than necessary. Nevertheless, a respectable phase error variance $\sim 0.03 \text{ rad}^2$ was measured over the 2 GHz measurement window.

II. RECENT WORK

Figure 2 shows a block diagram of a phase-locked coherent receiver, which contains photos of the PIC and EIC. The PIC contains a widely-tunable SGDBR LO laser (40 nm range) and a 90 degree hybrid along with monitoring detectors and adjustment amplifiers [8-10]. The EIC is a Costa's loop design for frequency and phase locking. At this writing simple phase locking with a 1 GHz capture range was demonstrated using the loop filter alone. Lower noise than that in Fig. 1 was observed, but detailed data is still being acquired. The linewidth of the

SGDBR laser was significantly narrowed by locking it to a narrow linewidth reference laser.

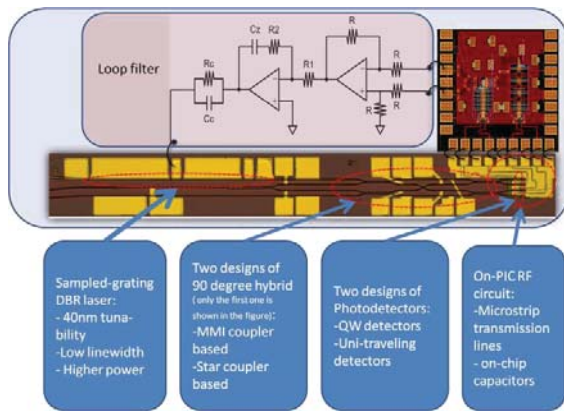


Fig. 2. Block diagram of phase-locked receiver with inserted photos of PIC and EIC. Widely-tunable SGDBR on-chip laser as well as external LO laser inputs possible; integrated optical hybrid and balanced I & Q detector pairs on-chip.

Figure 3 compares receiver output when the LO SGDBR laser is unlocked relative to a narrow linewidth input cw signal vs. the case of phase locking with a 100 MHz offset. A vast reduction in phase noise as well as a ‘clean’ 100 MHz optical interference waveform is observed.

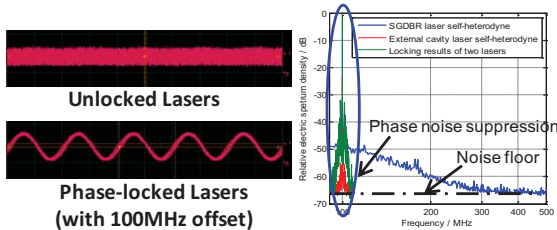


Fig. 3. Optical phase locked loop results.

Finally in Fig. 4 we illustrate the concept of a widely-tunable digitally-synthesized sweeping transmitter which might be relevant to a LIDAR system or some other sensor or communication system [9]. By using a single narrow-linewidth optical reference and two rf sources (one tunable) together with what could be one PIC (now two), we have proposed and partially demonstrated that we can digitally synthesize linear sweeps (or any other frequency pattern) up to 40 nm (5 THz) in width. A gain-flattened mode-locked ring laser is used to generate a comb spectrum up to this width. Currently 2 THz has been demonstrated as shown [11]. If one of the lines is locked to a stable reference, all of the lines are coherently referenced to it. The SGDBR can be tuned between lines using a millimeter wave source in the feedback electronics as shown. Then, in the next clock cycle the laser can jump to lock to the next mode-locked line and so forth.

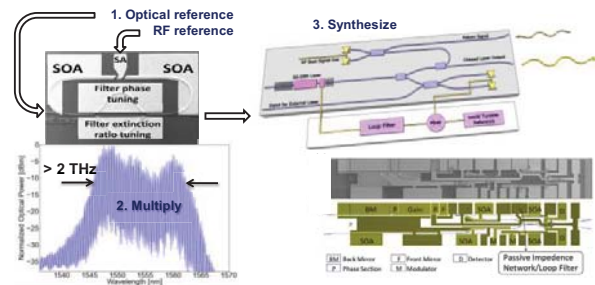


Fig. 4. Schematic of a digitally-synthesized optical transmitter capable of outputs over a 5 THz range with Hz level relative frequency accuracy.

REFERENCES

- [1] Y. Yamamoto and T. Kimura, “Coherent optical fiber transmission systems,” *IEEE J. Quantum Electron.*, vol. 17, no. 6, pp. 919-925, Jun. 1981.
- [2] R.J. Mears, L. Reekie, I.M. Jauncey and D. N. Payne, “Low-noise Erbium-doped fibre amplifier at 1.54 μ m,” *Electron. Lett.*, vol. 23, no. 19, pp.1026–1028, Sept. 1987.
- [3] N. S. Bergano and C. R. Davidson, “Wavelength division multiplexing in long-haul transmission systems”, *J. Lightwave Technol.*, vol.14, no. 6, pp. 1299-1308, Jun. 1996.
- [4] A. J. Rogers, "Polarization-optical time domain reflectometry: a technique for the measurement of field distributions," *Appl. Opt.*, vol. 20, pp. 1060-1074, 1981.
- [5] R. Tkach, “Optical Network Capacity: From Glut to Scarcity,” *OIDA Annual Meeting*, Santa Clara, CA, Dec. 1-2, 2009.
- [6] N. Nakazawa, K. Kikuchi, T. Miyazaki (eds.), *High Spectral Density Optical Communication Technologies, Optical and Fiber Communications Reports 6*, Springer-Verlag Berlin Heidelberg, vol. 6, pp 103-127, 2010.
- [7] S. Ristic, A. Bhardwaj, M.J. Rodwell, L.A. Coldren, and L.A. Johansson, “An optical phase-locked loop photonic integrated circuit,” *J. Lightwave Technol.*, vol. 28, no. 4, pp. 526-538, Feb. 15, 2010.
- [8] M. Lu, A. Bhardwaj, A. Sivanathan, L. Johansson, H. Park, E. Block, M. Rodwell, L. Coldren, “A widely-tunable integrated coherent optical receiver using a phase-locked loop,” *IEEE Photonics Conf (IPC'11)*, Arlington, Oct. 2011.
- [9] P. Binetti, M. Lu, E. Norberg, R. Guzzon, J. Parker, A. Sivanathan, A. Bhardwaj, L. Johansson, M. Rodwell, L. Coldren, “Photonic integrated circuits for coherent optical links, in press, *J. Quantum Electron.*, special issue on integrated optoelectronics, 2011.
- [10] L.A. Coldren et al, “High Performance InP-Based Photonic ICs—A Tutorial,” *IEEE J. Lightwave Tech.*, vol. 29, no. 4, pp. 554–570, Feb. 2011.
- [11] J.S. Parker, A. Bhardwaj, P.R.A. Binetti, Y.-J. Hung, C. Lin, L.A. Coldren, "Integrated 30GHz passive ring mode-locked laser with gain flattening filter," in *Proc. IEEE International Semiconductor Laser Conf.*, Kyoto, Japan, Sept. 26-30, 2010, Paper PD1; also to be published *IEEE J. Quantum Electron.*

Single-Chip Integrated Transmitters and Receivers

Larry A. Coldren^{1,2}, Leif Johansson¹, Mingzhi Lu¹, Abirami Sivananthan¹, and Mark Rodwell¹
ECE¹ and Materials² Departments, University of California, Santa Barbara, CA 93106
<coldren@ece.ucsb.edu>

Abstract—After many years in the research lab, photonic integrated circuits are emerging into practical commercial products with advantages not only in size, weight and power, but also in cost and performance. Recent advances in semiconductor-based devices will be reviewed.

As illustrated in Fig. 1, data traffic on the core fiber optic network and within data centers as well as the processing power of supercomputers has been growing exponentially for many years at a rate of between 100 to 500 times per decade [1]. This is faster than Moore's Law, and just as in the circuit design case, effectively parallel communication paths have been sought to keep up with the demand.

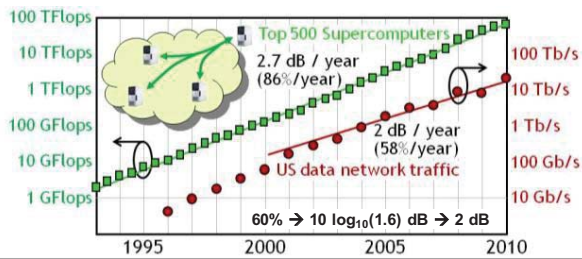


Fig. 1. Rate of growth in computer processing power and communication network bit-rate.

One common approach used in the rf-world has been to use advanced modulation formats that provide higher spectral efficiency, possibly leading to multiple bits/s of information transmission per Hz of bandwidth. This generally requires vector modulation approaches, acting on both the amplitude and phase of the optical field, as well as coherent receivers that recover the full vector field.

As it turns out coherent communication was intensively investigated some years ago (1980s), and this work stimulated work on photonic integration, because only with photonic integration could the various components be held together with enough stability and proximity. In those days, the primary goal was to increase receiver sensitivity and repeater spacing in fiber systems [2]. However, when wavelength division multiplexing (WDM) systems became more practical and inexpensive with the advent of the erbium-doped fiber amplifier (EDFA) these relatively costly and temperamental coherent communication approaches were put on the shelf for such fiber optic systems [3].

Nevertheless, the photonic integrated circuit (PIC) work they stimulated found new applications in the new WDM systems. For example, as illustrated in Fig. 2, widely-tunable (universal)

transmitters were widely desired. In fact, the integration of the sampled-grating distributed-Bragg-reflector (SGDBR) laser [4], with or without a Mach-Zehnder modulator, and some related products have been major success stories commercially, accounting for a large portion of dense WDM sources incorporated into systems over the past several years.

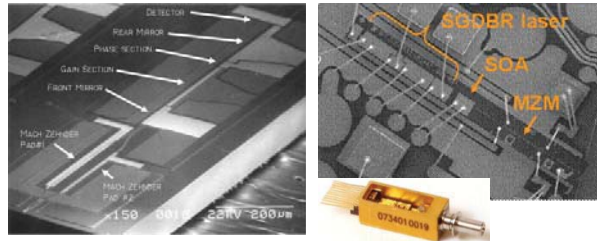


Fig 2. SEMs of SGDBR lasers integrated with Mach-Zehnder modulators (MZM)—left, early research result[5]; right, recent JDSU product, chip and TOSA[6].

Efforts on the technology to integrate more complex PICs have continued over the years, driven by the desire to make WDM more viable, the interest in “all photonic” networks, and most recently, a renewed interest in coherent, now mainly driven by spectral efficiency. Figure 3 shows an 8 x 8 photonic space switch that incorporates 8 all-optical wavelength-converters together with an arrayed waveguide grating router (AWGR). When first presented [7], this represented a major advance in the level and complexity of photonic integration.

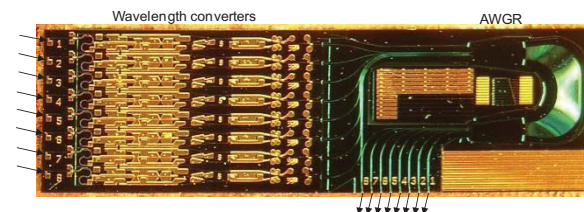


Fig. 3. Monolithic tunable optical router (MOTOR) chip with 8 SGDBR tuned wavelength converters feeding an AWGR to provide 8 spatially separated output, each operating at 40 Gb/s.

Figure 4 shows the layout of an advanced transmitter chip for polarization-multiplexed (PM) QPSK optical coherent communication demonstrated by Infinera. It has 10 parallel [x 2 for (PM)] channels operating at 10 GBaud for a net of 400 Gbits/s from one chip [8]. They have since demonstrated a single-chip with over 1 Tbit/s of net data transmission [9].

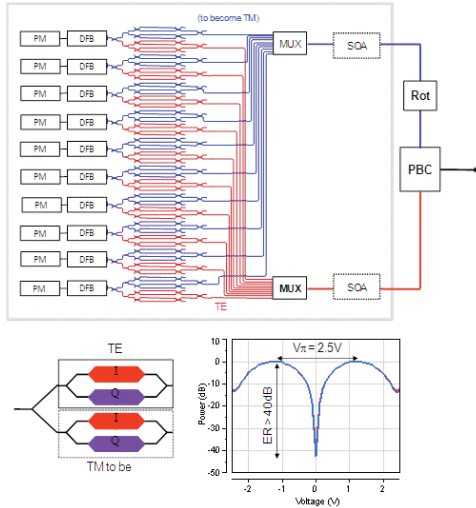


Fig. 4. Infinera PM-QPSK ($10 \times 40G$) – $10 \text{ GBaud} \times 4/\lambda$ —transmitter chip layout [8].

The recent resurgence of coherent techniques is mainly driven by social networking, HD video, and other exponentially growing data demands on the network [10,11]. This has driven a variety of research including our efforts, which differs from the mainstream in that we have been exploring integrated phase-locked loops (OPLL) in both our transmitters and receivers [12-15].

The common approach today is to use a loosely frequency-locked local oscillator at the receiver, which must have a fairly narrow linewidth, and then let a Digital Signal Processor (DSP) electronic chip track the phase and also perform a number of other signal conditioning functions. The problem with this approach is that the ADC and DSP combination require a lot of power to operate, and they are also relatively expensive to design and fabricate, if the market being served is relatively small.

As mentioned above, our efforts have focused on OPLL approaches which promise much higher efficiency operation, and much lower design and production costs. Again, as in the past, photonic integration as well as close integration with electronic ICs (or no ICs at all) [12-15] have the potential to vastly simplify coherent transmitters and receivers and make them much more robust. Environmental controls are relaxed, locking and capture ranges increased, and overall stability is significantly improved in a much smaller, lighter, less costly, and lower power package.

Figure 5 shows a block diagram of a phase-locked coherent receiver, which contains photos of the PIC and EIC. The PIC contains a widely-tunable SGDBR LO laser (40 nm range) and a 90 degree hybrid along with monitoring detectors and adjustment amplifiers [13,14]. The EIC is a Costa's loop design for frequency and phase locking. In operation, the linewidth of the SGDBR laser was significantly narrowed by locking it to a narrow linewidth reference laser.

Figure 6 compares receiver output when the LO SGDBR laser is unlocked relative to a narrow linewidth input cw signal vs. the case of phase locking with a 100 MHz offset. A vast reduction in phase noise as well as a 'clean' 100 MHz optical

CW1K.1.pdf interference waveform is observed. In fact, the linewidth of the reference laser is matched. CLEO Technical Digest © OSA 2012.

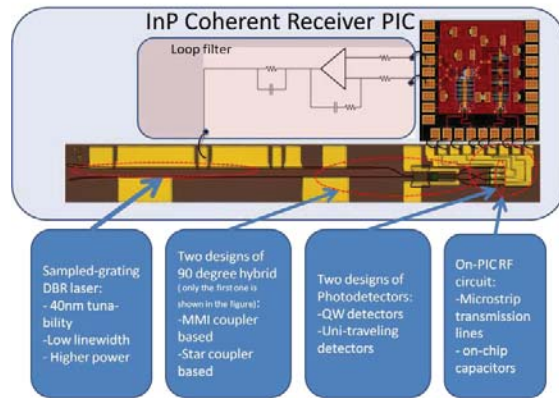


Fig. 5. OPLL coherent receiver.

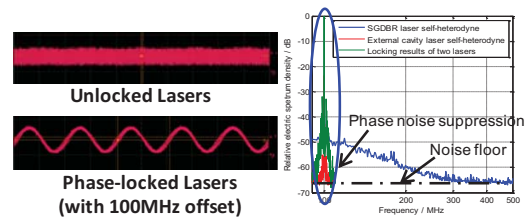


Fig. 6. Optical phase locked loop results.

REFERENCES

- [1] P. Winzer, *APC*, Shanghai, (Nov. 2011).
- [2] Y. Yamamoto and T. Kimura, *IEEE J. Quantum Electron.*, vol. 17, no. 6, pp. 919-925, (Jun. 1981).
- [3] N. S. Bergano and C. R. Davidson, *J. Lightwave Technol.*, vol. 14, no. 6, pp. 1299-1308, Jun. 1996.
- [4] L. A. Coldren, US Patent # 4,896,325 (January 1990).
- [5] J. S. Barton, et al, *ISLC*, TuB3, Garmish, (Sept, 2002).
- [6] B. Mason, et al, JDSU, private communication (2011).
- [7] S. Nicholes, et al, *IPRM '09*, paper WB1.2, Newport Beach (May, 2009).
- [8] C. Joyner, et al, *OFC*, San Diego, CA, Mar. 21-25, OWD3 (2010).
- [9] P. Evans, et al, *OFC*, Los Angeles, Mar. PDP7 (2011).
- [10] R. Tkach, *OIDA Annual Meeting*, Santa Clara, CA, (Dec. 1-2, 2009).
- [11] M. Nakazawa, K. Kikuchi, T. Miyazaki (eds.), *High Spec. Density Optical Com. Tech.s, Optical and Fiber Com. Reports 6*, Springer-Verlag, vol. 6, pp 103-127, 2010.
- [12] S. Ristic, et al *J. Lightwave Technol.*, vol. 28, no. 4, pp. 526-538, Feb. 15, (2010).
- [13] M. Lu, et al *IEEE Photonics Conf (IPC'11)*, Arlington, (Oct. 2011).
- [14] P. Binetti, et al *J. Quantum Electron.*, Special issue on integrated optoelectronics, (2012).
- [15] L.A. Coldren et al, *IEEE J. Lightwave Tech.*, vol. 29, no. 4, pp. 554-570, (Feb. 2011).



UC SANTA BARBARA
engineering

Introduction and Overview

The convergence of research and innovation.

- Why integration?
- Photonic IC technology—focus on InP
- Early development of PICs—serial and parallel approaches
- Coherent and WDM drove needs--tunable transmitters and receivers, or transmitter and receiver arrays resulted
- After focus on WDM due to EDFA, coherent has returned for more spectral efficiency
- Heterodyne vs. Intradyne—optical phase locked loops (OPLLs) for energy efficiency in sensors and communication
- What about Active Si-Photonics

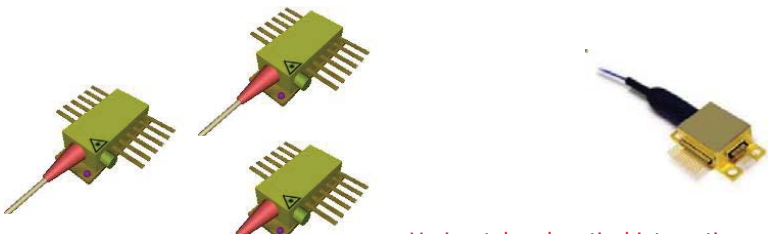
Why Integration

UC SANTA BARBARA
engineering

Motivation for Photonic Integration

The convergence of research and innovation.

- Reduced size, weight, power
- Improved performance (coupling losses, stability, etc.)
- Improved reliability (fewer pigtailed, TECs...)
- Cost



Horizontal and vertical integration possible
- multiple functionality and arrays of chips in one

1/18/2013 4

The convergence of research and innovation.

Oil & Gas



Structures



Aerospace



Medical--OCT

Bragg gratings:

- Temperature
- Pressure
- Displacement / Strain
- Damage/Delamination

Coherent Fiber Sensing

- Distributed Acoustics
- Vibration
- Flow
- Intrusion
- Perimeter Monitoring



New lasers, such as all-semiconductor very high-speed swept lasers (>kHz rates), are enabling new methodologies (photo courtesy of Insight Photonic Solutions)

The convergence of research and innovation.

Indium Phosphide

- Excellent active components
- Mature technology
- Complexity/propagation losses for passive elements

Silica on Silicon (PLC)

- Excellent passive components
- Mature technology
- Lack of active elements

Polymer Technology

- Low loss
- Passive waveguides
- Modulators
- No laser

Silicon Photonics

- Interconnects
- Integration with electronics
- Constantly improving performance
- No laser

Hybrid Solutions

- Most mature and widely used
- Driven by communication and sensor applications
- Examples
 - Widely tunable laser (SGDBR)
 - Externally modulated laser (EML)
 - EAM based
 - MZI based
 - Preamplified receiver
 - Transmitter/Receiver Arrays
 - Coherent (vector) transmitters and receivers
 - Wavelength converters

PIC Technology

Early Active PICs

The convergence of research and innovation.

Partially transmissive mirrors and active-passive integration needed

→ Etched grooves

- Tunable single frequency
- Laser-modulator
- Laser-detector

L.A. Coldren, B.I. Miller, K. Iga, and J.A. Rentschler, "Monolithic two-section GaInAsP/InP active-optical-resonator devices formed by RIE," *Appl. Phys. Letts.*, 38 (5) 315-7 (March, 1981).

First integrated InP (laser - X) devices



Early Active PICs

The convergence of research and innovation.

Partially transmissive mirrors and active-passive integration needed

→ Etched grooves

- Tunable single frequency
- Laser-modulator
- Laser-detector

L.A. Coldren, B.I. Miller, K. Iga, and J.A. Rentschler, "Monolithic two-section GaInAsP/InP active-optical-resonator devices formed by RIE," *Appl. Phys. Letts.*, 38 (5) 315-7 (March, 1981).

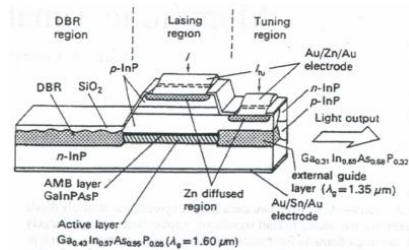
First integrated InP (laser - X) devices



→ DBR gratings and vertical couplers

- Tunable single frequency
- Combined integration technologies

Y. Tohmori, Y. Suematsu, Y. Tushima, and S. Arai, "Wavelength tuning of GaInAsP/InP integrated laser with butt-jointed built-in DBR," *Electron. Lett.*, 19 (17) 656-7 (1983).



Early Active PICs

The convergence of research and innovation.

Partially transmissive mirrors and active-passive integration needed

→ Etched grooves

- Tunable single frequency
- Laser-modulator
- Laser-detector

L.A. Coldren, B.I. Miller, K. Iga, and J.A. Rentschler, "Monolithic two-section GaInAsP/InP active-optical-resonator devices formed by RIE," *Appl. Phys. Letts.*, 38 (5) 315-7 (March, 1981).

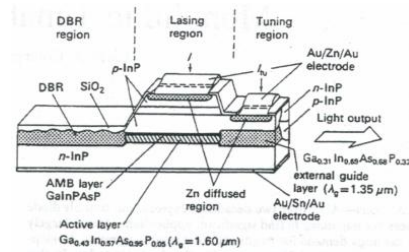
First integrated InP (laser - X) devices



→ DBR gratings and vertical couplers

- Tunable single frequency
- Combined integration technologies

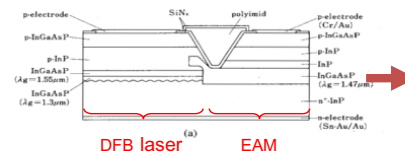
Y. Tohmori, Y. Suematsu, Y. Tushima, and S. Arai, "Wavelength tuning of GaInAsP/InP integrated laser with butt-jointed built-in DBR," *Electron. Lett.*, 19 (17) 656-7 (1983).



→ EML = electroabsorption-modulated laser

- Still in production today

M. Suzuki, et al., *J. Lightwave Technol.*, LT-5, pp. 1277-1285, 1987.



Coherent Communication Motivated Photonic Integration

The convergence of research and innovation.

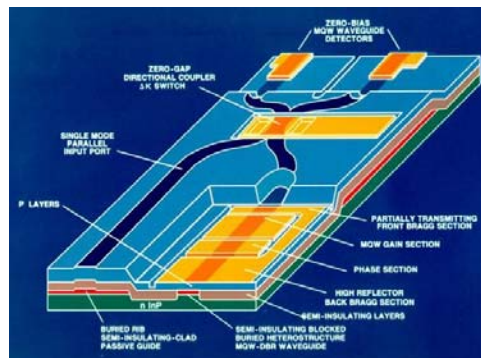
- In the 1980's coherent communication was widely investigated to increase receiver sensitivity and repeater spacing. It was also seen as a means of expanding WDM approaches because optical filters would not be so critical.

Y. Yamamoto and T. Kimura, "Coherent optical fiber transmission systems," *IEEE J. Quantum Electron.*, vol. 17, no. 6, pp. 919-925, Jun. 1981.

- This early coherent work drove early photonic integration efforts—Stability; enabled phase-locking

T. L. Koch, U. Koren, R. P. Gnall, F. S. Choa, F. Hernandez-Gil, C. A. Burrus, M. G. Young, M. Oron, and B. I. Miller, "GaInAs/GaInAsP multiple-quantum-well integrated heterodyne receiver," *Electron. Lett.*, vol. 25, no. 24, pp. 1621-1623, Nov. 1989

Integrated Coherent Receiver
(Koch, et al)



- The EDFA enabled simple WDM repeaters (just amplifiers) and coherent was put on the shelf

UC SANTA BARBARA engineering
The convergence of research and innovation.

PIC Enablers: Active-Passive Integration

Desire lossless, reflectionless transitions between sections

Vertical Twin-Guide BUTT-JOINT REGROWTH SELECTIVE AREA GROWTH OFFSET QUANTUM WELLS DUAL QUANTUM WELLS QUANTUM WELL INTERMIXING

Patterned Re-growth Low Passive Loss Low Passive Loss

3 Bandgaps usually desired
Need simple, high-yield process

UC SANTA BARBARA engineering
The convergence of research and innovation.

Offset Quantum Well Process

Active-Passive Region Definition Grating Formation InP/InGaAs Regrowth

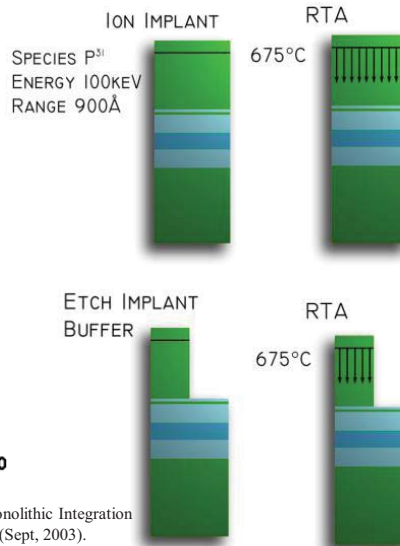
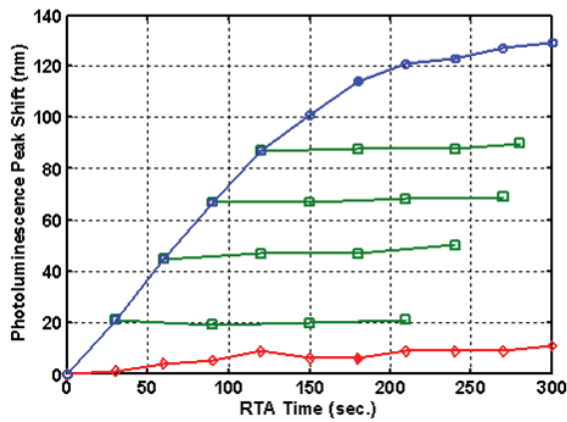
Metalization/Anneal Passivation/Implant InP Ridge Etch

- Most Mature SGDBR Fabrication Technology
- Requires Single 'Planar' MOCVD Regrowth

The convergence of research and innovation.

Simple/robust QWI process

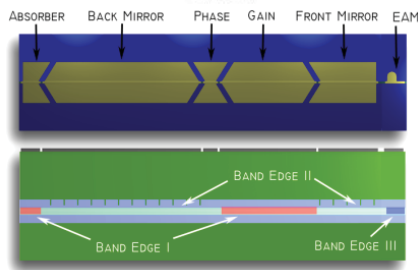
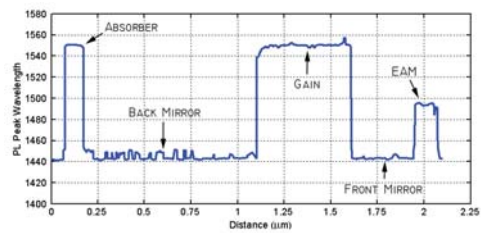
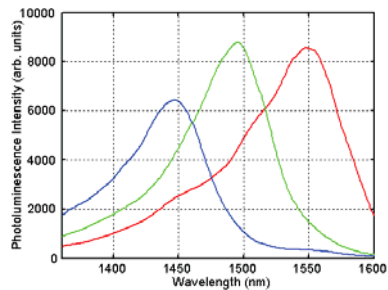
- Ability to achieve multiple band edges with a single growth & implant



E. Skogen et al, "Post-Growth Control of the Quantum-Well Band Edge for the Monolithic Integration of Widely-Tunable Lasers and Electroabsorption Modulators," *JSTQE*, 9 (5) pp 1-8 (Sept, 2003).

The convergence of research and innovation.

- Optimized band edges for various devices
- Three band edges across wafer
- Widely-tunable SGDBR laser/EAM



Raring, Skogen, Coldren, et al

UC SANTA BARBARA engineering
The convergence of research and innovation.

Lateral waveguides/couplers

Waveguide cross sections

Higher index contrast

MMI coupler

UC SANTA BARBARA engineering
The convergence of research and innovation.

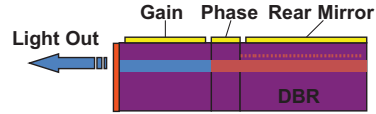
Desire for Practical Tunable Lasers Motivates Integration

- Both WDM and coherent communication systems desired tunable lasers
- Sensor systems also needed tunable sources
- Mechanically-tuned 'External-cavity' tunable lasers exist, but they tend to be costly, bulky, tune slowly, and are subject to vibration

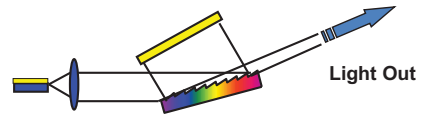
$m\lambda/2 = nL$

The convergence of research and innovation.

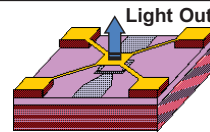
- DBR Lasers
 - Conventional DBR (<8 nm)
 - Extended Tuning DBR's (≥ 32 nm)



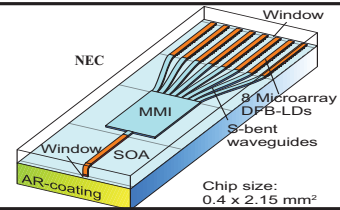
- External Cavity Lasers (≥ 32 nm)
 - Littman-Metcalf/MEMs
 - Thermally tuned etalon



- MEMS Tunable VCSEL (< 32 nm)
 - Optically or electrically pumped



- DFB Array (3-4 nm X #DFBs)
 - On-chip combiner + SOA
 - Or, off-chip MEMs combiner
 - Thermally tuned



Widely-Tunable-X PICs
(Mostly serial integration)

Sampled-Grating DBR: Monolithic and Integrable

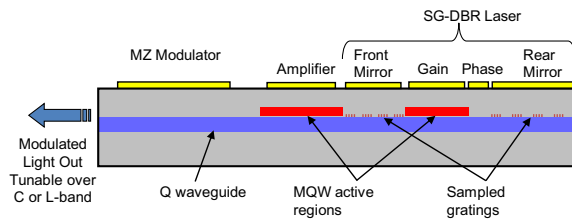
The convergence of research and innovation.

SGDBR+X widely-tunable transmitter:

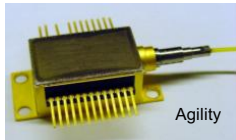
- Foundation of PIC work at UCSB

"Multi-Section Tunable Laser with Differing Multi-Element Mirrors," US Patent # 4,896,325 (January 1990)

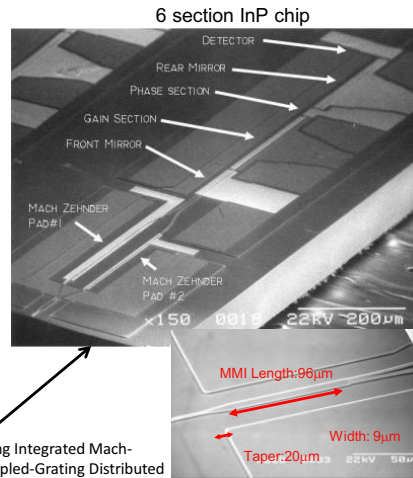
(UCSB'90-- → Agility'99-'05 → JDSU'05→)



- Vernier tuning over 40+nm near 1550nm
- SOA external to cavity provides power control
- Currently used in many new DWDM systems (variations)
- Integration technology for much more complex PICs

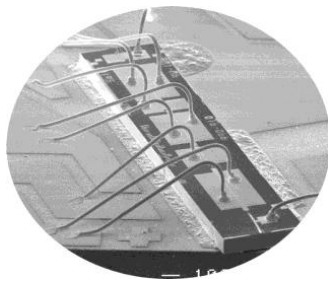


J. S. Barton, et al, "Tailorable Chirp using Integrated Mach-Zehnder Modulators with Tunable Sampled-Grating Distributed Bragg Reflector Lasers," ISLC, TuB3, Garmish, (Sept, 2002)

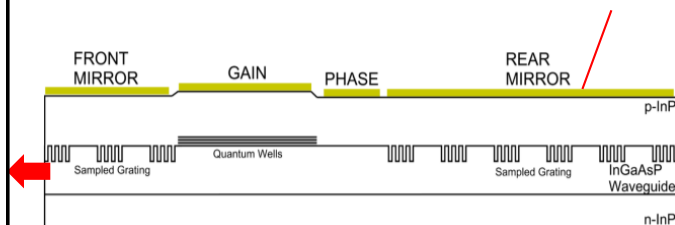


Sampled-Grating DBR Laser

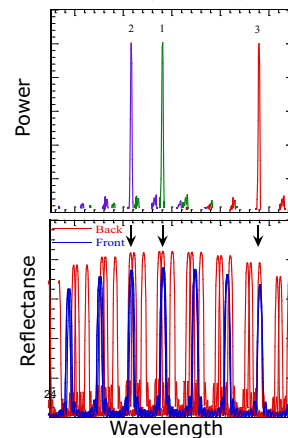
The convergence of research and innovation.



- Uses vernier effect for multiband tuning
- $\Delta\lambda/\lambda = N \times \Delta n/n$ by differential mirror tuning

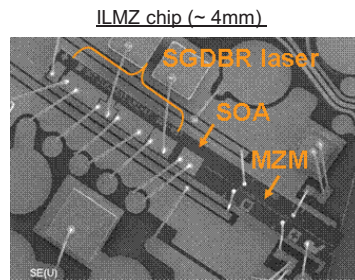


Supermode (multiband) tuning



The convergence of research and innovation.

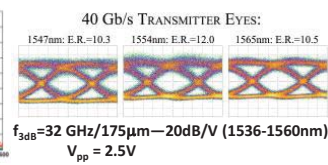
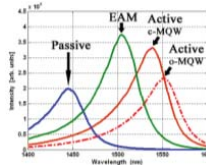
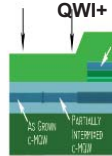
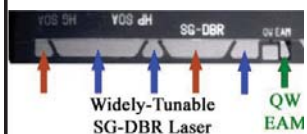
- Volume deployment typically needs form factors optimized for port count, size, power dissipation and cost
 - Transceiver module form factors are MSA driven and ecosystem is more mature
 - Photonic integration is essential to achieve cost, power and size roadmap
 - ILMZ is a good example of photonic integration



The convergence of research and innovation.

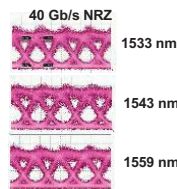
Research initiatives:

1. QWI/EAM :



J.W. Raring and L.A. Coldren, *JSTQE* 13, (1), pp. 3-14, (Jan. 2007)

2. Dual QW/TW-EAM :

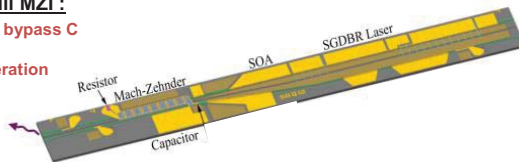


- 15 – 20 dB/V for 600 μm over range
- Open eyes for all wavelengths
 - 6 – 10 dB extinction with 2.1V

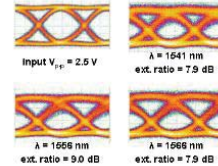
M. M. Dummer, et al, *OFC'08*, San Diego, Mar, 2008.

3. Series Push-Pull MZI :

- Integrated load R and bypass C
- 30 GHz Bandwidth
- 40 Gb/s error free operation
- Low/negative chirp



40 Gb/s eyes



A. Tauke-Pedretti, et al, *Photon. Tech. Lett.*, 18 (18) 1922-4 (2006).

UC SANTA BARBARA engineering

The convergence of research and innovation.

Evolution of InP Integration technology enables more functionality—Tranceivers/wavelength converters

Research initiatives: High-efficiency SOA-PIN Receiver & SGDBR-TW/EAM Transmitter

- Data format and rate transparent 5-40Gb/s
- No filters required (same λ in and out possible)
- Two-stage SOA pre-amp for high sensitivity & efficiency
- 2R regeneration possible
- Traveling-wave EAM with on chip loads; ~ 0 dB out/in optical insertion loss
- Only DC biases applied to chip—photocurrent directly drives EAM $\rightarrow 1\text{W}/40\text{ Gb/s} \rightarrow 25\text{ pJ/bit}$
- 40 nm wavelength tuning range

Eye Diagrams

5 Gb/s NRZ	10 Gb/s NRZ
20 Gb/s NRZ	40 Gb/s NRZ
20 Gb/s RZ	40 Gb/s RZ

M. Dummer et al. Invited Paper Th.2.C.1, ECOC 2008.

UC SANTA BARBARA engineering

The convergence of research and innovation.

More functionality: 8 x 8 MOTOR Chip

Research initiatives: (40 Gb/s per channel)

- 8 x 8 'all-optical' crossbar switch
- SOA – Mach-Zehnder Wavelength Converters
- Quantum-well intermixing (QWI) to shift bandedge for low absorption in passive regions
- Three different lateral waveguide structures for different curve/loss requirements

Monolithic Tunable Optical Router

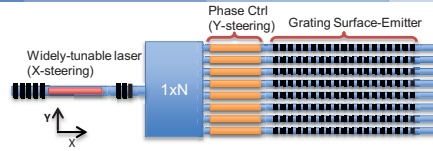
See S. Nicholes, et al, "Novel application of quantum-well intermixing implant buffer layer to enable high-density photonic integrated circuits in InP," *IPRM '09*, paper WB1.2, Newport Beach (May, 2009)

Free-space 2-D Beam Sweeper

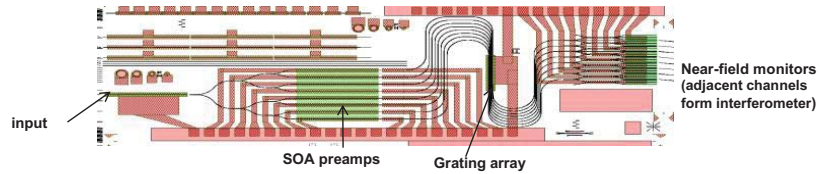
The convergence of research and innovation.

Research initiatives:

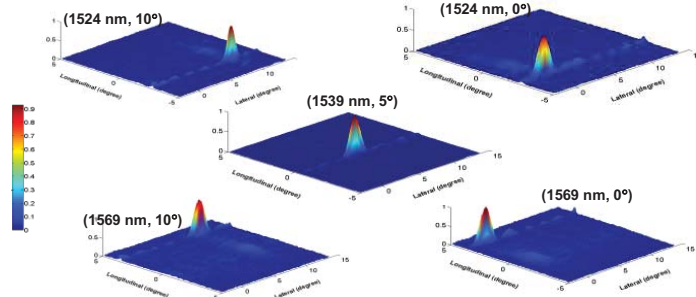
Concept: Wavelength sweeps beam in x-direction;
1-D phased array sweeps beam in y-direction



PIC layout:

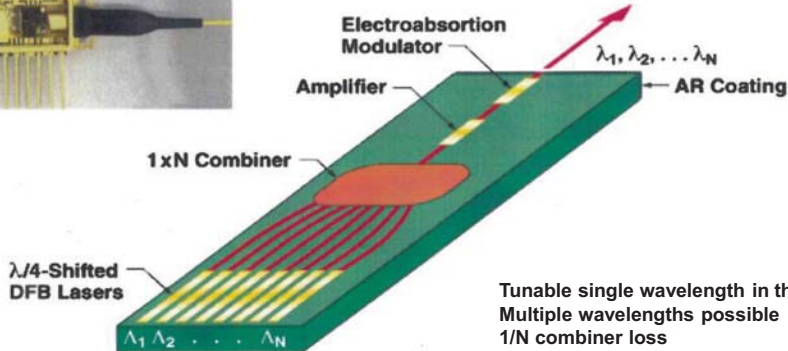
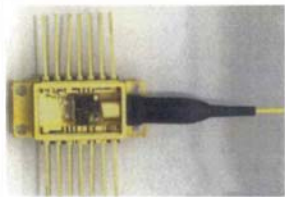


2-D beam sweeping results:
 $10^\circ \times 10^\circ$



Integrated Multi-Channel PICs
(Mostly parallel integration)

The convergence of research and innovation.



Tunable single wavelength in this case
Multiple wavelengths possible
1/N combiner loss

M. G. Young, et al., *Electron. Lett.*, 31, pp. 1835-1836, 1995.

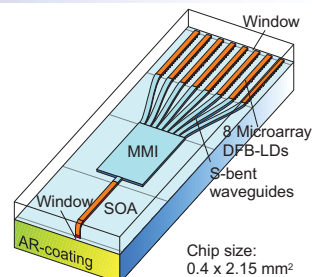
The convergence of research and innovation.

Feature

- DFB-LD-array-based structure
- Wide-band tunability
- Compact & stable
Multi- λ locker module

Performance

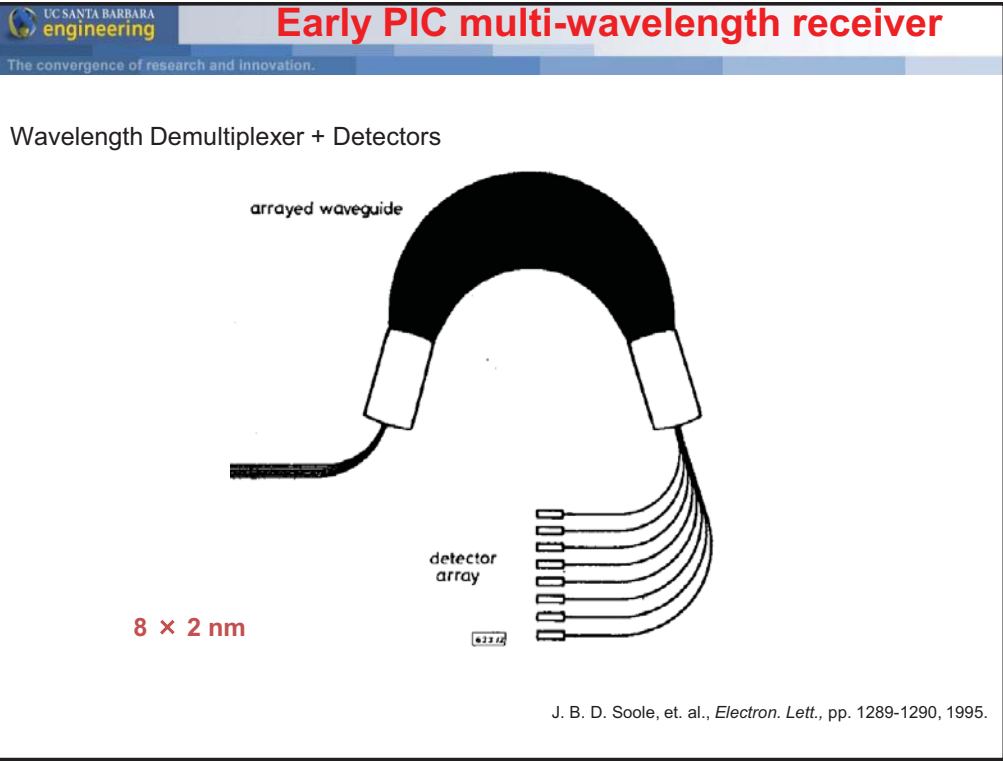
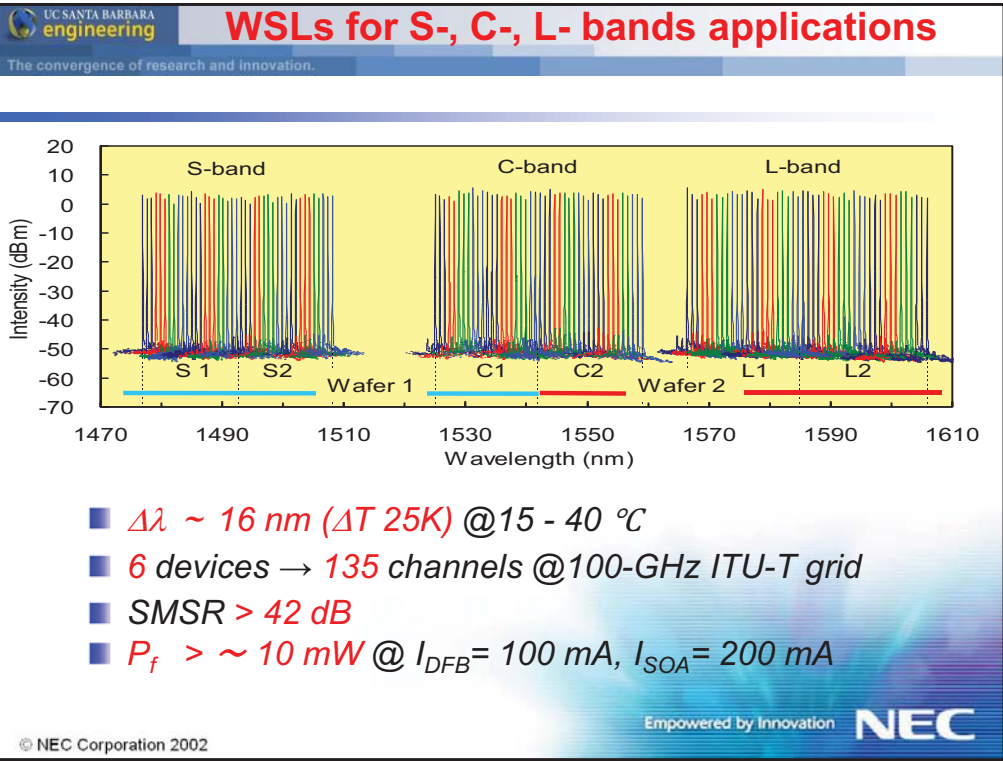
- WSLs for S-, C-, L- bands (OFC'02)
8 array, $\Delta\lambda \sim 16 \text{ nm}$ ($\Delta T = 25\text{K}$) x 6 devices
- Multi λ -locker integrated
Wide-band WSL module (OFC'02)
 $\Delta\lambda \sim 40 \text{ nm}$ ($\Delta T = 45\text{K}$)



Schematic of wide-band WSL

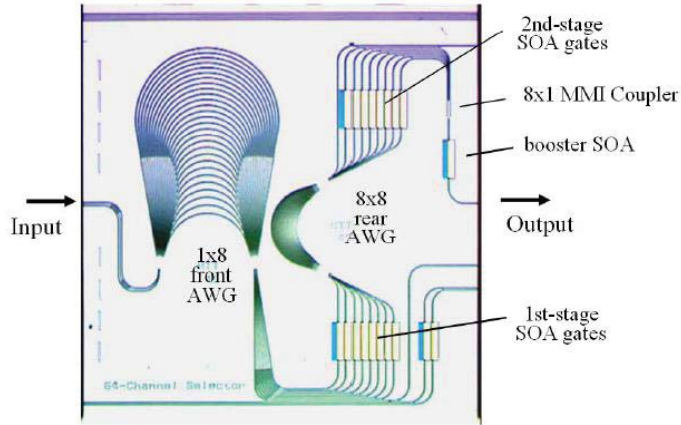


Multi λ -locker integrated
Wide-band WSL module



1/64 WDM Channel Selector

The convergence of research and innovation.



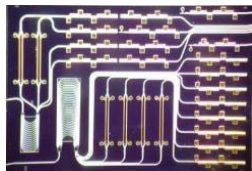
(chip size : 7.0 x 7.0 mm²)

Kikuchi (NTT), EL, Volume 39, Issue 3, p.312-314, 2003

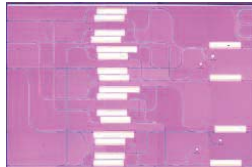
1/18/2013

ASICs made in the first EuroPIC MPW runs

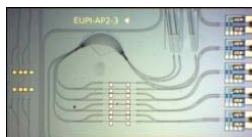
The convergence of research and innovation.



WDM transmitter



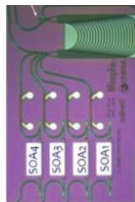
Fast optical 4x4 switch



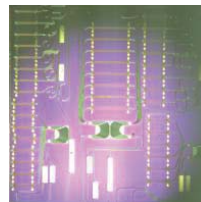
FBG readout chip



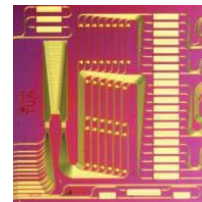
Pulse laser with variable rep rate



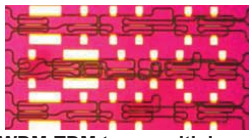
FF MW-laser



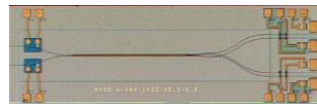
Pulse serialiser



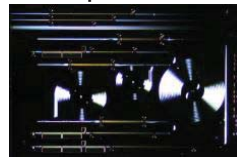
Pulse compressor



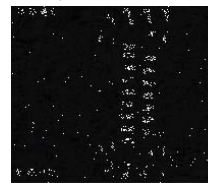
WDM-TDM transmultiplexer



QPSK receiver



60 GHz RoF transmitter



WDM crossconnect

UC SANTA BARBARA engineering **Widely Deployed Commercial "WDM" PICs**

The convergence of research and innovation.

EML's:

into XFP transceivers, etc.

Tunables & Selectable Arrays:

UCSB ↔ AGILITY ↔ JDSU

Santur

FURUKAWA ELECTRIC

courtesy of T. Koch

UC SANTA BARBARA engineering **Commercialization of WDM PICs: 2nd Gen. PICs**

The convergence of research and innovation.

Large-Scale DWDM Photonic Integrated Circuits

100Gb/s Receive

100Gb/s Transmit

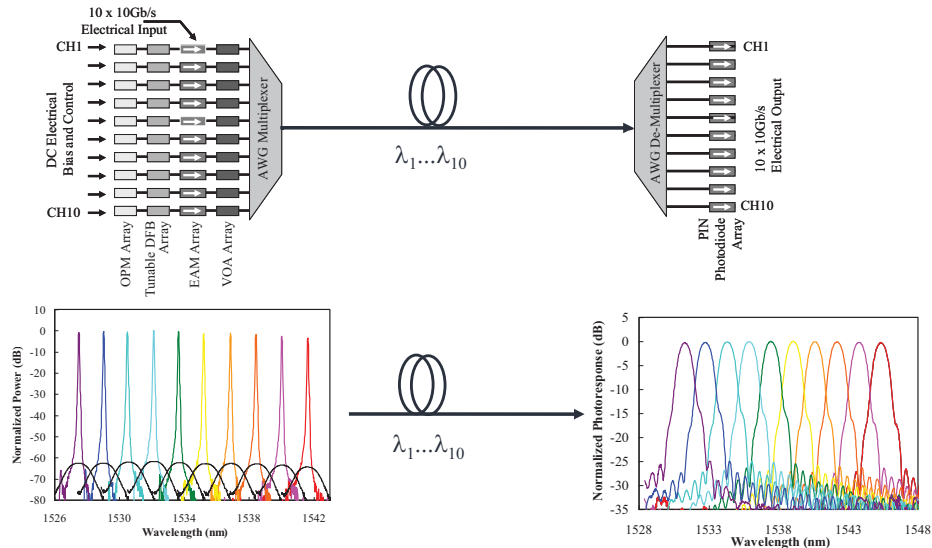
infinera

courtesy of C. Joyner

2004: First Commercial Large-Scale InP PICs

The convergence of research and innovation.

100 Gb/s (10 x 10Gb/s) Transmitter and Receiver PIC



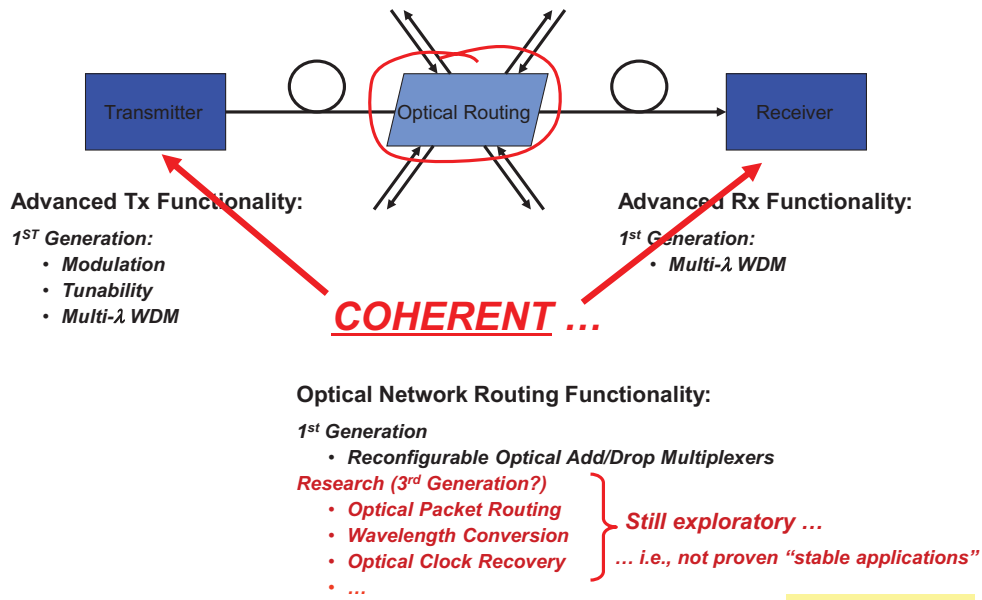
infinera

courtesy of F. Kish

What is the 3rd Generation of InP PICs??

The convergence of research and innovation.

– what are the critical “stable configurations”



courtesy of T. Koch

UC SANTA BARBARA engineering

Coherent returns to extend spectral efficiency++

The convergence of research and innovation.

- Vector modulation/coherent detection utilizes full complex field to enhance spectral efficiency
- Increase bit-rate without increasing baud rate

Binary modulation formats (1 bit/symbol):

- Optical duobinary / PSBT
- NRZ- / RZ-DPSK ("bipolar" ASK)

Quaternary (2 bits/symbol):

- NRZ- / RZ-DQPSK

Polarization-multiplexed QPSK (4 bits/symbol):

- Dual-Polarization QPSK

Other approaches for S.E. improvement include QAM (both amplitude and phase) and OFDM (Orthogonal Frequency Division Multiplexing → no guardbands)

Courtesy B. Mason

UC SANTA BARBARA engineering

Traveling-wave InP MZM DQPSK PIC

The convergence of research and innovation.

Wavelength range: L-band ($\lambda_{PL} = 1.47 \mu\text{m}$)
 RF input: Differential
 EO interaction length: 3 mm (Sub-MZMs),
 1.5 mm ($\pi/2$ -phase shifter)
 Chip size: **7.5 mm x 1.3 mm**

N. Kikuchi, ECOC, 10.3.1, 2007.

NTT

UC SANTA BARBARA engineering **First Multi-Channel QPSK Transmitter PIC**
 The convergence of research and innovation.

10 channels x 40 Gb/s net

AWG

Nested MZM

I Q

DFB

Tunable

PM

21.5Gb/s NRZ Balanced Receiver Eye

S21 Frequency Response

10 Log (S21) (dB, optical)

Frequency (GHz)

Small-signal BW > 20GHz

- 10 frequency-tunable DFB lasers with backside power monitors
- 10(I) + 10(Q) nested Mach-Zehnder modulator pairs
- 1 AWG
- 111 integrated elements in total on chip

S.W. Corzine, et al, OFC'08, PDP18, 2008

courtesy of C. Joyner

UC SANTA BARBARA engineering **2011: 500 Gb/s PM-QPSK Coherent PICs**
 The convergence of research and innovation.

Tx PIC Architecture (5 x 114 Gb/s)

PM DFB

TM-to-be

AWG

Rot

PBC

TE

AWG

- > 450 Integrated Functions
- 8 Different Integrated Functions

Rx PIC Architecture (5x 114Gb/s)

H Pot

V Pot

AWG

DFB LO

BPF

VOA

Optical Hybrid

Optical Hybrid

Q

I

Q

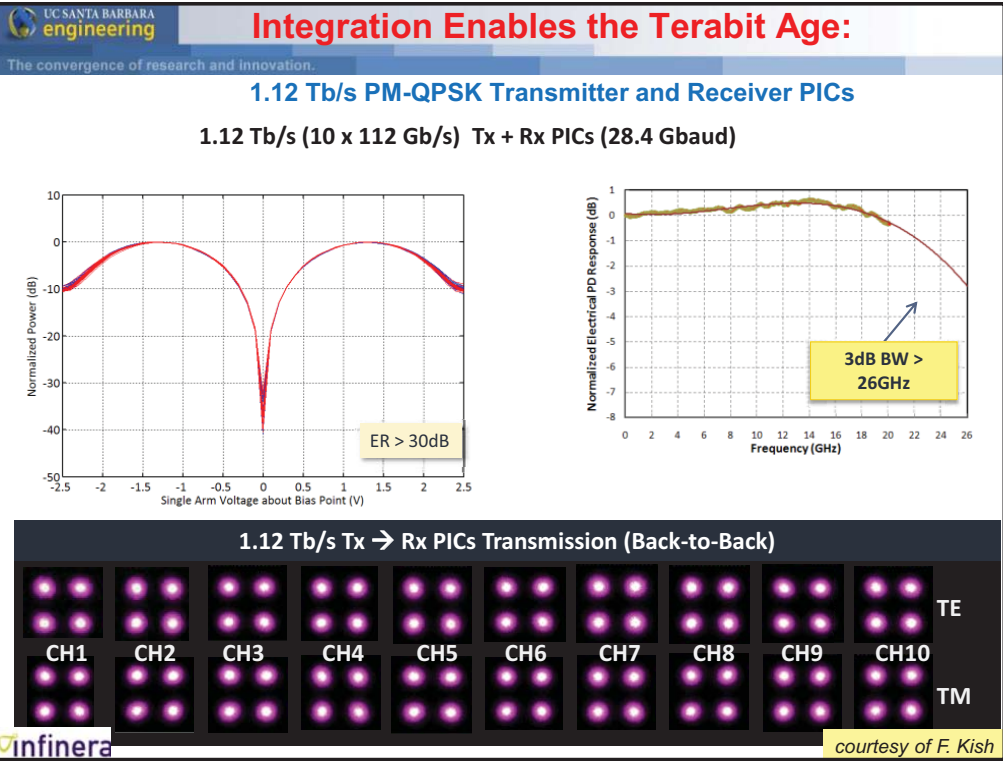
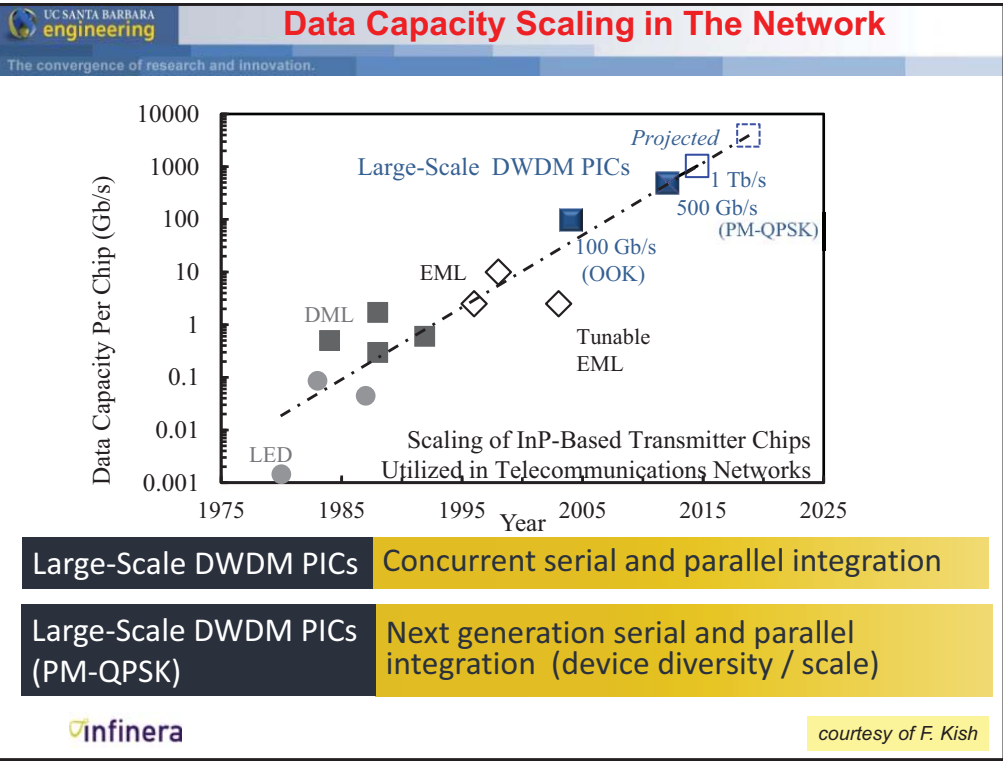
I

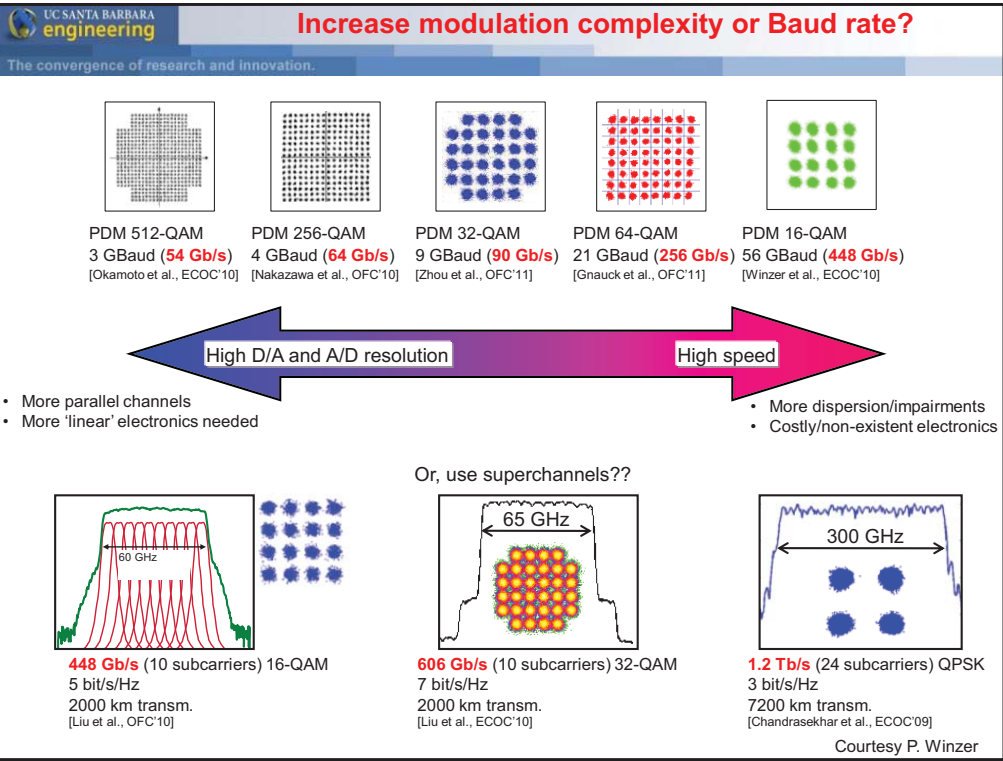
- > 150 Integrated Functions
- 7 Different Integrated Functions

10 tunable DFBs,
20 nested MZ modulators (40 total MZMs)
All of PIC sense and control functions

infinera

courtesy of F. Kish



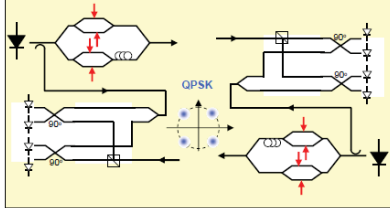


Optical Phase Locked Loops
To save Power and Cost?

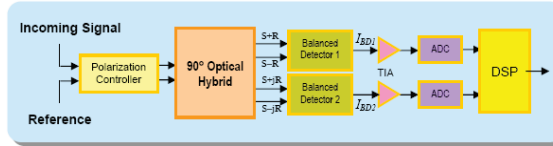
Intradyn or Heterodyne for generic sensor and short-reach communication applications?

Intradyn Coherent Detection

- Phase and polarization diversity
- Frequency-locked local oscillator
- Digital signal processing of received electrical signals
 - Electronic CD compensation
 - Electronic polarization demultiplex
 - Adaptive PMD compensation



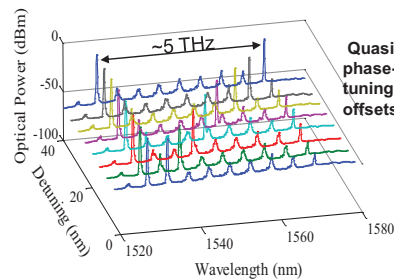
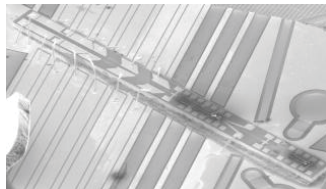
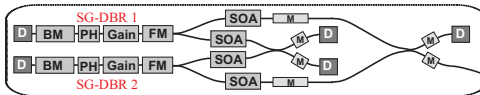
Typical Intradyn receiver architecture



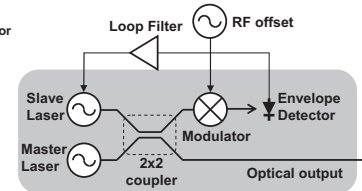
- ❖ Use 'Intradyn' without phase-locked LOs, or do we need true Heterodyne detection?
 - Desire data-rate independent generic chips—when are phase-locked narrow-linewidth LOs desired?
 - High-speed A/Ds & DSPs require lots of power and are expensive to design, especially as data rate increases
 - Some impairments can be removed with much slower, lower-power, lower-cost signal-processing circuits

Integrated Optical Phase Locked Loops (OPLLs): provide a new stable control element

- Offset locking of two SGDBRs → viable using close integration of PICs with electronics in a OPLL
- Hz-level relative frequency control, potentially over 5 THz

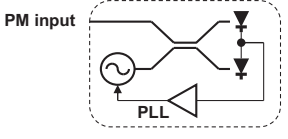
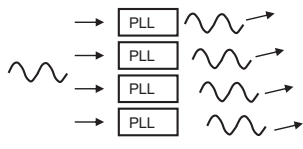
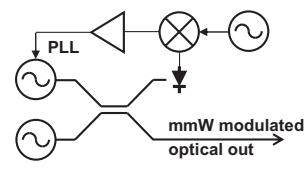


Quasi-continuous phase-locked digital tuning up to 5 THz offsets possible



UC SANTA BARBARA engineering
The convergence of research and innovation.

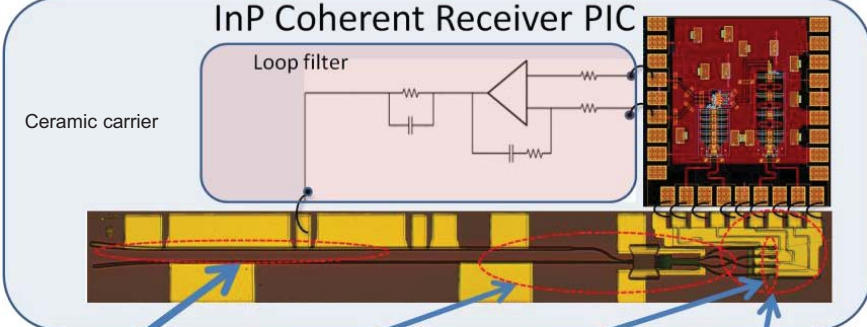
Applications/Challenges

<p>Coherent receiver</p>  <p>Costa's Loop for BPSK, QPSK demodulation Complex DSP circuits not required, but simpler ones can be added for CD and PMD Challenge: Develop receivers for high speed (>100Gbaud) or high constellations (n-QAM) Matched with development of coherent sources</p>	<p>LIDAR</p>  <p>Very rich/challenging area Locking tunable lasers Arrays of locked OPLLs Swept microwave reference Time / Phase encoding of directed output Need for rapid scanning and locking rates</p>	<p>mmW / THz generation</p>  <p>Locking of two tunable lasers Requires high-speed, high-power UTC photodiode Speed determined by UTC photodiode and feedback electronics: Can be very high Combined with antenna designs for complete TRX links with free-space path</p>
---	---	--

All require close integration of electronics with photonics

UC SANTA BARBARA engineering
The convergence of research and innovation.

OPLL Receiver Layout

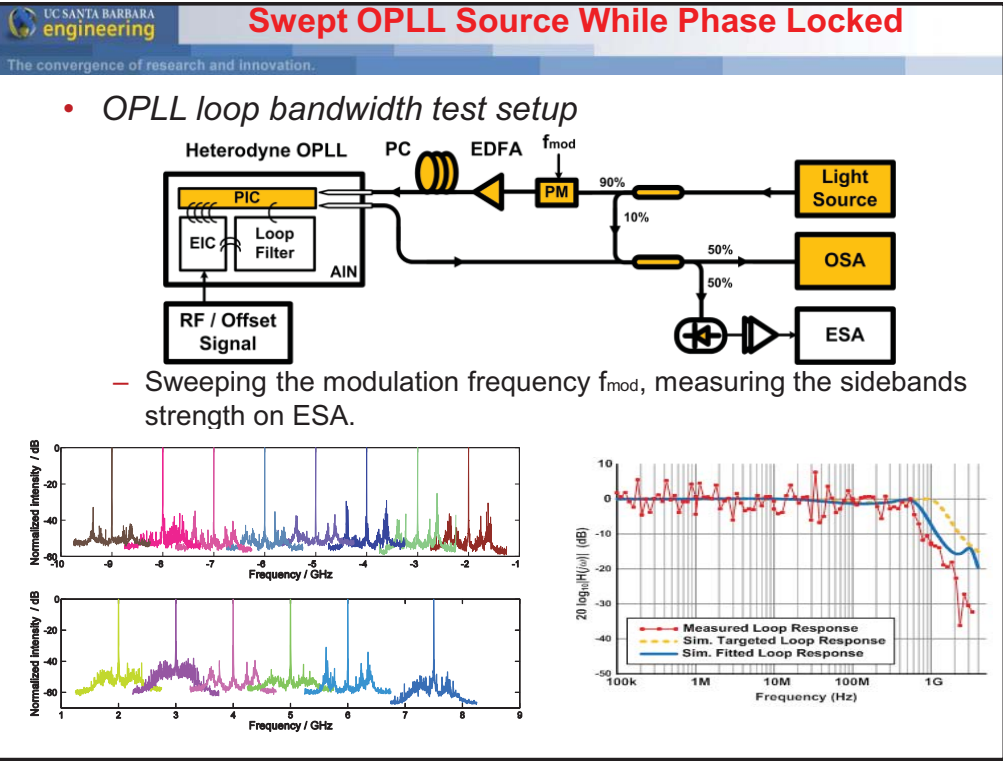
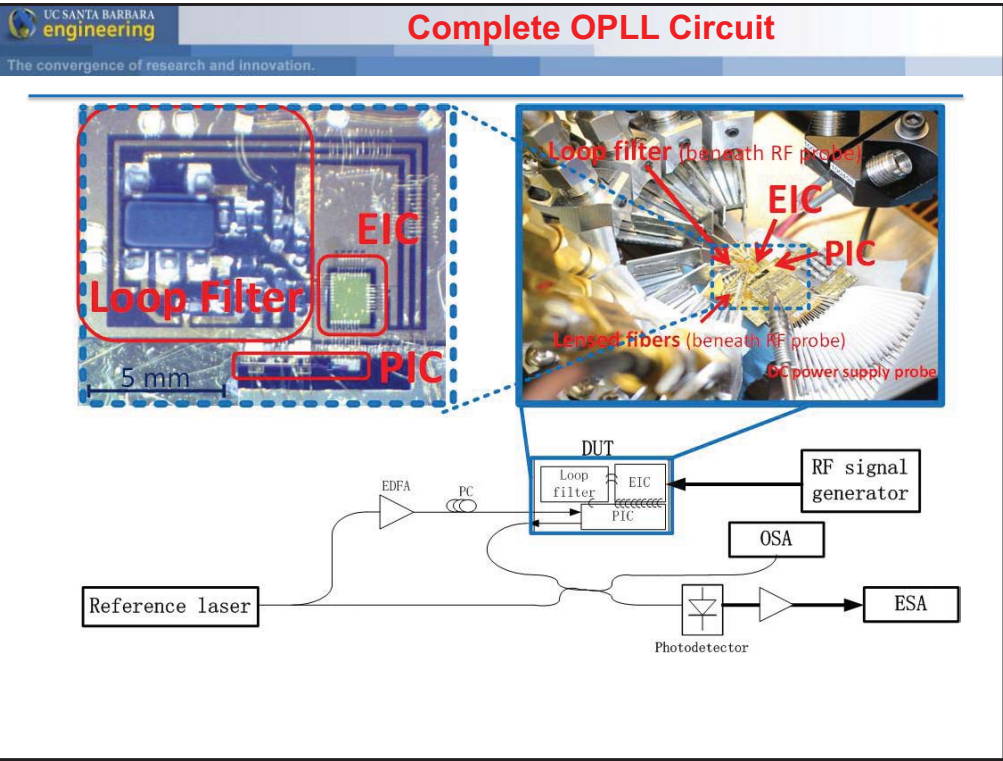


InP Coherent Receiver PIC

Ceramic carrier

Loop filter

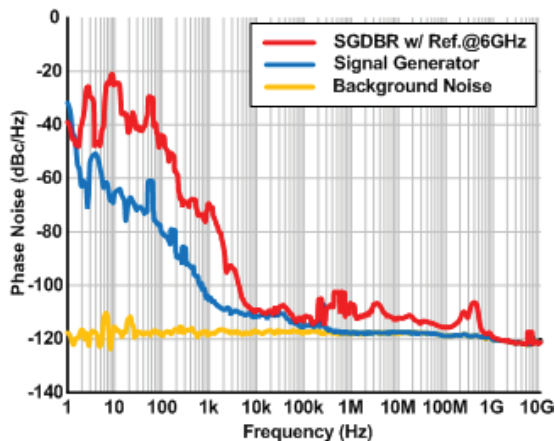
<p>Sampled-grating DBR laser:</p> <ul style="list-style-type: none"> - 40nm tunability - Low linewidth - Higher power 	<p>Two designs of 90 degree hybrid (only the first one is shown in the figure):</p> <ul style="list-style-type: none"> - MMI coupler based - Star coupler based 	<p>Two designs of Photodetectors:</p> <ul style="list-style-type: none"> - QW detectors - Uni-traveling detectors 	<p>On-PICRF circuit:</p> <ul style="list-style-type: none"> - Microstrip transmission lines - on-chip capacitors
---	--	--	---



Heterodyne Phase Noise (Swept Source)

The convergence of research and innovation.

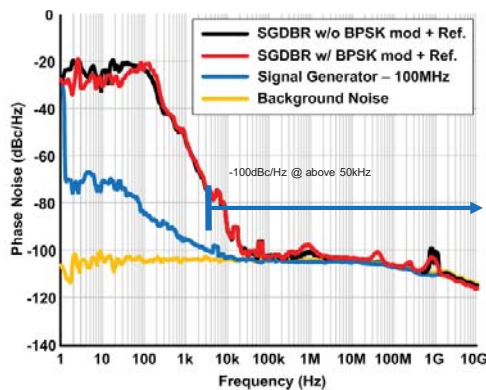
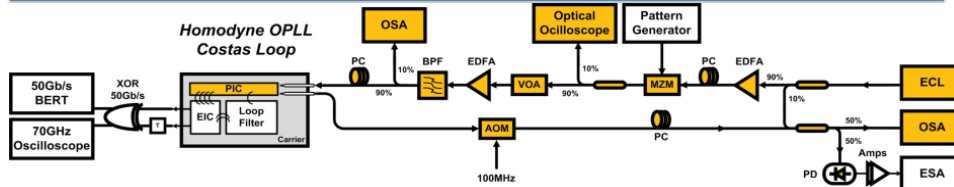
- Phase noise is comparable to commercial RF synthesizer
 - < -100 dBc/Hz phase noise above 5 kHz
 - 0.03 rad² phase error variance (Integration from 100Hz)



Homodyne BPSK OPLL Receiver (Phase Noise)

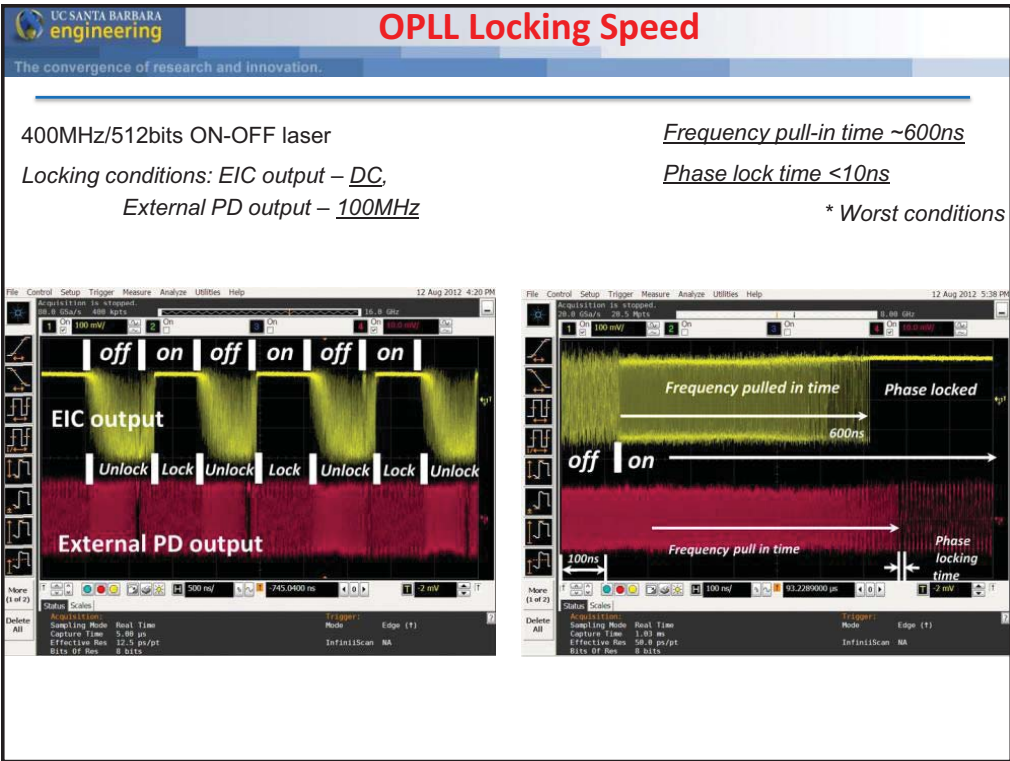
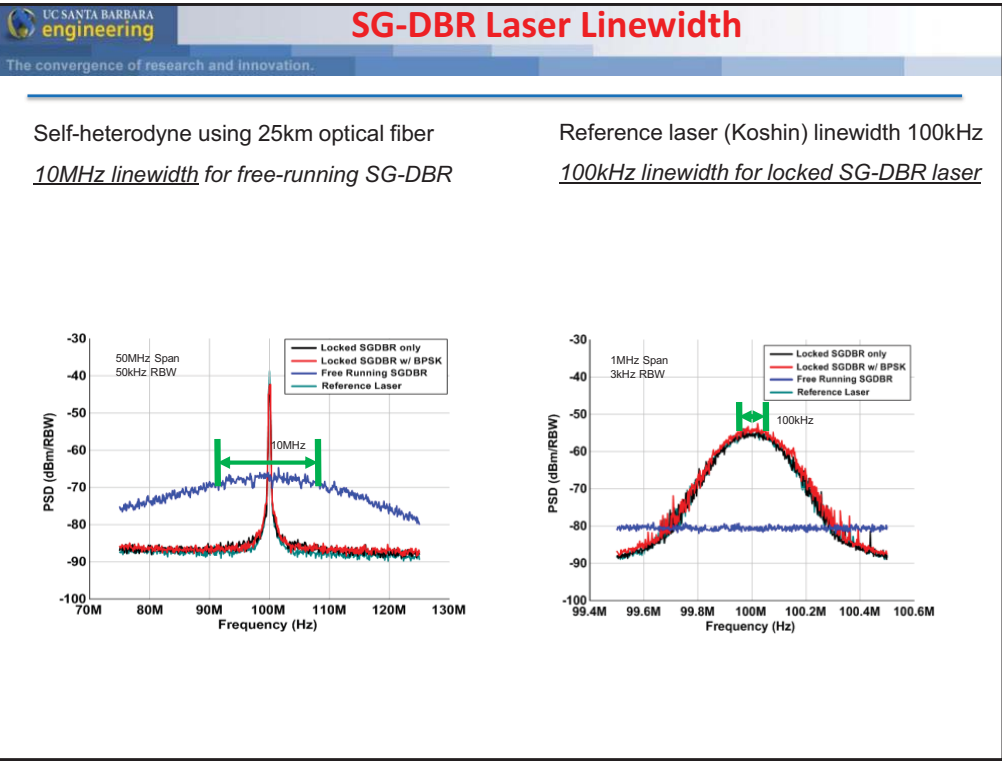
The convergence of research and innovation.

See Postdeadline Th3A.2 Room A



Cross correlation between SG-DBR and reference lasers

-100dBc/Hz @ above 50kHz

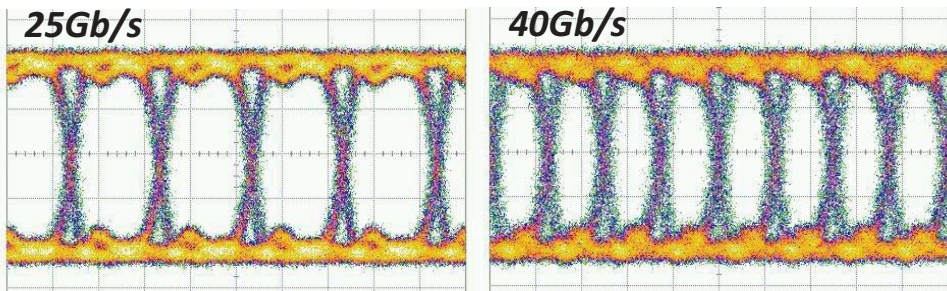
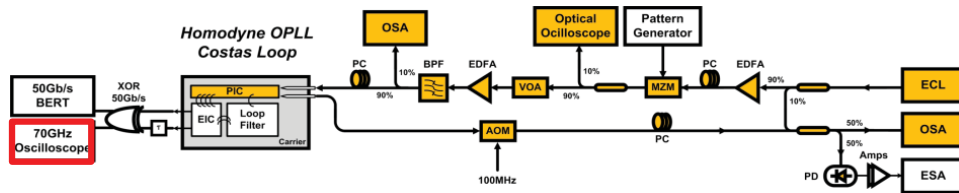


BPSK Data Reception—Eyes

The convergence of research and innovation.

PRBS $2^{31}-1$ signals – up to 40Gb/s BPSK data

Open eye diagrams for 25Gb/s and 40Gb/s



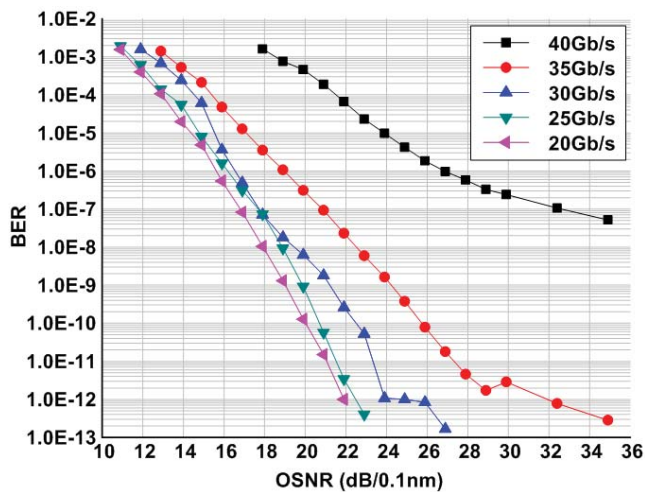
BPSK Data Reception—BERs

The convergence of research and innovation.

See Postdeadline Th3A.2 Room A

BER vs. OSNR (20Gb/s to 40Gb/s)

Error-free up to 35Gb/s, $< 1.0E-7$ @ 40Gb/s



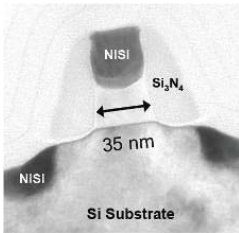
What about Si-Photonics for Active PICs?

UC SANTA BARBARA engineering
The convergence of research and innovation.

Why Silicon Photonics?

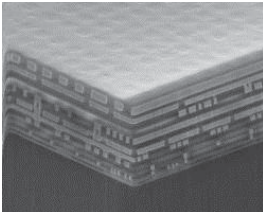
- Harness unprecedented process control platform that gives ever-increasing functionality per unit area at low cost

65 nm Generation Transistors ...
but already moving to 22nm!!

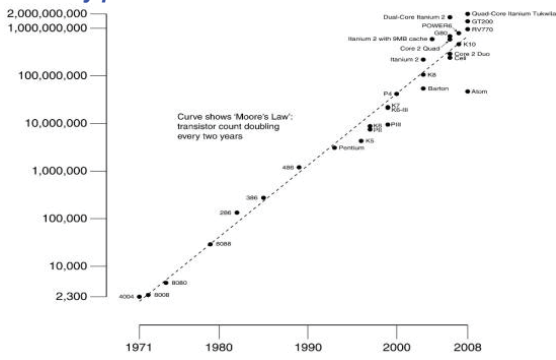


From Intel Corp.

Outrageous multi-layer metalizations ...



From ICE Corp.



Curve shows Moore's Law: transistor count doubling every two years

- 2 Billion transistors onto a chip at low cost?
 - Huge \$\$ annual investments to achieve extreme quality of materials, precision of fab tools, process yields
- IC product development team project done when tape-out complete!
 - Extreme predictability, mature CAD tools

CMOS IC Development – a world of difference from most of today's photonic chip design

courtesy of T. Koch

Why Silicon Photonics?

The convergence of research and innovation.

In brief:

- 1) Cost
- 2) Performance
- 3) "Saving Moore's Law"

—very different drivers

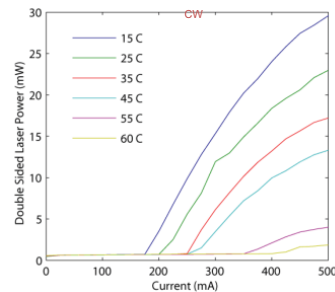
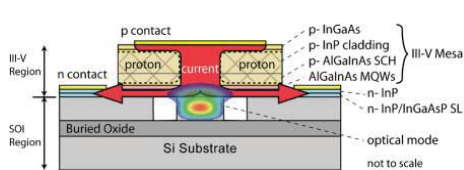
- **But can one get access to these state-of-the-art Si fabs? Likely not—however, probably can gain access to last generation fabs generating legacy EIC products**

Performance reasons:

- **Ultra-high index contrast**
 - Low bending losses, compact devices
 - Benefits of TM polarization for some apps
- **High performance actives? Lower power devices?**
 - High confinement, small active volumes ...??
- **Potential for on-board integrated electronics**
 - Reduced parasitics, eliminate impedance matching issues ...→ no 50 Ω loads !!!
 - Low-cost, highly sophisticated CMOS drive, preamp, digital processing, ...
 - Proliferation of new applications?
- **Critical to continued scaling of traditional electronic functionality?** *courtesy of T. Koch*

Hybrid-Si Laser via Wafer Bonding

The convergence of research and innovation.



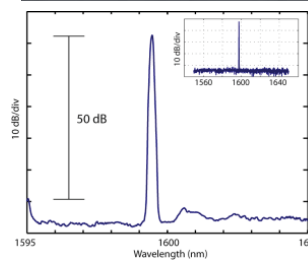
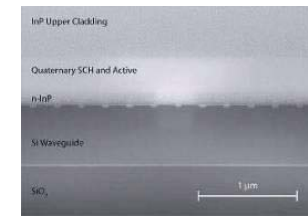
Integrated AlGaInAs-silicon evanescent racetrack laser and photodetector

Alexander W. Fang¹, Richard Jones², Hyundai Park¹, Oded Cohen¹, Omri Raday³, Mario J. Paniccia², & John E. Bowers¹

5 March 2007 / Vol. 15, No. 5 / OPTICS EXPRESS 2316



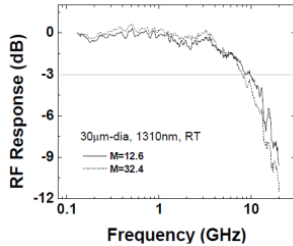
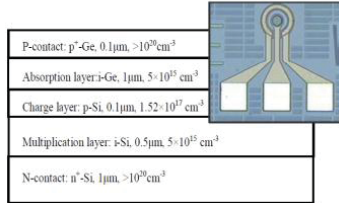
DFB Cross section



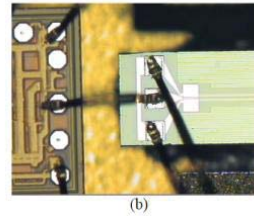
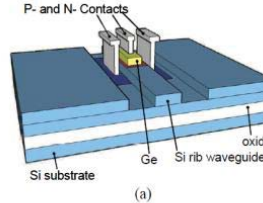
Bowers, et al, 2009

– Outperforming InP!!

Normal-incident mesa-type Ge/Si APDs



Waveguide type Ge/Si APDs



Receiver results @ 10 Gb/s with TIA:

- 28dBm (normal incident type)
- 30.4 dBm (waveguide type)



Invited Paper at GFP 2009:

WB6 11:45 AM - 12:15 PM (Invited)

Monolithic Ge/Si Avalanche Photodiodes, Y. Kang, M. Morse, M. Paniccia, Intel Corporation, Santa Clara, CA, USA, M. Zadka, Y. Saad, G. Sarid, Numonyx Israel Ltd, Kiryat Gat, Israel, A. Pauchard, Chemin de Crey-Derrey 152, Chatef-St-Denis, Switzerland, W. S. Zaoui, H.-W. Chen, D. Dai, J. E. Bowers, University of California - Santa Barbara, Santa Barbara, CA, USA, H.-D. Liu, D. C. McIntosh, X. Zheng and J. C. Campbell, University of Virginia, Charlottesville, VA, USA

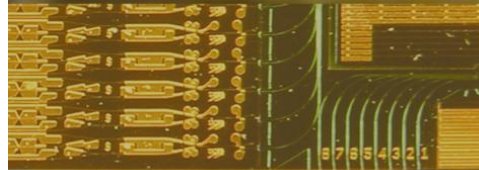
Summary

- **Active InP-based Photonic ICs** can be created with size, weight, power and stability as well as system performance metrics superior to discrete solutions in many situations. If produced in some volume, the cost can be much lower.
- Coherent approaches will be greatly improved by the use of Photonic Integration, and numerous sensor applications may be enabled in addition to higher-spectral-efficiency communications.
- Close integration of control/feedback electronics will be desirable in many future PIC applications—it is required for low-cost Optical Phase Locked Loop (OPLL) systems with conventional semiconductor lasers, but efficiency can be high.
- New high-volume (client) applications may emerge as low-cost ,high-performance PIC/EIC transmitter/receiver engines are developed—interconnect, computing, sensing, communication, etc.
- Active integrated Si-photonics is rapidly emerging, and many applications are being explored. Integrated PIC/EIC devices would appear to be compelling, but not on the horizon yet.

- Available now
- Worked examples throughout
- New homework problems
- New material:
 - VCSELs
 - GaN lasers
 - DFB, MMI, AWGR, & other component design
 - FTP site with software and color figs

SECOND EDITION

Diode Lasers and Photonic Integrated Circuits



Larry A. Coldren
Scott W. Corzine
Milan L. Mašanović



WILEY
Publishers Since 1807

Copyrighted Material

From Tunable Lasers to Photonic Integration

Larry A. Coldren
Electrical & Computer Engineering and Materials Departments
University of California, Santa Barbara, CA 93106
Email: coldren@ece.ucsb.edu

Abstract: This paper will review some of the author's efforts in the development of commercially-viable widely-tunable lasers and photonic integrated circuits (PICs). Recent work on integrated transmitters and receivers as well as optical phase-locked loops using such PICs will be emphasized.

Introduction

Early efforts at Bell Labs to create multiple-section tunable single-frequency lasers using etched slots indicated the ability to tune over wide ranges using the vernier effect[1-3]. However, all-active devices were limited due to carrier clamping, and thus, it later became obvious that active-passive structures, such as those pursued in Prof. Suematsu's group at TIT[4,5], were more desirable. This line of thinking led to the invention of the multi-element mirror concept[6] and associated widely-tunable lasers[7], which have become very important commercially[8]. The research also became the basis for a large activity on photonic integrated circuits (PICs), since the robust combination of different active and passive regions, DBR reflectors, and waveguide junctions were developed from this tunable laser work. Examples in recent years include: 1) widely-tunable transmitters, incorporating a sampled-grating DBR (SGDBR) laser, either electro-absorption (EA) or Mach-Zehnder (MZ) modulators, semiconductor-optical-amplifiers (SOAs), and monitoring photodiodes (PDs)[9-10], 2) widely-tunable transceivers (or wavelength converters), incorporating an SOA-PD receiver stage and an SGDBR-SOA-EA (or MZ) transmitter stage [11-12], and 3) an "all-optical" monolithic tunable optical router (MOTOR) PIC that operated as an 8 x 8 space switch using wavelength converters as the switching fabric[13].

Most recently, coherent transmitters[14] and receivers[15] with Hz-level tracking accuracy, either to a reference or the incoming carrier, respectively, have been demonstrated using optical phase-locked loops (OPLLs). These utilize PICs that again incorporate widely-tunable SGDBRs, but now with optical hybrids and balanced detector pairs. These are closely co-packaged with custom electronic ICs that provide feedback to the tuning section for the phase and frequency locking. Very stable operation has been demonstrated for the first time in an OPLL with a large tuning range as well as rapid tuning and locking capability.

The Widely-Tunable Sampled-Grating DBR (SGDBR) Laser

In 1988 the first patent was filed on the multi-section tunable laser with differing multi-element mirrors, and it issued in January of 1990. Although initially constructed with etched-grooves, the preferred embodiment quickly became the Sampled-Grating Distributed-Bragg-Reflector (SGDBR) laser. Considerable research on other widely-tunable lasers was also carried out in the 1990s at UCSB [16,17], but none appeared to be as simple to create or as high in performance as the SGDBR. Full C-band tuning with reasonable output powers was demonstrated. The monolithic integration of the SGDBR with SOAs, EAMs, MZMs, and PDs was also demonstrated. In 1998 Agility Communications was formed to commercialize widely-tunable lasers, transmitters, and transponders, all using the SGDBR at their core as the laser engine. After some measure of success, the company was acquired by JDSU in 2005, and today the SGDBR in various integrated forms in various modules is a key product for JDSU [8].

Photonic Integrated Circuits (PICs)

As already indicated, the SGDBR became the basis of a large amount of PIC research at UCSB in the 1990s, and this continues to the time of this writing. Some of the most recent work has involved the integration of widely-tunable transmitters and receivers for coherent communication and sensing applications. These include both PICs and electronic ICs (EICs) closely co-packaged on the same carrier to create OPLLs as indicated in Fig. 1. The loop bandwidth has been measured to be about 1.1 GHz—a record level. The novel IC design provides both frequency and phase locking for wide capture and stable phase locking, even while sweeping an offset source in heterodyne operation. As shown by the illustrated data, the normally relatively wide linewidth of the SGDBR (> 1MHz) will duplicate the reference to which it locks, it can be continuously swept, while phase locked, over about a mode spacing by an rf source, and good eyes and BER can be demodulated from phase-modulated data. It is important to note that the optical carrier can be recovered, and phase locking can occur, well past the dispersion limit of the data (~10x) after the signal is propagated through a length of fiber.

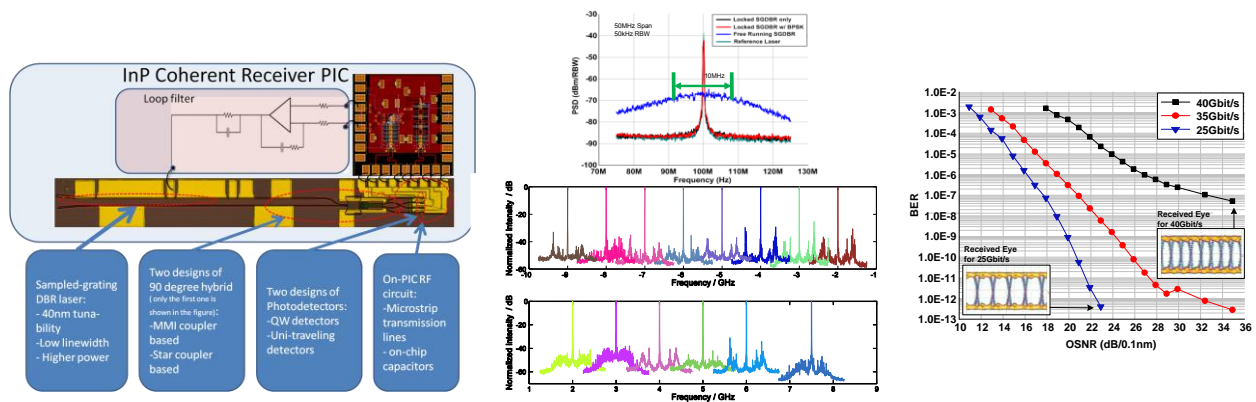


Fig. 1. (left) Schematic of OPLL with photos of PIC and EIC; (center-top) demonstration of linewidth reduction when locked to a narrow linewidth reference; (center-bottom) demonstration of continuous tuning while phase locked; (right) BPSK-BER data up to 40 Gb/s—limited by detector bandwidth [14, 15].

References

1. L.A. Coldren, B.I. Miller, K. Iga, and J.A. Rentschler, *Appl. Phys. Lett.*, **38** (5) 315 (Mar. 1981).
2. K.J. Ebeling, L. A. Coldren, B.I. Miller, and J.A. Rentschler, *Electron. Lett.*, **18** (21) 901 (Oct. 1982).
3. L.A. Coldren and T.L. Koch, *J. Quantum Electron.*, **20** (6) 659-682 (June, 1984).
4. Y. Abe, K. Kishino, Y. Suematsu, and S. Arai, *Electron. Lett.*, **17** (25) 945 (1981).
5. Y. Tohmori, Y. Suematsu, Y. Tushima, and S. Arai, *Electron. Lett.*, **19** (17) 656 (1983).
6. L.A. Coldren, US Patent #4,896,325 (Jan., 1990)
7. V.J. Jayaraman, A. Mathur, L.A. Coldren, and P.D. Dapkus, *13th IEEE Int. Semiconductor Laser Conf.*, Takamatsu, Japan, PD-11 (Sept., 1992).
8. See online: <http://www.jdsu.com/products/optical-communications>
9. A. Tauke-Pedretti, M.N. Sysak, J.S. Barton, J.W. Raring, L.A. Johansson, and L.A. Coldren, *Photon Tech Letts.*, **18** (18) 1922 (Sept., 2006).
10. J.W. Raring and L.A. Coldren, *IEEE JSTQE*, **13** (1) 3-14 (Jan., 2007).
11. A. Tauke-Pedretti, M.M. Dummer, M.N. Sysak, J.S. Barton, J. Klamkin, J.W. Raring, and L.A. Coldren, *J. Lightwave Tech.*, **26** (1) 91 (Jan., 2008).
12. M.M. Dummer, J. Klamkin, A. Tauke-Pedretti, and L.A. Coldren, *IEEE JSTQE*, **15** (3) 494- 503 (May, 2009).
13. S.C. Nicholes, M. Masanovic, B. Jevremovic, E. Lively, L.A. Coldren, and D. Blumenthal, *J. Lightwave Tech.*, **28** (4) 641-650 (Feb., 2010).
14. M. Lu, H. Park, E. Bloch, A. Sivanathan, A. Bhardwaj, Z. Griffith, L. A. Johansson, M.J. Rodwell, and L.A. Coldren, *Opt. Express*, **20**, 9736-9741 (2012).
15. H-C Park, M. Lu, E. Bloch, T. Reed, Z. Griffith, L. Johansson, L. Coldren, and M. Rodwell, *ECOC'12*, post-deadline paper (2012).
16. Z-M Chuang and L.A. Coldren, *SPIE OCCC'92*, Taiwan, pap **1813-44** (Dec., 1992).
17. Z-M Chuang and L.A. Coldren, *J. Quantum Electron.*, **29** (4) 1071-1080 (Apr., 1993).



Larry A. Coldren is the Fred Kavli Professor of Optoelectronics and Sensors at UC-Santa Barbara, CA. He received his Ph.D. in EE from Stanford and spent 13 years in research at Bell Labs before joining UCSB in 1984, where he holds appointments in ECE and Materials. He co-founded Optical Concepts, acquired as Gore Photonics, to develop novel VCSEL technology; and later Agility Communications, acquired by JDSU, to develop widely-tunable integrated transmitters.

At Bell Labs Coldren worked on SAW filters and tunable coupled-cavity lasers using novel RIE technology. At UCSB he continued work on multiple-section lasers, in 1988 inventing the widely-tunable multi-element mirror concept, now used in numerous commercial products. He has also made seminal contributions to efficient VCSEL designs. His group continues efforts on high-performance InP-based photonic integrated circuits (PICs) and high-speed, high-efficiency VCSELs.

He has authored or co-authored over a thousand journal and conference papers, a number of book chapters, a textbook, and has been issued 65 patents. An original member of ISI's highly-cited researchers database, he now has over seventeen thousand citations with an H-index of over sixty. He is a Fellow of the IEEE, OSA, and IEE, a recipient of the 2004 John Tyndall and 2009 Aron Kressel Awards, and a member of the National Academy of Engineering.

Single-chip integrated transmitters and receivers

Larry A. Coldren,^{*} Leif A. Johansson, Mingzhi Lu, Hyun-chul Park, John Parker, Abirami Sivanathan, and Mark Rodwell

Department of Electrical and Computer Engineering, University of California, Santa Barbara, California 93106, USA

^{*}coldren@ece.ucsb.edu

Abstract: Compared to traditional optics, photonic integrated circuits have advantages in size, weight, performance, reliability, power consumption, and cost. The size and stability also enable them to realize unique functions in coherent optics. Optical phase-locked loop (OPLL) based transmitters and receivers are examples. With photonic integration, the loop bandwidth of the OPLL can increase by orders of magnitude, and stable OPLLs have been achieved with closed-loop bandwidths >1 GHz.

©2012 Optical Society of America

OCIS codes: (250.5300) Photonic integrated circuits; (060.0060) Fiber optics and optical communications; (060.1660) Coherent communications; (250.0250) Optoelectronics.

References and links

1. T. L. Koch, U. Koren, R. P. Gnall, F. S. Choa, F. Hernandez-Gil, C. A. Burrus, M. G. Young, M. Oron, and B. I. Miller, "GaInAs/GaInAsP multiple-quantum-well integrated heterodyne receiver," *Electron. Lett.* **25**(24), 1621–1623 (1989).
2. J. S. Barton, E. J. Skogen, M. L. Mašanović, S. P. DenBaars, and L. A. Coldren, "Tailorable chirp using integrated Mach-Zehnder modulators with tunable sampled-grating distributed Bragg reflector lasers," *ISLC, TuB3, Garmish* (2002).
3. L. A. Coldren, S. C. Nicholes, L. Johansson, S. Ristic, R. S. Guzzon, E. J. Norberg, and U. Krishnamachari, "High Performance InP-Based Photonic ICs—A Tutorial," *J. Lightwave Technol.* **29**(4), 554–570 (2011).
4. A. W. Fang, H. Park, O. Cohen, R. Jones, M. J. Paniccia, and J. E. Bowers, "Electrically pumped hybrid AlGaInAs-silicon evanescent laser," *Opt. Express* **14**(20), 9203–9210 (2006).
5. M. M. Dummer, J. Klamkin, A. Tauke-Pedretti, and L. A. Coldren, "A bit-rate-transparent monolithically integrated wavelength converter," *ECOC, Th.2.C.1, Belgium* (2008).
6. D. F. Welch, F. A. Kish, R. Nagarajan, C. H. Joyner, R. P. Schneider, Jr., V. G. Dominic, M. L. Mitchell, S. G. Grubb, T.-K. Chiang, D. D. Perkins, and A. C. Nilsson, "The realization of large-scale photonic integrated circuits and the associated impact on fiber-optic communication systems," *J. Lightwave Technol.* **24**(12), 4674–4683 (2006).
7. S. C. Nicholes, M. L. Mašanović, J. Barton, E. Norberg, E. Lively, B. Jevremović, L. A. Coldren, and J. Daniel, Blumenthal, "Novel application of quantum-well intermixing implant buffer layer to enable high-density photonic integrated circuits in InP," *IPRM, WB1.2, Newport Beach* (2009).
8. F. A. Kish, D. Welch, R. Nagarajan, J. L. Pleumeekers, V. Lal, M. Ziari, A. Nilsson, M. Kato, S. Murthy, P. Evans, S. Corzine, M. Mitchell, P. Samra, M. Missey, S. DeMars, R. Schneider, M. Reffle, T. Butrie, J. Rahn, M. Van Leeuwen, J. Stewart, D. Lambert, R. Muthiah, H. Tsai, J. Bostak, A. Dentai, K. Wu, H. Sun, D. Pavinski, J. Zhang, J. Tang, J. McNicol, M. Kuntz, V. Dominic, B. Taylor, R. Salvatore, M. Fisher, A. Spannagel, E. Strzelecka, P. Studenkov, M. Raburn, W. Williams, D. Christini, K. Thomson, S. Agashe, R. Malendevich, G. Goldfarb, S. Melle, C. Joyner, M. Kaufman, and S. Grubb, "Current status of large-scale InP photonic integrated circuits," *IEEE J. Sel. Top. Quantum Electron.* **17**(6), 1470–1489 (2011).
9. J. E. Bowers, A. Ramaswamy, L. A. Johansson, J. Klamkin, M. Sysak, D. Zibar, L. Coldren, M. Rodwell, L. Lembo, R. Yoshimitsu, D. Scott, R. Davis, and P. Ly, "Linear coherent receiver based on a broadband and sampling optical phase-locked loop," *IEEE Int. Meeting on Micro. Photon.*, 225–228 (2007).
10. R. S. Guzzon, E. J. Norberg, and L. A. Coldren, "spurious-free dynamic range in photonic integrated circuit filters with semiconductor optical amplifiers," *IEEE J. Sel. Top. Quantum Electron.* **48**(2), 269–278 (2012).
11. W. H. Guo, P. R. A. Binetti, C. Althouse, A. Bhardwaj, J. K. Doylend, H. P. M. M. Ambrosius, L. A. Johansson, and L. A. Coldren, "InP photonic integrated circuit for 2D optical beam steering," *Post-deadline paper, IEEE Photonics Conf., Arlington* (2011).
12. J. K. Doylend, M. J. R. Heck, J. T. Bovington, J. D. Peters, L. A. Coldren, and J. E. Bowers, "Two-dimensional free-space beam steering with an optical phased array on silicon-on-insulator," *Opt. Express* **19**(22), 21595–21604 (2011).
13. S. Ristic, A. Bhardwaj, M. Rodwell, L. Coldren, and L. Johansson, "An optical phase-locked loop photonic integrated circuit," *J. Lightwave Technol.* **28**(4), 526–538 (2010).

14. R. J. Steed, F. Pozzi, M. J. Fice, C. C. Renaud, D. C. Rogers, I. F. Lealman, D. G. Moodie, P. J. Cannard, C. Lynch, L. Johnston, M. J. Robertson, R. Cronin, L. Pavlovic, L. Naglic, M. Vidmar, and A. J. Seeds, "Monolithically integrated heterodyne optical phase-lock loop with RF XOR phase detector," *Opt. Express* **19**(21), 20048–20053 (2011).
15. M. Lu, H. Park, E. Bloch, A. Sivanathan, A. Bhardwaj, Z. Griffith, L. A. Johansson, M. J. Rodwell, and L. A. Coldren, "Highly integrated optical heterodyne phase-locked loop with phase/frequency detection," *Opt. Express* **20**(9), 9736–9741 (2012).
16. M. Lu, H. Park, E. Bloch, A. Sivanathan, Z. Griffith, L. A. Johansson, M. J. Rodwell, and L. A. Coldren, "A Highly Integrated Optical Phase-locked Loop for Laser Wavelength Stabilization," *IEEE Photon. Conf.*, ThR 2 (2012).
17. H. Park, M. Lu, E. Bloch, T. Reed, Z. Griffith, L. Johansson, L. Coldren, and M. Rodwell, "40Gbit/s coherent optical receiver using a Costas loop," *ECOC*, post-deadline (2012).
18. M. Lu, H. Park, E. Bloch, A. Sivanathan, J. Parker, Z. Griffith, L. A. Johansson, M. J. Rodwell, and L. A. Coldren, "A photonic integrated circuit for a 40 Gbaud/s homodyne receiver using an optical Costas loop," *IEEE Photon. Conf.*, post-deadline (2012).
19. E. Skogen, J. Barton, S. Denbaars, and L. Coldren, "A quantum-well-intermixing process for wavelength-agile photonic integrated circuits," *IEEE J. Sel. Top. Quantum Electron.* **8**(4), 863–869 (2002).
20. J. Parker, M. Lu, H. Park, E. Bloch, A. Sivanathan, Z. Griffith, L. A. Johansson, M. J. Rodwell, and L. A. Coldren, "Offset locking of an SG-DBR to an InGaAsP/InP mode-locked laser," *IEEE Photon. Conf.*, ThR 3 (2012).
21. J. S. Parker, P. R. A. Binetti, Y.-J. Hung, and L. A. Coldren, "Frequency tuning in integrated InGaAsP/InP ring mode-locked lasers," *J. Lightwave Technol.* **30**(9), 1278–1283 (2012).
22. E. Bloch, H. Park, M. Lu, T. Reed, Z. Griffith, L. Johansson, L. Coldren, D. Ritter, and M. Rodwell, "A 1-20 GHz InP HBT phase-lock-loop IC for optical wavelength synthesis," *IEEE Int. Micro. Symposium* (2012).

1. Introduction

Since the invention of the first semiconductor laser fifty years ago, significant efforts have been devoted to the area of photonic integration [1–21]. Not only have the photonic integrated circuits (PICs) become more functional, the integration scale has also gone up significantly. Currently, researchers have demonstrated the ability to integrate most of the optical components on a single chip, including: lasers, modulators, detectors, amplifiers, phase shifters, couplers, and polarization rotators. By integration, the size, weight, and combined insertion loss of the optical components decrease greatly. Within the footprint of a millimeter scale, the full function of transmitting, receiving, filtering, or even O-E-O conversion can be realized [5].

Besides size and weight, smaller power consumption is also an advantage for photonic integration. Semiconductor lasers, amplifiers and other integrated components can have quite high wall-plug efficiency. By integrating a lot of components monolithically, the insertion loss will be greatly reduced, less optical power will be needed, and total thermoelectric cooler (TEC) power consumption will also decrease significantly.

Photonic integrated systems also have better performance and are more reliable. Integration makes the system much more stable and more resistive to environment fluctuations, compared to free-space optics and fiber-pigtailed components. Large-scale integration also cuts down the number of fiber couplers, which not only decreases the insertion loss, but also improves the reliability of the system.

As the most important driving force of photonic integration, the ever-increasing data stream of fiber optic communication requires the transmitters and receivers to have a smaller footprint, higher bandwidth efficiency, higher data rate, lower power consumption, and relatively low cost [6]. Therefore, a large number of integrated transmitter and receivers have been demonstrated in the recent literature and released on the market. An 8-by-8 tunable optical router has been demonstrated, operating at 40 Gb/s per channel [7]. 500 Gb/s monolithic transmitters and receivers are already on the market, and 1 Tb/s monolithic transmitters and receivers have been realized and will be commercially available soon [8].

Furthermore, besides improving and replacing the already-existing system, PICs have an important role of creating new optical systems that are difficult or even impossible to be realized using free-space optics or fiber-pigtailed components, especially in the area of coherent optics. The stability of the PIC enables the possibility of full engineering control

over the phase of light. A series of PICs have been demonstrated with superior performance, such as a linear analog receiver with push-pull modulators and an optical feedback loop [9], several designs of tunable and programmable microwave photonic filters [10], 2D beam-steering PICs [11,12], and several prototypes for optical phase-locked loops [13–18].

The phase-locked loop (PLL) was proposed in 1930s and has been widely used in most of the communication systems that we are using today, including FM radios, cell phones, computers, and GPS. The optical phase-locked loop (OPLL) on the other hand, was realized in 1965, yet it has never been sold commercially. The major reason behind this has been the difficulties of building stable OPLL using traditional optic building blocks, such as free-space lenses and fiber-pigtailed devices, because a stable OPLL needs a very short loop delay and the bulk optics are simply too big and lack stability. However, photonics integration has solved the loop delay problem and makes the OPLL more accessible for real applications.

In this paper, we will overview recent advances in photonic ICs for coherent communications and sensing applications within our research groups at UCSB. The commonly-used integration platform and integration technology will be introduced. Taking the advantage of the compactness and phase stability of integration, several OPLL PIC engines have been built based on the same integration platform and integration technology for coherent optics applications. A phase-locked tunable transmitter that might be useful in communication or sensor systems, and a homodyne coherent receiver based on Costas loop are included as examples.

2. Integration technology

Before diving into the specific PICs and the transmitter/receiver performance, it is worth describing the technology that allows us to achieve the integration of different optic components without compromising device performances. Several commonly used integration platforms and active/passive definition technologies are illustrated in Ref [3]. based on InGaAsP/InP material system, including vertical twin-guide, butt-joint regrowth, selective area regrowth, offset quantum wells, dual quantum wells and quantum well intermixing (QWI) technology [19]. Among all these, QWI platform has advantages of high gain, low loss in passive section, almost no reflection in the active/passive transition and simple fabrication, while offset quantum well and butt-joint are also widely used in academia and industry research. The structure of the QWI platform is shown in Fig. 1 as well as a scanning electron microscope (SEM) picture.

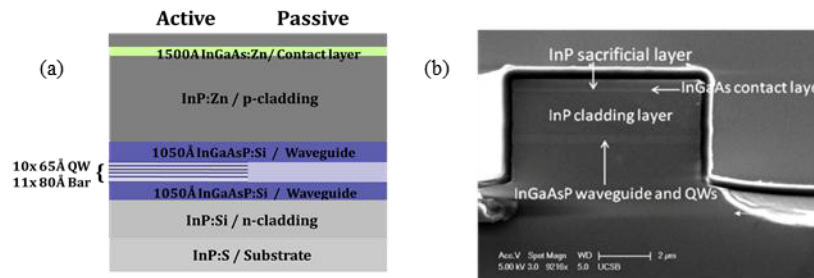


Fig. 1. (a) The epitaxial structure of the QWI platform. (b) A SEM picture of the cross section of a waveguide based on QWI platform.

The QWI process starts with a base epitaxial structure including waveguide layers, centered quantum wells and a 450 nm InP buffer layer above them. A selective-area phosphorous implant is then carried out with a energy of 100 keV and a dose of $5 \times 10^{14} \text{ cm}^{-2}$ to create point defects. By annealing at 675 °C, vacancies move through the quantum-well region, intermixing barriers with wells, and the photoluminescence (PL) peak blue-shift increases linearly for the first 80 nm. The maximum PL peak shift can be as large as 130 nm,

which ensures low-loss at the operating wavelength. Therefore, active and passive areas are defined on the wafer. Moreover, multiple bandwidth band edges are also possible to achieve on the same wafer. By removing the 450 nm InP implanted buffer layer on top of the waveguide layer, PL blue shift will be stopped even when further annealing is carried out. Figure 2 shows the QWI process and the peak photoluminescence peak shift as a function of annealing time [19].

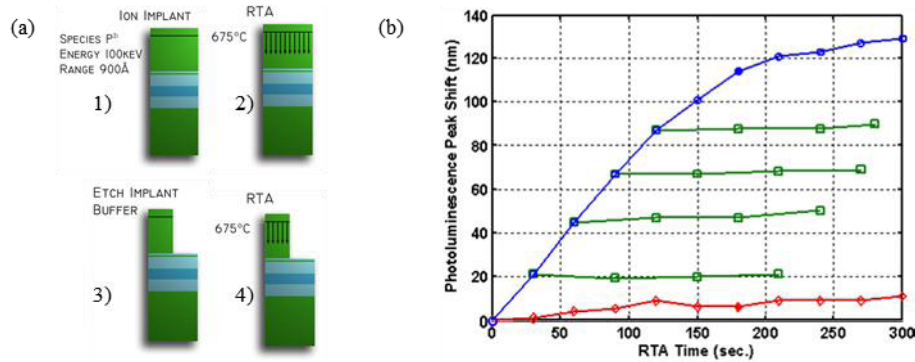


Fig. 2. (a) shows the QWI process. (b) The photoluminescence peak shift as a function of anneal time, showing the initial linear increase in the peak shift and the complete halting of the peak shift for samples for which the implant buffer layer has been etched. Symbols indicate nonimplanted (triangles), implanted (circles), and samples with partial anneal followed by the removal of the implant buffer layer (squares).

After QWI, the buffer layer is removed, gratings are defined by electron-beam lithography, and a blanket P-InP cladding and P-InGaAs contact regrowth will be carried out. Thus, the p-i-n photodiode is formed.

Following that is the waveguide definition. Both surface ridge waveguides and deeply etched waveguides are frequently used. The surface ridge waveguide has better heat dissipation and less reflection, but the waveguide bending angle is limited because of the crystallographic wet etch process. On the other hand, the deeply etch waveguide has a higher mode confinement, and has more design flexibilities to achieve sharp bends and rings. The process of the surface ridge waveguide is fairly straightforward. A Methane/Hydrogen/Argon reactive ion etch (RIE) is used, and PECVD Si_3N_4 acts as the hard mask. An HCl-based crystallographic wet etch is used to finish the waveguide definition. As for the deeply etched waveguide, they are defined with photoresist on a Cr/ SiO_2 bilayer hardmask. The Cr is etched using a low power Cl_2/O_2 ICP-RIE etch, and SF_6/Ar ICP-RIE is used for a vertical SiO_2 etch. The resulting 600 nm SiO_2 mask acts as a hardmask to define the InGaAsP/InP deeply etched waveguides using a $\text{Cl}_2/\text{H}_2/\text{Ar}$ ICP-RIE etch with the substrate temperature of 200 °C.

After the waveguide definition, N-contact etch and top N metal deposition, BCB definition, P contact open and P metal deposition will be carried out in sequence. Capacitors, RF transmission lines are also defined simultaneously.

By using the integration platform and the process flow shown above, different optic components can be integrated on one single InGaAsP/InP substrate. A series of PICs have been fabricated at UCSB based on this platform and fabrication process [10,11,13,15–18,20,21], including the OPLL-based single-chip transmitter and receiver engines, which are going to be shown in the following sections.

3. Single-chip integrated transmitters

Using the integration technologies illustrated in Section 2, the concept of an OPLL-based, Hertz-accuracy, widely-tunable transmitter has been proven. The transmitter includes a heterodyne OPLL and a mode-locked laser chip. This can provide a terahertz chirped LIDAR

transmitter that can potentially sweep over a more than 2.5 THz (even 5 THz, depending on the width of the comb source) range with Hertz level accuracy.

The architecture of the OPLL is shown in Fig. 3. It includes a PIC, an electronic IC (EIC) and a loop filter. All the photonics components are integrated on a single PIC, including a widely-tunable sampled-grating DBR (SG-DBR) laser, an optical 90 degree hybrid, four quantum well photodetectors, and microstrip transmission lines. Conducting substrate is chosen, and QWI is used to define the active and passive area. The process flow is as discussed in Section 2. Both surface and deeply etched waveguides are defined on the same device. The picture of the PIC is shown in Fig. 4(a) and the cross sections are shown in Fig. 4(b).

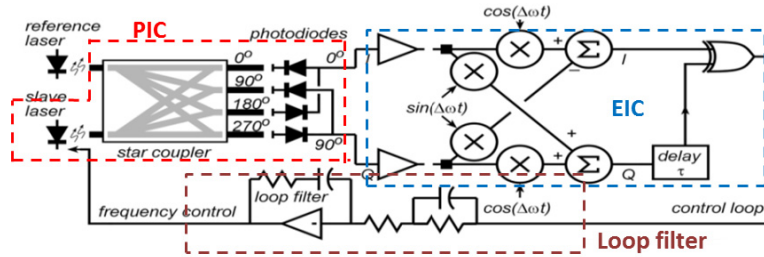


Fig. 3. The architecture of the heterodyne OPLL.

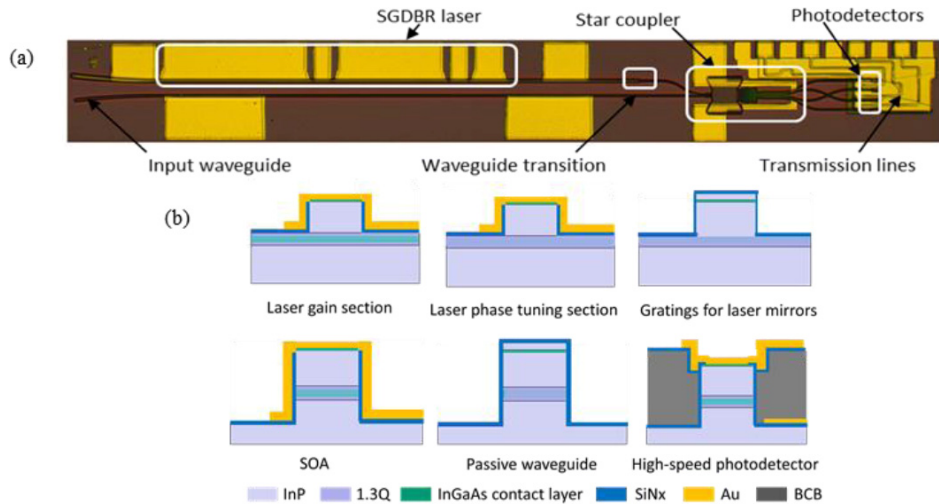


Fig. 4. Shows a picture of the fabricated PIC and the cross sections of the integrated components.

The PIC, EIC and loop filter are connected together using wirebonding. A reference laser is coupled into the PIC using lensed fiber and mixed with the on-PIC SG-DBR laser in the 90 degree hybrid. I/Q signals are then generated and detected in the four photodetectors, and feedback to the SG-DBR laser phase tuning section through the EIC and the loop filter. On the EIC, limiting amplifiers, a single-sideband mixer (SSBM) and a quadrice correlator phase/frequency detector are integrated. The details of the EIC can be found in Ref [22]. Because all the photonics components are integrated within a footprint of millimeter scale, the delay in the photonics part is only 40 ps, and total loop delay is around 200ps, which is mainly from the EIC and the interconnections. The size of the whole OPLL system is 10 mm \times 10 mm. The picture of this heterodyne OPLL is shown in Fig. 5.

First, in order to verify that the OPLL system is working, we used a commercial external cavity continuous-wave laser as the reference laser. By applying different RF frequency

references, the SG-DBR laser can phase lock to the reference laser with different frequency offsets. The phase/frequency detector enables the OPLL to function not only as a phase lock system, but also as a frequency locking system. This means that the phase/frequency of the SG-DBR laser will be stably lock to the reference, even if the SG-DBR laser free-running frequency drifts out of the phase locking bandwidth. The single-sideband mixer enables the OPLL to phase lock at either a positive or a negative frequency offset between SG-DBR and the reference laser. The sign of the offset frequency is set by a control signal to the EIC. The test setup is shown in Fig. 5.

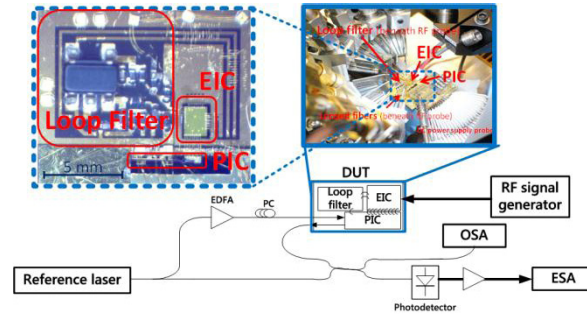


Fig. 5. The schematics of the OPLL test setup is shown in the lower part of this figure. Thinner lines indicate fiber connections and thicker lines show the RF cable connections. Pictures of the OPLL are also shown.

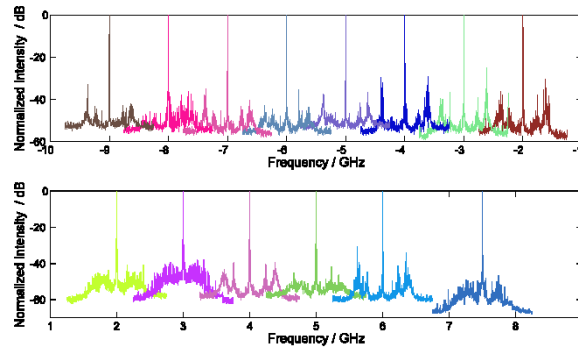


Fig. 6. Shows the beating tones of the two lasers when they are phase locked at various frequency offsets: -9 GHz, -8 GHz, -7 GHz, -6 GHz, -5 GHz, -4 GHz, -3 GHz, -2 GHz, 2 GHz, 3 GHz, 4 GHz, 5 GHz, 6 GHz, and 7.5 GHz.

Offset locking has been achieved with an offset frequency from -9 GHz to -1.5 GHz and from + 1.5 GHz to + 7.5 GHz, and the locking spectra are shown in Fig. 6. The phase error variance is 0.03 rad^2 , integrated from 100 Hz to 10 GHz. The closed-loop bandwidth of the OPLL is around 400 MHz. Approximately 10 GHz pull-in range and > 15 GHz hold-in range has been achieved.

Besides the heterodyne OPLL, another important building block of this LIDAR transmitter engine is an InGaAsP/InP mode-locked laser [21]. An SEM of the mode-locked laser is shown in Fig. 7(a). The offset quantum well integration platform is used with deeply etched waveguides. A similar MLL has shown more than 2.5 THz comb width, while here a relative narrow comb is used on purpose for the demonstration of phase locking a CW laser to a MLL. The beating spectrum of two lasers is shown in Fig. 7(b). The SG-DBR in the OPLL system is phase locked to one of the comb lines of the MLL with a frequency offset of 6.5 GHz. A strong beating tone is observed at 6.5 GHz, as well as two tones at 11.69 and 24.69 GHz (i.e. $18.19 \pm 6.5 \text{ GHz}$), corresponding to the adjacent comb lines of the MLL. The MLL

repetition rate is 18.19 GHz. 13 GHz peak is the harmonic of the 6.5 GHz offset frequency. The narrow beat observed indicates the high coherence between the MLL and the comb. The MLL linewidth is 100 MHz, whereas the linewidth of the 6.5 GHz beat term is < 800 kHz.

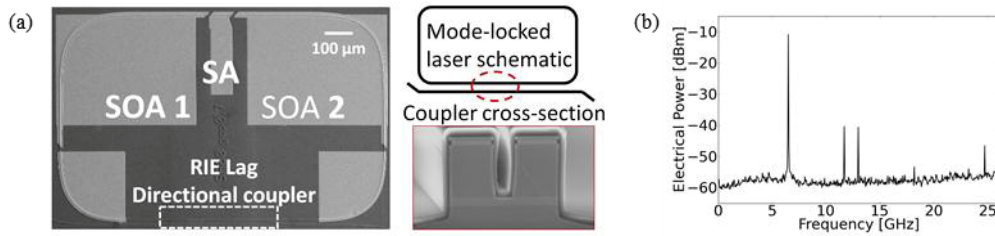


Fig. 7. (a) shows SEM pictures of the MLL and its cross section as well as the schematic. (b) Frequency spectrum of SG-DBR beating with the MLL measured on an electrical spectrum analyzer (RBW 50 kHz). The offset locking frequency is 6.5 GHz.

The offset frequency between MLL and SG-DBR laser is set by the RF reference. By changing the RF frequency, the frequency of the SG-DBR laser can be swept from one comb line to the adjacent one, and then offset lock to this line. This can be continued through all the comb lines, and a quasi-continuous frequency sweeping could be achieved, with the sweeping range as large as the width of the comb [20]. The bandwidth of the RF synthesizer, EICs and photodetectors only needs to be as large as the spacing between the MLL lines.

Furthermore, since the PIC in the OPLL system and the MLL share a similar integration platform and almost the same fabrication process, monolithically integrating these two PICs is viable.

4. Single-chip integrated receivers

With the exponential increase of internet data stream, a lot of effort has been devoted to the research of coherent receivers, while most are focused on DSP based intradyne receivers. Compared to other types of receivers, homodyne receivers have a high sensitivity, and no DSP is needed for short or mid-distance communication, where dispersion is not severe. Most of the research on the homodyne receivers was carried out in 1980s before the invention of EDFA, while the loops proved hard to stabilize. One of the major problem that researcher were facing was, again, the loop bandwidth, which is limited by the loop delay. Expensive external cavity lasers were commonly used as the LO laser because of the high requirement on the linewidth and stability introduced by the limited loop bandwidth.

By integration, we successfully achieved a homodyne coherent receiver within a footprint of 10 mm × 10 mm [17,18]. The total loop delay is only 120 ps. The design is based on optical Costas loop, and the architecture is shown in Fig. 8. Compared to the heterodyne OPLL architecture shown in Fig. 8, there is no SSBM in this EIC, and loop filter parameters are different. The receiver system also includes a PIC, an EIC and a loop filter.

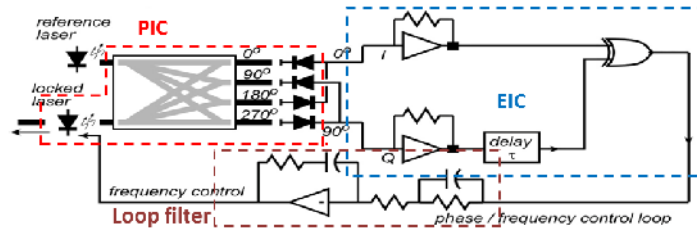


Fig. 8. The architecture of the homodyne coherent receiver.

The functionality of this PIC is the same as the one used in the heterodyne receiver, while the performance is improved. Uni-travelling-carrier (UTC) photodetectors are integrated, and

30 GHz 3-dB bandwidth and 18 mA saturation current are achieved. As for the processing, UTC layers need to be regrown and UTC photodetectors need to be defined after the QWI. The rest of the process steps remain the same. In order to reduce the reflection in the PIC and avoid injection locking, the whole device is based on surface ridge waveguide structure. The picture of the PIC and the cross sections are shown in Fig. 9(a)(b).

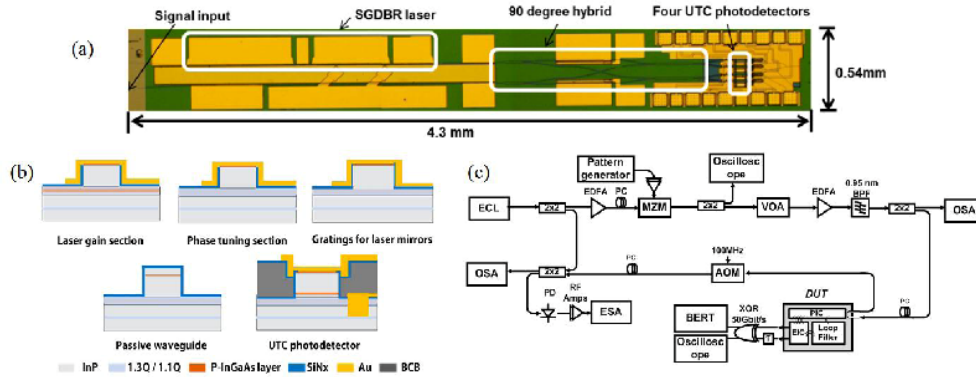


Fig. 9. (a) shows the microscope picture of the fabricated PIC. (b) shows the cross sections of the integrated components on this PIC. (c) The setup for the coherent receiver testing.

The test setup is shown in Fig. 9(c). 1.1 GHz closed-loop bandwidth has been realized. The test results show that the OPLL is very stable, and 40 Gb/s BPSK signal has been demodulated successfully. Bit error rates with different input OSNRs are plotted in Fig. 10, and the eye diagrams are also shown.

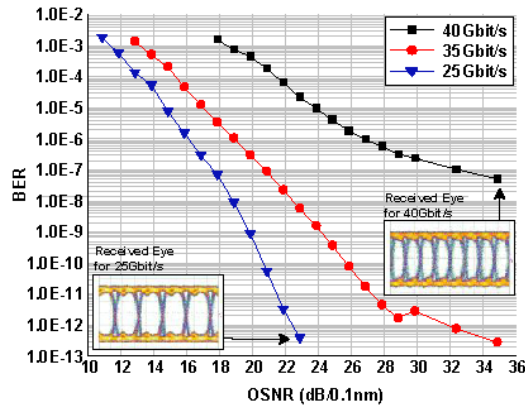


Fig. 10. BER vs. OSNR for 25G to 40Gb/s and received eye outputs for 25Gb/s and 40Gb/s.

5. Conclusions

In this paper, we overview the advantage of optical integration, and two examples of optical phase-locked loops are illustrated. Not only can photonic integration replace and improve the existing optic systems, it also has an important role of creating new optical systems that are difficult or even impossible to be realized using free-space optics or fiber-pigtailed components, especially in the area of coherent optics. The OPLL-based widely-tunable transmitter and homodyne receiver are feasible to build and operate due to photonic integration.

Acknowledgment

This work is supported by DARPA PICO project. A portion of this work is done in the UCSB nanofabrication facility, part of NSF funded NNIN network. The EIC fabrication is done at Teledyne Scientific.

I. Photonic Integrated Circuits

B. Integrated Mode-Locked Lasers

Monolithically Integrated Gain-Flattened Ring Mode-Locked Laser for Comb-Line Generation

John S. Parker, Ashish Bhardwaj, Pietro R. A. Binetti, Yung-Jr. Hung, and
Larry A. Coldren, *Fellow, IEEE*

Abstract—We demonstrate broadband comb-line generation from an integrated multiple quantum well InGaAsP/InP passively mode-locked laser (MLL) with a gain flattening filter (GFF) based on an asymmetric Mach-Zehnder interferometer. The intracavity filter flattens the nonuniform gain profile of the semiconductor material providing a more uniform net cavity gain. The GFF MLL has a -10 dB comb span of 15 nm (1.88 THz), the widest spectral width yet demonstrated for an integrated QW MLL at 1.55 μm . The measured optical linewidth at the center of the comb is 29 MHz, the -20 dB RF linewidth 500 KHz, while the output spectrum is phase-locked to produce 900 fs pulses at a repetition rate of 30 GHz with 4.6 ps integrated jitter from 100 Hz to 30 MHz.

Index Terms—Comb-line generation, integrated optics, mode-locked lasers, optical communication, photonic integrated circuits.

I. INTRODUCTION

INTEGRATED InGaAsP/InP mode-locked lasers (MLLs) operating at 1.55 μm wavelength are very stable pulse sources that can be used in a variety of applications in high-speed optical communication such as optical time domain multiplexing and optical sampling. Since a single MLL generates multiple phase-locked lasing modes that coherently add up to form the short pulses, MLLs can also be used for frequency comb-line generation (i.e. a multiwavelength source [1]) in applications including offset frequency locking [2], and light detection and ranging (LIDAR).

For wavelength-division-multiplexing (WDM) applications, a broadband phase-locked comb of frequencies can be used for rejection of cross-talk to allow more closely spaced non-return-to-zero (NRZ) channels and a higher spectral density [3]. In coherent communication systems, such frequency combs can greatly reduce the required front- and back-end footprint and overhead for laser stabilization and carrier tracking [4]. For

Manuscript received July 19, 2011; revised September 22, 2011; accepted October 21, 2011. Date of publication October 28, 2011; date of current version January 5, 2012. This work was supported in part by the Defense Advanced Research Projects Agency (DARPA) Photonic Integrated for Coherent Optics (PICO) Program. A portion of this work was done at the UCSB Nanofabrication Facility, part of the National Science Foundation (NSF) funded NNIN Network.

J. S. Parker, A. Bhardwaj, P. R. A. Binetti, and L. A. Coldren are with the Department of Electrical and Computer Engineering, University of California, Santa Barbara, CA 93106 USA (e-mail: JParker@ece.ucsb.edu; Ashish.Bhardwaj@jdsu.com; pbinetti@gmail.com; coldren@ece.ucsb.edu).

Y.-J. Hung is with the Department of Electronic Engineering, National Taiwan University of Science and Technology, Taipei 106, Taiwan (e-mail: yungjrhung@gmail.com).

Color versions of one or more of the figures in this letter are available online at <http://ieeexplore.ieee.org>.

Digital Object Identifier 10.1109/LPT.2011.2174148

example, a frequency comb that spans 1 THz can provide 40 WDM channels, each having a bandwidth of 25 GHz and has a substantially smaller footprint than 40 single tone lasers. Furthermore, a single wavelength locker can provide stabilization for all of the comb's periodic frequency lines. A homodyne coherent receiver would typically require each channel to have its own local oscillator (LO) for carrier synchronization [5], [6] (e.g. 40 lasers and 40 optical phase-locked loops (OPLLs)). However, a single phase-locked comb with an OPLL can supply all necessary LOs for the incoming signals. Since all lasing lines are phase-locked and have fixed frequency spacing, this effectively locks all channels.

In a semiconductor MLL, the span of the comb is determined by the cavity dispersion and the gain competition between its various lasing modes. While the semiconductor medium can generate gain that spans over 100 nm, the gain competition arising from the nonuniform material gain as a function of wavelength limits the bandwidth of the resulting frequency comb. By applying an intracavity filter function as an inverse of the spectral shape of the material gain, the resulting gain flattening creates a more uniform spectral profile. This allows for wider combs as demonstrated with bench-top MLLs [7].

Previously, we have shown the generation of 600 fs pulses from a monolithically integrated 30 GHz MLL with an intracavity gain-flattening filter (GFF) [8]. Additionally, we have compared the frequency comb span of the GFF MLL to standard MLL designs on the same material platform and have shown an improvement $>2\times$ [9]. In this letter, we present optical linewidth, RF linewidth, single sideband phase noise measurements, and a -10 dB comb span of 15 nm (1.88 THz). This is the widest frequency comb generated from an integrated quantum well (QW) based MLL at 1.55 μm , with a span matching state-of-the-art quantum-dot (QD) and quantum-dash MLLs [10]. Moreover, such GFFs can be used to improve the gain flatness on any material platform, including: QDs, QWs, and bulk.

II. RING MLL FABRICATION

We have chosen ring-based mode-locked laser architecture due to its ease of integration with other components to realize highly versatile photonic integrated circuits (PICs). These rings and their couplers can be defined using low-cost and high throughput i-line photolithography, allowing ring MLLs to be placed anywhere on the PIC without the need for more complicated processing. Thus rings can overcome fabrication complexity faced by distributed Bragg reflector (DBR) and

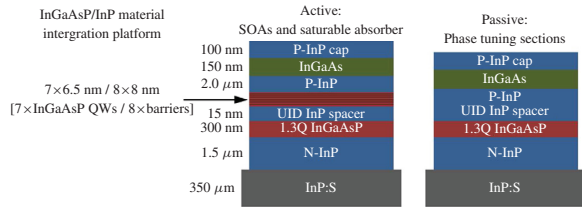


Fig. 1. Active sections (left) are used for the semiconductor optical amplifiers and the saturable absorber. The passive sections (right) are used for low-loss waveguides and phase tuning regions.

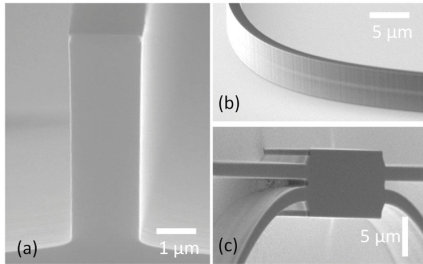


Fig. 2. Scanning electron microscope (SEM) images of the etched waveguide showing (a) 5 μm deep etch with vertical sidewalls, (b) waveguide bends with smooth sidewalls, and (c) multimode interference (MMI) couplers.

distributed feedback lasers (DFB) that require gratings defined by holography or electron-beam-lithography, which can be expensive with reduced yield.

A ring MLL with a GFF is designed and fabricated on an InGaAsP/InP offset quantum well (OQW) platform that consists of seven 0.9% compressively strained 6.5 nm QWs and eight -0.2% tensile strained 8 nm barriers that are epitaxially grown above a 300 nm thick 1.3Q InGaAsP layer as part of the base epi. Passive areas are defined using a selective wet-etch and a single blanket regrowth is done to cover the device with a p^+ -doped InP cladding, a p^{++} -doped InGaAs contact layer, and an InP capping layer to protect the InGaAs contact layer during device fabrication. The active material is used to define the semiconductor optical amplifiers (SOAs) and the saturable absorber (SA), whereas the passive material is used to define the low-loss waveguides and current injection based phase shifters, as shown in Fig. 1.

After regrowth, the waveguide is defined with photoresist on a Cr/SiO₂ bilayer hard mask. The Cr is etched using a low power Cl₂-based inductively coupled plasma (ICP), and the SiO₂ is etched using an SF₆/Ar based ICP. The resulting 600 nm SiO₂ mask acts as a hard-mask to define the InGaAsP/InP deeply etched waveguides using a Cl₂/H₂/Ar (9/18/2 sccm) ICP at a chamber pressure of 1.5 mT. The resulting etched features are shown in Fig. 2. After removing the SiO₂ mask, blanket deposition of a 350 nm isolation layer of silicon nitride is performed. Vias are opened for top-side p-metal contacts. N-metal contacts are realized through backside deposition of Ti/Pt/Au onto the n-doped conducting InP substrate.

The fully fabricated GFF MLL PIC has a round-trip cavity length of 2600 μm , corresponding to lasing lines spaced by

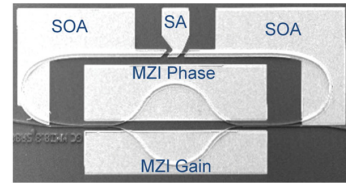


Fig. 3. SEM image of the GFF MLL PIC.

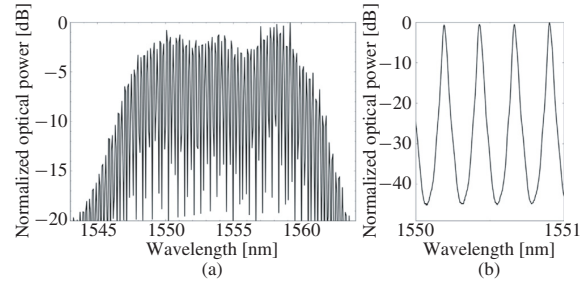


Fig. 4. Measured comb spectrum on optical spectrum analyzer (a) full span and (b) high-resolution measurement at 1550 nm showing 45 dB OSNR.

30 GHz, as shown in Fig. 3. The 600 μm asymmetric MZI filter uses 3 dB, i.e., 50–50, multi-mode interference (MMI) couplers to form two arms, which differ in length by 16 μm providing a free-spectral-range (FSR) of 40 nm. One of the arms of the MZI filter has an SOA that can be used to control the extinction ratio (ER) of the GFF, whereas the other arm has a phase shifter allowing adjustment of the filter zero.

III. PHASE LOCKED COMB GENERATION

The GFF MLL PICs are mounted on copper carriers and characterized at 10 $^{\circ}\text{C}$ using a thermo-electrical cooler (TEC). For passive mode-locking, the total drive current to the two 750 μm long ring SOAs (designated “SOA” in Fig. 3) is 110 mA with the 60 μm long SA biased at -4.5 V. The 460 μm long MZI gain section is driven at 31 mA with the 476 μm long MZI phase section set at 3 mA. The average power coupled into a lensed fiber is -6 dBm. The MZI filter gain and phase are adjusted to maximize the optical comb width as measured on an optical spectrum analyzer (OSA), shown in Fig. 4(a). The -10 dB span of the comb is 15 nm (1.88 THz) with lines spaced by 30 GHz as determined by the cavity length. As shown in Fig. 4(a), the ripple between adjacent lasing lines is several dB, while comb span is much wider. For this reason, the -3 dB bandwidth often provides a poor comparison between different comb spectra, and the -5 dB and -10 dB bandwidths are more useful for characterization [4].

The optical signal-to-noise ratio (OSNR) over the standard 0.1 nm bandwidth is >35 dB for all comb-lines, and 45 dB at the peak, as shown in Fig. 4(b).

For the temporal pulse measurements on a second-harmonic generation (SHG) based autocorrelator, the output from the GFF MLL is amplified using a 30 dBm erbium doped fiber amplifier (EDFA); this optical amplification is necessary for

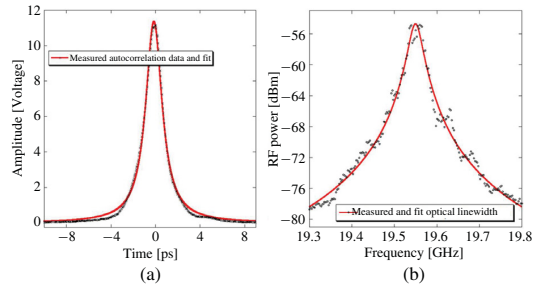


Fig. 5. (a) Measured and 900 fs Lorentzian fit pulse from an Inrad second harmonic generation based autocorrelator. (b) Heterodyne optical linewidth measurement of comb lasing line at 1555 nm. The Lorentzian linewidth fit has an FWHM of 29 MHz.

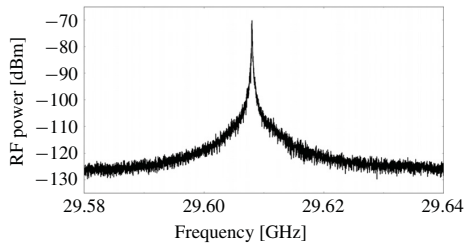


Fig. 6. Measured RF power from a 40 GHz photodiode with electrical signal analyzer (ESA). The -20 dB RF linewidth is 500 KHz (RBW = 50 KHz).

measurements on the autocorrelator. Fig. 5(a) shows the narrow pulses fit to a Lorentzian function with a full width half maximum (FWHM) of 900 fs and a corresponding time bandwidth product of 1.19, 5.4x larger than the time bandwidth limit of 0.22. Added sections of single mode and dispersion compensated fiber after the EDFA did not reduce the pulse width significantly, which suggests that the EDFA introduces higher-order dispersion into the broadband pulse.

The optical linewidth at the center of the comb is measured with a heterodyne method using a 40 GHz photodiode, ESA, and a narrow <100 KHz linewidth laser. Fig. 5(b) shows the Lorentzian fit optical linewidth with a FWHM of 29 MHz. The relative intensity noise (RIN) of a single mode is measured using a fiber Bragg filter centered at 1550 nm. The peak RIN is -82.6 dBc/Hz at 1.18 GHz for the 110 mA drive current.

Fig. 6 shows the measured RF power from the mode-locked laser using a 40 GHz photodiode and an electrical spectrum analyzer (ESA). A 30 dB low noise microwave amplifier boosts the electrical signal in the ESA (no EDFA is used). The RF power is measured to be 50 dB above the noise floor at 50 KHz resolution bandwidth (RBW). The -20 dB linewidth is as narrow as 500 KHz, demonstrating sub-MHz frequency stability between adjacent lasing lines. For use in coherent communication systems, incorporating active mode-locking into the cavity can further reduce this RF linewidth and provide precise frequency control over the mode spacing, thus enhancing the frequency stability between channels.

As shown in Fig. 7, the single sideband phase noise is measured from 100 Hz to 30 MHz with a corresponding RMS jitter value of 4.6 ps. Nearly half of the RMS jitter

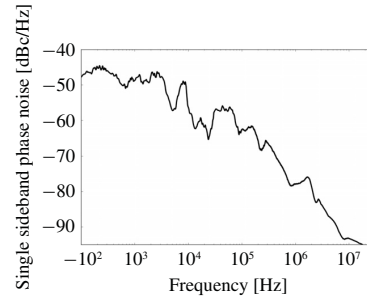


Fig. 7. Single sideband phase noise versus frequency. The integrated RMS jitter from 100 Hz to 30 MHz is 4.6 ps.

is accrued at <100 KHz, which is likely due to vibrations on the optical bench and thermal instability. In practice, such low frequency noise that remains after packaging can be easily handled with receiver tracking and stabilization. We are unable to characterize the phase noise above 30 MHz, as the single sideband phase noise goes below the ESA noise floor.

IV. CONCLUSION

We have presented an integrated GFF MLL PIC and have demonstrated the widest integrated MLL comb span from InP-MQW based material. Changes to the cavity length can be made to accommodate frequency spacing from 10 to 40 GHz with near MHz accuracy, as determined by optical lithography. For sub-MHz frequency accuracy, active-mode locking techniques can be used. This 1.88 THz phase-locked comb source can have important applications in coherent communication systems, offset locking, and phase-locked sources for WDM.

REFERENCES

- [1] P. J. Delfyett, *et al.*, "Optical frequency combs from semiconductor lasers and applications in ultrawideband signal processing and communications," *J. Lightw. Technol.*, vol. 24, no. 7, pp. 2701–2719, Jul. 2006.
- [2] U. Gliese, *et al.*, "A wideband heterodyne optical phase-locked loop for generation of 3–18 GHz microwave carriers," *IEEE Photon. Technol. Lett.*, vol. 4, no. 8, pp. 936–938, Aug. 1992.
- [3] A. D. Ellis and F. C. G. Gunning, "Spectral density enhancement using coherent WDM," *IEEE Photon. Technol. Lett.*, vol. 17, no. 2, pp. 504–506, Feb. 2005.
- [4] Y. B. M'Sallem, *et al.*, "Quantum-dash mode-locked laser as a source for 56-Gb/s DQPSK modulation in WDM multicast applications," *IEEE Photon. Technol. Lett.*, vol. 23, no. 7, pp. 453–455, Apr. 1, 2011.
- [5] M. J. Fice, A. Chiuchiarrelli, E. Ciarabella, and A. J. Seeds, "Homodyne coherent optical receiver using an optical injection phase-lock loop," *J. Lightw. Technol.*, vol. 29, no. 8, pp. 1152–1164, Apr. 15, 2011.
- [6] S. Ristic, A. Bhardwaj, M. J. Rodwell, L. A. Coldren, and L. A. Johansson, "An optical phase-locked loop photonic integrated circuit," *J. Lightw. Technol.*, vol. 28, no. 4, pp. 526–538, Feb. 15, 2010.
- [7] M. M. Mielke, G. A. Alphonse, and P. J. Delfyett, "Multiwavelength mode-locked semiconductor lasers for photonic access network applications," *IEEE J. Sel. Areas Commun.*, vol. 25, no. 3, pp. 120–128, Apr. 2007.
- [8] J. S. Parker, A. Bhardwaj, P. R. A. Binetti, Y.-J. Hung, C. Lin, and L. A. Coldren, "Integrated 30 GHz passive ring mode-locked laser with gain flattening filter," in *Proc. IEEE Int. Semicond. Laser Conf.*, Kyoto, Japan, Sep. 2010, paper PD1, pp. 1–2.
- [9] J. S. Parker, *et al.*, "Comparison of comb-line generation from InGaAsP/InP integrated ring mode-locked lasers," in *Proc. IEEE Conf. Lasers Electro-Opt.*, Baltimore, MD, May 2011, paper CTuV6, pp. 1–2.
- [10] J. P. Tourrenc, *et al.*, "Experimental investigation of the timing jitter in self-pulsating quantum-dash lasers operating at 1.55 μm ," *Opt. Exp.*, vol. 16, no. 22, pp. 17706–17713, 2008.

Theory and Design of THz Intracavity Gain-Flattened Filters for Monolithically Integrated Mode-Locked Lasers

John S. Parker, Robert S. Guzzon, Erik J. Norberg, Ashish Bhardwaj,
Pietro R. A. Binetti, and Larry A. Coldren, *Fellow, IEEE*

Abstract—We present the theory and design of a tunable gain-flattening filter for integrated mode-locked lasers (MLLs). The filter provides the inverse of the semiconductor spectral gain profile and produces a broad flattened net gain. This improves the performance of MLLs by allowing more modes to lase simultaneously. We demonstrate a gain-flattened MLL with a record 10 dB bandwidth of 2.08 THz, the widest frequency comb span for an integrated quantum-well-based laser at 1.55 μm . Gain-flattening theory is used to extend the integrated comb span to 40 nm. We use scattering matrices to investigate feed-forward filters based on asymmetric Mach–Zehnder interferometers (MZIs). We compare MZI filters designed for a fixed coupling value to those that use an active gain arm to adjust the extinction ratio. Tunable zero placement of these filters is achieved using a passive phase tuning arm. The optimized gain-flattening filter has a 5 dB extinction ratio and a 70 nm free-spectral-range. When the filter is incorporated into a ring MLL, simulations predict a 40 nm, i.e., 5 THz, comb span with a power variation <3.5 dB.

Index Terms—Integrated optics, mode-locked lasers, optical filters, photonic integrated circuits, quantum well devices, quantum well lasers, semiconductor laser, semiconductor optical amplifier.

I. INTRODUCTION

A FLATTENED gain spectrum is highly beneficial to photonic components in a wavelength division multiplexed (WDM) system, including: broadband amplifiers [1], tunable lasers [2], and multiwavelength sources such as mode-locked lasers (MLL) [3]. MLLs can provide low-noise and narrow linewidth phase-locked comb-lines with a set frequency spacing for applications including: optical signal processing [4], coherent communication [5], and spectroscopy [6]. Additionally, emerging applications in integrated laser offset locking

require a broadband stable frequency comb-line reference, which can be generated using a gain flattened mode-locked laser [7], [8]. However, the span of the frequency comb generated in integrated MLLs is limited by cavity dispersion and the flatness of the gain spectrum. The cavity dispersion is typically low for InP based material and can be compensated for by using an arrayed waveguide grating (AWG), or by optimizing the drive current and absorber bias of the MLL [9], [10]. Therefore, the generation of a flattened gain spectrum is crucial to improving the performance of MLLs. In this paper, we analyze the design of intracavity filters for enhanced gain flatness. To the best of our knowledge, this is the first paper on the design of intracavity integrated gain-flattening filters.

A flattened gain profile equalizes the output power at multiple wavelengths creating a more uniform comb across an optical band. Taking a broad historical view, two general approaches have been pursued: type I used material growth, whereas type II used filters to add loss at the peak gain.

Initial type I gain-flattening was focused on custom materials for WDM erbium-doped fiber amplifiers (EDFAs). In the early 1990's, experiments on EDFAs that used fluorozirconate glass instead of the standard silica core demonstrated improved gain flatness with <2 dB gain ripple over 30 nm bandwidth [11]. Such type I solutions had several advantages, including simplicity and power efficiency by avoiding a lossy external filter element.

For integrated devices, type I solutions have focused on tailoring the gain of the semiconductor material. For example, asymmetric quantum wells have been studied extensively on the InGaAs/GaAs and InGaAsP/InP material platforms, where a flat gain bandwidth with 1 dB ripple across 90 nm has been demonstrated [12]. These structures have used multiple quantum wells with different bandgaps to achieve flat gain profiles. While asymmetric quantum wells have shown promising results, the gain profile is highly dependent on pump current and the uniformity of the carrier distribution across the quantum wells [13]. Thus broad gain is only achievable over a narrow range of pump currents, or conversely, at a fixed gain. Additionally, devices based on asymmetric quantum wells are very sensitive to changes in material growth and operating temperature.

In type II gain-flattening approaches based on filters, bench-top EDFAs with thin film filters have been studied extensively, and commercial modules are readily available to flatten

Manuscript received August 1, 2011; revised September 27, 2011; accepted October 22, 2011. Date of current version January 24, 2012. This work was supported in part by the Defense Advanced Research Projects Agency Photonic Integration for Coherent Optics Program. A portion of this work was done in the UCSB Nanofabrication Facility, part of the National Science Foundation funded National Nanotechnology Infrastructure Network.

J. S. Parker, R. S. Guzzon, E. J. Norberg, P. R. A. Binetti, and L. A. Coldren are with the Department of Electrical Engineering, University of California, Santa Barbara, CA 93106 USA (e-mail: JJS Parker@gmail.com; rob.guzzon@gmail.com; norberg@ece.ucsb.edu; pbinetti@gmail.com; coldren@ece.ucsb.edu).

A. Bhardwaj was with the Department of Electrical and Computer Engineering, University of California, Santa Barbara, CA 93106 USA. He is now with JDS Uniphase Corporation, San Jose, CA 95134 USA (e-mail: Ashish.Bhardwaj@jdsu.com).

Color versions of one or more of the figures in this paper are available online at <http://ieeexplore.ieee.org>.

Digital Object Identifier 10.1109/JQE.2011.2174199

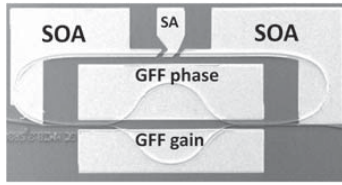


Fig. 1. Fabricated mode-locked laser with a gain-flattening filter (GFF).

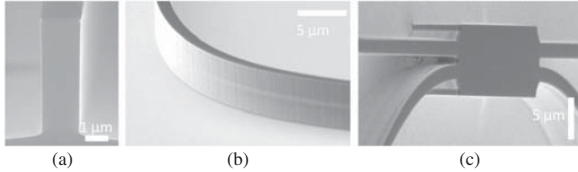


Fig. 2. Scanning electron microscope (SEM) images of the etched waveguide showing (a) $5\ \mu\text{m}$ deep etch with vertical sidewalls, (b) waveguide bends with smooth sidewalls, and (c) multimode interference (MMI) couplers.

the EDFA output. Prior to this, Bragg filters and acousto-optic filters were also studied for bench-top gain-flattening [14], [15]. Researchers have demonstrated broadband comb generation using bench-top gain flattened mode-locked laser by incorporating a spectrometer and spatial filter into their free-space optical set-up [16]. For integrated devices, silicon planar lightwave circuits (PLCs) have been demonstrated for EDFA gain-flattening [17]. Yet there has been minimal research done on integrated gain-flattening filters for use in mode-locked lasers.

Recently, we demonstrated an integrated intracavity gain-flattening filter (GFF) on InGaAsP/InP that doubled the locking bandwidth of a ring MLL [18], and provided far wider comb spans than any simple non-gain-flattened ring MLL fabricated on the same material platform [19]. The filter was an asymmetric Mach-Zehnder interferometer (MZI).

In this paper, we begin by demonstrating a $-10\ \text{dB}$ bandwidth of $2.08\ \text{THz}$ from the MZI-MLL. We were able to operate this device at a higher current density than our previous devices due to better metal evaporation and a lower p-type contact resistance, thus breaking our prior $1.8\ \text{THz}$ record, and producing the widest frequency comb that has yet been generated from an integrated quantum well (QW) based MLL at $1.55\ \mu\text{m}$ [19], [20]. In the remainder of the paper, we discuss the design optimization of monolithically integrated intracavity GFFs, targeting $5\ \text{THz}$, i.e. $40\ \text{nm}$, flattened gain bandwidth. We develop a general analytical formalism for calculating the change in threshold current density and the output power due to an intracavity gain flattening filter. Based on this approach, in the ideal case we show that the bandwidth can be flattened up to $40\ \text{nm}$ with $\sim 10\%$ reduction in the total output power. We use scattering matrices, to include the coupled cavity effects from incorporating an intracavity filter, and we compare MZIs designed for a fixed coupling value to those that use an active gain arm to adjust the extinction ratio. We show that for the optimized GFF incorporated into a ring mode-locked laser, simulations can achieve a $40\ \text{nm}$, i.e. $5\ \text{THz}$, comb span with a power variation $< 3.5\ \text{dB}$.

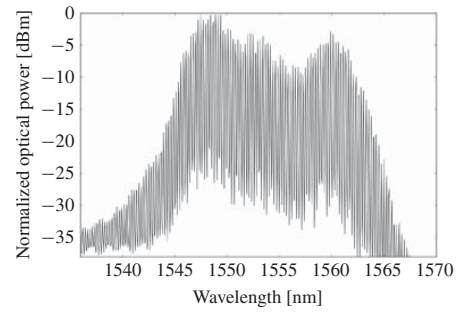


Fig. 3. Normalized optical power spectrum of optical comb generated from gain flattened mode-locked laser. The $-10\ \text{dB}$ comb span is $16.75\ \text{nm}$ ($2.08\ \text{THz}$).

It is to be noted that such versatile filters can be tailored for any semiconductor gain material including: quantum wells (QWs), quantum dots (QD), or bulk. Hence, these filters can provide improved bandwidth for most integrated mode-locked lasers. Furthermore, these filters can be dynamically tuned to tailor the gain spectrum after fabrication to account for changes in material growth and operating temperature variations.

II. FABRICATED GAIN-FLATTENED MODE-LOCKED LASER

The fabricated GFF-MLL is shown in Fig. 1. It has two $3\ \text{dB}$ multimode interference (MMI) couplers with two arms that differ in length by $16\ \mu\text{m}$ to form an intracavity asymmetric MZI; this filter has a free-spectral-range (FSR) of $39.7\ \text{nm}$. The MLL has a round-trip cavity length of $2600\ \mu\text{m}$ with two $750\ \mu\text{m}$ long SOAs, and a $60\ \mu\text{m}$ long SA. The GFF phase arm controls the filter's zero placement, while the GFF gain arm controls the filter's extinction ratio (ER).

This device is fabricated on an InGaAsP/InP offset quantum well (OQW) platform that contains seven 0.9% compressively strained QWs and eight -0.2% tensile strained barriers that are epitaxially grown above a $300\ \text{nm}$ 1.3Q InGaAsP layer as part of the base epi. Passive areas are defined by a selective wet-etch and a single blanket regrowth is used to cover the device with a p^+ -doped InP cladding, a p^{++} -doped InGaAs contact layer, and an InP capping layer to protect the InGaAs contact layer during device fabrication. The active material is used to define the semiconductor optical amplifiers (SOAs) and the saturable absorber (SA), whereas the passive material is used to define the low-loss waveguides and current injection based phase shifters.

After regrowth, the waveguide is defined with photoresist on a Cr/SiO₂ bilayer hard mask. The Cr is etched using a low power Cl₂-based inductively coupled plasma (ICP), and the SiO₂ is etched using an SF₆/Ar based ICP. The resulting $600\ \text{nm}$ SiO₂ mask acts as a hard-mask to define the InGaAsP/InP deeply etched waveguides using a Cl₂/H₂/Ar ($9/18/2\ \text{sccm}$) ICP at a chamber pressure of $1.5\ \text{mT}$. The resulting etched features are shown in Fig. 2. After removing the SiO₂ mask, blanket deposition of a $350\ \text{nm}$ isolation layer of silicon nitride is performed. Vias are opened for

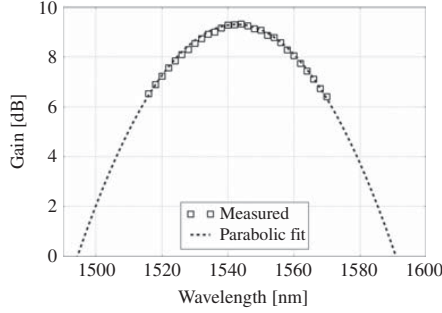


Fig. 4. Measured and parabolic fit gain spectrum. Parabolic fit [dB] = $9.3 - (1543 - \lambda)^2 / 250$.

topside p-metal contacts. N-metal contacts are realized through backside deposition of Ti/Pt/Au onto the n-doped conducting InP substrate. For more details on the fabrication and testing of the MLL-GFF, see [20].

When operating at 210 mA drive current, -2.1 V saturable absorber bias, 35 mA GFF gain current, and 15.5 mA GFF phase current, this device provides a -10 dB lasing bandwidth as wide as 16.75 nm, more than 2 THz, as shown in Fig. 3. Nevertheless, the flattened gain bandwidth can be improved further as this standard 7 QW material platform has more than 100 nm of positive gain bandwidth. In the next section, we examine intracavity gain-flattening using an ideal GFF, and then in Section IV and V using a realistic single-stage filter that can be monolithically integrated on InGaAsP/InP.

III. IDEAL PARABOLIC GAIN-FLATTENING FILTER

Semiconductor gain material has a near-parabolic gain profile due to the curvature of the valence and conduction bands. The parabolic profile fits well near the peak gain and deviates as the gain approaches transparency. The measured and parabolic fit for standard 7 offset-quantum well (OQW) gain material is shown in Fig. 4.

The gain peak is at 1543 nm and fits well to a parabola over a 50 nm range from 1518–1568 nm. The gain is measured by fiber coupling a 1 mW tunable laser into the input waveguide. Three 400 μm long SOAs are positioned serially along the waveguide. The first two are reverse biased at -3 V, and therefore act as photodetectors to record the input power from the tunable laser; the second SOA absorbs any light that is not captured in the first section. Then, the first SOA is forward biased, and the second and third SOAs are reverse biased at -3 V to record the amplified power. The peak gain is measured at ~ 4 kA/cm² for the 400 μm \times 1.8 μm SOA.

In the following mathematical derivation, we will use this parabolic fit to calculate the change in threshold gain and output laser power as we introduce an ideal GFF. The parabolic gain approximation for a 400 μm long SOA operating below saturation is calculated to be

$$g_{\text{SOA}, L=400 \mu\text{m}}(\lambda) = \left(9.3 - \frac{(1543 - \lambda)^2}{250} \right) \text{dB} \quad (1)$$

where λ is the wavelength in nm.

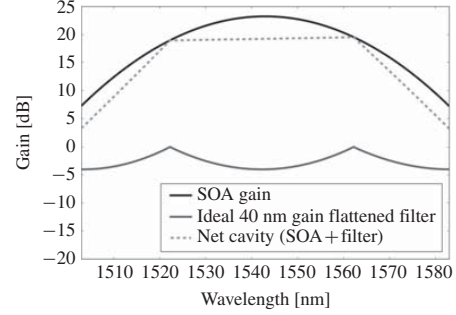


Fig. 5. Net cavity gain after insertion of ideal inverse parabolic gain-flattening filter.

Gain roll-off is the reduction in gain away from the peak gain wavelength, and it is represented by the denominator in the parabolic approximation. Furthermore, gain roll-off is proportional to the modal gain at the peak wavelength (g_{peak}), as is clearly evident since the SOA's positive gain bandwidth (i.e. gain above transparency) does not change with SOA length. For example, the OQW SOA at a current density of 4 kA/cm² has positive gain over a 96 nm span regardless of SOA length. However, the peak gain (g_{peak}) increases with length, hence, gain roll-off must increase with g_{peak} . A longer (or higher confinement factor) SOA will have a larger gain roll-off than a shorter (or lower confinement factor) SOA with the same current density. We define the SOA gain based on g_{peak} such that it is independent of length.

$$g_{\text{SOA}}(\lambda) = \left(g(N) - \frac{g_{\text{peak}}(\lambda_0 - \lambda)^2}{C_1} \right) \text{dB} \quad (2)$$

where g is a function of the carrier density, N , such that the maximum of $g(N) = g_{\text{peak}}$, and the parabolic gain roll-off coefficient is defined from Fig. 4 as $C_1 = 250 \times 9.3$ [nm²]. For critical flat gain applications, such as mode-locked lasers, we want the largest ratio of gain/roll-off. Based on (2), this can be achieved by driving the SOA near its peak gain when lasing. As gain clamping restricts the increase of gain above lasing, we aim to use the shortest SOA that allows the cavity to lase. We can define a net cavity gain that includes SOA gain and the added wavelength dependence of the filter

$$\begin{aligned} g_{\text{Net}}(\lambda) &= g_{\text{SOA}}(\lambda) - \text{loss}_{\text{Filter}}(\lambda) \\ \therefore g_{\text{Net}}(\lambda) &= g_{\text{SOA}}(\lambda) + g_{\text{Filter}}(\lambda) \end{aligned} \quad (3)$$

where the wavelength dependent loss is defined as a negative filter gain. The net gain per cavity round-trip is a function of the SOA gain profile and the filter transfer function. For the parabolic SOA profile shown in Fig. 4, the ideal GFF will have an inverse parabolic shape, as shown in Fig. 5.

The applied filter is assumed to have a periodic transfer function. The free-spectral-range (FSR) of the filter determines the bandwidth of the flattened gain region. The filter adds loss at the peak of the gain profile to equalize the gain. Therefore, to create a wider flat bandwidth, the ER of the filter must be increased. For a laser cavity, this results in a higher threshold gain and lower output power.

We can now calculate the increase in threshold gain with an ideal GFF. For a cavity resonator, the $g(N)$ term can be replaced with the threshold gain, g_{th} , as $g(N)$ does not change above lasing threshold. For a ring MLL, the nominal threshold gain (i.e. without the GFF turned on) can be calculated from the measured losses of each element in the ring. The internal losses measured from cleave back tests [21] on Fabry-Perot lasers are 3.5 dB/mm passive material internal loss and 4.3 dB/mm active material internal loss. We assume a minimum of two 3 dB couplers are necessary to create the GFF, each with measured insertion loss <1 dB. The saturable absorber (SA) loss is measured from a fabricated device to be ~ 1 dB from injecting the output pulses from the MLL, in [18], into a saturable absorber test structure, and measuring CW power on the SA and an 800 μm reversed biased SOA detector placed after it.

The nominal threshold gain (g_{th0}) for a 2600 μm circumference cavity with 1500 μm length active and 1100 μm length passive material is calculated as: internal loss + mirror loss (coupler transmission) + couplers insertion loss + SA loss = 10.3 dB + 3 dB + 2 dB + 1 dB = 16.3 dB. Assuming we have an ideal parabolic gain flattened filter, we can write the increased threshold gain (g_{th1}) after gain-flattening as

$$g_{th0}(\Delta\lambda) = \left(g_{th1} - \frac{g_{peak}(\Delta\lambda/2)^2}{C_1} \right) \text{dB} \quad (4)$$

where $\Delta\lambda$ is the gain flattened bandwidth.

We have replaced $g(N)$ with the new threshold gain after gain-flattening, g_{th1} . The gain at the edge of the gain flattened spectrum must be increased to equal to the previous peak wavelength gain, g_{th0} , to maintain lasing, i.e. the gain at $\lambda_0 + \Delta\lambda/2$ must be equal to the previous nominal threshold gain g_{th0} . However, we would like to define this expression in terms of g_{th1} to solve for the change in laser output power. Solving for g_{th1} , we calculate

$$g_{th1}(g_{th0}, \Delta\lambda) = g_{th0} + \frac{g_{peak}(\Delta\lambda/2)^2}{C_1}. \quad (5)$$

Using a logarithmic gain model [22], the threshold current density is related to the threshold gain by

$$J_{th1} = J_{tr} \exp(g_{th1}/g_0) \left[\text{A/cm}^2 \right] \quad (6)$$

where the J_{th1} and J_{tr} terms are the threshold and transparency current density respectively. The g_{th1} and g_0 terms are the threshold gain and gain constant respectively. A is the area of the active region in cm^2 (length \times width). The output power [23] for a semiconductor laser is given by

$$P_{out1}(I_{th}) = \eta_d \eta_i \frac{h\nu}{q} (I - I_{th}) \quad (7)$$

$$P_{out1}(J_{th}) = \eta_d \frac{h\nu}{q} A (J - J_{th}) \quad (8)$$

where η_d is the differential efficiency and η_i is the injection efficiency. We find the change in cavity output power by combining (5), (6), and (8)

$$P_{out} = \eta_d \frac{h\nu}{q} A \left(J - J_{tr} \exp\left(\frac{g_{th0} + g_{peak}(\Delta\lambda/2)^2}{C_1 g_0}\right) \right). \quad (9)$$

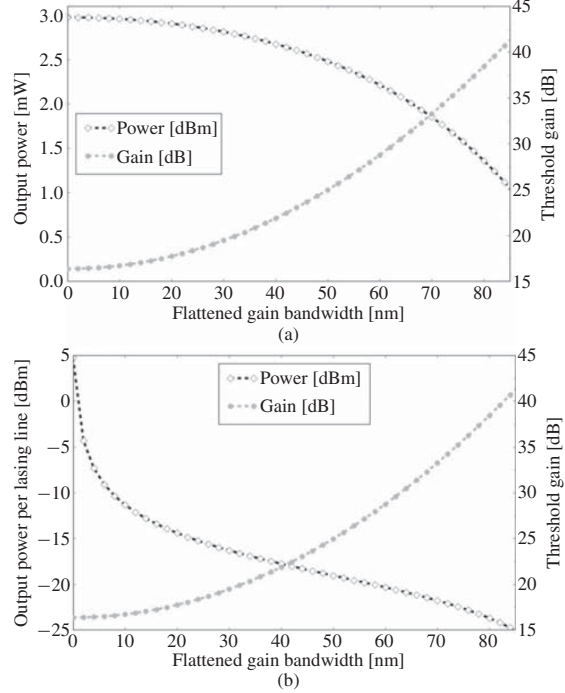


Fig. 6. (a) Laser output power and threshold gain versus flattened bandwidth of an ideal GFF. A larger flattened bandwidth requires added loss at the peak gain wavelength, increasing the threshold gain, and reducing the output power. The SOA drive current is fixed at 54 mA. The 40 nm flattened bandwidth has a 10% reduction in output power. (b) Output power per lasing line versus flattened bandwidth, assuming all modes within the flattened bandwidth lase. The output power per lasing line at 40 nm bandwidth is 22 dB lower than when the device operates with a single mode, i.e., 0 nm bandwidth.

The resulting plot of threshold gain and output power vs. gain flattened bandwidth is shown in Fig. 6(a). The drive current is held at 54 mA (e.g. $3I_{th}$) whereas the nominal threshold current is 18 mA with a measured injection efficiency of 0.6 ($J_{th} = 382 \text{ A/cm}^2$). For this material, $J_{tr} = 31 \text{ A/cm}^2/\text{well}$ and $g_0 = 650 \text{ cm}^{-1}$ are measured from broad-area laser cleave-back tests. Fig. 6(b) shows the output power in each of the lasing modes vs. gain flattened bandwidth. This plot uses the realistic assumption that all modes in the gain flattened bandwidth with equal round-trip gain are lasing simultaneously. The single lasing mode case occurs at 0 nm with 3 mW output, whereas at 40 nm flattened bandwidth there are 160 modes lasing with 20 μW per lasing line output power. At 40 nm bandwidth, the output power is divided amongst many lines resulting in greatly decreased power per line, see Fig. 6(b), whereas the total power is reduced only slightly, see Fig. 6(a).

IV. MACH-ZEHNDER INTERFEROMETER GAIN-FLATTENING FILTER

In the previous section, we developed theory based on an ideal GFF. In this section, we examine a realistic single-stage GFF that can be monolithically integrated with minimal added components. For use in MLLs, we want to minimize the filter unit delay to avoid coherence effects in pulse propagation.

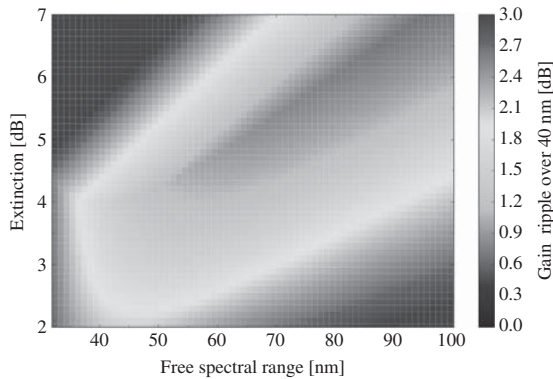


Fig. 7. Color map of gain ripple over a 40 nm bandwidth from variations in filter's extinction ratio and free spectral range.

For pulse widths of 1 ps we target delays $\ll 1$ ps. This limits us to path length differences of $\ll 80 \mu\text{m}$ in InP.

Feed-back filters, such as a coupled ring resonator, suffer from large loop delays much longer than the pulse width, which makes them unsuitable for short pulses. Feed-forward filters, such as a MZI, have short unit delays based on the difference in arm length. If we consider arms that differ in length by $< 20 \mu\text{m}$ (i.e. one quarter of the pulse width), we calculate a filter FSR > 32 nm. To compare MZI filter designs, the gain ripple (i.e. the maximum deviation in net gain) over a fixed 40 nm bandwidth is calculated for a range of FSR and ER, as shown in Fig. 7.

The filter flatness is improved as the FSR and ER are increased. Unlike the ideal GFF with an inverse parabolic profile, the MZI filter response matches the inverse parabola only near its center. Therefore, by increasing the FSR, the fit improves, however the threshold gain is increased as well due to a larger ER. The lowest ripple shown in Fig. 7 is 0.6 dB at an FSR of 100 nm with a 7 dB ER. However, by sacrificing a small amount of gain ripple we can use a lower ER, reduce the added loss from the applied filter, and operate with a lower threshold gain. By choosing 70 nm FSR, the optimal ER is 5 dB and the 40 nm gain ripple is 0.73 dB. The 70 nm FSR MZI filter response is shown in Fig. 8, along with the ideal inverse parabolic filter response. The ideal filter has an ER of 3.7 dB, whereas the optimized MZI filter is 1.3 dB greater.

This ER can be created by using equal power splitting couplers in the MZI with one variable amplitude arm by means of an SOA, or by using imbalanced power splitting couplers. The benefit of using the SOA is that variation to the ER can be made post-processing, which allows for dynamic control of the ER. However, a drawback of this approach is that the SOA in the amplitude arm is within the coupled-cavity system. Therefore, the carrier density in the amplitude arm cannot increase beyond the threshold carrier density of the laser before it gain-clamps, i.e. the gain per unit length cannot be higher in the amplitude filter arm than in the ring SOAs. This restricts the filter configurations. For example, consider a ring with a threshold gain of 15 dB with

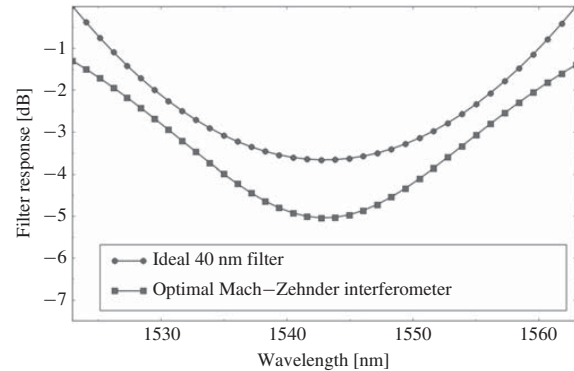


Fig. 8. Comparison of ideal gain-flattening filter and Mach-Zehnder interferometer filter response.

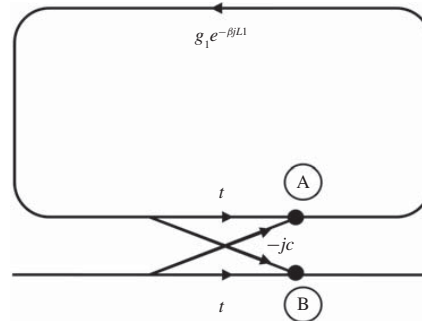


Fig. 9. Signal flow diagram of a single ring and coupler. Markers A and B designate nodes inside and outside of the ring cavity, respectively.

1500 μm of SOA in the ring and filter arms with a length of 500 μm . The maximum gain achievable in the amplitude filter arm would be approximately one-third of the threshold gain, i.e. 5 dB. When the gain arm is driven higher, its carrier density will clamp at N_{th} , preventing any further increase in gain.

For balanced power splitters, the desired 5 dB ER requires ~ 11 dB power difference in both arms. Hence, to achieve a 40 nm flattened bandwidth the amplitude arm must only be used as an absorbing element rather than a gain element. This loss greatly increases the threshold gain, and for this reason the imbalanced coupler is preferred. Furthermore, the long SOA necessary to provide either 11 dB gain or loss in the filter arm has its own wavelength dependence based on the semiconductor gain medium.

The alternative to using a variable gain (loss) arm is to use imbalanced couplers. To achieve this 5 dB ER, fixed couplers with 78% power bar-coupling are required. Assuming a 1 dB processing tolerance on the ER (i.e. 5 ± 1 dB, from Fig. 5), the fixed couplers must be between 75–82% bar-coupling. This can be achieved using reactive-ion etching (RIE) lag directional couplers, where two parallel deeply etched waveguides are separated by a narrow gap. This slows the etch rate between the waveguides and effectively forms a surface ridge directional coupler on a deeply etched waveguide in a single etch step. We have previously demonstrated RIE lag

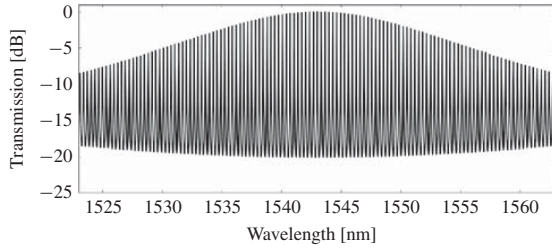


Fig. 10. Output power response of a single ring with coupler (A–B in Fig. 9). The variation in power response over the 40 nm spectrum is 8.5 dB.

directional couplers on non-gain-flattened ring mode-locked lasers with 90% bar-coupling, and we have shown that such couplers can be designed to provide arbitrary coupling from 1–99% [25]. Hence, the desired 5 THz comb generator using 78% couplers can be fabricated with realistic processing technology.

V. GAIN FLATTENED FILTER COUPLED CAVITY MODEL

In the previous sections, we have analyzed the GFF as a component. The ideal GFF has been compared to a practical MZI filter that can be implemented in a monolithically integrated photonic circuit. However, when the GFF is placed inside a cavity, the filter response becomes more complex due to coupled-cavity effects, i.e. each MZI arm forms a resonant cavity with the larger ring. To simulate the effects of the filter in the cavity, we make use of scattering parameters to calculate the full coupled-cavity response. The signal flow diagram for a single ring and coupler is shown in Fig. 9; the coupler has bar-coupling (t) and cross-coupling ($-jc$).

The amplitude transfer function from A to B, i.e. the transfer function of amplified spontaneous emission generated inside the ring seen at the output of the ring, is calculated as

$$H_{A-B}(\lambda) = \frac{-jcg_1(\lambda)\exp(-j\beta L_1)}{1 - tg_1(\lambda)\exp(-j\beta L_1)}. \quad (10)$$

Shown in Fig. 10, the power transmission out of the ring is calculated from the magnitude squared of the amplitude transfer function. All transfer functions are calculated at a pole response of 20 dB, which is typical for a lasing resonator, i.e. peak to trough extinction ratio is 20 dB. In this single ring without a filter, the wavelength dependent gain of the SOA causes the output transmission to vary by 8.5 dB over the 40 nm bandwidth and the pole response is decreased from 20 dB to ~ 10 dB.

A signal flow graph for the ring MLL with a GFF is shown in Fig. 11. This ring has two couplers. The ring path and two MZI arms have amplitude gains g_1 , g_2 , and g_3 .

The amplitude transfer function inside the ring (from A to A) is solved using Mason's rule [24]

$$H_{A-A}(\lambda) = \frac{-c^2 M_1(\lambda) M_3(\lambda) + t^2 M_1(\lambda) M_2(\lambda)}{1 - t^2 M_1(\lambda) M_2(\lambda) + c^2 M_1(\lambda) M_3(\lambda)} \quad (11)$$

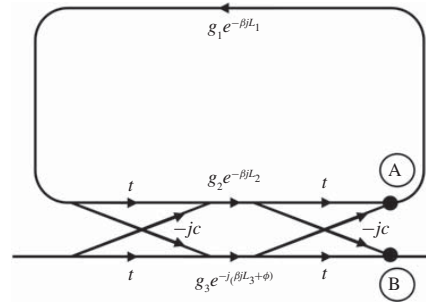


Fig. 11. Signal flow diagram of a ring with a gain-flattening filter. Markers A and B designate nodes inside and outside of the ring cavity, respectively.

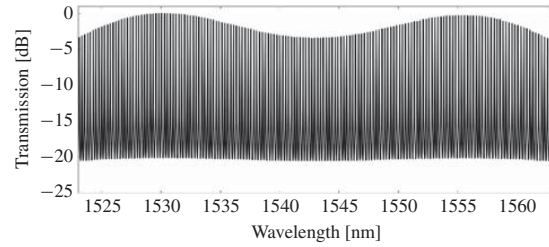


Fig. 12. Intracavity power response of a ring with a gain-flattening filter (A–A in Fig. 11). The variation in power response over the 40 nm spectrum is 3.4 dB.

$$M_1(\lambda) = g_1(\lambda)\exp(-j\beta L_1)$$

$$M_2(\lambda) = g_2(\lambda)\exp(-j\beta L_2)$$

$$M_3(\lambda) = g_3(\lambda)\exp(-j(\beta L_3 + \phi)).$$

The power transmission inside the ring with the GFF is plotted in Fig. 12. The small gain ripple calculated in Section IV by adding the filter and cavity gains is now enhanced by the resonant cavity operating at a high pole value of 0.82, i.e. a pole response magnitude of 20 dB. Over the 40 nm bandwidth, the 0.73 dB ripple in the net gain (calculated from the cascaded filter and SOA in Section IV) results in a 3.4 dB variation in the power response when these elements are placed inside a resonant cavity.

The response shown in Fig. 12 does not include the effect of coupling out of the cavity. To consider the output from the GFF-MLL, the transfer function from A to B is calculated as

$$H_{A-B}(\lambda) = \frac{-jctM_1(\lambda)M_3(\lambda) - jctM_1(\lambda)M_2(\lambda)}{1 - t^2M_1(\lambda)M_2(\lambda) + c^2M_1(\lambda)M_3(\lambda)}. \quad (12)$$

As shown in Fig. 12, the transfer function inside the ring (A–A) produces a flattened response compared to the single ring case, see Fig. 10. However, the output transfer function (A–B), as shown in Fig. 13, goes through the inverse GFF function when coupled out of the cavity. The transfer function (A–B) is degraded and the 40 nm transmission envelope has a 9.3 dB ripple, larger than the single ring by itself. Thus, while Fig. 13 achieves a flat response at the center of its comb, the comb profile falls off rapidly as it approaches the 40 nm bandwidth. To have the desired flat transfer function, covering the full 40 nm outside the cavity where it will be used, an

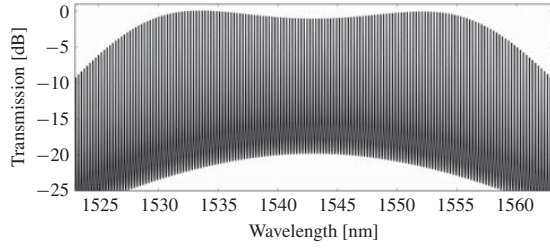


Fig. 13. Output power response of a ring with a gain-flattening filter (A–B in Fig. 11). The variation in power response over the 40 nm spectrum is 9.3 dB.

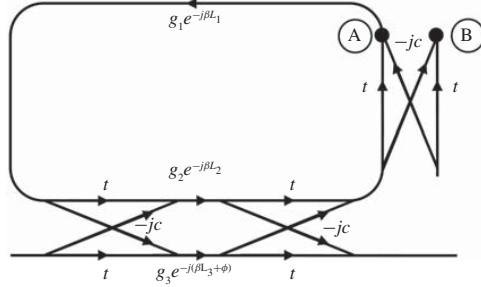


Fig. 14. Signal flow diagram of a ring with a gain-flattening filter and additional coupler. Markers A and B designate nodes inside and outside of the ring cavity respectively.

additional coupler is required to avoid passing the output comb spectrum through the inverse GFF. The cavity with an additional coupler is shown in Fig. 14 and shows the same spectral shape as Fig. 12, while in this case, the response is seen outside the ring. The draw-back of having an additional coupler is a slight increase in the threshold gain, ~ 2 dB, for the 22% cross-coupling with 1 dB insertion loss used in this example.

The transfer function with the additional coupler is shown in Fig. 15 and calculated as

$$H_{A-B}(\lambda) = \frac{jc^3 M_1(\lambda) M_3(\lambda) - jct^2 M_1(\lambda) M_2(\lambda)}{1 - t^3 M_1(\lambda) M_2(\lambda) + tc^2 M_1(\lambda) M_3(\lambda)}. \quad (13)$$

All transfer functions have been calculated based on the fixed 5 dB filter ER calculated in Section IV. Compared to the single ring and coupler, the addition of the GFF results in a 7 dB increase in the threshold gain and a reduction in output power from 3.0 mW to 2.7 mW, as calculated in Fig. 6(a) (e.g. the increase in threshold gain = 5 dB from GFF + 2 dB from added coupler). Ring MLLs built on a QW gain platform have typical comb spans < 1 THz [19], thus, the addition of the GFF reduces the laser output power by $\sim 17\%$ while increasing the comb bandwidth by > 5 X. However, the power per lasing line does decrease by $> 85\%$ as the total output power is divided over more modes.

VI. COMPARISON OF COUPLED CAVITY MODEL TO RESULTS

Using the coupled cavity model from Section V, we now compare the 2 THz measured comb from Fig. 3 to its simulated comb. The optical signal-to-noise ratio (OSNR) for the comb

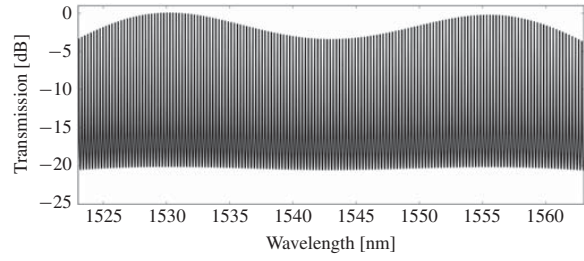


Fig. 15. Output power response of a ring with a gain-flattening filter and additional coupler (A–B in Fig. 14). The variation in power response over the 40 nm spectrum is 3.5 dB.

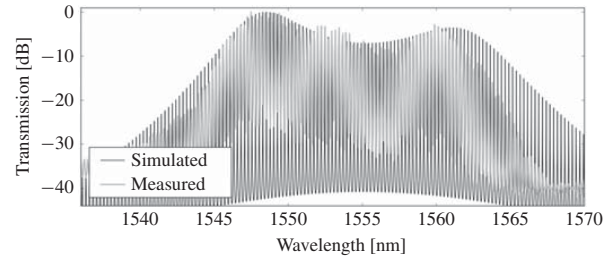


Fig. 16. Comparison of the measured and simulated power response from the gain-flattened mode-locked laser shown in Fig. 1. The -10 dB bandwidth is 16.75 nm and 19 nm for the measured and simulated spectrums, respectively.

is 35–45 dB, measured over narrow 1 nm spans with a high resolution OSA. The pole magnitude of the coupled cavity response matches this OSNR. As shown in Fig. 16, the simulated and measured combs have similar spectral profiles, yet the span of simulated comb is 19 nm, which is 13% wider than the measured bandwidth. Such deviation is like due to the limitations of the model, as it does not include material dispersion or the time-dependent effects of the saturable absorber. Nevertheless, the simulated and measured comb profiles match well, indicating that the coupled cavity approach can provide a reasonable estimate for the flattened gain profile of a mode-locked laser.

VII. CONCLUSION

We have demonstrated integrated gain-flattened MLLs with -10 dB bandwidths of over 2 THz, which are the widest reported comb spans for QW based MLLs. We have developed an analytical formalism for the reduction in output power from a gain-flattened mode-locked laser. We have presented the theory and design of an integrated intracavity gain-flattening filter for a ring mode-locked laser that provides a 40 nm flattened comb span with less than 3.5 dB power variation. The ideal gain-flattening filter for quantum well semiconductor material is shown to have an inverse parabolic profile, which can be approximated well over a 40 nm span by a single Mach–Zehnder interferometer. An integrated gain flattened mode-locked laser can provide broad comb-line generation for use in laser offset locking, in spectroscopy, and as a compact coherent WDM source.

REFERENCES

- [1] B. Clesca, D. Ronarc'h, D. Bayart, Y. Sorel, L. Hamon, M. Guibert, J. L. Beylat, J. F. Kerdiles, and M. Semenkoff, "Gain flatness comparison between erbium-doped fluoride and silica fiber amplifiers with wavelength-multiplexed signals," *IEEE Photon. Technol. Lett.*, vol. 6, no. 4, pp. 509–512, Apr. 1994.
- [2] L. A. Coldren, G. A. Fish, Y. Akulova, J. S. Barton, L. Johansson, and C. W. Coldren, "Tunable semiconductor lasers: A tutorial," *J. Lightw. Technol.*, vol. 22, no. 1, pp. 193–202, Jan. 2004.
- [3] H. Yasaka, Y. Yoshikuni, K. Sato, H. Ishii, and H. Sanjoh, "Multiwavelength light source with precise frequency spacing using mode-locked semiconductor laser and arrayed waveguide grating filter," in *Proc. IEEE Opt. Fiber Commun.*, Feb.–Mar. 1996, pp. 299–300.
- [4] P. J. Delfyett, S. Gee, M. T. Choi, H. Izadpanah, W. Lee, S. Ozharar, F. Quinlan, and T. Yilmaz, "Optical frequency combs from semiconductor lasers and applications in ultrawideband signal processing and communications," *J. Lightw. Technol.*, vol. 24, no. 7, pp. 2701–2719, Jul. 2006.
- [5] Y. B. M'Sallem, Q. T. Le, L. Bramerie, Q. Nguyen, E. Borgne, P. Besnard, A. Shen, F. Lelarge, S. LaRochelle, L. A. Rusch, and J. Simon, "Quantum-dash mode-locked laser as a source for 56-Gb/s DQPSK modulation in WDM multicast applications," *IEEE Photon. Technol. Lett.*, vol. 23, no. 7, pp. 453–455, Apr. 2011.
- [6] V. Gerginov, C. E. Tanner, S. A. Diddams, A. Bartels, and L. Hollberg, "High-resolution spectroscopy with a femtosecond laser frequency comb," *Opt. Lett.*, vol. 30, no. 13, pp. 1734–1736, 2005.
- [7] S. Ristic, A. Bhardwaj, M. J. Rodwell, L. A. Coldren, and L. A. Johansson, "An optical phase-locked loop photonic integrated circuit," *J. Lightw. Technol.*, vol. 28, no. 4, pp. 526–538, Feb. 2010.
- [8] C. F. C. Silva, A. J. Seeds, and P. J. Williams, "Terahertz span >60-channel exact frequency dense WDM source using comb generation and SG-DBR injection-locked laser filtering," *IEEE Photon. Technol. Lett.*, vol. 13, no. 4, pp. 370–372, Apr. 2001.
- [9] M. Kwakernaak, R. Schreieck, A. Neiger, H. Jackel, E. Gini, and W. Vogt, "Spectral phase measurement of mode-locked diode laser pulses by beating sidebands generated by electrooptical mixing," *IEEE Photon. Technol. Lett.*, vol. 12, no. 12, pp. 1677–1679, Dec. 2000.
- [10] M. J. R. Heck, P. Munoz, B. W. Tilma, E. A. J. M. Bente, Y. Barbarin, Y. S. Oei, R. Notzel, and M. K. Smit, "Design, fabrication and characterization of an InP-based tunable integrated optical pulse shaper," *IEEE J. Quantum Electron.*, vol. 44, no. 4, pp. 370–377, Apr. 2008.
- [11] D. Bayart, B. Clesca, L. Hamon, and J. L. Beylat, "Experimental investigation of the gain flatness characteristics for 1.55 μm erbium-doped fluoride fiber amplifiers," *IEEE Photon. Technol. Lett.*, vol. 6, no. 5, pp. 613–615, May 1994.
- [12] O.-K. Kwon, K.-H. Kim, E.-D. Sim, J.-H. Kim, H.-S. Kim, and K.-R. Oh, "Asymmetric multiple-quantum-well laser diodes with wide and flat gain," *Opt. Lett.*, vol. 28, no. 22, pp. 2189–2191, 2003.
- [13] C.-F. Lin, B.-R. Wu, L.-W. Lai, and T.-T. Shih, "Sequence influence of nonidentical InGaAsP quantum wells on broadband characteristics of semiconductor optical amplifiers–superluminescent diodes," *Opt. Lett.*, vol. 26, no. 14, pp. 1099–1101, 2001.
- [14] P. F. Wysocki, J. B. Judkins, R. P. Espindola, M. Andrejco, and A. M. Vengsarkar, "Broad-band erbium-doped fiber amplifier flattened beyond 40 nm using long-period grating filter," *IEEE Photon. Technol. Lett.*, vol. 9, no. 10, pp. 1343–1345, Oct. 1997.
- [15] S. F. Su, R. Olshansky, D. A. Smith, and J. E. Baran, "Flattening of erbium-doped fibre amplifier gain spectrum using an acousto-optic tunable filter," *Electron. Lett.*, vol. 29, no. 5, pp. 477–478, Mar. 1993.
- [16] M. M. Mielke, G. A. Alphonse, and P. J. Delfyett, "Multiwavelength modelocked semiconductor lasers for photonic access network applications," *IEEE J. Sel. Areas Commun.*, vol. 25, no. 3, pp. 120–128, Apr. 2007.
- [17] K. Suzuki, T. Kitoh, S. Suzuki, Y. Inoue, Y. Hibino, T. Shibata, A. Mori, and M. Shimizu, "PLC-based dynamic gain equaliser consisting of integrated Mach-Zehnder interferometers with C- and L-band equalising range," *Electron. Lett.*, vol. 38, no. 18, pp. 1030–1031, Aug. 2002.
- [18] J. S. Parker, A. Bhardwaj, P. R. A. Binetti, Y.-J. Hung, C. Lin, and L. A. Coldren, "Integrated 30 GHz passive ring mode-locked laser with gain flattening filter," in *Proc. 22nd IEEE Int. Semicond. Laser Conf.*, Kyoto, Japan, Sep. 2010, no. PD1, pp. 1–2.
- [19] J. S. Parker, P. R. A. Binetti, A. Bhardwaj, R. S. Guzzon, E. J. Norberg, Y.-J. Hung, and L. A. Coldren, "Comparison of comb-line generation from InGaAsP/InP integrated ring mode-locked lasers," in *Proc. IEEE Conf. Lasers Electro-Opt.*, Baltimore, MD, May 2011, no. CTuV6, pp. 1–2.
- [20] J. S. Parker, A. Bhardwaj, P. R. A. Binetti, Y.-J. Hung, and L. A. Coldren, "Monolithically integrated gain-flattened ring mode-locked laser for comb-line generation," *IEEE Photon. Technol. Lett.*, to be published.
- [21] L. Coldren and S. Corzine, "A phenomenological approach to diode lasers," in *Diode Lasers and Photonic Integrated Circuits*, K. Chang, Ed. New York: Wiley, 1995, pp. 52–54.
- [22] L. Coldren and S. Corzine, "Gain and current relations," in *Diode Lasers and Photonic Integrated Circuits*, K. Chang, Ed. New York: Wiley, 1995, pp. 171–174.
- [23] L. Coldren and S. Corzine, "Dynamic effects," in *Diode Lasers and Photonic Integrated Circuits*, K. Chang, Ed. New York: Wiley, 1995, pp. 190–191.
- [24] J. S. Parker, P. R. A. Binetti, Y.-J. Hung, E. J. Norberg, and L. A. Coldren, "RIE lag directional coupler based integrated InGaAsP/InP ring mode-locked laser," in *Proc. 69th IEEE Annu. Device Res. Conf.*, Santa Barbara, CA, Jun. 2011, pp. 263–264.
- [25] S. J. Mason, "Feedback theory-further properties of signal flow graphs," *Proc. Inst. Rad. Eng.*, vol. 44, no. 7, pp. 920–926, Jul. 1956.



John S. Parker received the B.S. degree in engineering from Harvey Mudd College, Claremont, CA, in 2007, and the M.S. degree in electrical and computer engineering from the University of California, Santa Barbara, in 2009, where he is currently pursuing the Ph.D. degree.

His current research interests include radio-frequency photonics, coherent communication, and compact components for dense photonic integrated circuits.



Robert S. Guzzon received the B.S. degree in electrical engineering and physics from Lehigh University, Bethlehem, PA, in 2007. He is currently pursuing the Ph.D. degree in electrical engineering with the University of California, Santa Barbara.

His current research interests include the design and fabrication of versatile photonic integrated microwave filter systems that achieve high spurious free dynamic range, large-scale photonics integration, and microwave photonic signal processing.



Erik J. Norberg received the B.S. and M.S. degrees in engineering nanoscience from Lund University, Lund, Sweden, in 2008. He is currently pursuing the Ph.D. degree in electrical engineering with the University of California, Santa Barbara.

He is currently working on the development of high dynamic range integrated optical filters for microwave signal processing. His current research interests include the design and metalorganic chemical vapor deposition growth of large scale photonic integrated circuits on InP.



Ashish Bhardwaj received the B.Sc. (honors) and M.Sc. degrees in physics from the Indian Institute of Technology, Kharagpur, India, in 1994 and 1996, respectively, and the Ph.D. degree in applied physics from the California Institute of Technology, Pasadena, in 2001.

He was with the Bell Laboratories, Lucent Technologies, Holmdel, NJ, as a Technical Staff Member from 2001 to 2007, where he was engaged in research on fast wavelength switching in tunable lasers for applications in optical packet switching.

He also led research in the design, fabrication, and characterization of large-scale monolithically integrated InP-based photonic integrated circuits employing semiconductor optical amplifiers. From 2007 to 2011, he was with the Department of Electrical and Computer Engineering, University of California, Santa Barbara, where he led research in the design and fabrication of monolithically integrated optical phase-locked loops as coherent receivers for high dynamic range radio-frequency/photonic links. He is currently with JDS Uniphase Corporation, Milpitas, CA.



Pietro R. A. Binetti received the Ph.D. degree in electrical engineering from the COBRA Research Institute, Eindhoven University of Technology, Eindhoven, The Netherlands, in 2009.

He is currently a Post-Doctoral Fellow with the University of California, Santa Barbara. His current research interests include the design, fabrication, and characterization of photonic integrated circuits for analog and digital applications.



Larry A. Coldren (S'67–M'72–SM'77–F'82) received the Ph.D. degree in electrical engineering from Stanford University, Stanford, CA, in 1972.

He is the Fred Kavli Professor of optoelectronics and sensors with the University of California (UCSB), Santa Barbara. After 13 years in the research area with Bell Laboratories, Holmdel, NJ, he joined UCSB in 1984, where he is currently with the Department of Materials and the Department of Electrical and Computer Engineering. In 1990, he co-founded optical concepts, later acquired as Gore

Photonics, to develop novel vertical-cavity surface-emitting laser (VCSEL) technology, and in 1998, he co-founded Agility Communications, Inc., Goleta, CA, later acquired by JDS Uniphase Corporation (JDSU), Milpitas, CA, to develop widely tunable integrated transmitters. At Bell Laboratories, he was initially on waveguided surface-acoustic-wave signal processing devices and coupled-resonator filters. He later developed tunable coupled-cavity lasers using novel reactive-ion etching technology that he created for the new InP-based materials. At UCSB, he continued work on multiple-section tunable lasers, in 1988, inventing the widely tunable multi-element mirror concept, which is currently used in some JDSU products. Near this time period, he also made seminal contributions to efficient VCSEL designs that continued to be implemented in practical devices till this day. More recently, his group has developed high-performance InP-based photonic integrated circuits as well as high-speed VCSELS, and they continue to advance the underlying materials growth and fabrication technologies. He has authored or co-authored over 1000 journals and conference papers, seven book chapters, and one textbook and has been issued 64 patents. He has presented dozens of invited and plenary talks at major conferences.

Prof. Coldren is a fellow of the Optical Society of America and a member of the National Academy of Engineering. He was a recipient of the John Tyndall and Aron Kressel Awards, in 2004 and 2009, respectively.

Integrated Phase-locked Multi-THz Comb for Broadband Offset Locking

John S. Parker, Abirami Sivananthan, Mingzhi Lu, Leif Johansson, Larry A. Coldren

Electrical and Computer Engineering Department, University of California at Santa Barbara, Santa Barbara, CA 93106-9560

Abstract: We demonstrate an integrated InGaAsP/InP 2.06 THz broadband comb for offset locking SG-DBR widely tunable lasers. The comb has 70 lasing lines and is generated using a hybrid mode-locked laser with intracavity gain flattening.

OCIS codes: 140.4050 Mode-locked lasers, 250.5300 Photonic integrated circuits, 280.3640 Lidar.

1. Introduction

Broadband combs have a multitude of applications including: injection locking laser arrays [1], sources for orthogonal frequency division multiplexing (OFDM) [2], and in metrology [3]. Emerging applications for broadband combs exist in offset locking devices. Such devices use the comb source as a reference for precise frequency positioning. Recently, offset locking of up to 15 GHz has been demonstrated with two monolithically integrated widely tunable SG-DBR lasers with an integrated optical phase-locked loop (OPLL) [4]. Additionally, offset locking to an external comb source has been used to phase-lock two DBR lasers at heterodyne frequencies <50 GHz [5].

When combined with comb sources, offset locked lasers can be positioned at any set frequency with Hz precision across the comb bandwidth. This enables higher spectral efficiency for dense wavelength division multiplexing systems (DWDM), allowing far greater channel density and frequency stability than with wavelength lockers. In another configuration, rather than keeping the offset frequency fixed, the tunable lasers can be swept across the comb lines for high-resolution light detection and ranging (LIDAR) functionality. To sweep between the multiple reference lines, the frequency of the SG-DBR OPLL is offset locked using an RF modulation signal from one comb line until it reaches the next. Upon reaching the adjacent comb line, the RF signal is reset and the OPLL locks to this new reference line allowing the sweep to continue until reaching the end of the comb span.

We have fabricated an integrated comb source with >2 THz bandwidth and <10 Hz frequency error between comb lines using an InGaAsP/InP quantum well (QW) based material platform. The comb is generated from a 30 GHz hybrid mode-locked laser with an intracavity gain flattening filter (GFF) based on an asymmetric Mach-Zehnder interferometer (MZI). The GFF provides the inverse spectral profile of the material gain, reducing gain competition between modes, and allowing more modes to lase simultaneously. This device is compatible with SG-DBR OPLLs, and provides the potential for single-chip integrated LIDAR systems with THz frequency sweeps. The resolution of a frequency modulator continuous-wave (FMCW) LIDAR system is roughly: $c / (2 \times \text{bandwidth}) \approx 75 \mu\text{m}$ (e.g. the topography on the face of a penny), for a 2 THz comb span.

2. Design and fabrication

A ring mode-locked laser architecture is chosen due to its ease of integration with other components, e.g. SG-DBR OPLLs, to realize highly versatile photonic integrated circuits (PICs). Such rings and their couplers are defined using low-cost and high throughput i-line photolithography, allowing ring MLLs to be placed anywhere on the PIC without the need for more complicated processing.

A ring MLL with a GFF is designed and fabricated on an InGaAsP/InP offset quantum well (OQW) platform that consists of seven compressively strained 6.5 nm QWs and eight tensile strained 8 nm barriers that are epitaxially grown above a 300 nm thick 1.3Q InGaAsP layer as part of the base epi. Passive areas are defined using a selective wet-etch and a single blanket regrowth is done to cover the device with 1.8 μm p+-doped InP cladding, a 150 nm p++-doped InGaAs contact layer, and a 400 nm InP capping layer to protect the InGaAs contact layer during device fabrication. The active material is used to define the semiconductor optical amplifiers (SOAs) and the saturable absorber (SA), whereas the passive material is used to define the low-loss waveguides and current injection based phase shifters, as shown in Fig. 1. The material structure and the fabrication steps are compatible with SG-DBR OPLLs, allowing both to be integrated monolithically without changes to the processing or device architecture.

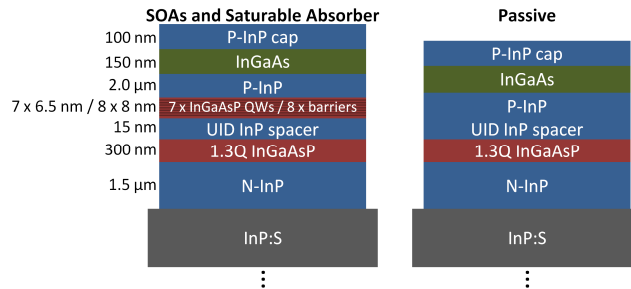


Fig. 1. Monolithic integration InGaAsP/InP platform that uses a 7 offset quantum well (QW) material layer structure. Active sections (left) are used for the semiconductor optical amplifier (SOA) and the saturable absorber. The passive sections (right) are used for low-loss waveguides and phase tuning regions.

After regrowth, the waveguide is defined with photoresist on a Cr/SiO₂ bilayer hard mask. The Cr is etched using a low power Cl₂-based inductively coupled plasma (ICP), and the SiO₂ is etched using an SF₆/Ar based ICP. The resulting 600 nm SiO₂ mask acts as a hard-mask to define the InGaAsP/InP deeply etched waveguides using a Cl₂/H₂/Ar (9/18/2 sccm) ICP and a 200°C heated chuck at a chamber pressure of 1.5 mT. The resulting etched features are shown in Fig. 2(a)-(c). After removing the SiO₂ mask, blanket deposition of a 350 nm isolation layer of silicon nitride is performed. Vias are opened for topside p-metal contacts. N-metal contacts are realized through backside deposition of Ti/Pt/Au onto the n-doped conducting InP substrate.

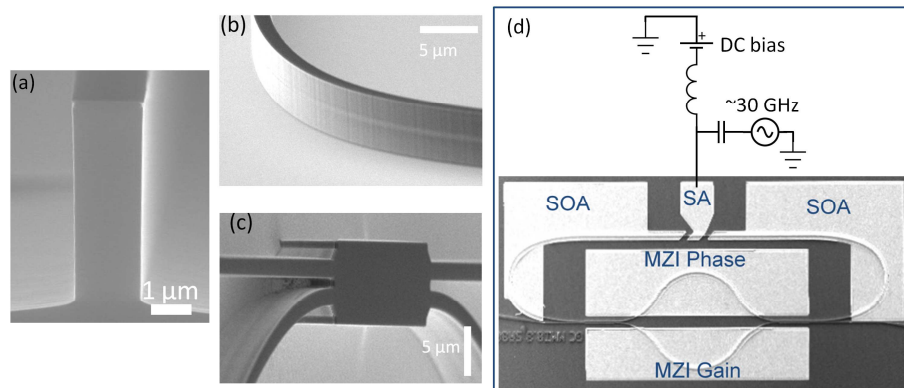


Fig. 2. Scanning electron microscope (SEM) images of the etched waveguide showing: (a) 5 μm deep etch with vertical sidewalls, (b) waveguide bends with smooth sidewalls, and (c) multimode interference (MMI) couplers. (d) A hybrid mode-locking schematic for the GFF MLL, showing an SEM image of the device with a DC biased and 30 GHz RF modulated saturable absorber (SA). The MZI gain arm allows tuning of the extinction ratio, while the phase arm allows placement of the filter zero.

The fully fabricated GFF MLL PIC, shown in Fig. 2(d), has a round-trip cavity length of 2600 μm, corresponding to lasing lines spaced by 29.5 GHz. The 600 μm asymmetric MZI filter uses 3 dB, i.e., 50-50, multi-mode interference (MMI) couplers to form two arms, which differ in length by 16 μm providing a free-spectral-range (FSR) of 40 nm. One of the arms of the MZI filter has an SOA that can be used to control the extinction ratio (ER) of the GFF, whereas the other arm has a phase shifter allowing adjustment of the filter zero.

3. Comb Generation

The device is biased at 210 mA drive current (~3x laser threshold), -2.6 V bias on the saturable absorber; the MZI filter is biased at 35 mA into the active filter arm to set the extinction ratio, and 17 mA into the passive phase tuning arm to set the filter zero. The RF beat tone under passive mode-locking is shown in Fig. 3(a) with a -20dB linewidth around 20 MHz and the peak at -75 dBm measured on the electrical spectrum analyzer (ESA) with a high-speed photodiode. A 15 dBm RF drive tone was applied to the saturable absorber, as shown in Fig. 2(d), to provide hybrid mode-locking (HML) and the resulting RF beat tone after HML is shown in Fig. 3(b). With HML, the RF linewidth FWHM is below the minimum resolution of the ESA (<10 Hz), and the noise pedestal at -75 dBm during passive mode-locking, has been decreased by 20 dB. The resulting RF tone is 35 dB above the background passively mode-

locked pedestal and >50 dB above the background noise.

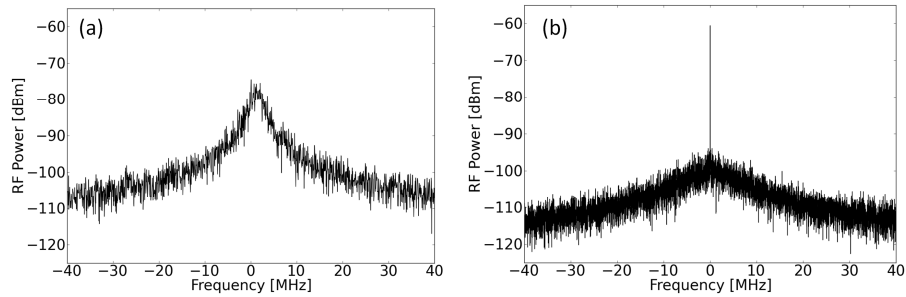


Figure 3: Normalized RF beat tones centered at 29.5 GHz from the GFF MLL under (a) passive mode-locking i.e. only a DC bias of -2.6V, and (b) under hybrid mode-locking with a 15 dBm RF signal applied. (RBW = 30 KHz).

The RF linewidth corresponds to the frequency error between adjacent lasing lines in the comb spectrum. By reducing the RF linewidth with HML, we are able to set the reference comb line spacing with a precise frequency and better than 10 Hz accuracy (as determined by the RF source). By using the HML configuration, the frequency error between comb lines is stabilized and immune to minor thermal or mechanical drift. The 2 THz comb span shown in Fig. 4 was taken after HML was achieved, indicating that HML does not limit broadband comb generation with this device. These results demonstrate that the frequency spacing between lasing lines can be stabilized on GFF MLLs, while maintaining >2 THz comb spans.

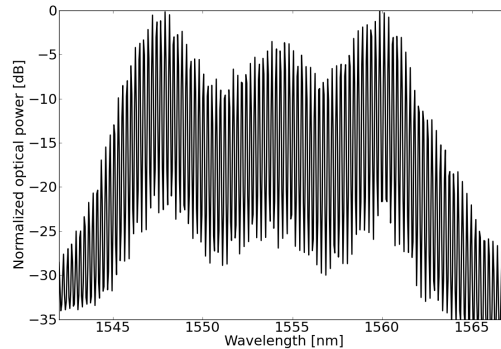


Figure 4: Optical spectrum from the GFF MLL under active mode-locking. The -10 dB span is 2.06 THz covering 70 lasing lines.

5. Conclusion

We have demonstrated a broadband 2 THz comb generator that can be integrated with SG-DBR OPLLs and enable single-chip high resolution LIDAR systems. The comb generated has <10 Hz error between comb lines and is a promising frequency reference to use in sweeping offset locked lasers.

Acknowledgements

This work was supported by the DARPA PICO program. A portion of the work was done in the UCSB nanofabrication facility, part of the NSF funded NNIN network.

References

- [1] S. Bennett, B. Cai, E. Burr, O. Gough, A.J. Seeds, "1.8-THz bandwidth, zero-frequency error, tunable optical comb generator for DWDM applications," *IEEE Photonics Technology Letters*, vol. 11, no. 5, pp. 551-553, May 1999.
- [2] N. Dupuis, C.R. Doerr, L. Zhang, L. Chen, N.J. Sauer, L.L. Buhl, D. Ahn, "InP-based comb generator for optical OFDM," *Optical Fiber Communication Conference and Exposition (OFC/NFOEC)*, March 6-10, 2011, paper PDPC8.
- [3] S.A. Diddams, D.J. Jones, J. Ye, S.T. Cundiff, J.L. Hall, J.K. Ranka, R.S. Windeler, "Direct RF to optical frequency measurements with a femtosecond laser comb," *IEEE Transactions on Instrumentation and Measurement*, vol. 50, no. 2, pp. 552-555, 2001.
- [4] S. Ristic, A. Bhardwaj, M.J. Rodwell, L.A. Coldren, and L.A. Johansson, "An optical phase-locked loop photonic integrated circuit," *J. Lightwave Technol.*, vol. 28, no. 4, pp. 526-538, Feb. 15, 2010.
- [5] L. Ponnampalam et al., "Monolithically Integrated Photonic Heterodyne System," *J. Lightwave Technol.*, vol. 29, no. 15, pp. 2229-2234, Aug. 1, 2011.

Frequency Tuning in Integrated InGaAsP/InP Ring Mode-Locked Lasers

John S. Parker, Pietro R. A. Binetti, Yung-Jr Hung, and Larry A. Coldren, *Fellow, IEEE*

Abstract—We demonstrate for the first time, continuous frequency tuning >40 MHz using symmetric phase tuning regions in an InGaAsP/InP 18 GHz passively mode-locked ring laser. Frequency tuning is achieved through current injection into passive waveguides, via the free-carrier plasma effect, which is enhanced by the concurrent increase in cavity losses from free-carrier absorption. Stable mode-locking with ~ 1 ps pulse-width is realized from -2.5 to -7.5 V bias on the saturable absorber and 170 to 290 mA drive current. The average RF power is 50 dB above the noise level over this regime.

Index Terms—Mode-locked laser, pulsed lasers, quantum well laser, ring laser, semiconductor laser.

I. INTRODUCTION

InGaAsP/InP mode-locked lasers (MLLs) operating at 1.55 μm wavelength are very stable pulsed sources, which makes them attractive components for high-speed optical fiber communication with optical-time-division-multiplexing (OTDM) [1], multi-wavelength sources for wavelength-division-multiplexing (WDM) [2], low-noise microwave oscillators [3], clock distribution systems [4], as well as for various applications in biological imaging [5]. MLLs built on a highly versatile InGaAsP/InP material platform provide the capability to create monolithically integrated systems-on-chip when combined with components that include: widely-tunable transmitters [6], balanced receivers [7], tunable optical filters [8], wavelength converters [9], and pulse-shapers [10]. New applications in microwave photonics may benefit from integrated mode-locked lasers used for high-frequency stable on-chip RF sources, such as the recently demonstrated integrated Optical Phase-Lock-Loop (OPLL) built on the InGaAsP/InP material platform [11].

Considerable work has been done in mode-locked laser cavity designs on InP including: Fabry–Perot (FP) [12], Distributed-Bragg-Reflector (DBR) [13], and ring resonator [14]. The ring

MLL has an advantage in that it can be defined entirely by photolithography without the need for electron beam lithography or holography to create DBR gratings, and it avoids repetition rate errors from cleaving, common on FP and DBR designs. Cleaving errors for conventional systems are at best $\pm 5 \mu\text{m}$, corresponding to ± 50 MHz on a 20 GHz DBR laser [15]. Such errors can be reduced by dry-etching the facets [16], however drawbacks do arise. Furthermore, the repetition rate on DBRs is determined by the effective penetration depth into the mirror sections, which is highly dependent on the grating etch depth, adding a further degree of repetition rate variation in processing.

For ring MLL, the repetition rate can be set entirely by optical lithography with better than 1 μm accuracy, i.e., 5 MHz repetition rate accuracy for a 20 GHz InGaAsP/InP MLL. Even greater precision is often necessary for optical communication and clocking applications. The drive current of the laser and the bias on the saturable absorber can be used to shift the repetition rate of the laser, however it is advantageous to fix these operating parameters at the most optimal mode-locking condition, e.g., lowest jitter, highest RF power, or narrowest pulse-width. Integrated hybrid or active mode-locking offers one solution, where by applying an RF drive signal on the saturable absorber an external microwave source determines the repetition rate. The RF drive signal must within the locking bandwidth and closely matched to a multiple of the cavity length for efficient power coupling from the RF source [15]. For this reason, tuning the cavity length to match the desired repetition rate is desirable for both hybrid and passive mode-locking.

Phase tuning pads alter the effective refractive index of the material, provide precise phase engineering of the passive ring length, and allow continuous tuning of the repetition rate. The effect is enhanced by increased cavity losses due to free-carrier absorption, which occurs from current injection in the passive sections. The phenomenon has been studied extensively to achieve frequency tuning in DBR MLL [15], [17], [18], and tuning as much as 400 MHz at a 40 GHz repetition rate has been demonstrated [17]. To our knowledge this is the first integrated ring MLL with phase pads, which has the advantage of avoiding gratings allowing for easier, less expensive processing, and the capability to determine the repetition rate entirely by lithography.

II. FABRICATION

A standard offset quantum well (QW) InGaAsP/InP integrated platform is used with 7 QWs positioned above a 300 nm tall 1.3 Q waveguide with a modal confinement factor of 7.1% [19]. A wet-etch removes the QWs for low loss passive waveguides followed by a single blanket 1.8 μm p+ InP cladding

Manuscript received October 27, 2011; revised January 07, 2012; accepted January 11, 2012. Date of publication January 13, 2012; date of current version April 04, 2012. This work was supported by the Defense Advanced Research Project Agency (DARPA) Photonic Integrated for Coherent Optics (PICO) program. A portion of this work was done in the UCSB nanofabrication facility, part of the National Science Foundation (NSF)-funded NNIN network.

J. S. Parker, P. R. A. Binetti, and L. A. Coldren are with the Department of Electrical and Computer Engineering, University of California, Santa Barbara, CA 93106 USA (e-mail: JParker@ece.uscb.edu).

Y.-J. Hung is with the Department of Electronic Engineering, National Taiwan University of Science and Technology, Taipei 106, Taiwan.

Color versions of one or more of the figures in this paper are available online at <http://ieeexplore.ieee.org>.

Digital Object Identifier 10.1109/JLT.2012.2184264

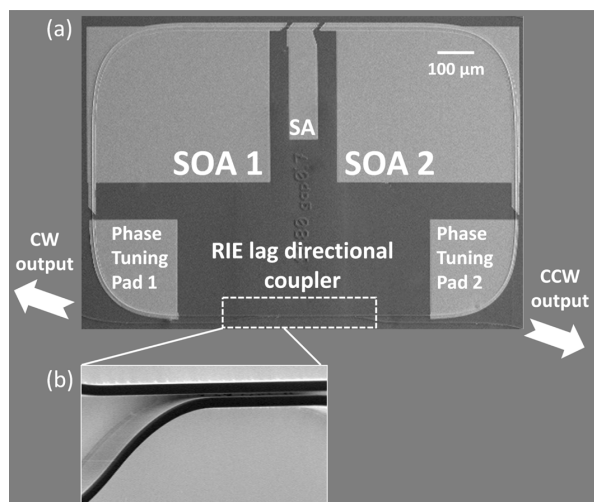


Fig. 1. (a) Scanning electron microscope (SEM) image of fabricated ring mode-locked laser with semiconductor optical amplifiers (SOAs), saturable absorber (SA), phase tuning pads, and directional coupler. (b) SEM side-view of two waveguides coming together to form the directional coupler.

regrowth, a 150 nm p++ InGaAs contact layer, and a 400 nm p+ InP protective cap. Waveguides are defined by stepper lithography on a photoresist/Cr/SiO₂ three-layer mask. The Cr is etched using a Cl₂/O₂ (23.3/6.8 sccm) inductively coupled plasma (ICP) reactive-ion etch (RIE) with 50 W ICP and 15 W bias power at 10 mT chamber pressure. The SiO₂ mask is etched with a SF₆/Ar (50/10 sccm) based ICP RIE using 600 W ICP and 50 W bias power at 7.5 mT. The SiO₂ is used to mask the InGaAsP/InP in Cl₂/H₂/Ar (9/18/2 sccm) ICP RIE with 850 W ICP power and 125 W bias power at 1.5 mT.

The RIE lag effect [20], which acts to slow the etch rate of smaller features, is used to define a 300 μm long directional coupler on a deeply etched 4400 μm ring with a single etch-step as shown in Fig. 1. Each of the two phase tuning pads are 500 μm long, the saturable absorber (SA) is 80 μm, and the two semiconductor optical amplifiers (SOAs) are 1200 μm. The remainder of the ring is passive waveguide. The waveguide width is 1.8 μm.

The directional coupler is chosen to minimize unwanted back-reflections in the ring structure, which would perturb stable MLL operation. The directional coupler has an etch depth of ~2.5 μm (150 nm etch into the waveguide layer at the center, and 175 nm etch into the waveguide layer at the edge), whereas the etch depth of the deeply etched waveguides is 3.61 μm (below the waveguide layer by 960 nm), as shown in Fig. 2. A deeply etched directional coupler needs an extremely narrow gap <300 nm to have appreciable coupling. This typically requires more complicated Electron-Beam-Lithography (EBL), while the severe RIE lag effect, due to reduced etch rates in high aspect-ratio features, necessitates long etch times. This high aspect-ratio etch is difficult to make vertical and smooth, which increases scattering losses.

We overcome these issues by adopting the single-etch process, which uses the RIE lag to our advantage and allows more streamlined processing of directional couplers

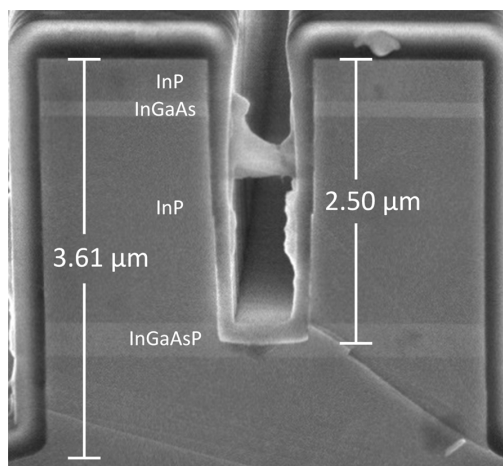


Fig. 2. SEM cross section of RIE lag directional coupler. The center etch depth is 150 nm into the waveguide layer. The outer etch depth is 960 nm below the waveguide layer.

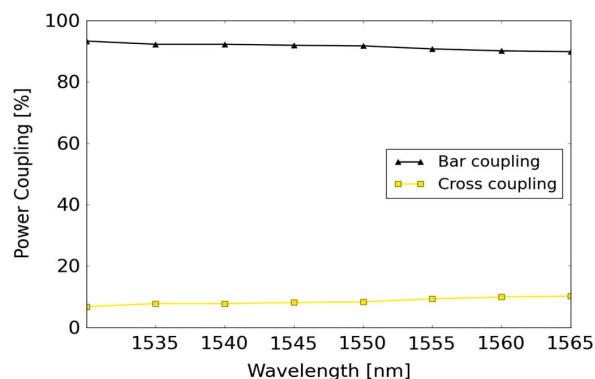


Fig. 3. Measured wavelength dependence of RIE lag directional coupler.

without the need for a separate surface ridge waveguide defined by wet-etching and deeply etched waveguide defined by dry-etching. The etch depth is controlled by timing the etch rate and measuring SEM cross-sections on a test sample. The 700 nm wide 300 μm long directional coupler has cross coupling of ~10% at 1550 nm, as shown in Fig. 3. This is measured by fiber coupling a tunable laser into the access waveguide of the directional coupler. To act as on-chip photodetectors, two 300 μm SOAs are placed symmetrically on the coupler output ports and reverse biased at -3 V. These couplers measure the incident optical power as the tunable laser is swept from 1530 to 1565 nm.

The directional coupler is simulated using RSoft BeamProp software as shown in Fig. 4. The results match well; the measured data falls between the simulated 125 and 150 nm etch depth curves. The simulation provides further insight into the tolerance of the device with etch depth, as shown in Fig. 5. For a fixed length, the cross-coupling is highly dependent on the etch depth and 300 μm length couplers can be fabricated with 1% to 80% power coupling. Fabrication tolerance is increased

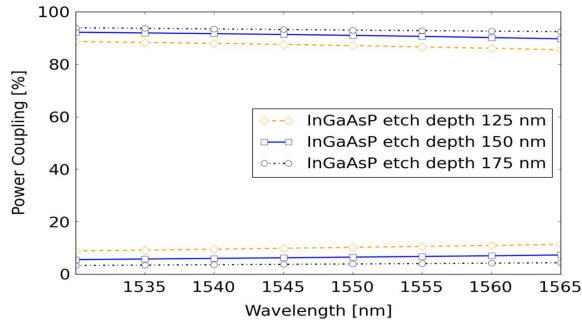


Fig. 4. Simulated wavelength dependence of RIE lag directional coupler.

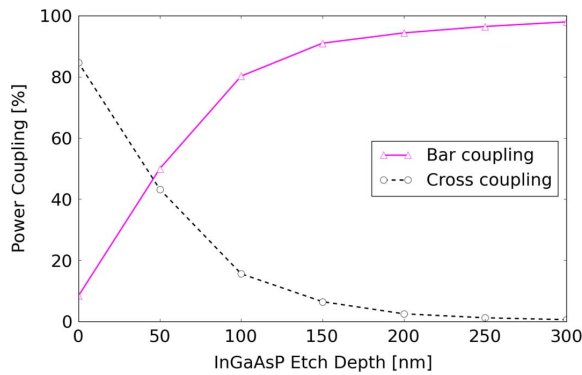


Fig. 5. Simulated etch depth dependence of RIE lag directional coupler.

by designing the lag coupler for deeper etch depths, where the slope of the coupling function changes more slowly.

After waveguide definition, the ridges are covered with 350 nm of SiN_x and vias are opened for P-type Pt/Ti/Pt/Au contacts. The backside substrate of the semiconductor is lapped to 110 μm thickness and N-type Ti/Pt/Au contacts are deposited. The P-type contacts are electrically isolated from each other using a proton implant, which provides 20 k Ω resistance between contacts spaced 10 μm apart.

III. MODE-LOCKING

Mode-locked lasers are soldered to copper blocks, placed on a thermo-electric cooler, and tested at 15°C. Mode-locking is typically defined as a peak RF power 25 dB above the noise floor. For our measurements, we add the criterion that the RF peak power must also be 25 dB above any side-peaks or undesirable frequency spurs.

We measure lasing threshold at 80 mA and peak mode-locked lasing power of 1.2 mW in each direction from on-chip reverse biased SOA detectors; the on-chip detectors are biased at transparency for off-chip testing. Based on the 10% coupler, we calculate the average lasing power inside the ring to be ~ 12 mW. The device has long access waveguides ~ 1500 μm ending in 7° flared waveguides with AR coatings to minimize back reflections. Lensed fiber is used to capture the output power with a measured coupling loss of 5 dB. The measured peak power off-chip is 200 μW (-7 dBm).

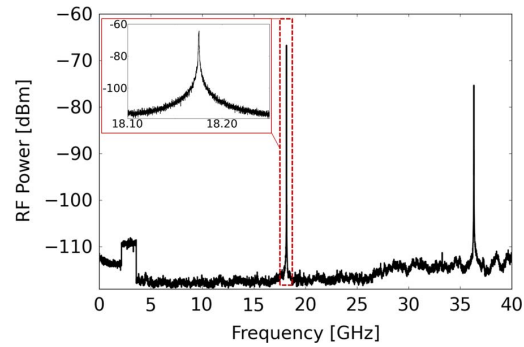


Fig. 6. Measured RF-spectrum $I_{\text{SOA}} = 210$ mA, $V_{\text{SA}} = -4.5$ V. The step discontinuity at 3 GHz is due to electronic amplifier.

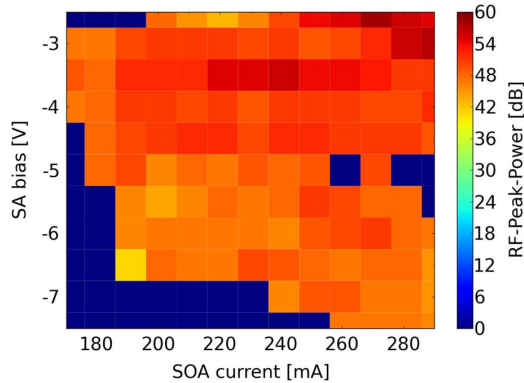


Fig. 7. RF peak power over the operating region. Average RF power is 50 dB above the noise. The blue regions of the color map are regions that did not meet the criterion for mode-locking.

SA and SOA settings are swept to map out the stable mode-locking regime. The sweeps are restricted to -2.5 to -7.5 V SA bias and 170–290 mA SOA drive current to focus on the central region of operation, in which more than 90% of the mode-locking regime occurs. The RF spectra of the fundamental and second harmonic from the ring MLL is shown in Fig. 6 from measurements on a Rohde Schwarz 50 GHz electrical spectrum analyzer (ESA) with a U² T 50 GHz photodiode. A 30 dB low noise amplifier is used to boost the RF signal, as the input power into the photodiode is quite low.

The raised plateau on the RF spectra at 3 GHz is due to distortion from the low noise amplifier and appears regardless of input signal. The RF peak power over the operating regime is shown in Fig. 7, and the -20 dB linewidth of the RF power in Fig. 8. The average -20 dB linewidth is 5.9 MHz, the minimum -20 dB linewidth is 1.5 MHz, and the average RF power is 50 dB.

The pulse-width variation is measured by an Inrad SHG autocorrelator (AC) and is shown in Fig. 9. Before the AC, the pulse-train is sent through a 30 dBm EDFA to provide enough optical power for clear autocorrelation traces. The signal-to-noise ratio (SNR) of these autocorrelation traces is as high as 13 dB, and most operating points are near this SNR; at the edges of the operating regime, the SNR decreases rapidly. The pulse-width map

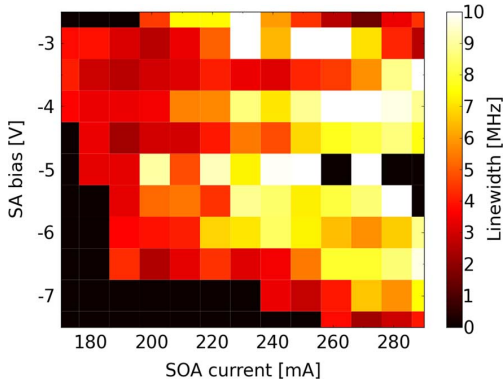


Fig. 8. RF –20 dB linewidth over the operating region. Average –20 dB linewidth is 5.9 MHz. The black regions of the color map are regions that did not meet the criterion for mode-locking. The white regions are mode-locked with a linewidth >10 MHz.

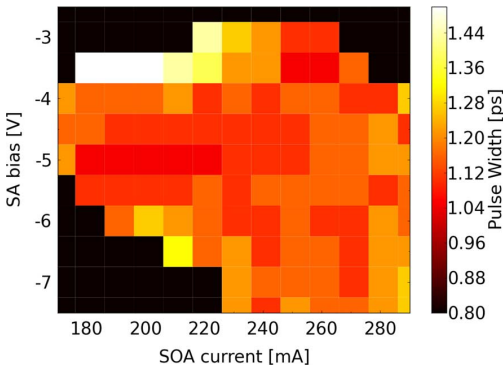


Fig. 9. Gaussian pulsewidth over the operating region. The black regions of the color map are regions that did not meet the criterion for mode-locking. The white regions are mode-locked with a pulse-width >1.5 ps.

is limited to autocorrelation traces with SNR > 6 dB, such that the amplitude at full-width-half-maximum (FWHM) is at least twice the noise level. At 3 dB SNR, the FWHM is obscured by the noise level; at 6 dB, the FWHM is significantly above the noise floor and allows clear measurements of the pulse-width. The cross-correlation is also measured to ensure that the pulses are indeed mode-locked.

For consistency, the pulse-widths are all measured assuming a Gaussian pulse shape. The Gaussian shape results in the widest FWHM after deconvolving the autocorrelation. However, the measured pulse shape does change over the operating regime and the Gaussian shape is not always the most accurate in fitting. In this case, the Gaussian shape provides a conservative upper limit on pulse-width (Lorentzian or hyperbolic secant fitting results in a narrower pulse-width). For example, the fit for a measured 1.1 ps Gaussian pulse is shown in Fig. 10, the hyperbolic secant has an $R^2 = 0.95$, whereas the Gaussian has an $R^2 = 0.90$.

The optical spectrum of the mode-locked laser is measured on the optical spectrum analyzer (OSA), as shown in Fig. 11 at –5 V reverse bias and 220 mA drive current, corresponding to a 1 ps pulse-width. The FWHM of the optical spectrum is 5.3 nm,

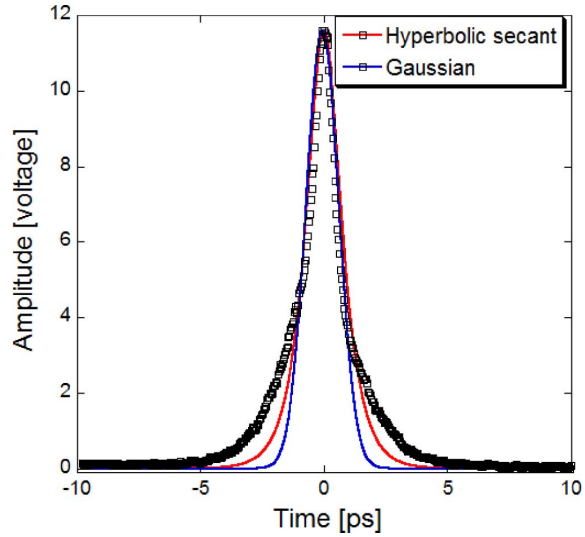


Fig. 10. Measured autocorrelation trace with hyperbolic secant and Gaussian curve fits, with R^2 values of 0.95 and 0.90, respectively. The operating conditions are 180 mA SOA current and –4 V reverse bias on the absorber.

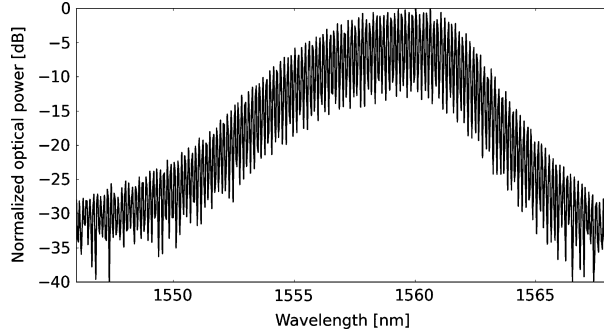


Fig. 11. Measured optical spectrum at 220 mA drive current and 5 V reverse bias on the saturable absorber. FWHM is 5.3 nm.

and the resulting time-bandwidth product is 0.66. The Gaussian time-bandwidth limit is 0.44. Hence, the output pulses from the MLL likely have a frequency chirp that is responsible for this deviation from the time-bandwidth limit.

There are some operating points that differ on the RF peak power and the pulse-width map, these measurements do not fit the criterion for RF tones >25 dB above side-spurs (on the RF map), and for autocorrelation traces with SNR >6 dB. These operating points might be acceptable for some applications, however this mode-locking is not ideal.

IV. FREQUENCY TUNING

Two 500 μm passive waveguide sections allow continuous frequency tuning of the fundamental mode-locked tone. By injecting carriers into the P-i-N junction in these regions, the carrier density is increased and the effective index of refraction of the material is decreased, due the free-carrier plasma effect. A lower effective index decreases the round-trip cavity flight-time and increases the repetition frequency. The total phase pad

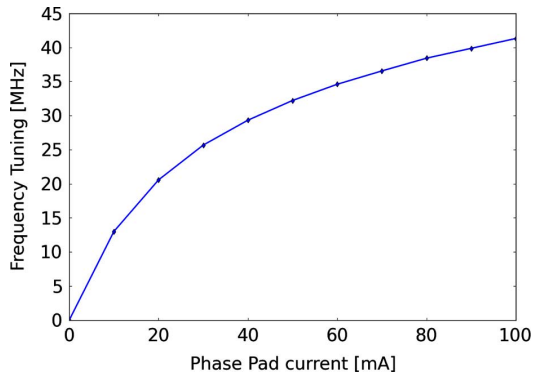


Fig. 12. Frequency tuning of the ring MLL by injecting current into both phase pads. The total phase pad length is $1000 \mu\text{m}$. Stable mode-locking is observed over the entire range of phase pad currents.

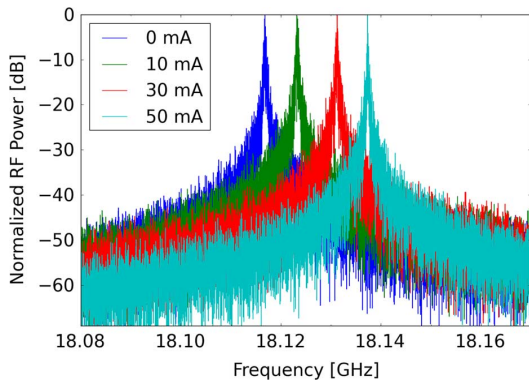


Fig. 13. RF spectra as the phase pad current in one pad is increased from 0 to 50 mA, and the frequency is tuned by ~ 20 MHz. Stable mode-locking occurs over the entire range of tuning currents.

length is $1000 \mu\text{m}$ or 22% of the total ring length. The frequency tuning is measured on the ESA for an SA bias of -4 V and an SOA drive current of 220 mA, as shown in Fig. 12. Mode-locking is maintained over the entire range of phase pad currents. The frequency shift of the RF spectra from a single phase pad is shown in Fig. 13.

The phase pads provide repetition rate frequency tuning of 41 MHz, for this $4400 \mu\text{m}$ cavity. To measure the refractive index shift of the phase pads, the ring is operated below lasing and the resonator comb shift is measured on an optical spectrum analyzer (OSA) with 0.06 nm resolution. From the OSA, phase tuning of $\sim 8\pi$ is measured, i.e., a change in the effective cavity length by $1.63 \mu\text{m}$ and an index shift in the phase pad sections of $5.3e-3$ (0.16%). Such an index shift, results in a change in the round-trip flight time by 0.037%. However, the repetition rate frequency tunes by 0.22%, due to an enhancement from the added loss of the phase pad as described in [17], [18]. This is a $\sim 6X$ enhancement factor (0.22%/0.037%) in repetition rate tuning due to the phase pad loss.

With the phase pads open, i.e., with a floating voltage, the propagation loss is 28 dB/cm. An intracavity method is used

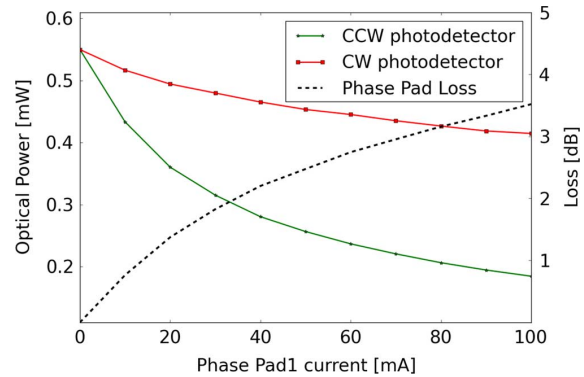


Fig. 14. Continuous-wave (not mode-locked) directional power tuning by asymmetrically biasing the phase pads. The plot shows output power in the clockwise (CW) and counter-clockwise (CCW) direction as a single phase pad is biased. The power is measured by on-chip photodetectors (not shown in Fig. 1).

to measure the added loss from tuning a single phase pad. In this measurement the SA in the MLL is forward biased at 2 V (i.e., the laser is free-running and not mode-locked) and the SOAs are driven at 120 mA to keep the ring just above lasing, thus preventing unidirectional operation as occurs under continuous-wave operation at high photon densities [21]. As shown in Fig. 14, at 0.55 mW output power both CW and CCW ports decrease as current to Phase Pad1 is increased. The phase pad loss is found from the difference between the two output directions. A phase change of π occurs at 3.5 mA phase pad current with an insertion loss of 0.6 dB.

This difference in output power shown in Fig. 14 is expected, and is well predicted by simple cavity geometry. Consider current applied to Phase Pad1, the CCW direction has the loss element before the output coupler, whereas the CW direction has the loss element after the output. In this case, both lasing directions have an equal increase in threshold gain due to the phase pad loss. However, the difference in output power between the two directions is entirely due to the single pass loss of the phase pad.

The common method to calculate the phase pad loss involves fiber coupling an off-chip laser into the structure, and using the ring SOAs in reverse bias as detectors to measure the change in optical transmission. Our measurements using this common method are in agreement, ~ 3 dB at 100 mA phase pad current, however fluctuations in coupled optical power due to vibrations and drift in the mechanical positioner are avoided using the intracavity method, reducing the uncertainty of the measurement.

A phase pad provides a tunable low-loss element inside the cavity, which can also be used to investigate the effects of carrier density in future mode-locking experiments. For lasers operating above lasing threshold, the carrier density clamps and is independent of drive current. Therefore, without changing the temperature, most lasers can only operate at a single specific current density. Since the phase pads add loss to the cavity, they can be used to precisely adjust the threshold gain and carrier density during lasing.

V. CONCLUSION

We have demonstrated the first integrated ring mode-locked laser with phase pads. The phase pads provide continuous frequency tuning of the repetition rate by >40 MHz. Ring mode-locked lasers with precise frequency tuning have applications in clocking and WDM data communication with tightly defined spacing for the frequency grid. We have presented a novel method using a ring laser to characterize the loss of the phase pads with high precision.

REFERENCES

- [1] V. Kaman and J. E. Bowers, "120 Gbit/s OTDM system using electroabsorption transmitter and demultiplexer operating at 30 GHz," *Electron. Lett.*, vol. 36, no. 17, pp. 1477–1479, 2000.
- [2] Y. B. M'Salleem, Q. T. Le, L. Bramerie, Q. Nguyen, E. Borgne, P. Besnard, A. Shen, F. Lelarge, S. LaRochelle, L. A. Rusch, and J. Simon, "Quantum-dash mode-locked laser as a source for 56-Gb/s DQPSK modulation in WDM multicast applications," *IEEE Photon. Technol. Lett.*, vol. 23, no. 7, pp. 453–455, Apr. 2011.
- [3] T. M. Ramond, A. Bartels, S. A. Diddams, L. Hollberg, and H. Kurz, "Low instability, low phase-noise femto-second optical frequency comb microwave synthesizer," in *Proc. IEEE Int. Freq. Control Symp. PDA Exhib. 17th Europ. Freq. Time Forum*, Tampa, FL, May 2003, pp. 168–171.
- [4] P. J. Delfyett, D. H. Hartman, and S. Z. Ahmad, "Optical clock distribution using a mode-locked semiconductor laser diode system," *J. Lightw. Technol.*, vol. 9, no. 12, pp. 1646–1649, Dec. 1991.
- [5] W. Drexler, "Ultrahigh-resolution optical coherence tomography," *J. Biomed. Opt.*, vol. 9, no. 1, pp. 47–74, 2004.
- [6] J. S. Barton, E. J. Skogen, M. L. Masanovic, S. P. Denbaars, and L. A. Coldren, "A widely tunable high-speed transmitter using an integrated SGDBR laser-semiconductor optical amplifier and Mach-Zehnder modulator," *IEEE J. Sel. Topics Quantum Electron.*, vol. 9, no. 5, pp. 1113–1117, Sep.-Oct. 2003.
- [7] J. Klamkin, A. Ramaswamy, L. A. Johansson, H.-F. Chou, M. N. Sysak, J. W. Raring, N. Parthasarathy, S. P. DenBaars, J. E. Bowers, and L. A. Coldren, "High output saturation and high-linearity uni-traveling-carrier waveguide photodiodes," *IEEE Photon. Technol. Lett.*, vol. 19, no. 3, pp. 149–151, Feb. 2007.
- [8] E. J. Norberg, R. S. Guzzon, S. C. Nicholes, J. S. Parker, and L. A. Coldren, "Programmable photonic lattice filters in InGaAsP/InP," *IEEE Photon. Technol. Lett.*, vol. 22, no. 2, pp. 109–111, Jan. 2010.
- [9] M. M. Dummer, M. N. Sysak, A. Tauke-Pedretti, J. W. Raring, J. Klamkin, and L. A. Coldren, "Widely tunable separate absorption and modulation wavelength converter with integrated microwave termination," *J. Lightw. Technol.*, vol. 26, no. 8, pp. 938–944, Aug. 2008.
- [10] M. J. R. Heck, P. Munoz, B. W. Tilma, E. A. J. M. Bente, Y. Barbarin, O. Yok-Siang, R. Notzel, and M. K. Smit, "Design, fabrication and characterization of an InP-based tunable integrated optical pulse shaper," *IEEE J. Quantum Electron.*, vol. 44, no. 4, pp. 370–377, Apr. 2008.
- [11] S. Ristic, A. Bhardwaj, M. J. Rodwell, L. A. Coldren, and L. A. Johansson, "An optical phase-locked loop photonic integrated circuit," *J. Lightw. Technol.*, vol. 28, no. 4, pp. 526–538, Feb. 2010.
- [12] M. J. R. Heck, A. Renault, E. A. J. M. Bente, O. Yok-Siang, M. K. Smit, K. S. E. Eikema, W. Ubachs, S. Anantathanasarn, and R. Notzel, "Passively mode-locked 4.6 and 10.5 GHz quantum dot laser diodes around $1.55 \mu\text{m}$ with large operating regime," *IEEE Sel. Topics Quantum Electron.*, vol. 15, no. 3, pp. 634–643, May–Jun. 2009.
- [13] I. Ogura, H. Kurita, T. Sasaki, and H. Yokoyama, "Precise operation-frequency control of monolithic mode-locked laser diodes for high-speed optical communication and all-optical signal processing," *Opt. Quantum Electron.*, vol. 33, pp. 709–725, 2001.
- [14] Y. Barbarin, E. A. J. M. Bente, M. J. R. Heck, Y. S. Oei, R. Nötzel, and M. K. Smit, "Characterization of a 15 GHz integrated bulk InGaAsP passive modelocked ring laser at $1.53 \mu\text{m}$," *Opt. Exp.*, vol. 14, no. 21, pp. 9716–9727, 2006.
- [15] R. Kaiser and B. Huttel, "Monolithic 40-GHz mode-locked MQW DBR lasers for high-speed optical communication systems," *IEEE J. Sel. Topics Quantum Electron.*, vol. 13, no. 1, pp. 125–135, Jan.–Feb. 2007.
- [16] J. S. Parker, E. J. Norberg, R. S. Guzzon, S. C. Nicholes, and L. A. Coldren, "High verticality InP/InGaAsP etching in Cl₂/H₂/Ar inductively coupled plasma for photonic integrated circuits," *J. Vac. Sci. Technol. B*, vol. 29, pp. 011016–011020, 2011.
- [17] H. F. Liu, S. A. Arahira, T. Kunii, and Y. Ogawa, "Tuning characteristics of monolithic passively mode-locked distributed Bragg reflector semiconductor lasers," *IEEE J. Quantum Electron.*, vol. 32, no. 11, pp. 1965–1975, Nov. 1996.
- [18] S. Arahira and Y. Ogawa, "Repetition-frequency tuning of monolithic passively mode-locked semiconductor lasers with integrated extended cavities," *IEEE J. Quantum Electron.*, vol. 33, no. 2, pp. 255–264, Feb. 1997.
- [19] L. A. Coldren, S. C. Nicholes, L. Johansson, S. Ristic, R. S. Guzzon, E. J. Norberg, and U. Krishnamachari, "High performance InP-based photonic ICs—A tutorial," *J. Lightw. Technol.*, vol. 29, no. 4, pp. 554–570, Feb. 2011.
- [20] Y. Shi, S. He, and S. Anand, "Ultracompact directional coupler realized in InP by utilizing feature size dependent etching," *Opt. Lett.*, vol. 33, no. 17, pp. 1927–1929, 2008.
- [21] M. Sorel, P. J. R. Laybourn, G. Giuliani, and S. Donati, "Unidirectional bistability in semiconductor waveguide ring lasers," *Appl. Phys. Lett.*, vol. 80, pp. 3051–3053, 2002.

Offset locking of an SG-DBR to an InGaAsP/InP mode-locked laser

John Parker¹, Mingzhi Lu¹, Hyunchul Park¹, Eli Bloch², Abirami Sivananthan¹, Zach Griffith³, Leif A. Johansson¹, member, IEEE, Mark J. Rodwell¹, Fellow, IEEE, and Larry A. Coldren¹, Fellow, IEEE

¹Department of Electrical and Computer Engineering, University of California, Santa Barbara, CA, 93106, USA.

²Department of Electrical Engineering, Technion – Israel Institute of Technology, Haifa 32000, Israel.

³Teledyne Scientific and Imaging Company, Thousand Oaks, 1049 Camino Dos Rios, CA, 91360, USA
Email: jparker@ece.ucsb.edu

Abstract—We demonstrate a Sampled Grating-Distributed Bragg Reflector (SG-DBR) laser offset locked at 6.5 GHz from a diode mode-locked laser comb using an integrated optical phase-locked loop (OPLL).

Keywords—coherent; optical frequency synthesis; optical phase-locked loop; wavelength stabilization.

Recently, highly-integrated optical phase-locked loops (OPLLs) have been demonstrated with 200-300 MHz loop bandwidths [1,2]. These OPLLs allow a tunable slave laser to clone the phase noise of any reference laser within their operating bandwidth. By offset locking an OPLL laser to a stable optical frequency comb, new applications emerge including: digitally synthesized optical frequency sweeps [3] for LIDAR, and THz frequency generation on an optical carrier [4].

In previous work, researchers have used OPLLs to lock two DBR lasers to an optical frequency comb, generating a high spectral purity 300 GHz tone [4]. This comb was generated using phase modulators and a narrow linewidth laser, yet the comb bandwidth was limited to 300 GHz. For many applications broader comb generation is needed, and integration with the OPLL laser improves stability and provides a more compact system. Frequency modulated (FM) InGaAsP/InP lasers have been used for comb generation >1 THz and as references for optical phase-locked loops, however the FM lasers typically suffer from nonuniform spectral power making frequency sweeps difficult [5]. Mode-locked lasers (MLLs) are another promising source for broadband comb generation, and flat bandwidths over 2 THz from a 30 GHz repetition rate monolithically integrated device have been demonstrated, as shown in Fig. 1 [6]. For this reason, many researchers are interested in combining broadband MLLs with OPLLs [4]. Towards this aim, we demonstrate the first offset locking of an SG-DBR laser to a diode MLL on an InGaAsP/InP platform.

For this demonstration, we use a MLL with a smaller repetition rate (18 GHz) and a much narrower spectral bandwidth than shown in Fig. 1. This choice of references allows us to observe the beat frequency between the locked OPLL laser and adjacent comb lines. The mode-locked laser is a ring cavity with length 4400 μm and more details of the fabrication and testing of this laser are described in [7]. Both SG-DBR and MLL are unpackaged and placed on separate

carriers and thermo-electric coolers. The MLL is operated at 106 mA drive current to the semiconductor optical amplifiers (SOAs) and -2 V reverse bias on the saturable absorber (SA).

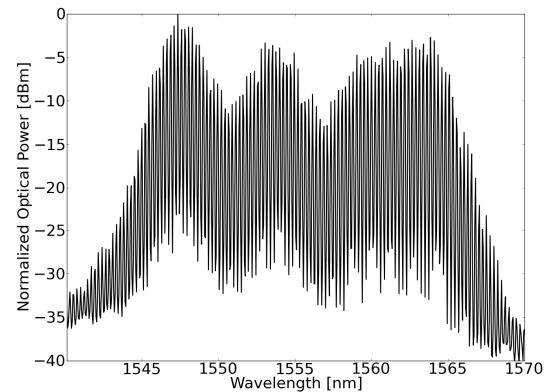


Fig. 1. Optical spectrum of a previously demonstrated InGaAsP/InP 30 GHz repetition rate MLL operating at 250mA drive current and -2.6 V reverse bias on the saturable absorber. Comb extends from 1545 to 1565nm.

The output from the MLL is captured with a lensed fiber and goes through an erbium doped fiber amplifier (EDFA), a 300 GHz optical band-pass filter to reduce the ASE noise from the EDFA, and into the SG-DBR OPLL photonic integrated circuit (PIC), shown in Fig. 2. In the OPLL PIC, the SG-DBR and MLL inputs are mixed using a star-coupler based 90 degree hybrid and detected. The electrical outputs from the detectors are wire-bonded to an EIC, mounted adjacent. The details about the EIC are discussed elsewhere [8]. The EIC feedback signal goes through an active loop filter and back to the phase modulator pad on the SG-DBR.

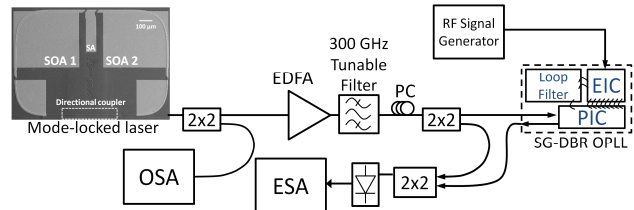


Fig. 2. Test set-up for offset locking the SG-DBR OPLL to the mode-locked laser. The MLL is shown in the top left. Semiconductor optical amplifier (SOA). Saturable absorber (SA). Erbium fiber doped amplifier (EDFA). Polarization controller (PC). Optical signal analyzer (OSA). Electrical spectrum analyzer (ESA).

The power requirement per optical line for stable offset locking is ~ 4 dBm in the fiber near 1550 nm operating wavelength. As the MLL output is only -10 dBm in the fiber and divided over several comb lines, the EDFA is necessary to provide adequate power levels. However, the ASE noise from the EDFA increases the DC photocurrent on the OPLL PIC and thereby reduces the AC saturation current, making correct operation of the EIC difficult. The tunable band pass filter removes this unwanted noise from the EDFA output. Monolithic integration of the SG-DBR and MLL on a single chip can avoid facet-to-fiber coupling losses and provide adequate power levels without the need for external gain.

To measure the OPLL tone, the output from the SG-DBR is mixed with the MLL in a 2x2 coupler, detected, and measured on an electrical signal analyzer (ESA), as shown in Fig. 3. Offset locking of the SG-DBR is demonstrated at exactly 6.5 GHz and remains locked for the duration of the test (>10 mins). The free-running MLL has a broad optical linewidth >100 MHz, which extends beyond the bandwidth of the loop filter below its peak amplitude. The -20 dB OPLL beat linewidth is ~ 800 kHz, and a significant widening in the noise pedestal is observed at 25 dB below the OPLL peak. There is a fiber length mismatch of 10m between the reference and OPLL laser paths, which is responsible for the interference fringes at ± 20 and ± 40 MHz from 6.5 GHz. Thus, the PIC laser is delayed 50 ns relative to the reference signal before mixing, and the reference laser frequency noise broadens the observed beat signal. Therefore, the actual beat linewidth is likely better than we observe. In future work, matched paths will be used.

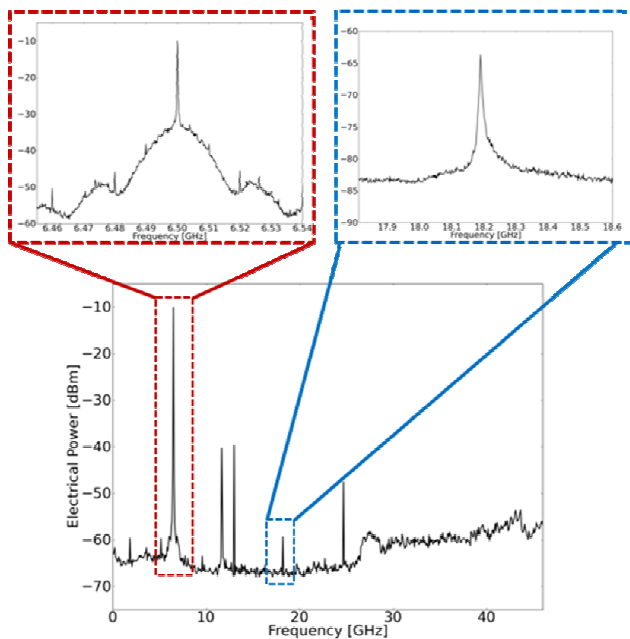


Fig. 3. Frequency spectrum of SG-DBR beating with the MLL measured on an electrical spectrum analyzer (RBW 50 kHz). The offset locking frequency is 6.5 GHz (upper left window, RBW 50 kHz), the second harmonic of it is visible at 13 GHz. The frequency beating between the SG-DBR OPLL and adjacent comb lines is visible at 11.69 GHz and 24.69 GHz. The mode-locked tone is shown at 18.19 GHz (upper right window, RBW 100 kHz).

The second harmonic of the OPLL beat tone is measured at exactly 13 GHz. The MLL beat tone is observed at 18.19 GHz. However, it is only 20 dB above the noise floor due to the optical filter which reduces the amplitude of the other comb lines. The beat tone between the adjacent comb lines and the SG-DBR are shown at 11.69 and 24.69 GHz (i.e. 18.19 ± 6.5 GHz). The -20 dB linewidth of these two beat tones are both 57 MHz, which is roughly the same -20 dB linewidth as the mode-locked tone at 18.19 GHz. This is expected, since MLL comb lines are nearly phase-locked (to the extent of the MLL beat tone shown at 18.19 GHz) and the OPLL is phase-locked to the central comb line, hence the OPLL is nearly phase-locked to the adjacent comb lines (to the extent of the MLL beat tone shown). To confirm that the mode-locked tone at 18.19 GHz is not an artifact of the OPLL, all beat tones (6.5, 11.69, 13, 24.69 GHz) except the MLL tone at 18.19 GHz vanish with the removal of the SG-DBR signal into the ESA.

The first demonstration of offset locking to a diode mode-locked laser has been demonstrated and preliminary results are shown. Improvements to optical linewidth and the stability of the diode mode-locked laser will greatly enhance the locking performance, and in future work both lasers can be monolithically integrated without significant change to the fabrication of the OPLL PIC.

Acknowledgment:

This work was supported by the Defense Advanced Research Project Agency (DARPA) Photonic Integration for Coherent Optics (PICO) program. A portion of this work was done in the UCSB nanofabrication facility, part of the National Science Foundation (NSF) funded NNIN network.

References:

- [1] M. Lu, H. Park, E. Bloch, A. Sivanathan, A. Bhardwaj, Z. Griffith, L. A. Johansson, M.J. Rodwell, L.A. Coldren, "Highly integrated optical heterodyne phase-locked loop with phase/frequency detection," *Opt. Express* **20**, 9736-9741 (2012).
- [2] S. Ristic, A. Bhardwaj, M.J. Rodwell, L.A. Coldren, and L.A. Johansson, "An Optical Phase-Locked Loop Photonic Integrated Circuit," *J. Lightw. Technol.* **28**, 526-538 (2010).
- [3] J. Jost, J. Hall, J. Ye, "Continuously tunable, precise, single frequency optical signal generator," *Opt. Express* **10**, 515-520 (2002).
- [4] R.J. Steed, L. Ponnampalam, M.J. Fice, C.C. Renaud, D.C. Rogers, D.G. Moodie, G.D. Maxwell, I.F. Lealman, M.J. Robertson, L. Pavlovic, L. Naglic, M. Vidmar, A.J. Seeds, "Hybrid Integrated Optical Phase-Lock Loops for Photonic Terahertz Sources," *Sel. Topics Quantum Electron.* **17**, 210-217 (2011).
- [5] C.C. Renaud, L. Ponnampalam, F. Pozzi, E. Rouvalis, D. Moodie, M. Robertson, A.J. Seeds, "Photonically enabled communication systems beyond 1000 GHz," in Proc. *Microwave photonics conference*, Gold Coast, Queensland, Australia, 55-58 (Sept. 9 - Oct. 3 2008).
- [6] J.S. Parker, A. Bhardwaj, P.R.A. Binetti, Y.-J. Hung, L.A. Coldren, "Monolithically Integrated Gain-Flattened Ring Mode-Locked Laser for Comb-Line Generation," *Photon. Technol. Lett.* **24**, 131-133 (2012).
- [7] J.S. Parker, P.R.A. Binetti, Y.-J. Hung, L.A. Coldren, "Frequency Tuning in Integrated InGaAsP/InP Ring Mode-Locked Lasers," *J. Lightw. Technol.* **30**, 1278-1283 (2012).
- [8] E. Bloch, H. Park, M. Lu, Thomas Reed, Zach Griffith, Leif Johansson, Larry Coldren, Dan Ritter, and Mark Rodwell, "A 1-20 GHz InP HBT phase-lock-loop IC for optical wavelength synthesis," Accepted by IEEE Int. Micro. Symposium (2012).

I. Photonic Integrated Circuits

C. Integrated Optical Phase-Locked Loops

Highly integrated optical heterodyne phase-locked loop with phase/frequency detection

Mingzhi Lu,^{1,*} Hyunchul Park,¹ Eli Bloch,² Abirami Sivananthan,¹
Ashish Bhardwaj,³ Zach Griffith,⁴ Leif A. Johansson,¹
Mark J. Rodwell,¹ and Larry A. Coldren^{1,5}

¹*ECE Department, University of California, Santa Barbara, California 93106, USA*

²*Department of Electrical Engineering, Technion-Israel Institute of Technology,
Haifa 32000, Israel*

³*Currently with JDSU Corporation, 80 Rose Orchard Way, San Jose, California 95134, USA*

⁴*Teledyne Scientific and Imaging Company, 1049 Camino Dos Rios, Thousand Oaks,
California 91360, USA*

⁵*Material Department, University of California, Santa Barbara, California 93106, USA*

[*mlu@ece.ucsb.edu](mailto:mlu@ece.ucsb.edu)

Abstract: A highly-integrated optical phase-locked loop with a phase/frequency detector and a single-sideband mixer (SSBM) has been proposed and demonstrated for the first time. A photonic integrated circuit (PIC) has been designed, fabricated and tested, together with an electronic IC (EIC). The PIC integrates a widely-tunable sampled-grating distributed-Bragg-reflector laser, an optical 90 degree hybrid and four high-speed photodetectors on the InGaAsP/InP platform. The EIC adds a single-sideband mixer, and a digital phase/frequency detector, to provide single-sideband heterodyne locking from -9 GHz to 7.5 GHz. The loop bandwidth is 400 MHz.

© 2012 Optical Society of America

OCIS codes: (250.5300) Photonic integrated circuits; (060.2840) Heterodyne; (060.1660) Coherent communications; (250.0250) Optoelectronic.

References and links

1. L. Enloe and J. Rodda, "Phase-locked loop," *Proc. IEEE* **53**, 165–166 (1965).
2. U. Gliese, T. N. Nielsen, M. Bruun, E. L. Christensen, K. E. Stubkjr, S. Lindgren, and B. Broberg, "A wideband heterodyne optical phase-locked loop for generation of 3-18 GHz microwave carriers," *IEEE Photon. Technol. Lett.* **4**, 936–938 (1992).
3. S. Ristic, A. Bhardwaj, M. Rodwell, L. Coldren, and L. Johansson, "An optical phase-locked loop photonic integrated circuit," *J. Lightwave Technol.* **28**, 526–538 (2010).
4. L. Ponnampalam, R. Steed, M. Fice, C. Renaud C. Rogers, D. Moodie, Maxwell, I. Lealman, M. Robertson, L. Pavlovic, L. Naglic, M. Vidmar, and A. Seeds, "A compact tunable coherent terahertz source based on an hybrid integrated optical phase-lock loop," 2010 IEEE Topical Meeting on Microwave Photonics (MWP), 151–154 (2010).
5. M. Fice, A. Chiuchiarelli, E. Ciamella, and A. Seeds, "Homodyne coherent optical receiver using an optical injection phase-lock loop," *J. Lightwave Technol.* **29**, 1152–1164 (2011).
6. L. Langley, M. Elkin, C. Edge, M. Wale, U. Gliese, X. Huang, and A. Seeds, "Packaged semiconductor laser optical phase-locked loop (OPLL) for photonic generation, processing and transmission of microwave signals," *IEEE Trans. Microw. Theory Tech.* **47**, 1257–1264 (1999).
7. A. Bhardwaj, Y. Li, R. Wang, S. Jin, P. Herczfeld, J. Bowers, and L. Coldren, "Monolithic integration of high linearity attenuated counter-propagating optical phase-locked loop coherent receiver," *Electron. Lett.* **47**, 1090–1092 (2011).

8. P. Binetti, M. Lu, E. Norberg, R. Guzzon, J. Parker, A. Sivananthan, A. Bhardwaj, L. Johansson, M. Rodwell, and L. Coldren, "Indium phosphide photonic integrated circuits for coherent optical links," *IEEE J. Quantum Electron.* **48**, 279–291 (2012).
9. N. Satyan, A. Vasilyev, G. Rakuljic, V. Leyva, and A. Yariv, "Precise control of broadband frequency chirps using optoelectronic feedback," *Opt. Express* **17**, 15991–15999 (2009).
10. M. Lu, A. Bhardwaj, A. Sivananthan, L. Johansson, H. Park, E. Bloch, M. Rodwell, and L. Coldren, "Widely-tunable integrated coherent optical receiver using a phase-locked loop," *IEEE Photonics Conf.*, Arlington, VA, ThL4 (2011).
11. N. Satyan, W. Liang, and A. Yariv, "Coherence cloning using semiconductor laser optical phase-lock loops," *IEEE J. Quantum Electron.* **45**, 755–761 (2009).
12. N. Satyan, W. Liang, A. Kewitsch, G. Rakuljic, and A. Yariv, "Coherent power combination of semiconductor lasers using optical phase lock loops," *IEEE J. Sel. Top. Quantum Electron.* **15**, 240–247 (2009).
13. R. Steed, F. Pozzi, M. Fice, C. Renaud, D. Rogers, I. Lealman, D. Moodie, P. Cannard, C. Lynch, L. Johnston, M. Robertson, R. Cronin, L. Pavlovic, L. Naglic, M. Vidmar, and A. Seeds, "Monolithically integrated heterodyne optical phase-lock loop with RF XOR phase detector," *Opt. Express* **19**, 20048–20053 (2011).
14. E. Bloch, H. Park, M. Lu, T. Reed, Z. Griffith, L. Johansson, L. Coldren, D. Ritter, and M. Rodwell, "A 1-20 GHz InP HBT phase-lock-loop IC for optical wavelength synthesis," Accepted by *IEEE Int. Micro. Symposium* (2012).
15. L. Coldren, "Monolithic tunable diode lasers," *IEEE J. Sel. Top. Quantum Electron.* **6**, 988–999 (2000).
16. C. Doerr, D. Gill, A. Gnauck, L. Buhl, P. Winzer, M. Cappuzzo, A. Wong-Foy, E. Chen, and L. Gomez, "Monolithic demodulator for 40-Gb/s DQPSK using a star coupler," *J. Lightwave Technol.* **24**, 171–174 (2006).
17. D. Messerschmitt, "Frequency detectors for PLL acquisition in timing and carrier recovery," *IEEE Trans. Commun.* **27**, 1288–1295 (1979).
18. J. Raring, M. Sysak, A. Pedretti, M. Dummer, E. Skogen, J. Barton, S. Denbaars, and L. Coldren, "Advanced integration schemes for high-functionality/high-performance photonic integrated circuits," in *Proc. IEEE SPIE*, San Jose, CA, Paper 6126-19 (2006).
19. E. Skogen, J. Barton, S. Denbaars, and L. Coldren, "A quantum-well-intermixing process for wavelength-agile photonic integrated circuits," *IEEE J. Sel. Top. Quantum Electron.* **8**, 863–869 (2002).

1. Introduction

Ever since the first demonstration of optical phase-locked loops (OPLL) [1], significant effort has been devoted for a wide range applications, as described in Ref. [2–7] and references therein. An OPLL is highly desirable for many applications, such as continuous-wave (CW) chirped LIDAR [4, 8, 9], coherent receivers [5, 7, 10], laser linewidth narrowing and "cloning" of another laser's properties [11, 12], and millimeter wave generation [4, 6].

Recent progress on heterodyne optical phase locking can be found in Ref. [3, 13]. By using an on-PIC modulator or an RF mixer, heterodyne locking can be achieved with a phase detector. However, without any frequency pull-in, the offset frequency cannot be easily tuned, and the locking range is limited. Every time the RF reference frequency is reset, either the master laser or slave laser in this OPLL needs to be adjusted to make sure the free running offset frequency is within the pull-in range of the phase-locked loop, which is normally several hundred MHz at most. Moreover, the loop cannot differentiate the sign of the frequency offset for heterodyne locking. In other words, there are two stable locking points for the heterodyne locking, one is at $\Delta f > 0$, and the other is at $\Delta f < 0$, where Δf is defined as follow.

$$\Delta f = f_{ref} - f_{slave} \quad (1)$$

In this work, we propose and demonstrate a new architecture of OPLL with both phase and frequency detection and a single-sideband mixer (SSBM) [14], which enable large-range frequency pull-in and offset frequency tuning within tens of GHz. We successfully achieved heterodyne locking from -9 GHz to 7.5 GHz, where the offset frequency is defined in Eq. (1).

In terms of OPLL design, one of the most important issues is loop delay. Considering the linewidth and the stability of the on-PIC slave laser, and the frequency pull-in error [14], a 300 MHz loop bandwidth is demanded as a minimum for stable phase locking. To achieve full functionality and keep a relatively short loop delay, a photonic integrated circuit (PIC) is

desired, as well as a high-speed electronic IC (EIC) and a carefully designed loop filter (LF). The architecture of the system is shown in Fig. 1. It is designed to be a second order phase-locked loop. The designed phase margin is 65 degree, and the amplitude margin is 7 dB.

On the PIC, we integrated a widely-tunable sampled-grating distributed-Bragg-reflector (SG-DBR) laser [15], a star-coupler-based optical 90 degree hybrid [16], four single-ended high-speed quantum well photodetectors, and microstrip transmission lines. The SG-DBR laser acts as the widely-tunable slave laser. By injecting current into the back and front mirrors, the reflection spectrum vernier can be tuned so that the laser can cover a 40 nm range. Meanwhile, the current injection into the phase section can tune the laser wavelength finely within one cavity mode, which is around 40 GHz.

The reference laser and the SG-DBR slave laser are mixed in the optical 90 degree hybrid. In-phase and quadrature signals are then generated, which are used for single-sideband mixing and phase/frequency detection. As for the 90 degree hybrid design, a 2-by-4 star coupler is used. We calculated a 2.3 degree error across 40 nm, and estimated about 4 dB loss. On each of the star coupler output waveguides, there is a $50\ \mu\text{m}$ - by - $3\ \mu\text{m}$ p-i-n waveguide photodetector. The electrical signal from the four photodetectors are led to the same side of the PIC using four $430\ \mu\text{m}$ long microstrip transmission lines for PIC-EIC interconnection. Bisbenzocyclobutene (BCB) is used as the dielectric between the signal lines and the RF ground. The RF pads on the PIC have the same pitch size as those on the EIC in order to assemble the PIC and EIC together for system testing.

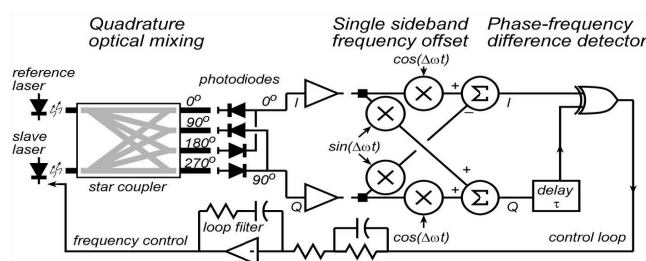


Fig. 1. The architecture of the OPLL.

On this EIC, transimpedance limiting amplifiers, a delay line, an XOR gate and a single-sideband mixer (SSBM) were integrated. The delay line and the XOR gate together act as a phase/frequency detector [14, 17]. The loop filter is a hybrid circuit built on an Aluminium Nitride carrier, using a voltage feedback operational amplifier as an active filter and integrator. The beating signal from the on-PIC photodetectors are finally negatively fed back to the SG-DBR laser phase section through the EIC and the loop filter.

The loop delay of this OPLL is approximately 200 ps, in which 40 ps is from the PIC, >100 ps is from the EIC and 50 ps from the LF and interconnections between them.

2. Fabrication

The PIC is integrated monolithically on a InGaAsP/InP centered quantum well (CWQ) platform [18]. The full epitaxial structure is show in Fig. 2 as well as a scanning electron microscope (SEM) picture. The fabrication started with a base epi, which includes the N-cladding layer, waveguide layers and quantum well layers. Active and passive areas were defined using quantum well-intermixing technology [19]. After that, the gratings of the SG-DBR laser were defined by electron beam lithography, and a methane/hydrogen/argon (MHA)-based RIE etching. Following the grating definition, a blanket p-cladding and p-contact layer regrowth was carried out using metalorganic chemical vapour deposition (MOCVD). After the regrowth, the next step is the waveguides definition. In order to have better heat dissipation and compactness

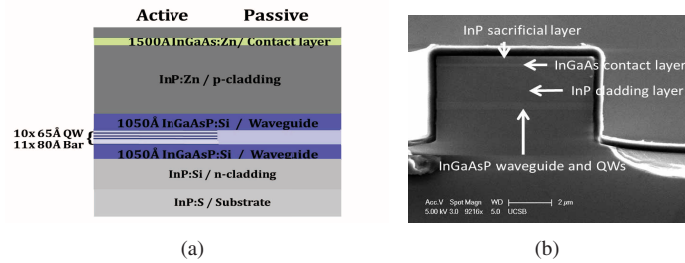


Fig. 2. Epitaxial structure of the integration platform. (a) shows the schematic illustration of the CQW InGaAsP/InP platform for active/passive device integration. (b) shows the cross section of a waveguide.

at the same time, we used surface ridge waveguides for the SG-DBR lasers and deeply-etched waveguides for the other parts of the devices. $\text{Cl}_2/\text{H}_2/\text{Ar}$ ICP-RIE dry etching as well as InP wet etching was used to defined the features. Following the waveguide etching was RF microstrip transmission lines definition and P-contact metal deposition. The RF lines were formed on BCB over a common ground plane. P-contact vias were opened and Pt/Ti/Pt/Au was then deposited as the P contact metal. To further decrease the passive waveguide loss, we implanted protons to the p-cladding layer of the passive waveguides. The wafer was then thinned down to $130\ \mu\text{m}$ for ease of cleaving. Backside Ti/Pt/Au metallization provided common cathode connections to the n-type substrate. After cleaving and anti-reflection coating of the waveguide facets, the samples were ready for testing. A microscope picture of the PIC is shown in Fig. 3.

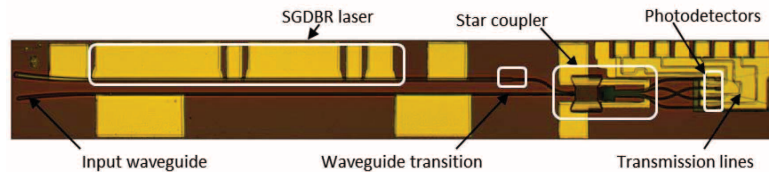


Fig. 3. A microscope picture of the fully fabricated device. SG-DBR laser, star coupler, photodetectors, and microstrip transmission lines are integrated on one single PIC.

The EIC was fabricated by Teledyne Scientific using 500 nm InP HBT technology. The working bandwidth of the EIC is 50 GHz [14].

3. Device characterization and system testing

The photonic IC was characterized before system testing. The measurement showed that the on-PIC SG-DBR laser can output up to 18 mW optical power measured by reverse biasing the semiconductor optical amplifier (SOA) at the output of the SG-DBR laser. The wavelength tuning range is 40 nm, from 1540 nm to 1580 nm. The tuning sensitivity of the phase tuning section is around 4-10 GHz/mA, depending on the cavity mode position relative to the reflection peak and the DC bias current. The bandwidth of the photodetector is measured by a lightwave network analyzer at 1550 nm wavelength. The 3 dB bandwidth is 18 GHz with -5 Volts bias and 12 GHz with -2 Volts bias. In actual system testing, the bias voltage is around -2 Volts, limited by the InP EIC. The star-coupler-based optical 90 degree hybrid is also characterized. Two laser signals were mixed in this hybrid and beat on the four on-PIC photodetectors. The waveforms from the photodetectors were obtained by a real-time oscilloscope with a sample rate of 40 Gsa/s. The measured phase error between I and Q is around 3 degrees and the phase errors between $I+$, $I-$ and $Q+$, $Q-$ are within 10 degrees. Measurements on the EIC are reported elsewhere [14].

After testing the PIC, EIC and LF separately, they were assembled together by wirebonding. Schematics of the OPLL test bed can be found in Fig. 4 and zoomed-in pictures are also shown.

All the system results were taken at 1543 nm wavelength. As mentioned in Section 1, the total loop delay is around 200 ps and therefore, the designed loop bandwidth is 500 MHz, mainly limited by the phase margin. Using lensed fiber, the reference laser signal was coupled into the PIC, and the SG-DBR laser signal was coupled out from the back mirror for monitoring purposes. The optical spectrum of the SG-DBR laser and the reference laser was measured by an optical spectrum analyzer (OSA) and their beat tone measured by an electrical spectrum analyzer (ESA) via a high speed photodetector. The reference laser has a linewidth of 100 kHz, while the linewidth of the SGDBR is above 100 MHz.

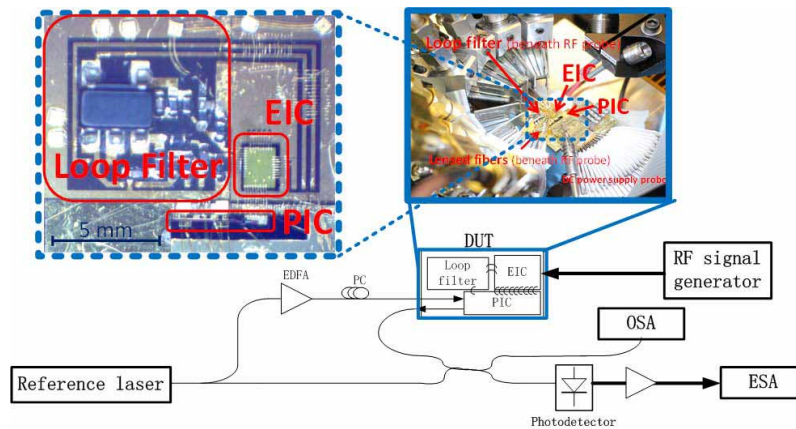


Fig. 4. The schematic of the OPLL test setup is shown in the lower part of this figure. Thinner lines indicate fiber connections and thicker lines show the RF cable connections. Pictures of the OPLL are also shown.

We define the frequency difference between the reference laser and the on-PIC SG-DBR laser in Eq. (1). f_{ref} is the frequency of the widely-tunable reference laser, and f_{slave} is the frequency of the SG-DBR laser. We successfully phase locked the SG-DBR laser to the reference laser with an offset Δf ranging from -9 GHz to +7.5 GHz. The sign of the offset frequency is designated by applying different control signals to the EIC. With a certain control signal to the EIC, the OPLL can only be heterodyne locked to one single frequency offset, either positive or negative. Figure 5 shows the optical spectra and electrical spectra when two lasers are phase locked with an offset of +6 GHz and -6 GHz. The optical spectra verify single-sideband locking.

With the phase/frequency detector, as long as the original beating frequency of the two lasers is within the bandwidth of the on-PIC photodetector and the expected locking wavelength of the SG-DBR laser is within the same cavity mode, heterodyne phase locking can be achieved. By *only* changing the RF reference frequency, we continuously shifted the SG-DBR frequency within the range of -9 GHz to -1.5 GHz, and also from 1.5 GHz up to 7.5 GHz with phase locking to the reference laser. In other words, within such a locking range the RF frequency can be arbitrarily set, and the OPLL will automatically phase lock. There was competition with injection locking due to intrachip reflections for offsets less than 1.5 GHz. The frequency offset is accurately defined by the RF source, normally within Hz or sub-Hz range. Figure 6 shows the electrical spectra of the phase-locked laser with various offsets. The electrical spectra also shows that the loop bandwidth is around 400 MHz.

4. Conclusion

In this work, we have successfully demonstrated the first highly-integrated optical phase-locked loop with phase/frequency detection and single-sideband heterodyne locking. By integrating an

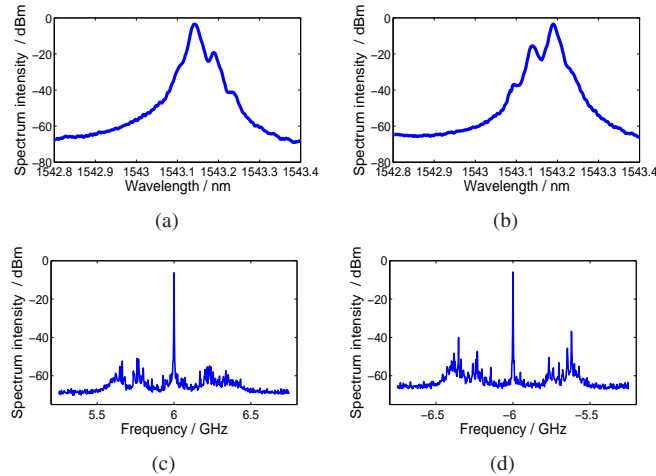


Fig. 5. (a) and (b) show the optical spectrums when two lasers are phase locked with a frequency difference of +6 GHz and -6 GHz. The reference laser has the higher power. (c) and (d) show the beating tones of the two laser when the offset frequency are +6 GHz and -6 GHz respectively, measured with 5 kHz resolution bandwidth.

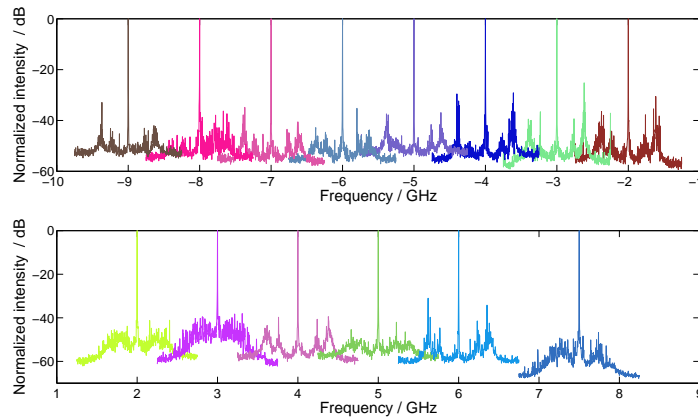


Fig. 6. Shows the beating tones of the two lasers when they are phase locked at various frequency offsets: -9 GHz, -8 GHz, -7 GHz, -6 GHz, -5 GHz, -4 GHz, -3 GHz, -2 GHz, 2 GHz, 3 GHz, 4 GHz, 5 GHz, 6 GHz, and 7.5 GHz.

optical 90 degree hybrid on the PIC and a SSBM on the EIC, single-sideband offset locking has been achieved within 16.5 GHz range. The OPLL loop bandwidth is 400 MHz.

It is anticipated that by replacing the continuous-wave (CW) reference laser with a phase-locked optical comb, e.g. a mode-locked laser, and then offset locking to different comb lines, the slave laser frequency could be possibly swept through several terahertz, while maintaining the coherent relationship to the original locking source. With several terahertz bandwidth, CW chirped LIDAR will have a depth resolution within the tens of micron range [8].

Acknowledgment

This work is supported by DARPA PICO project. A portion of this work is done in the UCSB nanofabrication facility, part of NSF funded NNIN network.

A Highly Integrated Optical Phase-locked Loop with Single-sideband Frequency Sweeping

Mingzhi Lu¹, Hyunchul Park¹, Eli Bloch², Abirami Sivananthan¹, Zach Griffith³, Ashish Bhardwaj⁴, Leif A. Johansson¹, *member, IEEE*, Mark J. Rodwell¹, *Fellow, IEEE*, and Larry A. Coldren¹, *Fellow, IEEE*

¹Department of Electrical and Computer Engineering, University of California, Santa Barbara, CA, 93106, USA.

²Department of Electrical Engineering, Technion-Israel Institute of Technology, Haifa 32000, Israel.

³Teledyne Scientific and Imaging Company, Thousand Oaks, 1049 Camino Dos Rios, CA, 91360, USA

⁴Currently with JDSU Corporation, 80 Rose Orchard Way, San Jose, CA 95134, USA.

Email: mlu@ece.ucsb.edu

Abstract: An optical phase-locked loop with a frequency detector and a single-sideband mixer has been proposed and demonstrated for the first time. Continuous frequency sweeping has been achieved.

OCIS codes: (250.5300) Photonic integrated circuits; (060.2840) Heterodyne (060.1660); Coherent communications; (250.0250) Optoelectronic.

Optical phase-locked loops synchronize the phase of a laser to that of an external laser, which is highly desirable for many applications, such as coherent receivers, linear frequency sweeping for LIDAR applications, and phased array microwave photonics systems. [1-3]

In this work, a highly integrated optically-locked loop has been demonstrated. Integrated with a 90 degree hybrid, an XOR gate as the frequency detector and a single-sideband mixer (SSBM), this OPLL has both phase detection and frequency detection modes. Furthermore, the optical 90 degree hybrid and the SSBM make the single-sideband locking possible. The testing results show that by simply changing the RF clock frequency, the offset frequency between the reference laser and the slave laser can be continuously tuned within a large frequency range. We achieved frequency detection and offset phase locking ranging from -9.5 GHz to +7.5 GHz. The sign of the frequency is defined by a control input of the EIC.

The architecture of the OPLL is shown in Fig. 1. It is composed by three parts: an InP photonic integrated circuit (PIC), an InP electronic integrated circuit (EIC), and a hybrid circuit as a loop filter. On the PIC, we integrated a sampled-grating DBR (SG-DBR) laser [4] with 40 nm continuous tuning range, a star-coupler-based optical 90 degree hybrid [5], four single-ended high-speed photodiodes, and microstrip transmission lines. The 90 degree hybrid provides both in-phase and quadrature signals, which are used for frequency detection and single-sideband mixing. The signal finally negatively feeds back to the SG-DBR laser phase section through the loop filter.

The PIC is designed and fabricated based on InGaAsP/InP centered quantum well structure requiring 18 lithography layers and one p-cladding regrowth. The quantum well intermixing (QWI) approach was used to define active and passive regions, and gratings were defined by e-beam lithography. For better heat dissipation and compactness, both surface ridge and deeply etched waveguides were fabricated on one PIC, and a low-loss waveguide transition was defined. BCB was used as the dielectric of the microstrip transmission lines.

On this EIC, we integrated four transimpedance limiting amplifiers as the first stage, following by a SSBM to introduce the frequency offset. A delay line and an XOR gate were also integrated on the EIC, together acting as a frequency detector. The designed frequency pull-in range is 50 GHz. The EIC is fabricated by Teledyne using 500nm InP HBT technology. The loop filter is a hybrid circuit using a current feedback operational amplifier as an active filter and integrator.

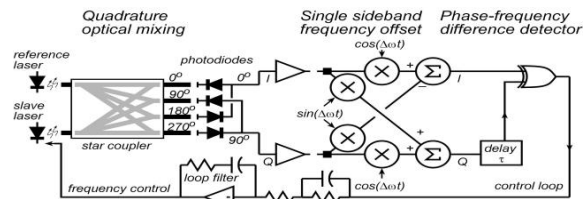


Fig. 1. The architecture of the OPLL consists of three parts: a photonic integrated circuit, an electrical integrated circuit and a loop filter.

Both PIC and EIC are soldered to AIN carriers and the loop filter is also built on an AIN carrier using discrete components and an operational amplifier. The PIC, EIC, and loop filter were connected together using wirebonds.

The carriers are carefully designed to decrease the loop delay as much as possible. The total loop delay in this system is estimated to be around 200 ps, and the designed loop bandwidth is approximately 500 MHz.

The experimental setup is shown in Fig. 2(a). Using lensed fibers, the reference laser was coupled into the PIC, and the SG-DBR laser was coupled out from the back mirror to beat with the reference laser off-chip for measurement purposes. The test setup is shown in Fig. 2(b).

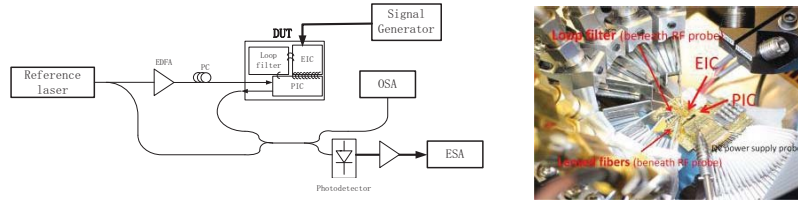


Fig. 2. The OPLL test setup. (a) The schematic of the test setup. Thinner lines show fiber connection and thicker lines show the RF cable connection. (b) shows the picture of the OPLL on the test setup.

We define the frequency different Δf as the frequency between the reference laser and the on-PIC SG-DBR laser, $\Delta f = f_{\text{ref}} - f_{\text{SG-DBR}}$. We successfully locked the SG-DBR laser to the reference laser with an offset Δf ranging from -9.5GHz to +7.5 GHz. By only changing the RF reference frequency, we continuously shifted the SG-DBR frequency within the range from -9.5 GHz to -2 GHz, and also from 2 GHz up to 7.5 GHz with phase locking to the reference laser, respectively. Fig. 3 shows the optical spectrums and electrical spectrums when two lasers are phase locked with an offset of +6 GHz and -6 GHz. The electric spectrums of the beating tones with different frequency offsets are shown in Fig. 4. The frequency sweeping is achieved by only changing the bias RF reference frequency on each figure. The loop bandwidth is around 400 MHz.

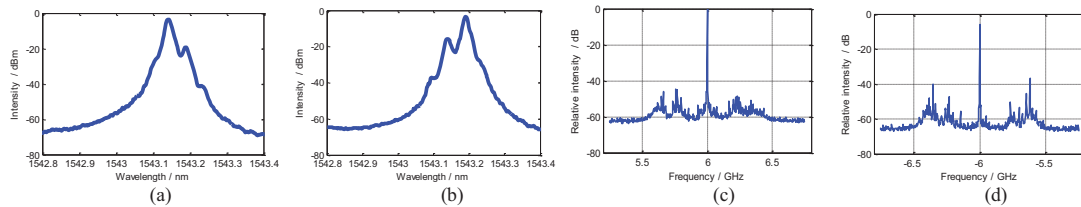


Fig. 3. (a) and (b) show the optical spectrums when two lasers are phase locked with a frequency different of +6 GHz and -6 GHz. (c) and (d) show the beating tones of the two laser when the offset frequency are +6 GHz and -6 GHz respectively.

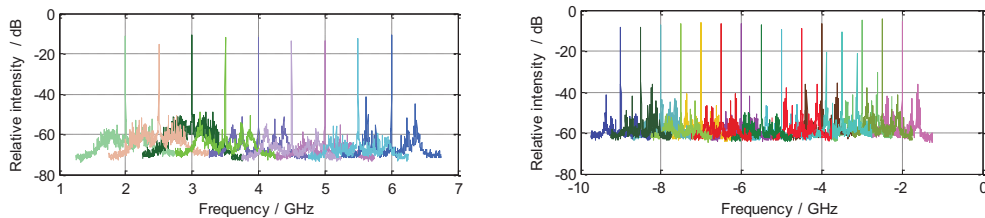


Fig. 4. Shows the beating tones of the two lasers when they are phase locked at different frequency offsets. All of them are 500 MHz apart.

Acknowledgement: This work is supported by DARPA PICO project.

References

- [1] Sasa Ristic, Ashish Bhardwaj, Mark J. Rodwell, Larry A. Coldren, and Leif A. Johansson, "An Optical Phase-Locked Loop Photonic Integrated Circuit," *Journal of Lightwave Technology*, Vol. 28, Issue 4, 2010, pp. 526-538.
- [2] Robert J. Steed, Francesca Pozzi, Martyn J. Fice, Cyril C. Renaud, David C. Rogers, Ian F. Lealman, David G. Moodie, Paul J. Cannard, Colm Lynch, Lillianne Johnston, Michael J. Robertson, Richard Cronin, Leon Pavlovic, Luka Naglic, Matjaz Vidmar, Alwyn J. Seeds, "Monolithically integrated heterodyne optical phase-lock loop with RF XOR phase detector," *Optics Express*, Vol. 19, No. 21, 2011.
- [3] N. Satyan, W. Liang, A. Kewitsch, G. Rakuljic, and A. Yariv, "Coherent power combination of semiconductor lasers using optical phase lock loops," *IEEE J. Sel. Topics Quantum Electron.*, vol. 15, no. 2, pp. 240-247, Mar./Apr. 2009.
- [4] Larry A. Coldren, "Monolithic tunable diode lasers," *IEEE Journal of Selected Topics in Quantum Electronics*, Volume: 6 Issue:6, 2000, pp.988-999.
- [5] Christopher R. Doerr, Douglas M. Gill, Alan H. Gnauck, IEEE, Lawrence L. Buhl, Peter J. Winzer, Mark A. Cappuzzo, A. Wong-Foy, Evans Yifan Chen, and L. T. Gomez, "Monolithic Demodulator for 40-Gb/s DQPSK Using a Star Coupler," *Journal of Lightwave Technology*, Vol. 24, Issue 1, 2006, pp. 171-174.

A 1-20 GHz InP HBT Phase-Lock-Loop IC for Optical Wavelength Synthesis

Eli Bloch¹, Hyunchul Park², Mingzhi Lu², Thomas Reed², Zach Griffith³, Leif A. Johansson²,
Larry A. Coldren², Dan Ritter¹ and Mark J. Rodwell².

¹Department of Electrical Engineering, Technion - Israel Institute of Technology, Haifa 32000, Israel.

²Department of ECE, University of California, Santa Barbara, CA, 93106, USA.

³Teledyne Scientific and Imaging, 1049 Camino Dos Rios, Thousand Oaks, CA, 91360, USA.

Abstract — We report a PLL IC for locking, at a controlled frequency offset between 1 and 20 GHz, the optical phase and optical frequency of a slave semiconductor laser to that of a reference semiconductor laser. The IC, implemented in a 500 nm InP HBT process, contains an ECL digital single-sideband mixer to provide phase-locking at a +/- 20 GHz offset frequency, and also contains a wideband phase-frequency detector to provide loop acquisition given up to +/-40 GHz initial frequency offset.

Index Terms — Phase locked loops, Mixers, Microwave circuits, Wavelength division multiplexing, Bipolar integrated circuits, Optoelectronic devices, High speed integrated circuits.

I. INTRODUCTION

In wavelength-division-multiplexed (WDM) optical communications systems, optical channel spacings, typically ~25 GHz, are determined by optical resonators coupled to diode lasers. In marked contrast, in microwave systems, frequencies are precisely determined by PLL/synthesis techniques. Using optical phase-lock-loops (OPLLs) [1], pairs of lasers can be locked in both optical phase and frequency. By introducing frequency offsets within the OPLL, the frequency difference between a pair of lasers can be set to this injected frequency, allowing wavelength spacings within WDM, LIDAR, and other optical systems to be set precisely and under digital control. This is optical wavelength synthesis.

Optical PLLs differ from microwave PLLs in that the oscillator frequency is vastly larger, 231 THz for a 1300 nm laser. The large initial frequency offset between lasers forces development of frequency difference detectors operating over 100 GHz bandwidth. Because optical frequencies cannot be divided under programmable control, other techniques must be developed for optical frequency synthesis.

An OPLL contains an optoelectronic IC (OEIC) comprising locked laser, interferometer, and photodiodes, a microwave electrical IC (EIC) containing frequency offset control and phase-frequency detectors, and a low-frequency (GHz) loop filter. OEIC design is described in [2]. Optical wavelength synthesis results will be reported separately [3]. Here we report design and performance of InP HBT optical wavelength synthesis ICs comprising of a 1-20 GHz *digital* single-sideband (SSB) mixer, and a +/- 40 GHz phase-frequency difference detector.

II. OPTICAL SYNTHESIZER DESIGN

In the OPLL (Fig. 1), the reference and slave laser are combined at (0°, 90°, 180°, 270°) phase offsets and interfered on photodiodes, producing photocurrents proportional to the cosine (I) and sine (Q) of the optical phase difference. The coupler and photodiodes thus form an I/Q mixer.

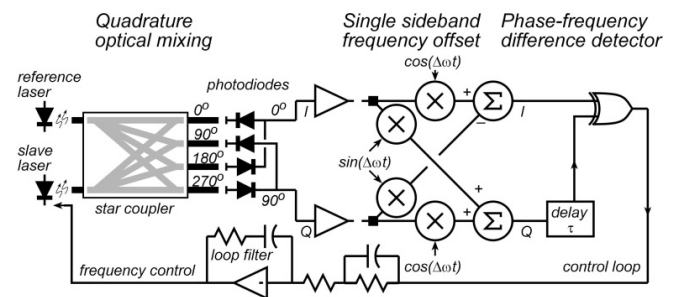


Fig. 1. Optical phase-locked-loop consisting of reference and locked lasers, 4-phase optical mixing, offset frequency injection with a single-sideband mixer, phase-frequency difference detector, and loop filter

To control optical frequency spacing, the slave laser must be locked to a controlled positive or negative frequency offset from that of the reference laser. The offset is introduced by shifting the I/Q photodetector signal frequencies using a two-stage (Weaver) single-sideband mixer implemented using quadrature optical and microwave mixers. The microwave mixer LO, provided by a microwave synthesizer, thus controls the optical frequency spacing. To permit tuning of this frequency offset over a wide +/- 1 to +/-20 GHz bandwidth, the electrical mixer is implemented digitally.

A PLL will not of itself acquire lock if the initial LO-RF offset frequency exceeds ~2-3 times the PLL loop bandwidth f_{loop} . At $\lambda=1300$ nm, +/- 0.02% wavelength detuning corresponds to a +/- 46 GHz offset frequency, much larger than the ~1 GHz f_{loop} feasible given the laser tuning characteristics. A Costas phase-frequency difference detector (PFD) provides an error signal proportional to the offset

frequency, permitting automatic loop acquisition for offset frequencies below +/- 40 GHz.

III. THEORY AND DESIGN

OEIC photocurrents vary significantly between fabricated OEICs; To make the loop parameters independent of such variations, PLL signals are converted to digital levels, and mixers and phase/frequency detectors are implemented in emitter-coupled logic (ECL).

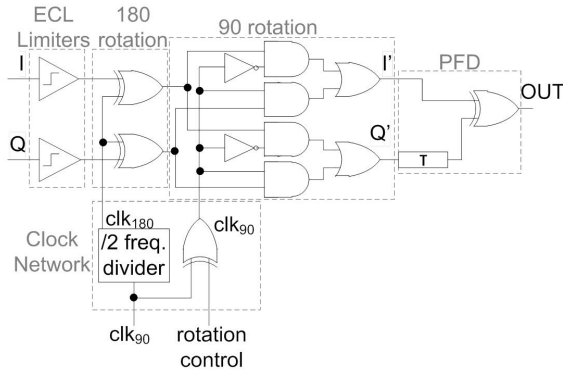


Fig. 2. Digital block diagram of the electrical PLL IC, consisting of input limiters, a digital SSB mixer implemented with 180° and 90° rotation blocks, and an phase-frequency difference detector implemented using a delay line and XOR gate. All digital blocks are in 2-level differential ECL.

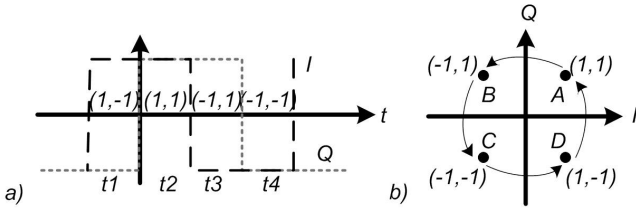


Fig. 3. Digitally limited I/Q signals for optical frequency offset. a) Time -domain square wave. b) Rotating constellation in the (I,Q) plane.

Subsequent to digital limiting, frequency shifts are introduced with a SSB mixer. This mixer, implemented digitally to permit a wide 20 GHz tuning range, is described in Fig. 1 and Fig. 2. Given a positive laser frequency offset f , the I/Q photocurrents rotate counterclockwise through the points (1,1), (-1,1), (-1,-1), (1,-1) in the (I,Q) plane (Fig. 3). For a negative frequency offset, $-f$, this rotation reverses. For zero frequency offset the constellation remains static at one of the four points as determined by the relative laser phases.

The digital SSB mixer provides a frequency offset by rotating this constellation, producing an output pair (I',Q'). It is formed of cascaded 180° and 90° rotation blocks. The 180° block rotates the (I,Q) state by 180° (i.e. A→C, B→D, etc.) when its input clock is 1 but provides no rotation when its input clock is 0. The 90° block rotates the (I,Q) state by 90° (i.e. A→B, B→C, etc.) when its input clock is 1 but provides no rotation when its input clock is 0. Applying high clock signals to both blocks rotates the state by 270°. Applying clock

signals f_{clk90}, f_{clk180} at a 2:1 frequency ratio to the 180° and 90° rotation blocks rotates the I'/Q' constellation and provides a frequency shifts f ; These signals are derived from a static frequency divider [4], (Fig. 2). Inverting the sign of f_{clk90} inverts the sign of the frequency offset.

The PFD is an ECL XOR gate with a delay line in the Q arm. To force equal transistor delays on both inputs, the gate uses two parallel multipliers with crossed inputs and shunt outputs. The PFD output (1) has one component proportional to the phase difference given zero frequency difference, and a second proportional to the frequency difference given zero phase difference.

$$I'(t) \oplus Q'(t - \tau) = \cos(2\pi\Delta f t + \theta) \sin(2\pi\Delta f (t - \tau) + \theta) \\ = 0.5 \sin(4\pi\Delta f t - 2\pi\Delta f \tau + 2\theta) + 0.5 \sin(2\pi\Delta f \tau) \quad (1)$$

In PLL frequency locking mode, when the frequency offset between the reference and the offset laser, Δf , does not match the clk_{90} frequency (i.e. $f_{clk90} \neq 2\Delta f$), the (I',Q') state rotates at the error frequency driving (Fig. 5) the PFD to provide a non-zero average output.

In phase locking mode, when the laser offset, Δf , matches the clk_{90} frequency (i.e. $f_{clk90} = 2\Delta f$) under a suitable rotation control sign, the relative phase between the lasers will change the I/Q signals phase relative to clk_{90} and clk_{180} . This will eventually result in (I',Q') state oscillating at a frequency $2f_{clk90}$ between states two adjacent states (A and B, B and C, etc.) with a duty cycle determined by the phase offset (Fig. 4). For a 90° (I,Q) phase relative to clk_{90} the oscillation is at 50% duty cycle, hence the PFD provides zero DC average output. This brings the system into lock.

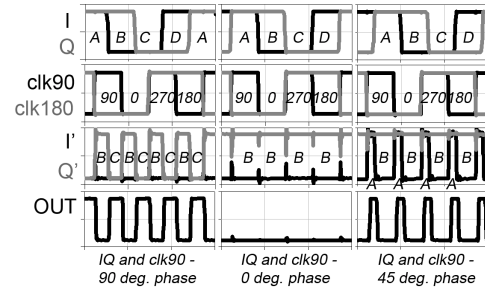


Fig. 4. SSB mixer at phase detection mode. Signal propagation as a function of various I/Q phase relative to clk_{90} . For 90° phase a 50% duty cycle output signal with zero average DC.

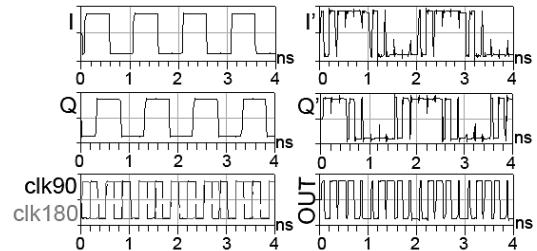


Fig. 5. SSB mixer at frequency locking mode. $f = 1$ GHz and $f_{clk90} = 3$ GHz. Since frequency lock occurs only for $f = 1.5$ GHz, the (I',Q') state will rotate at the error frequency of 0.5 GHz.

IV. EXPERIMENTAL RESULTS

The integrated SSBM chip was measured for phase and frequency detection using a sampling oscilloscope and a real time oscilloscope to observe and average the output signal. The optical I/Q signal was emulated by two synchronized microwave synthesizers while the clk_{90} signal was supplied by a third synthesizer. The applied input signals power was set to 0.4 mW for both the I/Q input and clk_{90} . Signals were delivered on-wafer using microwave wafer probes. The overall DC power for the IC was 5.3 W.

Fig. 6 shows experimental results. In Fig. 6a, the PFD output is measured as a function of phase difference with the emulated I/Q photocurrent signals set at 15 (20) GHz and with $f_{\text{clk}_{90}}$ set at 30 (40) GHz, i.e. with the system operating in phase-detection mode. The phase error signal varies ± 300 mV at 15 GHz offset and ± 120 mV at 20 GHz offset as the phase is varied through 360° . This indicates that the phase detector operates properly for frequency offsets as large as ± 20 GHz.

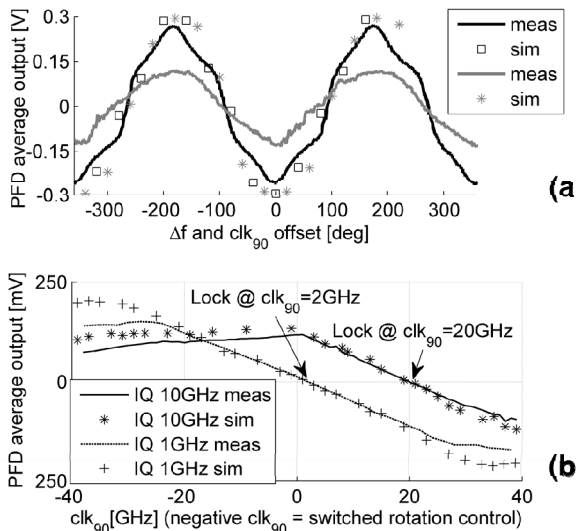


Fig. 6. PFD phase, frequency detection measurements. a) phase detection characteristics, measurement vs. simulation for $f = 20$ GHz, $\text{clk}_{90} = 40$ GHz (grey) and for $f = 15$ GHz, $\text{clk}_{90} = 30$ GHz (black). b) frequency detection characteristics, measurement vs. simulation for $f = 10$ GHz and $f = 1$ GHz.

In Fig. 6b, the PFD output is measured at a laser offset frequencies of $\Delta f = 1$ and 10 GHz, by adjusting SSB mixer LO frequency $f_{\text{clk}_{90}}$. This measured the PFD characteristics in frequency detection mode. The frequency detection characteristics show frequency error detection over a ± 40 GHz range, with zero frequency detector output when, as designed, the laser offset frequency is equal to $f_{\text{clk}_{90}}/2$. Fig. 7 shows the PFD output time waveforms in phase detection mode, as a function of phase offset, for $\Delta f = 2$ GHz and $f_{\text{clk}_{90}} = 4$ GHz. The IC (Fig. 8) area is 1.8 mm^2 .

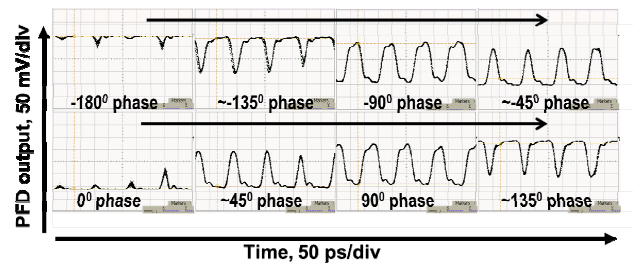


Fig. 7. PFD OUT measured waveforms in phase detection mode for $f = 2$ GHz and $f_{\text{clk}_{90}} = 4$ GHz.

V. CONCLUSION

We have demonstrated a novel broadband ± 20 GHz optical frequency synthesis IC in $0.5 \mu\text{m}$ InP HBT technology. Further work on a full optoelectronic system for single side band frequency offset locking is underway.

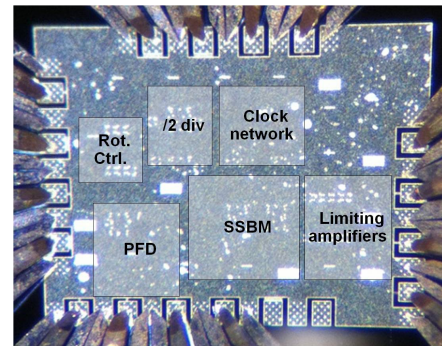


Fig. 8. IC chip image.

ACKNOWLEDGEMENT

The research was supported under the Defense Advances Research Projects Agency (DARPA) PICO program. The authors would like to thank Teledyne Scientific for MMIC Fabrication.

REFERENCES

- [1] R. J. Steed, L. Ponnampalam, M. J. Fice, C. C. Renaud, D. C. Rogers, D. G. Moodie, G. D. Maxwell, I. F. Lealman, M. J. Robertson, L. Pavlovic, L. Naglic, M. Vidmar and A. J. Seeds, "Hybrid Integrated Optical Phase-Lock Loops for Photonic Terahertz Sources," *Selected Topics in Quantum Electronics, IEEE Journal of*, vol. 17, pp. 210-217, 2011.
- [2] S. Ristic, A. Bhardwaj, M. J. Rodwell, L. A. Coldren and L. A. Johansson, "An Optical Phase-Locked Loop Photonic Integrated Circuit," *Lightwave Technology, Journal of*, vol. 28, pp. 526-538, 2010.
- [3] M. Lu, E. Bloch, H. Park, A. Sivanathan, A. Bhardwaj, L. A. Johansson, M. J. Rodwell and L. A. Coldren, "A highly integrated optical phase-locked loop with continuous frequency sweeping," *Submitted to CLEO 2012*.
- [4] Z. Griffith, M. Urteaga, R. Pierson, P. Rowell, M. Rodwell and B. Brar, "A 204.8GHz static divide-by-8 frequency divider in 250nm InP HBT," in *Compound Semiconductor Integrated Circuit Symposium (CSICS), 2010 IEEE*, 2010, pp. 1-4.

40Gbit/s Coherent Optical Receiver Using a Costas Loop

Hyun-chul Park⁽¹⁾, Mingzhi Lu⁽¹⁾, Eli Bloch⁽²⁾, Thomas Reed⁽¹⁾, Zach Griffith⁽³⁾, Leif Johansson⁽¹⁾, Larry Coldren⁽¹⁾, and Mark Rodwell⁽¹⁾

⁽¹⁾ ECE Department, University of California at Santa Barbara, Santa Barbara, CA 93106-9560, USA
hcpark@ece.ucsb.edu

⁽²⁾ Department of Electrical Engineering, Technion – Israel Institute of Technology, Haifa 32000, Israel

⁽³⁾ Teledyne Scientific & Imaging Company, 1049 Camino Dos Rios, Thousand Oaks, CA 91360, USA

Abstract For the first time, a highly integrated coherent optical receiver is demonstrated using a homodyne OPLL as a Costas loop. The OPLL shows 1.1GHz loop bandwidth, 120ps effective loop delay, and $10 \times 10 \text{mm}^2$ compact size of chip integration. The receiver exhibits 40Gbit/s BPSK reception with no latency.

Introduction

Coherent optical communication has resurged due to demand for higher sensitivity, data rates, and spectral efficiency^{1,2}. Recent approaches to coherent optical receivers have adopted coherent detection using a local oscillator (LO) laser, a polarization diversity 90° optical hybrid with balanced detectors, and digital signal processing (DSP), because advanced DSPs can manage phases and polarizations without a phase lock^{1,2}. However, they require high speed analog to digital converters (ADC) and complicated signal processing algorithms. They are also limited by data processing speed, cost, and power consumption^{2,3}.

The alternative coherent optical receiver is a homodyne optical phase locked loop (OPLL) based coherent detection also known as a Costas loop^{2,3}. It restores the phase of a carrier laser, and high-speed data are demodulated by a simple phase locked loop (PLL) without ADC and DSP. However, it has been regarded as challenging because of large loop delays which lead to a narrow loop bandwidth, and therefore, the OPLL cannot maintain stability against laser phase noise and frequency drift¹⁻³.

Recently, several OPLLs have been reported including a highly integrated homodyne OPLL using a high speed HEMT based loop filter with a loop bandwidth of 300MHz⁴, a heterodyne OPLL using an exclusive-OR (XOR) as a phase detector with a loop delay of 1.8ns⁵, and a highly integrated heterodyne OPLL using an integrated single side-band mixer and a phase frequency detector (PFD) with a loop delay of 0.2ns and loop bandwidth of 550MHz⁶.

OPLL based coherent optical receivers have been improved with modified OPLL topologies such as a decision driven OPLL with sub-carrier modulation⁷ and a digital OPLL using sampled I-Q signals and slow speed DSP for homodyne reception of PSK 40Gbit/s³. However, such OPLLs may require a narrow linewidth on

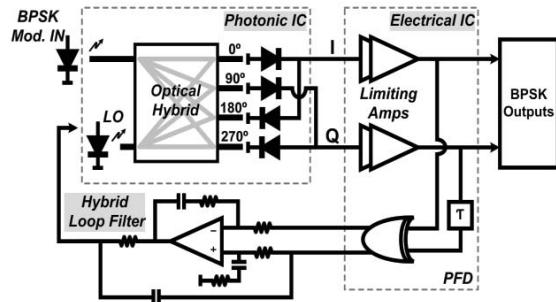


Fig. 1: A schematic of a homodyne OPLL and a BPSK receiver

transmitting and LO lasers due to a narrow loop bandwidth, and these OPLLs may need additional circuit blocks such as voltage controlled oscillators, a Mach-Zehnder modulator (MZM), an optical filter, and even ADC and DSP to recover the carrier signal.

In this paper, a highly integrated 40Gbit/s BPSK coherent optical receiver based on the homodyne OPLL and the Costas loop is demonstrated for the first time. The OPLL has achieved a large closed loop bandwidth of 1.1GHz by a significantly minimized loop delay of 120ps. In addition, digitally operating electrical circuits make the OPLL system less sensitive to external fluctuations and the PFD extends phase-lock and frequency pull-in ranges. The BPSK coherent receiver exhibits BER results of error-free ($\text{BER} < 10^{-12}$) up to 35Gbit/s and less than 10^{-7} for 40Gbit/s. The compact BPSK coherent optical receiver is integrated within $10 \times 10 \text{mm}^2$ and consumes less than 3W power.

Homodyne OPLL / Costas Loop

Design of Homodyne OPLL: The homodyne OPLL consists of three main blocks: a photonic IC (PIC), an electrical IC (EIC), and a hybrid loop filter as shown in Fig. 1. The fabricated PIC uses an InGaAsP/InP platform and integrates a widely (40nm) tunable sampled grating

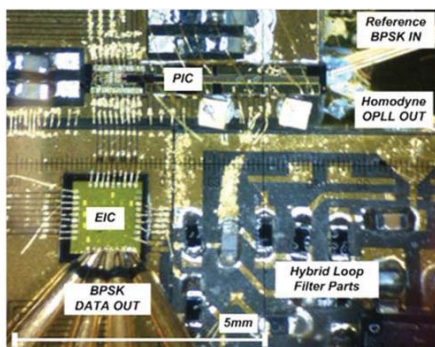


Fig. 2: A photograph of an implemented Costas loop based on a homodyne OPLL receiver

distributed Bragg reflector (SG-DBR) laser as an LO whose wavelength is tuned by current injection into front / back mirrors and a phase tuning diode. The received signal and LO laser are mixed by an integrated 90° optical hybrid and detected by uni-travelling carrier photodetectors (PD) for I-Q quadrature electrical current outputs. The optical hybrid has 48 - 52% balanced outputs, and the PDs show a 3-dB bandwidth of 30GHz and saturation currents of 18mA with -5V bias.

The EIC includes limiting amplifiers (LAs) and a PFD. It has been fabricated using Teledyne's 500nm InP HBT processes which have $300\text{GHz } f_t / f_{\text{max}}$, respectively. The LAs amplify the photocurrents to 0.3Vp-p digitized signals which contain only phase / frequency error information, and thus, the OPLL is more insensitive against photocurrent intensity variations. The PFD has been designed using XOR as a multiplier, and 10ps delay lines on the Q-path for 50GHz frequency pull-in ranges [8]. Integrating the LAs and PFD, the EIC has an operation bandwidth of larger than 50GHz and an extremely small electrical delay of $\sim 50\text{ps}$.

The loop filter has been designed using a feed-forward technique consisting of an integrator for a main path and a differentiator for a feed-forward path. A bulk operational amplifier (OPA) has been used to obtain high gain at DC and low frequencies, but the OPA has long propagation delays and could limit the OPLL's bandwidth performance. In order to minimize the delay effects and extend the loop bandwidth, the feed-forward path using a passive capacitor component has been applied. As a result, the effective loop delay of the loop filter becomes negligible and the loop bandwidth of the OPLL is only limited by delays from the PIC (40ps), EIC (50ps), and interconnections (30ps).

With a loop delay of 120ps, the targeted loop bandwidth of OPLL can be wider than 1GHz. A second order loop has been chosen to track the laser frequency drift, and the PFD has been

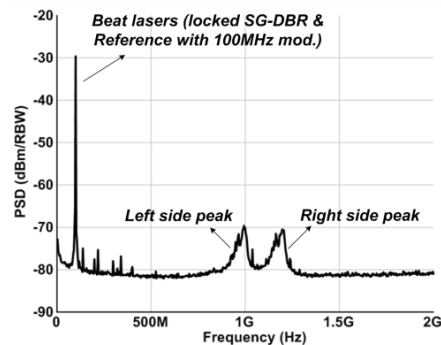


Fig. 3: A beat spectrum between a homodyne OPLL and a ref. laser with 100MHz mod. (RBW: 100kHz)

applied to extend frequency / phase acquisition performances. Loop characteristics of the PIC and EIC have been fully characterized, and parasitic effects have also been considered in the homodyne OPLL design.

Finally, the homodyne OPLL and the Costas loop have been implemented as shown in Fig. 2 within the compact size of $10 \times 10 \text{mm}^2$.

Costas Loop / BPSK Receiver: A homodyne OPLL can be used in an optical carrier phase recovery circuit as the Costas Loop. I and Q signals are mixed in the PFD and the PFD output has two stable lock conditions of 0 and π in one period. Therefore, the Costas loop can keep the lock for the BPSK modulated signals. The locked SG-DBR laser down-converts the modulated data. As a result, the homodyne OPLL can be used for the BPSK receiver without post digital signal processing. In the BPSK receiver, the down-converted data outputs from PDs are amplified / limited by the EIC blocks and the signals are split to the feedback loop and BPSK data detector.

Tests and experiment results

Homodyne OPLL tests: The homodyne OPLL for a coherent optical receiver has been realized as shown in Fig. 2. A Koshin Kogaku tunable laser has been used for a 1550nm external reference laser which has a linewidth of 100kHz. The SG-DBR laser has been locked to the reference laser and beat with the reference laser with a 100MHz acousto-optic modulator (AOM). The spectrum of the beat signals has been obtained using an electrical spectrum analyzer (ESA) as shown in Fig. 3 – peak tone at 100MHz, right side peak at 1.2GHz, and left side peak at 1.0GHz as an image frequency. From the spectral results, a closed loop bandwidth of 1.1GHz is observed. The homodyne OPLL can suppress wide frequency ranges of the SG-DBR laser phase noise and hold lock against laser frequency drift.

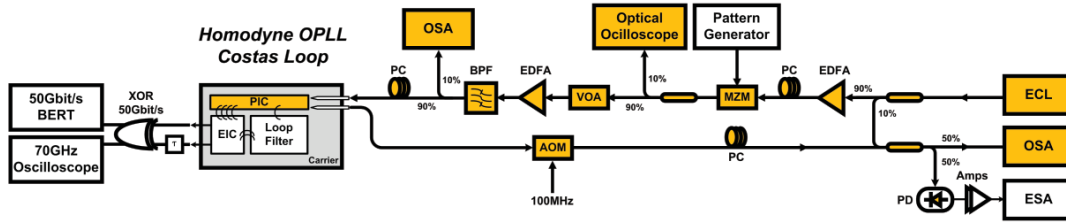


Fig. 4: A test setup of BER vs. OSNR for a Costas loop receiver (ECL: external cavity laser, PC: polarization controller, and OSA: optical spectrum analyzer)

BPSK Data Reception: To prove the BPSK coherent optical receiver performance, BER vs. OSNR has been measured using a test setup as shown in Fig. 4. A PRBS ($2^{31}-1$) pulse pattern generator and MZM have been used for BPSK optical data modulations up to 40Gbit/s, and OSNR has been controlled by a variable optical attenuator (VOA) before the Erbium doped fiber amplifier (EDFA) and 0.95nm optical band pass filter (BPF). Only I-differential outputs from the EIC are connected to 50Gbit/s BERT measurement through an external differential decoder using a 50Gbit/s XOR and 1bit-delay by phase shifters to solve the phase ambiguity of the Costas loop. At the same time, lock status of the SG-DBR has been monitored with an ESA.

A BER vs. OSNR has been measured for 25G to 40Gbit/s as shown in Fig. 5, and the BPSK receiver exhibits error-free ($BER < 10^{-12}$) up to 35Gbit/s and $BER < 10^{-7}$ for 40Gbit/s. Open received eye outputs for 25Gbit/s and 40Gbit/s are measured using a 70GHz sampled oscilloscope without the differential decoder. In addition, the linewidths of the locked SG-DBR laser with 25Gbit/s BPSK data and without the data are measured as shown in Fig. 6 using a self-heterodyne technique with a 25km fiber, and all locked SG-DBR lasers show the same linewidth of 100kHz as the reference laser. This means that the Costas loop with a 25Gbit/s BPSK data modulation can restore the carrier laser without degrading the linewidth and data reception performance.

This BPSK receiver consumes less than 3W (PIC < 0.5W, EIC < 2.2W, and loop filter < 0.1W).

Conclusions

A highly integrated coherent optical receiver has been demonstrated for the first time using the concept of a homodyne OPLL and a Costas loop. A stable homodyne OPLL has been designed with a PIC, a digitally operating EIC, and a feed-forward loop filter, achieving total effective loop delays of 120ps and a closed loop bandwidth of 1.1GHz. The coherent optical BPSK receiver exhibits error-free up to 35Gbit/s and less than 10^{-7} for 40Gbit/s with no latency and less than 3W power consumption.

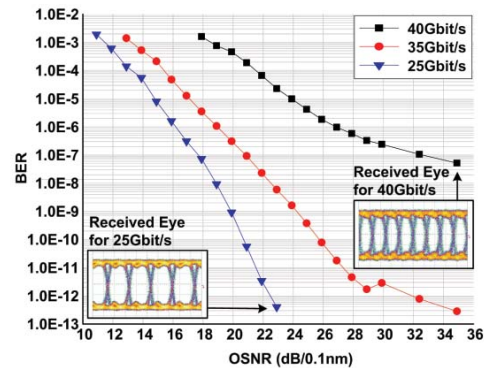


Fig. 5: BER vs. OSNR for 25G to 40Gbit/s and received eye outputs for 25G and 40Gbit/s

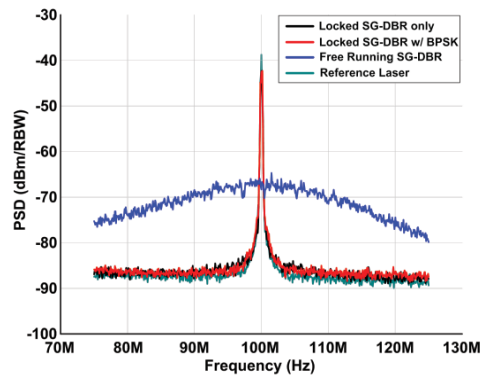


Fig. 6: Self-heterodyne linewidth measurements for locked SG-DBR w/o and w/ 25Gbit/s BPSK, free-running SG-DBR, and ref. lasers (RBW: 50kHz)

Acknowledgements

This work was supported by the Photonic Integration for Coherent Optics (PICO) through DARPA. A portion of this work was done in the UCSB nanofabrication facility, part of the NSF funded NNIN network. The author would like to thank Teledyne Scientific for EIC fabrications.

References

- [1] G. Li, Adv. Opt. Photon. **1**, 279-307 (2009).
- [2] K. Kikuchi, Springer, Chap. **2**, (2010).
- [3] T. Sakamoto et al., ECOC'10, P3.12, (2010).
- [4] S. Ristic et al., JLT **28**, 526-538 (2010).
- [5] R. Steeds et al., OE **19**, 20048-20053 (2011).
- [6] M. Lu et al., OE **20**, 9736-9741 (2012).
- [7] S. Camatel et al., OFC'06, OTu13, (2006).
- [8] E. Bloch et al., IMS2012, WEPN-4, (2012).

A Highly Integrated Optical Phase-locked Loop for Laser Wavelength Stabilization

Mingzhi Lu¹, Hyunchul Park¹, Eli Bloch², Abirami Sivananthan¹, Zach Griffith³, Leif A. Johansson¹, *member*, IEEE, Mark J. Rodwell¹, *Fellow*, IEEE, and Larry A. Coldren^{1,4}, *Fellow*, IEEE

¹Department of Electrical and Computer Engineering, University of California, Santa Barbara, CA, 93106, USA.

²Department of Electrical Engineering, Technion – Israel Institute of Technology, Haifa 32000, Israel.

³Teledyne Scientific and Imaging Company, Thousand Oaks, 1049 Camino Dos Rios, CA, 91360, USA

⁴Department of Materials, University of California, Santa Barbara, CA, 93106, USA.

Email: mlu@ece.ucsb.edu

Abstract—A highly integrated optical phase-locked loop (OPLL) has been applied to stabilize the semiconductor laser wavelength for the first time. Preliminary results show that the slave laser is stably phase-locked to a reference laser within 2.2 K temperature fluctuation.

Keywords—coherent; optical frequency synthesis; optical phase-locked loop; wavelength stabilization.

Coherent fiber optic communication is receiving a lot of interest recently. [1] However, whether used for long-haul or short-haul communication (e.g. PON), coherent receivers have high requirements on LO laser performance, such as narrower linewidth, and better wavelength stability. A lot of work has been done to stabilize the laser wavelength. For the commercialized laser module, a temperature-controlled external cavity is commonly applied. By locking the laser wavelength to the cavity through a photodetector and feedback circuits, the laser wavelength can be controlled within hundreds of MHz range. Work has also been done using optical injection phase-locked loop (OIPLL) [2]. By applying an OIPLL, the slave laser can stably injection lock to the reference laser or comb lines without an offset frequency.

Research on OPLL's started more than 50 years ago, but has proven to be difficult, mainly because of the loop delay and therefore the limited loop bandwidth. Although the loop bandwidth has been improved from MHz range to 200-300 MHz range [3,4] because of photonic integration, it is still not enough to maintain stable locking with small perturbations. A 0.2 K temperature change will easily make the OPLL lose locking. Therefore, it is not feasible to stabilize laser frequency using existing OPLLs.

In this paper, we propose and demonstrate an optical phase-locked loop with phase/frequency detection [5]. By incorporating both a phase detector and a frequency detector, the loop pull-in range and hold-in range become much larger compared to a traditional optical phase-locked loop with only a phase detector. Therefore, this OPLL is much easier to get phase locked and also more resistive to temperature fluctuation. The architecture of the system is shown in Fig. 1. Reference laser and slave tunable laser are mixed in a 90 degree hybrid. The in-phase and quadrature signals are then

generated and detected by four high-speed photodetectors. Trans-impedance limiting amplifiers, a single-sideband mixer, a phase/frequency detector (PFD) and an active loop filter are used in the electronic feedback path.

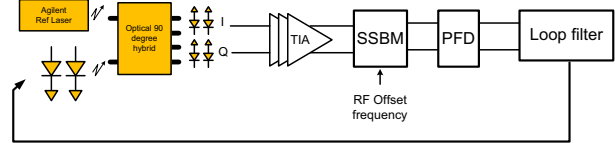


Fig. 1. The architecture of the optical phase-locked loop.

The system is composed of three blocks: a photonic integrated circuit (PIC), an electronic integrated circuit (EIC) and a loop filter (LF).

On the PIC, a widely-tunable sampled-grating distributed Bragg reflector (SG-DBR) laser, a star-coupler-based 90 degree hybrid, four quantum well photodetectors and four microstrip transmission lines were integrated [5]. A centered quantum well InGaAsP/InP integration platform was chosen to integrate all these optical components monolithically. The EIC is composed of limiting amplifiers, a digital single-sideband mixer and a phase/frequency detector as shown in Fig. 1. The phase/frequency detector is based on an RF delay line and an XOR gate [6], which is basically a quadri-correlator frequency detector. The EIC was fabricated using Teledyne's standard 500nm HBT fabrication line, and the f_{\max} of each transistor is 300 GHz. The details about the EIC are discussed elsewhere [6]. Loop filter was built on an AlN carrier using an operational amplifier and discrete surface-mount components.

The photonic IC, the electronic IC and a loop filter are closely interconnected via wire bonding, and the size of the whole OPLL is within one or two centimeter square. The test setup as well as the picture of the OPLL is shown in Fig. 2. We used a 100 kHz-linewidth Agilent external-cavity tunable laser as the reference laser and coupled into the PIC using a lensed fiber. The SG-DBR laser was coupled it out through the back mirror for monitoring purpose. The frequency of the free running SG-DBR laser drifts within hundreds of MHz range, and the linewidth is also much wider than that of the reference laser.

The open-loop response was first measured. By fixing the beating tone of the two lasers at 6 GHz and sweeping the RF

offset frequency, the output of the PFD was shown in Fig. 3. The frequency detection curve crosses zero volt point around 12 GHz, which is double of the locking frequency as designed.

The OPLL submount temperature is controlled by a thermoelectric temperature controller. The free-running SG-DBR laser shows 13.68 GHz/K temperature tuning sensitivity.

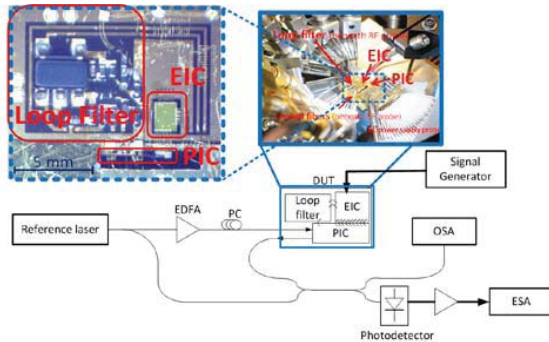


Fig. 2. The schematic of the OPLL test setup is shown in the lower part of this figure. Thinner lines indicate fiber connections and thicker lines show the RF cable connections. Pictures of the OPLL are also shown.

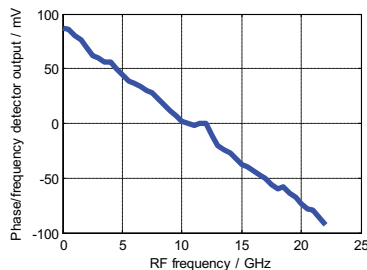


Fig. 3. Frequency detector open-loop response curve. The two lasers are offset by 6 GHz.

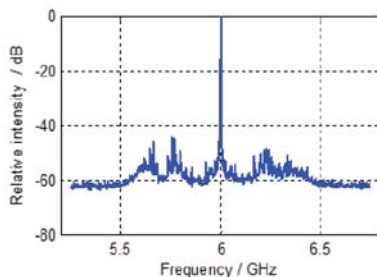


Fig. 4. The beating tones of the two lasers when the offset frequency is 6 GHz, measured with 5 kHz resolution bandwidth.

The electrical spectrum analyzer data of the beating between the reference and the locked slave laser is shown in Fig. 4, where the offset frequency is 6 GHz. By changing the RF reference frequency, we continuously shifted the SG-DBR frequency within the range from -9.5 GHz to -1.5 GHz, and also from 1.5 GHz up to 7.5 GHz with phase locking to the reference laser, respectively. [5] The phase-locked SG-DBR laser has the same wavelength stability as the Agilent reference laser and the linewidth has also been greatly improved as

indicated in Fig. 4. After phase locking the on-PIC SG-DBR laser to a reference laser with 6 GHz frequency offset, we tuned the submount temperature. The original submount temperature was set at 12°C. Typically a change in temperature leads to material dielectric index changes, therefore causing a wavelength shift of the laser. In this case, the feedback loop changes the current injected to the laser phase section accordingly to compensate for the temperature-dependent index change, keeping the laser wavelength stable and in lock. While tuning the temperature from 11.9 °C to 14.1 °C, the OPLL kept in locking status. The wavelength of the locked SGDBR is line narrowed and held constant for temperature changes up to 2.2 K--whereas an unlocked laser would drift by > 30 GHz. The measured voltage on the laser phase tuning diode is shown in Fig. 5. By applying the IV curve of the phase tuning diode, the temperature and current relation can be obtained (Fig. 5). At 11.8 °C and 14.2 °C, cavity mode hopping was observed so the OPLL lost locking at those temperatures.

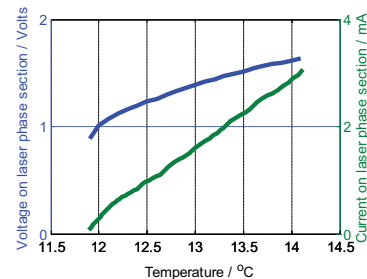


Fig. 5. DC voltage measured on the phase-locked SG-DBR laser phase tuning diode at different submount temperature. Current is obtained from the IV curve of the laser phase tuning diode.

In conclusion, by adopting a phase/frequency detector in the OPLL system, large frequency pull-in and hold-in ranges have been achieved. The wavelength of the locked SG-DBR laser is resistant to temperature fluctuations up to 2.2 °C.

Reference:

- [1] Frowin Derr, "Coherent optical QPSK intradyne system: concept and digital receiver realization," *Journal of Lightwave Technology*, Vol. 10, Issue 9, pp. 1290-1296 (1992).
- [2] L. A. Johansson and A. J. Seeds, "Generation and Transmission of Millimeter-Wave Data-Modulated Optical Signals Using an Optical Injection Phase-Lock Loop," *Journal of Lightwave Technology*, Vol. 21, Issue 2, pp. 511-520 (2003).
- [3] Sasa Ristic, Ashish Bhardwaj, Mark J. Rodwell, Larry A. Coldren, and Leif A. Johansson, "An Optical Phase-Locked Loop Photonic Integrated Circuit," *Journal of Lightwave Technology*, Vol. 28, Issue 4, pp. 526-538 (2010).
- [4] Robert J. Steed, et. al., "Monolithically integrated heterodyne optical phase-lock loop with RF XOR phase detector," *Optics Express*, Vol. 19, Issue 21, pp. 20048-20053 (2011)
- [5] Mingzhi Lu, Hyunchul Park, Eli Bloch, Abirami Sivananthan, Ashish Bhardwaj, Zach Griffith, Leif A. Johansson, Mark J. Rodwell, and Larry A. Coldren, "Highly integrated optical heterodyne phase-locked loop with phase/frequency detection," *Optics Express*, Vol. 20, Issue 9, pp. 9736-9741 (2012)
- [6] Eli Bloch, Hyunchul Park, Mingzhi Lu, Thomas Reed, Zach Griffith, Leif Johansson, Larry Coldren, Dan Ritter, and Mark Rodwell, "A 1-20 GHz InP HBT phase-lock-loop IC for optical wavelength synthesis," Accepted by IEEE Int. Micro. Symposium (2012).

A Photonic Integrated Circuit for a 40 Gbaud/s Homodyne Receiver Using an Optical Costas Loop

Mingzhi Lu¹, Hyunchul Park¹, Eli Bloch², Abirami Sivananthan¹, John Parker¹, Zach Griffith³, Leif A. Johansson¹, member, IEEE, Mark J. Rodwell¹, Fellow, IEEE, and Larry A. Coldren¹, Fellow, IEEE

¹Department of Electrical and Computer Engineering, University of California, Santa Barbara, CA, 93106, USA.

²Department of Electrical Engineering, Technion – Israel Institute of Technology, Haifa 32000, Israel.

³Teledyne Scientific and Imaging Company, Thousand Oaks, 1049 Camino Dos Rios, CA, 91360, USA.

Email: mlu@ece.ucsb.edu

Abstract—A highly-integrated optical Costas loop has been realized within a footprint of $10 \times 10 \text{ mm}^2$ by using a photonic integrated circuit. 40 Gbaud/s data demodulation has been achieved.

Keywords- photonic integration, coherent receiver; Costas loop; phase-locked loop

Coherent fiber optic communication is receiving a lot of interest recently. Compared to traditional optical receivers that are used for direct detection, coherent receivers have many advantages. They have high bandwidth efficiency, are more tolerant to noise, and are compatible with different modulation formats (such as multi-level amplitude/phase shift keying) [1-2]. Most efforts focusing on long-haul and metro systems today use an intradyne approach in which a free running local oscillator (LO) laser is mixed with the incoming signal, and digital signal processing is required to track the drift in the relative phase between the LO laser and the incoming laser signal. The high-speed digital signal processors that are being used for this have very high power consumption, limited speed, and high cost. In this work, we present the 40 Gbaud/s integrated homodyne coherent receiver with a simple architecture and low power consumption.

Although considerable research on homodyne phase-locked coherent receivers has been carried out [3-4], it was proved hard to implement because of the loop delay [3,5]. In terms of loop stability, a 100 MHz open-loop bandwidth requires roughly 1 ns loop delay, which is not feasible with fiber pigtailed components or micro optics.

In this work, a highly integrated Costas loop is proposed and demonstrated. By photonic and electronic integration, the whole receiver is realized within a footprint of $10 \text{ mm} \times 10 \text{ mm}$ area, and 120 ps loop delay is achieved. The architecture of the Costas loop is shown in Fig. 1. The receiver consists of three main parts: a photonic integrated circuit (PIC), and an electronic integrated circuit (EIC) and a hybrid loop filter.

The incoming signal and the LO are mixed in the optical 90 degree hybrid, and I/Q signals are generated on four photodetectors. The I/Q signals are mixed at the XOR gate on the EIC, and therefore the data-OPLL cross-talk is eliminated by the phase doubling. The XOR gate together with the delay

line works as a quadric-correlator frequency detector, and the XOR itself also acts as a phase detector. The phase/frequency error signals are then fed back to the laser phase tuning section through the loop filter.

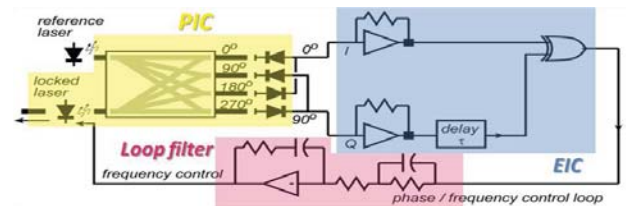


Fig. 1. The architecture of the OPLL.

On the PIC, a widely tunable sampled-grating DBR (SG-DBR) laser, a directional-coupler-based 90 degree hybrid, four uni-travelling-carrier (UTC) photodetectors and microstrip transmission lines are integrated monolithically. A centered-QW InGaAsP/InP integration platform is chosen, quantum well intermixing technology is used to define the active and passive area, and electron-beam lithography is applied to define the gratings. A blanket UTC layer regrowth and a blanket P-cladding regrowth are carried out, followed by waveguide definition using Methane/Hydrogen/Argon reactive-ion etching (RIE), and HCl-based crystallographic wet etch. This is followed by N-mesa definition and N-contact metal deposition. Helium implantation is used to isolate photodetectors. BCB is used as the dielectric for the RF transmission lines. Capacitors are also integrated for photodetector high-speed performance. After P-metal and pad metal deposition, the wafer is lapped down to $120 \mu\text{m}$ thick and cleaved. The picture and the cross sections of the fully-fabricated PIC are shown in Fig. 2 (a), (b).

The testing results show that the on-PIC SG-DBR laser can output around 30 mW power, measured by reverse biasing the boosting SOA on PIC. The tuning range is 40 nm and the threshold current is 30 mA. The UTC photodetectors have a 30 GHz 3-dB bandwidth. The measured data is shown in Fig. 3(c). There is no I/Q phase error introduced by the optical 90 degree hybrid. The four photodetectors have more than 1 mA AC current output with 4% power imbalance. The size of the PIC is $4.3 \text{ mm} \times 0.54 \text{ mm}$, and the light propagation delay is only 40 ps.

As for the EIC, four limiting amplifiers were integrated as the frond-end. A delay line and XOR gate are used as the

phase/frequency detector for the phase locking, and also act as the mixer for recovering the carrier phase. The loop filter is made on an AlN substrate using surface-mount components, including an operational amplifier. More detailed information about EIC and the loop filter can be found in [6].

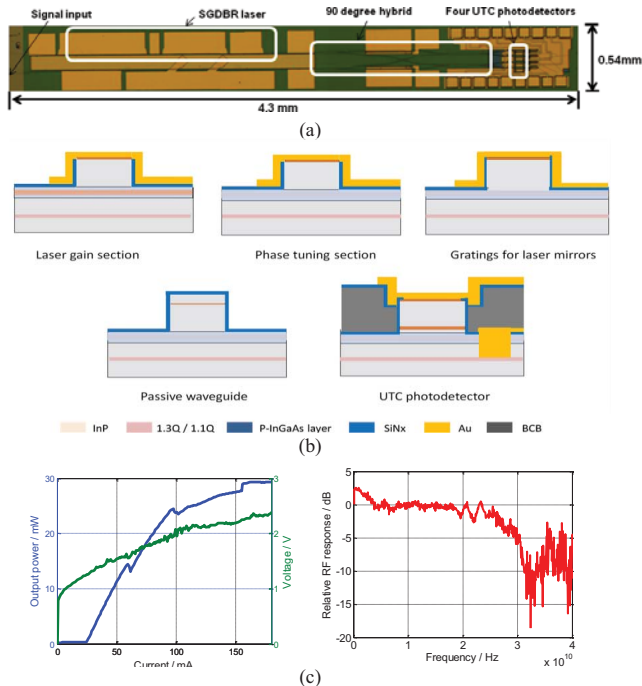


Fig. 2. (a) A microscope picture of the PIC; (b) shows the cross sections of the fabricated devices. (c) L-I-V curve of the SG-DBR laser and the bandwidth of the UTC photodetector.

The PIC, EIC, and loop filter are connected together using wirebonds. Because of the highly integration, a 120 ps total loop delay is achieved in this feedback system, and the designed closed-loop bandwidth is around 1 GHz.

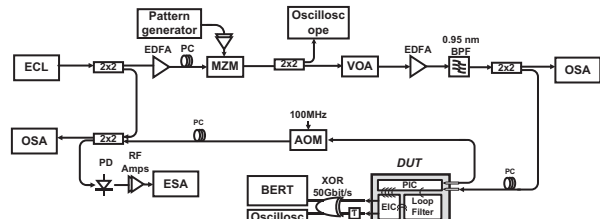


Fig. 3. The schematics of the test setup. (ECL: external-cavity laser, OSA: optical spectrum analyzer, ESA: electrical spectrum analyzer, MZM: Mach-Zehnder modulator, VOA: variable optical attenuator, PC: polarization controller, AOM: acousto-optic modulator, BERT: bit error rate tester, PD: photodetector.)

The experimental setup is shown in Fig. 3. $2^{31}-1$ PRBS data is applied to the transmitting laser using the NRZ BPSK format. A VOA and an EDFA are used to control the OSNR of the received signal. The BPSK signal is coupled into the PIC through a lensed fiber, and the power of the SG-DBR laser is coupled out through another lensed fiber, and beat with the transmitting laser on a high-speed photodetector for the monitoring purpose. Bit error rates (BERs) are also measured.

Due to the phase ambiguity of the Costas loop, a differential decoding circuit is applied. No differential encoding circuit is used in this system simply because the differential of PRBS is PRBS itself.

We successfully locked the SG-DBR laser to the transmitting laser. The beating spectrum measured by the ESA showed 1.1 GHz closed-loop bandwidth. BER is also measured with various OSNR of the input signal. Error free ($BER < 10^{-12}$) is achieved with a data rate up to 35 Gbit/s. Both measured BER and the theoretical BER are plotted in Fig. 4, and the difference between them is mainly due to the noise figure of on-PIC SOAs and on-EIC TIAs. The power consumption of the system is around 3 Watt, not including the TEC cooling.

More detailed information will be presented at the conference.

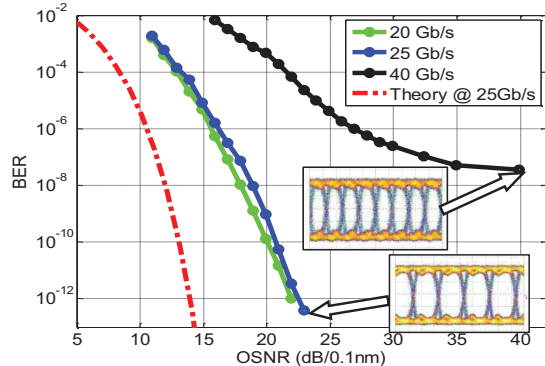


Fig. 4. BER vs. OSNR for 20 Gbit/s, 25 Gbit/s and 40 Gbit/s and the theoretical curve. Eye diagrams are also shown for 25 Gbit/s and 40 Gbit/s.

Acknowledgment

This work is mainly supported by DARPA PICO project. A portion of this work was done in the UCSB nanofabrication facility, part of the National Science Foundation (NSF) funded NNIN network.

Reference:

- [1] Frowin Derr, "Coherent optical QPSK intradyne system: concept and digital receiver realization," *Journal of Lightwave Technology*, vol. 10, Issue 9, 1992, pp. 1290-1296.
- [2] Andreas Beling, Norbert Ebel, Andreas Matiss, Günter Unterbörtsch, Markus Nölle, Johannes K. Fischer, Jonas Hilt, Lutz Molle, Colja Schubert, Frederic Verluise, and Ludovic Fulop, "Fully-Integrated Polarization-Diversity Coherent Receiver Module for 100G DP-QPSK," *Optical Fiber Communication Conference, Coherent I (OML)*, 2011.
- [3] Leonid G. Kazovsky, "Decision-driven phase-locked loop for optical homodyne receivers: Performance analysis and laser linewidth requirements," *Journal of Lightwave Technology*, vol. LT-3, No. 6, 1985.
- [4] Takahide Sakamoto, Akito Chiba, Atsushi Kanno, Isao Morohashi, Tetsuya Kawanishi, "Real-Time Homodyne Reception of 40-Gb/s BPSK Signal by Digital Optical Phase-Locked Loop," *ECOC*, P3.12, 2010.
- [5] Michael A. Grant, W. Craig Michie, Michael J. Fletcher, "The performance of optical phase-locked loops in the presence of nonnegligible loop propagation delay," *Journal of Lightwave Technology*, vl. LT-5, No. 4, 1987.
- [6] Hyun-chul Park, Mingzhi Lu, Eli Bloch, Thomas Reed, Zach Griffith, Leif Johansson, Lary Coldren, and Mark Rodwell, "40Gbit/s Coherent Optical Receiver Using a Costas Loop," *ECOC*, post-deadline, 2012.

40Gbit/s coherent optical receiver using a Costas loop

Hyun-chul Park,^{1,*} Mingzhi Lu,¹ Eli Bloch,² Thomas Reed,¹ Zach Griffith,³
Leif Johansson,¹ Larry Coldren,¹ and Mark Rodwell¹

¹ECE Department, University of California at Santa Barbara, Santa Barbara, CA 93106-9560, USA

²Department of Electrical Engineering, Technion – Israel Institute of Technology, Haifa 32000, Israel

³Teledyne Scientific & Imaging Company, 1049 Camino Dos Rios, Thousand Oaks, CA 91360, USA

*hcpark@ece.ucsb.edu

Abstract: A highly integrated 40Gbit/s coherent optical receiver is reported using a Costas loop as a homodyne optical phase locked loop (OPLL). A photonic IC, an electrical IC, and a hybrid loop filter are characterized, and the feedback loop system is fully analyzed to build a stable homodyne OPLL. All components are integrated on a single substrate within the compact size of $10 \times 10\text{mm}^2$, and a 1.1GHz loop bandwidth and a 120ps loop delay are achieved. The binary phase-shift keying receiver exhibits error-free ($\text{BER} < 10^{-12}$) up to 35Gbit/s and $\text{BER} < 10^{-7}$ for 40Gbit/s with no latency, and consumes less than 3W power.

©2012 Optical Society of America

OCIS codes: (060.1660) Coherent communications; (250.5300) Photonic integrated circuits; (350.4010) Microwaves.

References and links

1. K. Kikuchi, "Coherent optical communications: historical perspectives and future directions," in *High spectral Density Optical Communication Technology*, (Springer, 2010), Chap. 2.
2. G. Li, "Recent advances in coherent optical communication," *Adv. Opt. Photon.* **1**(2), 279–307 (2009).
3. K. Kikuchi, M. Fukase, and S. Kim, "Electronic post-compensation for nonlinear phase noise in a 1000-km 20-Gbit/s optical QPSK transmission system using the homodyne receiver with digital signal processing," OFC'2007 conference, OTuA2 (2007).
4. White paper - Driving 100G to the metro: <http://www.multi-phy.com/en-us/home.aspx>.
5. T. Sakamoto, A. Chiba, A. Kanno, I. Morohashi, and T. Kawanishi, "Real-time homodyne reception of 40-Gb/s BPSK signal by digital optical phase-locked loop," ECOC'2010 conference, P3.12 (2010).
6. M. Grant, W. Michie, and M. Fletcher, "The performance of optical phase locked loops in the presence of nonnegligible loop propagation delay," *J. Lightwave Technol.* **5**(4), 592–597 (1987).
7. T. Hodgkinson, "Costas loop analysis for coherent optical receivers," *Electron. Lett.* **22**(7), 394–396 (1986).
8. L. Kazovsky, "Balanced phase-locked loops for optical homodyne receivers: performance analysis, design considerations, and laser linewidth requirements," *J. Lightwave Technol.* **4**(2), 182–195 (1986).
9. S. Norimatsu and K. Iwashita, "PLL Propagation delay-time influence on linewidth requirements of optical PSK homodyne detection," *J. Lightwave Technol.* **9**(10), 1367–1375 (1991).
10. S. Ristic, A. Bhardwaj, M. Rodwell, L. Coldren, and L. Johansson, "An optical phase-locked loop photonic integrated circuit," *J. Lightwave Technol.* **28**(4), 526–538 (2010).
11. R. J. Steed, F. Pozzi, M. J. Fice, C. C. Renaud, D. C. Rogers, I. F. Lealman, D. G. Moodie, P. J. Cannard, C. Lynch, L. Johnston, M. J. Robertson, R. Cronin, L. Pavlovic, L. Naglic, M. Vidmar, and A. J. Seeds, "Monolithically integrated heterodyne optical phase-lock loop with RF XOR phase detector," *Opt. Express* **19**(21), 20048–20053 (2011).
12. M. Lu, H. Park, E. Bloch, A. Sivanathan, A. Bhardwaj, Z. Griffith, L. A. Johansson, M. J. Rodwell, and L. A. Coldren, "Highly integrated optical heterodyne phase-locked loop with phase/frequency detection," *Opt. Express* **20**(9), 9736–9741 (2012).
13. H. Philipp, A. Scholtz, E. Bonek, and W. Leeb, "Costas loop experiments for a 10.6 μm communications receiver," *IEEE Trans. Commun.* **31**(8), 1000–1002 (1983).
14. S. Norimatsu, K. Iwashita, and K. Sato, "PSK optical homodyne detection using external cavity laser diodes in Costas loop," *IEEE Photon. Technol. Lett.* **2**(5), 374–376 (1990).
15. L. Kazovsky, "Decision-driven phase-locked loop for optical homodyne receivers: performance analysis and laser linewidth requirements," *J. Lightwave Technol.* **3**(6), 1238–1247 (1985).
16. V. Ferrero and S. Camatel, "Optical phase locking techniques: an overview and a novel method based on single side sub-carrier modulation," *Opt. Express* **16**(2), 818–828 (2008).

17. H. Park, M. Lu, E. Bloch, T. Reed, Z. Griffith, L. Johansson, L. Coldren, and M. Rodwell, "40Gbit/s coherent optical receiver using a Costas loop," ECOC'2012 conference, PD Th.3.A, (2012).
 18. M. Lu, H. Park, E. Bloch, A. Sivananthan, J. Parker, Z. Griffith, L. A. Johansson, M. Rodwell, and L. Coldren, "A photonic integrated circuit for a 40 Gbaud/s homodyne receiver using an optical Costas loop," IPC'2012 conference, PD-4, (2012).
 19. M. Urteaga, R. Pierson, P. Rowell, M. Choe, D. Mensa, and B. Brar, "Advanced InP DHBT process for high speed LSI circuits," IPRM 2008. 20th International conference, 1–5 (2008).
 20. D. G. Messerschmitt, "Frequency detectors for PLL acquisition in timing and carrier recovery," IEEE Trans. Commun. **27**(9), 1288–1295 (1979).
 21. E. Bloch, H. Park, M. Lu, T. Reed, Z. Griffith, L. Johansson, L. Coldren, D. Ritter, and M. Rodwell, "A 1-20 GHz all-Digital InP HBT optical wavelength synthesis IC," IEEE Trans. Microw. Theory Tech. (to be published).
 22. R. C. Walker, "Designing bang-bang PLLs for clock and data recovery in serial data transmission systems," in phase-locking in high-performance systems, B. Razavi, Ed. New York: IEEE Press, 34–45 (2003).
 23. J. Crossley and E. Alon, "An energy-efficient Digital phase-locked loop with linear phase control," (2010), <http://bwrc.eecs.berkeley.edu/php/pubs/pubs.php/1294.html>.
-

1. Introduction

Digital coherent optical communication has been revived due to demand for increasing data-rates with high spectral efficiency and its superior sensitivity [1,2]. Recently, the majority of optical receivers use coherent detection based on high speed digital signal processing (DSP), because high data-rate signals can reach long distances even more than 1000km by compensating dispersion and other non-linear effects in the presence of DSPs [1–3]. On the other hand, short distance Ethernet networks for metro and access networks use intensity-modulation and direct-detection, because it might be redundant to use complicated analog-to-digital convertors (ADCs) and DSPs, and power consumption and product cost issues should also be considered [4]. The Costas loop by simple feedback loop configuration could be a promising solution for high speed optical receivers with energy efficiency and low cost.

However, the Costas loop as a homodyne optical phase locked loop (OPLL) has been regarded challenging because of long delay in the feedback loop due to the bulk size of photonic, electrical, and loop filter components [1,5]. This long loop delay limits the loop bandwidth which determines phase-noise suppression range for the local oscillator (LO) laser and track / hold ranges against received carrier signals. In this case, the OPLL requires stable and narrow linewidth reference sources for both the LO and transmitting lasers to keep a proper receiver system operation within a stable phase lock [6–9].

Recently, many OPLL researches have reported a relatively stable feedback loop using integration technology. A homodyne OPLL using a high speed HEMT for a small delay loop filter with a loop bandwidth of 300MHz [10], a heterodyne OPLL using an RF exclusive-OR (XOR) as a phase detector with loop delay of 1.8ns [11], and a highly integrated heterodyne OPLL using an integrated single side band mixer and a phase frequency detector (PFD) with delay of 0.2ns and closed loop bandwidth of 550MHz [12] have been published. OPLL based coherent optical receivers have been also developed. Costas receivers using homodyne OPLLs with below 10Gbit/s [13,14], decision-driven loops including sub-carrier modulation scheme [15,16], and a digital OPLL using a sampled I-Q signals with slow DSP for homodyne reception of PSK 40Gbit/s [5] have been published. However, the receivers still require a narrow linewidth on LO and transmitting lasers due to a narrow loop bandwidth, and they may need additional blocks such as voltage controlled oscillators, a Mach-Zehnder modulator, an optical filter, and even ADCs and DSPs to recover the carrier signal.

In this paper, as an extension of [17], a 40Gbit/s coherent optical receiver using a Costas loop is demonstrated. The characteristics of each components and feedback loop are fully analyzed to optimize the OPLL system with a novel loop filter design topology. The receiver is realized within a compact size of $10 \times 10\text{mm}^2$, and it exhibits a closed loop bandwidth of 1.1GHz and loop delays of 120ps. In addition, the digitally operating electrical circuits make the OPLL more robust against photocurrent fluctuations, and the PFD extends phase-lock and frequency pull-in ranges. As a result, a stable OPLL and binary phase-shift keying (BPSK)

coherent receiver error-free ($BER < 10^{-12}$) up to 35Gbit/s and $BER < 10^{-7}$ for 40Gbit/s are achieved. The BPSK receiver consumes less than 3W power.

2. A homodyne OPLL and loop analysis

A homodyne OPLL is designed with the concept of the schematics shown in Fig. 1. It mainly consists of a photonic integrated circuit (PIC), an electrical integrated circuit (EIC), and a hybrid loop filter.

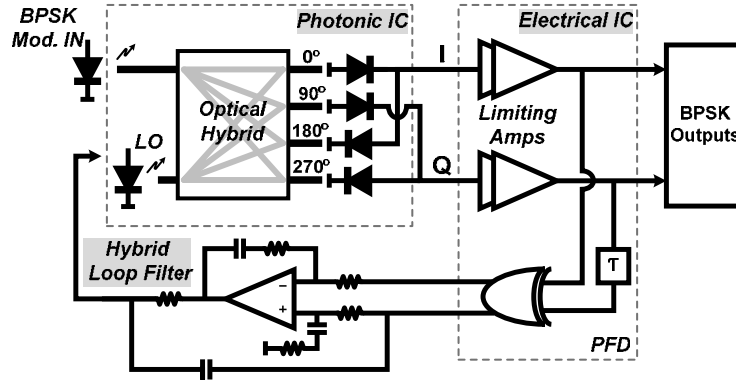


Fig. 1. A concept schematic for a homodyne OPLL structure using a Costas loop.

2.1 Photonic integrated circuit (PIC)

The fabricated PIC is based on the InGaAsP/InP platform. The PIC includes a widely tunable sampled grating distributed Bragg reflector (SG-DBR) laser which can be tuned over a 40nm wavelength span by current injection into front / back mirrors and a phase tuning section diode. The received signal and LO laser are mixed by an integrated 90° optical hybrid and down-converted by four uni-traveling carrier PDs for I-Q electrical outputs. The fabricated optical hybrid has $\pm 2\%$ imbalanced outputs and the PDs exhibit a 3-dB bandwidth of 30GHz and 18mA saturation current at $-5V$. The PIC chip size is $4.30 \times 0.56\text{mm}^2$ and has 40ps propagation delay. The details about this PIC can be found in [18].

2.2 Electrical integrated circuit (EIC)

The EIC has been designed using Teledyne's 500nm HBT process which has 300GHz f_t and f_{max} [19]. It includes input biasing circuits to supply $-2V$ bias on PIC PDs with 50Ω interface. Limiting amplifiers (LIAs) limit the PD outputs to 0.3Vp-p digitized signals containing only phase and frequency error information. Due to digital operations in the feedback system by LIAs, the OPLL system becomes less sensitive to the PIC's intensity variations. A PFD is composed of an XOR with a 10ps delay-line, which is called the quadricorrelator type, to cover a 50GHz frequency pull-in range [20]. The EIC chip size is $1.30 \times 1.20\text{mm}^2$ and has a 50ps propagation delay. The details about this EIC can be found in [21].

2.3 Hybrid loop filter

The hybrid loop filter has been implemented using a feed-forward technique consisting of an integrator for a main path and a differentiator for a feed-forward path. A bulk operational amplifier (OPA) is used to obtain high gain at DC and low frequencies, but the OPA has long delay which could limit the bandwidth of OPLLs. In order to minimize the delay effect, a passive capacitor is added on the feed forward path for only high frequencies. As a result, the effective loop delay by the loop filter becomes negligible, and the loop bandwidth is only limited by the delay from PIC, EIC, and interconnections (30ps) [17].

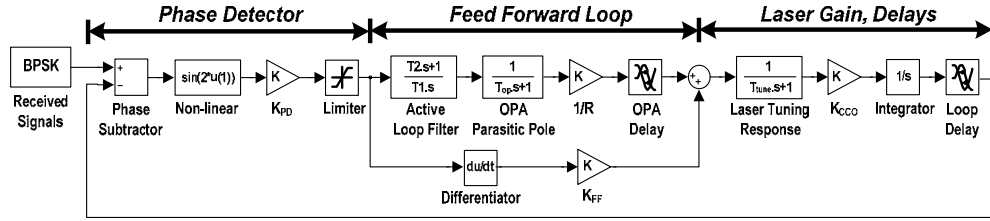


Fig. 2. Modeling for the OPLL analysis.

2.4 Feedback loop analysis

A phase based feedback loop analysis has been conducted using Matlab Simulink as shown in Fig. 2. A phase detector is modeled by sinusoidal and hard limiting non-linear function for the LIA chain and XOR-type binary phase detection [22]. The feed-forward loop is modeled with two independent paths. The integrator path includes a first order active loop filter, OPA's second order pole, a resistor, and the OPA delay. The differentiator path has a zero, and a coupling gain determined by a capacitor value. The feed-forward loop must avoid 180° phase difference between two paths to prevent an amplitude notch at the crossover frequency. In addition, a laser slow tuning response, laser tuning sensitivity, an integrator for frequency to phase transform, and total effective loop delay are modeled as shown in Fig. 2. Based on the model parameters, the open loop response $T(s)$ is expressed as

$$T(s) = K_{PD} \cdot K_{CCO} \cdot \frac{1}{\tau_{tune}s + 1} \cdot \left(\frac{\tau_2s + 1}{\tau_1s^2} \cdot \frac{1}{\tau_{op}s + 1} \cdot \frac{1}{R} \cdot e^{-\tau_{d,op}s} + \frac{C_{FF}}{2} \right) \cdot e^{-\tau_d s}, \quad (1)$$

where a linear equivalent phase detection gain $K_{PD} = 0.2 \sim 0.4 \text{ V/rad}$, a laser tuning sensitivity $K_{CCO} = 5.0 \times 10^{13} \text{ rad/sec/A}$, a laser slow tuning response τ_{tune} as a pole at 100MHz, active loop filter pole τ_1 and zero τ_2 determined at 0.17MHz and 2.2MHz, respectively, an OPA's second pole τ_{OP} at 200MHz, a resistor R of 500Ω, an OPA's delay $\tau_{d,OP}$ of 200ps, a coupling capacitor on feed-forward path C_{FF} of 1.0pF, and a total effective loop delay τ_d of 120ps are characterized. Especially, non-linear phase detector gain K_{PD} is approximated and optimized with a linear equivalent gain [23]. The open loop response $T(s)$ for the OPLL is obtained as shown in Fig. 3, and it shows that the total loop response follows the main path at low frequencies and the feed-forward path at high frequencies. From the response, the feedback loop response shows a natural frequency ω_n of $4.4 \times 10^9 \text{ rad/sec}$ (700MHz) and 65° phase margin.

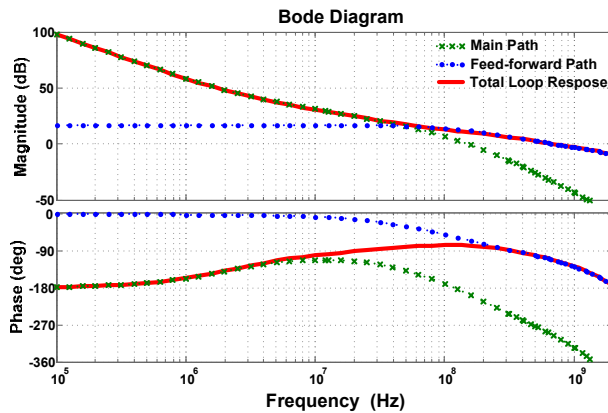


Fig. 3. A Bode diagram for the OPLL open loop response $T(s)$.

3. Implementation and experiment results

3.1 Integration for the OPLL

The OPLL for Costas loop receiver is realized as shown in Fig. 4. The fabricated PIC on the top, the EIC on the bottom left, and the hybrid loop filter on the bottom right are mounted on a single AlN substrate ($\epsilon_r = 9$ and thermal conductivity = 140~180W/m/K) within the total size of $10 \times 10\text{mm}^2$. They are connected by wire-bonds and transmission lines, and the feed-forward path (red arrow shown in Fig. 4) is minimized to decrease their interconnection delay. The loop filter uses a commercial voltage feedback OPA, Texas Instruments' LMH6609, which has 70dB open loop gain and 200MHz unity gain bandwidth. Together with discrete chip capacitors and resistors, the active loop transfer function has been realized.

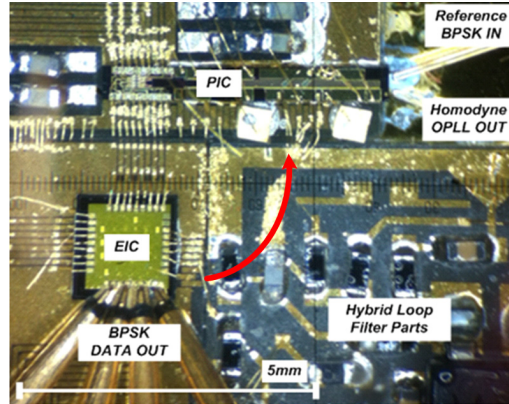


Fig. 4. A photograph of the Costas loop based on a homodyne OPLL receiver (Red arrow: feed-forward path).

3.2 Homodyne OPLL experiments

The homodyne OPLL has been tested to measure the closed loop bandwidth and locked SG-DBR laser linewidth performance. The test setup for the OPLL is explained in [17], and the OPLL has a 1.1GHz closed loop bandwidth as shown in Fig. 5(a), which is the widest loop bandwidth to the best of our knowledge. Peak beat tone is shown at 100MHz, and two side peak tones represent the closed loop bandwidth because of under damping shown at 1GHz – left peak as an image frequency and 1.2GHz – right peak as a real frequency. The linewidths for the un-locked SG-DBR laser, locked SG-DBR laser, and reference laser are measured and compared, as shown in Fig. 5(b), using a self-heterodyne linewidth measurement technique. The un-locked SG-DBR laser shows a broad linewidth of 10MHz, but the locked SG-DBR laser exhibits a linewidth of 100kHz which is the same as the reference laser linewidth. As a result, the wide loop bandwidth suppresses the SG-DBR laser's phase noise for broad frequency range, extends track and hold range against the received laser's carrier frequency drifts, and the Costas loop can catch the received laser carrier phase.

3.3 BPSK receiver experiments

To prove the Costas loop receiver performance, eye outputs and bit-error-ratio (BER) performance are measured. This test setup for the BPSK demodulation is explained in [17], and Figs. 6(a) and 6(b) show received open eye patterns for 25Gbit/s and 40Gbit/s, respectively. BER vs. optical signal-to-noise ratio (OSNR) is shown in Fig. 6(c), and it exhibits superior performance of error-free ($\text{BER} < 10^{-12}$) up to 35Gbit/s and $\text{BER} < 10^{-7}$ performance for 40Gbit/s. In addition, as shown in Fig. 5(b), the linewidth of the locked SG-DBR laser with 25Gbit/s BPSK data shows the same linewidth performance as the locked SG-DBR laser and the reference laser. This means that the Costas loop with a 25Gbit/s BPSK

data modulation can restore the carrier phase without degrading the linewidth and data reception performance.

This receiver system consumes less than 3W power (PIC < 0.5W, EIC < 2.2W, and loop filter < 0.1W), not including a thermoelectric controller power.

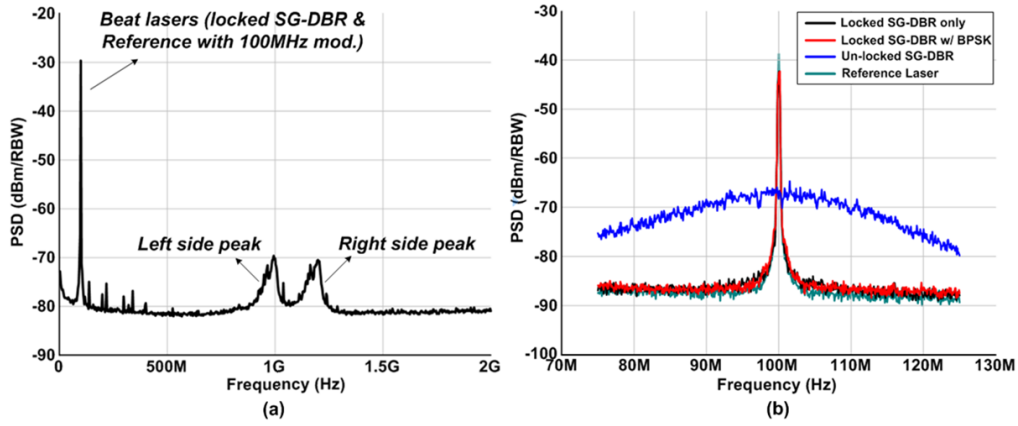


Fig. 5. Homodyne OPLL measurement results (a) Beat spectrum between the reference laser and locked SG-DBR laser, and (b) Measured linewidths: locked SG-DBR laser without BPSK modulation, locked SG-DBR laser with BPSK modulation, un-locked SG-DBR laser, and reference laser.

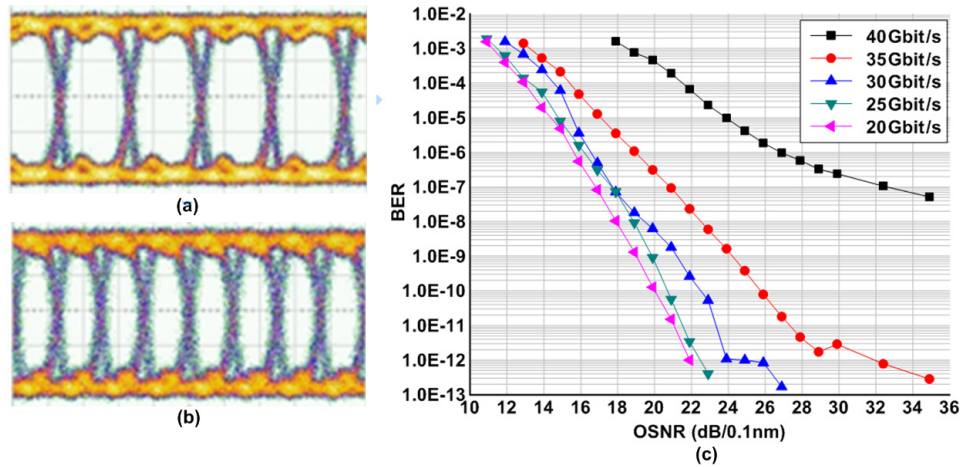


Fig. 6. BPSK data reception tests: (a) Received eye output for 25Gbit/s, (b) Received eye output for 40Gbit/s, and (c) BER vs. OSNR from 20Gbit/s to 40Gbit/s.

4. Conclusion

For the first time, a highly integrated homodyne OPLL based coherent optical receiver has been demonstrated using a Costas loop. A stable OPLL has been achieved within the compact size of $10 \times 10\text{mm}^2$, closed loop bandwidth of 1.1GHz, and 120ps loop propagation delay. The BPSK receiver based on the Costas loop exhibits error-free ($\text{BER} < 10^{-12}$) up to 35Gbit/s and $\text{BER} < 10^{-7}$ for 40Gbit/s. The receiver consumes less than 3W power. It might be a promising option for coherent optical receivers in short or mid distance optical communication with low power and low cost.

Acknowledgment

This work was supported by the Photonic Integration for Coherent Optics (PICO) through DARPA. A portion of this work was done in the UCSB nanofabrication facility, part of the NSF funded NNIN network. The author would like to thank Teledyne Scientific Company for EIC fabrications.

I. Photonic Integrated Circuits

D. Coherent Beam Steering PICs

Free-space Beam Steering in Two Dimensions Using a Silicon Optical Phased Array

J. K. Doyle^{*}, M. J. R. Heck, J. T. Bovington, J. D. Peters, L. A. Coldren, J. E. Bowers

Dept. of Electrical and Computer Engineering, University of California, Santa Barbara, California 93106, USA

[*doylend@ece.ucsb.edu](mailto:doylend@ece.ucsb.edu)

Abstract: We report an independently tuned 16-channel optical phased array fabricated in silicon for 2D free-space beam steering. The phased array was composed of silicon-on-insulator waveguide surface gratings integrated with thermo-optic phase tuners and was operated both using a control algorithm together with automated real-time far field image analysis to target and shape the beam, and using a lookup table without real-time feedback. The device exhibited $1.6^\circ \times 0.6^\circ$ beam width and 10 dB background suppression in the far field across a $20^\circ \times 14^\circ$ field of view. We show that by increasing the waveguide width from 1 μm to 3 μm we can suppress the side-lobe peaks by a factor of 2.

OCIS codes: (060.2605) Free-space optical communication; (280.0000) LIDAR; (130.4815) Optical switching devices;

Sponsored By:

Defense Advanced Research Projects Agency, Microsystems Technology Office (MTO)

Program: CHip-scale Integrated Photonic Phased Array (CHIPPA), Issued by DARPA/CMO under Contract No. HR0011-10-2-0003.

The views and conclusions contained in this document are those of the authors and should not be interpreted as representing official policies of the Defense Advanced Research Projects Agency or the U.S. Government.

1. Introduction

Free-space optical chip-to-chip and board-to-board interconnects offer advantages with respect to packaging and density over waveguide-based approaches due to parallelism [1] and obviation of the need for fiber attachment. The capability to steer the beam is important for such applications and others such as optical scanning, LIDAR, crossconnect switching, and in order to prevent optical misalignment and hence increased insertion loss and crosstalk [2,3] from thermal or mechanical disturbances. Among the approaches used to accomplish chip-scale free-space beam steering are tunable gain elements [4], piezo-electric micro-stages [5], reconfigurable liquid-crystal phase gratings [6], MEMS microlenses [7] and micromirrors [8].

An approach that avoids mechanical motion can be advantageous in terms of robustness and susceptibility to vibration, while compatibility with standard CMOS silicon processing by fabricating the device in the silicon-on-insulator (SOI) platform is desirable for ease of fabrication and on-chip electronic integration. Furthermore such a platform allows the integration of the free-space beam steerer with tunable optical sources [9,10] and amplifiers [11] via hybrid integration of III-V materials with SOI optical waveguides. Optical phased arrays using surface waveguide gratings in SOI have been demonstrated using a combination of wavelength scanning and a single thermo-optic phase tuner for a steering range of $2.3^\circ \times 14^\circ$ [12,13], but suffered from the lack of a means to actively eliminate phase errors introduced by fabrication variation and thermal crosstalk. An alternate technique in which a star coupler was integrated with a grating array such that wavelength alone could be used to scan the beam across the far field was also demonstrated [14], thus eliminating the need for phase tuning altogether at the expense of beam width (4°) and the ability to actively shape the wavefront. Individually phase-tuning the channels in an SOI waveguide optical phased array solves these problems and has been demonstrated for 1D beam steering in a silicon slab [15]. Suppression of side-lobes in such a device is important both to direct a higher fraction of optical power into the central peak (thus enhancing efficiency) and to avoid optical crosstalk between adjacent free-space optical links.

We here report a 16-channel independently tuned optical phased array fabricated in SOI for 2D free-space beam steering over a $20^\circ \times 14^\circ$ field of view with $1.6^\circ \times 0.6^\circ$ beam width, and we investigate the effect of rib waveguide width on far field side-lobe suppression. The emission outcoupling angle was determined by wavelength in one axis and by relative phase between emitters in the other axis. Resistive heaters were used to phase-tune individual channels via the thermo-optic effect, and a hill-climber optimization algorithm together with real-time far field

feedback from an automated image analyzer was used to minimize phase errors and suppress background peaks. Solution sets were recorded for wavelengths from 1525 nm to 1625 nm, where a solution was defined by meeting the condition in which beam intensity exceeded the maximum background peak height by 10 dB for a field of view chosen so as to exclude the side-lobes. The recorded phase solutions were then used to steer the beam without real-time feedback using a lookup table.

2. Fabrication

Rib waveguides were photolithographically defined in 500 nm top silicon, 1 μm buried oxide SOI. The waveguides had 1 μm width and 280 ± 20 nm trench depth. The beam was separated into 16 channels spaced at 100 μm intervals using 1×2 multi-mode interferometers (MMI), and a separate phase tuning element was fabricated on each channel by e-beam deposition of 72 nm / 75 nm nickel-chrome/gold to form $470 \mu\text{m} \times 4 \mu\text{m}$ resistive heaters adjacent to each waveguide with a 6.5 μm separation to avoid metal optical absorption. The top silicon between adjacent channels was etched to the buried oxide so as to minimize thermal crosstalk. The grating array was fabricated with 50% duty cycle, 600 nm pitch and 200 μm length using e-beam lithography and etched 75 nm deep. Within the grating array the waveguide spacing was 3.5 μm ; this spacing determined the angular separation between the central peak and side-lobes, and hence the angle over which the beam could be swept without introducing side-lobes into the field of view. Waveguide widths within the grating array of 1 μm , 2 μm , and 3 μm were used to evaluate the effect of rib widths on the side-lobe peaks. Schematic diagrams of the device and a scanning electron microscope image of the grating array are shown in Figure 1.

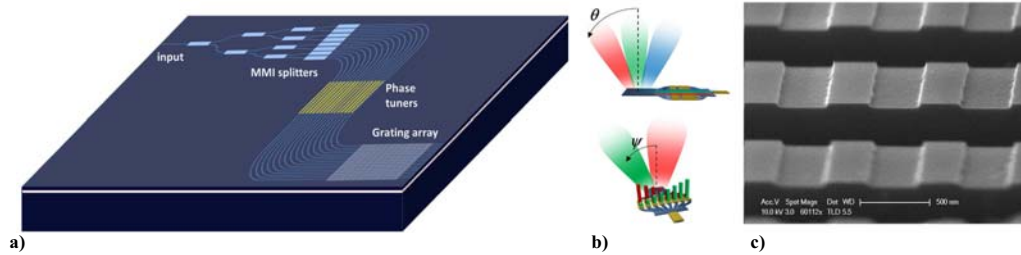


Fig. 1. a) Schematic diagram of the device. b) Illustration of the longitudinal θ emission angle determined by wavelength (top) and lateral emission angle ψ determined by phase (bottom). c) Scanning electron microscope image of the grating array.

3. Characterization

A high-numerical-aperture aspheric lens (NA = 0.83, effective focal length (EFL) = 15 mm) was used to collect the optical output and image it into the Fourier plane; two additional lenses (EFL 18 cm and 6 cm respectively) were used to image the Fourier plane onto an infrared camera for real-time far field imaging following the approach described in [16]. Polarization was aligned along the TE axis using a polarization controller. Beam steering in the longitudinal θ axis (i.e. the axis parallel to the waveguides) was determined by wavelength and measured to be $0.14^\circ/\text{nm}$ with a beam width (FWHM) of 0.6° for the 1 μm waveguide array, while steering in the ψ axis (i.e. the axis perpendicular to the waveguides) was determined by relative phase at the emitters.

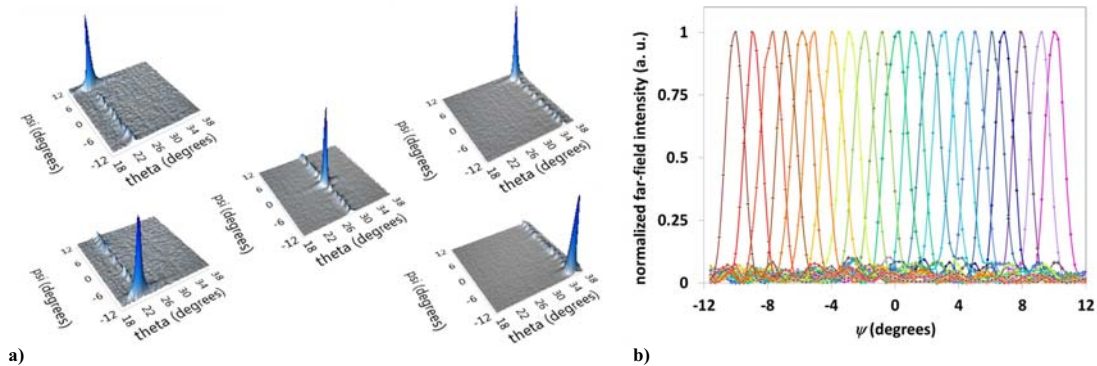


Fig. 2. a) Far field beam profiles for phase and wavelength set to steer the beam to the corners and center of the field of view. The low θ boundary (left) corresponds to emission at 1625 nm, the center corresponds to 1575 nm, and the high θ boundary (right) to 1525 nm. b) Cross sections in the ψ axis of the far field beam profile at 1555 nm for beam steering at 1° increments with 10 dB background suppression.

An optimization algorithm was used to solve for phase solutions with 10 dB background suppression within a 20° (ψ axis) \times 14° (θ axis) field of view at 1° increments. Once solved, these phase settings were stored in a lookup table and used to sweep the beam without real-time feedback. Measured profiles of the beam targeted to the corners and center of the field of view are shown in Figure 2(a); cross-sections of the beam in the ψ axis at a wavelength of 1555 nm are shown in Figure 2(b) for the 1 μm waveguide width array. Beam width in ψ was measured to be 1.6° .

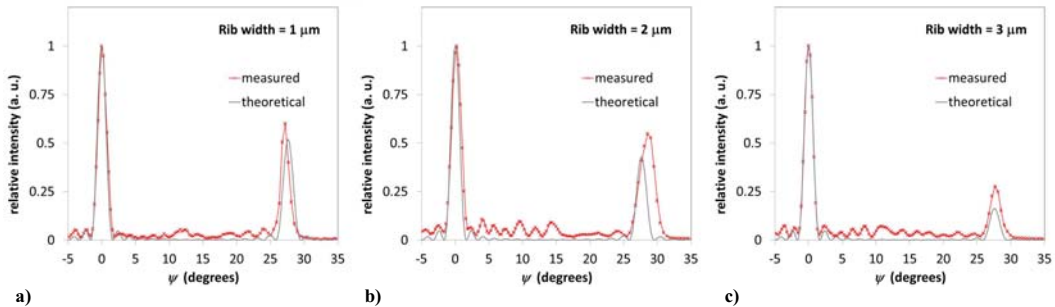


Fig. 3. Measured and calculated cross sections of the far field in ψ for 1625 nm wavelength showing the first side-lobe for a) 1 μm waveguide width, b) 2 μm waveguide width, and c) 3 μm waveguide width.

With waveguide spacing fixed at 3.5 μm , the relative power distribution in the side-lobes versus the central peak was determined by the emitter width, i.e. the rib waveguide width within the grating array. Measured and calculated cross-sections in ψ of the far field profile at 1625 nm are shown in Figure 3, where the calculated profile was determined by summing the far field contributions of emitter amplitudes corresponding to a cross-section at the grating etch depth (75 nm) of the fundamental mode for each waveguide width. As expected, side-lobe suppression improved for increased rib width, with side-lobe peak heights of 0.6, 0.55, and 0.28 relative to the central peak for rib widths of 1 μm , 2 μm and 3 μm respectively.

4. Summary and Conclusions

We have demonstrated a 16-channel optical phased array in silicon for 2D free-space beam steering with independently tuned channels. The device exhibited beam steering over a $20^\circ \times 14^\circ$ field of view with $1.6^\circ \times 0.6^\circ$ beam width and 10 dB background suppression. The effect of waveguide width on side-lobe suppression was investigated and found to decrease side-lobe peak power from 60% to 28% of the central peak height for waveguide widths ranging from 1 μm to 3 μm . This suggests that the efficiency of the optical phased array can be enhanced by optimizing the waveguide width.

5. References

- [1] L. J. Camp et al., "Guided-wave and freespace optical interconnects for parallel-processing systems: a comparison," *Appl. Opt.* **33**, 6168-6180 (1994).
- [2] V. N. Morozov et al., "Tolerance analysis for three-dimensional optoelectronic systems packaging," *Opt. Eng.* **35**, 2034-2044 (1996).
- [3] A. G. Kirk et al., "Design rules for highly parallel free-space optical interconnects," *IEEE J. Sel. Top. Quant. Electr.* **9**, 531-547 (2003).
- [4] N. W. Carlson et al., "Electronic beam steering in monolithic grating-surface-emitting diode laser arrays," *Appl. Phys. Lett.* **53**, 2275-2277 (1988).
- [5] M. Naruse et al., "Real-time active alignment demonstration for free-space optical interconnections," *IEEE Phot. Tech. Lett.* **13**, 1257-1259 (2001).
- [6] C. J. Henderson et al., "Free space adaptive optical interconnect at 1.25 Gb/s, with beam steering using a ferroelectric liquid-crystal SLM," *J. Lightwave Tech.* **24**, 1989-1997 (2006).
- [7] A. Tuantranont et al., "Optical beam steering using MEMS-controllable microlens array," *Sens. Actuators A, Phys.* **91**, 363-372 (2001).
- [8] D. M. Burns et al., "Optical beam steering using surface micromachined gratings and optical phased arrays," *Proc. SPIE* **3131**, 99-110 (1997).
- [9] A. W. Fang et al., "A Continuous Wave Hybrid AlGaInAs-Silicon Evanescent Laser," *IEEE Phot. Tech. Lett.* **18**, 1143-1145 (2006).
- [10] M. N. Sysak et al., "A hybrid silicon sampled grating DBR tunable laser," in *Group IV Photonics, 2008 5th IEEE International Conference on*, (Cardiff, Wales, 2008), pp. 55-57.
- [11] H. Park et al., "A Hybrid AlGaInAs-Silicon Evanescent Amplifier," *IEEE Phot. Tech. Lett.* **19**, 230-232 (2007).
- [12] K. Van Acoleyen et al., "Off-chip beam steering with a one-dimensional optical phased array on silicon-on-insulator," *Opt. Lett.* **34**, 1477-1479 (2009).
- [13] K. Van Acoleyen et al., "Two-dimensional optical phased array antenna on silicon-on-insulator," *Opt. Express* **18**, 13655-13660 (2010).
- [14] K. Van Acoleyen et al., "Two-Dimensional Dispersive Off-Chip Beam Scanner Fabricated on Silicon-On-Insulator," *IEEE Phot. Tech. Lett.* **23**, 1270-1272 (2011).
- [15] D. Kwong et al., "1 \times 12 Unequally spaced waveguide array for actively tuned optical phased array on a silicon nanomembrane," *Appl. Phys. Lett.* **99**, 051104 (2011).
- [16] N. Le Thomas et al., "Exploring light propagating in photonic crystals with Fourier optics," *J. Opt. Soc. Am. B* **24**, 2964-2971 (2007).

Improved Performance of Optical Beam Steering through an InP Photonic Integrated Circuit

Weihua Guo¹, Pietro R. A. Binetti¹, Chad Althouse¹, Huub P.M.M. Ambrosius², Leif A. Johansson¹, member, IEEE, and Larry A. Coldren¹, Fellow, IEEE

¹Department of Electrical and Computer Engineering, University of California, Santa Barbara, CA 93106, USA

²Electrical Engineering Department, Eindhoven University of Technology, Eindhoven, NL

Email: guow@ece.ucsb.edu

Abstract: Optical beam steering through an InP photonic integrated circuit has been improved in term of side-lobe suppression (13dB from -14° to 14° around the peak) and steering angle (10° by 28nm wavelength tuning).

OCIS codes: (250.5300) Photonic integrated circuits; (280.3640) Lidar;

1. Introduction

2D electronically controlled optical beam steering is envisaged to be very useful for light detection and ranging (LIDAR) [1-2]. In [2] we demonstrated an InP photonic integrated circuit (PIC) for this purpose. The critical part of the PIC is an optical phased array with embedded 2nd order gratings for emission vertical to the PIC plane. Wavelength is used to control the beam steering along the grating direction (longitudinal direction). An array of phase shifters is used to control the beam steering perpendicular to the grating direction (lateral direction). These two controls are independent of each other therefore a 2D beam steering can be realized. In [2] we demonstrated 10° of beam steering in the lateral direction and 5° in the longitudinal direction limited by the 40nm of wavelength tuning around 1550 nm. We also demonstrated 7-dB side-lobe suppression for the angle range from -14° to 14° around the peak. In this work we show that 13-dB side-lobe suppression has been achieved through controlling the amplitude of the emission across the array. We also show that through a 4-f lens system 10° of steering angle can be achieved in the longitudinal direction through 28nm wavelength tuning.

2. PIC layout and measurement setup

As shown in Fig. 1(a) the PIC consists of an input semiconductor optical amplifier (SOA) to compensate the coupling loss; a 1×2 MMI tree to split the input signal into 8 channels; SOAs and phase shifters (PS) in each channel to boost the signal power and control the signal phase; an emission array composed of SOAs with 2nd order gratings etched in the upper optical confinement layer of the waveguide core; and a monitor array which makes adjacent channels form interferometers to monitor the phase generated by the phase shifters. The emission array propagates downward through the substrate and an aperture opened in the bottom N-contact metal. The chip is mounted top-side up on an AlN carrier and then on a copper heat sink as shown in Fig. 1(b). Holes are opened in the carrier and the heat sink to allow the emission transmit through. Three lenses installed in lens tubes are used for the far-field imaging of which the first lens implements the Fourier transform and the second and third lenses project the far-field pattern onto an InGaAs infrared camera. Two lenses—one convex and one concave—can also be inserted above the first lens for far-field imaging to magnify the steering angle as introduced later on.

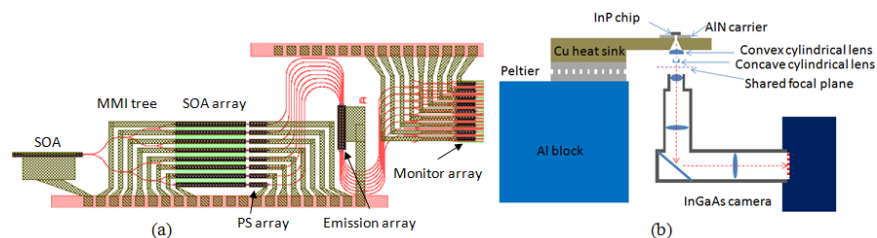


Fig. 1 (a) Schematic layout of the PIC; (b) Schematic of the measurement setup

3. Improved side-lobe suppression

In [2] we injected current into the SOAs in each channel through a single current source. Because the series resistance of these SOAs varies the current injected into each SOA is actually not the same which tends to make the amplitude of the emission across the array non-uniform and therefore harm the side-lobe suppression. To overcome the issue we use a strategy as shown in Fig. 2(a). We place two resistances in series for each channel before the

connection to the SOA: one variable from 0 to 50Ω and one fixed at 10Ω. A single voltage source is used to inject currents into all the SOAs in the channels and the current into each channel is adjusted through varying the variable resistance and monitored by the voltage drop across the fixed resistance. Through this way we ensure 100mA current uniformly injected across all channels. After this we adjust the phase shifter currents to optimize the far-field pattern in the lateral direction as implemented in [2]. Fig. 2(b) shows the optimized result which is the field distribution across the peak in the longitudinal and lateral directions. A side-lobe suppression of 13dB has been successfully demonstrated from -14° to 14° around the peak which actually corresponds to the theoretical value very well if assuming the emission is uniform across the array.

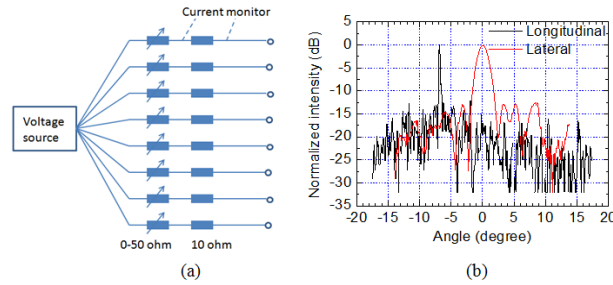


Fig. 2 (a) Schematic of the electrical setup for adjusting injection currents into the SOAs; (b) Optimized far-field pattern

4. Sweeping angle magnification through a 4-f system

To increase the sweeping angle in the longitudinal direction another 2 cylindrical lenses are inserted between the PIC and the lens for the Fourier transform as shown in Fig. 1(b). The sequence is a convex lens first followed by a concave lens. These two lenses share the same focal plane and the effective focal length of the convex lens is M times that of the concave lens. In our case according to the lens spec M equals 2.56. Theoretically we would expect an M times magnification of the steering angle. When the steering angle being magnified the beam divergence will also be magnified by the same amount. The experiment results are shown below where Fig. 3(a) plots the peak position in the longitudinal direction versus wavelength. We can see that the slope is 5.6° per 40 nm before inserting the 4-f system and is increased to 14.3° per 40 nm after. The magnification is therefore 2.55 which is in good agreement with the theoretical prediction. Fig. 3(b) shows the far-field distribution in the longitudinal direction. Without or with the 4-f system the beam divergence angle (full width at half maximum) is 0.2° and 0.5°, respectively. So a magnification of 2.5 times is seen which is also close to the theoretical prediction. With the angular magnification a 10° steering angle can therefore be achieved through 28nm wavelength tuning.

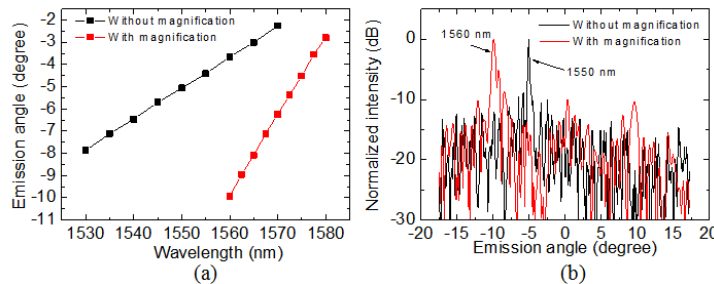


Fig. 3 (a) Peak position in the longitudinal direction versus wavelength; (b) Field distribution in the longitudinal direction.

5. Summary

In summary we have demonstrated improved performance of electronically controlled 2D beam steering from an InP PIC. Through controlling the emission across the array we demonstrated improved (13 dB) side-lobe suppression. We also demonstrated wider steering angle in the longitudinal direction through inserting a 4-f lens system.

6. Reference

- [1] K. Van Acoleyen, W. Bogaerts, J. Jagerska, N. Le Thomas, R. Houdre, and R. Baets, "Off-chip beam steering with a one-dimensional optical phased array on silicon-on-insulator," *Opt. Lett.* 34, 1477-1479 (2009).
- [2] W. H. Guo, P. R. A. Binetti, C. Althouse, A. Bhardwaj, J. K. Doylend, H. P. M. M. Ambrosius, L. A. Johansson, and L. A. Coldren, "InP photonic integrated circuit for 2D optical beam steering." Post-deadline paper, IEEE Photonics 2011 (IPC11), Arlington, Virginia, USA, 2011.

InP Photonic Integrated Circuit with an AWG-like design for Optical Beam Steering

Weihua Guo¹, Pietro R. A. Binetti¹, Chad Althouse¹, Huub P.M.M. Ambrosius², Leif A. Johansson¹, member, IEEE, and Larry A. Coldren¹, Fellow, IEEE

¹Department of Electrical and Computer Engineering, University of California Santa Barbara, CA93106, USA

²Electrical Engineering Department, Eindhoven University of Technology, Eindhoven, NL

Abstract — Optical beam steering through an InP PIC with an AWG-like design has been demonstrated. Good far-field pattern has been kept without resetting the phase shifter currents when changing the input wavelength to steer the beam.

Index Terms — Photonic integrated circuits, optical beam steering, LIDAR.

I. INTRODUCTION

Similar to electronically scanned phased array Radar, electronically controlled optical beam steering is useful for light detecting and ranging (LIDAR). It also finds applications in 3D imaging, precision targeting, guidance and navigation, etc. Different methods have been tried to achieve electronically controlled optical beam steering [1-3]. In [4-5] we demonstrated electronically controlled 2D optical beam steering through an InP photonic integrated circuit (PIC). The critical part of the PIC is a waveguide array with embedded 2nd-order gratings for out-of-plane emission. An array of phase shifters is used to add a phase slope across the waveguide array so as to steer the beam perpendicularly to the waveguide in the array (lateral direction) [4]. The input wavelength is changed to steer the beam along the waveguide in the array (longitudinal direction) because the emission angle of the grating depends on wavelength [4]. Because of phase errors caused by imperfect fabrication, we normally need to optimize the phase shifter currents to generate a good beam—narrow beam width and high side-lobe suppression for the far-field pattern. Because it is a 2D scan it would be preferable not to reset the phase shifter currents when changing wavelength. In this work, we show that through an AWG-like design, i.e. all the channels use bends with the same radius and the same length, the far-field pattern of the beam can keep a good shape and high side-lobe suppression when changing the input wavelength even when we do not reset the phase shifter currents.

II. PIC LAYOUT

The PIC layout is shown in Fig. 1. After amplification by a preamplifier—the leftmost semiconductor optical amplifier (SOA), the input signal is split into eight channels by a 1×8

splitter consisting of cascaded 1×2 MMI's. Each channel then has its own SOA and phase shifter to boost the power and control the phase. After passing through some additional waveguides consisting mostly of bends with the same radius and the same total bending angles (1.5π), the signal enters into the waveguide array region as shown in Fig. 1.

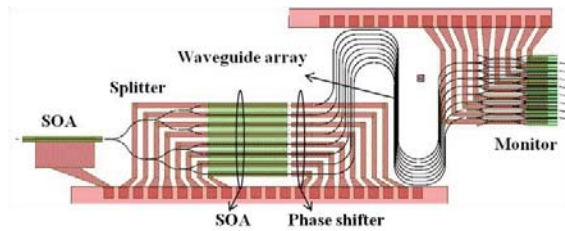


Fig. 1. Layout of the PIC.

Each waveguide in the waveguide array is passive and has embedded 2nd-order gratings etched into the upper optical confinement layer of the waveguide core and buried by the regrown P-doped cladding layers. These gratings scatter the signal from the waveguide out of the plane, upward and downward. There is an aperture in the N-contact metal which is on the backside of the thinned-down substrate. This aperture is aligned to the gratings so that the downward emission can transmit through and be detected in our measurement setup. The additional bending waveguides are added to make all the channels have the same length from the end of the phase shifters to the beginning of the 2nd-order gratings. They are needed because the spacing between the SOA array and the waveguide array for emission is different: the former is 100 μm but the latter is only 5.5 μm . After passing through the waveguide array for emission, some signal which is still left in the waveguide passes through additional bending waveguides and then enters into the monitor array. These additional bending waveguides are needed due to the same reason as those added before the grating array. The monitors integrated on chip are used to monitor the phase difference between adjacent channels through interferometer structures formed by adjacent channels. All waveguides used in the PIC including both active and passive waveguides are deep ridge waveguides which allow small bend radius—200 μm —to be used. Because

of the relatively long bends and the tight bend radius, it is better to use the same bend radius and the same total bend length in each channel so that their influence on phase can cancel each other. This is a rule quite generally followed by AWG designs especially when waveguides with strong optical confinement are used [6].

III. PIC FABRICATION

The PIC as being introduced in the above section includes both passive and active waveguides. The active-passive integration has been realized by using the quantum well intermixing technique [7-8]. Starting from a base wafer structure as shown in Fig. 2 (a), phosphorous ions are implanted into the top sacrificial InP layer to produce defects in the area intended to be passive. These defects are then thermally driven down through the quantum well layers to cause component mixture between the barrier and well materials. This is the so-called quantum well intermixing process which increases the bandgap of the quantum wells in the implanted area. After intermixing, the top InP sacrificial layer is removed by wet etching then the 2nd-order gratings are patterned by using electron beam lithography and etched into the upper optical confinement layer of the waveguide core. After that a P-doped InP cladding layer is re-grown above followed by the highly P-doped InGaAs contact layer. The full wafer structure after regrowth is schematically shown in Fig. 2 (b). The waveguides are patterned by using the I-line wafer stepper and are etched by using ICP with the Cl₂/H₂/Ar plasma [9]. The etch depth is about 5 μm so all the waveguides including both active and passive waveguides are deeply etched ridge waveguides. After waveguide etching is the SiN_x isolation layer deposition followed by via opening for the P-metal and P-metal deposition. Then the wafer is thinned down and N-metal is put on the backside of the wafer. An aperture has been opened in the N-metal which is aligned to the grating area to allow the downward emission from the grating to transmit through.

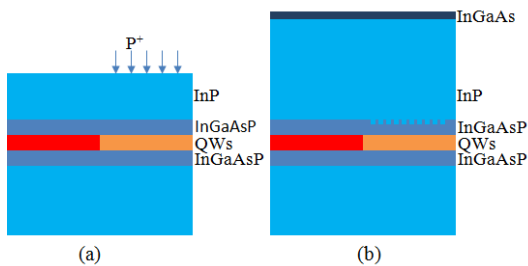


Fig. 2. Schematic wafer structure before regrowth (a) and after regrowth (b).

III. MEASUREMENT

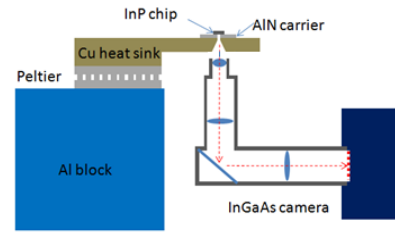
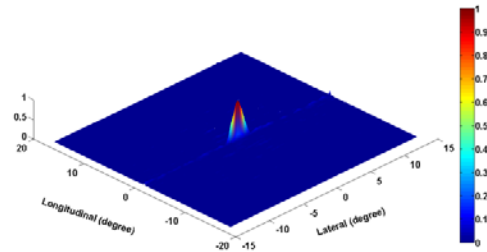
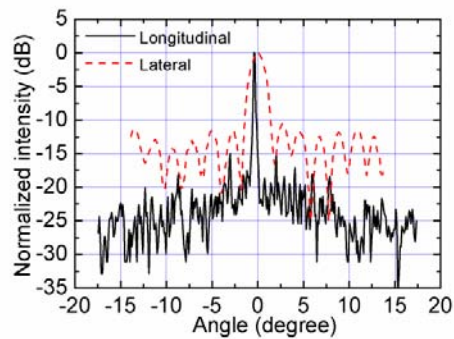


Fig. 3. Schematic of the measurement setup.



(a)



(b)

Fig. 4. (a) Far-field pattern when the beam pointing at zero degree in the lateral direction and the input wavelength is 1540 nm; (b) Intensity distribution across the peak in the lateral and longitudinal direction.

The measurement setup is schematically shown in Fig. 3. The PIC is mounted facing-up onto an AlN carrier. There are holes in the carrier and the Cu heat sink which are aligned to the aperture of the N-contact metal of the PIC so that the downward emission can be captured by the imaging system as shown in Fig. 3. The imaging system consists of three lenses with folded optical path and an InGaAs infrared camera. The first lens projects the far-field pattern of the emission onto its lower focal plane. The far-field pattern is then magnified and

projected onto the detector plane of the infrared camera by the other two lenses. The imaging system is able to capture the far-field from -17 to 17 degrees in the longitudinal direction and from -14 to 14 degrees in the lateral direction with an angle resolution of ~ 0.1 degree. For the following measurement the on-chip SOAs are all biased at 100 mA. The eight channel SOAs are biased by a single current source. To account for the series resistance difference of the SOAs, a variable resistor network has been used as demonstrated in [5]. The eight phase shifters are controlled by eight current analog outputs from a DAC card. The input signal is from an external cavity tunable laser fiber coupled into the chip. The tuning range is set from 1530 to 1560 nm.

First, the input wavelength is set to 1540 nm. The phase shifter currents are optimized by the Particle Swarm Optimization (PSO) algorithm to make the beam point at zero degree in the lateral direction and to maximize the side-lobe suppression ratio in the angle range from -14 to 14 degrees [4]. The resulted 2D far-field pattern is plotted in Fig. 4 (a) which shows that a nice clean beam has been obtained. The intensity distribution across the peak in the lateral and longitudinal direction is shown in Fig. 4 (b). A side-lobe suppression of 10 dB has been achieved. The 3-dB beam width in the lateral direction is 1.7 degrees which is in close agreement of the theoretical value of 1.8 degrees, assuming the emission amplitude is uniform across the eight channels. In the longitudinal direction the beam is much narrower because a very long (500 μm) and slowly attenuating grating has been used. Then, we steer the beam to different angles in the lateral direction by repeating the above optimization process around the lateral angles from -6 to 6 degrees with a step of 2 degrees. The results are shown in Fig. 5. The array spacing is 5.5 μm which determines that the angle spacing between two adjacent diffraction orders is 16 degrees, as it can be clearly seen from Fig. 5.

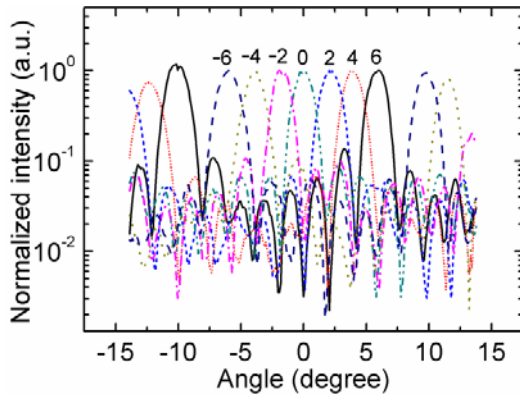


Fig. 5. Intensity distribution in the lateral direction when the beam steered to lateral angles from -6 to 6 degrees with a step of 2 degrees.

After this, we steered the beam back to the lateral zero-degree angle and then changed the wavelength from 1530 to 1560 nm. Without changing the phase shifter currents, the far-field pattern in the lateral direction is recorded and plotted in Fig. 6. When changing the wavelength, the gain of the SOAs on-chip varies due to the limited gain bandwidth and the fixed current injections to the SOAs. This influences the output power as seen from Fig. 6. But the 3-dB beam width and the side-lobe suppression keep nearly the same, ~ 2.0 degrees and 10 dB, respectively. For the wavelength of 1550 nm which is the gain peak, the emission is a little bit too strong to saturate the infrared camera which causes the peak of the recorded field distribution to be cut-off. The design not only keeps the length of all the channels the same but also uses the same bends: the same bend radius and the same total bending angles. Furthermore all the SOAs and phase shifters are arranged to have the same positions relative to the splitter and to the grating array. All of these help to achieve the effect shown in Fig. 6. But there is also one penalty from these additional waveguides—the added loss. Our passive waveguides typically have a loss of about 2 dB/mm. So these additional waveguides contribute to a loss of about 4 dB due to their ~ 2 mm length.

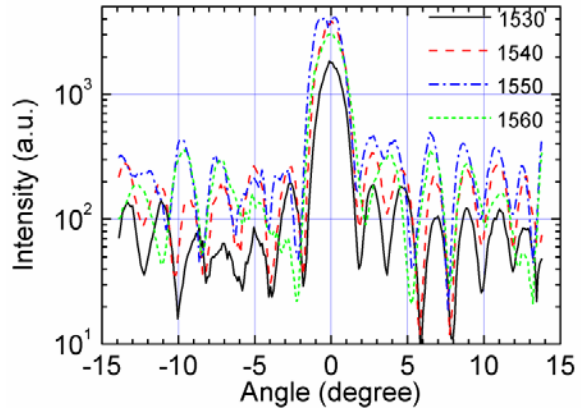


Fig. 6. Far-field pattern in the lateral direction for the input wavelength of 1530, 1540, 1550, and 1560 nm.

IV. SUMMARY

In summary we have demonstrated an InP PIC for optical beam steering: when we change the input wavelength to steer the beam the array of phase shifters does not need to reset the bias currents in order to preserve the beam shape and the side-lobe suppression. The AWG-like design employed in the PIC uses bends with the same radius and the same total length in each channel. This ensures that the influences from these bends cancel with each other even when a very tight bend radius—200 μm —has been used.

ACKNOWLEDGEMENT

This work is supported by DARPA SWEEPER project.

REFERENCES

- [1] D. P. Resler, D. S. Hobbs, R. C. Sharp, L. J. Friedman, and T. A. Dorschner, "High-efficiency liquid-crystal optical phased-array beam steering," *Opt. Lett.*, vol. 21, no. 9, pp. 689-691, May 1996.
- [2] A. Tuantranont, V. M. Bright, J. Zhang, W. Zhang, J. A. Neff, Y. C. Lee, "Optical beam steering using MEMS-controllable microlens array," *Sens. Actuators A: Phys.*, vol. 91, no. 3, pp. 363-372, Jul. 2001.
- [3] K. Van Acoleyen, W. Bogaerts, R. Baets, "Two-dimensional dispersive off-chip beam scanner fabricated on silicon-on-insulator," *IEEE Photon. Technol. Lett.*, vol. 23, no. 17, pp. 1270-1272, Sep. 2011.
- [4] W. H. Guo, P. R. A. Binetti, C. Althouse, A. Bhardwaj, J. K. Doylend, H. P. M. M. Ambrosius, L. A. Johansson, and L. A. Coldren, "InP photonic integrated circuit for 2D optical beam steering," Post-deadline paper, IEEE Photonics 2011 (IPC11), Arlington, Virginia, USA, 2011.
- [5] W. H. Guo, P. R. A. Binetti, C. Althouse, H. P. M. M. Ambrosius, L. A. Johansson, and L. A. Coldren, "Improved performance of optical beam steering through an InP photonic integrated circuit," CW1K, CLEO, San Jose, CA, USA, 2012.
- [6] H. Takahashi, I. Nishi, and Y. Hibino, "10 GHz spacing optical frequency division multiplexer based on arrayed-waveguide grating," *Electron. Lett.*, vol. 28, no. 4, pp. 380-382, Feb. 1992.
- [7] E. J. Skogen, J. S. Barton, S. P. Denbaars, and L. A. Coldren, "A quantum-well-intermixing process for wavelength-agile photonic integrated circuits," *IEEE J. Select. Topics Quantum Electron.*, vol. 8, no. 4, pp. 863-869, Jul./Aug. 2002.
- [8] P. R. A. Binetti, M. Z. Lu, E. J. Norberg, R. S. Guzzon, J. S. Parker, A. Sivananthan, A. Bhardwaj, L. A. Johansson, M. J. Rodwell, and L. A. Coldren, "Indium phosphide photonic integrated circuits for coherent optical links," *IEEE J. Select. Topics Quantum Electron.*, vol. 48, no. 2, pp. 279-291, Feb. 2012.
- [9] J. S. Parker, E. J. Norberg, R. S. Guzzon, S. C. Nicholes, and L. A. Coldren, "High verticality InP/InGaAsP etching in Cl₂/H₂/Ar inductively coupled plasma for photonic integrated circuits," *J. Vac. Sci. Technol. B*, vol. 29, no. 1, Jan./Feb. 2011.

Very Fast ($>10^7$ degree/s) 2D Optical Beam Steering through an InP Photonic Integrated Circuit

Weihua Guo¹, Pietro R. A. Binetti¹, Chad Althouse¹, Huub P.M.M. Ambrosius², Leif A. Johansson¹, member, IEEE and Larry A. Coldren^{1,3}, Fellow, IEEE

¹Department of Electrical and Computer Engineering, University of California Santa Barbara, CA 93106, USA.

²Electrical Engineering Department, Eindhoven University of Technology, Eindhoven, NL.

³Department of Materials, University of California Santa Barbara, CA 93106, USA.

Email: guow@ece.ucsb.edu

Abstract—Very fast ($>10^7$ degree/s) 2D optical beam steering through an InP photonic integrated circuit has been demonstrated.

Keywords—Lidar; optical beam steering; photonic integrated circuit

I. INTRODUCTION

Electronically controlled optical beam steering has many potential applications such as light detection and ranging (LIDAR), 3D imaging, precision targeting, etc. Several methods have been demonstrated before to achieve this goal [1-2]. One of the advantages of electronically controlled beam steering is that the beam can potentially be swept between different directions very fast. In [3] we demonstrated electronically controlled 2D optical beam steering through an InP photonic integrated circuit (PIC). In this work we show that the InP based PIC can sweep the beam in 2D very fast, with the actual sweeping speed higher than 10^7 degree/s.

II. LAYOUT OF THE PIC

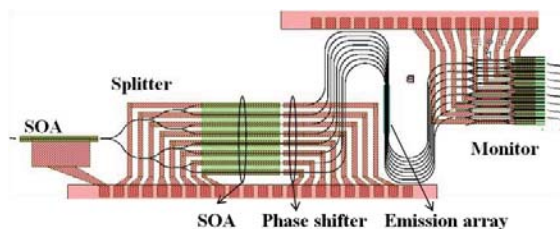


Fig. 1 Layout of the InP PIC

Fig. 1 shows the layout of the PIC. It consists of an input semiconductor optical amplifier (SOA); a 1×8 splitter consisting of cascaded 1×2 MMIs; SOAs followed by phase shifters in each channel; the emission array consisting of a passive waveguide array of which each waveguide has buried 2^{nd} -order gratings for the out-of-plane emission; an array of interferometer monitors monitoring the phase difference between adjacent channels. The gratings are etched in the upper confinement layer of the waveguide core and buried by the re-grown P-doped cladding layers. The emission from the grating goes equally upward and downward. The far-field of the downward emission is captured by an imaging system backed up by an infrared camera. The 2D beam steering

mechanism is as explained in [3]: when changing the input wavelength the beam is swept along the grating (horizontally in the image taken by the camera – see Fig. 2); when adding a phase slope across the array through those phase shifters, the beam is swept perpendicular to the grating (vertically in the image).

III. EXPERIMENT

The input signal to the PIC is fiber coupled from another InP PIC hosting a sampled-grating DBR (SGDBR) laser. As described in [4], the SGDBR laser source consists of a back mirror section, phase section, gain section, front mirror section, and a front SOA section. The currents injected into all these sections are fixed except the front mirror section which is controlled by a function generator (FG). The DC offset of the FG is used to select the super modes of the SGDBR laser which are 6 nm apart. First the DC voltage is set at 0.99 V to peak up a super mode at 1540 nm. All the SOAs in the PIC are injected with 100 mA current. All eight channel SOAs have current injected through a single current source. To account for the unavoidable series resistance difference, variable resistors are connected in series to these SOAs and adjusted to make the current injected into each SOA the same. Seven of the eight phase shifters connected with 50Ω resistors in series, are controlled by seven FGs. First the DC offsets of the FGs are adjusted to optimize the phase profile across the emission array in order to make a good beam pointing at the vertical 0° angle. The far-field image taken by the camera is shown in Fig. 2 (a). A spot corresponding to the 0^{th} order diffraction beam can be clearly seen. Then the DC offset is adjusted to make the 0^{th} order beam pointing at -10° . Now the $+1^{\text{st}}$ order diffraction beam which is 16° apart from the 0^{th} order diffraction determined by the $5.5 \mu\text{m}$ array pitch, is also captured by the camera as seen from Fig. 2 (b). The imaging system can capture $\pm 14^\circ$ vertically. Then the FGs are set to output square waves at 1 MHz repetition frequency with the DC offsets being the average of the above two DC sets and the peak-to-peak amplitude being the differences. These FGs are synchronized by using one of them as the master FG whose synchronization output is split and used to trigger the other slave FGs. The square wave sweeps the beam between the two angles -0° and -10° at 1 MHz speed, which is much faster than the 60 Hz frame rate of the camera. The image taken by the camera shows the spots corresponding to the two angles

simultaneously as seen from Fig. 2 (c). We also put a detector 15 cm above the grating array. The detector is positioned to maximize its output signal when the 0th order beam is pointed at 0°. When the beam is quickly sweeping between the two angles 0° and -10°, the signal from the detector is recorded by an oscilloscope and shown in Fig. 2 (d). A square wave is clearly seen even as the signal captured is very weak. The square wave result means that the sweeping speed has reached $10^\circ/0.5 \mu\text{s} = 2 \times 10^7 \text{ degree/s}$.

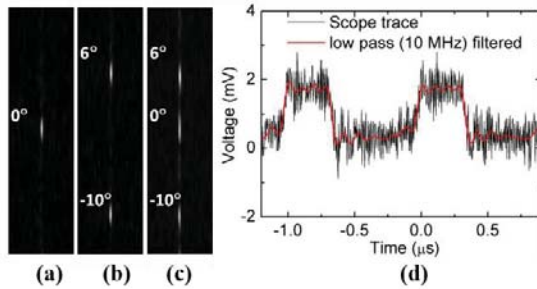


Fig. 2 (a)-(c) Images taken by the infrared camera when the 0th order beam is pointed at 0° and -10° and swept between them; (d) Scope trace when fast sweeping between 0° and -10°.

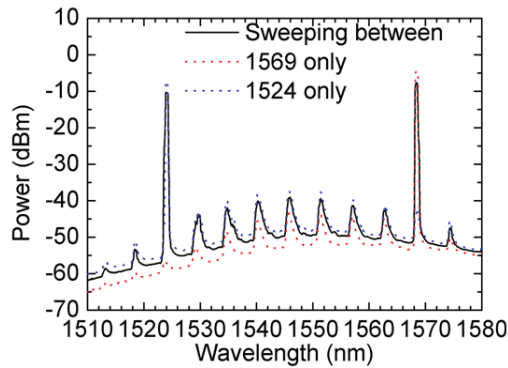


Fig. 3 Output spectrum of the SGDBR laser.

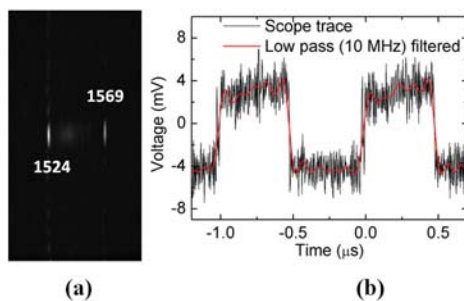


Fig. 4 (a) Image taken by the infrared camera and (b) scope trace when the SGDBR laser is fast switching between 1569 and 1524 nm.

To demonstrate the fast beam steering in the perpendicular direction, we sweep the beam along the grating by quickly changing the output wavelength of the SG-DBR laser. The phase shifter biases are recovered to DC and optimized to make the 0th order beam pointing at 0° vertically. First the DC offset of the FG that controls the front mirror of the SGDBR laser, is set at 1.62 and 1.81 V, respectively. The output wavelength of the SG-DBR laser is 1569 and 1524 nm, respectively as seen from Fig. 3. Then the FG is set to output a square wave at 1 MHz with the DC offset being 1.71 V and peak-to-peak amplitude being 0.19 V. This square wave makes the output of the SG-DBR laser switch very fast between these two wavelengths. Because the scanning speed of the optical spectrum analyzer is rather slow it captures the two wavelengths simultaneously as seen from Fig. 3. For the same reason the camera captures the two spots simultaneously corresponding to the two beams pointing at two angles θ apart horizontally, as seen from Fig. 4 (a). To make sure the wavelength is really switching at 1 MHz speed, we tap 5% of the output of the SG-DBR laser and pass it through a 0.35 nm filter. The transmission is recorded by a fast photodiode with TIAs. The response from the PD is recorded by the oscilloscope and the scope trace is shown in Fig. 4 (b). It is seen that a switching speed of 1 MHz is achieved, which corresponds to a sweeping speed of $1.2 \times 10^7 \text{ degree/s}$.

IV. SUMMARY

So in summary, very fast sweeping ($>10^7 \text{ degree/s}$) has been demonstrated for 2D beam steering through an InP photonic integrated circuit.

Acknowledgement

This work is supported by DARPA SWEEPER project.

Reference:

- [1] P. F. McManamon, T. A. Dorschner, D. L. Corkum, L. J. Friedman, D. S. Hobbs, M. Holz, S. Liberman, H. Q. Nguyen, D. P. Resler, R. C. Sharp, and E. A. Watson, "Optical phased array technology," *Proc. IEEE* vol. 84, 1996, pp. 268-298.
- [2] K. Van Acoleyen, W. Bogaerts, J. Jagerska, N. Le Thomas, R. Houdre, and R. Baets, "Off-chip beam steering with a one-dimensional optical phased array on silicon-on-insulator." *Opt. Lett.*, vol. 34, 2009, pp. 1477-1479.
- [3] W. H. Guo, P. R. A. Binetti, C. Althouse, A. Bhardwaj, J. K. Doylend, H. P. M. M. Ambrosius, L. A. Johansson, and L. A. Coldren, "InP photonic integrated circuit for 2D optical beam steering." Post-deadline paper, IEEE Photonics 2011 (IPC11), Arlington, Virginia, USA, 2011.
- [4] L. A. Coldren, "Monolithic tunable diode lasers," *IEEE J. Sel. Topics Quantum Electron.*, vol. 6, 2000, pp. 988-999.

InP Photonic Integrated Circuit with On-chip Monitors for Optical Beam Steering

Weihua Guo¹, Pietro R. A. Binetti¹, Chad Althouse¹, Huub P.M.M. Ambrosius², Leif A. Johansson¹, member, IEEE, and Larry A. Coldren¹, Fellow, IEEE

¹Department of Electrical and Computer Engineering, University of California, Santa Barbara, CA 93106, USA

²Electrical Engineering Department, Eindhoven University of Technology, Eindhoven, NL

Email: guow@ece.ucsb.edu

Abstract: Optical beam steering controlled by an array of phase shifters from an InP photonic integrated circuit has been demonstrated with the help from on-chip monitors.

OCIS codes: (250.5300) Photonic integrated circuits; (280.3640) Lidar;

1. Introduction

Electronically controlled optical beam steering is potentially useful for a number of applications such as light detection and ranging (LIDAR), 3D imaging, precision targeting, guidance and navigation, etc. Recently, we have demonstrated an InP photonic integrated circuit (PIC) for 2D optical beam steering controlled electronically [1]. The critical part of the PIC is an optical waveguide array with embedded 2nd-order gratings for out-of-plane emission. An array of phase shifters is used to generate a phase slope across the waveguide array which steers the beam perpendicularly to the waveguide (lateral direction). The embedded 2nd-order gratings have the emission angle dependent on wavelength, which is used to steer the beam along the waveguide by varying the input wavelength (longitudinal direction). The 2D beam steering has thus been achieved by controlling the input wavelength and the array of phase shifters simultaneously. In our first demonstration, the beam is steered to different angles in the lateral direction by blindly optimizing the phase shifter bias currents through the particle swarm optimization (PSO) algorithm [1]. This would become tedious if sweeping with very small angle steps is required. It becomes even more problematic if the currents injected into the phase shifters need to be re-optimized when changing wavelength. In this work, we show that through integrated on-chip monitors the phase shifters can be characterized on-site, so the dependence of the generated phase shift on injected current, i.e. the phase-current curve, can be established. Then the phase slope across the array required by a specific steering angle can be set directly by referring to the established phase-current curves.

2. PIC layout

Fig.1 (a) shows the layout of the PIC which consists of the input semiconductor optical amplifier (SOA), the 1×2 MMI tree which splits the input into eight channels, an SOA array and a phase shifter array which are used to boost the power and control the phase of each channel, then the waveguide array with embedded 2nd-order gratings for the out-of-plane emission, and the monitor array. Additional bends are added to make each channel have equal length in order to prevent additional differential phase generated when changing wavelength. Fig. 1 (b) shows the blown-up of the monitors. Each channel is split into three equal parts by a 1×3 MMI. Two close parts from two adjacent channels are combined by a 1×2 MMI to form interferometers with the interference monitored by a photodiode (PD) as seen from Fig. 1 (b). Two additional waveguides are added at the output interface of the MMI to guide away the destructive interference so as to increase the interference extinction ratio. For the following measurement we bias the SOAs at 100 mA each. The input wavelength is fixed at 1540 nm. The 8 phase shifters are controlled by 8 current analog outputs from a DAC card.

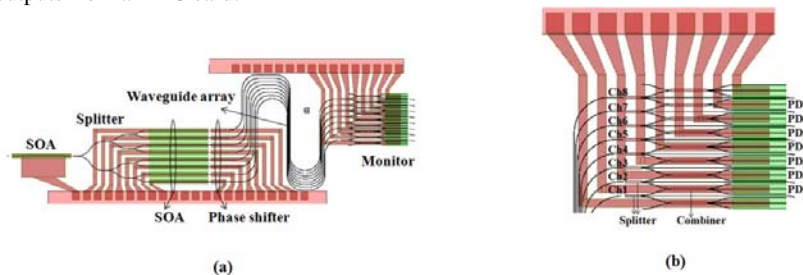


Fig. 1 (a) Layout of the PIC; (b) Blown-up of the monitor array

3. On-site characterization of the phase shifters

For on-site characterization of the phase shifters, we fix the current injected into the i^{th} channel phase shifter at 1 mA and increase the $(i+1)^{\text{th}}$ channel phase shifter current from 1 mA to 20 mA and then record the i^{th} PD signal. The

channels and PDs are numbered as shown in Fig. 1 (b). The results are shown in Fig. 2 (a) as dashed curves with i from 1 to 7. Then we fit these curves with a theoretical model to find the phase $\Delta\phi_i(I)$ which is the phase of the $(i+1)^{\text{th}}$ channel relative to the i^{th} channel when the i^{th} channel phase shifter is injected with 1 mA current. Equation (1) represents the model where C_i i from 0 to 4, are fitting parameters, $\Delta\psi$ represents the initial phase difference. The fit is shown in Fig. 2 (a) as solid lines.

$$V(I) = C_0[1 + \exp(-2\alpha) + 2\exp(-\alpha)\cos(\Delta\phi)] + C_1 \quad (1)$$

$$\Delta\phi = \Delta\psi + C_2\sqrt{I} + C_3I, \quad \alpha = C_4(\Delta\phi - \Delta\psi)$$

We repeat the above process for all the channels. The reference phase for the series of phase curves $\Delta\phi_i(I)$, i from 1 to 7, is not unified. We can make them all refer to the first channel when its phase shifter is biased at 1 mA. To achieve this we just need to move the curve $\Delta\phi_i(I)$ vertically according to $\phi_{i+1}(I) = \Delta\phi_i(I) + \sum_{j=1}^{i-1} \Delta\phi_j(I=1\text{ mA}), i=1\dots7$.

$\phi_1(I)$ is zero because the first channel refers to itself. $\phi_i(I)$ is the phase-current curve we obtain through on-site characterization of the phase shifters.

4. Calibrating the phase-current curves

Once we have the phase-current curves for all the phase shifters, we can steer the beam by setting the phase slope across the waveguide array directly. For the beam to point to angle θ , we need a phase slope of $\phi_i = 2\pi(i-1)d \sin(\theta)/\lambda$, where d is the array pitch and λ is the wavelength. First we make the angle θ equal to zero. From the phase-current curves we have just obtained, we find a set of currents I_i which are suppose to make each channel have the same phase. But the far-field pattern is not very good as we set these currents because of two reasons: 1) the phase error accumulation which is produced when we move the phase reference from adjacent channels to the first channel; and 2) not necessarily equal phase across the array makes a good pattern pointing at angle 0 because there could be variations from grating to grating. To handle these issues we optimize the far-field pattern around the current sets I_i through the PSO algorithm. A new current set I'_i has been found which are not far away from the original I_i but generates far better far-field pattern. Based on this we calibrate our original phase-current curves according to $\phi'_i(I) = \phi_i(I) - \phi_i(I'_i)$ which makes the new curves have nominal zero phase at I'_i . The new phase-current curves $\phi'_i(I)$ are the basis of our beam steering and are shown in Fig. 2 (b).

5. Beam steering

To steer the beam, we just need to find out the currents from the calibrated phase-current curves according to the phase required by the formula $\phi_i = 2\pi(i-1)d \sin(\theta)/\lambda$. Fig. 2 (c) shows the far-field distribution when the beam is steered from -6 degree to 4 degree with a step of 2 degree. The plot shows that the good beam shape and side-lobe suppression has been kept when we steer the beam. The waveguide array pitch is $5.5 \mu\text{m}$ which makes the $\pm 1^{\text{st}}$ order diffraction beam be 16 degree apart from the 0^{th} order diffraction. This can also be clearly seen from Fig. 2 (c).

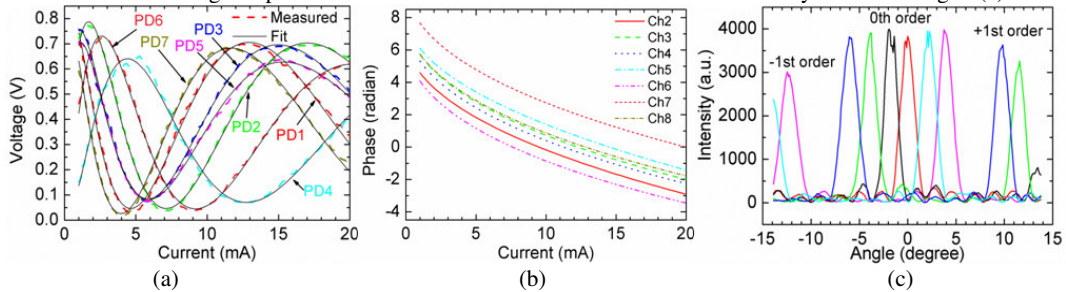


Fig. 2 (a) PD response v.s. phase shifter current (b) Phase-current curves (c) Far-field pattern in the lateral direction

6. Summary

In summary we have demonstrated beam steering with the help from on-chip monitors. These monitors help establish the phase-current curves of the phase shifters. The beam is thus steered by setting the phase slope across the array directly.

7. References

- [1] W. H. Guo, P. R. A. Binetti, C. Althouse, A. Bhardwaj, J. K. Doylend, H. P. M. M. Ambrosius, L. A. Johansson, and L. A. Coldren, "InP photonic integrated circuit for 2D optical beam steering," Post-deadline paper, IEEE Photonics 2011 (IPC11), Arlington, Virginia, USA, 2011.

Hybrid III/V silicon photonic source with integrated 1D free-space beam steering

J. K. Doylend,* M. J. R. Heck, J. T. Bovington, J. D. Peters, M. L. Davenport, L. A. Coldren, and J. E. Bowers

Department of Electrical and Computer Engineering, University of California, Santa Barbara, California 93106, USA

*Corresponding author: doylend@ece.ucsb.edu

Received July 31, 2012; revised September 10, 2012; accepted September 10, 2012;
posted September 11, 2012 (Doc. ID 173459); published October 9, 2012

A chip-scale optical source with integrated beam steering is demonstrated. The chip was fabricated using the hybrid silicon platform and incorporates an on-chip laser, waveguide splitter, amplifiers, phase modulators, and surface gratings to comprise an optical phased array with beam steering across a 12° field of view in one axis. Tuning of the phased array is used to achieve 1.8° (steered axis) \times 0.6° (nonsteered axis) beam width with 7 dB background suppression for arbitrary beam direction within the field of view. © 2012 Optical Society of America

OCIS codes: 250.5960, 280.3640, 250.5300, 250.3140, 200.2605.

Optical phased arrays [1] have gained interest as an elegant means of nonmechanical beam steering for free-space board-to-board adaptive optical interconnects [2] and light detection and ranging (LiDAR) [3]. Fabrication of the system as an integrated photonic circuit can reduce both size and packaging complexity, and the use of silicon-on-insulator (SOI) for such an integrated device enables the incorporation of standard CMOS fabrication techniques, while also permitting hybrid integration of III-V gain materials with planar SOI waveguides for electrically pumped amplifiers [4] and single-wavelength lasers [5]. Chip-scale optical phased arrays using an off-chip laser have been reported [6–9], but eliminating external lasers and fiber coupling by integrating the laser/amplifiers on-chip is desirable.

In this work we report the first demonstration of a self-contained, steerable free-space optical source comprising an optical phased array integrated with a laser and amplifiers on-chip such that the beam can be generated, shaped, and steered in one dimension without off-chip optical components.

Design. Schematics of the device are shown in Fig. 1. A source laser was coupled to a semiconductor optical amplifier (SOA) preamplifier followed by a 1×8 multimode interferometer (MMI) splitter to separate the beam into eight channels. MMIs were used rather than a star coupler in order to minimize loss and for continuity with the previously demonstrated beam steerer reported in [9]. Each channel was then separately amplified, phase adjusted, and emitted from a surface grating array to form a beam in the far field. S-b-bends after the splitter separated the waveguides by $150 \mu\text{m}$ to reduce the thermal power density of the array; additional S-bends after the phase modulators reduced the separation to $5.5 \mu\text{m}$ for the grating array output. The whole device was $16 \text{ mm} \times 4 \text{ mm}$ in size and was fabricated on SOI with 500 nm top silicon and $1 \mu\text{m}$ buried oxide (BOX). The rib waveguides were etched 275 nm deep and were $1 \mu\text{m}$ wide throughout most of the device, but were widened to $3 \mu\text{m}$ prior to the grating array in order to increase far field power in the main beam relative to the side lobes [10]. The surface gratings were separately etched 50 nm deep with 550 nm pitch and 20% duty cycle in order to distribute the emission along the full $200 \mu\text{m}$ length of the grating array, thus maintaining a narrow beam in the far field along the

longitudinal θ axis (i.e., parallel to the waveguides) [9]. The waveguides within the grating array were arranged with $5.5 \mu\text{m}$ pitch for a total array lateral dimension of $44 \mu\text{m}$; these dimensions were chosen in order to maintain overall beam width in the lateral ϕ axis (i.e., perpendicular to the waveguides) of 1.8° while keeping the side lobes outside of the 12° field of view.

Fabrication. Rib waveguides were photolithographically defined and etched in SOI, after which phase modulator diodes were produced within the top silicon via ion implantation of boron and phosphorus. These phase modulators were operated in forward bias to provide local heating to the waveguide, thus thermo-optically adjusting the effective index of the guided mode. Trenches between the phase modulators were etched to the BOX to improve thermal isolation. Following a high-temperature dopant anneal, gratings were patterned using e-beam lithography. III-V quantum well laser material was wafer-bonded to the SOI and the laser and SOA mesas were then patterned and etched, with metal contacts defined by e-beam evaporation and liftoff. Hard-baked SU8 photoresist and PECVD SiO_2 were used as buffer layers over the waveguides with vias etched through them prior to probe-pad metal e-beam evaporation and lift off.

Results. The phase tuning efficiency was measured by recording the far field pattern produced by adjacent pairs of channels as phase was tuned, and was determined to be $97 \text{ mW}/\pi$, similar to what has been observed for conventional heaters overlaying silicon rib waveguides with the same BOX thickness [11]. With the laser and

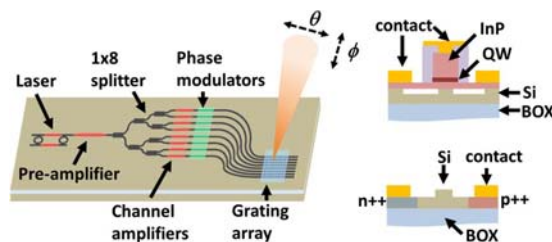


Fig. 1. (Color online) Schematics (not to scale) of the overall device (left), cross-section of the gain elements (right top), and cross-section of the phase modulators (right bottom). QW = quantum wells, Si = silicon, BOX = buried oxide.

preamplifier each pumped at 250 mA, each channel's SOA was individually turned on and its current adjusted for uniform power output to the far field. One of the eight waveguides (channel 5) was found to be damaged such that no signal power could be attained from its SOA; this channel was therefore turned off and only the remaining seven were used to produce the beam.

With seven channels biased for uniform optical output (pump currents ranged from 107 to 163 mA) and the chip mounted on a stage held at 18 °C, current in the SOAs and phase tuners was cycled at 125 Hz, 20% duty cycle (1.6 ms dwells) in order to reduce on-chip heating from the phase tuners. The preamplifier current was cycled at 10% duty cycle (0.8 ms dwells) with a 0.8 ms delay relative to the other elements in order to blank the beam while the SOAs and phase modulators were being turned on and adjusted. A far field imaging system together with a LabVIEW feedback control algorithm similar to that described in [9] were used to adjust the relative phases for shaping and pointing the beam across a 12° range at 1° increments. These phase settings were then used in a lookup table such that the beam could be steered without external feedback, and were found to be stable over several days (the requirement for occasional recalculation was attributed to changes in the thermal contact between the chip and the stage, which can be mitigated by soldering); this stability is a benefit of eliminating optical alignment through integration.

With constant preamplifier current, beam power varied by 3.2 dB across the steering range due to variations in overall heating at each phase setting (and thus SOA gain); it was found that varying preamplifier current from 245 to 290 mA provided 3.4 dB power adjustment without measurable detriment to beam width or background suppression, and is therefore sufficient to compensate for variations in far field output versus steering angle. The normalized far field beam profiles in the ϕ axis are shown in Fig. 2 together with the dependence of beam power on steering angle and preamplifier current. Beam position accuracy of 0.3° was achieved with background suppression of >7 dB for all solved beam positions (the theoretical best background suppression with channel 5 switched off was 8.4 dB). The beam cross-section in both axes for the $\phi = 0^\circ$ case is shown in Fig. 3.

The modeled beam profile in θ was calculated using scattering propagation constant $\alpha = 164 \text{ cm}^{-1}$, which was measured by imaging the scattered intensity versus propagation length along the grating in the near field. Full width half-maximum (FWHM) beam width was measured to be 1.8° in ϕ and 0.6° in θ . The discrepancy between the modeled and measured beam width in θ was attributed to mode evolution within the grating.

Using the solved lookup table to steer the beam to a photodetector positioned in the far field (8 cm distance), beam power with 250 mA pre-amplifier current was measured to be 4.1 μW (quasi-cw), which is comparable to that achievable with the passive chip reported in [9] using an off-chip 1 mW fiber-coupled laser, although 6 dB lower than that required for a commercially viable board-to-board adaptive interconnect [2]. The on-chip laser output was measured by operating the preamplifier in reverse bias as a photodiode. For 250 mA laser current and -3 V preamplifier bias, 66 μA photocurrent was measured

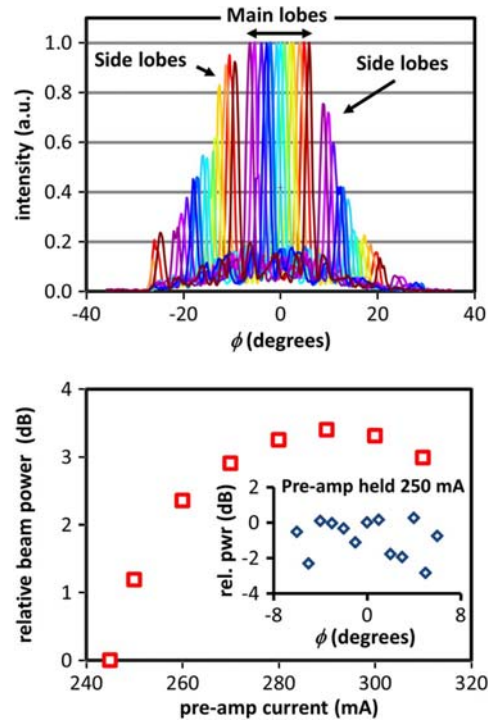


Fig. 2. (Color online) Normalized far field beam cross-sections measured for beam positions from $\phi = -6^\circ$ to $\phi = 6^\circ$ at 1° increments (top), and relative beam power measured versus preamplifier current (bottom). The inset shows variation of beam power with steering angle for constant preamplifier current.

indicating on-chip laser power of 110 μW for photodiode responsivity of 0.6 A/W.

By calculating the power lost to side lobes (-6.6 dB), backside emission from the grating (-6.3 dB), excess loss in the 1×8 MMI tree (-3 dB corresponding to measured -1 dB per splitter [9]), and propagation loss (-4.8 dB) the amplifying elements are estimated to provide 6.4 dB gain.

The beam energy required for short-range (i.e., <2 km) imaging LiDAR is at least 15 μJ [12]; the output power limitation observed in this work was attributed to on-chip heating. This can be mitigated by introducing thermal shunts through the BOX, soldering the chip to a heat sink, and employing electro-optic rather than thermo-optic phase modulation.

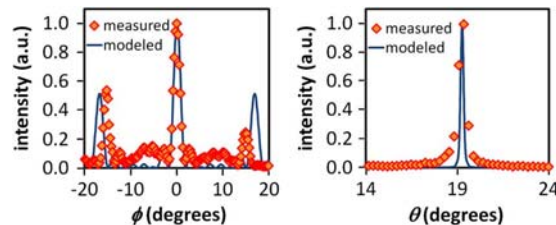


Fig. 3. (Color online) Measured far-field beam cross-sections in ϕ (left) and θ (right) of the far field beam for the phased-array solution at $\phi = 0^\circ$. The discrepancy between measured and modeled side-lobe position was attributed to lens Seidel aberrations.

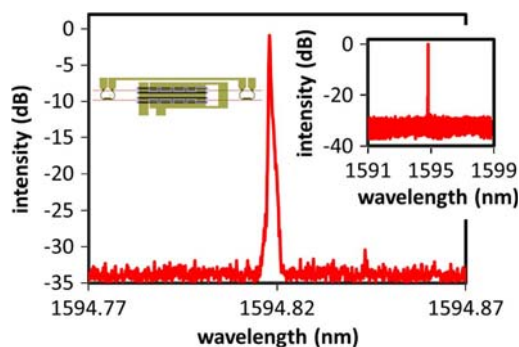


Fig. 4. (Color online) Optical spectrum (resolution: 40 MHz) of the free-space output demonstrating single wavelength operation (inset: right) from the on-chip source laser (inset: left).

The source laser incorporated a dual ring-coupled cavity similar to the design described in [13] to provide single-wavelength operation. The spectral characteristics of the laser were measured with an APEX 2051A optical spectrum analyzer by collecting the free-space optical output from the combined laser/preamplifier/SOA. The beam spectrum thus obtained is shown in Fig. 4. Laser linewidth was less than 40 MHz with 30 dB sidemode suppression. Since the laser in the device was integrated with amplifiers, the LIV characteristic was measured indirectly: (a) by operating the preamplifier in reverse bias (-3 V) to act as a photodiode, (b) by using the imaging lens system to measure the optical power versus on-chip laser current while holding/pulsing the SOAs as described above, and (c) by recording the signal strength of the laser peak on the optical spectrum analyzer (OSA). These data represent power at different stages in the on-chip link budget and are therefore shown normalized in Fig. 5.

The nonzero emitted power for the far field power monitor measurement was due to amplified stimulated emission (ASE) emitted from the amplifier array during the $800 \mu\text{s}$ delay between SOA and preamplifier turn-on. The laser exhibited threshold current of 120 mA corresponding to 2.0 kA/cm^2 threshold current density, which is comparable to other CW single-wavelength hybrid lasers [5].

Conclusion. A hybrid silicon photonic integrated circuit phased array incorporating a laser, amplifiers, and individual phase tuning for free-space beam steering has been demonstrated, achieving 12° tuning range in the far field with $4.1 \mu\text{W}$ main lobe beam power, 7 dB background suppression, and 0.3° pointing accuracy. Future work will incorporate wavelength tuning of the laser for two-dimensional steering, on-chip interferometers, and photodiodes for internal feedback concerning the far field beam shape, a larger emission array for improved far field spatial resolution, and electro-optic phase modulation for high-speed beam steering.

The authors thank Pietro Binetti, Weihua Guo, Chad Althouse, and Scott Rodgers for useful discussions. This

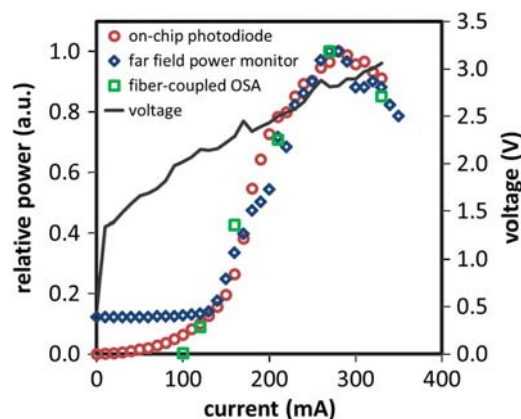


Fig. 5. (Color online) Normalized measurements of (a) the on-chip photocurrent from the preamplifier held at -3 V bias, (b) power coupled to a Newport 818 power meter using the far field imaging system, and (c) peak signal fiber-coupled to the APEX 2541 OSA.

research was supported by the DARPA Sweeper program, grant no. HR0011-10-2-0003. Jonathan Doylend's work was supported in part by a Natural Sciences and Engineering Research Council of Canada Post-doctoral Fellowship.

References

1. P. F. McManamon, P. J. Bos, M. K. Escuti, J. Heikenfeld, S. Serati, X. Huikai, and E. A. Watson, *Proc. IEEE* **97**, 1078 (2009).
2. C. J. Henderson, D. G. Leyva, and T. D. Wilkinson, *J. Lightwave Technol.* **24**, 1989 (2006).
3. A. Schweinsberg, Z. Shi, J. E. Vornehm, and R. W. Boyd, *Opt. Express* **19**, 15760 (2011).
4. H. Park, Y.-H. Kuo, A. W. Fang, R. Jones, O. Cohen, M. J. Paniccia, and J. E. Bowers, *IEEE Photon. Technol. Lett.* **19**, 230 (2007).
5. A. W. Fang, M. N. Sysak, B. R. Koch, R. Jones, E. Lively, Y. Kuo, D. Liang, O. Raday, and J. E. Bowers, *IEEE J. Sel. Top. Quantum Electron.* **15**, 535 (2009).
6. K. Van Acoleyen, W. Bogaerts, J. Jagerská, N. Le Thomas, R. Houdré, and R. Baets, *Opt. Lett.* **34**, 1477 (2009).
7. K. Van Acoleyen, H. Rogier, and R. Baets, *Opt. Express* **18**, 13655 (2010).
8. D. Kwong, A. Hosseini, Y. Zhang, and R. T. Chen, *Appl. Phys. Lett.* **99**, 051104 (2011).
9. J. K. Doylend, M. J. R. Heck, J. T. Bovington, J. D. Peters, L. A. Coldren, and J. E. Bowers, *Opt. Express* **19**, 21595 (2011).
10. J. K. Doylend, M. J. R. Heck, J. T. Bovington, J. D. Peters, and J. E. Bowers, in *Optical Fiber Communication Conference*, OSA Technical Digest Series (Optical Society of America, 2012), paper OM2J.1.
11. R. Jones, J. K. Doylend, P. Ebrahimi, S. Ayotte, O. Raday, and O. Cohen, *Opt. Express* **15**, 15836 (2007).
12. J. A. Overbeck, M. S. Salisbury, M. B. Mark, and E. A. Watson, *Appl. Opt.* **34**, 7724 (1995).
13. B. Liu, A. Shakouri, and J. E. Bowers, *IEEE Photon. Technol. Lett.* **14**, 600 (2002).

InP Photonic Integrated Circuit for 2D Optical Beam Steering

Weihua Guo¹, Pietro R. A. Binetti¹, Chad Althouse¹, Huub P.M.M. Ambrosius², Leif A. Johansson¹, member, IEEE, and Larry A. Coldren¹, Fellow, IEEE

¹Department of Electrical and Computer Engineering, University of California, Santa Barbara, CA 93106, USA

²Electrical Engineering Department, Eindhoven University of Technology, Eindhoven, NL

Email: guow@ece.ucsb.edu

Abstract: 2D optical beam steering through an InP photonic integrated circuit with on-chip monitors and an AWG-like structure has been demonstrated.

OCIS codes: (250.5300) Photonic integrated circuits; (280.3640) Lidar;

Electronically controlled 2D optical beam steering is potentially useful for applications like LIDAR, 3D imaging, precision targeting, guidance and navigation, etc. Recently, we have demonstrated an InP photonic integrated circuit (PIC) for this purpose [1-2]. Fig.1 (a) shows the layout of the PIC which consists of the input semiconductor optical amplifier (SOA), the 1×2 MMI tree which splits the input into eight channels, an SOA array and a phase shifter array which are used to boost the power and control the phase of each channel, then the waveguide array with embedded 2nd-order gratings for the out-of-plane emission, and the monitor array. The mechanism for 2D beam steering is that: the array of phase shifters is used to add a phase slope across the waveguide array so as to steer the beam perpendicularly to the waveguide in the array (lateral direction); the input wavelength is changed to steer the beam along the waveguide in the array (longitudinal direction) because the emission angle of the grating depends on wavelength [1]. As shown in Fig. 1 (a) additional bends are added to make each channel have equal length. All these bends use the same radius (200 μm) and the same total lengths. Such AWG-like structure prevents additional differential phase being generated when changing wavelength. Fig. 1 (b) shows the blown-up of the monitors. Each channel is split into three equal parts by a 1×3 MMI. Two close parts from two adjacent channels are combined by a 1×2 MMI to form interferometers with the interference monitored by a photodiode (PD) as seen from Fig. 1 (b). In this work we show that the on-chip monitors and the AWG-like PIC structure have made the 2D beam steering easier.

The monitors can be used to characterize the phase shifters on-site so that the dependence of the generated phase shift on injected current, i.e. the phase-current curve, can be established. Then the phase slope across the array required by a specific steering angle θ , which is $\phi_i = 2\pi(i-1)d \sin(\theta)/\lambda$ where d is the array pitch and λ is the wavelength, can be set directly by referring to the established phase-current curves. The result is shown in Fig. 1 (c).

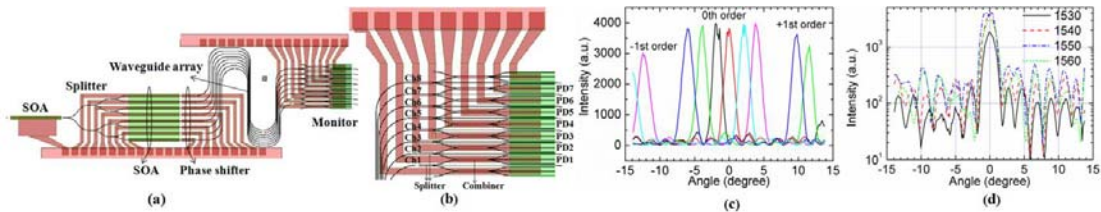


Fig. 1 (a) Layout of the PIC; (b) Blown-up of the monitor array; (c) Far-field pattern in the lateral direction for the input wavelength of 1540 nm and different steering angles; (d) Far-field pattern in the lateral direction for the input wavelength of 1530, 1540, 1550, and 1560 nm.

Also because the PIC takes an AWG-like structure, the far-field pattern of the beam keeps having a good shape and high side-lobe suppression (~2.0 degree 3dB beam width and 10 dB side-lobe suppression from -15 to 15 degree) when changing the input wavelength even when we do not reset the phased shifter currents as shown in Fig. 1 (d).

In summary we have demonstrated 2D optical beam steering through an InP PIC with on-chip monitors and an AWG-like structure.

References

- [1] W. H. Guo, P. R. A. Binetti, C. Althouse, A. Bhardwaj, J. K. Doylend, H. P. M. M. Ambrosius, L. A. Johansson, and L. A. Coldren, "InP photonic integrated circuit for 2D optical beam steering," Post-deadline paper, IEEE Photonics 2011 (IPC11), Arlington, Virginia, USA, 2011.
- [2] W. H. Guo, P. R. A. Binetti, C. Althouse, H. P. M. M. Ambrosius, L. A. Johansson, and L. A. Coldren, "Improved performance of optical beam steering through an InP photonic integrated circuit," CWIK, CLEO2012, San Jose, CA, USA, 2012.

II. Vertical-Cavity Surface-Emitting Lasers (VCSELs)

Frequency Dependent Polarization Dynamics in Vertical Cavity Surface Emitting Lasers with Electrical Injection

Ajit V. Barve^a, Yan Zheng^a, Leif Johansson^a and Larry Coldren^{a,b,*}

^aDepartment of Electrical and Computer Engineering, University of California Santa Barbara, CA 93106, USA

^bDepartment of Materials, University of California Santa Barbara, CA 93106, USA

Abstract—We report on the polarization dynamics in VCSELs with a small frequency modulation. The polarization state of a VCSEL is shown to be controlled by only changing the frequency of the modulation to electrical injection.

Understanding and controlling the polarization properties of vertical cavity surface emitting lasers (VCSEL), is of critical importance for the applications in communication networks with polarization sensitive elements, as well as other important applications, such as, medical imaging, environmental monitoring and military. VCSEL modes are transverse electromagnetic (TEM) in nature due to the vertical structure. The polarization orientation in the lateral direction is hard to control due to the symmetric nature of typical VCSELs. Crystalline symmetries generally give rise to two dominant linear polarization directions, oriented along $\langle 110 \rangle$ and $\langle 1\bar{1}0 \rangle$ axes. These linear polarization modes are usually bistable and exhibit polarization switching at certain bias currents. Various techniques have been previously used to control the polarization state of a VCSEL, such as, asymmetric current injection [1], controlled stress etc. In this paper we report, for the first time, on the complex high frequency polarization dynamics occurring near the polarization switching point. We demonstrate that the polarization state of a VCSEL can be altered by changing only the frequency of electrical modulation, while keeping all other parameters fixed. These results not only enable a new method for polarization control in VCSELs, but also underline the complex dynamics near the polarization switching point.

Highly strained VCSEL material with InGaAs/GaAs quantum well active region, operating at 1060nm was chosen for this study. The VCSEL under test has a circular mesa of 14 μ m diameter. A tapered oxide aperture, with oxidation length of 3 μ m, was used to confine the carriers and provide index guiding. The substrate of the bottom-emitting VCSEL was antireflection coated to minimize the optical feedback. The polarization dependent light-current (LI) curve of this VCSEL is shown in Fig. 1. This VCSEL shows type I polarization switching (switching from high to low wavelength) around 0.78mA of bias.

In order to study the frequency dependence of its polarization properties, the VCSEL was electrically modulated with a network analyzer, operating at 130MHz to 20GHz frequency range, at a modulation power of 1mW. This corresponds to a current swing of approximately 300 μ A peak to peak, which is much lower than the bias current. Light emitted from the bottom was focused onto a multimode optical fiber using aspheric lens and mirror assembly, after passing through a polarizer. The signal was detected using a 25GHz infrared photodetector, the output of which was amplified and fed to the network analyzer. The modulation transfer function was measured at several different DC biases, and the resulting responses were plotted in two dimensional contour plots, shown in Fig. 2.

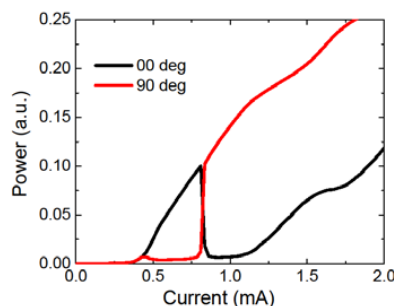


Fig. 1. VCSEL L-I with a polarizer showing polarization switching at 0.78mA.

It is clear from Fig. 2 that even though all other parameters are unchanged, the polarization direction can be controlled by varying the frequency of modulation. For instance, above 0.7mA, the polarization switching to 90° occurs only above 4GHz. Below 4GHz, both the polarization modes are coexisting. The exact nature of this frequency response depends on the modulation amplitude. For example, at the modulation power of -10dBm, the optical power goes from 90° to 0° between 3-4GHz, and goes back into 90° polarization mode above 4GHz. The small increase in modulation response in 0° polarization response shown in Fig. 2(a) is due to a higher order mode. It should be noted that these phenomena are not thermally driven, as the modulation

This work was supported by DARPA, via STTR with Ziva Corp.

frequencies are much higher than typical thermal cutoff frequencies for polarization switching, which are less than 1MHz [2].

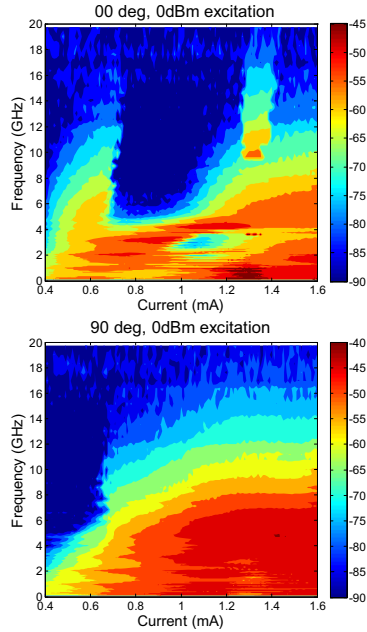


Fig. 2. Frequency response of VCSEL for two different polarization directions as a function of bias current, showing frequency dependent polarization switching.

In order to estimate the polarization switching extinction ratio that can be obtained by changing the frequency, a DC measurement of power was carried out on this VCSEL under high frequency continuous wave (CW) electrical modulation. Results are shown in Fig. 3. It is clear that the ratio of power going into each polarization can be controlled by the frequency of modulation. It should be emphasized that only the averaged DC power was measured in this experiment. High extinction ratio of 18dB was obtained just by changing the CW modulation frequency.

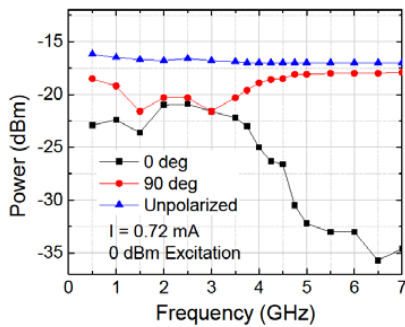


Fig. 3. DC power in different polarization modes of VCSEL under different frequency modulation.

Fig. 4. shows optical spectra at two different frequencies of modulation. VCSEL was biased at 0.72mA, with an RF power of 0dBm superimposed on the DC bias. The optical modes are broadened, probably due to chirping as a result of modulation. It can be seen that at 3GHz modulation, the fundamental mode consists of two orthogonal polarizations with equal intensity. As the frequency of modulation increases to 6GHz, the power shorter wavelength mode decreases as compared to the longer wavelength mode. Unpolarized spectrum is simply the sum of the spectra for two orthogonal polarizations.

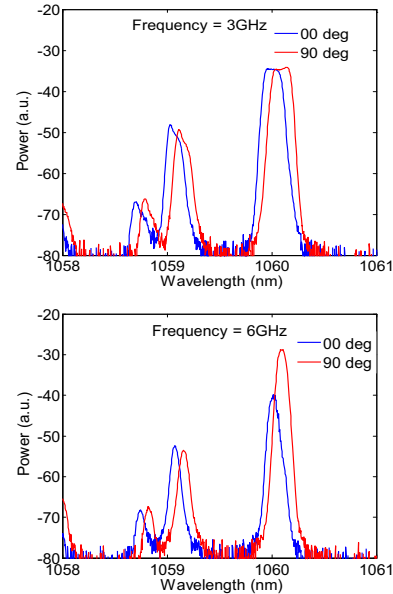


Fig. 4. Optical spectrum obtained from the VCSEL biased at 0.72mA of DC current, with constant frequency modulation of (a) 3GHz and (b) 6GHz..

In conclusion, the polarization state of a VCSEL can be altered purely by changing the modulation frequency of electrical injection. High extinction ratios obtained by this method suggest the potential for this technique for polarization control, possibly at high modulation speeds. Measurements reported here also important towards understanding the complex physics behind the frequency dependent polarization dynamics in VCSELs.

Disclaimer: The views expressed are those of the authors and do not reflect the official policy or position of the Department of Defense or the U.S. Government.
Approved for Public Release, Distribution Unlimited

References:

[1] Augustin et al, IEEE Photon. Technol. Lett., 16(3), pp 708, 2004
[2] Verschaffelt et al, IEEE J. Quantum Electron., 39(10), pp 1177, 2003

Ultra-compact intra-cavity contacts for multi-terminal VCSEL power enhancement

Chin-Han Lin¹, Brian J. Thibeault¹, Yan Zheng¹, John S. Parker¹, Mark J. W. Rodwell¹, and Larry A. Coldren^{1,2}

¹Department of Electrical and Computer Engineering, University of California, Santa Barbara, CA93106, USA

²Department of Materials, University of California, Santa Barbara, CA93106, USA

Phone: 1-805-893-7065 Fax: 1-805-893-4500 Email: chinhan@ece.ucsb.edu

Abstract – We demonstrate ultra-compact intra-cavity contacts fabricated with an embedded Al₂O₃ etch-stop, which effectively shorten the cavity length and enhance the output power of a multi-terminal VCSEL.

I. Introduction

As the conventional diode vertical-cavity surface-emitting lasers (VCSELs) gained huge process in the communication and sensing area [1], multi-terminal VCSELs have also become very intriguing due to their novel functionalities [2]-[4]. These complex devices normally incorporate lengthened cavity designs and extra intra-cavity contacts. A lengthened cavity and the insertion of extra highly-doped layers inevitably lead to a smaller confinement factor Γ , a higher internal loss α_i , and thus a higher threshold current I_{th} . The differential quantum efficiency (DQE) η_d , determined by the injection efficiency η_i , the internal loss α_i , and the mirror loss α_m according to (1), will also be reduced as a result.

$$\eta_d = \eta_i \frac{\alpha_m}{\alpha_m + \alpha_i} \quad (1)$$

The combined effect of a higher I_{th} and a lower DQE is a reduction in the output power. Moreover, a higher I_{th} also means a lower differential gain and a lower modulation speed. To address these issues that multi-terminal VCSELs commonly share, a way to make compact intra-cavity contacts is very desirable.

II. Wet thermal oxide as the embedded etch-stop

To compress the cavity length and enhance device yield, we developed an etch-stop process by tailoring the composition of the first AlGaAs DBR layer that is directly adjacent to the quantum wells (QWs), so an elongated Al₂O₃ layer will form after the wet thermal oxidation together with the oxide aperture. This wet thermal Al₂O₃ is impervious to Cl₂-based dry-etch and can be easily removed with a selective wet-etch, making an embedded etch-stop feasible.

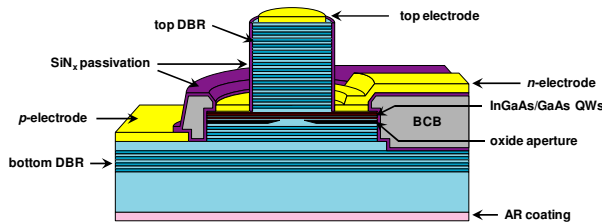


Fig. 1. Schematic of a compact cavity three-terminal VCSEL.

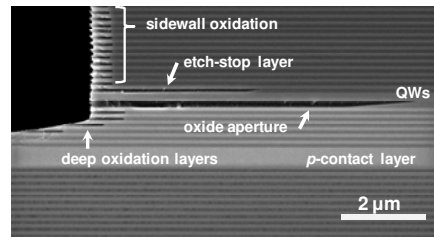


Fig. 2. Cross-sectional SEM image of various oxide structures.

To demonstrate this process, we designed a compact cavity three-terminal VCSEL with the embedded Al₂O₃ etch-stop, with schematic is shown in Fig. 1. The SEM image of various oxide structures (after wet thermal oxidation) is shown in Fig. 2. It is crucial to design the layer structure carefully so the etch-stop extends long enough to protect the quantum well layer completely, but also short enough so the optical mode will only be confined by the oxide aperture, otherwise extra loss will be induced. The InGaAs/GaAs quantum wells, sandwiched by the oxide aperture and the etch-stop layer, are grown with delta-doped silicon in the barriers to provide two-dimensional electron gas (2DEG) carrier injection from the ring contact. As a result, no extra etch buffer layer is required, the cavity length is kept minimal, and the doping within the cavity is minimized.

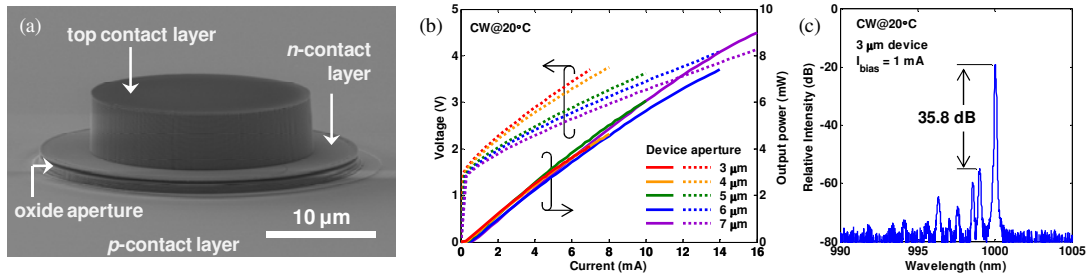


Fig. 3. (a) SEM image of the double mesa, after etch-stop removal. (b) L-I-V curves. (c) lasing spectrum of a 3 μm device with $I_{\text{bias}} = 1 \text{ mA}$.

III. Device Fabrication

The base structure was grown on semi-insulating GaAs (100) substrate with a bottom emission configuration. First dry-etching down to the p -contact layer was used to define the outer mesa. Afterwards, wet thermal oxidation simultaneously created the oxide aperture and the etch-stop layer, which endured the second inner mesa dry-etch and allowed over-etching for good uniformity. The Al_2O_3 etch-stop and the residual $\text{Al}_2\text{O}_3/\text{GaAs}$ sidewall were removed with AZ400K developer, exposing the smooth intra-cavity n -contact layer, as shown in Fig. 3(a). A vertical silicon nitride sidewall was created through a semi self-aligned process [5] to isolate the ring n -contact and the top DBRs. The ring n -contact, p -contact and top n -contact metals were deposited separately, followed by annealing, BCB planarization, electrode pads deposition, and backside anti-reflection (AR) coating.

IV. Experimental Results

The fabricated devices were tested with a dc setup. Fig. 3(b) shows the voltage and output power versus current (L-I-V) curves for devices with apertures ranging from 3 μm to 7 μm in diameter. The lasing wavelength is around 1000 nm. All of these devices have a sub-mA threshold current, with a differential quantum efficiency around 54%, and a threshold voltage around 1.54 V, just slightly above the bandgap. The series resistance decreases as the aperture scales up, from 298 Ω for the 3 μm device, to 156 Ω for the 7 μm device. Due to the nature of dual intra-cavity carrier injection, larger devices support multiple higher order modes. The 3 μm device supports single-mode operation up to 1.6 mA of bias current (Fig. 3(c)).

V. Conclusion

We have demonstrated the novel method of fabricating ultra-compact intra-cavity contact layers for VCSELs with the assist of an embedded Al_2O_3 etch-stop layer. Compact cavity three-terminal VCSELs were fabricated, and threshold currents and output powers were on par with those of state-of-the-art diode VCSELs. The series resistance can be further reduced by increasing the delta-doping in the quantum well barriers, or by introducing modulation doping at the optical nodes in the p -contact layer.

Acknowledgment

This work was supported by DARPA through a STTR with Ziva Corp. and by NSF through a GOALI program. A portion of this work was done in the UCSB nanofabrication facility, part of the NSF funded NNIN network.

References

- [1] A. Larsson, "Advances in VCSELs for Communication and Sensing," *IEEE J. Sel. Topics Quantum Electron.*, Vol. 17, No. 6, pp. 1552-1557 (November/December 2012).
- [2] C.-H. Lin, Y. Zheng, M. J.W. Rodwell, L. A. Coldren, "First Demonstration of Modulation via Field-Induced Charge-Separation in VCSEL," *22nd IEEE International Semiconductor Laser Conference*, post-deadline session, PD2, Kyoto, Japan (Sept. 26-30, 2010).
- [3] Y. Zheng, C.-H. Lin, L. A. Coldren, "Control of Polarization Phase Offset in Low Threshold Polarization Switching VCSELs," *Photonic Technology Letters*, **23**, (5), pp. 305-307 (March 1, 2011).
- [4] C. Chen, P. O. Leisher, C. Long, D. M. Grasso, and K. D. Choquette, "High Speed Electro-Absorption Modulation of Composite Resonator Vertical Cavity Laser," *IET Optoelectron.*, Vol.3, No. 2, pp. 93-99 (2009)
- [5] M. Urteaga, R. Pierson, P. Rowell, B. Brar, Z. Griffith, M. Dahlström, M.J.W. Rodwell, S. Lee, N. Nguyen, C. Nguyen, "Wide Bandwidth InP DHBT Technology Utilizing Dielectric Sidewall Spacers," *Proc. IEEE International Conference on Indium Phosphide and Related Materials*, Kagoshima, Japan (May 31-June 4, 2004).

P-type δ -doping of highly-strained VCSELs for 25 Gbps operation

Yan Zheng[†], Chin-Han Lin[†], Ajit V. Barve[†], Larry A. Coldren^{†*}

Departments of [†]Electrical and Computer Engineering and ^{*}Materials, University of California, Santa Barbara, CA 93106

Abstract—We present the utilization of δ -doping to mitigate the rise in nonlinear gain compression in highly-strained InGaAs VCSELs and compare it with unstrained and undoped active region designs. High speed 25 Gbps operation is also demonstrated.

Keywords- VCSELs, optical interconnect, highly-strained, δ -doping

I. INTRODUCTION

The rapidly expanding web of servers and racks are increasingly being connected optically. These optical interconnects can carry more data, are faster and do not heat up. However with the growing number of connections, they also need to be energy efficient. Vertical cavity surface emitting lasers (VCSELs) have long been recognized as a key component for optical interconnects because of their small size, speed and low power consumption.

Recent progress has shown that by moving to highly-strained quantum wells with wavelengths around 1060 nm highly-energy-efficient VCSELs [1] can be achieved. This is because increased strain enhances differential gain and reduces the gain transparency condition [2]. However, strain has been linked to an increase in nonlinear gain compression, mainly through carrier heating [3], which can reduce the modulation bandwidth. One method to address this issue is to increase intraband scattering events by adding modulation doping to the active region [4].

In this report we compare two sets of highly-strained 1060 nm VCSELs and demonstrate that nonlinear gain compression can be suppressed with δ -doping. The doped VCSEL also shows superior intrinsic characteristics compared to commercial 850 nm VCSELs. A maximum $f_{3\text{dB}}$ bandwidth of 18.5 GHz and large signal operation of 25 Gbps is achieved.

II. DEVICE DESIGN

We grew the VCSELs on (100) semi-insulating GaAs substrates using molecular beam epitaxy (MBE) system. The bottom mirror consisted of unintentionally doped (UID) GaAs/AlAs followed by a $1 \frac{3}{4} \lambda$ thick layer of Si doped GaAs to form an intracavity n-contact layer. The tapered oxide aperture layer is $\frac{1}{2} \lambda$ thick and is placed so that the tip of the taper occurs at the standing wave null. Four periods of deep oxidation layers are grown after that to reduce capacitance. The top mirror consists of GaAs/AlGaAs

mirrors that are bandgap-engineered for low resistance and low optical loss. Details of this design can be found in [5].

The active region is surrounded by an asymmetric $\text{Al}_{0.3}\text{Ga}_{0.7}\text{As}$ separate confinement heterostructure (SCH) that is parabolically graded down to GaAs spacers. Three 8 nm thick highly-strained $\text{In}_{0.3}\text{Ga}_{0.7}\text{As}$ quantum wells (QWs) are separated by 8 nm GaAs barriers. Growth is stopped halfway into the barrier and the surface is δ -doped with carbon using a carbon tetrabromide (CBr_4) precursor. We found that by pausing growth after each doped layer residual dopants in the chamber could be pumped out more thoroughly thereby reducing the probability of incorporating nonradiative recombination centers into the QWs. Once inside the barrier, carbon will move very little compared to beryllium because of its low diffusion coefficient [6]. The finished device is shown in Fig. 1.

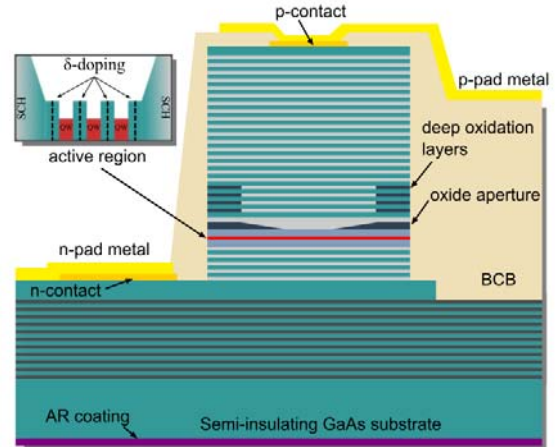


Fig. 1 Schematic showing notable components of the VCSEL. The inset is an expanded view of the active region with the δ -doping regions labeled.

III. RELATIVE INTENSITY NOISE

Although increasing strain is known to enhance differential gain, it is suspected that nonlinear gain compression, ϵ , is also simultaneously enhanced. We investigated this by simulating fits to relative intensity noise (RIN) measurements to extract the damping rate, γ , which is an indicator of the laser's intrinsic modulation bandwidth. Because the K -factor in the damping rate relation (1) is a function of both differential gain, $\partial g / \partial N$ and ϵ , it is useful to

This work was supported by DARPA via a STTR with Ziva Corp.

solve for the individual contribution to γ from these terms using (2) and (3).

$$\gamma = Kf_r^2 + \frac{1}{\tau_c} \quad (1)$$

$$f_r = \frac{1}{2\pi} \sqrt{\frac{\Gamma v_g \eta_i \partial g / \partial n (I - I_{th})}{qV}} \quad (2)$$

$$K = \frac{(2\pi)^2}{v_g} \left(\frac{\epsilon}{\partial g / \partial n} + \frac{1}{\alpha_i + \alpha_m} \right) \quad (3)$$

The light output was coupled into a multimode fiber using a collimating aspheric lens and a fiber port. The threshold current for $\sim 8 \mu\text{m}$ diameter doped and undoped VCSEL was around $300 \mu\text{A}$. From broad area laser measurements, the internal loss, α_i was determined to be 5.5 cm^{-1} and 11.5 cm^{-1} for the undoped and δ -doped material respectively.

Calculated and measured values for our highly-strained VCSELS are compared against a 850 nm GaAs MQW VCSEL [7] shown in Table I. There is a very noticeable enhancement in $\partial g / \partial n$ going from an unstrained GaAs to a highly-strained $\text{In}_{0.3}\text{Ga}_{0.7}\text{As}$ QW design accompanied by a large increase in ϵ . However, the addition of δ -doping mitigates the rise in ϵ and cuts the K -factor by over 50%.

TABLE I.
EFFECT OF δ -DOPING ON HIGHLY-STRAINED VCSELS

	$\partial g / \partial n \text{ (cm}^2\text{)}$	$\epsilon \text{ (cm}^3\text{)}$	$K\text{-factor (ns)}$
<i>Undoped 850 nm GaAs VCSEL [7]</i>	$7.19 \text{ e-}16$	$2.5 \text{ e-}17$	0.393
<i>Undoped 1060 nm In_{0.3}Ga_{0.7}As VCSEL</i>	$2.35 \text{ e-}15$	$1.2 \text{ e-}16$	0.442
<i>δ-doped 1060 nm In_{0.3}Ga_{0.7}As VCSEL</i>	$2.54 \text{ e-}15$	$3.0 \text{ e-}17$	0.202

IV. MODULATION RESPONSE

High speed modulation testing revealed a $f_{3\text{dB}}$ bandwidth of 18.5 GHz and 16.5 GHz for the δ -doped and undoped VCSELS respectively. The parasitic free $f_{3\text{dB}}$ bandwidth calculated from the relation $f_{3\text{dB}}|_{\text{max}} = 2\pi\sqrt{2}/K$ indicates that the δ -doped VCSEL has a max bandwidth of 44 GHz while the undoped VCSEL has only a 20 GHz max bandwidth. The large difference is a result of the reduced damping in doped VCSELS. Both devices however, are limited by electrical parasitic and thermal limits. Error-free operation at 25 Gbps was achieved using a δ -doped $8 \mu\text{m}$ aperture device. The data-rate to power dissipation ratio is 2.5 Gbps/mW which is 400 fJ/bit .

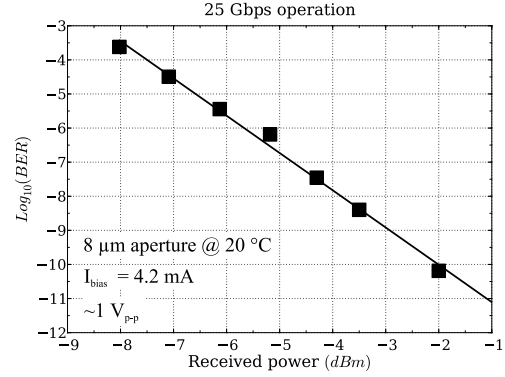


Fig. 2 Bit error rate for a δ -doped $8 \mu\text{m}$ device.

V. CONCLUSION

We have shown that despite the increase in differential gain, highly-strained active regions also have a much higher nonlinear gain compression coefficient. For efficient operation, doping in the active region is essential to mitigating this effect by enhancing the intraband scattering rate and reducing damping.

ACKNOWLEDGMENT

We would like to thank Leif Johansson and John Garcia for their help on the high speed measurements. A portion of this work was done in the UCSB nanofabrication facility, part of the NSF funded NNIN network.

REFERENCES

- [1] K. Takaki, S. Imai, S. Kamiya, H. Shimizu, Y. Kawakita, K. Hiraiwa, T. Takagi, H. Shimizu, J. Yoshida, T. Ishikawa, N. Tsukiji and A. Kasukawa, "1060-nm for inter-chip optical interconnection," *Proc. SPIE 7952*, 795204, 2010.
- [2] L.A. Coldren, Y.-C. Chang, Y. Zheng, C.-H. Lin, "Efficient sources for chip-to-chip to box-to-box communication within data centers," *IEEE Photonics Society Summer Topical Meeting Series*, paper no. TuD2.1, pp.205-206, July, 2010.
- [3] M. Willatzen, T. Takahashi, and Y. Arakawa, "Nonlinear gain effects due to carrier heating and spectral holeburning in strained-quantum well lasers," *IEEE Transactions Photonics Technology Letters*, vol. 4, no. 7, pp. 682-685, 1992.
- [4] A. Schonfelder, S. Weisser, I. Esquivias, J. D. Ralston, and J. Rosenzweig, "Theoretical investigation of gain enhancements in strained In/sub 0.35/Ga/sub 0.65/As/GaAs MQW lasers via p-doping," *Photonics Technology Letters, IEEE*, vol. 6, no.4, pp. 475 - 478, 1994.
- [5] Y.-C. Chang and L.A. Coldren, "Optimization of VCSEL Structure for High-Speed Operation," *Proc. IEEE International Semiconductor Laser Conference*, ThA1, Sorrento, Italy, September 14-18, 2008.
- [6] E. F. Schubert, *Doping in III-V Semiconductors*, Cambridge, UK: Cambridge University Press, 1993, pp.190.
- [7] C. Ji, J. Wang, D. Soderstrom and L. Giovane, "20-Gb/s 850-nm Oxide VCSEL Operating at 25C-70C," *Photonics Technology Letters, IEEE*, vol. 22, no. 10, pp. 670 -672, may15, 2010.

Electro-thermal Single-mode Tuning in Field-Induced Charge-Separation Lasers

Chin-Han Lin¹, Yan Zheng¹, Leif A. Johansson¹, Mark J. W. Rodwell¹, and Larry A. Coldren^{1,2}

¹Department of Electrical and Computer Engineering, University of California, Santa Barbara, CA 93106, USA

²Department of Materials, University of California, Santa Barbara, CA 93106, USA

Phone: 1-805-893-7065 Fax: 1-805-893-4500 Email: chinhan@ece.ucsb.edu

Abstract – We demonstrate the wavelength tunability via electro-thermal effect of field-induced charge-separation lasers (FICSLs). A large 6.6 nm tuning range is achieved with only 4.6 mA of tuning current. This high tuning efficiency persists up to about 40 kHz.

I. Introduction

We have demonstrated a novel Field-Induced Charge-Separation Laser (FICSL) in a Vertical-Cavity Surface-Emitting Laser (VCSEL) embodiment, which promises to increase the modulation bandwidth via modulating the gain directly [1][2]. Recently, it was discovered that by adding the doping in the off-state well to decrease the minority carrier lifetime, the non-radiative recombination rate in this region could be increased. As a result, an intra-cavity electro-thermal tuning region was formed where electrons and holes recombined and emitted phonon energy. This enables FICSLs to be operated as a tunable VCSEL for wavelength division multiplexing (WDM) systems, complementing the well-studied MEMS tunable VCSELs [3][4] as well as other electro-thermal tunable VCSELs [5].

II. Intra-cavity electro-thermal tuning region

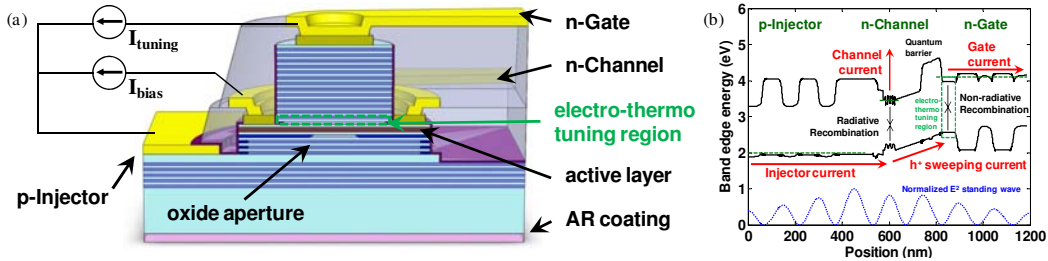


Fig. 1. (a) Schematic of a FICSL showing an intra-cavity electro-thermo tuning region (b) Band diagram showing different current flows

The schematic of a FICSL is shown in Fig. 1a, with the one-dimensional band-edge diagram near the active region along the longitudinal direction shown in Fig. 1b. To separate electrons and holes, a quantum barrier was deliberately created through bandgap engineering. When a gate bias is applied, holes are driven away from the quantum well into the off-state well, and start to accumulate. As the off-state well is doped n-type, holes and electrons will recombine at a rate determined by the doping level. This recombination rate can be pre-determined by material growth: the higher the n-doping is, the shorter the minority carrier (hole) lifetime, and the higher the recombination rate will be.

At equilibrium, electrons and holes consumed by binomial recombination have to be replenished from the gate and the injector respectively. According to Kirchhoff's circuit law, the hole current flowing into the off-state well has to be equal to the electron current supplied by the gate, and equal to the recombination current in the off-state well. The hole current coming from the injector will be split into two streams: the radiative recombination current which contributes to the lasing mode, as well as the hole sweeping current into the off-state well. As the optical output power was predominantly determined by the radiative recombination in the quantum wells, the non-radiative recombination in the off-state change the lattice temperature in proximity, resulting in an index change as well as a cavity mode shift. The lasing wavelength will be tuned as a result.

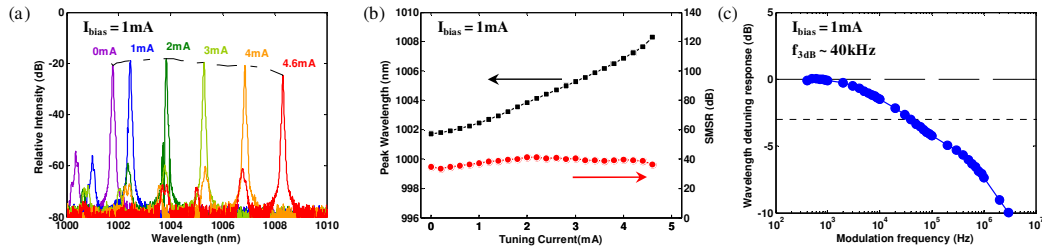


Fig. 2. Room temperature wavelength tuning of a 3 μm device with $I_{\text{bias}} = 1 \text{ mA}$ (a) lasing spectra with different I_{tuning} . (b) Peak wavelength and side mode suppression ratio (SMSR) vs. I_{tuning} . (c) Dynamic tuning characteristics with a cut-off frequency $f_{3\text{dB}} \sim 40 \text{ kHz}$.

III. Device Design

To demonstrate the tuning effect, a p-i-n-i-n three-terminal device was grown and fabricated, similar to the structure reported before [1]. The doping level in the off-state well was increased to reduce the hole life-time and promote recombination. Devices with smaller oxide apertures were fabricated to suppress side modes and allow single-mode operation.

IV. Experimental Results

Two current sources were required for characterization: one for the constant bias current, I_{bias} , and the other for the variable tuning current, I_{tuning} , with the configuration shown in Fig. 1a. A device with a 3 μm aperture was chosen as it operated with single-mode up to 1.6 mA of I_{bias} . The spectra were recorded by an optical spectrum analyzer (OSA) with the side-mode suppression ratio (SMSR) calculated accordingly. Fig. 2a shows the lasing spectra, and Fig. 2b shows the peak wavelengths and SMSRs with different I_{tuning} . A continuous tuning of 6.6 nm was achieved with 0 to 4.6 mA of tuning current, while the device maintained single-mode within this tuning range. The wavelength change versus stage temperature was characterized to be 0.0698 nm/ $^{\circ}\text{C}$.

The dynamic characterization was performed by driving the device with a sinusoidal I_{tuning} with a function generator. The wavelength detuning was then determined by the spacing between the two major peaks on the OSA. For the 3 μm device, the detuning at low frequencies was around 1.69 nm. At high frequencies, this mode spacing decreased with a 3dB cut-off frequency around 40 KHz, as shown in Fig. 2c.

V. Conclusion

We have demonstrated the electro-thermo wavelength tuning model for FICSLs. The minority carrier lifetime in the off-state well was reduced by doping to accelerate non-radiative recombination, creating an intra-cavity electro-thermo tuning region to change the cavity mode location. Both static and dynamic experimental results were presented, showing large tuning range with single mode operation.

Acknowledgement

This work was supported by DARPA through a STTR with Ziva Corp. and by NSF through a GOALI program. A portion of this work was done in the UCSB nanofabrication facility, part of the NSF funded NNIN network.

References

- [1] C.-H. Lin, Y. Zheng, M. J. W. Rodwell, L. A. Coldren, *22nd IEEE International Semiconductor Laser Conference*, PD2 (2010).
- [2] C.-H. Lin, Y. Zheng, M. Gross, M. J. W. Rodwell, L. A. Coldren, *Proc. Optical Fiber Communication Conference*, OWD5 (2011).
- [3] C. J. Chang-Hasnain, *IEEE Journal of Selected Topics in Quantum Electronics*, vol.6, no. 6, pp. 978-987 (2000).
- [4] C. Gierl, T. Gruendl, P. Debernardi, K. Zogal, C. Grasse, H. A. Davani, G. Böhm, S. Jatta, F. Küppers, P. Meißner, and M.-C. Amann, *Optics Express*, vol. 19, no. 18, pp. 17336-17343 (2011).
- [5] Y. Uchiyama, T. Kondo, K. Takeda, A. Matsutani, T. Uchida, T. Miyamoto, and F. Koyama, *Japanese Journal of Applied Physics*, vol. 44, pp. L214-L215 (2005).

Fast Polarization Modulation in Vertical Cavity Lasers with Electrical RF Injection

Ajit V. Barve^a, Yan Zheng^a, Leif Johansson^a, Alok Mehta^c, Anis Husain^c, and Larry Coldren^{a,b,*}

^aDepartment of Electrical and Computer Engineering, University of California Santa Barbara, CA 93106, USA

^bDepartment of Materials, University of California Santa Barbara, CA 93106, USA

^cZiva Corporation, San Diego, CA 92121, USA

Abstract—We report on a new method for fast electrical modulation of the polarization state of a simple, two terminal VCSEL. By biasing the VCSEL with a gated RF signal, polarization can be modulated at more than a GHz rate, which is fastest for electrical modulation of polarization.

It is well known that VCSEL modes are transverse electromagnetic (TEM) in nature due to the vertical structure. Crystalline symmetries generally give rise to two dominant linear polarization directions, oriented along $\langle 110 \rangle$ and $\langle \bar{1}\bar{1}0 \rangle$ axes. These linear polarization modes are usually bistable and exhibit polarization switching at certain bias currents. Understanding and controlling the polarization properties of VCSEL is of critical importance for applications in communication networks with polarization sensitive elements, medical imaging, environmental monitoring and military. Various techniques have been previously used to control the polarization state of a VCSEL, such as, asymmetric current injection [1], controlled stress, electro-optic birefringence etc. Fast polarization modulation has been previously achieved by optically injection locking to polarized laser pulses. However, for the ease of control and scaling, being able to modulate the polarization with electrical injection is particularly attractive. So far, the polarization modulation of VCSEL with electrical injection has been limited to less than 5MHz, due to thermal nature of switching mechanisms [2].

We have previously reported [3] on the complex high frequency polarization dynamics occurring near the polarization switching point by injecting a RF frequency electrical current into the VCSEL. In this paper we report, for the first time, on a controlled polarization modulation at 1.35GHz, which is, by far, the fastest reported for electrically injected VCSELs. We demonstrate that the polarization state of a VCSEL can be altered by changing only the frequency of modulation, while keeping all other parameters fixed. This method does not require any special fabrication steps or

packaging and thus is suitable for commercially available two terminal VCSELs.

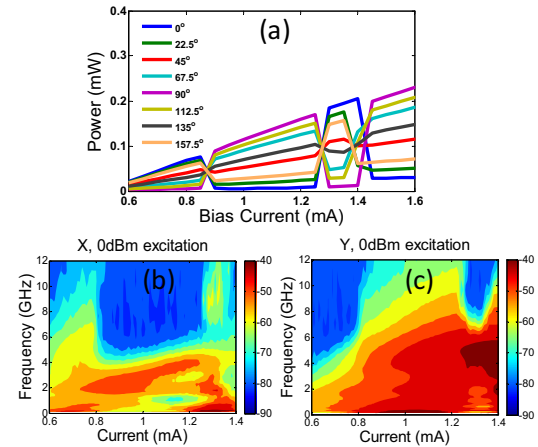


Fig. 1. (a) VCSEL L-I curve at different polarizer angles. (b,c) Polarized S_{21} measurements as a function of bias current, showing frequency dependent polarization switching for X (0°) and Y (90°) polarizations

Highly strained VCSEL material with InGaAs/GaAs quantum well active region, operating at 1060nm was chosen for this study. The VCSEL under test has a circular mesa of $14\mu\text{m}$ diameter. A tapered oxide aperture, with oxidation length of $3\mu\text{m}$, was used to confine the carriers and provide index guiding. The substrate of the bottom-emitting VCSEL was antireflection coated to minimize the optical feedback. The polarization angle dependent light-current (LI) curve of this VCSEL is shown in Fig. 1 (a). Transitions after 1.4mA are due to the higher order lateral mode. Polarized frequency response curves (S_{21}) of this VCSEL, subjected to 0dBm nominal modulation power are shown in Fig. 1(b)-(c). For this measurement, the light emitted from the bottom of the VCSEL was focused onto a multimode optical fiber using aspheric lens and mirror assembly, after passing through a polarizer. The signal was detected using a 25GHz infrared photodetector, the output of which was amplified and fed to the network analyzer. The modulation

This work was supported by DARPA, via STTR with Ziva Corp.

transfer function was measured at several different DC biases, and the resulting responses were plotted in two dimensional contour plots, shown in Fig. 1.

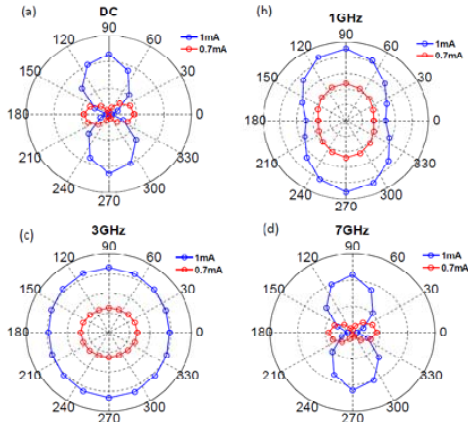


Fig. 2. Polarization angle dependent power measurements at two different bias currents in (a) DC conditions and with RF injection of frequency (b) 1GHz (b) 3GHz and (d) 7GHz.

Interestingly, even though at DC conditions high extinction ratio polarization switching is observed, a rich frequency dependence of this extinction ratio is obtained as the RF signal is applied to the VCSEL. For RF frequencies below 4GHz, the S_{21} parameter is significant in both the polarizations, which is in sharp contrast to DC measurements. This can be visualized with polar plots of output power at different polarization angles, for the same DC bias current, as shown in Fig. 2. VCSEL was subjected to RF injection of various frequencies and at 0dBm nominal modulation power for this measurement. Plots obtained at no RF injection, and with RF injection at 1GHz, 3GHz and 7GHz frequencies are shown in Fig. 2(a), (b), (c) and (d), respectively. It can be clearly seen that, without any RF injection, X (0°) and Y (90°) modes are dominant at 0.7mA and 1.0mA current, respectively. As RF modulation is applied, below 4GHz, the VCSEL polarization selection is drastically altered and it emits nearly equal power in all the polarization directions. At higher RF frequencies, response becomes similar to that in DC conditions.

In order to estimate the speed of the polarization modulation, the VCSEL was subjected to periodic burst of RF currents with the nominal modulation power of 0dBm. These periodically gated RF bursts were generated by passing a

constant frequency RF signal and a square wave through a double-balanced mixer circuit. The VCSEL output was passed through a polarizer, then focused onto a multimode optical fiber, detected with a high frequency detector, amplified and fed to an oscilloscope. A low pass filter was used after the amplifier to reduce the carrier RF signal by approximately 10dB. Fig. 3 shows the time-domain response for X and Y polarized outputs at different modulation frequencies. The frequency of the RF source was kept constant at 4 GHz, and the modulation power of was 5dBm. Fig. 3 (a) shows the time averaged response for a modulation frequency of 50MHz. It is clear that the polarization mode changes from dominant X mode to dominant Y mode as we go from 'on' to 'off' state of the RF burst. Fig. 3 (b) shows the response at 1.35GHz square wave frequency at 1.05mA of DC bias applied to the VCSEL. Output of X and Y channels are nearly 180° out of phase, indicating the dominant polarization changing between the two modes, in less than 350ps. This is, by far, the fastest reported polarization modulation using electrical injection.

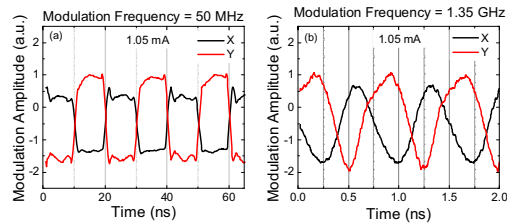


Fig. 3. Polarization modulation response for VCSEL in X and Y polarizations for modulation frequency of (a) 50 MHz (b) 1.35 GHz at 1.05 mA bias.

In conclusion, a new way of electrically modulating the polarization of VCSELs is reported. By injecting the electrical RF signal into the VCSEL, the state of the polarization can be altered at more than a GHz rate, much beyond the thermally limited modulation speeds.

Disclaimer: The views expressed are those of the authors and do not reflect the official policy or position of the Department of Defense or the U.S. Government. Approved for Public Release, Distribution Unlimited

References:

[1] Augustin et al, IEEE PTL, 16(3), 708, 2004
 [2] Verschaffelt et al, IEEE J. Quantum Electron., 39(10), pp 1177, 2003
 [3] Barve et al, IEEE Photonics Conference, TuF 3, 2012.



Ultrafast polarization modulation in vertical cavity surface emitting lasers with frequency dependent current injection

A. V. Barve,¹ Y. Zheng,¹ L. Johansson,¹ A. Mehta,² A. Husain,² and L. Coldren¹

¹Department of Electrical and Computer Engineering, University of California, Santa Barbara, California 93117, USA

²Ziva Corporation, San Diego, California 92121, USA

(Received 15 October 2012; accepted 3 December 2012; published online 18 December 2012)

We report on a polarization modulation in vertical cavity surface emitting lasers (VCSEL), based on RF electrical injection. Complex polarization dynamics in the single mode regime is studied as a function of RF frequency and power at different bias currents. It has been observed that the polarization state of the VCSEL can be altered by changing the frequency of RF current modulation. Time resolved measurements show that by injecting periodic bursts of RF modulation in the VCSEL, it is possible to change the dominant polarization between the two orthogonal modes at gigahertz rates. © 2012 American Institute of Physics. [<http://dx.doi.org/10.1063/1.4772540>]

It is well known that vertical cavity surface emitting lasers (VCSEL) emit in one of the two orthogonal polarization modes.^{1,2} The polarization orientation in the lateral direction is hard to control due to the symmetric nature of typical VCSELs. Crystalline symmetries generally give rise to two dominant linear polarization directions, oriented along $\langle 110 \rangle$ and $\langle 1\bar{1}0 \rangle$ axes. The selection of one of the two linear polarization modes depends on various factors such as temperature, geometry, stress, location of cavity mode with respect the gain peak, and thus exhibit polarization switching at certain bias currents. Theoretical analysis of polarization properties of VCSELs has been carried out with rate equations that include the spin sublevels in conduction and valance bands.^{3,4} Various techniques have previously been used to control the polarization state of a VCSEL, such as, asymmetric current injection,^{5–7} controlled stress,⁸ electro-optic birefringence,⁹ which typically require more than two contacts per VCSEL or special packaging. Polarized optical injection is a popular method for dynamically controlling the state of polarization of a VCSEL, to create all optical polarization flip-flops.^{10,11} Although polarization switching up to 10 GHz has been demonstrated with this technique, it requires high speed optical pulses with two different polarizations, for set and reset switches. Polarization control through electrical injection is an attractive alternative. Although it is possible to control the state of the polarization by simply modulating the bias current,¹² it is a slow effect due to the thermal nature of the polarization switching process, with speeds limited to sub-MHz regimes.¹³ Current modulation experiments have been previously reported to analyze the nonlinear dynamics of VCSEL in gain switched regime,¹⁴ with observations of frequency doubling behavior.

In this letter, we introduce a technique for polarization modulation in VCSELs, with electrical RF frequency injection. It has been observed that it is possible to alter the power going into each polarization mode by simply varying the frequency of RF injection, while keeping all the other parameters, such as, bias current, temperature etc., the same. The polarized modulation response of VCSELs at several different bias currents and different modulation depths have been

measured to explore the complex nature of polarization modulation under these conditions. DC measurements, such as light power output-current-voltage (LIV) measurements and optical spectral measurements under these conditions confirm the power transfer in two different polarization modes as a function of RF frequency. Since this effect occurs at GHz frequencies, this polarization modulation is not driven by thermal effects and therefore can be extremely fast. To estimate the speed of the polarization modulation with this effect, VCSELs have been subjected to high speed bursts of electrical RF injection, and their polarized output have been measured in the time domain. These measurements reveal that this effect leads to fast modulation of polarization between X and Y polarized modes, above 1 GHz frequencies, which is more than an order of magnitude faster than other electrical injection techniques to control the polarization of a VCSEL.

VCSELs used for these measurements have a highly strained InGaAs/GaAs quantum-well (QW) active region, for 1060 nm operation. These VCSELs were grown on (100) semi-insulating GaAs substrates using a molecular beam epitaxy (MBE) system. The bottom mirror consisted of 18 periods of unintentionally doped (UID) GaAs/AlAs distributed Bragg reflectors (DBR), followed by a 1.75λ thick layer of Si doped GaAs to form an intracavity n-contact layer. The tapered oxide aperture layer was 0.5λ thick and was placed so that the tip of the taper occurs at the standing wave null. Four periods of deep oxidation layers are grown after that to reduce the capacitance. The p-type top mirror consists of GaAs/AlGaAs DBRs that are bandgap-engineered for low resistance and low optical loss. Details of this design can be found in Zheng *et al.*¹⁵ The active region is surrounded by an asymmetric $\text{Al}_{0.3}\text{Ga}_{0.7}\text{As}$ separate confinement heterostructure (SCH) that is parabolically graded down to GaAs spacers. Three 8 nm thick highly strained $\text{In}_{0.3}\text{Ga}_{0.7}\text{As}$ quantum wells are separated by 8 nm GaAs barriers, δ -doped with carbon using a carbon tetrabromide (CBr_4) precursor. The material was processed into circular-mesa VCSELs with varying diameters. The electrical and optical confinement was provided with tapered oxide apertures, with a total

oxidation length of $3\ \mu\text{m}$. The devices have a simple two contact geometry with a bottom emitting configuration. The substrate was coated with an antireflection (AR) layer of magnesium oxide (MgO) to avoid optical feedback.

Polarization sensitive LIV measurements on two $14\ \mu\text{m}$ mesa diameter devices, from different parts of the processed wafer are shown in Figs. 1(a) and 1(b). Polarization switching with high extinction ratio for single mode operation below the bias current of $1.4\ \text{mA}$, and a threshold current of $0.5\ \text{mA}$, was obtained. In both the devices (devices A and B), the dominant polarization mode changes from longer wavelength mode (Y-polarized) to shorter wavelength mode (X-polarized) (type I switching), and then back to longer wavelength mode (type II switching). However, these switching occur at different biases, as shown in Figs. 1(a) and 1(b). The difference in switching characteristics is due to nonuniformity during fabrication. All the devices tested showed a response similar to either device A or device B. For modulation response measurements, a RF signal from a high-speed network analyzer was injected into the VCSEL, on top of the DC bias current, using a bias-T. The light output from the VCSEL was then focused onto a 45° mirror, using an AR coated aspheric lens. A wire-grid polarizer was inserted in the beam path. The light was then coupled to a multimode fiber (MMF) using a second AR coated lens and detected using a high speed multimode detector. The electrical signal was amplified and fed back to the calibrated network analyzer to measure S_{21} , the electrical modulation transfer function of the VCSEL. The modulation transfer function was measured at several different DC biases and the resulting responses were plotted in two-dimensional contour plots, shown in Figs. 1(c)–1(f) for device A and Figs. 1(g)–1(j) for device B.

Figs. 1(c) and 1(d) show the response for X and Y polarizations in device A, for a nominal RF modulation amplitude of $-10\ \text{dBm}$, which corresponds to approximately $0.2\ \text{mA}$ peak to peak current variation in the VCSEL. Interestingly, at a bias current around $0.95\ \text{mA}$, there is a pronounced dip

in the frequency response of Y-polarized modulation, and a corresponding peak in X-polarized modulation response, near the relaxation resonance frequency. Results for device B at $-10\ \text{dBm}$ RF excitation are shown in Figs. 1(g) and 1(h) for X and Y polarizations, respectively. The nature of the modulation response curve changes as the RF modulation power is increased to $0\ \text{dBm}$ (approximately $0.60\ \text{mA}$ peak to peak current swing), as shown in Figs. 1(e) and 1(f) for device A and Figs. 1(i) and 1(j) for device B. For these powers, at bias currents higher than a polarization switching bias of $\sim 0.8\ \text{mA}$, significant modulation response is observed in both polarizations, which is very different than the DC behavior for a single-mode operation. It should be noted that these phenomena are not thermally driven, as the RF frequencies are much higher than typical thermal cutoff frequencies for polarization switching, which are less than $1\ \text{MHz}$.¹³

In order to verify that the actual power in different polarization modes is being varied, L-I-V measurements were carried out with the RF injection on. Fig. 2(a) shows the plot of LI curves at two different RF frequencies in both the polarizations for device B, for $5\ \text{dBm}$ RF excitation. Only the DC optical power is measured in this measurement. This shows the same trend as in Figs. 1(e), 1(f), 1(i), and 1(j), where the VCSEL starts emitting similar powers in both polarizations near the RF frequency of $2\text{--}4\ \text{GHz}$. For example, for $4\ \text{GHz}$ excitation, the VCSEL is emitting with similar powers in both the polarizations, until a bias current of $\sim 1.2\ \text{mA}$. This is in sharp contrast with the DC LIV curves shown in Figs. 1(a) and 1(b), as well as the L-I curve for $7\ \text{GHz}$ excitation. It should be noted that the current-voltage curve (not shown here) is identical for all the RF frequencies. Fig. 2(b) shows the optical spectrum measured at X and Y polarizations, for no RF excitation, and at $4\ \text{GHz}$ and $7\ \text{GHz}$ excitations at $1.05\ \text{mA}$ of DC bias. It is clear that for DC conditions with no RF injection, Y-polarized mode (longer wavelength mode) is $23\ \text{dB}$ higher than the X-polarized

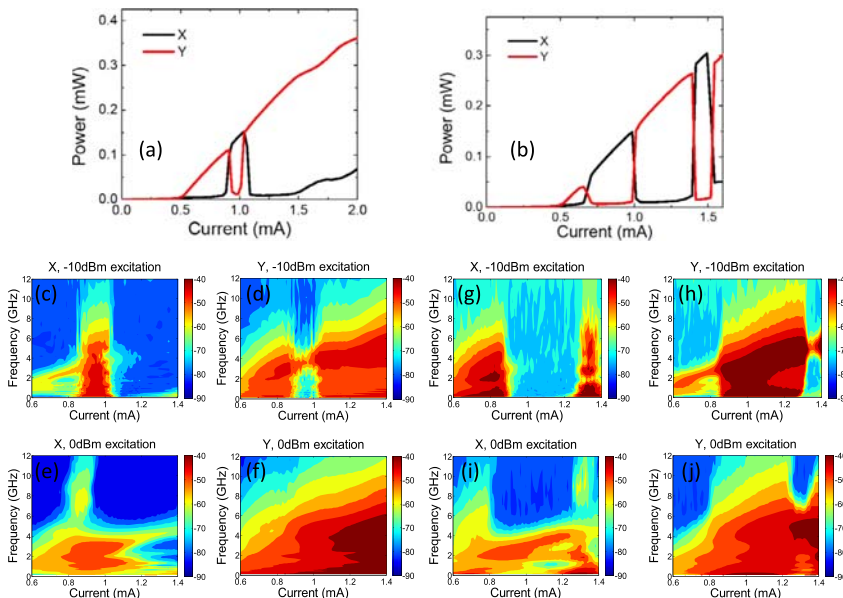


FIG. 1. Polarized optical power versus bias current curves for (a) device A and (b) device B. Polarization dependent modulation response as a function of bias for device A is plotted in (c) and (d) for X and Y polarization, respectively, for $-10\ \text{dBm}$ excitation. (e) and (f) show the corresponding curves for $0\ \text{dBm}$ modulation. (g)–(j) show the corresponding plots for device B, with $-10\ \text{dBm}$ and $0\ \text{dBm}$ modulation powers.

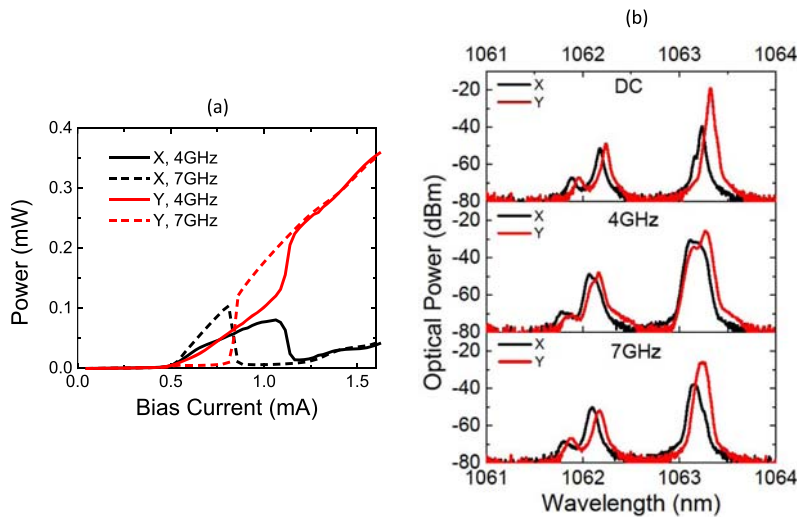


FIG. 2. Frequency dependent DC measurements for device B, showing (a) polarized L-I curves, at two different frequencies and (b) Polarized optical spectra.

mode at 1.05 mA. However, for RF excitation at 4 GHz, both the modes show nearly equal output. The Y-polarized mode starts dominating again as the frequency is increased further, with a 12 dB higher power than the X-polarized mode at 7 GHz RF frequency, at 1.05 mA. This measurement confirms that the power going into each polarization mode can be varied by simply changing the frequency of RF excitation.

To estimate the speed of the polarization modulation by changing the RF frequency or power, we set up a time domain polarization modulation measurement. The set up for the measurement is shown in Fig. 3. A constant frequency RF signal and a square wave are passed through a double-balanced mixer, to generate a gated RF signal. The inset in Fig. 3 shows an example of this mixing, with the green curve showing the square wave generated by a bit-rate generator and the black curve showing the gated RF signal. The small modulation in the “off” region is due to a small leakage of RF signal through the mixer. This gated RF signal is then applied across the VCSEL, along with a DC bias, with a bias-T circuit. The VCSEL output is passed through a

polarizer, then focused onto a MMF, detected with a high frequency detector, amplified and fed to an oscilloscope. A low pass filter is used to reduce the carrier RF signal by approximately 10 dB. The oscilloscope is synchronized to the square wave generator, but not with the RF generator, which results in varying phase of RF signal at the start of “on” region, as can be seen from the inset.

Fig. 4 shows the time domain response for X and Y polarized outputs at different modulation frequencies and bias currents with this configuration. The frequency of the RF source was kept constant at 4 GHz, and the modulation power was 5 dBm. Fig. 4(a) shows the response for a modulation frequency of 50 MHz. It is clear that the polarization mode changes from dominant X mode to dominant Y mode as we go from “on” to “off” state of the RF burst. The waveforms have been averaged in time to reduce the noise. This polarization modulation can be observed till much higher frequencies of the square wave. For example, Fig. 4(b) shows the response at 1.35 GHz square wave frequency at 1.05 mA of DC bias applied to the VCSEL. Output of X and Y channels are nearly 180° out of phase, indicating the

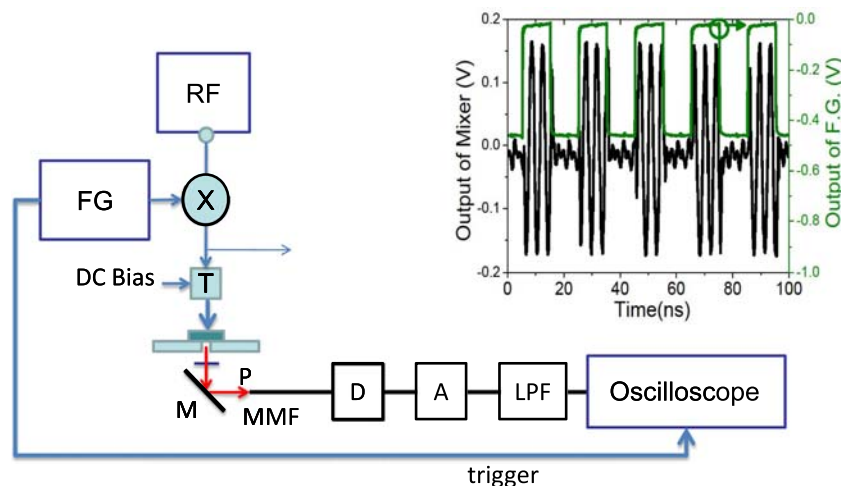


FIG. 3. Set up for time domain measurements. Different components are: RF—RF generator, FG—function generator for variable frequency square wave generation, X—frequency mixer, T—bias tee circuit, M—mirror, MMF—multi-mode optical fiber, P—polarizer, D—detector, A—amplifier, LPF—low pass filter. The inset shows the output of FG (green) and output of the mixer (black), showing periodic bursts of RF signal.

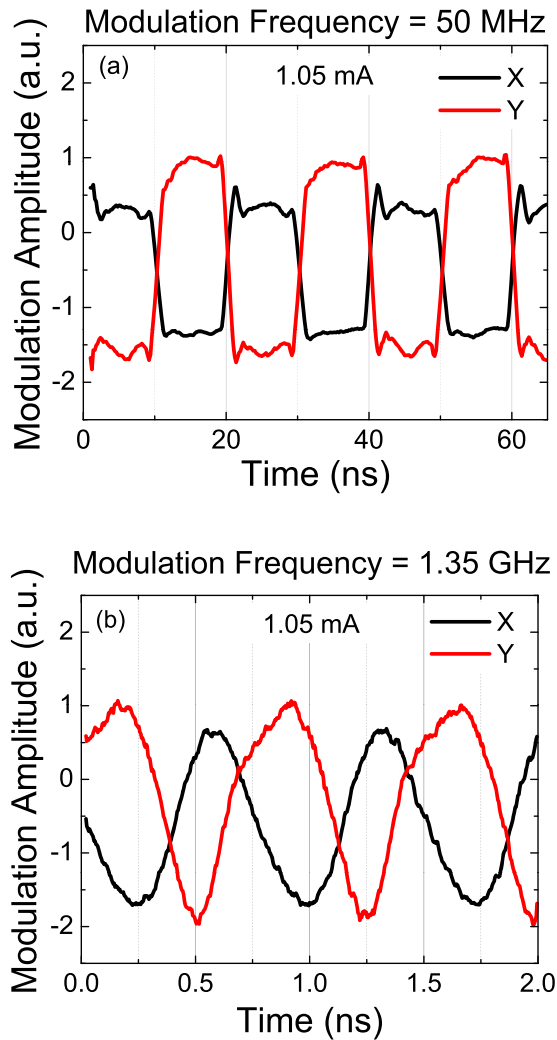


FIG. 4. Time domain modulation response for VCSEL in X and Y polarizations for modulation frequency of (a) 50 MHz, (b) 1.35 GHz at 1.05 mA bias current.

dominant polarization changing between the two modes, in less than 350 ps. This is, by far, the fastest reported polarization modulation using electrical injection. As the modulation frequency is increased further, the modulation frequency and RF frequency become comparable, and the modulation envelop is not clearly defined. Thus, it should be noted that the actual polarization modulation can be faster than the 1.35 GHz reported here. The high modulation frequencies

indicate that the polarization modulation is not caused by thermal effects.

In conclusion, a technique of electrically modulating the polarization of VCSELs is reported. By injecting the electrical RF signal into the VCSEL, the state of the polarization can be altered at high speeds. Polarized transfer function measurements at different modulation amplitudes reported here reveal complex polarization dynamics near the polarization switching point of a single mode VCSEL. These findings have been supported by optical spectral measurements and LIV measurements under various RF injection conditions. Time domain experiments reveal that polarization can be modulated by changing the RF frequency or power at speeds as high as 1.35 GHz.

This work was supported by DARPA, via STTR with Ziva Corp.

Disclaimer: The views expressed are those of the authors and do not reflect the official policy or position of the Department of Defense or the U.S. Government.

Distribution Statement "A" (Approved for Public Release, Distribution Unlimited).

¹G. Verschaffelt, K. Panajotov, J. Albert, B. Nagler, M. Peeters, J. Danckaert, I. Veretennicoff, and H. Thienpont (Association of Polish Electrical Engineers (SEP), 2001).

²K. D. Choquette, R. P. Schneider, K. L. Lear, and R. E. Leibenguth, *IEEE J. Sel. Top. Quantum Electron.* **1**(2), 661 (1995).

³M. San Miguel, Q. Feng, and J. V. Moloney, *Phys. Rev. A* **52**(2), 1728 (1995).

⁴J. Martin-Regalado, F. Prati, M. San Miguel, and N. B. Abraham, *IEEE J. Quantum Electron.* **33**(5), 765 (1997).

⁵L. M. Augustin, E. Smalbrugge, K. D. Choquette, F. Karouta, R. C. Strijbos, G. Verschaffelt, E. J. Geluk, T. G. van de Roer, and H. Thienpont, *IEEE Photon. Technol. Lett.* **16**(3), 708 (2004).

⁶Y. Zheng, C.-H. Lin, and L. A. Coldren, *IEEE Photon. Technol. Lett.* **23**(5), 305 (2011).

⁷Y. Sato, K. Furuta, T. Katayama, and H. Kawaguchi, *IEEE Photon. Technol. Lett.* **20**(17), 1446 (2008).

⁸K. Panajotov, B. Nagler, G. Verschaffelt, A. Georgievski, H. Thienpont, J. Danckaert, and I. Veretennicoff, *Appl. Phys. Lett.* **77**(11), 1590 (2000).

⁹M. S. Park, B. T. Ahn, B.-S. Yoo, H. Y. Chu, H.-H. Park, and C. J. Chang-Hasnain, *Appl. Phys. Lett.* **76**(7), 813 (2000).

¹⁰H. Kawaguchi, *Opto-Electron. Rev.* **17**(4), 265 (2009).

¹¹D. L. Boiko, G. M. Stephan, and P. Besnard, *J. Appl. Phys.* **86**(8), 4096 (1999).

¹²K. D. Choquette, K. L. Lear, R. E. Leibenguth, and M. T. Asom, *Appl. Phys. Lett.* **64**(21), 2767 (1994).

¹³G. Verschaffelt, J. Albert, B. Nagler, M. Peeters, J. Danckaert, S. Barbay, G. Giacomelli, and F. Marin, *IEEE J. Quantum Electron.* **39**(10), 1177 (2003).

¹⁴K. Panajotov, I. Gatara, A. Valle, H. Thienpont, and M. Sciamanna, *IEEE J. Quantum Electron.* **45**(11), 1473 (2009).

¹⁵Y. Zheng, C.-H. Lin, A. V. Barve, and L. A. Coldren, in *IEEE Photonics Conference IPC2012* (IEEE, 2012), pp. 131–132.

III. Materials and Device Technology

Coalescence of InP Epitaxial Lateral Overgrowth by MOVPE with V/III Ratio Variation

NICK JULIAN,^{1,3} PHIL MAGES,^{1,4} CHONG ZHANG,¹ JACK ZHANG,²
STEPHAN KRAEMER,² SUSANNE STEMMER,² STEVEN DENBAARS,^{1,2}
LARRY COLDREN,^{1,2} PIERRE PETROFF,^{1,2} and JOHN BOWERS^{1,2}

1.—Department of ECE, University of California Santa Barbara, Santa Barbara, CA 93106, USA.
2.—Department of Materials, University of California Santa Barbara, Santa Barbara, CA 93106, USA.
3.—e-mail: njulian@engineering.ucsb.edu. 4.—e-mail: pmages@ece.ucsb.edu

The effects of V/III ratio and seed window orientation on the coalescence of epitaxial lateral overgrowth InP over SiO₂ using metal organic vapor-phase epitaxy with tertiary butyl phosphine were investigated. Parallel lines having $\theta = 60^\circ$ and 30° off [011] were coalesced, and their lateral growth rate variation with V/III was measured. Coalescence of lines separated by narrow angles in a star-like pattern was also studied. We find the greatest extent of coalescence to occur when the window stripe is oriented just off of the (010) directions. V/III ratio strongly affects the extent of coalescence, showing an alternating enhancement or inhibition depending on which side of the (010) direction the stripes are oriented. The variation in quality of coalesced material between stripes separated by narrow angles is examined with cross-sectional transmission electron microscopy, illustrating the most problematic growth directions under two V/III ratio conditions.

Key words: Metal organic vapor-phase epitaxy (MOVPE), metal organic chemical vapor deposition (MOCVD), OMVPE, selective-area growth (SAG), epitaxial lateral overgrowth (ELO), coalescence, heteroepitaxy

INTRODUCTION

Indium phosphide (InP) plays a significant role in modern photonic devices. Its heteroepitaxial integration onto silicon would yield significant improvements in the cost and efficiency of optoelectronic integrated circuits intended for use in the computing and telecommunications industries. A promising method for realizing such material integration is epitaxial lateral overgrowth (ELO). In this method a growth-inhibiting layer is patterned with windows opening to the substrate, forcing growth into a limited area until protruding out of the windows, at which point it is then able to propagate laterally with the hope of coalescing with

neighboring lateral growths. There are then two significant sources for defects to appear in the grown layer. Defects may propagate through the mask openings, or they may also be generated during coalescence. We limit this study to homoepitaxial ELO of InP on InP substrates to explore methods of maximizing the area of defect-free overgrowth as well as minimizing coalescence-related defects with respect to ELO mask design and growth conditions. This restriction to homoepitaxy allows us to be certain that any defects present in the grown material are due solely to phenomena associated with lateral overgrowth, coalescence, and interaction with the ELO mask. The stress fields and defects arising from thermal and lattice mismatch with a Si substrate, which would vary with seed layer thickness, composition, and defect density, would introduce uncertainty when attempting to attribute defect formation purely to mask design and growth conditions. We observed that variations

Presented at EMC 2011, University of California Santa Barbara June 22–24, 2011.
(Received August 15, 2011; accepted February 16, 2012; published online March 22, 2012)

in window stripe direction had the most profound effect on sidewall morphology, demonstrating two classes of stripe orientation near $\langle 010 \rangle$ having fast lateral growth, which respond in distinct ways to changes in V/III precursor partial pressure ratio.

In this paper we describe the results of ELO growth and coalescence using two categories of mask pattern: parallel stripes and a star-like configuration of 32 intersecting arms separated by 5.625° . Special note is taken of the morphological variation of growth through stripes oriented just off of the $\langle 010 \rangle$ family of directions with V/III ratio, and our use of these variations to achieve lateral coalescence. We attribute the morphological variations primarily to the growth rate anisotropies of the facets involved, and note the introduction of capillary mass transport within regions undergoing coalescence. We present cross-sectional transmission electron microscopy (TEM) images of coalesced material between ranges of stripe orientations separated by narrow angles in a star-like configuration to evaluate their quality.

EXPERIMENTAL PROCEDURES

To create the mask patterns for ELO growth, we first deposited approximately 200 nm of SiO_2 via plasma-enhanced chemical vapor deposition (PECVD) at 250°C with a low deposition rate. We then applied a thin (20 nm) layer of chromium, upon which we defined the contours of our ELO windows using conventional photolithography. Inductively coupled plasma (ICP) etching was used to first etch the windows into chromium, then photoresist was removed. ICP etching was used again to open the windows into SiO_2 , and then to selectively remove the remaining chromium. This hard-mask process minimizes contamination from polymerized photoresist, which otherwise tends to stick to the InP and SiO_2 surfaces after the initial ICP etching. Before growth, the native InP oxide was removed with a dip in undiluted 90 wt.% to 98 wt.% sulfuric acid, followed by a short rinse in deionized water.

Growth was then carried out on (100) InP substrates in a 2-inch horizontal metal organic vapor-phase epitaxy (MOVPE) reactor using trimethylindium (TMI) and tertiary butyl phosphine (TBP) precursors and hydrogen as carrier gas at 350 Torr and 615°C . This growth temperature was experimentally determined to minimize unwanted nucleation on our particular SiO_2 surfaces. Partial pressures of TBP were varied from 0.22 Torr to 4.1 Torr, yielding V/III ratios ranging from 50 to 496 and growth rates between 0.5 Å/s and 8 Å/s. However, growth rates faster than 4 Å/s were seen to increase chaotic variations in the growth morphology. All growths in this study were thus limited to a rate of 4 Å/s or less. Due to the lower pressure limit of our reactor, this restricts us to V/III ratios greater than or equal to 124.

Analysis was performed using scanning electron microscopy and cross-sectional TEM. The cross-sectional TEM samples were prepared using a focused ion beam (FIB) to excavate and thin the regions of interest into lamellae of approximately 200 nm thickness.

RESULTS

Morphological Characteristics and Variation with V/III Ratio

A striking feature of the resulting growth over star-like patterns was their variation with stripe direction. In Fig. 1 we see two of these samples grown with V/III ratios of 124 and 248, where the growth of arms through windows oriented along the $\langle 010 \rangle$ directions is unlike its neighbors. These $\langle 010 \rangle$ arms have large stable facets, while the growth through windows on either of their sides has regions in which coalescence has progressed outward from the center of the star. This coalescence extends a shorter distance for angles further away from the $\langle 010 \rangle$ arms. It is also apparent from Fig. 1 that the widths of the arms nearest $[0\bar{1}0]$ increase with distance from the pattern center, and to a slightly greater extent than the arms farthest from $[0\bar{1}0]$.

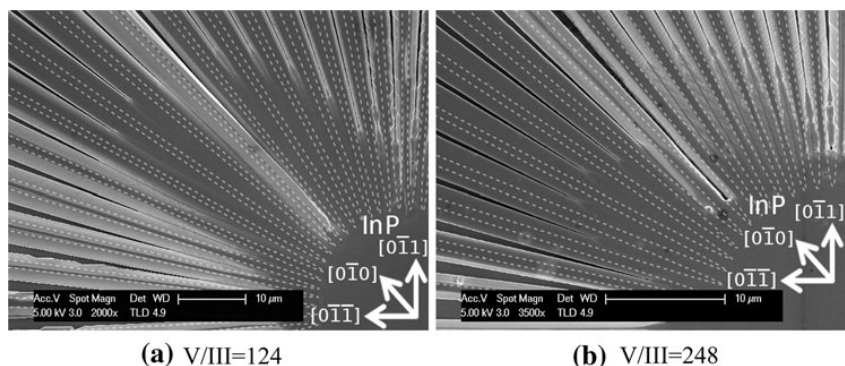


Fig. 1. Overview of coalescence behavior with variations in direction and V/III ratios of (a) 124 and (b) 248. Dashed lines outline the overgrown boundaries of $0.8\text{-}\mu\text{m}$ -wide windows through which growth initiated.

This may be attributed to a growth rate enhancement from the widening SiO_2 mask. Such growth rate enhancements occur when precursors diffuse from the SiO_2 mask onto a preferred growth facet.¹ For the lower V/III ratio of 124, arms rotated toward $[0\bar{1}1]$ away from $[0\bar{1}0]$ ($\theta < 45^\circ$ when measured from $[0\bar{1}1]$) show a greater angular range of complete coalescence, whereas fewer of the arms rotated toward $[0\bar{1}\bar{1}]$ ($\theta > 45^\circ$) have fully coalesced. These contrasting effects are reversed when the V/III ratio is increased to 248. Under this condition, the coalescence of a greater number of arms toward $[0\bar{1}\bar{1}]$ ($45^\circ < |\theta| < 90^\circ$) advanced, while coalescence of the arms rotated toward $[0\bar{1}1]$ ($\theta < 45^\circ$) was incomplete. In addition, at this magnification we can see that the sidewalls of these two groups of arms differ. A closer view of the parallel stripes shown in Fig. 2 illustrates in greater detail the morphological differences between the arms of these two directional groups and their response to V/III variation. For $\theta = 30^\circ$ we see sidewalls consisting of jagged steps, which we refer to as a “fillet” character for convenience. These steps appear to contain $\{101\}$ and $\{111\}$ facets, as highlighted on the inset rhombicuboctahedron which shows all low index facet families for zincblende crystals that could be visible in this view. For growths neighboring $[0\bar{1}0]$ with $|\theta| < 45^\circ$, an increase in V/III ratio causes the

top (100) facet to be narrower, with taller fillet sidewalls. For growths neighboring $[0\bar{1}0]$ with $45^\circ < |\theta| < 90^\circ$ we see smooth sidewalls which transform into an overhanging ledge when the V/III ratio is raised from 124 to 248. For this direction, there are no obvious low-index facet formations other than (100) . We refer to these as having “dovetail” character.

Lateral Growth of Parallel Stripes

We then investigated lateral growth of parallel stripes from each of the two directional classes: 30° off of $[0\bar{1}1]$ with fillet character and 60° off of $[0\bar{1}1]$ with dovetail character. For both categories, the lateral growth of stripes separated by $2.5\ \mu\text{m}$ slowed as the total open field thickness (OFT) growth was increased, as shown in Fig. 3a, b. Only the growths of dovetail character along 60° achieved coalescence over a $2.5\text{-}\mu\text{m}$ spacing for either V/III ratio. The lateral growth rate of this orientation also increased significantly with increasing V/III ratio, achieving coalescence with as little as 0.9 OFT (marked by a star in Fig. 3b) when using V/III of 409. The absolute TBP pressure was held constant for each of these except for the rightmost point of Fig. 3b. The plot of lateral growth versus V/III ratio in Fig. 3c shows that lateral growth for both stripe directions

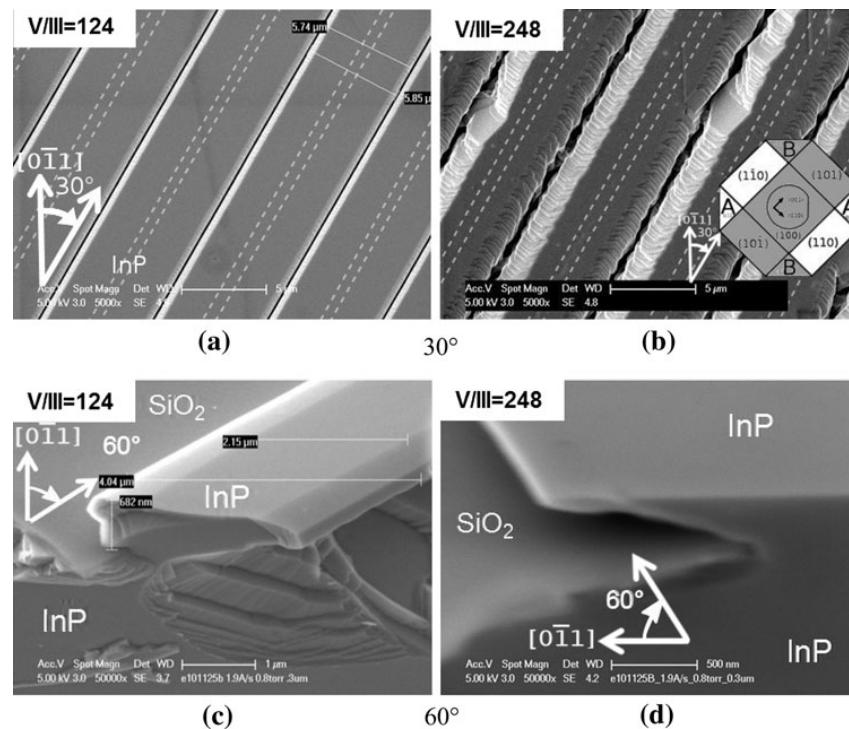


Fig. 2. Morphological variation of stripes oriented 30° (a, b) and 60° (c, d) with V/III ratios of 124 (a, c), and 248 (b, d). The inset of (b) highlights on a rhombicuboctahedron the facet planes nearest the sidewalls of 30° stripes. Dashed lines outline the overgrown $0.8\text{-}\mu\text{m}$ -wide ELO mask openings.

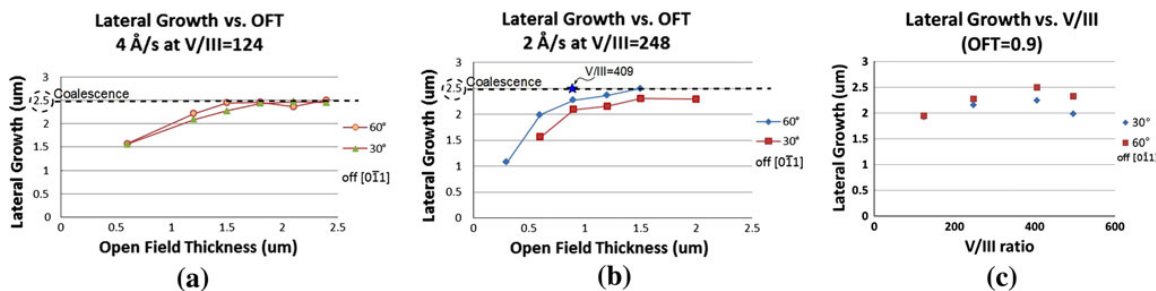


Fig. 3. Lateral growth of parallel stripes separated by $2.5 \mu\text{m}$ of SiO_2 for (a) $V/\text{III} = 124$, (b) $V/\text{III} = 248$, and (c) variation with V/III ratio.

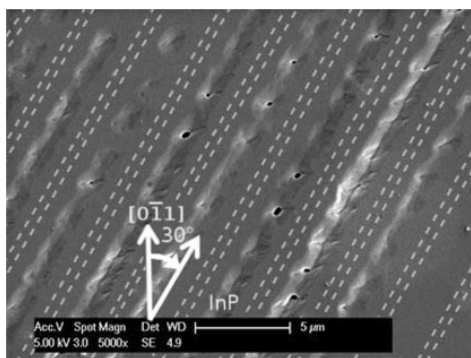


Fig. 4. Multipoint two-zipper-mode coalescence of parallel stripes 30° off of $[0\bar{1}1]$ having small SiO separation. Dashed lines outline the overgrown $0.8\text{-}\mu\text{m}$ -wide ELO mask openings.

incurs maximal enhancement between V/III ratios of 248 and 406, while this enhancement is less effective for orientations 30° off of $[0\bar{1}1]$ (fillet sidewalls) than for orientations 60° off of $[0\bar{1}1]$ (dovetail). The difference between the two increases monotonically with V/III , and the enhancement of 30° stripes ceases with V/III of 496.

Behavior During Coalescence

The coalescence behavior of parallel stripes 30° off of $[0\bar{1}1]$ is captured in Fig. 4. Here coalescence is initiated at multiple points, over a narrower mask separation than reported above, and proceeds in what Yan et al. term a two-zipper mode with high likelihood of forming defects when coalescence completes and the voids shown finally close.²

Introducing a nonzero angle between growth fronts helps to avoid this two-zipper coalescence, as shown previously in Fig. 1, allowing what Yan² denotes as a one-zipper coalescence mode. Looking more closely at the coalescence taking place between these arms separated by 5.625° , shown in Fig. 5, helps to illustrate the evolution of one-zipper coalescence. For the directions having fillet sidewalls, specifically between arms having $\theta = 39.375^\circ$ and 33.75° , we see that coalescence is initiated from the bottom of the growth for V/III ratios of both 124

and 248 in Fig. 5a, b. The surface morphology of the coalescent region in both cases is noticeably different from the nearby fillet steps. As coalescence proceeds up toward the top surface, this less jagged shape begins to consume more area than the large steps. For both V/III ratios we see that the steps become curved. For the lower V/III of 124 the steps yield to the new coalescent surface without recourse. For higher V/III of 248 the steps initially yield to the smoother morphology, but return at least once more further into the circle before they disappear entirely.

Examining the analogous coalescent regions for directions having smooth sidewalls, or dovetail character, we see in Fig. 5c, d that coalescence proceeds from the bottom surface to the top for V/III of 124, a behavior shared with the fillet sidewall directions. However, in this case the separation between sidewalls near the top (100) surface in the region of coalescence is not as wide. For V/III of 248 the coalescence does not appear to initiate from below at the mask surface, but coalescence is only visible along the top (100) surface.

Cross-Sectional TEM

To examine the quality of coalesced material we present cross-sectional TEM images in Fig. 6b–d. The dark lines shown in the sample overview TEM (Fig. 6b) can be assigned to bending contours resulting from the curvature of this $20\text{-}\mu\text{m}$ -long 200-nm thin lamellae as it is suspended by opposite ends. Figure 6a shows the region to be examined as it was being prepared by FIB. This region covers the coalescence of several stripe pairs separated by narrow angles of 5.625° , specifically those having $28.125^\circ < |\theta| < 67.5^\circ$, which includes areas containing both fillet and smooth sidewall characteristics. Two layers of platinum were initially deposited over the regions of interest to protect them from the ion beam. For V/III of 124, in Fig. 6c, we see a coalescence-related defect between arms rotated 61.875° and 56.25° away from $[0\bar{1}1]$, corresponding to the coalescence behavior of smooth sidewall growths shown in Fig. 5c. In contrast we do not yet see any defects forming between the two sets of arms within the angular range of 28.125° to 39.375°

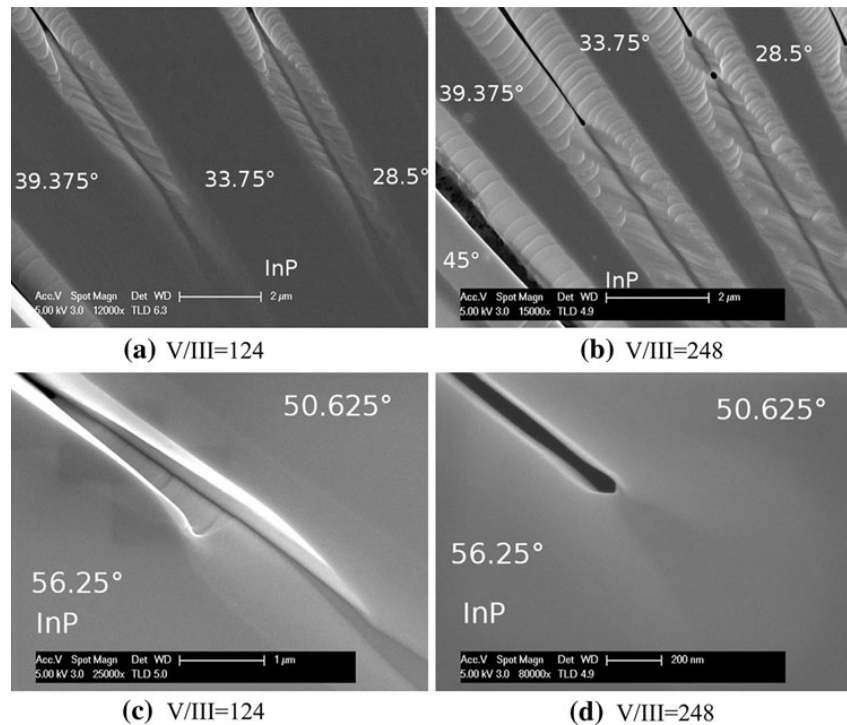


Fig. 5. Coalescence regions between arms oriented (a, b) 39.375°, 33.75°, 28.5° and (c, d) 56.25°, 50.625° off of $[0\bar{1}1]$, for V/III ratios of (a, c) 124, and (b, d) 248. Images (c, d) are at higher magnification due to smaller feature size.

for this lower V/III ratio, as shown in Fig. 6d, corresponding to orientations having jagged or fillet sidewalls. Figure 6e–g shows TEM images of a similar lamella grown with higher V/III ratio of 248. Here we notice a defect within coalescence of fillet-style sidewalls. This appears to be a dislocation which originated at the junction of neighboring fillet sidewalls. The coalescence of dovetail sidewalls does not show any obvious defects for this higher V/III ratio, although they do introduce spacious voids directly below coalescence due to their dovetail cross-sectional shape.

DISCUSSION

Morphological Characteristics and Variation with V/III Ratio

To maximize the useful area of material grown via ELO, it is desirable to maximize the extent of lateral overgrowth per OFT growth, and to optimize the quality of material at coalescence regions. We have demonstrated a correlation of these two features with growth morphology, and their response to V/III ratio adjustment. It is therefore useful to investigate the mechanisms causing these morphological variations for future optimization.

It was noted in a previous section that the steps along sidewalls of fillet category, present only on stripes just off of $\langle 010 \rangle$ having $|\theta| < 45^\circ$ measured

from the $[0\bar{1}1]$ direction, contain planes appearing to be $\{101\}$ and $\{111\}A$ facets, as seen in Fig. 2b. In contrast, the stripes having $45^\circ < |\theta| < 90^\circ$ did not show such low-index facet formation on their upper sidewalls. The following question arises: Why do the slow-growing $\{111\}B$ facets not appear on the lateral growth sidewalls, while the fast-growing $\{111\}A$ facets fail to congeal with neighboring $\{101\}$ facets to form a smooth high-index plane sidewall?

Following Asai and others, we offer a speculative explanation of this morphological phenomenon using a dangling bond model.^{3,4} As is usual, we assume that, once an indium atom incorporates onto a site, its dangling bonds are swiftly occupied by phosphorus due to excess supply. Growth is then limited by indium incorporation, the rate of which is subject to precursor decomposition anisotropies of the different crystallographic planes and surface diffusion of indium atoms along the local chemical potential gradient (“capillarity”), which is linearly dependent on the surface free energy.^{5–7} Figure 7 shows each of the configurations of atomic planes involved, including both concave and convex intersections of step facets. At each site of possible indium atom incorporation is a number quantifying the total change in dangling bonds if an indium atom were to attach there. Negative change in the number of dangling bonds represents a reduction in surface energy upon indium incorporation, and

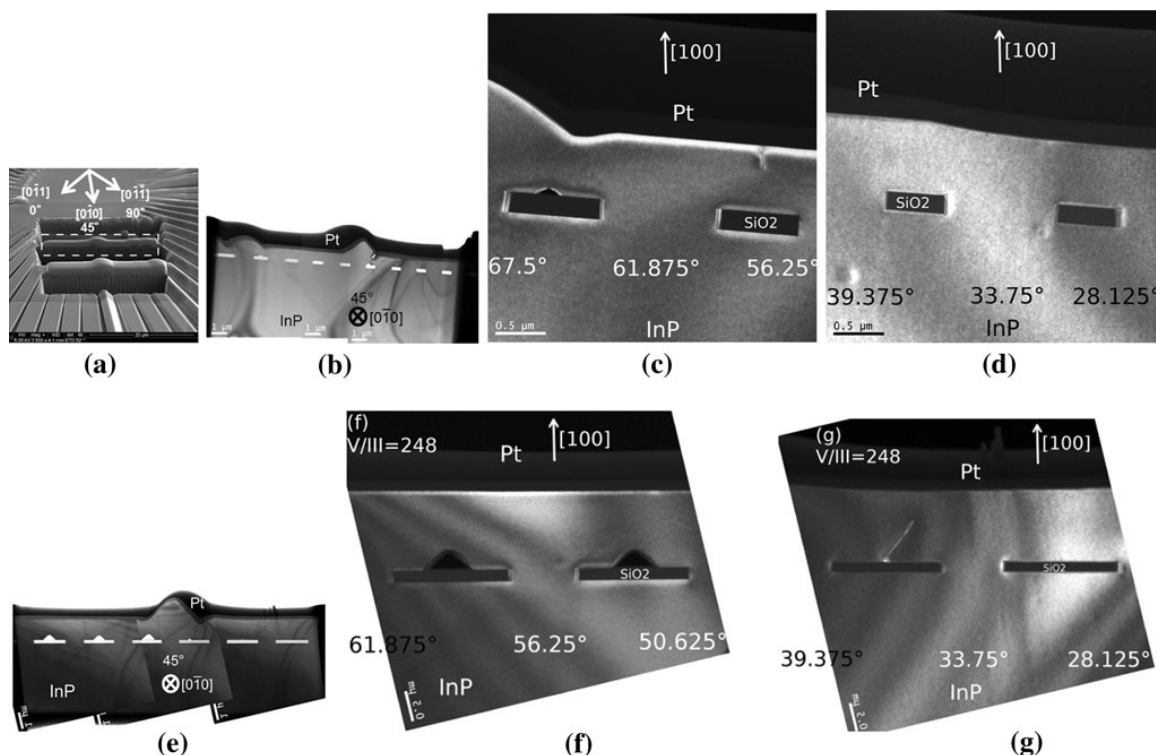


Fig. 6. (a) Location of lamellae to be examined on star-like pattern, after initial excavation. Bright-field TEM overview of lamellae for V/III ratios of (b) 124 and (e) 248. Dark-field TEM of coalesced regions showing defect locations for V/III of 124 (c, d) and 248 (f, g). Triangular dark areas in (f) correspond to voids which do not fill once formed.

positive change represents a potential energy barrier for incorporation.

A possible explanation to our question could be found by looking near the kink sites where planes intersect, marked by grey circles in Fig. 7. The concave intersection of (111)B with the relevant {110} plane contains an energetically favorable site for indium incorporation, having a dangling bond change of -2 , while indium incorporation at the convex intersection is energetically inhibited by a dangling bond change of $+2$. Such an arrangement encourages minimization of (111)B facet step height and the appearance of a macroscopically smoother surface for $45^\circ < \theta < 90^\circ$. In contrast, the kink sites at both intersections of (111)A and (110) surfaces are energetically unfavorable compared with sites elsewhere on the (111)A surface. This contributes to the preferred growth and maintenance of the (111)A planes, as observed, and may contribute to inhibition of capillarity or mass transport effects between these two planes at this temperature.

A consequence of our analysis is that growth of arms with fillet sidewall character progresses laterally through the flow of very large steps consisting of (111)A facets flowing over neighboring {101} facets.

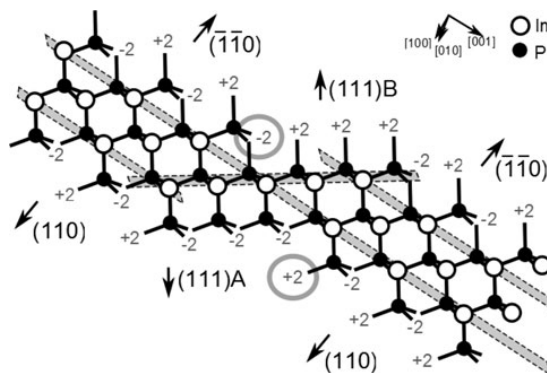


Fig. 7. Ball-and-stick model of the atomic configuration, with change in dangling bonds noted for relevant intersections of $(\bar{1}10)$, (111)B, (111)A, and (110) planes.

Before resuming the analysis of our growths, it is desirable to propose a hierarchy of growth rates amongst low-index facets. Growth on (111)A planes is often reported as the most substantial, while (111)B planes usually show very little growth.^{5,8} On the {110} faces the dangling bond change alternates between $+2$ and -2 between neighboring locations.

This mixture decreases the likelihood of In incorporation, and thus {110} faces should grow more slowly than (111)A planes. Sun⁴ uses a dangling bond theory to argue that, under high V/III ratio, {110} facets have higher growth rates than (100) facets in hydride vapor-phase epitaxy (HVPE). They attribute this to energetically favorable initiation of each {110} layer at the intersection of {110} and (100). Thus, the theoretical hierarchy of facet growth preference under high V/III ratio, from highest to lowest, is: (111)A, {110}, (100), and lastly (111)B.

Coalescence

In a previous section it was demonstrated that the extent to which coalescence completes between stripes separated by 5.625° on a star-like pattern is dependent on the V/III ratio (Fig. 1). In particular, those oriented less than 45° off of [0 $\bar{1}1$] were coalesced to a greater extent than those oriented with $45^\circ < \theta < 90^\circ$ off of [0 $\bar{1}1$] for a lower V/III ratio of 124, while these roles were reversed for V/III of 248. This may be partially attributed to the preferential step flow directions of growth on the (100) facet demonstrated by Asai et al.³ Step flow in the [0 $\bar{1}1$] direction on the (100) plane is essentially constant for a wide range of V/III, as is the cumulative vertical growth, while step flow in the [011] direction is slower than [0 $\bar{1}1$] for low V/III, and faster than [0 $\bar{1}1$] for higher V/III.

For higher V/III this correlates with greater lateral growth of stripes with $45^\circ < \theta < 90^\circ$ off [0 $\bar{1}1$], as explained in the previous section. Due to the flat top and sharp sidewalls of these dovetail stripes, coalescence of a small region is completed very soon after initiation and the space between neighboring arms fills completely. For $\theta < 45^\circ$, having fillet sidewalls, faster [0 $\bar{1}1$] step flow direction on the (100) plane correlates with faster {101} plane growth, whose vertical expansion inherently opposes complete coalescence by expanding the gap between the tops of the arms. The lengthening of {110} planes requires taller (111)A steps to conform to the angle of the growth stripe.

For lower V/III ratio, {110} layer initiation at the upper intersection with (100) slows, and thus so does the entire {110} growth rate. For $45^\circ < \theta < 90^\circ$, this eliminates the overhanging dovetail growth, resulting in less lateral extension and forcing coalescence to initiate at the bottom of the sidewall. A defect may then be formed as seen in Fig. 6c when the top and bottom of opposite arms simultaneously converge. For $\theta < 45^\circ$, lower {110} growth preference enhances the deposition on the (111)A step faces while decreasing the vertical growth rate. This results in lower fillet sidewall heights, and thus coalescence proceeding from the bottom up would complete sooner.

The coalescence of parallel stripes at $\theta = 30^\circ$ away from [0 $\bar{1}1$], those having fillet sidewalls, was likely

inhibited by the decrease in growth rate enhancement due to decreased precursor flux from the diminishing SiO₂ mask area between growth fronts, a mechanism noted by Kayser et al.¹ In contrast, the coalescence of stripes 60° away from [0 $\bar{1}1$], having a dovetail profile, was not as inhibited by this effect at high V/III ratio. This may be attributed to the decreasing area of preferred growth surface on the sidewall, requiring the incorporation of fewer and fewer atoms per lateral growth distance, the supply of which was enhanced by the preference for step flow on the (100) surface toward the [011] direction at high V/III ratio.³

It is important to note in Fig. 5 that the (111)A facets on each step near the coalescence region have shrunk and appear to curve toward (100) at the top, and either (011) or (0 $\bar{1}1$) at the bottom. This phenomenon is also seen further away from coalescent regions, but is far less pronounced. In these regions where (111)A intersects with (100) or any region neighboring coalescence, we cannot rule out capillarity or mass transport effects involving the (111)A plane. The introduction of coalescent surfaces between arms changes the chemical potential profile, influencing the balance between capillary mass transport and facet growth rate anisotropies,^{5,7,9} and thus may be causing the curvature of the steps. The defects, or lack thereof, seen under TEM in Fig. 6d, h for fillet sidewall growths ($|\theta| < 45^\circ$ off [0 $\bar{1}1$]) are indicative of the need to balance growth rate anisotropies of facets with capillary mass transport to achieve optimal material. It is likely that the defect of Fig. 6g resulted from two-zipper growth mode occurring after two opposing (111)A facets collided. The lack of defect in Fig. 6d indicates sufficient capillary mass transport to avoid such colliding facets. This demonstrates an alternation between facet growth dominance and capillary mass transport dominance by V/III ratio adjustment.

CONCLUSIONS

We have demonstrated coalescence of ELO-grown InP between sidewalls of two types, and their variation with V/III ratios ranging from 124 to 496. Parallel lines oriented $\theta = 60^\circ$ off [0 $\bar{1}1$] coalesced over $2.5 \mu\text{m}$ separation with as little as $0.9 \mu\text{m}$ OFT growth, while parallel lines with $\theta = 30^\circ$ did not coalesce for this separation and OFT. Using a star-like pattern we examined the coalescence of stripes just off of $\langle 010 \rangle$, each separated by 5.625° . We showed the introduction of a coalescent morphology which differs from the surrounding stripe sidewalls and contributes to the presence or lack of coalescence-related defects, shown in cross-sectional TEM. Two V/III ratios, 124 and 248, were seen to span a range in which complete coalescence could be alternated between those arms having $|\theta| < 45^\circ$ and those having $45^\circ < |\theta| < 90^\circ$. This was attributed to established growth rate anisotropies,

and the observation of possible capillary mass transport at the coalescent region. For both V/III ratios examined under TEM, defects appeared amongst those coalescent regions whose sidewall types were also unfavorable for complete vertical coalescence.

ACKNOWLEDGEMENT

The authors would like to thank DARPA MTO and Intel Corporation for financial support, as well as NNIN and MRL for use of their facilities. The MRL Central Facilities are supported by the MRSEC Program of the NSF under Award No. DMR05-20415; a member of the NSF-funded Materials Research Facilities Network (www.mrfn.org). Funding by DARPA MTO and Intel Corporation.

REFERENCES

1. O. Kayser, R. Westphalen, B. Opitz, and P. Balk, *J. Cryst. Growth* 112, 1 (1991).
2. Z. Yan, Y. Hamaoka, S. Naritsuka, and T. Nishinaga, *J. Cryst. Growth* 212, 1 (2000).
3. H. Asai, *J. Cryst. Growth* 80, 2 (1987).
4. Y.T. Sun, E.R. Messmer, D. Soderstrom, D. Jahan, and S. Lourduoss, *J. Cryst. Growth* 225, 1 (2001).
5. E. Pelucchi, V. Dimastrodonato, A. Rudra, K. Leifer, E. Kapon, L. Bethke, P.A. Zestanakis, and D.D. Vvedensky, *Phys. Rev. B* 83, 20 (2011).
6. G. Biasiol, F. LeLarge, K. Leifer, and E. Kapon, *J. Cryst. Growth* 195, 1 (1998).
7. M. Ozdemir and A. Zangwill, *J. Vac. Sci. Technol. A* 10, 684 (1992).
8. M. Gibbon, J.P. Stagg, C.G. Cureton, E.J. Thrush, C.J. Jones, R.E. Mallard, R.E. Pritchard, N. Collis, and A. Chew, *Semicond. Sci. Technol.* 8, 6 (1993).
9. F. Lelarge, G. Biasiol, A. Rudra, A. Condo, and E. Kapon, *Microelectron. J.* 30, 4 (1999).

Regrowth-free high-gain InGaAsP/InP active-passive platform via ion implantation

John S. Parker,^{1,*} Abirami Sivananthan,¹ Erik Norberg,² and Larry A. Coldren¹

¹Electrical and Computer Engineering Department, University of California at Santa Barbara, Santa Barbara, CA 93106, USA

²Aurion Inc., 130 Robin Hill Road #300, Goleta, CA 93117, USA
jparker@ece.ucsb.edu

Abstract: We demonstrate a regrowth-free material platform to create monolithic InGaAsP/InP photonic integrated circuits (PICs) with high-gain active and low-loss passive sections via a PL detuning of >135 nm. We show 2.5 μm wide by 400 μm long semiconductor optical amplifiers with >40 dB/mm gain at 1570 nm, and passive waveguide losses <2.3 dB/mm. The bandgap in the passive section is detuned using low-energy 190 keV channelized phosphorous implantation and subsequent rapid thermal annealing to achieve impurity-induced quantum well intermixing (QWI). The PL wavelengths in the active and passive sections are 1553 and 1417 nm, respectively. Lasing wavelengths for 500 μm Fabry-Perot lasers are 1567 and 1453 nm, respectively.

©2012 Optical Society of America

OCIS codes: (250.3140) Integrated optoelectronic circuits; (140.4480) Optical amplifiers; (140.5960) Semiconductor lasers.

References and links

1. Y. Cheng, J. Pan, S. Liang, W. Feng, Z. Liao, F. Zhou, B. Wang, L. Zhao, H. Zhu, and W. Wang, "Butt-coupled MOVPE growth for high-performance electro-absorption modulator integrated with a DFB laser," *J. Cryst. Growth* **308**(2), 297–301 (2007).
2. M. Aoki, M. Suzuki, H. Sano, T. Kawano, T. Ido, T. Taniwatari, K. Uomi, and A. Takai, "InGaAs/InGaAsP MQW electroabsorption modulator integrated with a DFB laser fabricated by band-gap energy control selective-area MOCVD," *J. Quantum Electron.* **29**(6), 2088–2096 (1993).
3. T. K. Ong, Y. C. Chan, Y. L. Lam, and B. S. Ooi, "Wavelength tuning in InGaAs/InGaAsP quantum well lasers using pulsed-photoabsorption-induced disordering," *Appl. Phys. Lett.* **78**(18), 2637–2639 (2001).
4. T. K. Ong, O. Gunawan, B. S. Ooi, Y. L. Lam, Y. C. Chan, Y. Zhou, A. S. Helmy, and J. H. Marsh, "High-spatial-resolution quantum-well intermixing process in GaInAs/GaInAsP laser structure using pulsed-photoabsorption-induced disordering," *J. Appl. Phys.* **87**(6), 2775–2779 (2000).
5. B. C. Qiu, A. C. Bryce, R. M. de la Rue, and J. H. Marsh, "Monolithic integration in InGaAs-InGaAsP multiquantum-well structure using laser processing," *IEEE Photon. Technol. Lett.* **10**(6), 769–771 (1998).
6. H. S. Djie, T. Mei, J. Arokiaraj, C. Sookdhis, S. F. Yu, L. K. Ang, and X. H. Tang, "Experimental and theoretical analysis of argon plasma-enhanced quantum-well intermixing," *J. Quantum Electron.* **40**(2), 166–174 (2004).
7. H. S. Djie, C. Sookdhis, T. Mei, and J. Arokiaraj, "Photonic integration using inductively coupled argon plasma enhanced quantum well intermixing," *Electron. Lett.* **38**(25), 1672–1673 (2002).
8. K.-H. Lee, J. O'Callaghan, B. Roycroft, C. L. Daunt, H. Yang, J. H. Song, F. H. Peters, and B. Corbett, "Quantum well intermixing in AlInGaAs MQW structures through impurity-free vacancy method," *Proc. SPIE* **7604**, 76040J, 76040J-7 (2010).
9. S. K. Si, D. H. Yeo, H. H. Yoon, and S. J. Kim, "Area selectivity of InGaAsP-InP multiquantum-well intermixing by impurity-free vacancy diffusion," *IEEE J. Sel. Top. Quantum Electron.* **4**(4), 619–623 (1998).
10. J. Zhao, Z. C. Feng, Y. C. Wang, J. C. Deng, and G. Xu, "Luminescent characteristics of InGaAsP/InP multiple quantum well structures by impurity-free vacancy disordering," *Surf. Coat. Tech.* **200**(10), 3245–3249 (2006).
11. S. Charbonneau, E. S. Koteles, P. J. Poole, J. J. He, G. C. Aers, J. Haysom, M. Buchanan, Y. Feng, A. Delage, F. Yang, M. Davies, R. D. Goldberg, P. G. Piva, and I. V. Mitchell, "Photonic integrated circuits fabricated using ion implantation," *IEEE J. Sel. Top. Quantum Electron.* **4**(4), 772–793 (1998).
12. P. J. Poole, S. Charbonneau, G. C. Aers, T. E. Jackman, M. Buchanan, M. Dion, R. D. Goldberg, and I. V. Mitchell, "Defect diffusion in ion implanted AlGaAs and InP: Consequences for quantum well intermixing," *J. Appl. Phys.* **78**(4), 2367–2371 (1995).
13. M. Pantouvaki, C. C. Renaud, P. Cannard, M. J. Robertson, R. Gwilliam, and A. J. Seeds, "Fast tuneable InGaAsP DBR laser using quantum-confined stark-effect-induced refractive index change," *IEEE J. Sel. Top. Quantum Electron.* **13**(5), 1112–1121 (2007).

14. M. Paquette, V. Aimez, J. Beauvais, J. Beerens, P. J. Poole, S. Charbonneau, and A. P. Roth, "Blueshifting of InGaAsP-InP laser diodes using a low-energy ion-implantation technique: comparison between strained and lattice-matched quantum-well structures," *IEEE J. Sel. Top. Quantum Electron.* **4**(4), 741–745 (1998).
15. V. Aimez, J. Beauvais, J. Beerens, D. Morris, H. S. Lim, and B. S. Ooi, "Low-energy ion-implantation-induced quantum-well intermixing," *IEEE J. Sel. Top. Quantum Electron.* **8**(4), 870–879 (2002).
16. M. Chicoine, A. Francois, C. Tavares, S. Chevobbe, F. Schiettekatte, V. Aimez, J. Beauvais, and J. Beerens, "Effects of damage accumulation on quantum well intermixing by low-energy ion implantation in photonic devices," *Proc. SPIE* **5260**, 423–431 (2003).
17. D. Barba, B. Salem, D. Morris, V. Aimez, J. Beauvais, M. Chicoine, and F. Schiettekatte, "Ion channeling effects on quantum well intermixing in phosphorus-implanted InGaAsP/InGaAs/InP," *J. Appl. Phys.* **98**(5), 054904–054908 (2005).
18. E. J. Skogen, J. W. Raring, J. S. Barton, S. P. DenBaars, and L. A. Coldren, "Postgrowth control of the quantum-well band edge for the monolithic integration of widely tunable lasers and electroabsorption modulators," *IEEE J. Sel. Top. Quantum Electron.* **9**(5), 1183–1190 (2003).
19. J. W. Raring and L. A. Coldren, "40-Gb/s Widely Tunable Transceivers," *IEEE J. Sel. Top. Quantum Electron.* **13**(1), 3–14 (2007).
20. W. Guo, Q. Lu, M. Nawrocka, A. Abdullaev, J. O'Callaghan, M. Lynch, V. Weldon, and J. F. Donegan, "Integrable Slotted Single-Mode Lasers," *IEEE Photon. Technol. Lett.* **24**(8), 634–636 (2012).
21. M. Silver and E. P. O'Reilly, "Optimization of long wavelength InGaAsP strained quantum-well lasers," *J. Quantum Electron.* **31**(7), 1193–1200 (1995).
22. T. Takeda, S. Tazawa, and A. Yoshii, "Precise ion-implantation analysis including channeling effects," *IEEE Trans. Electron Devices* **33**(9), 1278–1285 (1986).
23. J. Bausells, G. Badenes, and E. Lora-Tamayo, "Calculation of channeling effects in ion implantation," *Nucl. Instrum. Meth. B* **55**(1-4), 666–670 (1991).
24. Y.-F. Lao, H. Wu, and Z.-C. Huang, "Luminescent properties of annealed and directly wafer-bonded InAsP/InGaAsP multiple quantum wells," *Semicond. Sci. Technol.* **20**(6), 615–620 (2005).
25. C. Blaauw, B. Emmerstorfer, D. Kreller, L. Hobbs, and A. J. Springthorpe, "Effects of S, Si, or Fe dopants on the diffusion of Zn in InP during MOCVD," *J. Electron. Mater.* **21**(2), 173–179 (1992).
26. E. F. Schubert, C. J. Pinzone, and M. Geva, "Phenomenology of Zn diffusion and incorporation in InP grown by organometallic vapor-phase epitaxy (OMVPE)," *Appl. Phys. Lett.* **67**(5), 700–702 (1995).
27. N. Yoshimoto, Y. Shibata, S. Oku, S. Kondo, and Y. Noguchi, "Design and demonstration of polarization insensitive Mach-Zehnder switch using a lattice-matched InGaAs/InAlAs MQW and deep-etched high-mesa waveguide structure," *J. Lightwave Technol.* **17**(9), 1662–1668 (1999).

1. Introduction

The InGaAsP/InP heterostructure is one of the most widely used material systems for 1.55 μm telecommunication lasers and photonic integrated circuits (PICs). Numerous methods have been investigated to create an InGaAsP/InP monolithically integrated platform with both active (material with optical gain) and passive (material with low propagation loss) sections. These include butt-joint regrowth [1], selective area regrowth (SAG) [2], and quantum-well disordering [3–19], often referred to as quantum-well intermixing (QWI), in which the quantum well and barrier compositions are interdiffused.

Only QWI can shift the bandgap post-growth, and can thus alleviate complexities arising from regrowth and provide cost savings by avoiding additional growths. Regrowth contamination is unavoidable in most facilities, especially from silicon, which as an N-type InP dopant can be detrimental to correct placement of the p-i-n junction, and hence for efficient carrier injection into the QWs. QWI provides the lowest refractive index discontinuity between active-passive sections as the overall material composition in the waveguide remains the same, while the composition in the QWs and barriers is shifted. This is highly beneficial as reflections caused by refractive index discontinuities make on-chip lasers unstable through unwanted optical feedback.

Many techniques have demonstrated QWI, with varying trade-offs. These include photo-absorption induced disordering (PAID) [3–5], inductively coupled plasma quantum well intermixing (ICP-QWI) [6, 7], impurity-free vacancy disordering (IFVD) [8–10], and impurity-induced disordering (IID) [11–19]. In all methods, defects are diffused through the material with a rapid thermal anneal (RTA) above 600 $^{\circ}\text{C}$, and the extent of the disordering is measured by the change in the wavelength of the photoluminescence peak (PL).

IID relies on ion implantation of a benign atom, e.g. phosphorous or arsenic, to create vacancies near the QWs. To reduce the implant energy yet still achieve large >100 nm blue shifts, many researchers have implanted without the p-type cladding grown, and then regrow

to finish the device [18, 19]. For gratings definition on the waveguide, this regrowth is necessary, however avoiding this regrowth can reduce fabrication time, improve yield, and reduce risks inherent in regrowth near the p-i-n junction. Towards this aim, recent work has demonstrated that higher-order gratings can be successfully fabricated from the top of the laser structure, providing excellent side-mode-suppression (>50 dB), without the need for regrowth [20].

Early regrowth-free experiments demonstrated maximum shifts of 90 nm for 3 MeV P⁺ ions implanted into an InP laser structure at 7° tilt, whereas 200 keV implants produced <35 nm shifts [12]. The QWs were located 1.85 μm below the upper InP surface, and >1.5 MeV energy was necessary to create any defects near the QWs. However, there are several drawbacks to MeV implants including: a thick dielectric or metal implant mask is necessary to block the implant for nonintermixed regions (e.g. 3 MeV P⁺ simulated with the Stopping Range of Ions in Solids software (SRIM) shows the necessary SiO₂ mask thickness to be >2.75 μm), and the majority of ion implantation vendors only provide single-ionized energies <200 keV. Reduction of ion energy below 200 keV allows for ease of manufacturing, yet angled implants at keV energies can only provide limited bandgap shifts for full laser structures. For example, a 37 nm PL blue shift was demonstrated for the phase and grating sections of a DBR using 100 keV P⁺ at 7° tilt [13]. Some researcher have overcome the ion energy limitation by using doubly charged ions for which a 100 nm blue shift was demonstrated using 360 keV P⁺⁺ at 7° tilt [14, 15].

To avoid regrowth with <200 keV implant energy, one solution is to implant deeper using ion channeling. Compared to angled implantation, ion channeling has an increased implantation depth, results in a greater PL shift in the QWs, and has a lower density of nonradiative recombination centers after RTA [17]. Yet, ion channeling is avoided in silicon CMOS and bipolar technology. Angled (i.e. nonchannelized) implantation produces a near gaussian implant profile at the desired depth, whereas channeling creates a broad implant profile that varies with implant angle. For Si CMOS, precise junction placement is achieved via implantation and any angular spread over the sample results in an implant depth variation. However, for PIC applications requiring only two waveguide bandgaps, a high-gain active and a low-loss passive, the implant depth tolerances are much greater than in CMOS. For example, a passive section may simply need to be low-loss with a PL detuned by ~110 nm from the active section. An extreme variation in detuning of as much as 20% (± 11 nm) across a wafer due to implant and RTA results in a passive loss variation of only ~1 cm⁻¹ [18]; this is less than 0.5 dB loss for extremely large 1 mm long passive components. In this case, a material platform with 20% detuning variation in the intermixed regions can be acceptable for many PIC components including: semiconductor optical amplifiers, QW detectors, star couplers and arrayed waveguide gratings, multimode interference couplers, and passive waveguides.

In this paper, we demonstrate that ion channeling, i.e. 0° tilt, can provide this much needed reduction in implant energy for regrowth-free fabrication of lasers with active and passive sections. A blue shift of >135 nm is achieved using a 190 keV phosphorous implant with a subsequent 670 °C RTA for 120 s. This is the largest blue shift yet demonstrated for regrowth-free IID, and greater than the PL shift shown using 7° tilt 3 MeV P⁺ [12], meanwhile the implant energy used is 15X lower and the anneal temperature is 30 °C below that used in [12]. Previous studies demonstrate the benefits of ion-channeling on intermixing InGaAsP QWs; however, only a 42 nm blue shift is shown and the structure used requires a cladding and contact regrowth [17]. One of the main concerns for regrowth-free processing is diffusion of the p-type Zn dopant during the RTA. To examine the effects of Zn diffusion, we present Secondary Ion Mass spectroscopy (SIMS), passive loss, and active gain measurements from devices fabricated with this method. A thick layer structure is used in the experiment to examine the feasibility of the process at the upper limits of p-cladding designs, where the QWs are placed 2.45 μm from the surface, as shown in Fig. 1(a). The majority of laser structures will have thinner cladding layers and can use lower implant energy to achieve this detuning.

a) regrowth-free material platform

b) regrowth-required material platform

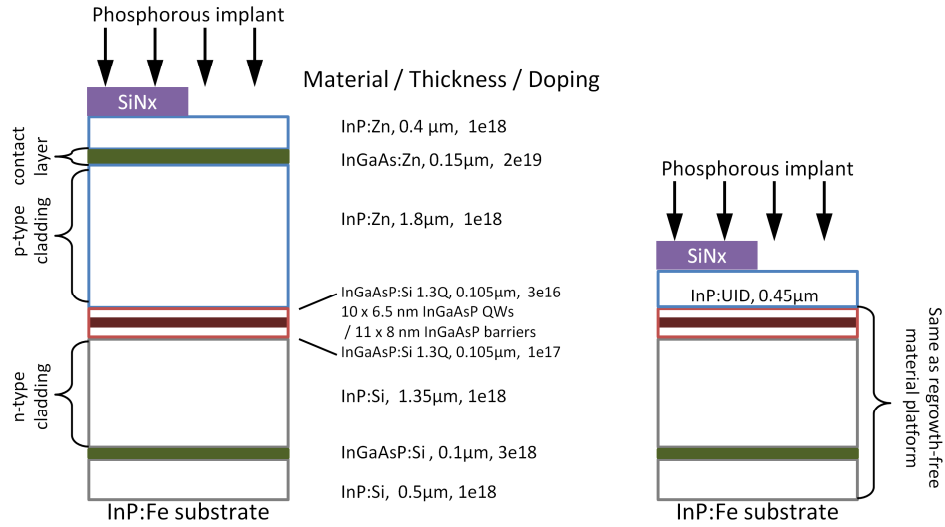


Fig. 1. Cross-sections of the two material platforms investigated for impurity-induced disordering. SiNx acts as a mask to prevent phosphorous implantation into the active regions. (a) The regrowth-free material platform that requires no additional growth steps to fabricate active-passive laser structures. Ions are implanted into the passive (nonmasked) regions and channel through the InP lattice to reach the QWs. (b) The material platform that requires additional regrowth steps for the p-type cladding and contact layers.

It is important to note that in much of the previously mentioned work [3–7, 11, 12, 14–17], 5.5–6.0 nm $\text{In}_{0.53}\text{Ga}_{0.47}\text{As}$ QWs with 10–20 nm $\text{In}_{0.74}\text{Ga}_{0.26}\text{As}_{0.55}\text{P}_{0.45}$ barriers ($\lambda_g = 1.26$) are used to create narrow wells with a high compositional different between QW and barrier, enhancing the effect of disorder on the bandgap. High composition variation and narrow QWs can provide a larger bandgap detuning, yet they do limit the flexibility and performance compared to the InGaAsP/InGaAsP (QW / barrier) material platform [21]. In this study, 6.5 nm (0.9% compressively strained) $\text{In}_{0.735}\text{Ga}_{0.265}\text{As}_{0.845}\text{P}_{0.155}$ QWs and 8 nm $\text{In}_{0.735}\text{Ga}_{0.265}\text{As}_{0.513}\text{P}_{0.487}$ barriers are used.

2. Methodology

The critical angle for high-energy ion implantation can be approximated by [22]:

$$\Phi_c = \sqrt{\frac{Z_1 Z_2 q^2}{2\pi\epsilon_0 E d}} \quad (1)$$

where Z_1 and Z_2 are the atomic numbers of the implant species and the target, respectively. E is the energy of the implant, ϵ_0 is the permittivity of free space, and d is the atomic separation or lattice constant. From this equation, the critical angle is proportional to the square root of the atomic number. For compounds such as InP, a geometric average of the two species is typically used for Z_2 . For InP, we use $Z \approx \sqrt{Z_{In} Z_P} = 27$, which leads to a 38% larger critical angle for implantation than for Si. The approximation in Eq. (1) requires an additional correction factor for lower energy implants [23], such as 190 keV:

$$\Phi_c' = \sqrt{\frac{\Phi_c \sqrt{1.5a}}{d}} \quad (2)$$

where a is the Thomas-Fermi screening radius for P^+ in InP, 0.11-0.12 Å. We find that the critical angle for ion channeling P^+ into InP at 190 keV is $\sim 3^\circ$. Hence, there is a $\pm 3^\circ$ margin for error on the implant while still achieving channeling for the majority of ions.

3. Results and discussion

The QW structures are grown on semi-insulating (100) InP iron-doped 2" wafers by metalorganic chemical vapor deposition (MOCVD) at 600-650 °C. A 2.5 cm x 2.5 cm sample is patterned with 600 nm of plasma enhanced chemical vapor deposition (PECVD) SiNx and sent for phosphorous implant at 190 keV, $2e15$ ions/cm² dose with a 200 °C stage temperature, and a $0^\circ \pm 1^\circ$ tilt angle. The SiNx is twice as thick as the implant depth predicted by SRIM simulation, to assure that the active regions are fully protected by the mask and that no vacancies are created in the active region. After implant, the SiNx is removed using BHF and surface defects are removed with a 1 min O₂ descum in a Gasonics remote ashing chamber at 250 °C. Afterward, the sample is dipped in 8% (by volume) phosphoric acid for 2 min and rinsed in deionized water, to remove native oxide formed by the ash, and solvent cleaned to remove acid residue. 40 nm of PECVD SiNx is deposited each side of the sample, and a subsequent 2 min 670 ± 3 °C RTA in N₂ is used to diffuse the vacancies. Afterward, the SiNx is removed using BHF, and standard photolithography and wet-etches are used to define 2.5 μm wide surface ridge lasers with top N-side Ni/AuGe/Ni/Au and P-side Pt/Ti/Pt/Au contacts. The InGaAs is removed between the P-side contacts for electrical isolation, the substrate is thinned to 120 μm for cleaving, and the sample is tested on a thermo-electric cooled copper stage.

The PL of the passive section near the wafer's center is measured at 1417 nm with an adjacent active PL at 1553 nm, as shown in Fig. 2. The full-width-at-half-maximum (FWHM) and each corresponding PL peak wavelength are listed in Table 1. For these measurements, the pump laser wavelength is 980 nm with 0.75-1.00 W/mm² power at the wafer surface. The higher powers are necessary for clear PL in the passive areas as the PL intensity decreases from the as-grown PL. The higher pump powers in this range account for a 5% increase in FWHM, when tested on the same sample, therefore slight deviations in the FWHM are due to the range of pump powers. There is variation in the passive PL of ± 10 nm over the processed sample area (a 14% variation in total blue shift), whereas the active variation is ± 2 nm, which matches the as-grown wafer. The larger variation in passive PL results from nonuniformity in the ion implantation and the RTA. The RTA has a ~ 5 °C temperature gradient across the sample with the thermo-couple placed at the center. The largest PL shift occurs at the hotter side of the wafer, indicating that temperature variation in the RTA is more significant than implant variation for samples of this size. The total PL shift from the as-grown sample is 139 nm, with a detuning between the active and passive regions of 136 nm.

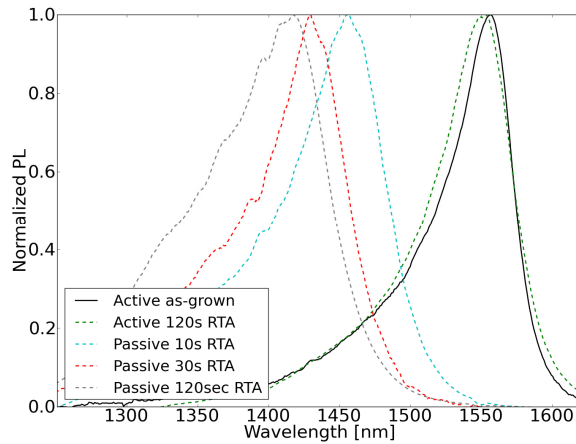


Fig. 2. (Regrowth-free sample) PL shift due to impurity-induced disordering during rapid thermal anneal (RTA) at 670 °C for InGaAsP/InGaAsP QWs and barriers with 1.8 μm InP:Zn cladding, 0.1 μm InGaAs:Zn contact, and 0.4 μm InP:Zn cap layers.

Table 1. PL during 670 °C RTA on regrowth-free sample

	As-grown	Active 120s	Passive 10s	Passive 30s	Passive 120s
PL [nm]	1556	1553	1455	1429	1417
FWHM [nm]	57	64	80	75	103

For comparison to a regrown QWI sample, intermixing is conducted using the well established method described in [18, 19] using a 450 nm InP:UID implant buffer above the QWs, as shown in Fig. 1 (b). The sample is angled at 7° tilt and P⁺ implanted at 100 keV, 5e14 ions/cm² dose with a 200 °C stage temperature. This structure has no Zn doped regions, and provides insight into the channelized defect location and the effect of the Zn doping during intermixing. The PL shift is shown in Fig. 3, with the FWHM and PL peak wavelengths listed in Table 2. The InP:UID clad PL shift is 134 nm with a detuning of 120 nm between the active and passive regions, post-RTA. This sample has the layer structure proposed in [18] and designed for post-QWI InP buffer removal and regrowth. The as-grown PL shift of 14 nm during QWI is common for this platform, due to diffusion of surface defects into the QWs, as used in IFVD for bandgap detuning. The regrowth-free layer structure, shown in Table 1, has only a 3 nm shift during QWI as diffusion of surface defects does not reach the QWs with this thicker structure.

Determining the phosphorous depth after implant is challenging as SIMs cannot differential the implanted P⁺ ions from the phosphorous in InP material structure. Rutherford backscattering spectrometry (RBS) can be used to investigate defect distributions within crystals, but high RBS sensitivity is required to analyze implant induced defects at 200 °C due to in situ diffusion, and low defect concentration often cannot be resolved [16]. Channelized implants are complicated to simulate, and accurate models in use for channeling in Si require large experimental data sets for interpolation. However, angled implants can be simulated with higher accuracy. For the 7° tilt 100 keV P⁺ implant, SRIM predicts a 110 nm mean depth, 53 nm straggle, and a maximum depth of 250 nm. Therefore, in Fig. 3 the implanted ions are >300 nm from the QWs. As shown in Table 1 and 2, the channelized ion implant 2.45 μm above the QWs shifts the PL faster than the angled implant 550 nm above the QWs. After a 30 s RTA, 1429 nm and 1493 nm PLs are observed for the channelized and angled ion implant, respectively. The rates of PL detuning suggests that channelized defects are at an equal or closer distance from the QWs after implant, that is <300 nm. However, doping (Zn vs. UID), defect concentration, defect distribution, and the type of defects formed do influence the diffusion of vacancies for QWI.

Comparing the InP:Zn cladding to the UID cladding, there is a dramatic increase in the FWHM for the InP:Zn intermixed passive sections. The InP:UID sample has no Zn in the structure, and therefore has no Zn diffusion into the QWs during the RTA process. There are two mechanisms for the Zn doping to cause PL broadening. In the first, Zn enhances the monolayer variations in the QW thicknesses. Minor spatial variation in QW thickness is frequently observed during RTA and quantum well disordering [24]. In the second, Zn incorporation in the QWs causes intraband carrier scattering, and leads to homogenous broadening.

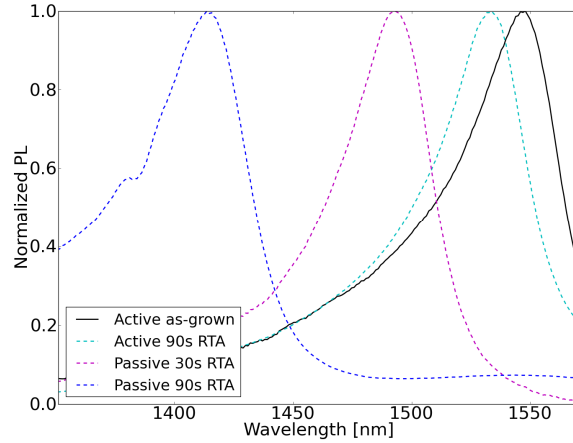


Fig. 3. (Sample requiring regrowth) PL shift due to impurity-induced disordering during rapid thermal anneal (RTA) at 670 °C for InGaAsP/InGaAsP QWs and barriers with 450 nm InP:UID buffer layer, see layer structure in Fig. 1(b).

Table 2. PL during 670 °C RTA on sample requiring regrowth

	Active-as-grown	Active 90s	Passive 30s	Passive 90s
Peak PL [nm]	1548	1534	1493	1414
FWHM [nm]	56	52	48	63

The Zn doping profiles of the regrowth-free as-grown and passive (after implant and RTA) are examined using Secondary Ion Mass spectroscopy and shown in Fig. 4. The Zn doping in the InGaAs contact layer has been reduced from $1.5 \times 10^{19} \text{ cm}^{-3}$ to $1 \times 10^{19} \text{ cm}^{-3}$, and Zn doping has diffused into the separate confinement heterostructure (SCH) and QWs. The Zn doping level in the QWs is $\sim 1.5 \times 10^{17} \text{ cm}^{-3}$, with Zn doping in the SCH from $1 \times 10^{17} \text{ cm}^{-3}$ to $2.5 \times 10^{17} \text{ cm}^{-3}$. The Zn doping decreases abruptly to $8 \times 10^{16} \text{ cm}^{-3}$ at the InP-SCH interface; the reason for this dip is unknown yet it has been observed on the SIMS characterization for two additional QWI samples. The Si doping inhibits the Zn diffusion for concentration of Zn below Si, which likely explains why the tail of the Zn diffusion does not extend into the lower cladding with $1 \times 10^{18} \text{ cm}^{-3}$ Si, whereas the SCH with 3×10^{16} - $1 \times 10^{17} \text{ cm}^{-3}$ Si has a minimal effect [25]. The Zn diffusion is much greater for the implanted samples due to defect assisted diffusion. Without added vacancies present, typical Zn at $1 \times 10^{18} \text{ cm}^{-3}$ concentration in InP diffuses $< 22 \text{ nm}$ at 700 °C for 120 s, using the diffusion constants measured in [26].

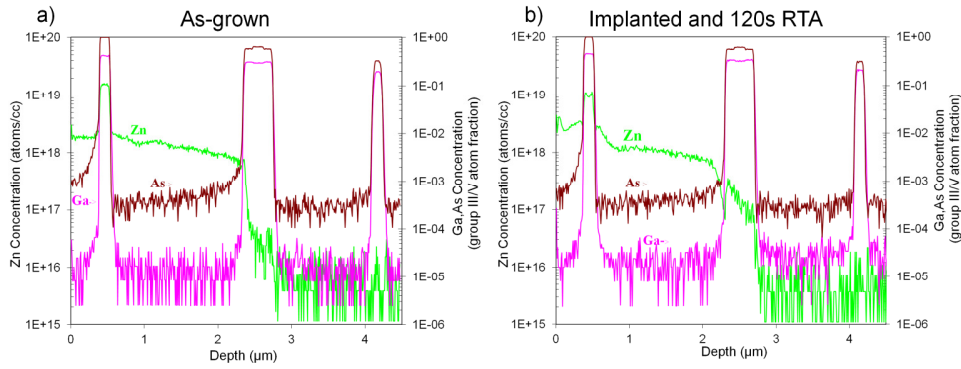


Fig. 4. Secondary Mass Ions spectroscopy of (a) the as-grown regrowth-free InGaAsP/InP material, and (b) passive areas of the regrowth-free material after 190 keV P⁺ implant and subsequent 120 s anneal at 670 °C. The material structure is shown in Fig. 1(a).

The losses of the passive waveguides are characterized by measuring the transmission $|S_{21}|^2$ of cleaved Fabry-Perot (FP) cavities, as shown in Fig. 5. The TE polarization of an ASE source is selected with a polarization beam splitter (PBS) and launched into the waveguide using a lensed fiber. The FP response is captured with a second lens fiber and measured on an optical spectrum analyzer (OSA) with 0.06 nm resolution. The $|S_{21}|^2$ response from one of these test structures is shown in Fig. 6. The average TE mode passive loss from a set of 5 adjacent FP structures with length 1775 μm is $5.5 \pm 1 \text{ cm}^{-1}$, i.e. 2.3 dB/mm; the uncertainty arises from fiber drift affecting the fit of $|S_{21}|^2$. These passive losses are confirmed by measuring the change in differential quantum efficiency for active-passive (500 μm -700 μm) lasers during cleave-back, with an extracted passive loss of $6 \pm 2 \text{ cm}^{-1}$. The free carrier absorption loss resulting from Zn and Si doping in InP has been reported on in literature [27]. With these numbers, a modal free carrier absorption loss 4 cm^{-1} is estimated from Rsoft BeamProp simulation using the layers and doping concentrations measured by SIMS, see Fig. 4(b).

By preventing Zn diffusion into the SCH and reducing the Zn doping to $5 \times 10^{17} \text{ cm}^{-3}$ in the lower half of the p-type cladding, the estimated free carrier absorption losses can be reduced to $\sim 2 \text{ cm}^{-1}$. Therefore, passive propagation losses would benefit greatly from an optimized doping set-back or super-lattice, to inhibit the p-type doping from entering the SCH layer after the intermixing process. Further investigation is required as super-lattices can be detrimental to intermixing by capturing defects and reducing their diffusion to the QWs. Due to the high doping level in the contact layer, some Zn diffusion out of the InGaAs during RTA is likely, which results in a higher contact resistance in the passive sections. A QWI process followed by regrowth has the potential for less Zn diffusion in the SCH, i.e. lower free-carrier absorption, and additional functionality provided by the multiple growths. A prior study investigated multiple regrowths on a QWI sample with a UID set-back layer, and measured passive loss of 1.8 cm^{-1} [19]. The trade-off with additional growth steps is the added cost and time involved in loading the samples in the reactor, and the risk of contamination (or reduced yield) at the regrowth interface from silicon (as n-type dopant) and other processing contaminants. As growth is increasingly centralized and wafers shipped away for each growth, minimizing the numbers of regrowths is desirable. Certain PIC designs, such as those involving untraveling carrier (UTC) detectors or varying QW placement in the cladding [19], will always require multiple growths, whereas others can be made regrowth-free.

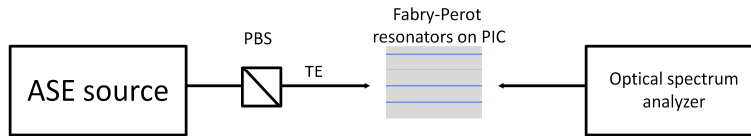


Fig. 5. Test set-up for measurement of TE polarized optical losses of passive Fabry-Perot resonators. Amplified spontaneous emission (ASE). Polarization beam splitter (PBS).

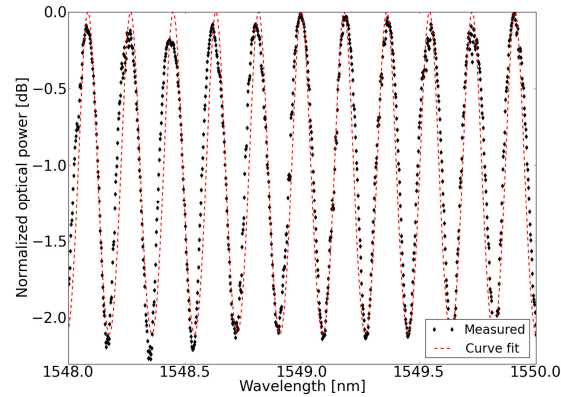


Fig. 6. (Regrowth-free sample) Measured $|S_{21}|^2$ response of 1775 μm long Fabry-Perot resonators with ASE input. Lower losses correspond to higher extinction values in the response. Curve fit is 5.5 cm^{-1} propagation loss.

The active waveguides are characterized by measuring the large signal gain of an optical mode through a semiconductor optical amplifier (SOA). Three 400 μm SOAs are cascaded serially. For the gain test, the first SOA is reverse biased at -1 V to detect the coupled optical power then it is forward biased up to 2 V to provide gain to this optical mode. The second SOA is reverse biased to detect the gain provided by the first SOA. The electrical isolation between the two sections is $>5\text{ k}\Omega$, and current leakage is measured and subtracted from total current in order to measure the optical gain. The measurement uncertainty is $\pm 2\text{ dB/mm}$ due to fiber coupling drift and current leakage. The optical gain peak is at 1570 nm for a set $25\text{ }^\circ\text{C}$ stage temperature. A 1 mW tunable laser is fiber coupled into the test structure, and gain of 40 dB/mm is measured at 6.3 kA/cm^2 , as shown in Fig. 7.

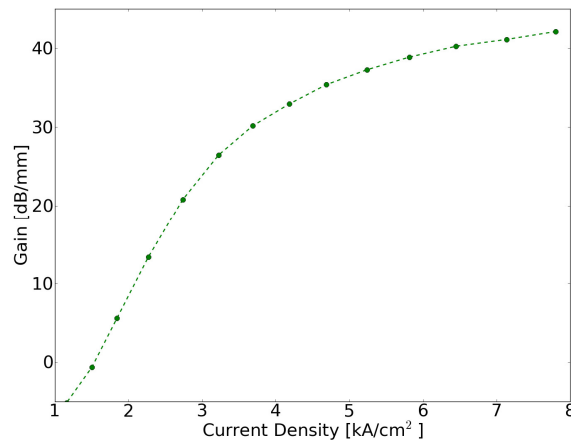


Fig. 7. (Regrowth-free sample) Measured large signal gain vs. current density for a 400 μm active semiconductor optical amplifier at $25\text{ }^\circ\text{C}$. Injection efficiency of 75% assumed.

The pulsed lasing of active FP cavities is measured using 1 μ s current pulses and a large area InGaAs photodetector. The threshold currents for 500 μ m x 2.5 μ m lasers at ~1567 nm and 1452 nm are shown in Table 3. The lasing spectra of the two lasers at 1.1 I_{th} is shown in Fig. 8. The pulsed threshold current for the intermixed laser is ~2X higher, likely caused by broadening of the gain spectrum and Zn diffusion into the QWs increasing the internal loss through free-carrier absorption.

Table 3. Fabry-Perot pulsed and cw threshold currents on regrowth-free sample

	Lasing at 1567nm*	Lasing at 1452nm*
I_{th} (mA), J_{th} (kA/cm ²) Pulsed	19, 1.14	42, 2.52
I_{th} (mA), J_{th} (kA/cm ²) CW	22, 1.32	53, 3.18

*lasing wavelength measured under CW operation

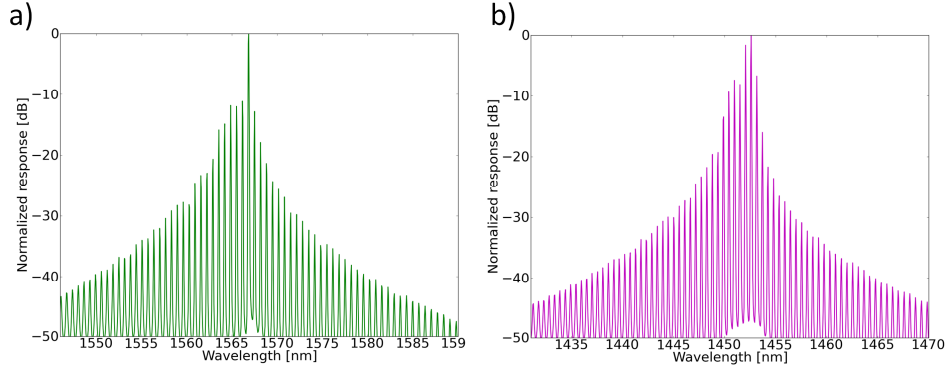


Fig. 8. Regrowth-free sample (a) optical spectra of Fabry-Perot laser made from active material with PL 1553 nm at 1.1 I_{th} , and (b) made from passive material with PL 1417 nm at 1.1 I_{th} .

3. Conclusion

We have shown ridge lasers fabricated with a regrowth-free active-passive InGaAsP/InP platform, using a channelized phosphorous ion implantation at 190 keV. The quantum wells are positioned 2.45 μ m below the implanted surface, indicating that this process is even suitable for material platforms with thick cladding layers. The active sections have high gain >40 dB/mm, whereas the passive sections have losses <2.3 dB/mm. This process is promising for the creation of large-area regrowth-free PICs, and for rapid optimization of new photonic components where fast processing turnaround time is required. By avoiding regrowth defects and interface contamination, high-yield and high-performance photonic components can be fabricated.

Acknowledgment

This work was supported by the Defense Advanced Research Projects Agency (DARPA) under the Photonic Integrated for Coherent Optics (PICO) program. A portion of this work was conducted in the UCSB nanofabrication facility, part of the NSF funded NNIN network.

Multi-Valued Stability Map of Injection-Locked Semiconductor Laser

Marko M. Krstić, Jasna V. Crnjanski, Milan L. Mašanović, Leif A. Johansson, *Member, IEEE*, Larry A. Coldren, *Fellow, IEEE*, and Dejan M. Gvozdić

Abstract—We present a novel and detailed analysis of the locking range and the stability map for side-mode injection-locked in-plane semiconductor multimode lasers. By including the usually neglected unlocked modes in our model, we predict a multi-valued locking range and stability map for this type of lasers. We also explain and relate, the previously noticed slave laser bistability phenomenon with the multi-valued character of the locking range and stability map, and experimentally validate our findings. Moreover, we find that the unstable operating region, commonly found in literature by stability analysis of the injection-locked mode alone, is actually much smaller.

Index Terms—Stability map, locking range, multimode semiconductor lasers, multi-valued functions, bistability

I. INTRODUCTION

INJECTION locking is a general phenomenon observed in many disciplines such as physics, engineering, biology, etc. For the first time, it was observed by C. Huygens, who noticed that the pendulums of two clocks on the wall move in unison if the clocks are hanged close to each other [1]. Later, other examples of this phenomenon were observed, such as human circadian rhythm locking to the length of day [1], or the locking of the Moon's to the Earth's rotation. Over time, injection locking has been used in a number of engineering applications comprising oscillators: electrical [2], microwave [3], or optical i.e. lasers [4]. Semiconductor lasers are a type of electrically driven oscillators in which the number of supported oscillations or modes can be controlled by various feedback mechanisms, providing single- or multi-mode operation. For a multimode laser, a sophisticated method to control oscillations in this (slave) laser relies on synchronization with another (master) laser, i.e. on the technique of injection locking.

The stable locking regime of an injection-locked laser is usually characterized by a stability map, which is represented by a set of ordered pairs comprising angular frequency of

detuning $\Delta\omega$ between the master and the slave laser free-running frequencies, and the injection power ratio r (i.e. the ratio of the photon density S_{inj} injected into the slave laser and the photon density S_m of the injection-locked mode of the slave laser) for which the slave laser is stably locked to the master laser. Such map has previously been thought to be a single-valued function on $\Delta\omega$ and r [5-8]. However, in this paper, we show that the slave laser behavior is far more complex and that the stability map is a multivalued function. We arrive at this important conclusion, which revises the current understanding of the locking and the stability map, by studying, theoretically and experimentally, the effects of a side-mode injection into a Fabry-Perot in-plane quantum well laser.

In the prior work on the analysis of the stability maps [6, 7], the unlocked slave laser modes have not been taken into account, although it has been suggested that the unlocked modes should be included into the consideration in the case of their collateral excitation or gain suppression effects during the injection locking [5, 8]. Even in the case of unstable injection locking, followed by a variety of peculiar and chaotic effects, researchers were still focused only on the injection-locked mode [4, 9]. Here, we show that unlocked modes significantly impact the locking range, as well as the boundaries of the stable locking in the regions where the stability map is a single-valued function. As a consequence of the multivalued character of the stability map, we show that the bistability of the slave laser occurs within the region which was previously considered stable [5, 6]. Although the bistability was previously noticed [7, 8], it was never fully explored and explained. In this work, we also experimentally confirm and correlate this bistability with our modeling results.

In Section II, we present the model of the multimode rate equations (MREs) used in our work. In Section III, we show the locking map and theoretically explain its multi-valued character. Section IV relates mapping of stationary points from $\Delta\omega$ - r space with phase plots and provides analysis of the stability plots. In Section V, we present the experiment and its results, which we compare with our theoretical findings. Finally, in Section VI, we provide the conclusion of this paper.

II. MODEL

The dynamics of the injection-locked slave laser is described by a system of multimode rate equations [10] with

Manuscript received October 31, 2012. Major part of this work was supported by the Serbian Ministry of Education and Science (project Photonics Components and Systems 171011).

M. M. Krstić, J. V. Crnjanski and D. M. Gvozdić are with School of Electrical Engineering, University of Belgrade, Serbia (corresponding author D. M. Gvozdić: +381 11 3370-060; fax: +381 11 321-8331; e-mail: gvozdic@etf.bg.ac.rs).

M. M. Mašanović, L. A. Johansson, and L. A. Coldren are with ECE Department, University of California, Santa Barbara, CA 93106, USA.

extra terms describing the locking phenomenon [4-10]. We consider a Fabry-Perot slave laser whose emission in the free-running regime is centered at the photon energy $\hbar\omega_0 = 0.8$ eV ($\lambda_0 = 1.55$ μm). The material gain spectrum used in the model, $g(n, \omega)$, where n stands for the carrier density and ω for the angular photon frequency, is asymmetric. It reaches its maximum ($g_{th} = 1222$ cm^{-1}) at the threshold carrier concentration $n = n_{th} = 2.85 \times 10^{18}$ cm^{-3} and at the angular frequency $\omega = \omega_0$, corresponding to the central (dominant) mode. Due to the gain asymmetry with respect to ω , the number of side modes which can be supported by the laser cavity is $l_1 = 170$ for $\omega < \omega_0$ and $l_2 = 120$ for $\omega > \omega_0$.

The multimode rate equations describe the photon density for each mode in the mode ensemble. Since the phase and the photon density equations of the injection-locked side-mode are coupled with the photon density and the phase of injected light, it is necessary to add separate photon density and the phase equation of the injection-locked mode to the MRE system. Thus, the system comprises $l_1 + l_2 + 3$ nonlinear differential equations. One of the equations deals with the carrier concentration (n) dynamics, $l_1 + l_2 + 1$ equations describe the time dependence of the photon density of both the injection-locked m -th mode (S_m) and other longitudinal modes (S_j), including the central mode ($j = 0$), while the last equation describes the time evolution of the phase difference θ_m between the free-running and the injection-locked state [10]:

$$\frac{dn}{dt} = \frac{I}{qV} - [A_{SRH} n + R_{sp}(n) + C_A n^3] - \sum_{j=-l_1}^{l_2} v_g g(n, \omega_j) S_j, \quad (1)$$

$$\frac{dS_j}{dt} = \Gamma v_g g(n, \omega_j) S_j - \frac{S_j}{\tau_p} + \Gamma \beta_{sp} R_{sp}(n), \quad j \neq m, \quad (2)$$

$$\begin{aligned} \frac{dS_m}{dt} = & \Gamma v_g g(n, \omega_m + \Delta\omega) S_m - \frac{S_m}{\tau_p} \\ & + \Gamma \beta_{sp} R_{sp}(n) + 2k_c \sqrt{S_m S_{inj}} \cos \theta_m, \end{aligned} \quad (3)$$

$$\frac{d\theta_m}{dt} = \frac{\alpha}{2} \left[\Gamma v_g g(n, \omega_m + \Delta\omega) - \frac{1}{\tau_p} \right] - \Delta\omega - k_c \sqrt{\frac{S_{inj}}{S_m}} \sin \theta_m. \quad (4)$$

In (1) $I = 1.2I_{th}$ is the current of the slave laser ($I_{th} = 2.45$ mA), $R_{sp}(n)$ is the total spontaneous optical emission rate, $A_{SRH} = 1.1 \times 10^8$ s^{-1} is the Shockley-Reed-Hall and $C_A = 5.82 \times 10^{-29}$ $\text{cm}^6 \text{s}^{-1}$ is the Auger recombination constant, while $V = 7.83 \times 10^{-12}$ cm^3 is the volume of the active area, corresponding to a laser width $w = 1.2$ μm and the laser cavity length $L = 250$ μm . In the system of MREs $\tau_p = (\Gamma v_g g_{th})^{-1} = 2.04$ ps stands for the photon lifetime, $\Gamma = 0.056$ is the confinement factor, $v_g = c/n_g$ is the group velocity with $n_g = 4.2$, $k_c = 1.13 \times 10^{11}$ s^{-1} is the external light coupling factor, $\alpha = 3$ is the linewidth enhancement factor, $\Delta\omega$ is the frequency detuning between the master and slave lasers, while $\beta_{sp} = 2.15 \times 10^{-4}$ is the spontaneous emission coupling factor, defined as the ratio of spontaneous emission coupling rate to the lasing mode and

total spontaneous emission rate. Finally, S_{inj} is the injected photon density, which is proportional to the injected optical power P_{inj} and is given by relation $S_{inj} = \tau_p \Gamma P_{inj} / (\eta_0 \hbar \omega V)$, where $\eta_0 = 0.33$ is the optical efficiency. All numerical values for these quantities in our model are taken from [10]. The angular frequencies of side longitudinal mode j and injection-locked mode m are denoted by ω_j and ω_m , respectively. We define ω_j as the longitudinal mode frequency, separated from the dominant mode frequency ω_0 by integer multiple (j) of intermodal spacing, i.e. $\omega_j = \omega_0 + j(\pi c/n_g L)$, which for the injection-locked mode order $j = m$ yields $\omega_m = \omega_0 + m(\pi c/n_g L)$. As already defined, the frequency of the dominant mode ω_0 is the lasing frequency in the free-running regime, corresponding to the modal gain maximum, at $n = n_{th}$. Since our model does not account for the variation of the group refractive index n_g with frequency or carrier density, the frequencies of all of the modes are fixed with respect to the carrier density variation in the laser and the dominant mode frequency ω_0 . An implicit frequency variation with carrier density change for the injection-locked mode is taken into account only by (7). However, the frequency detuning $\Delta\omega$ between the master and slave laser is defined with respect to the injection locked mode frequency ω_m , which is the closest to the frequency of injected signal from the master laser. In our computation, injected optical power P_{inj} and the photon density in any of the modes are at least two orders of magnitude smaller than those necessary to trigger the mechanism of nonlinear gain suppression which is therefore neglected in our computation.

The system of MREs (1)-(4), can be rewritten in a more compact form, in which instead of the injected photon density S_{inj} we introduce r , previously defined as the injection power/slave laser power ratio:

$$\frac{dn}{dt} = \frac{I}{qV} - Q(n) - \sum_{j=-l_1}^{l_2} v_g g(n, \omega_j + \delta_{jm} \Delta\omega) S_j \quad (5)$$

$$\frac{dS_j}{dt} = A_j(n) S_j + B(n) + \delta_{jm} 2k_c \sqrt{r} S_j \cos \theta_j \quad (6)$$

$$\frac{d\theta_m}{dt} = \frac{1}{2} \alpha A_m(n) - \Delta\omega - k_c \sqrt{r} \sin \theta_m \quad (7)$$

In addition, we define $B(n) = \Gamma \beta_{sp} R_{sp}(n)$ as the effective spontaneous emission, $A_j(n) = \Gamma v_g g(n, \omega_j + \delta_{jm} \Delta\omega) - \tau_p^{-1}$ as the effective rate of stimulated photon generation for mode j , and Q as the total recombination rate, representing the sum of $R_{sp}(n)$ and nonradiative recombination rates. The equation (6) applies on all modes, injection-locked and unlocked, which is regulated by Kronecker delta δ_{jm} .

III. LOCKING RANGE ANALYSIS

Starting from the stationary equations (6) for $j = m$ and (7), assuming that $B(n)$ is negligible in comparison to the other terms, the stationary value for θ_m is:

$$\theta_m = \text{Arcsin} \left[-\frac{\Delta\omega}{\sqrt{rk_c^2(1+\alpha^2)}} \right] - \arctan(\alpha). \quad (8)$$

The first term in (8) is the generalized inverse sine, given by $\varphi(-1)^z + z\pi$, where $\varphi = \arcsin\{-\Delta\omega/[k_c(1+\alpha^2)^{1/2}r^{1/2}]\}$ is its principal value, while z is an integer, which has a physical meaning only for $z \in \{0, 1\}$. By introducing $\psi = \arctan(\alpha)$, (8) yields:

$$r = \frac{\Delta\omega^2}{k_c^2(1+\alpha^2)\sin^2(\theta_m + \psi)}, \quad (9)$$

which for real θ_m , and extreme values for $\sin(\theta_m + \psi) = \pm 1$ defines the boundaries between the injection-locked and the four wave mixing (FWM) regions [6]. However, an additional condition comes from the fact that in the locked range $\cos(\theta_m) > 0$ [11]. The locking boundary can be derived from the condition $\cos(\theta_m) = 0$, which according to (8) can be converted to $\sin(\theta_m) = -1$ for $\Delta\omega > 0$ and to $\sin(\theta_m) = +1$ for $\Delta\omega < 0$. Insertion of $\sin(\theta_m) = \pm 1$ into the stationary form of (7) leads to $\alpha A_m(n)/2 = \Delta\omega - \text{sgn}(\Delta\omega)k_c r^{1/2}$. If the injection-locked mode is the central mode ($m = 0$) at $n = n_{th}$, then $A_m(n) = 0$. In this case, the locking boundary is given by $\Delta\omega = \pm k_c r^{1/2}$ or $r = (\Delta\omega/k_c)^2$ (dash-dot line in Fig. 1), where $\Delta\omega$ is given in units of Ω ($\Omega = 10^{10}$ rad/s). This can also be derived from (9), by taking into account that for $\theta_m = \pm\pi/2$, $\sin(\pm\pi/2 + \psi) = \pm(1 + \alpha^2)^{-1/2}$. If m is a side mode ($m \neq 0$), the stationary photon densities corresponding to $\cos(\theta_m) = 0$ are given by $S_j = -B(n)/A_j(n)$ for all modes. Thus, (5) can be written with respect to n as:

$$\frac{I}{qV} - Q(n) + \sum_{-l_1 \leq j \leq l_2} \nu_g g(n, \omega_j + \delta_{jm} \Delta\omega) \frac{B(n)}{A_j(n)} = 0 \quad (10)$$

The solution to (10) in this case is $n_c < n_{th}$. It represents the stationary state of the laser, for which $A_m(n_c) < 0$. This last condition remains valid whether besides the central mode, we take into account all other side modes, a few side modes (including injection-locked mode) or only injection-locked mode $m \neq 0$. Therefore, the new locking boundaries (Fig. 1) can be found from $\alpha A_m(n_c)/2 = \pm(|\Delta\omega| - k_c r^{1/2})$, leading to $r_{\pm} = \{[\pm|\Delta\omega| - \alpha A_m(n_c)/2]/k_c\}^2$ where (+) corresponds to positive and small negative $\Delta\omega$ (r_+ boundary), while (-) is used for sufficiently large negative $\Delta\omega$ (r_- boundary). However, for the r_+ boundary, this condition imposes an additional, more rigid constraint, which due to the negative value of $A_m(n_c)$, additionally rises the boundary of r , leading to a shrinkage of the locking range (c.f. Fig.1). In this case, $\theta_m \in (-\pi/2, -\psi]$, since the other branch of φ in (4) i.e. $\pi - \varphi$ leads to $\cos(\theta_m) < 0$ and cannot be included in consideration. However, for the r_- boundary, it is possible to include both branches of φ (i.e. φ and $\pi - \varphi$), since for both of them $\cos(\theta_m)$ can be positive. In this case, $\theta_m \in \{[-\psi, 0] \cup (0, \pi/2)\}$ comprises $\theta_m = \pi/2 - \psi$, corresponding to the FWM boundary due to fact that $\sin(\theta_m + \psi) = 1$. This means that for $\Delta\omega < 0$, FWM boundary divides θ_m range in two segments, $\theta_m \in [-\psi, \pi/2 - \psi]$ and $\theta_m \in$

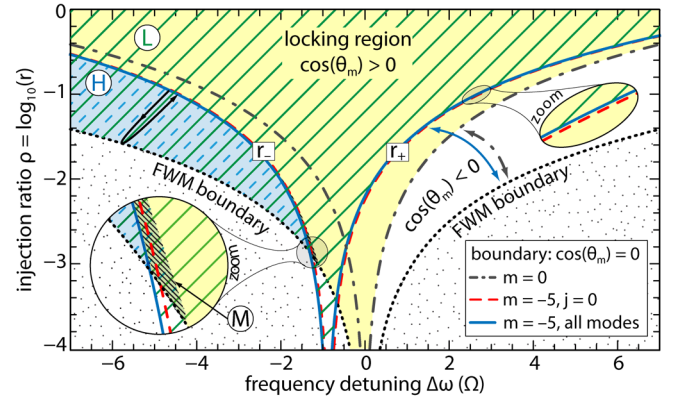


Fig. 1. Locking range for the injection into: the side mode $m = -5$ with all unlocked modes included (single and double hatched); the central mode $m = 0$, excluding unlocked modes (shaded). Boundary condition $\cos(\theta_m) = 0$ for injection into: $m = 0$ excluding unlocked modes (dash-dot line); $m = -5$ with the central mode ($j = 0$) included (dash line); $m = -5$ with all unlocked modes included (solid line). Distribution of the roots of Eq. (11): L (hatched), H (dense-hatched), M (double-hatched) for all modes included.

$[\pi/2 - \psi, \pi/2]$. Since FWM boundary corresponds to the smallest r for a given $\Delta\omega$, it can be concluded that the locking range in the $\Delta\omega$ - r space is folded down along the FWM boundary, leading to the overlap of the two locking regions in the r -range between the FWM boundary and r_- (dash and solid line hatched region in Fig. 1). For small negative detuning ($\Delta\omega \approx -1.13\Omega$), the left FWM boundary crosses the locking range [$\cos(\theta_m) \geq 0$]. The intersection of the FWM and the $\cos(\theta_m) = 0$ boundary is possible, since at this point and its vicinity, there is more than one stationary solution, which can satisfy either one or the other condition imposed by these two boundaries. Within the locking range, the FWM boundary sets θ_m to $\pi/2 - \psi$, but it becomes irrelevant, since on its both sides, injection locking is possible. The folding down along FWM boundary and overlap of the locking regions between FWM and corresponding r boundaries is also valid for $m = 0$. Since we are more interested in the injection-locking into side modes, we do not show this case in Fig. 1.

The locking range shown in Fig. 1, which accounts for the unlocked modes, exhibits a nonzero detuning offset for small injection ratios r . The essential reason for this is in our definition of ω_m , and the uneven increase of the frequencies for the dominant mode and side longitudinal modes when the carrier density increases. The dominant frequency ω_0 is the lasing frequency corresponding to $n = n_{th}$, while ω_m is the frequency for the injection-locked side-mode, defined in the free-running regime by $\omega_m = \omega_0 + m(\pi c/n_g L)$. This definition for ω_m overestimates its value for $n \leq n_{th}$, since the gain change due to the carrier density change is smaller for the side mode m than for the dominant mode 0. Assuming a constant linewidth enhancement factor for both modes, a smaller gain change of the side mode leads to its smaller frequency change. Thus, the frequency maximum of a side mode m , which occurs at $n = n_{th}$, is smaller than one predicted by $\omega_m = \omega_0 + m(\pi c/n_g L)$, which accounts for the dominant mode frequency increase. The correction term for the injection-locked mode frequency ω_m , i.e. the frequency shift of the side-mode frequency ω_m , is proportional to its gain defect. For example, the gain defect is zero ($A_m = 0$) for the dominant mode $m = 0$

(ω_0), and it is negative ($A_m < 0$) for any side mode $m \neq 0$ (ω_m). Therefore, side modes should exhibit a negative frequency shift (red shift) with respect to the frequencies given by $\omega_m = \omega_0 + m(\pi c/n_g L)$. This shift is taken into account by the first term in (7), and for small or negligible injection ratio r ($r \approx 0$), in the stationary state ($d\theta_m/dt = 0$), it can be compensated only by the negative detuning offset $\Delta\omega$, as noticed in Fig. 1.

IV. STABILITY MAP ANALYSIS

From the stationary equations (6) for $j = m$ and (7), one can eliminate $\cos(\theta_m)$ and $\sin(\theta_m)$ and derive an equation with respect to the carrier concentration n :

$$[\alpha A_m(n) - 2\Delta\omega]^2 + [A_m(n) + B(n)/S_m]^2 - 4k_c^2 r = 0. \quad (11)$$

S_m can be expressed as a function of n , using the stationary form of (5) as:

$$S_m = \frac{I}{qV} - Q(n) + \frac{\sum_{-1 \leq j \leq l_2, j \neq m} v_g g(n, \omega_j) B(n)}{v_g g(n, \omega_m + \Delta\omega) A_j(n)}. \quad (12)$$

Obviously, (11) is a nonlinear equation, solutions of which are stationary concentrations n_s dependent on $\Delta\omega$ and r . By solving (11) numerically, we find that for any $\Delta\omega$ - r pair in the locking range (hatched region in Fig. 1), there is at least one, basic solution, which we denote as n_L , while two additional solutions may appear for $\Delta\omega < -1.13\Omega$ (crossing of FWM and r_- boundary). In Fig. 1, L denotes the region where there is only one solution (n_L), H is the region where each $\Delta\omega$ - r point represents two solutions (2nd order root), the basic solution n_L and one more denoted as n_H , while M is the narrow 3rd order root region, which in addition to n_L and n_H comprises solution n_M . In further text, by n_s we denote any of the roots n_L , n_H , or n_M . The locking boundary r_- separates the H - and M -regions (c.f. Fig. 1), and with the FWM boundary outlines the H -region. For the more negative detuning ($\Delta\omega < -2\Omega$), the M -region is compressed into a line and it can be barely seen.

Each n_s determines one pair of injected photon density $S_{inj}^{(s)}$ and injection-locked mode photon density $S_m^{(s)}$. For a given $S_{inj}^{(s)}$, phase plots dn/dt - n may exhibit either one [Fig. 2(b)] or three [Fig. 3(b)-(d)] n -values, representing stationary points, which we denote in increasing order ($n_{sp}^{(1)} \leq n_{sp}^{(2)} \leq n_{sp}^{(3)} \leq n_{th}$) as in [10]. Here, we analyze how the n_s roots map into these stationary points.

The root n_L from the region L corresponds to a pair $S_{inj}^{(L)}$ and $S_m^{(L)}$ for which there is only one stationary point in dn/dt - n phase plot, denoted as $n_{sp}^{(1)}$. Similarly, a point from the M -region [c.f. Fig. 2(a)], maps into stationary points $n_{sp}^{(1)}$ for each of three corresponding roots n_s [Fig. 2(b)], all having different $n_{sp}^{(1)}$ values, since $S_{inj}^{(s)}$ is different for each of them.

The points from the H -region exhibit a more complex mapping. Each point from the H -region represents two roots, n_L and n_H , with two corresponding injection densities $S_{inj}^{(L)}$ and $S_{inj}^{(H)}$. However, the mapping into the stationary points of the phase plot dn/dt - n , shows that n_L always maps into $n_{sp}^{(1)}$, while n_H , may map either into $n_{sp}^{(2)}$ or $n_{sp}^{(3)}$ or even into $n_{sp}^{(1)}$.

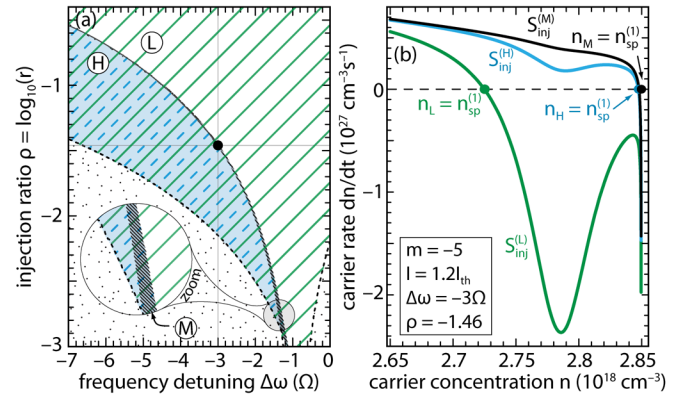


Fig. 2. (a) Distribution of roots of Eq. (11): L (hatched), H (shaded double-hatched), M (dark-dense-shaded) for all unlocked modes included. The dot corresponds to $\Delta\omega$ - r pair, for which all three roots occur simultaneously. (b) dn/dt - n plots for all three roots and their corresponding stationary point $n_{sp}^{(1)}$ for $S_{inj}^{(L)} > S_{inj}^{(H)} > S_{inj}^{(M)}$.

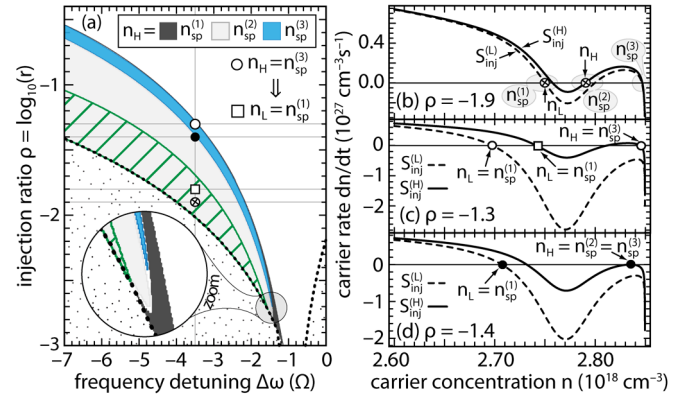


Fig. 3. (a) Partition of the H -region, with respect to the type of the stationary point n_H . The region $n_L = n_{sp}^{(1)}$ (hatched) coexisting with $n_H = n_{sp}^{(3)}$. (b) dn/dt - n plot and mapping of n_L and n_H into stationary points for $\Delta\omega = -3.5\Omega$ and $\rho = -1.9$. Same for (c) $\rho = -1.3$ and (d) $\rho = -1.4$. In (c) n_L for $\rho = -1.8$ (square dot) coexists with n_H for $\rho = -1.3$ (open dot), sharing the same injected power.

in the vicinity of the r_- boundary. Fig. 3(a) shows the full picture of the H -region partition with respect to the type of stationary point n_H . In order to provide a deeper analysis of the mapping we study character of the dn/dt - n phase plots [Fig. 3(b)-(d)] corresponding to the H -region for a fixed detuning $\Delta\omega = -3.5\Omega$ and three different values of r (or ρ , where $\rho = \log_{10} r$), shown by circular dots in Fig. 3(a). Fig. 3(b) shows that for $\rho = -1.9$, n_L and n_H map into points $n_{sp}^{(1)}$ and $n_{sp}^{(2)}$. For $\rho = -1.3$ [Fig. 3(c)] the situation is similar, with the exception that n_H maps into $n_{sp}^{(3)}$, while for the critical value $\rho = -1.4$, n_H maps into a point at which $n_{sp}^{(2)}$ and $n_{sp}^{(3)}$ merge in the single point [Fig. 3(d)]. As it was already mentioned, one can see from all these examples that n_L always maps into $n_{sp}^{(1)}$.

This analysis shows that a point from the H -region maps into two points (n_L and n_H) each representing one stationary point in dn/dt - n phase plot [e.g. Fig. 3(b)]. Each of these points corresponds to one injected photon density $S_{inj}^{(s)}$ and simultaneously exists with other stationary points, corresponding to the same injected photon densities, $S_{inj}^{(L)}$ or $S_{inj}^{(H)}$, but different r i.e. ρ . In these and similar cases [solid lines in Fig. 3(c) and (d)], coexistence of the stationary points may provide multistability.

Thus, we further study the range of r (ρ), for which

multistability may occur. We again analyze $dn/dt-n$ plots for $\Delta\omega = -3.5\Omega$ and find that for $S_{inj}^{(L)}$ and $\rho > -1.7$, there is only one stationary point i.e. $n_{sp}^{(1)}$ [dashed lines in Figs. 3(c) and (d)]. In other cases, multistability becomes feasible, since for a fixed $S_{inj}^{(s)}$ and consequently different r -values there are three coexisting stationary points, $n_L = n_{sp}^{(1)}$, $n_H = n_{sp}^{(2)}$ and $n_H = n_{sp}^{(3)}$. Fig. 3(a) shows that mapping of n_H from the H -region into $n_{sp}^{(2)}$ or $n_{sp}^{(3)}$, leads to the partition of the H -region into two disjunctive subsets. However, for a fixed $S_{inj}^{(s)}$ and detuning, each point from one subset has a corresponding point in the other [Figs. 3(b)-(d)]. In other words, for a fixed $S_{inj}^{(s)}$, $n_{sp}^{(2)}$ and $n_{sp}^{(3)}$ always accompany each other. Therefore, both subsets of the H -region represent ranges of multistability for stationary points $n_{sp}^{(2)}$ and $n_{sp}^{(3)}$. It thus remains for us to find the multistability range corresponding to $n_L = n_{sp}^{(1)}$.

In order to do that, we search for the r -range for which $n_L = n_{sp}^{(1)}$ [e.g. square dot in Fig. 3(c)] coexists with points $n_{sp}^{(3)}$ [open dot in Fig. 3(c)] and $n_{sp}^{(2)}$ for a fixed $S_{inj}^{(s)}$. For any given $\Delta\omega$, we find this range by calculating the photon density of the injection-locked mode $S_m^{(L)}$ for injected density $S_{inj}^{(L)} = S_{inj}^{(H)}$, where $S_{inj}^{(H)}$ corresponds to $n_H = n_{sp}^{(3)}$ and $n_{sp}^{(2)}$. This finally yields $r = S_{inj}^{(H)}/S_m^{(L)}$. Fig. 3(a) depicts the hatched part of the H -region, in which $n_L = n_{sp}^{(1)}$ coexists with $n_H = n_{sp}^{(3)}$ and $n_{sp}^{(2)}$ for the same $S_{inj}^{(s)}$. Moreover, in the vicinity of the r -boundary, there is a third narrow subset in which n_H maps into $n_{sp}^{(1)}$, which is irrelevant for multistability.

After identifying the areas in the $\Delta\omega-r$ space where $n_{sp}^{(1)}$, $n_{sp}^{(2)}$ and $n_{sp}^{(3)}$ coexist, we investigate their stability. This is done by calculating the eigenvalues of the linearized rate equations system (5)-(7), under the assumption of a small perturbation [10]. We simultaneously analyze how the number of modes included in the analysis affects the stability. For that, we investigate three cases, for which we take into account (i) the injected side-mode $m = -5$ only, (ii) the injected side-mode $m = -5$ and the central mode $j = 0$, and finally (iii) the injection-locked mode $m = -5$ and all unlocked modes. The stationary point is considered stable if all eigenvalues of the system lie in the left-half of the complex plain, which in the cases (i)-(iii) correspond to 3, 4 and $l_1 + l_2 + 3$ eigenvalues, respectively [6, 10]. For the case (i), $n_L = n_{sp}^{(1)}$ corresponding to the L - and the H -region in Fig. 4(a) [shaded area, shaded area beneath the single hatched region and cross-hatched area in Fig. 4(a)] reproduces the common stability plot as predicted by earlier works [5, 6]. The union of the unlocked (blank area) and unstable region (cross-hatched area) for $n_L = n_{sp}^{(1)}$ in Fig. 4(a) is usually classified as the region of nonlinear dynamics [6]. However, Fig. 4(a) also show the root loci $n_H = n_{sp}^{(2)}$, outlining the H -region [single hatched region in Fig. 4(a)], which appear even in the single side-mode analysis. As has been explained previously, the stationary points $n_H = n_{sp}^{(2)}$ represent an additional layer on the top of $n_L = n_{sp}^{(1)}$ root loci in the H -region. A closer inspection shows that $n_H = n_{sp}^{(2)}$ root behave as repelling fixed point, not attracting one, as should be in case of a stable stationary point. The same is confirmed by the small signal analysis. Since the region for $n_H = n_{sp}^{(2)}$ is fully unstable and represents the layer which overlaps $n_L = n_{sp}^{(1)}$ layer in the H -region, one can conclude n_H region

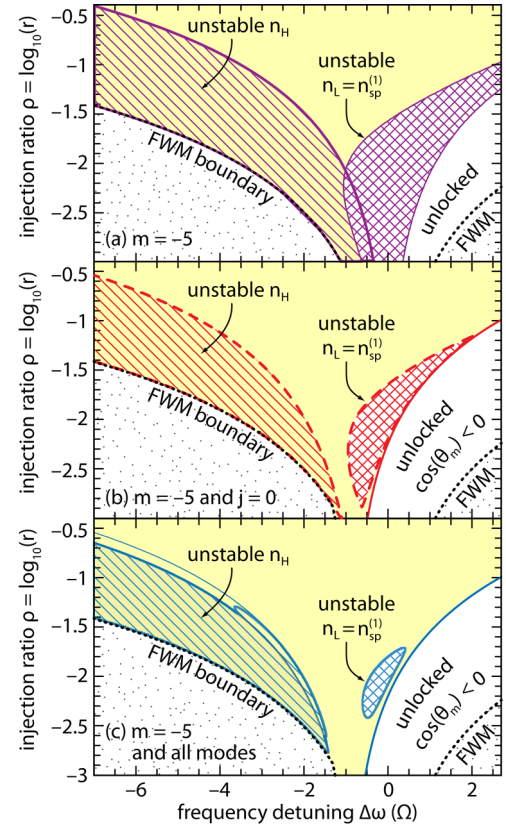


Fig. 4. (a) Stability plot for injection-locked mode $m = -5$ alone. Stable (shaded) and unstable (hatched) part of the locking range. The whole H -region is unstable. (b) Same, for two modes included i.e. injection-locked mode $m = -5$ and $j = 0$. The whole H -region is unstable. (c) Same, for all modes included. The whole subset $n_H = n_{sp}^{(2)}$ is unstable, while $n_H = n_{sp}^{(3)}$ is unstable only for small negative detuning. For all three cases, n_L is stable in the whole H -region (shaded under hatched).

actually does not manifests its presence nor intersect $n_L = n_{sp}^{(1)}$ layer. Therefore, this single hatched layer can be ignored in the case (i), while the stability map remains as the one predicted in [5, 6]. Although the H -region in the case (ii) besides $n_H = n_{sp}^{(2)}$, comprises $n_H = n_{sp}^{(3)}$, we find that similarly as in the case (i), n_H is fully unstable for the whole H -region [c.f. Fig. 4(a) and (b)]. However, it is found in the case (iii) that $n_H = n_{sp}^{(2)}$ is always unstable, while $n_H = n_{sp}^{(3)}$ is unstable only for a small negative detuning [Fig. 4(c)]. For all three cases, n_L corresponding to the H -region stays stable (shaded beneath the hatched region). It can be seen in Fig. 4(b) and (c) that unstable region for $n_L = n_{sp}^{(1)}$ from Fig. 4(a), diminishes as the number of modes increases.

In addition to the repelling fixed point instability related to the stationary point $n_H = n_{sp}^{(2)}$, which can be also confirmed by the asymptotic Lyapunov stability check based on the small signal analysis, we find that a different type of instability is related to the other stationary points. In fact, instabilities which occur for positive detuning for $n_L = n_{sp}^{(1)}$ and for negative detuning for $n_H = n_{sp}^{(3)}$ are related to the supercritical Hopf bifurcation, for which the laser operates on only one mode with the oscillatory output, while the suppressed modes follow the same oscillatory behavior. In the stable regions and for the fixed conditions, the slave laser remains in one of the stable points and in the injected mode over the entire range.

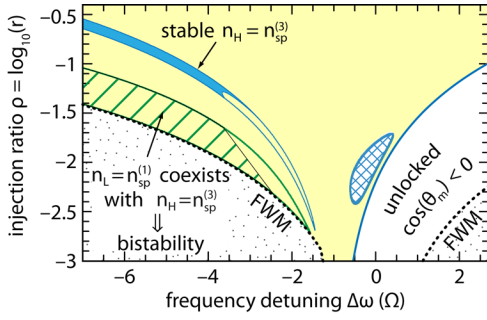


Fig. 5. Stable region for $n_H = n_{sp}^{(3)}$ (dark shaded) and the part of $n_L = n_{sp}^{(1)}$ (hatched) coexisting with it, for a fixed injection photon density S_{inj} , providing bistability. All modes are included.

However, the multivalued character of the locking range allows coexistence of the two stable, attractive fixed points for a sufficiently large negative detuning. As we show next, these stable points may provide shifting between modes as a result of injection power (or detuning) variation.

Since $n_H = n_{sp}^{(3)}$ is a stable state for a sufficiently large negative detuning (Fig. 5), we conclude that this part of locking and stability plot diagram comprises two stable solutions n_L and $n_H = n_{sp}^{(3)}$ and represents multi-valued function in $\Delta\omega$ - r space. In addition, for fixed injected densities $S_{inj}^{(s)}$, the state $n_H = n_{sp}^{(3)}$ coexists with $n_L = n_{sp}^{(1)}$ (hatched part in Fig. 5). Therefore, we conclude that the bistability becomes feasible as a result of the multivalued character of the locking and stability plot. This result confirms that inclusion of unlocked modes in the analysis of the stability map is crucial for multimode in-plane lasers. It is not clear, whether this effect is relevant for monomode in-plane lasers. However, it can be expected that in the case of the sufficient suppression of side modes, monomode lasers can be treated as before, i.e. regardless the influence of the unlocked modes. Recent investigation of nanostructure lasers based on quantum dashes [4, 12], suggest that our findings may help to understand some of bistability effects found there. Moreover, this complete model can be useful in investigation of the bandwidth and the modulation response of injection-locked multimode lasers [13, 14] and their dynamics in general. In addition, it can be used to study the injection locked lasers in all-optical flip-flop element applications, to investigate the switching time between the bistable states more precisely, previously analyzed only by a single-mode model [15]. Our model can also be of interest if the injection locking includes more than one master signal, as in the case of dual injection [16], etc.

V. EXPERIMENT

In order to validate our findings regarding bistability, we conduct an experiment [Fig. 6(a)], in which for a slave Fabry-Perot laser we measure the side-mode-suppression-ratio (SMSR) of the injection-locked mode $m = -5$ (with respect to the dominant mode) versus the injection power P_{inj} [Fig. 6(b)]. We set $\Delta\omega = -5\Omega$ and $I = 1.4I_{th}$. The decrease and then the increase of P_{inj} clearly show a hysteresis, which proves the existence of the bistability. By using the measured power corresponding to S_m for $m = -5$ and P_{inj} , we generate the r

versus SMSR plot [Fig. 6(c)]. Since the laser used in this experiment has a larger active region volume than the one used in our calculations we qualitatively compare Fig. 6(c) with Fig. 5 for a fixed negative detuning. The upper branch of the hysteresis loop [Fig. 6(b)] falls into a smaller r -range ($\rho < 0.5$) [Fig. 6(c)]. This corresponds to the hatched region in the Fig. 5 for which $n_L = n_{sp}^{(1)}$ coexists with $n_H = n_{sp}^{(3)}$, sharing the same P_{inj} . For $\rho > 0.5$, corresponding to the upper branch outside of the hysteresis loop, we find only one stable stationary point. This result is supported by Fig. 5, which shows a stable region between the hatched and shaded areas, corresponding to the part of the upper branch outside of the bistability range [c.f. inset in Fig.6(c)]. For a sufficiently large r ($\rho > 1.1$), there is an additional stable stationary point corresponding to lower branch of the hysteresis loop and $n_H = n_{sp}^{(3)}$ region in Fig. 5. The fact that for this range of r , we have two different values of SMSR, i.e. two different injected powers P_{inj} for one r , confirms the conclusion that the shaded region in Fig. 5 represents the multi-valued function. The lower branch outside of the loop, corresponds to $n_H = n_{sp}^{(1)}$ [Fig. 3(a)], which as we already mentioned, is not related to the bistability region. However, the experimental results suggest that the region corresponding to $n_H = n_{sp}^{(1)}$ comprises a somewhat wider r -range than one predicted by our theory, which proposes almost horizontal line for $n_H = n_{sp}^{(1)}$ part in Fig. 6(c). It is likely that small injected powers in this case may cause a measurement uncertainty and consequently the small noticed discrepancy between the theory and the experiment. It is also possible that the experimental results include not only the H -, but also the M -region, which supports multiplicity of $n_{sp}^{(1)}$ point. Therefore, the mapping shown in Fig. 6(c) completely resembles distribution of r -values in Fig. 5 and thin region $n_H = n_{sp}^{(1)}$ in Fig. 3(a).

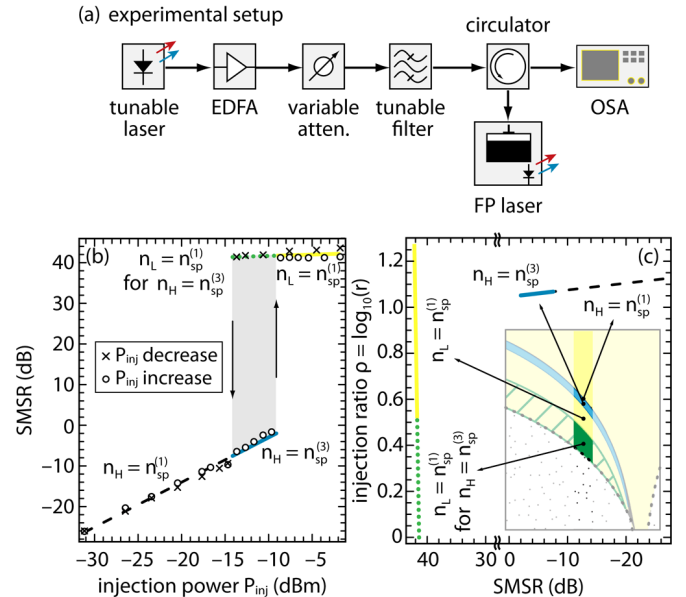


Fig. 6. (a) Experimental setup (b) Measured SMSR for the mode $m = -5$ versus injection power P_{inj} . (c) Branches of the hysteresis from (b), mapped into r -SMSR space: (left) upper branch within (dots) and outside (solid) bistability range; (right) lower branch within (solid) and outside (dash) bistability range. (Inset) Schematic distribution of the hysteresis branches in the locking and the stability plot.

VI. CONCLUSION

We show that the inclusion of the central and other unlocked modes in an injection-locked laser considerably modifies the commonly defined locking range map, ordinarily obtained by analysis of the injection-locked side-mode alone. For sufficient negative detuning, the locking range is degenerated and folded down between the FWM and the locking range boundary where $\cos(\theta_m) = 0$. Moreover, for a small r , this range is shifted towards the negative detuning. The folding down of the locking range leads to a multiplicity of the stationary points and consequently to the slave laser bistability. Qualitative agreement between our theory and our experiment has been found in this work. The stability analysis shows that when all of the modes are included in the numerical analysis, the potential bistability regions are generally stable, except for small negative detuning. However, if only the dominant and injection-locked modes are included in the stability analysis, the bistability cannot be observed since the folded part of the locking region becomes fully unstable.

Additionally, for a positive detuning, the inclusion of all unlocked modes predicts shrinkage of the unstable region on the stability map. All these results considerably modify the shape and features of the common single-valued locking and stability map [5].

REFERENCES

- [1] A. E. Siegman, *Lasers*. University Science Books, Mill Valley, CA, 1986.
- [2] R. Adler, "A Study of Locking Phenomena in Oscillators," *Proc. IRE*, vol. 34, pp. 351-357, 1946.
- [3] M. J. Fice, A. Chiuchiarelli, E. Ciaramella, A. J. Seeds, "Homodyne Coherent Optical Receiver Using an Optical Injection Phase-Lock Loop," *J. Lightw. Technol.*, Vol. 29, no. 8, pp. 1152-1164, 2011.
- [4] M. C. Pochet, N. A. Naderi, V. Kovanis, and L. F. Lester, "Modeling the Dynamic Response of an Optically-Injected Nanostructure Diode Laser," *IEEE J. Quantum Electron.*, vol. 47, pp. 827-833, 2011.
- [5] J. Ohtsubo, *Semiconductor Lasers: Stability, Instability, Chaos*. Springer-Verlag, Berlin, Germany, 2008.
- [6] A. Murakami, "Phase locking and chaos synchronization in injection-locked semiconductor lasers," *IEEE J. Quantum Electron.*, vol. 39, pp. 438-447, 2003.
- [7] T. B. Simpson, J. M. Liu, K. F. Huang, and K. Tai, "Nonlinear dynamics induced by external optical injection in semiconductor lasers," *Quantum Semiclass. Opt.*, vol. 9, no. 5, pp. 765-784, 1997.
- [8] T. B. Simpson, "Mapping the nonlinear dynamics of a distributed feedback semiconductor laser subject to external optical injection," *Opt. Commun.*, vol. 215, pp. 135-151, 2003.
- [9] S. Wiczorek, B. Krauskopf, and D. Lenstra, "Multipulse Excitability in a Semiconductor Laser with Optical Injection," *Phys. Rev. Lett.*, vol. 88, pp. 063901-063904, 2002.
- [10] M. M. Krstić, J. V. Crnjanski, and D. M. Gvozdić, "Injection Power and Detuning-Dependent Bistability in Fabry-Perot Laser Diodes," *IEEE J. Selected Topics Quantum Electron.*, vol. 18, no. 2, pp. 826-833, 2012.
- [11] C. H. Henry, N. A. Olsson, and N. K. Dutta, "Locking range and stability of injection locked 1.54 μm InGaAsP semiconductor lasers," *IEEE J. Quantum Electron.*, vol. 21, no. 8, pp. 1152-1156, 1985.
- [12] A. Hurtado, M. Nami, I. D. Henning, M. J. Adams, L. F. Lester, "Bistability patterns and nonlinear switching with very high contrast ratio in a 1550 nm quantum dash semiconductor laser", *Appl. Phys. Lett.*, vol. 101, pp. 161117-161121, 2012.
- [13] A. G. R. Zliti, M. M. Krstić, and D. M. Gvozdić, "Modulation Response and Bandwidth of Injection-Locked Fabry-Perot Laser Diodes," *Phys. Scripta*, vol. T149, pp. 014033-014037, 2012.

- [14] X. Jin and S. L. Chuang, "Bandwidth enhancement of Fabry-Perot quantum-well lasers by injection locking," *Solid State Electron.*, vol. 50, pp. 1141-1149, 2006.
- [15] D. M. Gvozdić, M. M. Krstić and J. V. Crnjanski, "Switching time in optically bistable injection-locking semiconductor lasers," *Opt. Lett.*, vol. 36, pp. 4200-4202, 2011.
- [16] C. W. Chow, C. S. Wong, H. K. Tsang, "All-optical NRZ to RZ format and wavelength converter by dual-wavelength injection locking," *Opt. Commun.*, vol. 209, pp. 329-334, 2002.

Marko M. Krstić received his dipl. inž. and M.S. degrees in electrical engineering from the University of Belgrade, Serbia, in 2007 and 2009, respectively. He is currently working toward his Ph.D. degree in electrical engineering at the University of Belgrade.

In 2009, he joined the academic staff at the School of Electrical Engineering, University of Belgrade, where he currently works as a Teaching and Research Assistant. His general interests are in the area of modeling and simulation of semiconductor lasers and fiber-optics.

Jasna V. Crnjanski received her dipl. inž. and M.S. degrees in electrical engineering from the University of Belgrade, Serbia, in 2002 and 2007, respectively. She is currently working toward her Ph.D. degree at the University of Belgrade.

In 2002, she joined the School of Electrical Engineering, University of Belgrade, where she works as a Teaching and Research Assistant. Her research interests are in the area of modeling of optical properties of semiconductor nanostructures. She has co-authored more than 10 publications. **Milan Mašanović** (S'98-M'04) received the dipl. inž. degree from the School of Electrical Engineering, University of Belgrade, Belgrade, Yugoslavia, and the M.S. and Ph.D. degrees from the University of California at Santa Barbara, Santa Barbara, in 1998, 2000, and 2004, respectively, all in electrical engineering.

He is currently an Associate Project Scientist at the University of California at Santa Barbara, and one of the principals at Freedom Photonics LLC, a photonic integration company he co-founded in Santa Barbara, CA. His current research interests are in the areas of semiconductor lasers and photonic integrated circuits. He has co-authored more than 85 research papers, given numerous invited talks and has co-authored one graduate-level text book.

Dr. Mašanović was the recipient numerous awards and fellowships, including the 2004 IEEE Lasers and Electro-Optics Society Graduate Student Fellowship Award. He serves on technical program committees for a number of conferences in the area of integrated photonics.

Leif A. Johansson (M'04) received the Ph.D. degree in engineering from University College London, London, U.K., in 2002.

He is currently a Research Scientist with the University of California, Santa Barbara, and a principal at Freedom Photonics LLC, a photonic integration company he co-founded in Santa Barbara, CA. His current research interests include design and characterization of integrated photonic devices for analog and digital applications and analog photonic systems and subsystems.

He has co-authored more than 100 papers, and presented at numerous conferences.

Larry A. Coldren (S'67-M'72-SM'77-F'82) received the Ph.D. degree in electrical engineering from Stanford University, Stanford, CA, in 1972.

He is the Fred Kavli Professor of optoelectronics and sensors with the University of California (UCSB), Santa Barbara. After 13 years in the research area with Bell Laboratories, Holmdel, NJ, he joined UCSB in 1984, where he is currently with the Department of Materials and the Department of Electrical and Computer Engineering. In 1990, he co-founded optical concepts, later acquired as Gore Photonics, to develop novel vertical-cavity surface-emitting laser (VCSEL) technology, and in 1998, he co-founded Agility Communications, Inc., Goleta, CA, later acquired by JDS Uniphase Corporation (JDSU), Milpitas, CA, to develop widely tunable integrated transmitters. At Bell Laboratories, he was initially on waveguided surface-acoustic-wave signal processing devices and coupled-resonator filters. He later developed tunable coupled-cavity lasers using novel reactive-ion etching technology that he created for the new InP-based materials. At UCSB, he continued work on multiple-section tunable lasers, in 1988, inventing the widely tunable multi-element mirror concept, which is currently used in some JDSU products. Near this time period, he also made seminal contributions to efficient VCSEL designs that continued to be implemented in practical devices till this day. More recently, his group has developed high-performance InP-based photonic integrated circuits as well as high-speed VCSELs, and they continue to advance the underlying materials growth and fabrication

technologies. He has authored or co-authored over 1000 journals and conference papers, seven book chapters, and one textbook and has been issued 64 patents. He has presented dozens of invited and plenary talks at major conferences.

Prof. Coldren is a fellow of the Optical Society of America and a member of the National Academy of Engineering. He was a recipient of the John Tyndall and Aron Kressel Awards, in 2004 and 2009, respectively.

Dejan M. Gvozdić was received his M.S. and Ph.D. degrees in electrical engineering from University of Belgrade, Serbia, in 1992 and 1995, respectively.

In 1989, he joined the School of Electrical Engineering, University of Belgrade, where he is now a Professor of Physical Electronics, Quantum Electronics and Optical Communications. His general research interests are modeling and simulation of optoelectronic devices as nanostructure lasers, optical amplifiers, photodetectors and since recently spintronic effects.

Dr. Gvozdić has authored and co-authored over 30 peer-reviewed journal papers. He is a recipient of several scientific awards, and has been working as a referee for a number of IEEE publications and conferences.